UNIVERSITY OF CALIFORNIA
RIVERSIDE

Biomimetic Self-Assembled Cages: Catalysis, Synthesis, and Guest Exchange

A Dissertation in partial satisfaction of
the requirements for the degree of

Doctor of Philosophy

in

Chemistry

by

Bryce da Camara

September 2023

Dissertation Committee:
Dr. Richard J. Hooley, Chairperson
Dr. Christopher Switzer
Dr. Kevin G. M. Kou

The Dissertation of Bryce da Camara is approved:

Committee Chairperson

University of California, Riverside

Acknowledgements

"Veni, vidi, vici"

Gaius Julius Caesar, 46 A.D.

Most emerging researchers and educators understand that achieving a PhD requires significant effort and dedication, unlike the effortless victory described by Julius Caesar in the Battle of Zela against the Kingdom of Pontus. As Caesar famously proclaimed, "I came, I saw, I conquered." However, the path of research is often challenging, akin to the uphill battle and misguided strategies of the Kingdom of Pontus. Despite occasional chaos in academia, it is a fulfilling and rewarding journey. Research can be a solitary pursuit, but like Caesar and his legionnaires, researchers rely on support networks and mentors to overcome obstacles and accomplish monumental tasks such as completing a PhD thesis.

It goes without saying that this thesis would not have been possible without Professor Hooley who adopted me into his lab halfway through my second year. I'm eternally grateful and honored to be one of your students. Your ability to string together seemingly unrelated experimental phenomena into a compelling and intriguing research narrative is amazing. Thank you for all your patience, advice, and shaping my analytical thinking skills, and research capabilities. See you later!

I would also like to acknowledge the sacrifice and hard work of my mother Diane and Father Antonio. Dad, I watched you work religiously throughout my childhood, adolescence, and early adult life with brute like discipline. Embodying a level of attention to detail that I continually aspire to assimilate into my own work. Mom, thank you for all the life lessons, the wisdom, love, and support. Without your patience I would surely not

have gotten this far. To my sister Melissa, I am inspired by your contagious joyfulness and adventurous spirit as you embark on your journey through your 20s, while I am transitioning into a new phase of life, called my 30s. Thank you for sending me all the memes and funny snapchats. I miss the COVID times when we were all locked down as a family.

To my undergraduate research advisor Professor Lydia McKinstry thank you for taking me into your research lab and pushing me to develop my own research project. In hindsight the idea was rather silly, but it proved to me that synthetic organic chemistry is a subject I'm deeply passionate about and this passion has sustained me through my graduate studies. Professor Paula Schofield, I miss your British wit and am thankful that you appointed me as your teaching assistant twice, which provided me invaluable experience that directly translated to being a teaching assistant in graduate school. Professor Ratna Roy…Ratnadi I miss you and Davidbi, greatly. Neither of you taught me any chemistry but you taught me about life and how to live. I miss our long conversations in the evening after dance rehearsals and the Odissi community. Thank you for helping shape me into the person I am today which has been critical to finding success in graduate school.

To my first mentor in graduate school Zachary Palchak, you were very patient and spent a lot of time teaching me how to be a successful graduate student and I'm so glad you have seen so much success at Lubrizol. To my OG cohort mates Courtney and Briana, thank you for all your support, fun and lively conversations, and memories. Connor Woods, thank you for lessening my workload and being imperturbably kind and rocking my world at Catan. José Luis Moreno Jr. I will miss being lane buddies and goofing around, thank

you for your kindness, patience, and receptivity. Noa Bar Ziv, it has been a pleasure working with you and I cannot wait to see tripodal two out into the world. Ryan, you're quite funny, I'm excited to see your successes over the course of your PhD career. To Komal and Lucas, I cannot think of a better duo for taking up the reigns of the lab's leadership, with due time.

In addition to this there are numerous other colleagues that it has been a pleasure and joy to share short and long conversations with. Whether it was early or late, in the NMR room or the courtyard, they have all aided in helping me move forward to accomplish my PhD. Notably I would like to extend a special thanks to members of the Kou, Martin, and Lavallo lab. For very intellectually stimulating conversations and much needed goofing off.

To my fellow biochemistry and biology friends, Rachael, Alex, and Marcello, I want to express my heartfelt gratitude for welcoming me into your circle. Whether it's the relaxed and fun dinners we've shared, where we've bonded over good food and laughter, or the laid-back TV nights when we've indulged in our favorite shows, these experiences have made graduate school survivable. I truly appreciate the camaraderie and support you've shown me throughout my PhD journey. Thank you for making this experience more enjoyable and memorable, come visit us in San Diego! In addition to this…Rachael thank you for being a part of the trail trio. I have loved backpacking and exploring Southern California's highly rugged and beautiful trail systems with you.

Miranda Brooke Rose, thank you for being an immovable force of light and support during the latter portion of my PhD career and for getting me into ultramarathoning. Our

highly intellectually stimulating conversations and trail excursions have provided a much-needed balance to my life that in turn has fortified my work ethic and health. Without you I cannot say for sure that I would have been as successful as I have been during this time. I'm so proud of what you have accomplished in your PhD career and am glad we've both made it to the other side. I'm so excited for what life has in store for us.

The text of this dissertation, in part or in full, is a reprint of the material as they appear in the following publications:

Chapter 2: da Camara, B.; Woods, C.Z.; Sharma, K.; Wu, H.; Farooqi, N.S.; Chen, C.; Julian, R. R.; Vander Griend, D.A.; Hooley, R. J. "Catalytic Inhibition of Base-Mediated Reactivity by a Self-Assembled Metal-Ligand Host" *Chem. Eur. J.* **2023**, e202302499.

Chapter 3: da Camara, B.; Dietz, P. C.; Chalek, K. R.; Mueller, L. J.; Hooley, R. J. Selective, Cofactor-Mediated Catalytic Oxidation of Alkanethiols in a Self-Assembled Cage Host. *Chem. Commun.* **2020**, *56*, 14263–14266.

Chapter 4: da Camara, B.; Bar Ziv, N.; Carta, V.; Mota Orozco, G. A.; Wu, H.-T.; Julian, R. R.; Hooley, R. J. Gated, Selective Anion Exchange in Functionalized Self-Assembled Cage Complexes. *Chem. Eur. J.* **2022**, e202203588.

The co-author Richard J. Hooley listed in these publications directed and supervised the research which forms the basis for this dissertation. All other co-authors listed in these publications contributed technical expertise.

Dedication

This thesis is dedicated to my late grandparents: Roza, Clara, Leonard, and Avo

ABSTRACT OF THE DISSERTATION

Biomimetic Self-Assembled Cages: Catalysis, Synthesis, and Guest Exchange

by

Bryce da Camara

Doctor of Philosophy, Graduate Program in Chemistry
University of California, Riverside, September 2023
Dr. Richard J. Hooley, Chairperson

Self-assembled cages are produced *via* self-assembly using metal ligand subcomponents that form a variety of polyhedral species that are capable of mimicking enzymatic catalysis and substrate recognition. A spacious Fe_4L_6 tetrahedral cage acts as a catalytic inhibitor in base-mediated reactions. By introducing 5 % of this Fe_4L_6 cage complex the conjugate addition between ethyl cyanoacetate and β-nitrostyrene, catalyzed by proton sponge, is significantly reduced from 83 % to less than 1 % under identical conditions. The catalytic inhibition mechanism is unique and unusual: the octacationic Fe_4L_6 cage enhances the acidity of exogenous water in acetonitrile by favorably binding the conjugate acid of the basic catalyst which ultimately moderates its basicity. This inhibition only occurs with the Fe_4L_6 host possessing a spacious cavity. Smaller tetrahedra or Fe_2L_3 helicates exhibit minimal inhibition.

The same spacious M_4L_6 tetrahedral cage catalyzes the oxidative dimerization of alkanethiols *via* favorable coencapsulation of two molecules of thiol and a redox active metallic cofactor. The host supplies its own metallic cofactor from partial disassembly of the cage structure, depositing Fe(II) into solution. Remarkably, the host enables size-selective oxidation and can discriminate between alkanethiols of identical reactivity based solely on their sizes *via* selective molecular recognition.

A series of Zn_4L_4 self-assembled cages with functional groups appended to their exterior were synthesized. The unfunctionalized analogues possess freely rotating aryl groups in the ligand, while the introduction of inert functional groups acts as a "doorstop," preventing rotation and slowing down guest exchange rates. The cages have identical charges and cavities, and the anion exchange process is regulated by multiple factors, including anion size, anion leaving group, and the electronic and steric nature of the pendant groups. The external groups regulate associative and dissociative exchange mechanisms which contribute to anion selectivity and exchange rates. Slight changes to the cage's molecular architecture can vary binding affinities for similar anions like PF_6^- and SbF_6^- by up to 400-fold in identically sized cavities. Lastly, this work concludes with a brief discussion on larger functionalized ligands that can form spacious M_4L_4 cages. These cages can internally orient functional groups, potentially serving as biomimetic catalysts.

Table of Contents

List of Tables

List of Figures

Chapter 1 - Self-Assembled Cages as Biomimetic Catalysts

1.1. From Alchemy to Biomimetic Self-Assembled Hosts

Before Boyle established the scientific method, the field of chemistry was known as alchemy. Despite the distinct methodologies and theories of alchemy compared to contemporary chemistry, the endeavors and discoveries of alchemists provided valuable insights and knowledge that laid the foundation for the emergence and evolution of the field of chemistry. This was achieved even in the absence of the technologies and resources that expedite the research goals of modern chemists. The emergence of chemistry began after Marie-Anne Pierrette Paulze Lavoisier and Antoine-Laurent de Lavoisier established quantification and data-driven decision-making, in part by incinerating diamonds, that led to the discovery of the Law of Conservation of Mass in the 18th century.[1] Many others contributed, such as Scheele, Dalton, Davy, Berzelius, Gay-Lussac, Avogadro, and Kekulé. Some of these contributions were mathematically-driven, such as the law of multiple proportions proven by Dalton.[2] Others were more peculiar, such as the isolation of phosphorus from distilling human urine by Hennig Brandt. The first intended organic synthesis was achieved by Wöhler in 1828,[3] who synthesized urea. Followed by the first carbon-carbon bond forming reaction discovered by Wöhler's student, Kolbe,[2] this preceded transition metal catalysis which was first observed in 1927.[4] The collective work from early chemists, as well as advancements in structural theory and analytical techniques, provided the momentum for organic chemistry to be recognized as a well-established discipline in the early 20th century.[3]

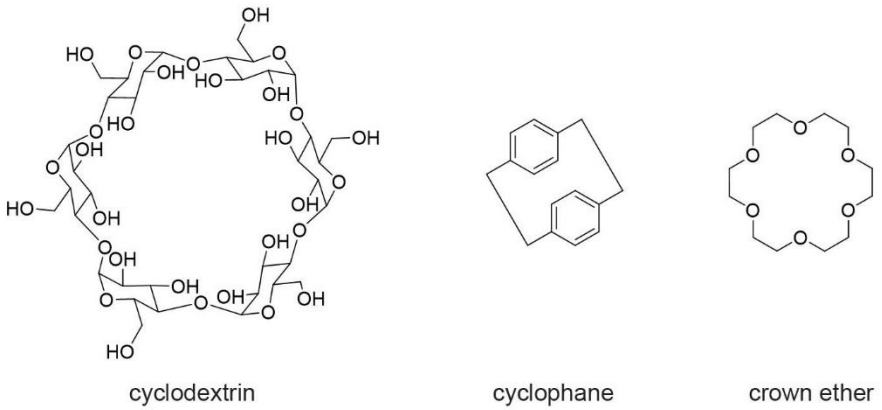

Figure 1.1. Early molecules in the field of supramolecular chemistry.

During the 19-20th century significant advancements were made in the synthesis of complex natural products[5–9] and methodology development,[10–14] as well as the beginning of a new niche in organic chemistry: supramolecular chemistry, which is the study of molecular recognition and high-order assemblies formed by noncovalent interactions.[15] Some of the first compounds synthesized in this field were cyclophanes,[16] crown ethers,[17] and cyclodextrins[18] (Figure 1.1). Cyclodextrins are cyclized units of glucopyranosides composed of 6, 8, or 10 sugars referred to as α, β, and γ, respectively. The hydroxyls are externally oriented, rendering the macrocycle hydrophilic, while its interior cavity is hydrophobic. As cyclodextrins are water-soluble, they bind organic molecules in aqueous solution v*ia* hydrophobic driving forces. The range of species that can be bound by cyclodextrins is quite large and includes (but is not limited to) aliphatic hydrocarbons, aldehydes, ketones, alcohols, aromatics, and polar organic substrates.[19] Cyclodextrins mimic protein substrate recognition, as their molecular recognition capabilities are easily altered by substituting the alcohols for other functional groups.[19] As well as the hydrophobic effect, which is only applicable in aqueous solution, other weak forces, such

CH-π[20] and π-π[21] interactions, can be exploited to drive molecular recognition of neutral polar and non-polar substrates in organic solvents.

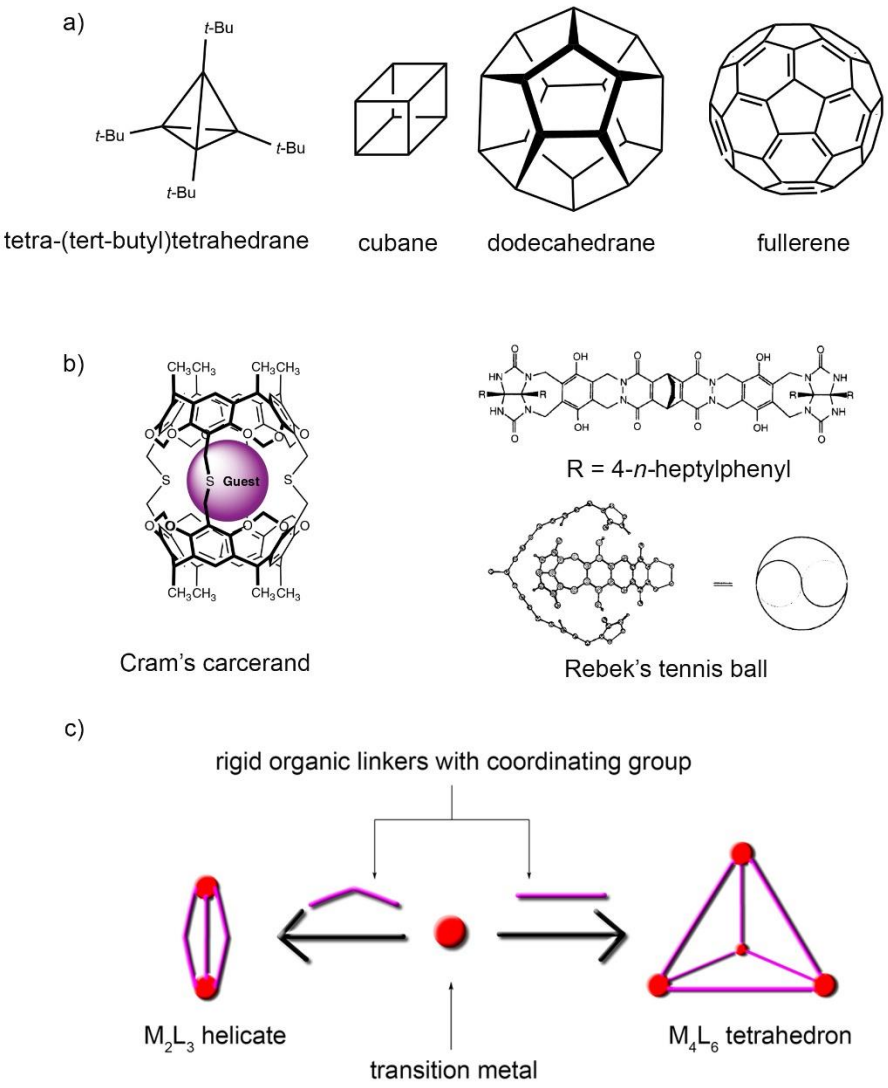

Figure 1.2. a) Structures of covalent polyhedra; b) Examples of larger cages, Cram's carcerand, and Rebek's tennis ball;[22,23] c) Self-assembly cartoon conveying two simple geometries that are accessible from slightly different ligands using the same transition metal.[24] Reprinted with permission from ref 22, copyright 1997, Nature and ref 23, copyright 2012, John Wiley & Sons.

Herein lies the key difference between small molecule catalysis and enzymatic catalysis: molecular recognition, which occurs in the enzyme's active site when guest molecules are bound. Enzyme substrate recognition allows substantial rate enhancements and various forms of chemical selectivity that researchers are interested in performing with small molecules.[25,26] The synthesis of enzymes is too challenging to be practical for applications in a synthetic lab,[27] but advancements in enzyme directed evolution[28] and bioengineering[29] have facilitated the use of enzymes in a variety of academic and industrial contexts. Alternatively, supramolecular hosts possess cavities, much like enzymes, and are capable of molecular recognition which can provide a means for accessing new biomimetic reactivity.

Tetra(*tert*-butyl)tetrahedrane,[30] cubane,[31] dodecahedrane,[32] and fullerenes[33,34] (Figure 1.2a) are covalently structured polyhedra each possessing internal cavities. Fullerene is the largest of these polyhedra, and has a volume of ~ 150 Å^3,[35] and can be synthesized with Li^+ or H_2 inside. The guests are not binding within fullerene, as they cannot leave. Even through extensive on developing techniques for the external functionalization of fullerenes,[36] fullerenes are not adept for biomimetic catalysis, as they are too small for endohedral functionalization or the molecular recognition of multiple reaction components for they do not possess portals to mediate guest capture and release. Larger supermolecules exist, such as Cram's carcerand[37,38] and Rebek's tennis ball,[22,39] which possess larger cavities than fullerene but their molecular recognition properties are not easily altered, as they lack synthetic handles that would promote derivatization (Figure 1.2b). Alternatively, self-assembled cages are produced from commercially available metal salts and easily

synthesizable ligands (Figure 1.2c). They possess well defined geometries and usually have internal cavities. The internal cavities of self-assembled cages are capable of molecular recognition and are easily altered synthetically, thus they are good candidates for mimicking enzymatic catalysis.

1.2. Self-Assembled Cages: Design, Synthesis, and Topology

Self-assembled cages are composed of transition metals and ligands and can possess many stoichiometries abbreviated as M_xL_y. The first reported M_4L_6 self-assembled cage was serendipitously produced by Saalfrank and co-workers.[40–42] While there were prior examples of metallic macrocycles in the literature, they were deemed too small to be classified as hosts for guest molecules.[43–45] Early work by Raymond,[46–48] Fujita,[49,50] Ogura,[51] Saalfrank,[40,52,53] Piguet,[54] and Lehn[55] developed the design principles required for constructing self-assembled cages. Self-assembled cages are produced from ligands possessing coordinating groups that can coordinate metals. Through complementary chemical interactions involving the approach angle of ligands, bite angle of coordinating groups, and preferred geometry of the metal, the ligands and metals form superstructures with well-defined shapes and cavities.[46] The most common ligand coordinating groups are pyridines, iminopyridines, and catechols, although phosphines, benzimidazolates, and nitriles have also been used.[56,57] The most common metals used as vertices are Pd^{2+}, Pt^{2+}, Fe^{2+} and Ga^{3+}, but Cd^{2+} and Pb^{2+} have also been successfully employed.[56–59] The final shape of the self-assembly process is topologically rich (Figure 1.3) and determined primarily by the stoichiometry, shape of ligand, metal geometry, temperature, and concentration.[56,57]

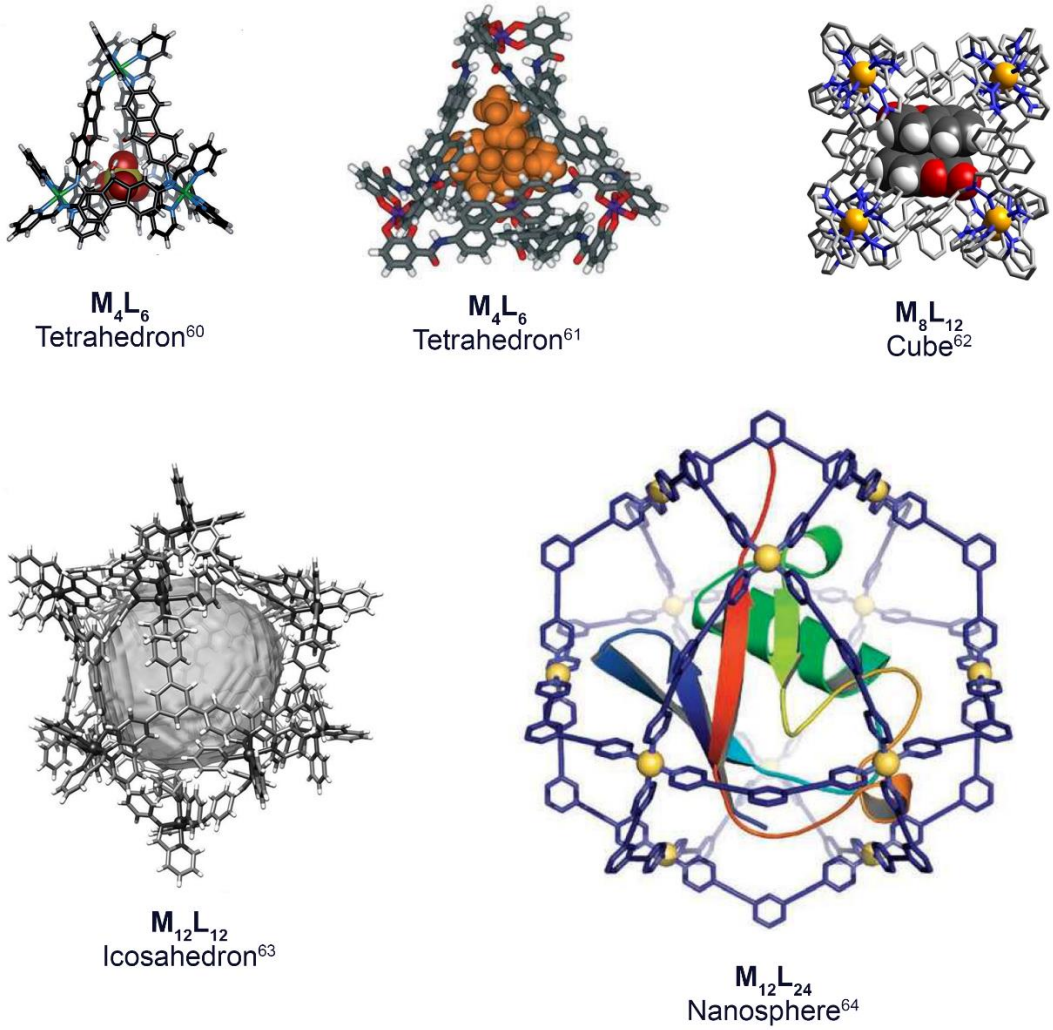

Figure 1.3. Self-assembled cage complexes of differing stoichiometry and geometric shapes.[60–64] Reprinted with permission from ref 60-63, copyright 2014, 2008, 2020, 2013, Wiley, and ref 64, copyright 2012, Macmillan Publishers Limited.

By making minor modifications in reaction conditions, the final geometry of the cage can potentially be altered (Figure 1.4a). Subcomponent self-assembly of helicate **1.1** and icosahedron **1.2** have identical sub-components, but **1.1** is favored when using dilute conditions and **1.2** is favored when using concentrated conditions.[65] Both **1.1** and **1.2** can be converted to tetrahedron **1.3** upon recognition of a suitably sized anion. In addition to

this, subtle changes in the structure of ligands can have significant impacts on the geometry of the self-assembled cage.

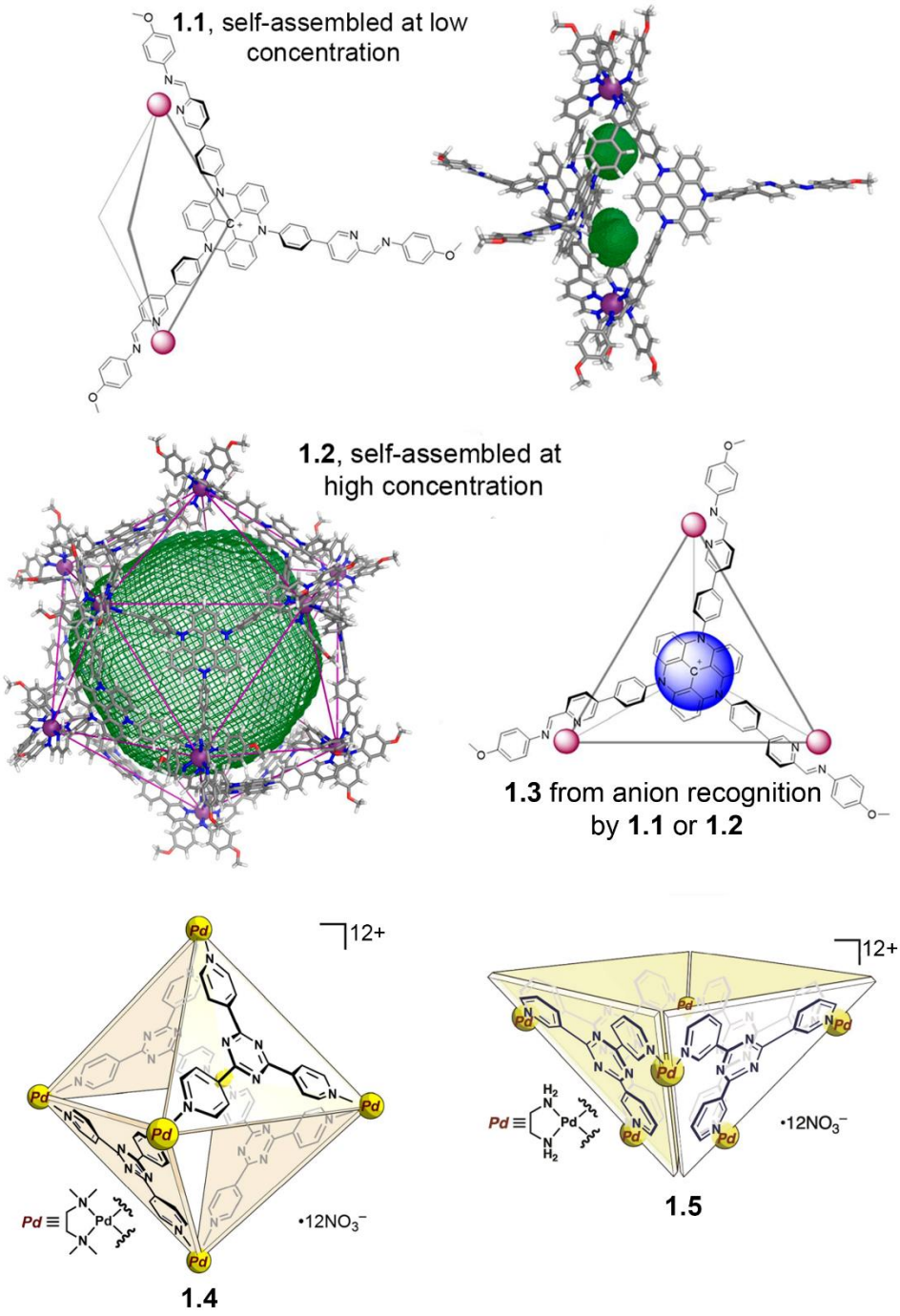

Figure 1.4. a) Architectural switching between self-assembled cages from using different reaction conditions and anion recognition; b) minor modification of ligand dictates geometry of self-assembly outcome.[65,66] Reprinted with permission from ref 65, copyright 2022, American Chemical Society, and ref 66, copyright 2022, Wiley.

In the case of octahedron **1.4** and "half-bowl" **1.5**, (Figure 1.4b) the coordinating pyridyl nitrogen's position is changed, and under identical self-assembly conditions the resultant geometries are distinct.[67] In addition to the requirement for ligands to have coordinating groups, it is crucial that they exhibit a relatively flat and rigid structure. Ligands that possess excessive flexibility, generally, tend to have a larger number of potential conformations, making it difficult for them to maintain a stable and rigid configuration during the assembly process.[68] In addition to changes in ligands and concentration of the sub-components to mediate control over the structural outcomes of self-assembled cages, ligand conformation and temperature can also impact the stereochemical outcomes of the subcomponent self-assembly process.[69]

Octahedral metal complexes composed of hetero bis-bidentate ligands form different stereochemical isomers based on the relative orientation of coordinating groups around the metal center and are described as meridional (*mer)* and facial (*fac*) (Figure 1.5).[69–72] The relative orientations of the *fac* substituents have handedness described as *Λ* (left) and Δ (right), which produces three diastereomers for M_4L_6 self-assembled cages.[69] These diastereomers are *T* (*ΛΛΛΛ*/ΔΔΔΔ) which is homochiral and results in a single set of proton signals, C_3 (*ΛΛΛ*Δ/ΔΔΔ*Λ*) which is heterochiral and results in 4 sets of proton signals, and S_4 (*ΛΛ*ΔΔ/ΔΔ*ΛΛ*) which is achiral and results in 3 sets of proton signals. Small modifications of the ligand scaffold can produce conformational changes that alter the stereochemical information that is conferred onto these self-assembled cages.

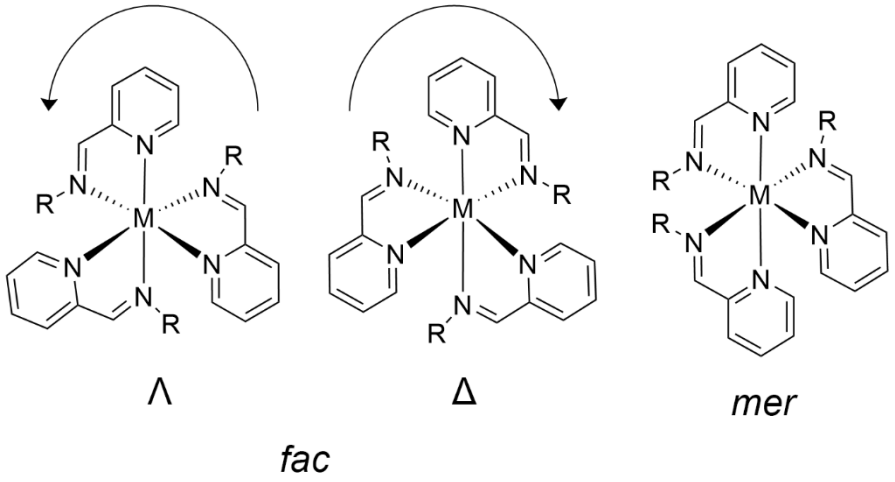

Figure 1.5. Metal centered stereoisomers of bis-bidentate iminopyridine complexes.

When using bis-bidentate ligands, heterochiral metal centers are created in self-assembled cages **1.7**-**1.9** by the ligand linkages adopting a *syn* or *anti* configuration (Figure 1.6a). For cage **1.7**, the ligand linkage is *anti*, the chelators are on opposite sides of the metal, and thus both metal centers are homochiral (Figure 1.6a). Compared to cage **1.8** the coordinating groups are *syn*, meaning they are on the same face of both metal vertices, thus the metal centers are heterochiral. The methylated aryl rings attached to the phenylene core of the ligand that forms cage **1.8** are coplanar, and perpendicular to the central ring in their lowest energy conformation. Because of this, the ligand prefers the *syn* arrangement, thus the cage almost exclusively forms diastereomers S_4 and C_3 as they have the greatest number of *syn* linkages between metal centers (Figure 1.6b).

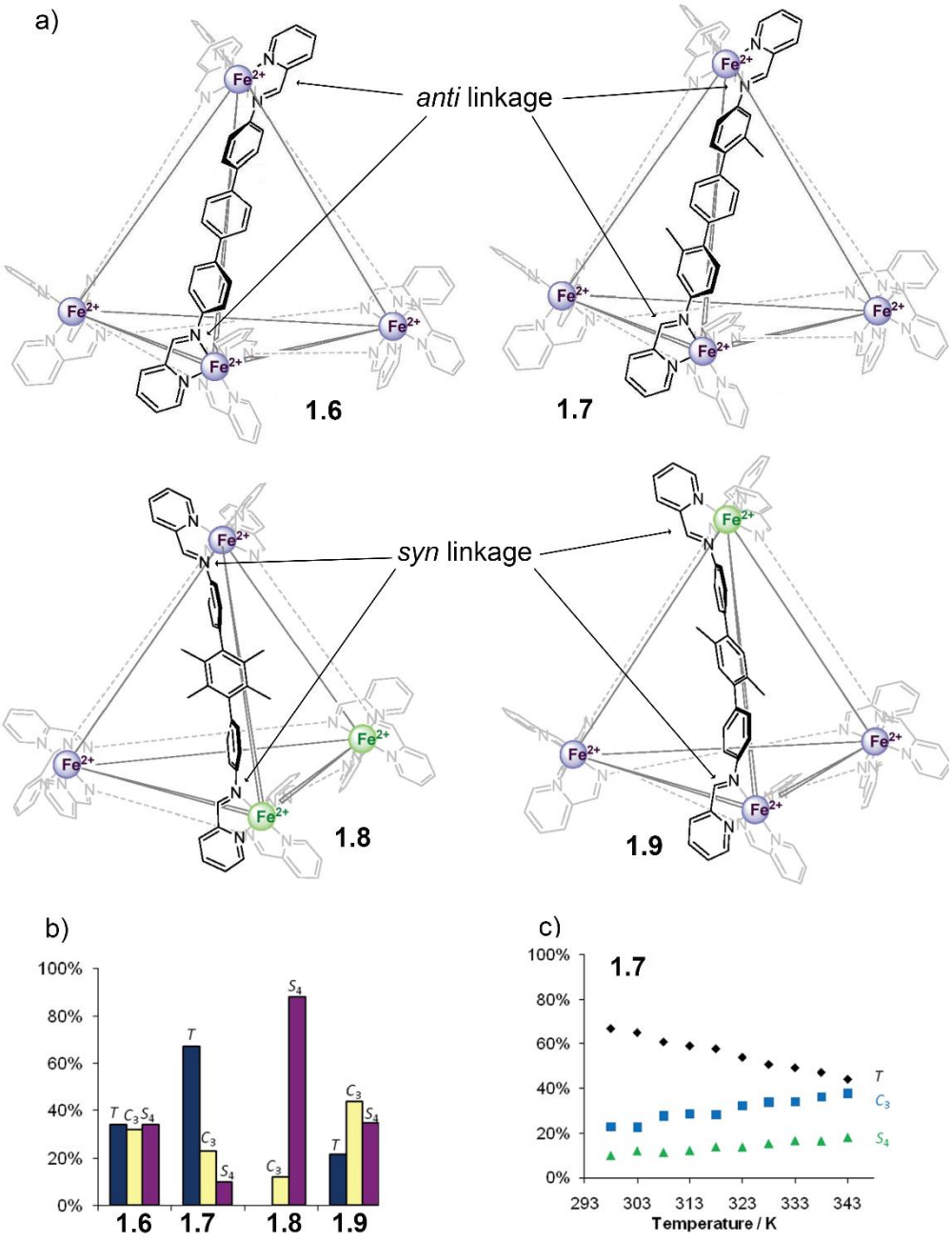

Figure 1.6. a) Tetrahedral self-assembled cages with various substituted phenylene rings; b) diastereomer distributions of cages **1.6-1.7**; c) diastereomer distribution because of temperature change for cage **1.7**.[69] Reprinted with permission from ref 69, copyright 2011, American Chemical Society.

When the aryl rings attached to the phenylene core are not forced to be coplanar and can freely rotate, the resulting diastereomeric distribution is more statistical, e.g., cages **1.6**

and **1.9**. For cage **1.7** the methylated peripheral rings prefer being trans which is translated to the coordination sites that adopt the *anti*-configuration and result in preferentially forming the *T* symmetric cage. Additionally, racemization at the Fe^{2+} centers is possible, thus the diastereomeric distribution can be affected by temperature (Figure 1.6c). In addition to their stereochemical intricacy, self-assembled cages architectural complexity and variability translates to a broad range of applications within the chemical space of molecular recognition.

1.3. Self-Assembled Cages and Their Molecular Recognition Properties

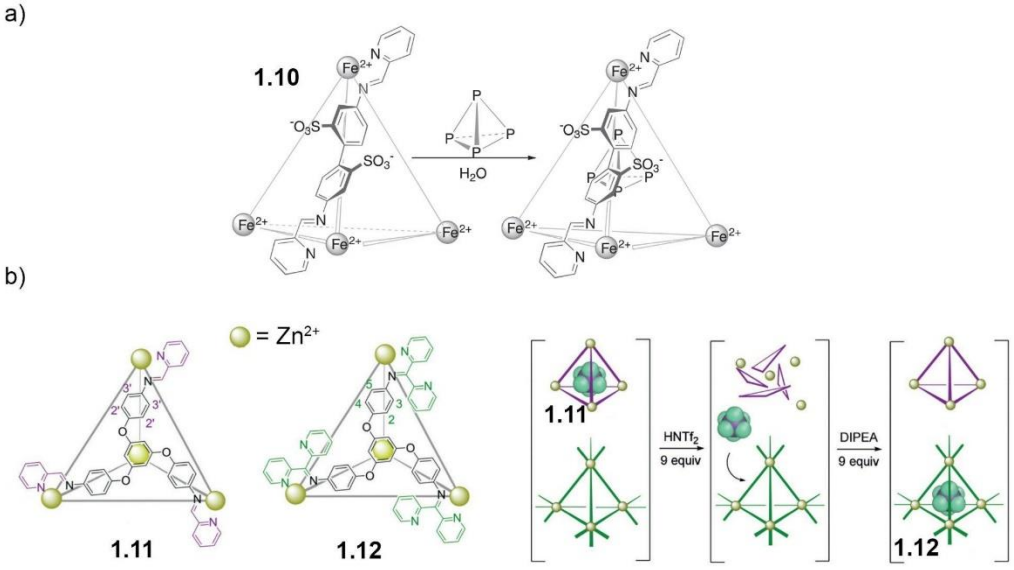

Figure 1.7. a) Binding and subsequent air stabilization of white phosphorus (P_4) in a self-assembled cage; b) anion recognition and transfer between two tetrahedral hosts.[73,74] Reprinted with permission from ref 75, copyright 2009, American Association for the Advancement of Science and ref 76, copyright 2020, Wiley.

The entrances and cavities of self-assembled cages play a crucial role in facilitating the ingress/egress of guests. Host-guest interactions within these cages can be approached from two distinct paradigms: kinetics and thermodynamics.[75,76] Kinetics focuses on the rate at

which guests enter or exit the cage, providing insights into the dynamics of the exchange process. Thermodynamics, on the other hand, examines the binding affinity of a guest within the host, revealing the strength of their interaction. Kinetics and thermodynamics do not necessarily have to be correlated. One might be tempted to assume that a slow exchanging guest has a much higher binding affinity but if the concentration of the host:guest complex in solution is sufficiently low we know that this is not that case. Likewise, rapid capture and release of guests does not mean they do not have high affinity for the host, only that they exchange rapidly. If guest exchange is slow relative to the ^{1}H nuclear magnetic resonance (NMR) time scale, the bound and unbound host can be seen on the ^{1}H NMR spectrum.[77] If host/guest kinetics are rapid on the ^{1}H NMR timescale, this results in the need to use faster methods to analyze guest binding, such as Ultraviolet-Visible spectroscopy (UV-Vis).[78]

Cage **1.10** binds white phosphorus (P_4) within its hydrophobic cavity which stabilizes it against air and water (Figure 1.7a).[73] Interestingly, even though P_4 is very soluble in heptane, the addition of heptane to a solution of **1.10**•P_4 does not result in removal of P_4 from **1.10**, but in the presence of a competitive guest, such as benzene, P_4 is displaced. Cage **1.10** is also a good host for other "small" organic molecules, such as cyclopentane, cyclohexane and methylcyclopentane, but shows minimal selectivity amongst these guests, as there is non-optimal size and shape fitting between the host and guests.[77,79] The cavity size of cage **1.10** was made larger by using a different metallic subcomponent Co^{2+}. This produced a structural analogue of **1.10** with an expanded cavity as the coordination bonds

between the ligand and metal center were longer. This resulted in binding of larger saturated alkanes.[79]

Cages **1.11** and **1.12** bind non-coordinating soft anions *via* favorable Coulombic attractive forces (as the cages have an overall 8+ charge).[74,80] Cage **1.12** is self-assembled from a different aldehyde subcomponent than **1.11**, which restricts its cavity expansion upon guest encapsulation, resulting in a tighter cavity fit for guest binding. This in turn allows **1.12** to bind a smaller fluorinated anion, BF_4^-, which **1.11** cannot bind as it does not fill up enough void space for stabilizing CH-F interactions. Selective anion binding in similar cages will be discussed thoroughly in chapter 4. As the aldehyde subcomponent of **1.12** provides the host with a basic nitrogen moiety, it is more stable to acid than **1.11**. Upon addition of acid to a solution of **1.11**•SbF_6, cage **1.11** decomposes, releases SbF_6^-, which is captured by **1.12** (Figure 1.7b). In addition to simple organic substrates and anions, self-assembled cages can encapsulate an array of guests, e.g., cisplatin,[81] sucrose,[82] fullerene,[83] and even enzymes.[64]

When a host molecule captures a single molecular species, it results in the formation of 1:1 host:guest complexes. These complexes are referred to as binary complexes, because they involve the interaction between one host and one guest molecule. In most cases solvent is expelled from the host cavity preceding guest binding which provides an entropic driving force. Once in the cavity the fit between guest and host determines its affinity. If a guest is too large, its movement within the cavity may be restricted and overly organized, which is entropically unfavorable.[75] However, if it is too small then it cannot take advantage of all

the possible van der Waals interactions which decreases affinity. Hosts also have the capability to form higher order complexes beyond the binary complexes. In such cases, multiple guest molecules can be accommodated within the host cavity, leading to the formation of higher order complexes. Correct size matching between host cavities and guest molecules with the correct thermodynamic driving forces leads to the formation of 1:2, 1:3, and 1:4 homoternary complexes.[62,75] The binding of multiple of the same guest typically relies on exploiting favorable van der Waals forces between the guests within the host cavity to overcome the entropic penalties of binding multiple species.[75] On the other hand, the formation of 1:2 or more heteroternary complexes is much rarer, as complimentary interactions between two different guests in the host cavity cannot readily be used to overcome the entropic barrier of binding multiple guests.[75,84,85] The binding modes and molecular recognition capabilities of hosts is critical to their capacity to mediate biomimetic catalysis.

1.4. Challenges in Catalysis with Self-Assembled Cages

The binding of substrates by self-assembled cages can mediate catalysis. These hosts must bind, activate, and most importantly, *release* guests. If substrates are concealed from reactants within a host cavity, they can be made unreactive, like in the case of **1.10**•P_4. Obviously, the goal is for guests to bind but if guest release is too slow this can cause substrate inhibition, as guests are not favorably released. Alternatively, if guest uptake is too slow, substrates cannot be sufficiently activated and thus binding cannot positively affect catalysis. Assuming the host can bind two molecules to mediate a reaction, the binding of one large product, over two smaller reactants, is entropically favorable and can

result in product inhibition.[86] Most importantly species must be bound and released, the effective liberation of the cage cavity is of the utmost importance to enhance turnover, which represents the central characteristic of an exceptional catalyst. The structures of self-assembled cages can also be delicate, so reagents and conditions must be chosen wisely. Lastly, if a self-assembled cage exists as a series of stereoisomers, this can complicate ^{1}H NMR analysis of the reactions, which adds an additional layer of complexity when designing an appropriate molecular transformation to study. Many self-assembled cages have been produced since their inception but very few are catalytically active.

1.5. Reactions Mediated by Unfunctionalized Cages

A reaction occurs due to the proximity of two molecules. If two molecules are confined within a cage cavity, reactivity can be enhanced, as the "effective concentration" of reaction components is increased. From being confined in a cavity, substrates may undergo otherwise unfavorable reaction pathways due to selective molecular recognition and preorganization of the substrates within the host cavity. Fujita and coworkers successfully synthesized two cages with the same stoichiometry, Pd_6L_4, octahedral cage **1.4** and its "half-bowl" variant **1.5**. Although the frameworks are made from hydrophobic aromatic ligands, due to the overall 12+ charge and solubilizing counterions, they are water soluble and possess hydrophobic cavities.[67]

Cages **1.4** and **1.5** bind organic molecules *via* hydrophobic driving forces in aqueous solution, which produces heteroternary complexes that are observable on the ^{1}H NMR time scale.[67] Once bound, the substrates are unable to leave, unless the solution is extracted with

an organic solvent, as **1.13** and **1.14** are not favorably solvated by water. The cavity of **1.4** is spacious enough to bind substrates **1.13** and **1.14**, which was unambiguously confirmed *via* single crystal X-Ray diffraction (scXRD). Once bound, substrates **1.13** and **1.14** undergo a Diels-Alder reaction to produce **1.15**, using a stoichiometric amount of **1.4** (Figure 1.8a). Interestingly, the cycloaddition occurs at the terminal arene ring of the anthracene derivative **1.13**, due to the preorganization of substrates within **1.4**. When using other reagents the regioselectivity occurs on the central ring of the anthracene derivative **1.13**.[87] Fujita also discovered that "half-bowl" **1.5** can catalyze the Diels-Alder reaction between **1.13** and **1.14** but the unusual regioselectivity observed when using **1.4** is not conserved.

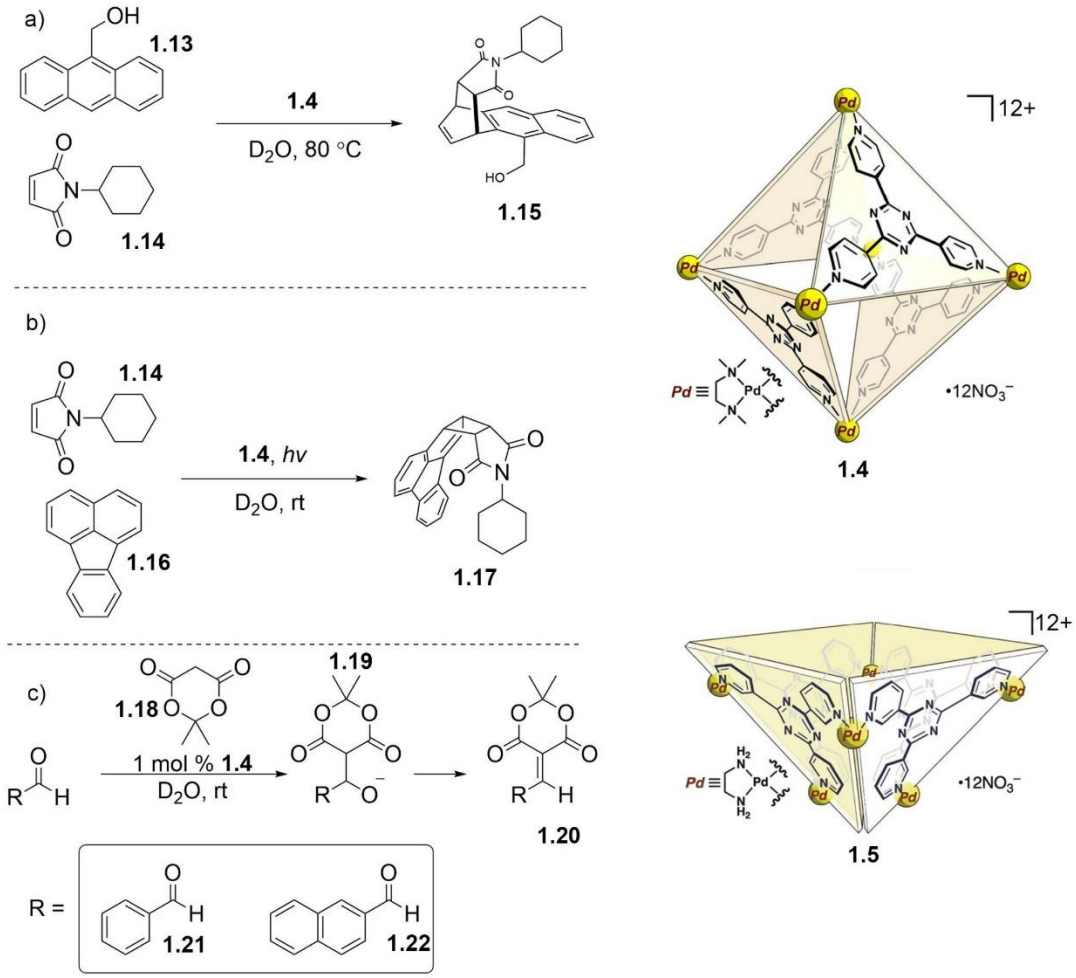

Figure 1.8. a) Stoichiometric Diels-Alder reaction mediated by **1.4** leading to unusual regioselectivity,[67] b) [2 + 2] olefin cross photoaddition mediated by stoichiometric amount of **1.4**,[88] c) Knoevenagel condensation catalyzed by **1.4** with various aldehyde substrates.[88,89 65,66] Reprinted with permission from ref 66, copyright 2022, Wiley.

Other ternary complexes involving **1.4** are possible, as the binding of **1.10** and **1.12** within **1.4** has been reported.[88] Fluoranthene **1.16** is an inert aromatic compound but when the ternary complex **1.4**·(**1.14**+**1.16**) forms and is exposed to an ultra-high pressure mercury lamp, a [2 + 2] photocycloaddition produces cycloadduct **1.17** (Figure 1.8b). Given all the potential reaction sites of **1.16**, it is remarkable a single regioisomeric product was observed, driven by optimal organization of substrates within the cavity of **1.4**. The

binding and preorganization of substrates within the cavity of **1.4** directs a highly selective cycloaddition.

Turnover is a significant problem for **1.4** as the products bind just as favorably as the starting materials for the cycloaddition reactions. One way around this is to choose a reaction where an unfavorable intermediate can be stabilized within the cavity of **1.4** and the resulting product can be favorably solvated by water, which positively promotes turnover by freeing the cavity. Due to the overall 12+ charge of cage **1.4**, it can also bind negatively charged organic species *via* Coulombic attractive forces, as well as π-π stacking between the host and guest. Under neutral conditions in water the anionic intermediate of dimedone, **1.18**, is not favorably formed but in the presence of **1.4** it is stabilized, which promotes the Knoevenagel condensation of **1.18**, and various aryl aldehydes **1.21**-**1.22** (Figure 1.8c). The conversion of substrate **1.21** was 58 % lower compared to **1.22**, as **1.21** is a weaker binding bound guest. When 9-anthraldehyde, was used the conversion also dropped by 33 % compared to **1.22**, because the ensuing anionic intermediate was too large to be favorably encapsulated. In contrast, **1.5** showed limited activity for the Knoevenagel reaction. Even though **1.4** and **1.5** possess the same 12+ charge, **1.4** has an enclosed cavity which likely helps stabilize the negative charge of intermediate **1.18** *via* restricted egress, which in turn promotes reactivity.

Cage **1.23** self-assembles from a bidentate catechol ligand that defines the edges of the tetrahedral structure which is anchored by Ga^{3+} metallo-vertices. The tetrahedron **1.23** is soluble in water, and other polar solvents, due to its overall 12- charge conferred by the

charge of ligand and the metal vertices.[48] As such, it has a strong affinity for cations ions. The naphthyl panels are able to twist and contort to facilitate host egress and ingress and the cavity of the cage has an approximate volume of 300-500 Å^3.[48,90,91] **1.23** is a self-assembled host composed of a racemic mixture of *ΔΔΔΔ*-**1.23** and *ΛΛΛΛ*-**1.23**, which can be enantioenriched by installing a chiral arm on the ligand framework which produces structures **1.24** and **1.25**, the chirality of the structures was confirmed *via* circular dichroism and scXRD analysis.[92]

Cage **1.23** binds various ammonium substrates, e.g., **1.26**, that vary in their steric bulkiness.[93] When in solution, **1.26** can undergo a [3,3]-sigmatropic rearrangement to produce an iminium ion that is hydrolyzed to aldehyde **1.27** (Figure 1.8b). The reaction occurs in solution, albeit slowly, as **1.26** is conformationally flexible and must adopt a rigid chair-like conformation to be converted to **1.27**. When **1.26** binds within **1.23**, it is conformationally restricted due to the tight binding pocket of **1.23**. This preorganization forces **1.26** to adopt a reactive chair-like conformation and leads to rate accelerations up to 854-fold compared to the background reaction. Notably, if **1.26** is made bulkier, the rate accelerations are significantly higher due to the tighter binding of the substrate within **1.23**.

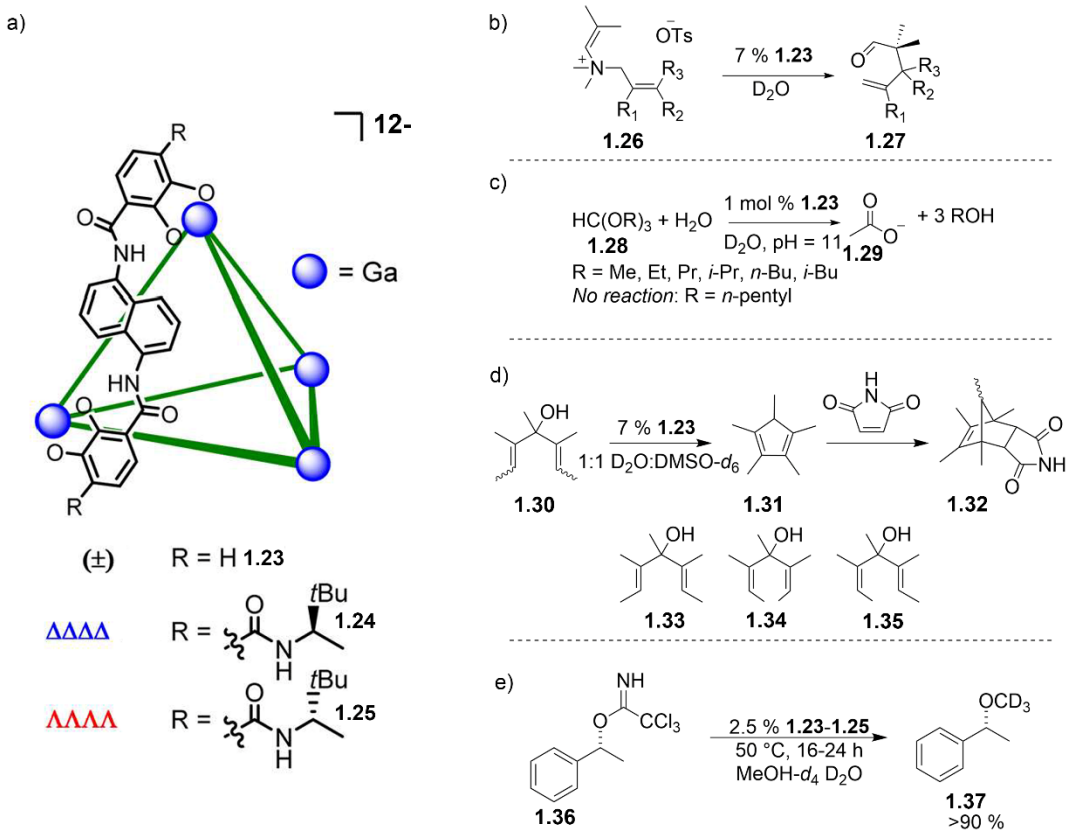

Figure 1.9. a) Chemdraw structure of racemic and enantioenriched catechol cages;[94] b) aza-Cope rearrangement catalyzed by cage **1.19**;[93] c) hydrolysis of orthoformates *under basic conditions* catalyzed by **1.19**;[95] d) enzyme like catalysis of the Nazarov cyclization;[86] e) stereochemical retention of S_N1 reaction.[94] Reprinted with permission ref 92, copyright 2014, American Chemical Society.

Various types of organic nitrogenous bases become protonated in the cavity of **1.23**, even when the pH of the solution is a unit higher than the amine's pKa.[96] This has important implications for biomimetic catalysis, as kinetically inaccessible reactive intermediates might be stabilized in the cavity of **1.23**. This is elegantly illustrated in the acid-catalyzed hydrolysis of orthoformates *under basic conditions* catalyzed by **1.23** (Figure 1.9c). Hydrolysis of orthoformates, for example **1.28**, is favored under acidic conditions. The cavity of **1.23** is chemically different from the basic bulk solution as it stabilizes kinetically inaccessible reactive intermediates. When **1.28** is bound, protonation is favored within the

cavity of **1.23**, as the environment possesses an overall negative charge. After two subsequent hydrolysis steps **1.29** is produced. Other carbocation intermediates can also be stabilized by **1.23**.

A series of pentadienols **1.30** were synthesized and used as reactants for the Nazarov cyclization, a reaction that proceeds through a carbocation intermediate before a 4π electrocyclization to produce **1.31** (Figure 1.9d).[86] To mitigate product inhibition maleimide was added to the reaction mixture to produce the Diels-Alder adduct **1.32** for determining the enhanced reaction rates. In the presence of the host the carbocation intermediate is stabilized and substantial rate enhancements were observed, on the order of 10^6 for **1.35** and 10^5 for **1.34**, which is a similar magnitude as that shown by some enzyme-catalyzed reactions.[25,97–99] Employing racemic cage **1.23** and enantioenriched cages **1.24** and **1.25** did not impact the stereoselectivity during the conversion of a racemic mixture of **1.36** to **1.37** (not shown). However, using enantiomerically enriched **1.36**, the *S_N1 reaction resulted in a product with stereochemical retention* (Figure 1.9e). This phenomenon was attributed to the planar cation intermediate being positionally fixed within cavities **1.23-1.25**. Cages **1.4**, **1.5**, and **1.23-1.25**, through molecular recognition and preorganization of substrates in their cavities, mediate and catalyze a variety of reactions in unexpected ways, e.g. unusual regioselectivity and significant rate accelerations.[66,100–106]

Cubic cage **1.38** was made by the Ward group and self-assembled from tetradentate bisimidazole-pyridine ligands possessing Co^{2+} metallo-vertices (Figure 1.10).[107] The superstructure possesses an overall 16+ charge and analysis of the crystal structure reveals

hydroxide anions are localized around the edges of the cubic structure (Figure 1.10a). Importantly, the portal entrances into the cavity are sufficiently large, facilitating facile host ingress and egress, which can be regulated via changes in pH.[108,109] Hydroxide anions coordinate to the cage exterior and can be used to catalyze the Kemp elimination, leading to rate accelerations on the order of 10^6 compared to the background reactivity in D_2O at pH = 10 (Figure 1.10b).[110] These hydroxide anions are reminiscent of cofactors mediating enzymatic catalysis. As the host portals are large and the product is negatively charged, it is easily expelled and solvated by water, thus product inhibition is not seen. The rate could be controlled by anion metathesis of surface bound hydroxides with other anions such as acetate or SO_4^{2-}, which lead to an increase or decrease in product formation, depending on alkalinity.[111] Additionally, various phenolates could be employed as opposed to basic anions where the rate was found to be proportional to their respective basicity.[112]

Cubic cage **1.38** is privileged, as it can stabilize highly nucleophilic and basic hydroxide anions around its exterior and use them to mediate the Kemp elimination, but most self-assembled cages are not able to persist in the presence of strong nucleophiles. The use of anions at the cages interface is reminiscent of enzymes using cofactors to mediate reactions. This type of reactivity can also be mimicked using self-assembled cages.

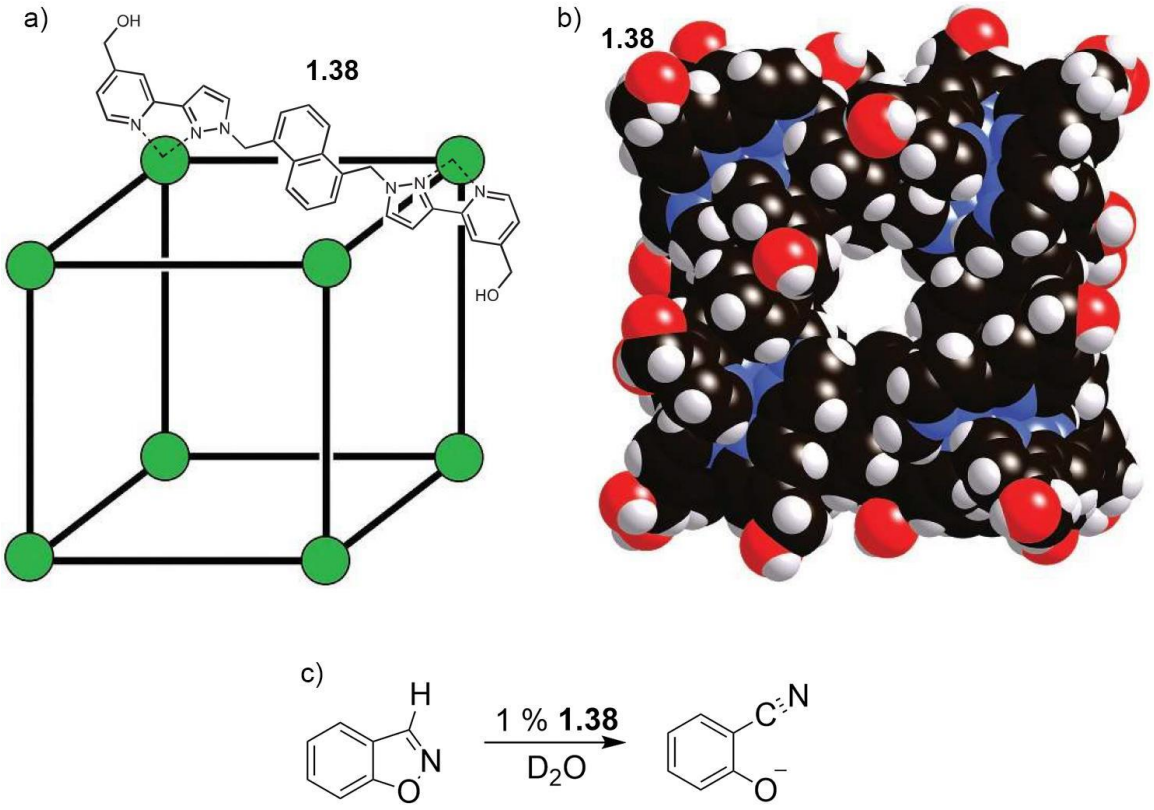

Figure 1.10. a) Chemdraw structure of bis-imidazole-pyridine cubic cage and scXRD structure depicting hydroxide ions localized on the edges; b) Kemp elimination catalyzed by **1.38.**[110] Reprinted with permission ref 108, copyright 2016, Macmillan Publishers Limited.

1.6. Self-Assembled Cages Using Cofactors for Biomimetic Catalysis

Enzymes directly participate in the reactions they catalyze, and one example of this is the use of cofactors. Apoenzymes are inert enzymes but when they bind a cofactor they activate it for the transformation of organic substrates, where all constituents are simultaneously bound.[26,113] Self-assembled cages usually do not possess multiple binding pockets, like enzymes, they are limited to a single cavity. To mimic cofactor-mediated enzymatic catalysis, self-assembled cages need to have a sufficiently large cavity for the formation of ternary and quaternary complexes. V-shaped ligands can be used to produce

self-assembled nanospheres that have a volume of 1,000 Å^3 or more, and have a stoichiometry of $M_{12}L_{24}$.[114] These ligands are easily synthesized via Sonogashira coupling and the central benzene ring is conveniently positioned for the incorporation of functional groups to bind cofactors (Figure 1.10a).

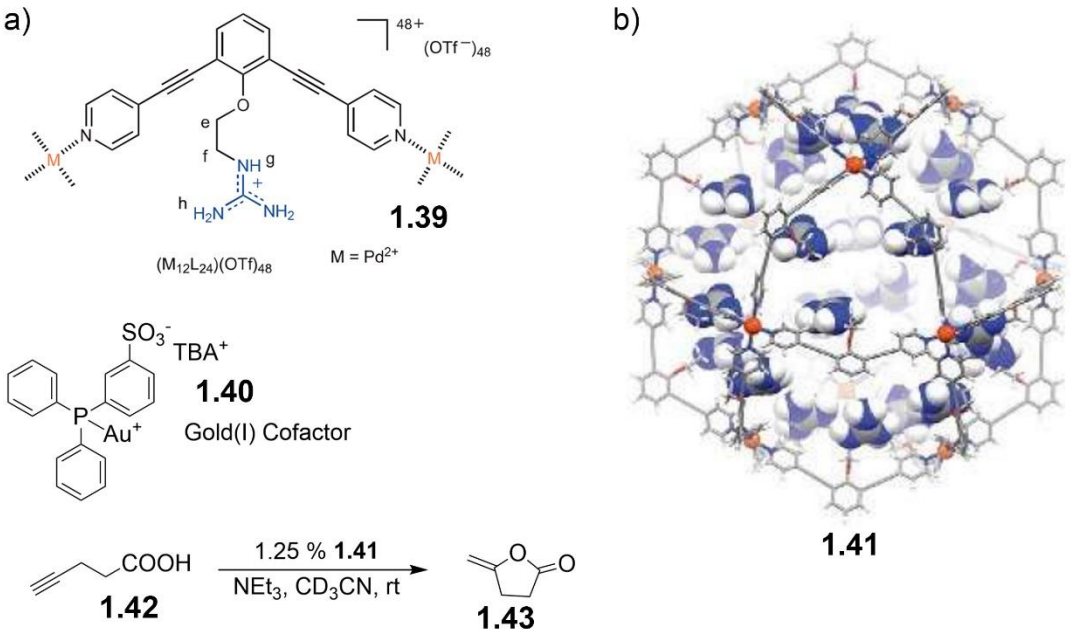

Figure 1.11. a) V-shaped ligand, Au(I) cofactor, and reaction catalyzed by nanosphere **1.41**; b) PM3-Spartan-Modeled $Pd_{12}L_{24}$ sphere.[114] Reprinted with permission ref 112, copyright 2016, Macmillan Publishers Limited.

Nanosphere **1.41** (Figure 1.11b) is self-assembled from ligand **1.39** and possesses a guanidinium functional group that is endohedrally oriented and acts as a H-bond donor. A consequence of this is that it can bind sulfonate containing Au(I) species, such as **1.40**. This increases the effective concentration of the catalytic Au(I) species within the large nanosphere **1.41**. This nanosphere does not possess appreciable electrostatic interactions to bind substrate **1.42**, and instead acts as a discrete phase within the bulk solution. Nanodroplet **1.41** catalyzes the conversion of **1.42** to **1.43** with greater efficiency than the

Au(I) catalyst employed without **1.41**. Nanosphere **1.41** mimics enzymatic cofactor catalysis as it concentrates catalytically active Au(I) species resulting in greater reaction efficiency (Figure 1.11a).

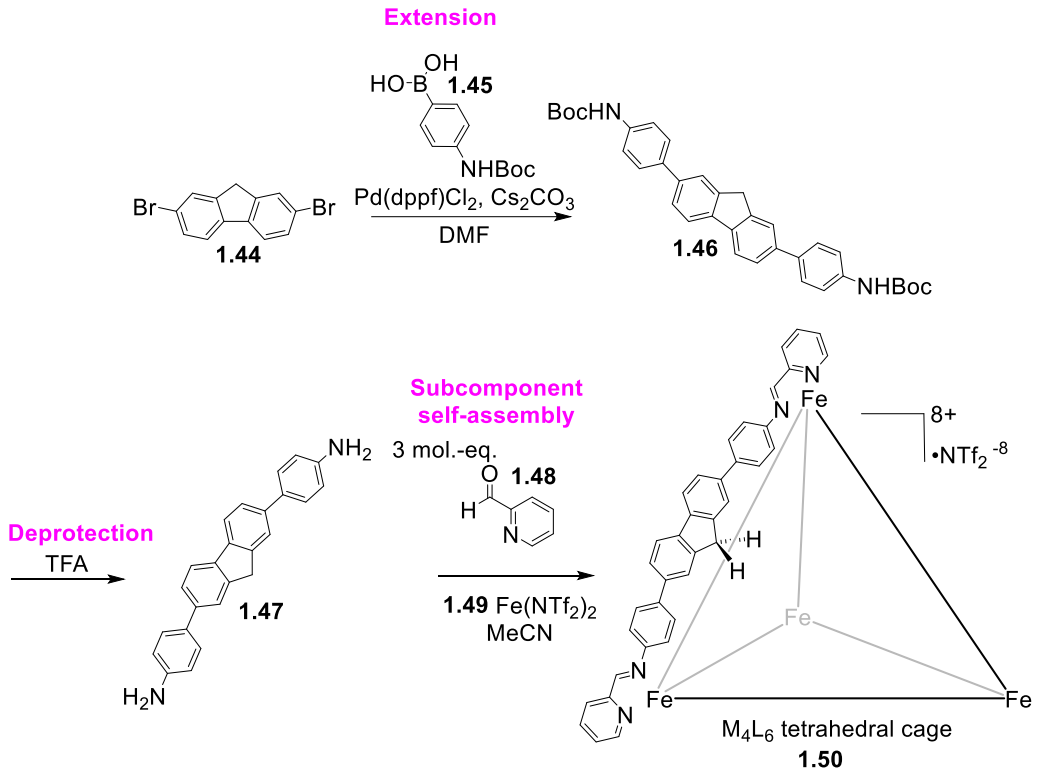

Figure 1.12. Reaction scheme of synthetic path to M_4L_6 tetrahedral cage which acts as a holoenzyme mimic.[115]

A different strategy for increasing the cavity size of self-assembled cages is using larger ligands (Figure 1.12). Hooley and co-workers have demonstrated that **1.44** can undergo Suzuki coupling with **1.45** to yield ligand precursor **1.46**, and subsequently ligand **1.47** is made by deprotecting **1.46**. Subcomponents **1.47**, **1.48**, and **1.49** self-assemble into a M_4L_6 tetrahedral cage as a distribution of three different diastereomers: *C*$_3$, *S*$_4$, and *T*.[115] The cage possesses a large cavity with an approximate volume of 572 Å^3, thus it should be able to form tertiary and quaternary host:guest complexes. Initial guest binding studies by ^{1}H

NMR spectroscopy revealed little evidence for binding. Subtle changes were observed but they were not significant for determining binding affinities or stoichiometries of guests inside of cage **1.50** as the in/out kinetics were rapid. Luckily, UV-Vis spectroscopy is a faster analysis method that indicated **1.50** binds polar organic substrates bearing polar functional groups, which will be discussed in detail in chapter 2.

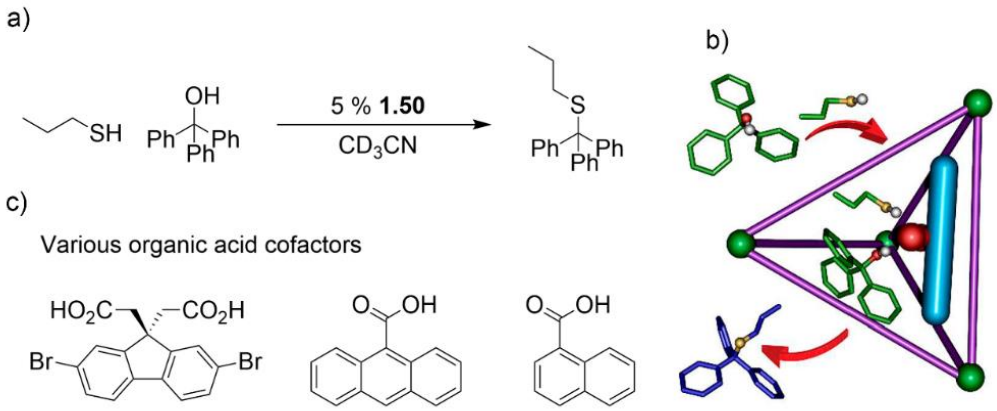

Figure 1.13. a) Holoenzyme mimic thioetherification of triphenylmethanol; b) cartoon of ternary complex likely leading to nucleophile rate dependance in the S_N1 reaction; c) example of some organic acid cofactors employed.[116] Reprinted with permission ref 114, copyright 2019, American Chemical Society.

The self-assembled M_4L_6 cage **1.50** exhibits the capability to co-encapsulate multiple aryl organic acid guests, allowing these acids to serve as cofactors for nucleophilic substitution reactions catalyzed by the cage (Figure 1.13).[115,116] Size, shape, binding affinity, and binding stoichiometry strongly influence both the kinetics and mechanism of the thioetherification of triphenylmethanol. In some cases, the rate is enhanced in the presence of **1.50** and the S_N1 reaction rate *has a higher dependance on the concentration of the nucleophile* with specific reaction components. The selective molecular recognition

taking place within the interior of **1.50** controls these unexpected outcomes of the substitution reaction.

1.7. Endohedrally Functionalized Self-Assembled Cages

In addition to using a cofactor, enzymes also have active sites furnished with reaction prone functional groups that mediate catalysis. Synthesizing cages with functional groups that are endohedrally oriented comes with many challenges. Functional groups that are reactive and possess the ability to coordinate may interfere with the self-assembly process. If the cage is too small, steric repulsions can rotate the groups externally. As nanospheres are exceedingly large, appending functional groups into their cavities is possible.

Functionalized ligand **1.51** was synthesized with a diaryl ether linkage incorporating an aryl phosphine Au(I) species that produced nanosphere **1.53**, which has Au(I) concentrated within its interior (Figure 1.14a). An inert analogue of **1.53** was made from unfunctionalized ligand **1.52** that produced nanosphere **1.54**. Nanosphere **1.53** acts as a synthetic enzyme active site for the intramolecular hydroalkoxylation of allenol (Figure 1.14), while cage **1.54** is inactive for the reaction. Ph_3PAuCl was used as a control for the hydroalkoxylation of allenol and was found to be catalytically inactive under similar conditions, even at 24 mol % loading. As Au(I) is concentrated within nanosphere **1.53**, it can effectively catalyze the hydroalkoxylation of allenol by providing a phase within the solution composed of reactive Au(I) species appended to the interior of the nanosphere. Importantly, free Au(I) salts in the bulk solution used as a control cannot catalyze this

reaction. Nanosphere **1.53** also selectively produces the 5-membered ring product, and the 6-membered ring is not observed.

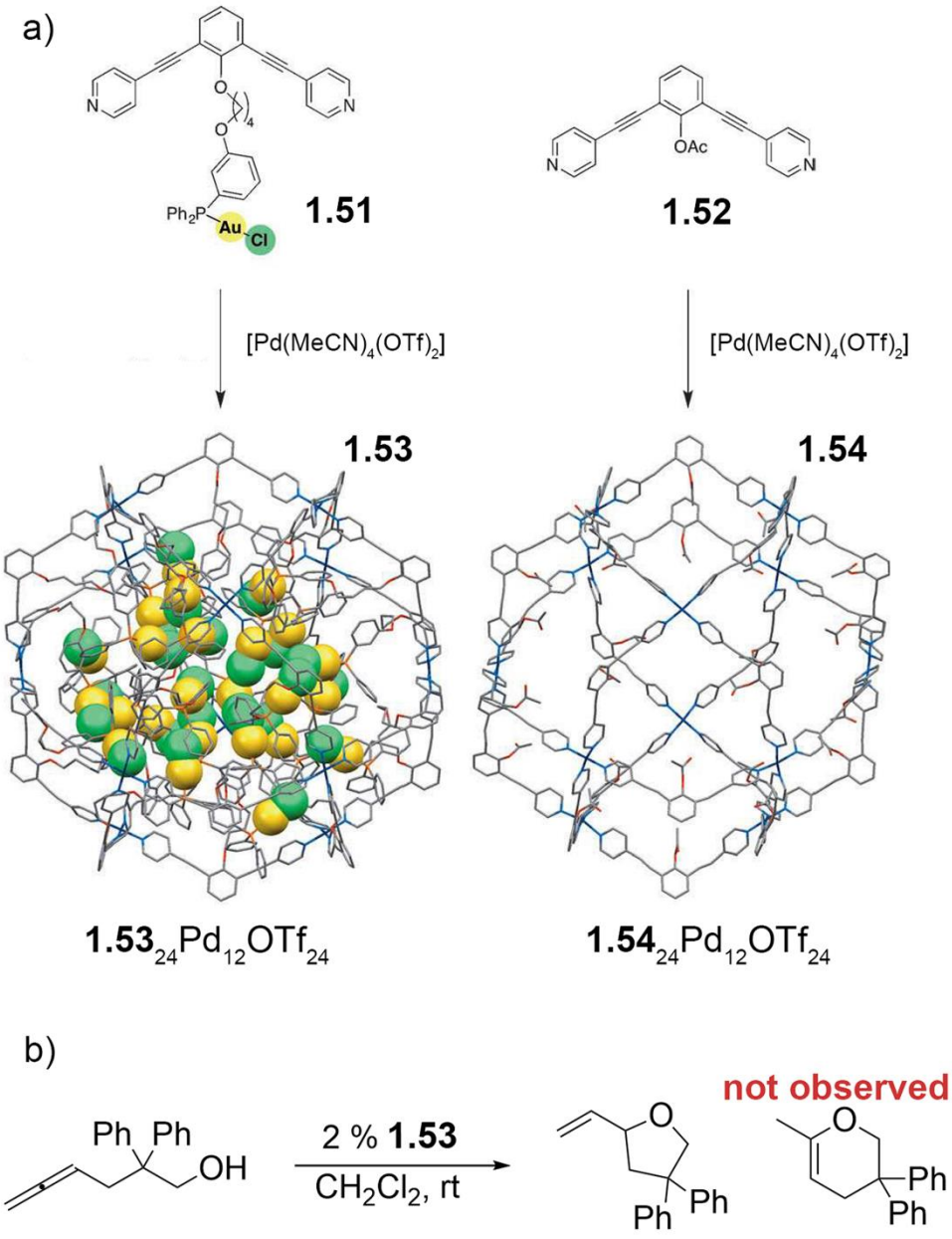

Figure 1.14. a) Formation of two different $M_{12}L_{24}$ nanospheres, **1.53** that contains internal Au(I) catalysts and **1.54** that is internally "empty"; b) allene hydroxylation reaction catalyzed by **1.53**.[117] Reprinted with permission ref 115, copyright 2014, Wiley.

This synthetic technology was also used to promote cascade catalysis. MacMillan's catalyst was installed onto ligand **1.56** and (2,2,6,6-tetramethylpiperidin-1-yl)oxyl (TEMPO) was installed onto ligand **1.55**. Subsequently, they were used to synthesize the self-assembled nanospheres **1.58** and **1.57**, respectively.[118] TEMPO and MacMillan's catalyst are incompatible in bulk solution but by being chemically isolated in their own endohedrally functionalized nanospheres, a cascade oxidation-Diels-Alder reaction was promoted (Figure 1.15). Nanospheres have proven to be an effective strategy for the installation of functional groups to mimic enzyme active sites. As their cavities are massive, they lack a critical feature of enzymatic catalysis: molecular recognition for there are no van der Waal's interactions to exploit for binding guests. If functional groups can be appended to smaller self-assembled cages, this can be circumvented.

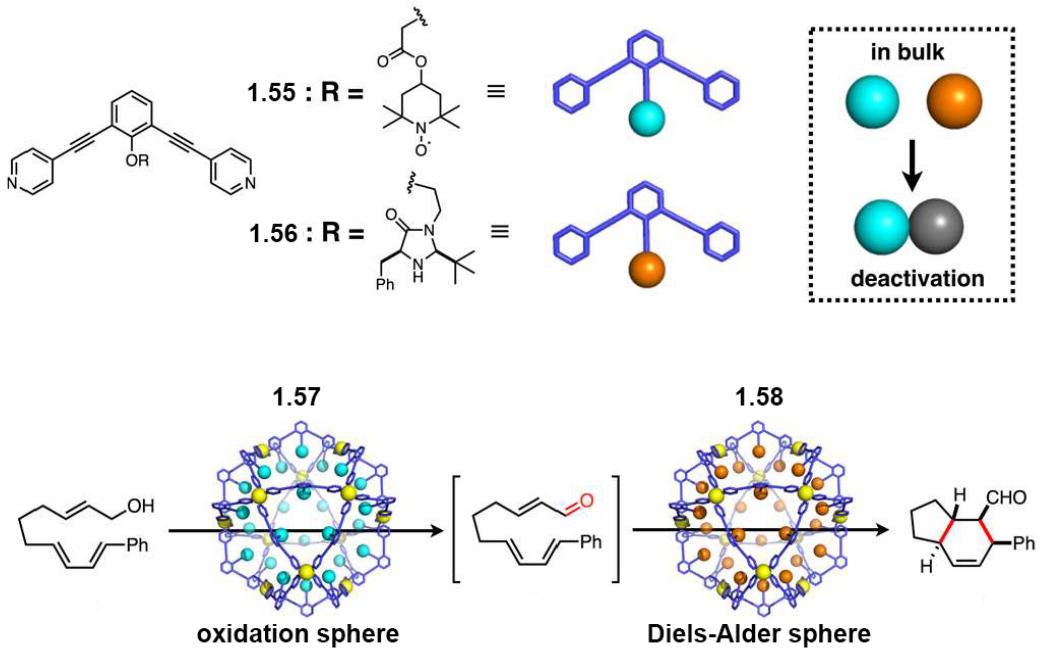

Figure 1.15. Cascade catalysis mediated by internally functionalized nanospheres.[118] Reprinted with permission ref 116, copyright 2017, American Chemical Society.

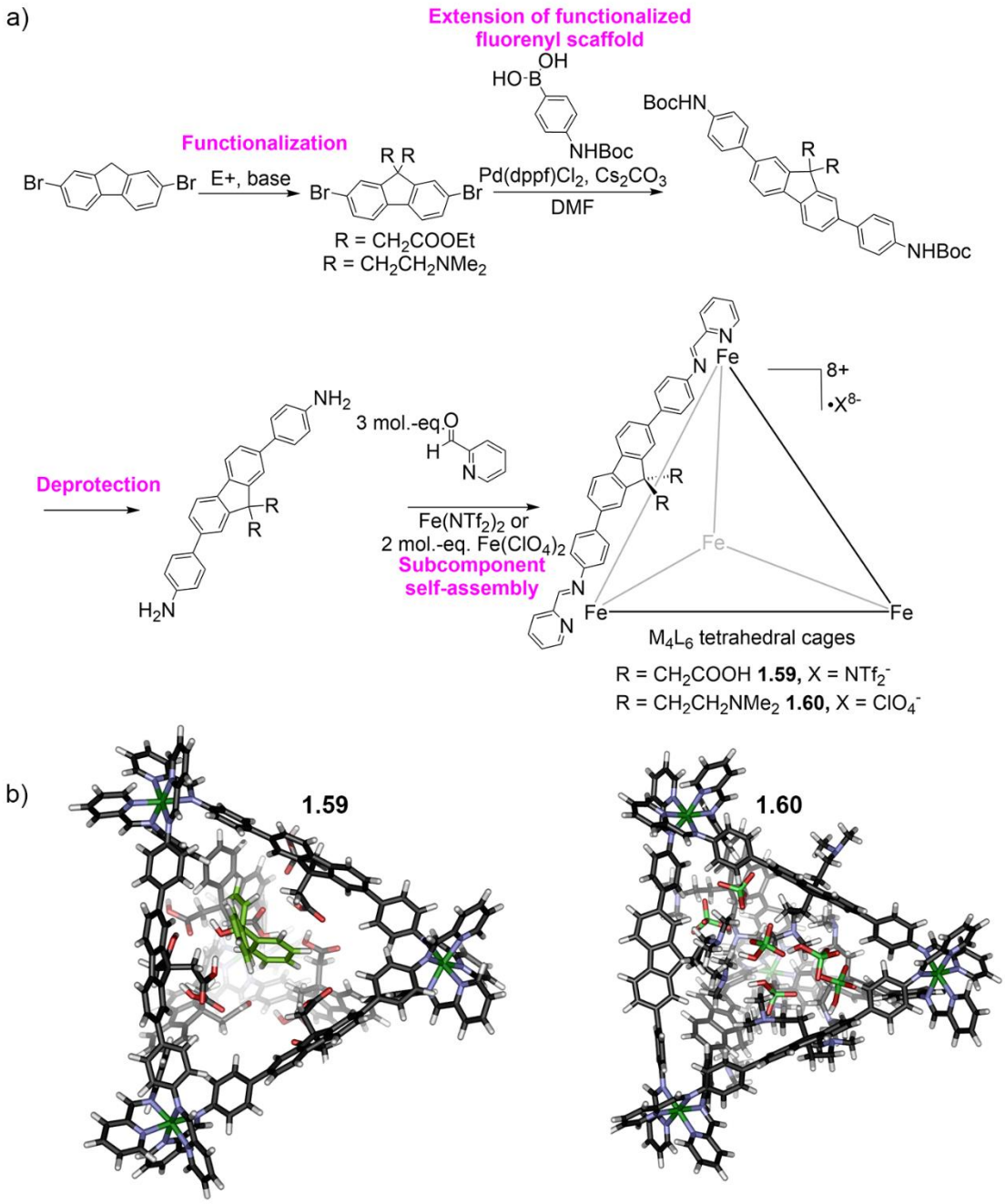

Figure 1.16. a) Synthetic route to functionalized self-assembled cages; b) Spartan energy minimized models of **1.59** with a guest and **1.60** which is templated with 12 ClO_4^- anions, 6 are shown for clarity.[115,123]

The initial versions of internally functionalized self-assembled cages developed by the Hooley lab were insufficiently sized for facilitating organic transformations. [60,119–122] The

fluorenyl scaffold garnered significant interest due to the presence of reactive benzylic protons, capable of facile substitution with various functional groups (Figure 1.16). The synthesis of functionalized cage **1.59** and **1.60** is almost identical to their unfunctionalized predecessor **1.50**, where the functional groups are installed before Suzuki coupling in both cases (Figure 1.15). As is common with Fe-iminopyridine self-assembled cages, they exist as a mixture of S_4, C_3, and *T* diastereomers and possess portals that are sufficiently large to facilitate smooth ingress/egress of guests.

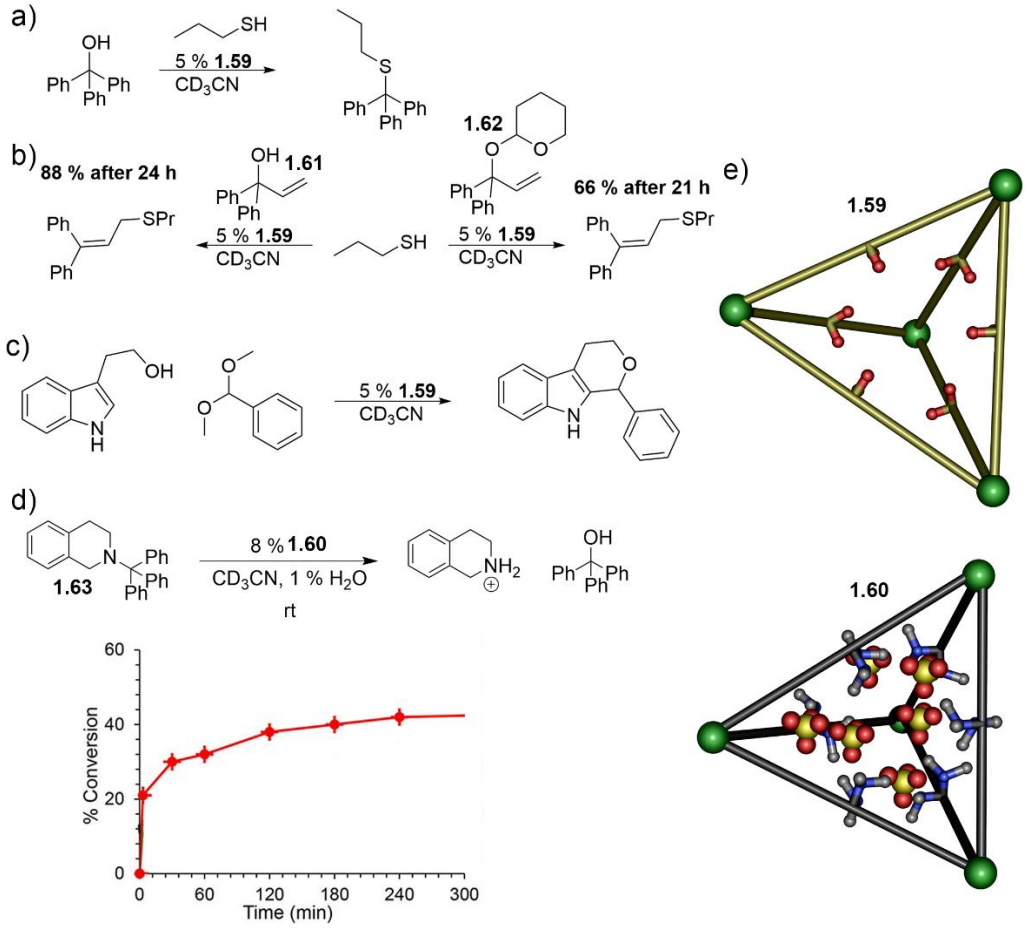

Figure 1.17. a) Thioetherification catalyzed by acid cage; b) size and shape selective catalysis of oxocarbenium ion reactions; c) Oxa-Pictet-Spengler reaction; d) detritylation of **1.63** using "base" cage **1.60**; e) cartoons of acid cage **1.59** and "base" cage **1.60**.[115,123–126] Reprinted with permission 114, copyright 2019, American Chemical Society and ref 124, copyright 2022, Wiley.

Cage **1.59** has its carboxylic acid groups internally oriented, providing polar and H-bonding interactions for binding guests. The first example of its use as a catalyst was the hydrolysis of benzaldehyde dimethyl acetal that was accelerated 1000-fold. It was then applied to a more elaborate multistep transformation, the thioetherification of triphenylmethanol (Figure 1.17a), where it accelerated the rate of substitution by up to 1000-fold. Like **1.50**, the reaction's molecularity was influenced by the components

involved being selectively recognized by **1.59**, the molecularity was up to *bimolecular for the S_N1 reaction*. Not only is **1.59** able to enhance reactivity, but it also can lead to other unique and unexpected reaction outcomes. This is exemplified by the stark difference in reactivity between **1.61** and **1.62** (Figure 1.17b). Where the tetrahydropyran protected electrophile, that shows greater reactivity with a small molecule catalyst, reacts *slower* than its less reactive unprotected counterpart, likely due to favorable preorganization of the basic oxygens coordinating to the acid functional groups of **1.59**. Furthermore, **1.59** can also catalyze complex multistep transformations such as the oxa-Pictet-Spengler reaction (Figure 1.17c), these types of multistep organic transformations are rarely performed by supramolecular catalysts.

In efforts towards accessing base mediated reactions, cage **1.60** was synthesized but was only accessible when all twelve endohedrally oriented amines were protonated with $HClO_4$, giving the final structure an overall +20 charge, which required the use of excess $Fe(ClO_4)_2$.[123] The structure is highly unusual. To self-assemble into the cage, the amines must be protonated, resulting in a +12 charge in the cavity of the octacationic structure. These ammoniums are not kinetically trapped, as they can be deprotonated without the cage disassembling. The amines possessed a sliding scale of basicity with an approximate 6 pKa unit difference between the first and last protons. This is nicely illustrated by the reaction profile diagram of the detritylation of **1.63** (Figure 1.17). Initially the detritylation is fast, as the first protons removed from **1.60** are the most acidic, which rapidly slows down at ~ 30 % conversion. The "base cage" synthetically replicates the regulation of side chain basicity observed in proteins. The molecular recognition properties of **1.50**, **1.59** and

1.60 allow them to effectively bind polar organic molecules which comprise most organic transformations, thereby increasing the possible reaction scope of these biomimetic catalysts. Subtle changes in substrates have large effects on the kinetics and mechanisms of the reactions discussed thus far. They are large enough to bind multiple reaction components and incorporate internally oriented functional groups, thus they are exceptional enzyme mimics.

1.8. Conclusion

In an idealized synthetic environment, simple commercially available building blocks could be submitted to a single pot procedure to render complex molecular architectures where atoms and connectivity are easily altered at the chemist's discretion. One method of obtaining new reactivity is using self-assembled cages as biomimetic catalysts. Many challenges of biomimetic catalysis have been resolved, yet a vast array of reaction types is still inaccessible. To broaden the reaction scope of biomimetic cage catalysts, new cages must be synthesized and new reaction types, with already existing hosts, must be tested. The aim of my thesis is to broaden the reaction scope of biomimetic hosts by surveying reaction types using already existing cages while also looking towards synthesizing new ligand scaffolds for the synthesis of new internally functionalized biomimetic cages.

References

(1) Bell, M. S. *Lavoisier in the Year One: The Birth of a New Science in an Age of Revolution*; W. W. Norton & Company, 2005.

(2) Nicolaou, K. C. The Emergence of the Structure of the Molecule and the Art of Its Synthesis. *Angew. Chem. Int. Ed.* **2013**, *52*, 131–146.

(3) Nicolaou, K. C. Organic Synthesis: The Art and Science of Replicating the Molecules of Living Nature and Creating Others like Them in the Laboratory. *Proc. R. Soc. A.* **2014**, *470*, 20130690.

(4) *C. R. Acad. Sci.* **1924**, 330.

(5) Woodward, R. B.; Ayer, W. A.; Beaton, J. M.; Bickelhaupt, F.; Bonnett, R.; Buchschacher, P.; Closs, G. L.; Dutler, H.; Hannah, J.; Hauck, F. P.; Itô, S.; Langemann, A.; Le Goff, E.; Leimgruber, W.; Lwowski, W.; Sauer, J.; Valenta, Z.; Volz, H. The Total Synthesis of Chlorophyll. *J. Am. Chem. Soc.* **1960**, *82*, 3800–3802.

(6) Woodward, R. B. The total synthesis of vitamin B_{12}. *Pure Appl. Chem.* **1973**, *33*, 145–178.

(7) Corey, E. J.; Kang, M.-C.; Desai, M. C.; Ghosh, A. K.; Houpis, I. N. Total Synthesis of (±)-Ginkgolide B. *J. Am. Chem. Soc.* **1988**, *110*, 649–651.

(8) Nicolaou, K. C.; Aversa, R. J. Maitotoxin: An Inspiration for Synthesis. *Isr. J. Chem.* **2011**, *51*, 359–377.

(9) Nicolaou, K. C.; Heretsch, P.; Nakamura, T.; Rudo, A.; Murata, M.; Konoki, K. Synthesis and Biological Evaluation of QRSTUVWXYZA' Domains of Maitotoxin. *J. Am. Chem. Soc.* **2014**, *136*, 16444–16451.

(10) Hock, H.; Lang, S. Autoxydation von Kohlenwasserstoffen, IX. Mitteil.: Über Peroxyde von Benzol-Derivaten. *Ber. dtsch. Chem. Ges. A/B* **1944**, *77*, 257–264.

(11) Prier, C. K.; Rankic, D. A.; MacMillan, D. W. C. Visible Light Photoredox Catalysis with Transition Metal Complexes: Applications in Organic Synthesis. *Chem. Rev.* **2013**, *113*, 5322–5363.

(12) Johansson Seechurn, C. C. C.; Kitching, M. O.; Colacot, T. J.; Snieckus, V. Palladium-Catalyzed Cross-Coupling: A Historical Contextual Perspective to the 2010 Nobel Prize. *Angew. Chem. Int. Ed.* **2012**, *51*, 5062–5085.

(13) Albright, H.; Davis, A. J.; Gomez-Lopez, J. L.; Vonesh, H. L.; Quach, P. K.; Lambert, T. H.; Schindler, C. S. Carbonyl-Olefin Metathesis. *Chem. Rev.* **2021**, *121*, 9359–9406.

(14) MacMillan, D. W. C. The Advent and Development of Organocatalysis. *Nature* **2008**, *455*, 304–308.

(15) Huang, F.; Anslyn, E. V. Introduction: Supramolecular Chemistry. *Chem. Rev.* **2015**, *115*, 6999–7000.

(16) Cram, D. J.; Cram, J. M. Cyclophane Chemistry: Bent and Battered Benzene Rings. *Acc. Chem. Res.* **1971**, *4*, 204–213.

(17) Pedersen, C. J. Cyclic Polyethers and Their Complexes with Metal Salts. *J. Am. Chem. Soc.* **1967**, *89*, 7017–7036.

(18) Breslow, R.; Campbell, P. Selective Aromatic Substitution within a Cyclodextrin Mixed Complex. *J. Am. Chem. Soc.* **1969**, *91*, 3085–3085.

(19) Rekharsky, M. V.; Inoue, Y. Complexation Thermodynamics of Cyclodextrins. *Chem. Rev.* **1998**, *98*, 1875–1918.

(20) Nishio, M. CH/π Hydrogen Bonds in Crystals. *CrystEngComm* **2004**, *6*, 130–158.

(21) Ronson, T. K.; Meng, W.; Nitschke, J. R. Design Principles for the Optimization of Guest Binding in Aromatic-Paneled $Fe^{II}_4L_6$ Cages. *J. Am. Chem. Soc.* **2017**, *139*, 9698–9707.

(22) Kang, J.; Rebek, J., Jr. Acceleration of a Diels-Alder Reaction by a Self-Assembled Molecular Capsule. *Nature* **1997**, *385*, 50–52.

(23) Warmuth, R. *Carcerands and Hemicarcerands*; John Wiley & Sons, Ltd, 2012.

(24) Holloway, L. R.; Bogie, P. M.; Lyon, Y.; Julian, R. R.; Hooley, R. J. Stereoselective Postassembly CH Oxidation of Self-Assembled Metal-Ligand Cage Complexes. *Inorg. Chem.* **2017**, *56*, 11435–11442.

(25) Radzicka, A.; Wolfenden, R. A Proficient Enzyme. *Science* **1995**, *267*, 90–93.

(26) Richter, M. Functional Diversity of Organic Molecule Enzyme Cofactors. *Nat. Prod. Rep.* **2013**, *30*, 1324–1345.

(27) Gutte, B.; Merrifield, R. B. The Synthesis of Ribonuclease A. *J. Biol. Chem.* **1971**,

246, 1922–1941.

(28) Fasan, R.; Jennifer Kan, S. B.; Zhao, H. A Continuing Career in Biocatalysis: Frances H. Arnold. *ACS Catal.* **2019**, *9*, 9775–9788.

(29) Galanie, S.; Thodey, K.; Trenchard, I. J.; Filsinger Interrante, M.; Smolke, C. D. Complete Biosynthesis of Opioids in Yeast. *Science* **2015**, *349*, 1095–1100.

(30) Maier, G.; Pfriem, S.; Schäfer, U.; Matusch, R. Tetra-Tert-Butyltetrahedrane. *Angew. Chem. Int. Ed. Engl.* **1978**, *17*, 520–521.

(31) Fleischer, E. B. X-Ray Structure Determination of Cubane. *J. Am. Chem. Soc.* **1964**, *86*, 3889–3890.

(32) Ternansky, R. J.; Balogh, D. W.; Paquette, L. A. Dodecahedrane. *J. Am. Chem. Soc.* **1982**, *104*, 4503–4504.

(33) Kroto, H. W.; Heath, J. R.; O'Brien, S. C.; Curl, R. F.; Smalley, R. E. C60: Buckminsterfullerene. *Nature* **1985**, *318*, 162–163.

(34) Krätschmer, W.; Lamb, L. D.; Fostiropoulos, K.; Huffman, D. R. Solid C60: A New Form of Carbon. *Nature* **1990**, *347*, 354–358.

(35) Adams, G. B.; O'Keeffe, M.; Ruoff, R. S. Van Der Waals Surface Areas and Volumes of Fullerenes. *J. Phys. Chem.* **1994**, *98*, 9465–9469.

(36) Vougioukalakis, G. C.; Roubelakis, M. M.; Orfanopoulos, M. Open-Cage Fullerenes: Towards the Construction of Nanosized Molecular Containers. *Chem. Soc. Rev.* **2010**, *39*, 817–844.

(37) Cram, D. J.; Karbach, S.; Kim, Y. H.; Baczynskyj, L.; Kallemeyn, G. W. Shell Closure of Two Cavitands Forms Carcerand Complexes with Components of the Medium as Permanent Guests. *J. Am. Chem. Soc.* **1985**, *107*, 2575–2576.

(38) Cram, D. J. The Design of Molecular Hosts, Guests, and Their Complexes (Nobel Lecture). *Angew. Chem. Int. Ed. Engl.* **1988**, *27*, 1009–1020.

(39) Wyler, R.; de Mendoza, J.; Rebek, J. A Synthetic Cavity Assembles through Self-Complementary Hydrogen Bonds. *Angew. Chem. Int. Ed. Engl.* **1993**, *32*, 1699–1701.

(40) Saalfrank, R. W.; Stark, A.; Peters, K.; von Schnering, H. G. The First "Adamantoid" Alkaline Earth Metal Chelate Complex: Synthesis, Structure, and Reactivity. *Angew. Chem. Int. Ed. Engl.* **1988**, *27*, 851–853.

(41) Saalfrank, R. W.; Burak, R.; Breit, A.; Stalke, D.; Herbst-Irmer, R.; Daub, J.; Porsch, M.; Bill, E.; Müther, M.; Trautwein, A. X. Mixed-Valence, Tetranuclear Iron Chelate Complexes as Endoreceptors: Charge Compensation through Inclusion of Cations. *Angew. Chem. Int. Ed. Engl.* **1994**, *33*, 1621–1623.

(42) Saalfrank, R. W.; Stark, A.; Bremer, M.; Hummel, H.-U. Formation of Tetranuclear Chelate(4-) Ions of Divalent Metals(Mn, Co, Ni) with Idealized *T* Symmetry by Spontaneous Self-Assembly. *Angew. Chem. Int. Ed. Engl.* **1990**, *29*, 311–314.

(43) Pryde, A. J.; Shaw, B. L.; Weeks, B. Large Ring Compounds Involving Trans-Bonding Bidentate Ligands. *Chem. Commun.* **1973**, *1249*, 947–948.

(44) Maverick, A. W.; Klavetter, F. E. Cofacial Binuclear Copper Complexes of a Bis(.Beta.-Diketone) Ligand. *Inorg. Chem.* **1984**, *23*, 4129–4130.

(45) Maverick, A. W.; Buckingham, S. C.; Yao, Q.; Bradbury, J. R.; Stanley, G. G. Intramolecular Coordination of Bidentate Lewis Bases to a Cofacial Binuclear Copper(II) Complex. *J. Am. Chem. Soc.* **1986**, *108*, 7430–7431.

(46) Caulder, D. L.; Raymond, K. N. The Rational Design of High Symmetry Coordination Clusters. *J. Chem. Soc. Dalton Trans.* **1999**, 1185–1200.

(47) Caulder, D. L.; Raymond, K. N. Supermolecules by Design. *Acc. Chem. Res.* **1999**, *32*, 975–982.

(48) Parac, T. N.; Caulder, D. L.; Raymond, K. N. Selective Encapsulation of Aqueous Cationic Guests into a Supramolecular Tetrahedral $[M_4L_6]^{12-}$ Anionic Host. *J. Am. Chem. Soc.* **1998**, *120*, 8003–8004.

(49) Kusukawa, T.; Fujita, M. Encapsulation of Large, Neutral Molecules in a Self-Assembled Nanocage Incorporating Six Palladium(II) Ions. *Angew. Chem. Int. Ed Engl.* **1998**, *37*, 3142–3144.

(50) Fujita, M. Metal-Directed Self-Assembly of Two- and Three-Dimensional Synthetic Receptors. *Chem. Soc. Rev.* **1998**, *27*, 417–425.

(51) Fujita, M.; Ogura, K. Transition-Metal-Directed Assembly of Well-Defined Organic Architectures Possessing Large Voids: From Macrocycles to [2] Catenanes. *Coord. Chem. Rev.* **1996**, *148*, 249–264.

(52) Saalfrank, R. W.; Burak, R.; Reihs, S.; Löw, N.; Hampel, F.; Stachel, H.-D.; Lentmaier, J.; Peters, K.; Peters, E.-M.; von Schnering, H. G. Synthesis and Structure of Tetra- and Octanuclear Chelate Complexes—Exohedral Guest

Exchange in Tetrahemispheraplexes. *Angew. Chem. Int. Ed Engl.* **1995**, *34*, 993–995.

(53) Saalfrank, R. W.; Bernt, I.; Uller, E.; Hampel, F. Template-Mediated Self Assembly of Six- and Eight-Membered Iron Coronates. *Angew. Chem. Int. Ed. Engl.* **1997**, *36*, 2482–2485.

(54) Piguet, C.; Bernardinelli, G.; Hopfgartner, G. Helicates as Versatile Supramolecular Complexes. *Chem. Rev.* **1997**, *97*, 2005–2062.

(55) Hasenknopf, B.; Lehn, J.-M.; Boumediene, N.; Dupont-Gervais, A.; Van Dorsselaer, A.; Kneisel, B.; Fenske, D. Self-Assembly of Tetra- and Hexanuclear Circular Helicates. *J. Am. Chem. Soc.* **1997**, *119*, 10956–10962.

(56) Leininger, S.; Olenyuk, B.; Stang, P. J. Self-Assembly of Discrete Cyclic Nanostructures Mediated by Transition Metals. *Chem. Rev.* **2000**, *100*, 853–908.

(57) Seidel, S. R.; Stang, P. J. High-Symmetry Coordination Cages via Self-Assembly. *Acc. Chem. Res.* **2002**, *35*, 972–983.

(58) Brooker, S.; Hay, S. J.; Plieger, P. G. A Grid Complex $[CuL_2]^{4+}$ and a Mixed-Valent Complex $[Cu^{II}Cu^{I}L(MeCN)_2]^{3+}$ of the Pyridazine-Containing Macrocycle L. *Angew. Chem. Int. Ed.* **2000**, *39*, 1968–1970.

(59) Zhang, D.; Ronson, T. K.; Xu, L.; Nitschke, J. R. Transformation Network Culminating in a Heteroleptic $Cd_6L_6L'_2$ Twisted Trigonal Prism. *J. Am. Chem. Soc.* **2020**, *142*, 9152–9157.

(60) Young, M. C.; Holloway, L. R.; Johnson, A. M.; Hooley, R. J. A Supramolecular Sorting Hat: Stereocontrol in Metal-Ligand Self-Assembly by Complementary Hydrogen Bonding. *Angew. Chem. Int. Ed.* **2014**, *53*, 9832–9836.

(61) Biros, S. M.; Yeh, R. M.; Raymond, K. N. Design and Formation of a Large Tetrahedral Cluster Using 1,1'-Binaphthyl Ligands. *Angew. Chem. Int. Ed.* **2008**, *47*, 6062–6064.

(62) Taylor, C. G. P.; Argent, S. P.; Ludden, M. D.; Piper, J. R.; Mozaceanu, C.; Barnett, S. A.; Ward, M. D. One Guest or Two? A Crystallographic and Solution Study of Guest Binding in a Cubic Coordination Cage. *Eur. J. Chem.* **2020**, *26*, 3054–3064.

(63) Bilbeisi, R. A.; Ronson, T. K.; Nitschke, J. R. A Self-Assembled $[Fe(II)_{12}L_{12}]$ Capsule with an Icosahedral Framework. *Angew. Chem. Int. Ed.* **2013**, *52*, 9027–9030.

(64) Fujita, D.; Suzuki, K.; Sato, S.; Yagi-Utsumi, M.; Yamaguchi, Y.; Mizuno, N.; Kumasaka, T.; Takata, M.; Noda, M.; Uchiyama, S.; Kato, K.; Fujita, M. Protein Encapsulation within Synthetic Molecular Hosts. *Nat. Commun.* **2012**, *3*, 1093.

(65) Zhang, D.; Gan, Q.; Plajer, A. J.; Lavendomme, R.; Ronson, T. K.; Lu, Z.; Jensen, J. D.; Laursen, B. W.; Nitschke, J. R. Templation and Concentration Drive Conversion Between a $FeII_{12}L_{12}$ Pseudoicosahedron, a $FeII_4L_4$ Tetrahedron, and a FeII2L3 Helicate. *J. Am. Chem. Soc.* **2022**, *144*, 1106–1112.

(66) Takezawa, H.; Fujii, Y.; Murase, T.; Fujita, M. Electrophilic Spirocyclization of a 2-Biphenylacetylene via Conformational Fixing within a Hollow-Cage Host. *Angew. Chem. Int. Ed.* **2022**, *61*, e202203970.

(67) Yoshizawa, M.; Tamura, M.; Fujita, M. Diels-Alder in Aqueous Molecular Hosts: Unusual Regioselectivity and Efficient Catalysis. *Science* **2006**, *312*, 251–254.

(68) Martín Díaz, A. E.; Lewis, J. E. M. Structural Flexibility in Metal-Organic Cages. *Front. Chem.* **2021**, *9*, 706462.

(69) Meng, W.; Clegg, J. K.; Thoburn, J. D.; Nitschke, J. R. Controlling the Transmission of Stereochemical Information through Space in Terphenyl-Edged Fe_4L_6 Cages. *J. Am. Chem. Soc.* **2011**, *133*, 13652–13660.

(70) Kieffer, M.; Pilgrim, B. S.; Ronson, T. K.; Roberts, D. A.; Aleksanyan, M.; Nitschke, J. R. Perfluorinated Ligands Induce Meridional Metal Stereochemistry to Generate M_8L_{12}, $M_{10}L_{15}$, and $M_{12}L_{18}$ Prisms. *J. Am. Chem. Soc.* **2016**, *138*, 6813–6821.

(71) Meng, W.; Ronson, T. K.; Nitschke, J. R. Symmetry Breaking in Self-Assembled M_4L_6 Cage Complexes. *Proc. Natl. Acad. Sci. U. S. A.* **2013**, *110*, 10531–10535.

(72) Ehnbom, A.; Ghosh, S. K.; Lewis, K. G.; Gladysz, J. A. Octahedral Werner Complexes with Substituted Ethylenediamine Ligands: A Stereochemical Primer for a Historic Series of Compounds Now Emerging as a Modern Family of Catalysts. *Chem. Soc. Rev.* **2016**, *45*, 6799–6811.

(73) Mal, P.; Breiner, B.; Rissanen, K.; Nitschke, J. R. White Phosphorus Is Air-Stable within a Self-Assembled Tetrahedral Capsule. *Science* **2009**, *324*, 1697–1699.

(74) Xu, L.; Zhang, D.; Ronson, T. K.; Nitschke, J. R. Improved Acid Resistance of a Metal-Organic Cage Enables Cargo Release and Exchange between Hosts. *Angew. Chem. Int. Ed.* **2020**, *59*, 7435–7438.

(75) Rizzuto, F. J.; Von krbek, L. K. S.; Nitschke, J. R. Strategies for Binding Multiple

Guests in Metal-Organic Cages. *Nat. Rev. Chem*. **2019**, *3*, 204–222.

(76) Hof, F.; Craig, S. L.; Nuckolls, C.; Rebek, J., Jr. Molecular Encapsulation. *Angew. Chem*. *Int. Ed.* **2002**, *41*, 1488–1508.

(77) Mal, P.; Schultz, D.; Beyeh, K.; Rissanen, K.; Nitschke, J. R. An Unlockable-Relockable Iron Cage by Subcomponent Self-Assembly. *Angew*. *Chem*. *Int. Ed.* **2008**, *47*, 8297–8301.

(78) Brynn Hibbert, D.; Thordarson, P. The Death of the Job Plot, Transparency, Open Science and Online Tools, Uncertainty Estimation Methods and Other Developments in Supramolecular Chemistry Data Analysis. *Chem*. *Commun*. **2016**, *52*, 12792–12805.

(79) Ronson, T. K.; Giri, C.; Beyeh, N. K.; Minkkinen, A.; Topić, F.; Holstein, J. J.; Rissanen, K.; Nitschke, J. R. Size-Selective Encapsulation of Hydrophobic Guests by Self-Assembled M_4L_6 Cobalt and Nickel Cages. *Chem*. *Eur. J.* **2013**, *19*, 3374–3382.

(80) Ferguson, A.; Staniland, R. W.; Fitchett, C. M.; Squire, M. A.; Williamson, B. E.; Kruger, P. E. Variation of Guest Selectivity within $[Fe_4L_4]^{8+}$ Tetrahedral Cages through Subtle Modification of the Face-Capping Ligand. *Dalton Trans.* **2014**, *43*, 14550–14553.

(81) Lewis, J. E. M.; Gavey, E. L.; Cameron, S. A.; Crowley, J. D. Stimuli-Responsive Pd_2L_4 Metallosupramolecular Cages: Towards Targeted Cisplatin Drug Delivery. *Chem*. *Sci.* **2012**, *3*, 778–784.

(82) Zhang, D.; Ronson, T. K.; Lavendomme, R.; Nitschke, J. R. Selective Separation of Polyaromatic Hydrocarbons by Phase Transfer of Coordination Cages. *J. Am. Chem*. *Soc.* **2019**, *141*, 18949–18953.

(83) Lu, Z.; Ronson, T. K.; Heard, A. W.; Feldmann, S.; Vanthuyne, N.; Martinez, A.; Nitschke, J. R. Enantioselective Fullerene Functionalization through Stereochemical Information Transfer from a Self-Assembled Cage. *Nat. Chem.* **2022**, *15*, 405–412.

(84) Chen, J.; Rebek, J., Jr. Selectivity in an Encapsulated Cycloaddition Reaction. *Org. Lett.* **2002**, *4*, 327–329.

(85) Sawada, T.; Fujita, M. A Single Watson-Crick G x C Base Pair in Water: Aqueous Hydrogen Bonds in Hydrophobic Cavities. *J. Am*. *Chem*. *Soc.* **2010**, *132*, 7194–7201.

(86) Hastings, C. J.; Pluth, M. D.; Bergman, R. G.; Raymond, K. N. Enzymelike Catalysis of the Nazarov Cyclization by Supramolecular Encapsulation. *J. Am. Chem. Soc.* **2010**, *132*, 6938–6940.

(87) Stuhlmann, F.; Jäschke, A. Characterization of an RNA Active Site: Interactions between a Diels-Alderase Ribozyme and Its Substrates and Products. *J. Am. Chem. Soc.* **2002**, *124*, 3238–3244.

(88) Nishioka, Y.; Yamaguchi, T.; Kawano, M.; Fujita, M. Asymmetric [2 + 2] Olefin Cross Photoaddition in a Self-Assembled Host with Remote Chiral Auxiliaries. *J. Am. Chem. Soc.* **2008**, *130*, 8160–8161.

(89) Murase, T.; Nishijima, Y.; Fujita, M. Cage-Catalyzed Knoevenagel Condensation under Neutral Conditions in Water. *J. Am. Chem. Soc.* **2012**, *134*, 162–164.

(90) Davis, A. V.; Fiedler, D.; Seeber, G.; Zahl, A.; van Eldik, R.; Raymond, K. N. Guest Exchange Dynamics in an M_4L_6 Tetrahedral Host. *J. Am. Chem. Soc.* **2006**, *128*, 1324–1333.

(91) Davis, A. V.; Raymond, K. N. The Big Squeeze: Guest Exchange in an M_4L_6 Supramolecular Host. *J. Am. Chem. Soc.* **2005**, *127*, 7912–7919.

(92) Zhao, C.; Sun, Q.-F.; Hart-Cooper, W. M.; DiPasquale, A. G.; Toste, F. D.; Bergman, R. G.; Raymond, K. N. Chiral Amide Directed Assembly of a Diastereo- and Enantiopure Supramolecular Host and Its Application to Enantioselective Catalysis of Neutral Substrates. *J. Am. Chem. Soc.* **2013**, *135*, 18802–18805.

(93) Fiedler, D.; Bergman, R. G.; Raymond, K. N. Supramolecular Catalysis of a Unimolecular Transformation: Aza-Cope Rearrangement within a Self-Assembled Host. *Angew. Chem. Int. Ed.* **2004**, *43*, 6748–6751.

(94) Zhao, C.; Toste, F. D.; Raymond, K. N.; Bergman, R. G. Nucleophilic Substitution Catalyzed by a Supramolecular Cavity Proceeds with Retention of Absolute Stereochemistry. *J. Am. Chem. Soc.* **2014**, *136*, 14409–14412.

(95) Pluth, M. D.; Bergman, R. G.; Raymond, K. N. Acid Catalysis in Basic Solution: A Supramolecular Host Promotes Orthoformate Hydrolysis. *Science* **2007**, *316*, 85–88.

(96) Pluth, M. D.; Bergman, R. G.; Raymond, K. N. Making Amines Strong Bases: Thermodynamic Stabilization of Protonated Guests in a Highly-Charged Supramolecular Host. *J. Am. Chem. Soc.* **2007**, *129*, 11459–11467.

(97) Skouta, R.; Wei, S.; Breslow, R. High Rates and Substrate Selectivities in Water

by Polyvinylimidazoles as Transaminase Enzyme Mimics with Hydrophobically Bound Pyridoxamine Derivatives as Coenzyme Mimics. *J. Am. Chem. Soc.* **2009**, *131*, 15604–15605.

(98) Marinescu, L. G.; Bols, M. Very High Rate Enhancement of Benzyl Alcohol Oxidation by an Artificial Enzyme. *Angew. Chem. Int. Ed.* **2006**, *45*, 4590–4593.

(99) Mock, W. L.; Irra, T. A.; Wepsiec, J. P.; Adhya, M. Catalysis by Cucurbituril. The Significance of Bound-Substrate Destabilization for Induced Triazole Formation. *J. Org. Chem.* **1989**, *54*, 5302–5308.

(100) Leung, D. H.; Fiedler, D.; Bergman, R. G.; Raymond, K. N. Selective C-H Bond Activation by a Supramolecular Host-Guest Assembly. *Angew. Chem. Int. Ed.* **2004**, *43*, 963–966.

(101) Leung, D. H.; Bergman, R. G.; Raymond, K. N. Scope and Mechanism of the C-H Bond Activation Reactivity within a Supramolecular Host by an Iridium Guest: A Stepwise Ion Pair Guest Dissociation Mechanism. *J. Am. Chem. Soc.* **2006**, *128*, 9781–9797.

(102) Wang, Z. J.; Brown, C. J.; Bergman, R. G.; Raymond, K. N.; Toste, F. D. Hydroalkoxylation Catalyzed by a Gold(I) Complex Encapsulated in a Supramolecular Host. *J. Am. Chem. Soc.* **2011**, *133*, 7358–7360.

(103) Leung, D. H.; Bergman, R. G.; Raymond, K. N. Highly Selective Supramolecular Catalyzed Allylic Alcohol Isomerization. *J. Am. Chem. Soc.* **2007**, *129*, 2746–2747.

(104) Bierschenk, S. M.; Bergman, R. G.; Raymond, K. N.; Toste, F. D. A Nanovessel-Catalyzed Three-Component Aza-Darzens Reaction. *J. Am. Chem. Soc.* **2020**, *142*, 733–737.

(105) Pluth, M. D.; Bergman, R. G.; Raymond, K. N. Catalytic Deprotection of Acetals in Basic Solution with a Self-Assembled Supramolecular "Nanozyme." *Angew. Chem. Int. Ed.* **2007**, *46*, 8587–8589.

(106) Yoshizawa, M.; Miyagi, S.; Kawano, M.; Ishiguro, K.; Fujita, M. Alkane Oxidation via Photochemical Excitation of a Self-Assembled Molecular Cage. *J. Am. Chem. Soc.* **2004**, *126*, 9172–9173.

(107) Whitehead, M.; Turega, S.; Stephenson, A.; Hunter, C. A.; Ward, M. D. Quantification of Solvent Effects on Molecular Recognition in Polyhedral Coordination Cage Hosts. *Chem. Sci.* **2013**, *4*, 2744–2751.

(108) Cullen, W.; Turega, S.; Hunter, C. A.; Ward, M. D. pH-Dependent Binding of

Guests in the Cavity of a Polyhedral Coordination Cage: Reversible Uptake and Release of Drug Molecules. *Chem. Sci.* **2015**, *6*, 625–631.

(109) Turega, S.; Cullen, W.; Whitehead, M.; Hunter, C. A.; Ward, M. D. Mapping the Internal Recognition Surface of an Octanuclear Coordination Cage Using Guest Libraries. *J. Am. Chem. Soc.* **2014**, *136*, 8475–8483.

(110) Cullen, W.; Misuraca, M. C.; Hunter, C. A.; Williams, N. H.; Ward, M. D. Highly Efficient Catalysis of the Kemp Elimination in the Cavity of a Cubic Coordination Cage. *Nat. Chem.* **2016**, *8*, 231–236.

(111) Ludden, M. D.; Taylor, C. G. P.; Tipping, M. B.; Train, J. S.; Williams, N. H.; Dorrat, J. C.; Tuck, K. L.; Ward, M. D. Interaction of Anions with the Surface of a Coordination Cage in Aqueous Solution Probed by Their Effect on a Cage-Catalysed Kemp Elimination. *Chem. Sci.* **2021**, *12*, 14781–14791.

(112) Cullen, W.; Metherell, A. J.; Wragg, A. B.; Taylor, C. G. P.; Williams, N. H.; Ward, M. D. Catalysis in a Cationic Coordination Cage Using a Cavity-Bound Guest and Surface-Bound Anions: Inhibition, Activation, and Autocatalysis. *J. Am. Chem. Soc.* **2018**, *140*, 2821–2828.

(113) Banerjee, R.; Ragsdale, S. W. The Many Faces of Vitamin B12: Catalysis by Cobalamin-Dependent Enzymes. *Annu. Rev. Biochem.* **2003**, *72*, 209–247.

(114) Wang, Q.-Q.; Gonell, S.; Leenders, S. H. A. M.; Dürr, M.; Ivanović-Burmazović, I.; Reek, J. N. H. Self-Assembled Nanospheres with Multiple Endohedral Binding Sites Pre-Organize Catalysts and Substrates for Highly Efficient Reactions. *Nat. Chem.* **2016**, *8*, 225–230.

(115) Holloway, L. R.; Bogie, P. M.; Lyon, Y.; Ngai, C.; Miller, T. F.; Julian, R. R.; Hooley, R. J. Tandem Reactivity of a Self-Assembled Cage Catalyst with Endohedral Acid Groups. *J. Am. Chem. Soc.* **2018**, *140*, 8078–8081.

(116) Ngai, C.; Bogie, P. M.; Holloway, L. R.; Dietz, P. C.; Mueller, L. J.; Hooley, R. J. Cofactor-Mediated Nucleophilic Substitution Catalyzed by a Self-Assembled Holoenzyme Mimic. *J. Org. Chem.* **2019**, *84*, 12000–12008.

(117) Gramage-Doria, R.; Hessels, J.; Leenders, S. H. A. M.; Tröppner, O.; Dürr, M.; Ivanović-Burmazović, I.; Reek, J. N. H. Gold(I) Catalysis at Extreme Concentrations inside Self-Assembled Nanospheres. *Angew. Chem. Int. Ed.* **2014**, *53*, 13380–13384.

(118) Ueda, Y.; Ito, H.; Fujita, D.; Fujita, M. Permeable Self-Assembled Molecular Containers for Catalyst Isolation Enabling Two-Step Cascade Reactions. *J. Am.*

Chem. Soc. **2017**, *139*, 6090–6093.

(119) Johnson, A. M.; Hooley, R. J. Steric Effects Control Self-Sorting in Self-Assembled Clusters. *Inorg. Chem.* **2011**, *50*, 4671–4673.

(120) Young, M. C.; Johnson, A. M.; Gamboa, A. S.; Hooley, R. J. Achiral Endohedral Functionality Provides Stereochemical Control in Fe(II)-Based Self-Assemblies. *Chem. Commun.* **2013**, *49*, 1627–1629.

(121) Johnson, A. M.; Young, M. C.; Zhang, X.; Julian, R. R.; Hooley, R. J. Cooperative Thermodynamic Control of Selectivity in the Self-Assembly of Rare Earth Metal-Ligand Helices. *J. Am. Chem. Soc.* **2013**, *135*, 17723–17726.

(122) Young, M. C.; Johnson, A. M.; Hooley, R. J. Self-Promoted Post-Synthetic Modification of Metal–Ligand M_2L_3 Mesocates. *Chem. Commun.* **2014**, *50*, 1378–1380.

(123) Ngai, C.; Wu, H.-T.; da Camara, B.; Williams, C. G.; Mueller, L. J.; Julian, R. R.; Hooley, R. J. Moderated Basicity of Endohedral Amine Groups in an Octa-Cationic Self-Assembled Cage. *Angew. Chem. Int. Ed.* **2022**, *61*, e202117011.

(124) Ngai, C.; da Camara, B.; Woods, C. Z.; Hooley, R. J. Size- and Shape-Selective Catalysis with a Functionalized Self-Assembled Cage Host. *J. Org. Chem.* **2021**, *86*, 12862–12871.

(125) Ngai, C.; Sanchez-Marsetti, C. M.; Harman, W. H.; Hooley, R. J. Supramolecular Catalysis of the Oxa-Pictet-Spengler Reaction with an Endohedrally Functionalized Self-Assembled Cage Complex. *Angew. Chem. Int. Ed.* **2020**, *59*, 23505–23509.

(126) Bogie, P. M.; Holloway, L. R.; Ngai, C.; Miller, T. F.; Grewal, D. K.; Hooley, R. J. A Self-Assembled Cage with Endohedral Acid Groups Both Catalyzes Substitution Reactions and Controls Their Molecularity. *Chem. Eur. J.* **2019**, *25*, 10232–10238.

Chapter 2 - Catalytic Inhibition of Base Mediated Processes by a Self-Assembled Cage Host

2.1. Introduction

Certain hosts are capable of binding multiple species within the interior cavity which has allowed the mimicry of cofactor-mediated enzymatic catalysis.[1] The most common strategy for achieving this is using large nanospheres or resorcinarene hexamers that have internal cavity volumes of greater than 1300 Å^3. These large assemblies mediate many types of reactions such as gold-catalyzed cyclizations,[1] iminium-catalyzed conjugate additions,[2] and carbonyl-olefin metatheses.[3] Alternatively, smaller cages can also employ reactive species such as OH^- sequestered around the hosts ligand edges to facilitate base-catalyzed transformations.[4–6] Previous work from our group has demonstrated that a hollow Fe_4L_6 self-assembled cage (**1.50**), colloquially called the fluorene cage, is capable of acting as a holoenzyme mimic for the thioetherification of triphenylmethanol.[7] The following chapter is focused on using the fluorene cage for analogous base-mediated processes.

2.2. Molecular Recognition of Unfunctionalized Fluorenyl Self-Assembled Cage

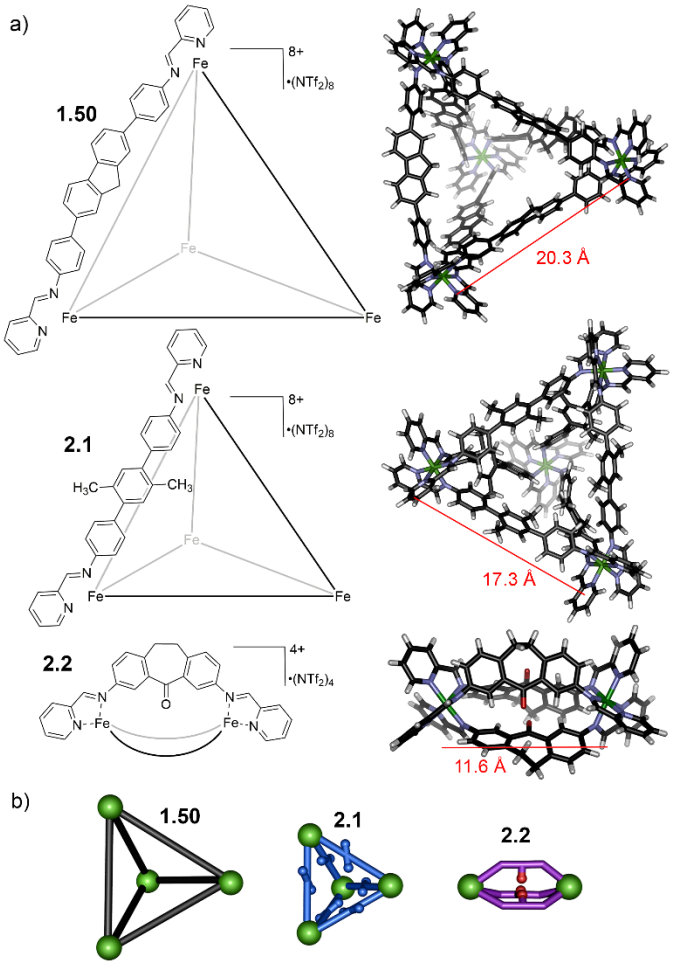

Figure 2.1. a) Cage structures and AM1 forcefield energy minimized models of cages; b) cartoons of supramolecular structures.

The spacious unfunctionalized fluorene cage, **1.50**, possesses a cavity volume of 572 $Å^3$ and large panel gaps that stretch 20 Å across between each metal vertex.[8] In solution the cavity is filled with, at most, 11 molecules of MeCN (50.5 $Å^3$) or 8 molecules of MeCN and plus one molecule of NTf_2^- (144 $Å^3$), although other variations could be possible. The solvent molecules and NTf_2^- anion exchange faster than the NMR time scales of their respective nuclei, 0.2 s – 0.4 ms for ^1H and 0.2 s – 13 µs for ^{19}F.[9] Thus the exchange of

acetonitrile solvent molecules and NTf_2^- anion(s) is not observable *via* NMR spectroscopy. As the cage interior is large the binding of multiple guests within the cavity is possible. The addition of cage **1.50** to solutions containing neutral polar organic molecules in CD_3CN created small perturbations in both the cage's and guests' ^1H NMR resonances. This was surprising as it is uncommon that self-assembled cages of this size can bind organic substrates without exploiting hydrophobic or Coulombic driving forces.[10,11] These small perturbations most likely resulted from binding interactions, but they were not significant enough to determine binding affinities or modes of guests. The detection of these slight variations in the magnetic resonances in the ^1H NMR spectra served as an early indication of the fluorene cage's capacity for molecular recognition.

UV-Vis titrations have been a vital tool for investigating the molecular recognition properties of cage **1.50**. Sophisticated mathematical algorithms have been employed to rigorously analyze the variations in absorbance of the UV signature of the fluorene cage during titrations[12,13]. These algorithms calculate the binding affinity, K_a, by relating the changes in absorbance at two points to determine the following quantities: [HG], [H], and [G] as a function of added guest. These values are then used to calculate K_a. Furthermore, by modeling the binding isotherms using 1:1 and 1:2 binding models and assessing their fit, it becomes possible to determine if the most favorable binding stoichiometry is 1:1 or 1:2. By determining the binding behavior of guests within the fluorene cage, this analysis becomes a powerful tool for explaining and designing biomimetic catalytic reactions. From these studies it was determined that the fluorene cage, **1.50**, shows high affinity (K_a = 50 – 100 x 10^3 M^1) for neutral, polar substrates such as anthroic acid and alkanethiols in CH_3CN,

but shows minimal affinity for neutral organic molecules that possess no polar groups, such as adamantane (Figure 2.1).[7,14] The driving force for binding arises from entropically favorable displacement of solvent molecules into solution. As well as favorable CH-π or π-π interactions between the ligand edges of the self-assembled cage structure and guest molecules. The cage can bind large organic substrates such as triphenylmethanol, which has a molecular volume of 264 $Å^3$ (Figure 2.2). The binding of guest(s) that exceeds the fluorene cage's cavity volume is not impossible, and can occur if portions of the guest sufficiently extend out of the fluorene cage's large panels. Cage **1.50** does not possess high selectivity for a specific subset of molecules and can bind multiple substrates simultaneously. This lack of selectivity and ability to form homo and hetero-ternary complexes is crucial for its capability to act as a holoenzyme mimic, and favorably affects the activation, transformation, and release of organic molecules.

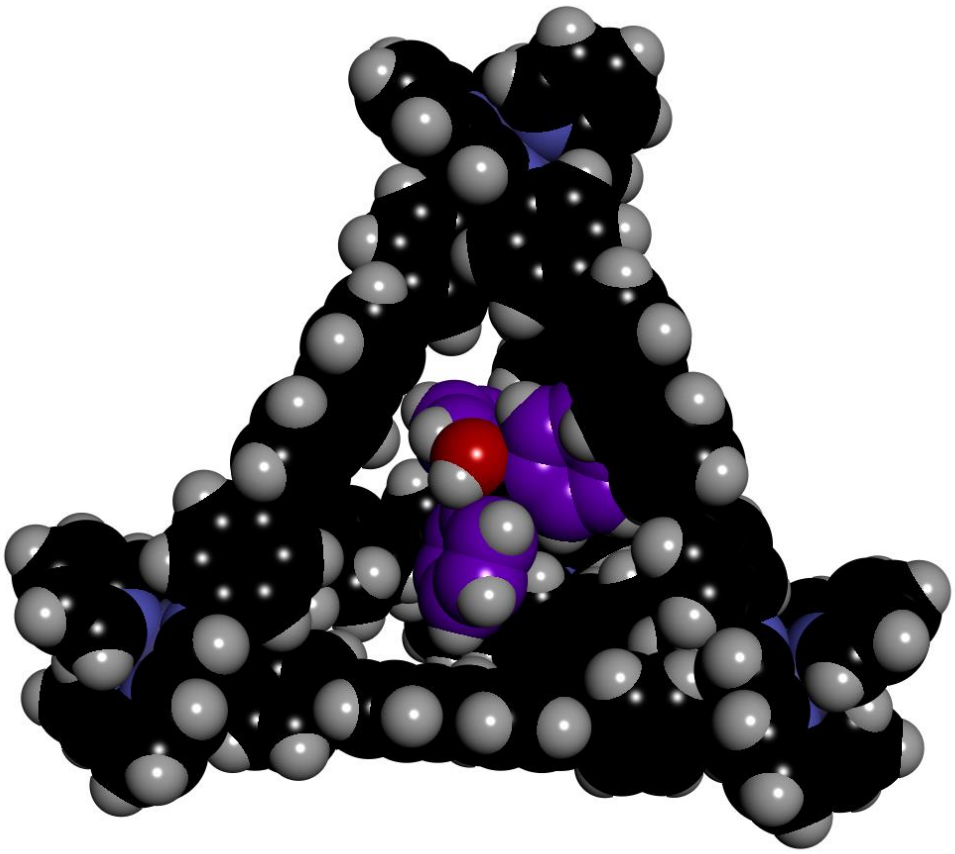

Figure 2.2. Spartan energy minimized molecular model of *S*$_4$-**1.50**•triphenylmethanol, triphenylmethanol carbons are highlighted in purple for clarity (Hartree-Fock).

2.3. A Self-Assembled Cage Catalytically Inhibits a Conjugate Addition

As **1.50** acts as holoenzyme mimic for the thioetherification of triphenylmethanol, an acid-catalyzed S_N1 reaction, the logical next step was to explore its effect on base-mediated reactions. The initial tests were simple, and we asked the question: What is the effect on the base catalyzed conjugate addition of ethylcyanoacetate and β-nitrostyrene in the presence of the fluorene cage, **1.50**? Due to the sensitivity of the fluorene cage to different tertiary amines, caution was exercised in identifying a suitable base catalyst for mediating the conjugate addition without causing cage degradation. Glutarimide catalyst **2.3** and the bifunctional thiourea catalyst **2.5** (see Figure 2.3) were synthesized as they are large enough

to bind in the fluorene cage, do not cause appreciable cage decomposition, and should be able to catalyze base mediated conjugate addition. It was expected that **2.3** and **2.5** are sufficiently large and will favorably bind in the cavity of the fluorene cage. While bound, the glutarimide and thiourea catalyst will leave ample space within the cavity of the fluorene cage for other reaction components to bind simultaneously. The concurrent binding of the base catalyst, electrophile, and nucleophile was anticipated to result in enhanced reaction rates and the possibility of size selectivity, as these phenomena were previously observed in the thioetherification of triphenylmethanol.

The reaction outcomes were unexpected. In the presence of 5 % fluorene cage and 30 % glutarimide catalyst, the reaction was catalytically inhibited, yielding 8 % after 24 h. When the reaction was repeated in the absence of fluorene cage, the reaction proceeded smoothly, with 72 % conversion after 24 h (Figure 2.3).These experiments were repeated with the bifunctional thiourea catalyst, **2.5**, and the results were like the outcomes of using the glutarimide cofactor, but the inhibition effect was less pronounced. In the presence of the fluorene cage the bifunctional thiourea catalyst produced the addition product in 6 % yield and without the fluorene cage gave 60 % of the addition product. In attempts to counteract the inhibition, a stronger base catalyst was employed 1,8-bis(dimethylamino)naphthalene, otherwise known as the proton sponge.[15] Using the more basic proton sponge the inhibition effect was even more pronounced. When 15 % proton sponge was used, in the absence of cage, 80 % conversion was observed after only 75 mins at ambient temperature, but in the presence of 5 % fluorene cage, less than 1 % of the addition product was observed.

To validate that this catalytic inhibition of the conjugate addition was due to the fluorene cage's molecular recognition properties, these conjugate additions were repeated with other self-assembled structures. Structurally similar xylene cage **2.1** features a smaller cavity with an internal volume of 252 $Å^3$ compared to cage **1.50**. The xylene cage exhibits significantly weaker binding affinity towards guests in comparison to its larger fluorene cage counterpart, which is discussed in greater detail in chapter 3. These differences in size and binding strength highlight the distinct characteristics and capabilities of these two self-assembled cages. Helicate **2.2** possesses no cavity and has never been observed to bind any type of guest molecule. Repeating the conjugate addition with the glutarimide (**2.3**) and proton sponge (**2.4**) catalysts, some small inhibition effects were observed in the presence of the smaller tetrahedron **2.1** and the helicate **2.2** (Figure 2.3). The Fe_4L_6 xylene cage (**2.1**) reduced the % conversions to 43 % and 44 % when cofactors **2.3** and **2.5** were used, respectively. Similarly, suberone helicate **2.2** reduced the % conversions to 67 % and 42 % when cofactors **2.3** and **2.5** were used, respectively. As the reaction conditions were identical in all scenarios, clearly the molecular recognition capacity of the fluorene cage is the cause of the catalytic inhibition.

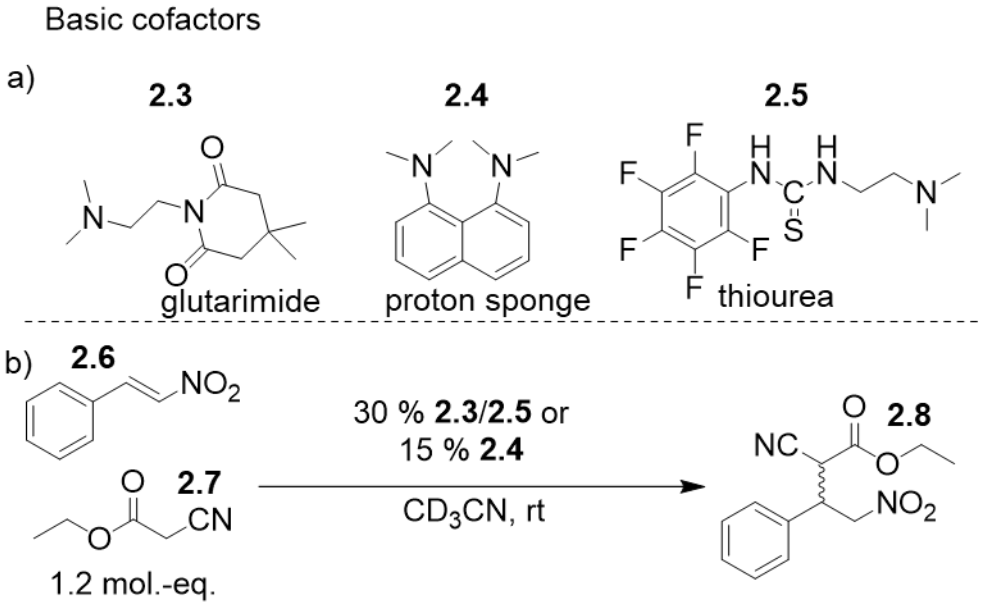

c)

Cofactor	Cage	t (mins)	% conversion
2.3	No cage	1,440	72
2.3	5 % **2.2**	1,440	67
2.3	5 % **2.1**	1,440	43
2.3	5 % **1.50**	1,440	8
2.4	No cage	75	80
2.4	5 % **2.2**	69	42
2.4	5 % **2.1**	74	44
2.4	5 % **1.50**	62	0.5
2.5	No cage	1,440	60
2.5	5 % **1.50**	1,440	6

Figure 2.3. a) Molecules containing basic functional groups to be used as cofactors; b) reaction scheme for conjugate addition; c) % conversion for different combinations of cofactors and cages. [**1.50**/**2.1**/**2.2**] = 1 mM, [**2.6**] = 20 mM, [**2.7**] = 24 mM, [**2.3** or **2.4**] = 6 mM, [**2.4**] = 3 mM, CD_3CN, 298 K.

The catalytic inhibition effect of the fluorene cage is surprising and could be caused by multiple factors. The most immediate hypothesis is that the fluorene cage is sequestering the base catalyst from the reaction solution. There is certainly "enough space" in the

fluorene cage cavity to bind three molecules of proton sponge per molecule of fluorene cage. This stoichiometry though is likely highly unfavorable and there is no evidence to suggest that it is possible. The sequestration of 6 molecules of either the glutarimide or bifunctional thiourea catalyst is not physically possible, the fluorene cage cavity is too small for this stoichiometry. The fluorene cage's ability to bind various polar neutral species with comparable affinities and rapid ingress/egress lends itself to its effectiveness as a host for acid-mediated reactions. Consequently, binding only the base should not significantly impede the reaction, as any guest can freely exit and enter the host.

The next most reasonable proposition for inhibiting a base mediated reaction is quenching of the base catalyst by acidic protons. The only source of acidic protons in the reaction media is H_2O. Upon this realization closer attention was paid to the water peak in the ^1H NMR spectra for the conjugate addition reactions and it was observed that there was significant broadening in the presence of **1.50**. This is typical with charged species, but the broadening was much more significant than what had been observed in previous studies. It was decided the first step to illuminating the cause of the inhibition mechanism was to study the effects of the supramolecular cages **1.50**, **2.1** and **2.2** had on cofactors **2.3** and **2.4** and whether the cofactors were basic enough to self-protonate in CD_3CN.

The ^1H NMR spectrum of the cage complex **1.50•2.3** showed clear evidence of *protonation* in solution with cage **1.50**. Exogenous water is obviously the proton source and is clearly being made more acidic in the presence of **1.50**. To further substantiate that this is indeed due to the selective molecular recognition of fluorene cage **1.50**, ^1H NMR

spectra of the glutarimide and proton sponge are shown in a variety of environments (Figure 2.4). The triplet corresponding to the CH_2^b of the glutarimide cofactor **2.3** appears at δ 2.35 ppm, whereas for the fully protonated HCl salt, **2.3**H^+, peaks are shifted downfield to δ 3.22 ppm. In the presence of cage **1.50** in wet CD_3CN, the CH_2^b triplet in the free base **2.3** shifts downfield to δ 3.11 ppm. This shift is not due to encapsulation of the cofactor in the cavity of cage **1.50**, as the peripheral geminal methyls' chemical shifts do not change. This effect is present with the xylene cage and suberone helicate but to a much lesser extent. Importantly, when anhydrous CD_3CN is employed the chemical shift of the CH_2^b protons are more up field and are almost identical in their chemical shift to the glutarimide cofactor in solution by itself. These results conclusively demonstrate that exogenous water in solution is being made more acidic in the confines of the fluorene cage's cavity. This is verified by the fact that when water is removed from solution the equilibrium is more favored towards the free base as demonstrated by the chemical shift of CH_2^b of the glutarimide cofactor. Furthermore, the presence of a small, broad peak at δ 4.28 ppm corresponding to NH^+ in the 2D NOESY spectrum (Figure 2.5) indicates chemical exchange peaks with the broadened H_2O peak. This observation verifies that in solution with the fluorene cage the glutarimide base catalyst is protonated by water in CD_3CN. These experiments were then repeated with the proton sponge (**2.4**), where the changes in the protonation state in various environments are similar to that seen with the glutarimide cofactor. The exchange rate of the protons for the glutarimide catalyst and proton sponge are different, though. For the glutarimide catalyst the exchange is fast on the NMR timescale and thus the downfield shift is indicative of the averaged position (Figure 2.4).

Whereas with the more basic proton sponge the proton exchange is slow relative to the NMR timescale and so both the protonated and unprotonated species are visible on the ^{1}H NMR spectrum. The fluorene and xylene cage had the most pronounced effect on the protonation state of the proton sponge, where in both cases the **2.4**H^{+} was dominant, while the suberone helicate **2.3** had hardly any effect on the proton sponge's protonation state. In the case of the fluorene cage, when water was removed from solution, the proton sponge's free base was the dominant species, meaning that *water is necessary* to produce the conjugate acid from the free base catalyst. These results corroborate that this unusual catalytic inhibitory activity is genuinely from the selective molecular recognition of the fluorene cage.

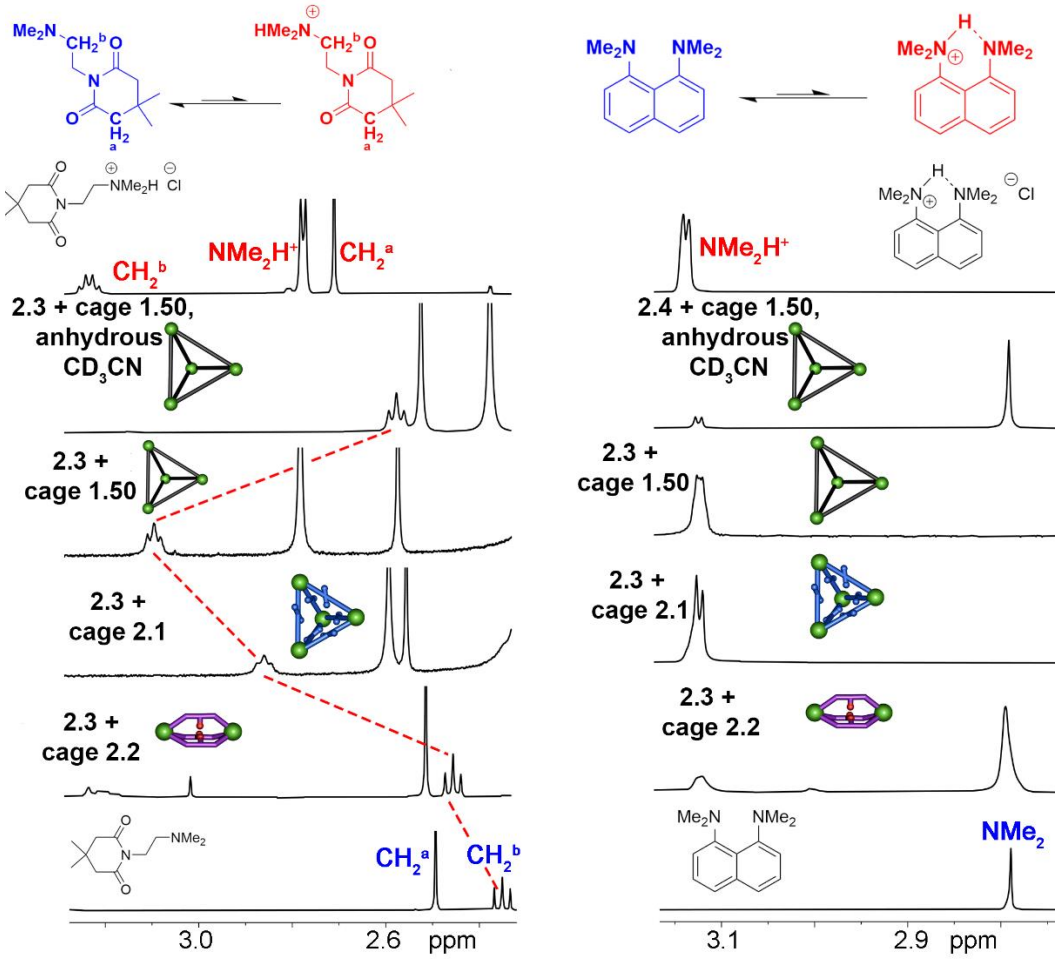

Figure 2.4. ^{1}H NMR spectrum of cofactors 1 mM mixtures of **2.3** and **2.4** + cages **1.50**, **2.1**, and **2.2** in wet CD_3CN and rigorously anhydrous CD_3CN, allowed to sit at room temperature for 24 h before acquisition, CD_3CN, 400 MHz, 298 K). [**1.50**/ **2.1**/**2.2**] = 1.0 mM, [**2.3**] = 1.0 mM, [**2.4**] = 1.0 mM, 24 h, CD_3CN, 298 K.

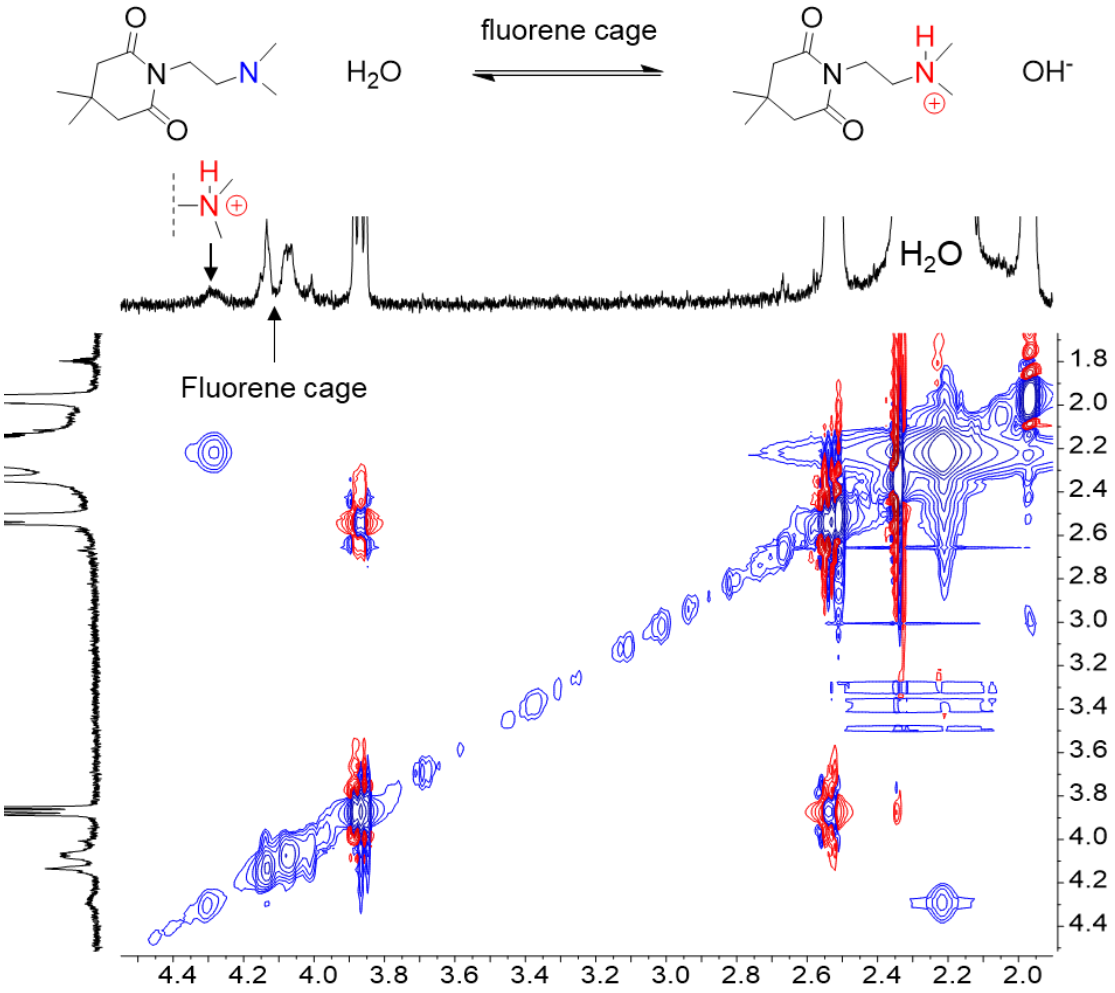

Figure 2.5. gNOESY NMR spectrum of 1.0 mM **1.50** and **2.3** (CD_3CN, 400 MHz, 298 K, mixing time = 300 ms).

To more thoroughly investigate the inhibitory phenomena the reaction kinetics were examined under both anhydrous and wet conditions to definitively confirm that water-induced protonation of the base catalysts, driven by **1.50**, is the root cause of catalytic inhibition. Pseudo-first order rate plots were utilized to analyze the kinetics of the reaction, employing cofactors **2.3** and **2.5** in the presence and absence of cage **1.50**. This analysis was conducted under both dry and wet conditions, providing a comprehensive understanding of water's role in the catalytic inhibition process.

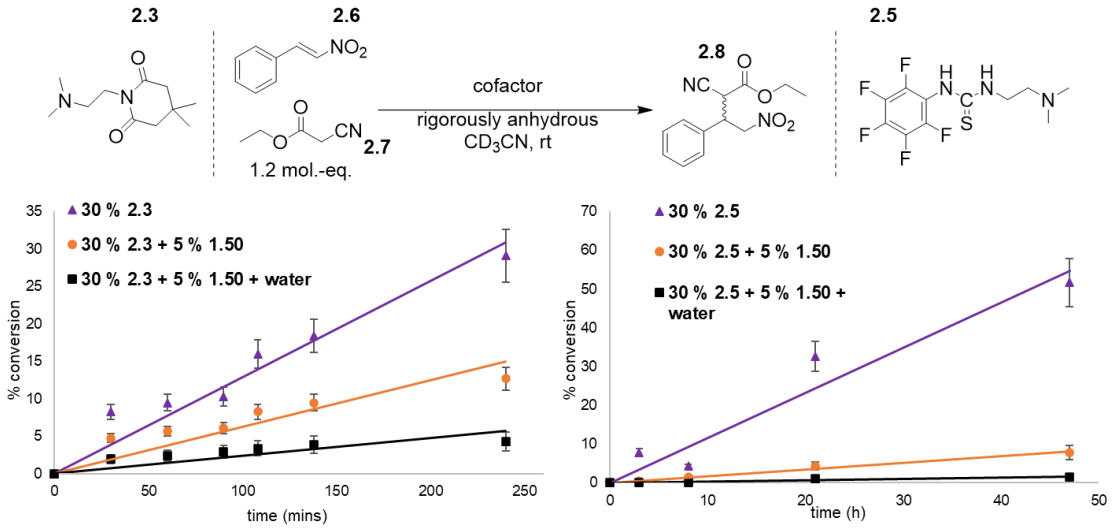

Figure 2.6. Pseudo-first order rate plots for the conjugate of **2.6** and **2.7** to **2.8** using rigorously anhydrous CD_3CN. Under three different conditions: 30 % **2.3** or **2.5**, 30 % **2.3** or **2.5** + 5 % **1.50**, and 30 % **2.3** or **2.5** + 5 % **1.50** + H_2O, [H_2O] = 6 mM. [**1.50**] = 1 mM, [**2.6**] = 20 mM, [**2.7**] = 24 mM, [**2.3**/**2.4**] = 6 mM, CD_3CN, 298 K.

When using glutarimide catalyst **2.3** in the presence of fluorene cage **1.50**, the rate of the reaction was half as fast compared to the no cage reaction under anhydrous conditions (Figure 2.6). When water is added, the rate is ¼ that of the no cage anhydrous control. Clearly, removing water in the reaction mixture when using catalyst **2.3** and cage **1.50** *decreases* the inhibitory effect. The continuation of the inhibition, even when water is removed from the reaction solution, is not completely understood. The ^{1}H NMR spectra revealed no detectable amount of water in the reaction mixture but obviously that does not mean trace amounts were not absorbed from the atmosphere. Moreover, cage **1.50** is produced from a condensation reaction and likely can form adducts with water, thus the addition of fluorene cage to any solution likely results in the addition of small amounts of water to the mixture. Water, in conjunction with the molecular recognition of the fluorene cage, is the cause of the catalytic inhibition. The story is rather different using the bifunctional thiourea catalyst **2.5**. The differences between the anhydrous and water added

reactions using cofactor **2.5** and cage **1.50** are minute. Both are significantly slower compared to when the reaction is studied in the absence of the fluorene cage. Structurally, the major difference between **2.3** and **2.5** is the acidic thiourea protons of **2.5**. Likely, the bifunctional catalyst **2.5** can self-protonate which is enhanced by the fluorene cage cavity, thus the rates of the anhydrous and wet reactions are highly similar. The fluorene cage increases the acidity of water which results in the protonation of cofactors **2.3** – **2.5**. This is the cause of the inhibitory phenomenon and results in moderate to strong rate decelerations of the conjugate addition.

2.4. Mechanistic Analysis of Catalytic Inhibition

All the experimental data thus far supports the hypothesis that in the presence of the fluorene cage 1.50, exogenous water becomes more acidic and protonates nitrogenous base catalysts, in turn this creates OH^-. The two most compelling reasons for this could be that the fluorene cage binds OH^- stronger than H_2O. Alternatively, if the cage binds the conjugate acids stronger than their free base counterparts, this will drive equilibrium to the right (Figure 2.4). In both situations OH^- is created from the deprotonation of water to form the conjugate acid salts.

If OH^- is forming from the deprotonation of water, two questions get raised: why is the cage still intact and why does it not mediate the addition reaction? The ligands that form cage **1.50** are bis-iminopyridines, activated by the Fe^{2+} metallo-vertices. Reasonably any amount of OH^- should hydrolyze the ligand linkages resulting in cage disassembly. Ward has shown a self-assembled Co^{2+}-pyridylpyrazole cube that has OH^- localized around the

cage exterior in water, but the coordinating ligands are not susceptible to hydrolysis in that case, as opposed to the imine-based ligands in **1.50**.[4,6,16,17] What seems likely, given the peculiar circumstances of the catalytic inhibition, is that in the presence of **1.50** amines are favorably protonated, creating OH^- that is sequestered by the cage.

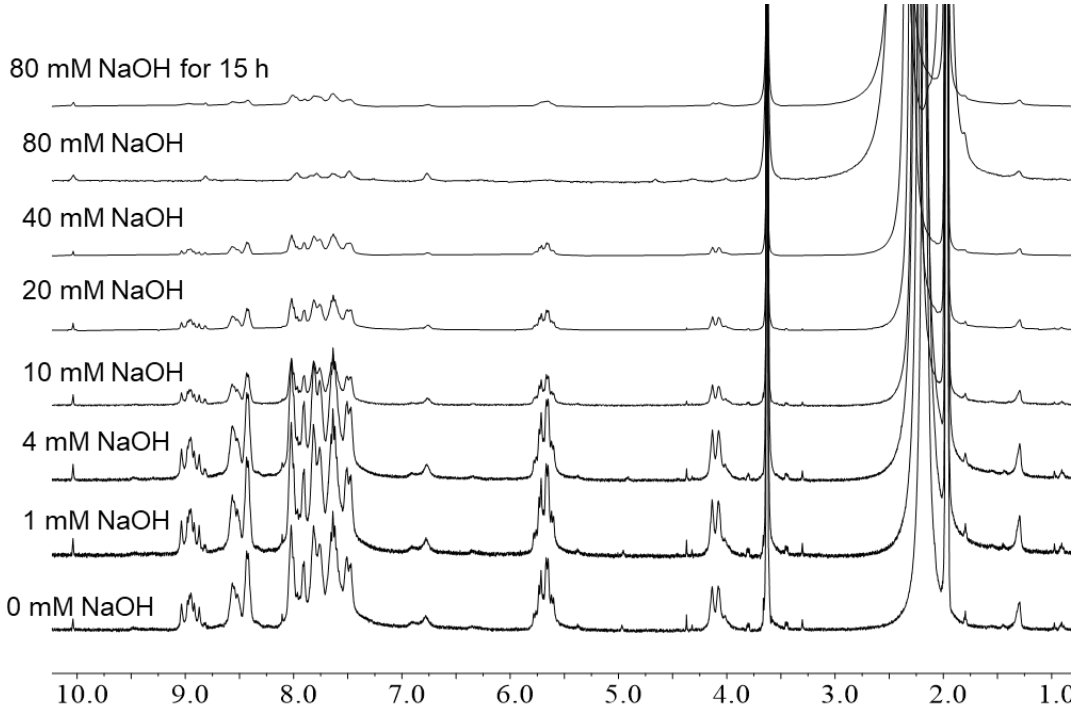

Figure 2.7. ^{1}H NMR NaOH titration into a solution of fluorene cage. [**1.50**] = 1.0 mM, CD_3CN, 298 K.

To begin elucidating the capacity for **1.50** to sequester OH^- from solution, a simple ^{1}H NMR titration was performed (Figure 2.7). If OH^- is formed through the deprotonation of water, the maximum concentration of hydroxide during the addition reactions would be 6 mM, which corresponds to the highest concentration of the cofactor employed in the inhibition experiments. Surprisingly, cage **1.50** is tolerant to the addition of NaOH. Even at 40 mol.-eq. only ~ 10 % of cage decomposition has occurred (Figure 2.7). At 80 mol.-eq. decomposition of **1.50** is more pronounced, where more than half the cage has

disassembled, and over a 15 h period the cage is no longer present in solution. Clearly **1.50** is tolerant to small amounts of OH^- in solution under conditions similar to those seen in the inhibition reactions. This observation provides further support to the hypothesis that hydroxide anions can be effectively sequestered around the ligand edges of the fluorene cage. As a result, these hydroxide anions are not readily available to participate in base-mediated reactions. Therefore, the binding modes and affinities of nitrogenous bases within the cavity of **1.50** become exponentially more complex, as it is a complex mixture of many distinct species in equilibrium. The presence of multiple species in equilibrium with each other adds complexity to extracting the binding and molecular recognition events from UV-Vis titrations.

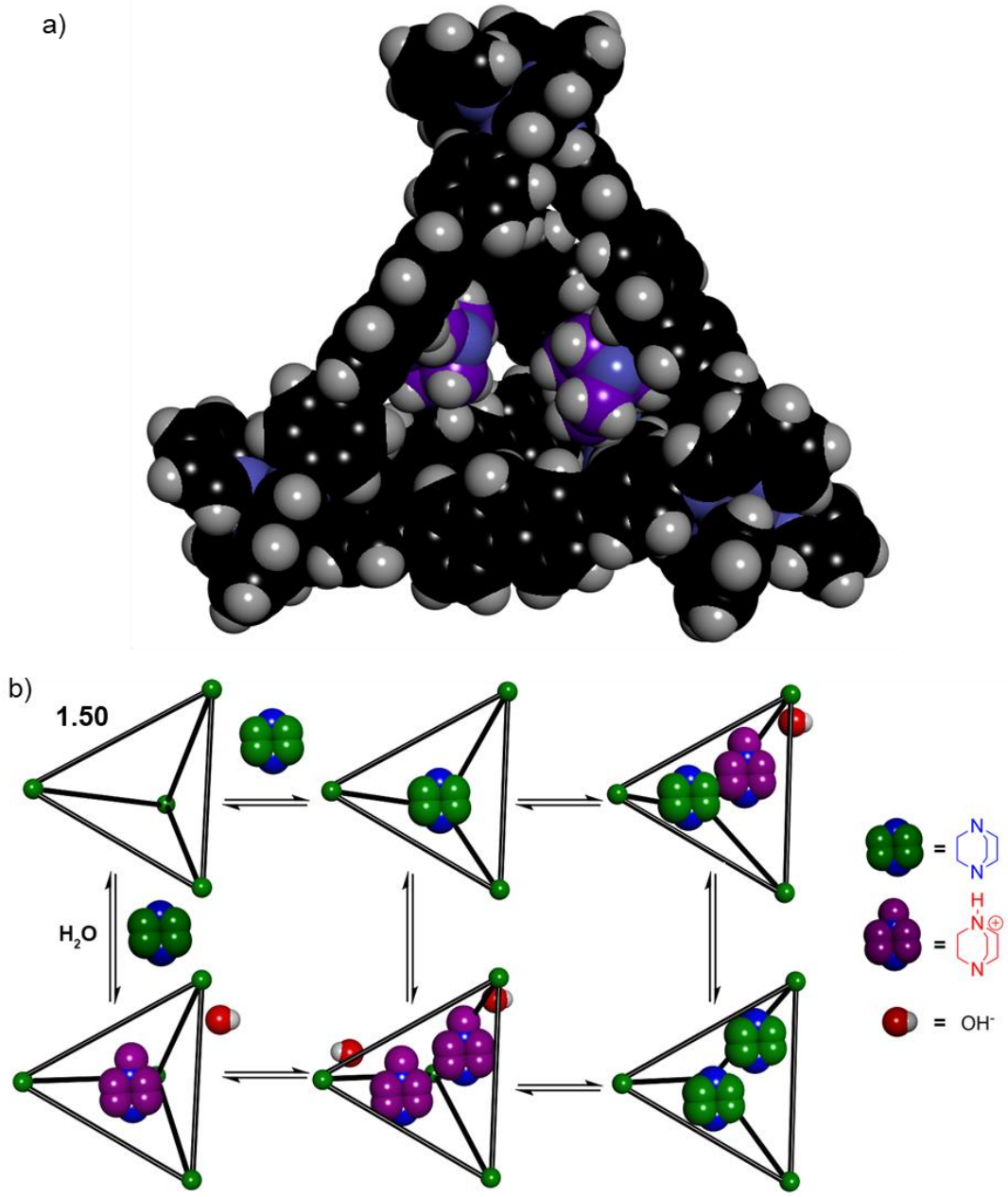

Figure 2.8. a) Spartan energy minimized molecular model of *S*$_4$-**1.50**•(DABCO)$_2$, DABCO carbons highlighted in purple for clarity, demonstrating the spacious cavity of the fluorene cage can bind two molecules of DABCO (Hartree-Fock); b) cartoon of a few possible fluorene cage equilibrium species when DABCO is protonated from deprotonation of exogenous water producing OH^-.

Using UV-Vis binding titrations, it is relatively straightforward to determine the binding affinities and preferred stoichiometries of neutral guests when they do not generate

new guest species in solution. Analyzing the binding of the base catalysts using UV-Vis becomes significantly more challenging because there are numerous species in equilibrium with each other. The base catalyst in solution with H2O and the fluorene cage gives rise to the formation of a new guest species. For example, the deprotonation of water generates hydroxide anions as a new guest species (Figure 2.8b). In addition to the neutral base guest, which can bind to the cage interior as its free base or conjugate acid, there is also the possibility of hydroxide anions being bound to the cage exterior. The presence of these numerous species adds a layer of intricacy to the analysis of binding events in solution. To explore this further, we conducted various tests and analyzed the data using SIVVU to tentatively decipher the contributors to the changes in UV-Vis absorption spectra. To elucidate the binding of guests accurately using SIVVU a collaboration with Professor Douglas A. Vander Griend, the developer of SIVVU, was formed. SIVVU is a mathematical modeling software written in the form of Matlab that uses equilibrium-restricted factor analysis (ERFA) to deconvolute UV-Vis binding titrations of complex equilibria involving multiple chemically distinct species.[18] By extracting the molar absorptivity curves of each species from the UV-Vis binding titration, the concentrations of chemical species can be calculated using the Beer-Lambert law (Figure 2.9a). We chose 1,4,-diazabicyclo[2.2.2]octane (DABCO) as a guest for it is a bicyclic symmetrical nitrogenous base and is a good size and shape for forming ternary complexes with 1.50 (Figure 2.8a). These titrations were performed by Ph.D. candidate Connor Z. Woods. Upon addition of DABCO, the base can bind inside the host in multiple different stoichiometries, or it can be protonated by exogenous water and the resulting products (either hydroxide

anions or DABCO-H+) can be bound, again in different stoichiometries, including homo and hetero-ternary complexes (or higher) (Figure 2.8b).

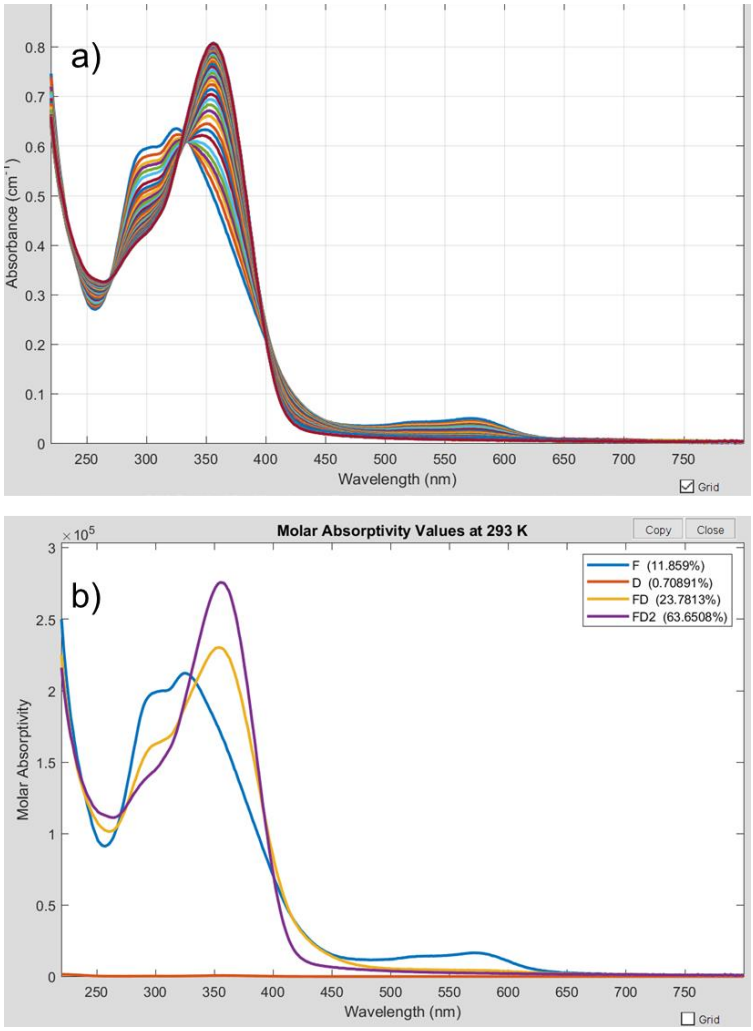

Figure 2.9. a) UV-Vis binding titration of DABCO into a solution of **1.50**, b) molar absorptivity curves for **1.50**, **1.50**•DABCO, and **1.50**•$DABCO_2$ produced by deconvolution using SIVVU on the UV-Vis titration spectrum.

Testing the binding affinities of DABCO and DABCO-H^+ in dry and wet CH_3CN answered two important questions: firstly, does the binding of nitrogenous bases and their conjugate acids change when MeCN is more wet, secondly, does **1.50** bind ammonium salts stronger than their free base counterparts? Titration of DABCO into a dry solution of

1.50 (3 μM **1.50** in acetonitrile) results in easily visualizable changes in absorbance, consistent with binding (Figure 2.9a). It should be noted the process was performed in air, so small amounts of water likely absorbed during the titrations. This process was repeated with DABCO into a solution of "wet" acetonitrile (3 μM **1.50** in acetonitrile with a 0.09 M H_2O). The isosbestic point shifts throughout the titration which is indicative that the solution is composed of many chemically distinct species in equilibrium with each other. This was then repeated with the triflate salt of DABCO-H^+ under identical conditions for both the "dry" and wet variants of the binding experiment. Under "wet" conditions DABCO bound more favorably compared to "dry" conditions, with almost a 1 kcal mol^{-1} greater affinity (Figure 2.10). Clearly water affects the binding of nitrogenous bases by cage **1.50** in acetonitrile, in this case the binding was enhanced, but the actual species contributing to the changes in the UV signature of the fluorene cage are not analyzable, it could be OH^-, DABCO, or DABCO-H^+. In the case of titrant DABCO-H^+, when the solution is "dry", the affinity is higher compared to the free base. One reason for this is other equilibrium states such as the free base of DABCO are less prevalent in the "dry" solution. Importantly, this data confirms that the octacationic fluorene cage **1.50** preferentially binds cationic ammonium salts over their free base counterparts.

Table 2.1. Binding affinities of DABCO and DABCO-H^+ for self-assembled cage **1.50**. [**1.50**] = 3.0 μM, CH_3CN, 298 K.

Guest	$LogK_1$	$LogK_2$
DABCO (dry)	6.1	5.3
DABCO (wet)	7.1	5.9
DABCO-H^+ (dry)	7.4	6.1
DABCO-H^+ (wet)	6.7	5.1

2.5. Moderated Basicity, Knoevenagel Condensations, and Towards Chemoselectivity

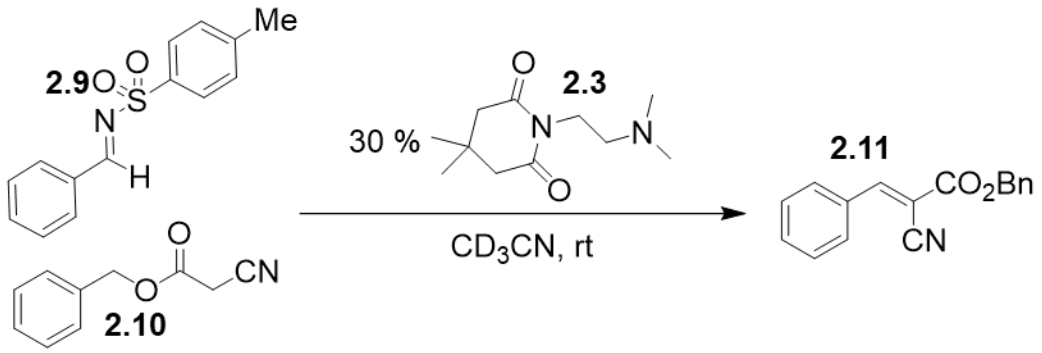

Cage	t (mins)	% conversion
No cage	240	75
5 % suberone helicate (**2.2**)	240	40
5 % xylene cage (**2.1**)	240	28
5 % fluorene cage (**1.50**)	240	24

Figure 2.10. Inhibited formation of Knoevenagel product in the presence and absence of various supramolecular structures.

If a reaction was only partially inhibited, selective molecular recognition by cage **1.50** could result in new types of reactivity that differ significantly from the bulk solution. As the glutarimide cofactor **2.3** was not fully protonated by cage **1.50**, it was the primary candidate for this task. We sought a new reaction with a more reactive electrophile to discover new biomimetic reactivity. Thus, reactions that proceed through a highly reactive iminium-like cation, such as a Knoevenagel condensation with a sulfonamide masked aldehyde (**2.9**), were considered.

The use of the fluorene cage **1.50** resulted in a lower yield of the alkylidene product from the sulfonamide masked aldehyde (**2.9**), with only 24 % conversion after 4 h (Figure 2.10). Interestingly, the Knoevenagel condensation reaction was significantly faster than

the conjugate addition between ethylcyanoacetate and β-nitrostyrene. As the Knoevenagel condensation was not completely inhibited, we recognized the potential of this reaction for uncovering new reactivity that was previously inaccessible through the conjugate addition reaction. The xylene cage **2.1** exhibited a similar inhibitory effect on the Knoevenagel condensation, producing 28 % of the alkylidene product after 4 h. On the other hand, the suberone helicate **2.2** showed the smallest inhibitory effect, resulting in the conversion to the alkylidene product **2.11** at 40 % after 4 h. Even though the reaction was inhibited we considered that the fluorene cage's ability to selectively recognize and bind certain molecules with significant variability may lead to unique reactivity.

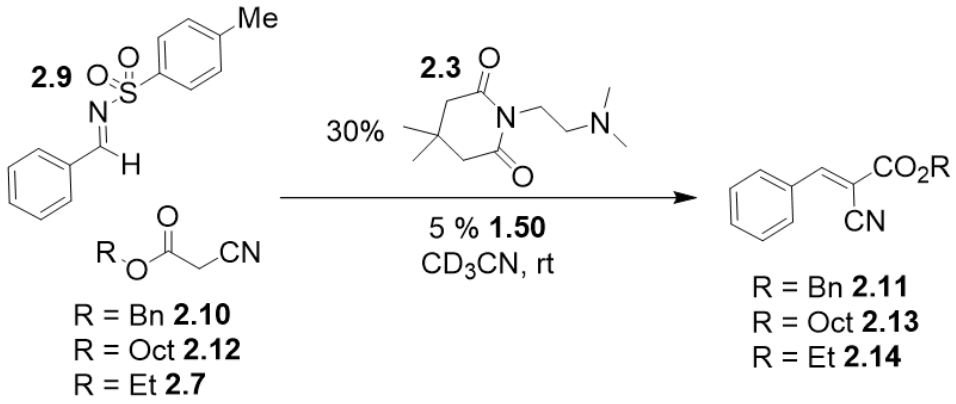

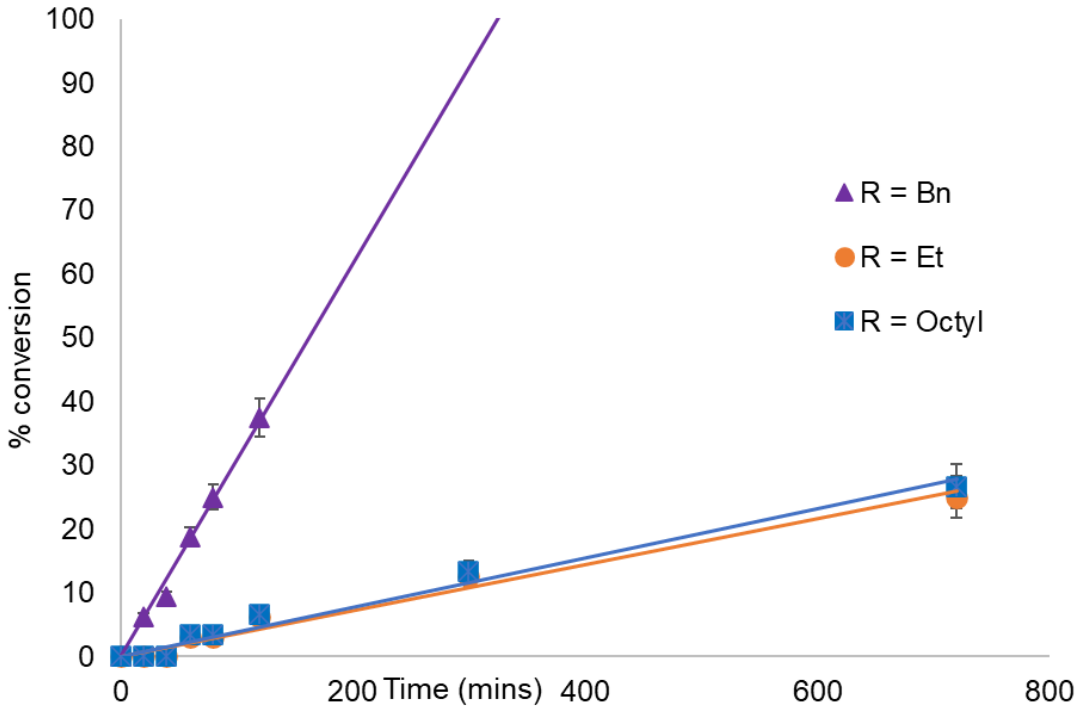

Figure 2.11. Reaction profile diagram for the Knoevenagel condensation with various cyanoacetates in the presence of 5 mol % **1.50**. [**1.50**/**2.1**/**2.2**] = 1.0 mM, [**2.9**] = 20 mM, [**2.7**/**2.10**/**2.12**] = 24 mM, [**2.3**] = 6.0 mM, CD_3CN, 298 K.

Three cyanoacetate nucleophiles were chosen: benzylcyanoacetate (**2.10**), octylcyanoacetate (**2.12)**, and ethylcyanoacetate (**2.7**). Using the fluorene cage inhibitor, the most significant differences in their reactions rates were between the benzyl and the

alkyl substituted cyanoacetates (Figure 2.11). Initially it was not clear if this was because of the selective molecular recognition of fluorene cage **1.50** enhancing the reactivity of benzyl nucleophile **2.10**. To investigate this, we performed a competitive nucleophile study as a control under identical reaction conditions (Figure 2.12). Surprisingly, benzylcyanoacetate (**2.10**) was more reactive than its alkyl variant (**2.7**) with and without cage (Figure 2.13). Without cage the benzyl alkylidene product **2.11** was produced in 60 % conversion after 5 h, in comparison to the ethyl alkylidene product **2.14** produced in 40 % conversion (Figure 2.12). The ratio between the benzyl and ethyl alkylidene products was 1.5:1.0 (**2.11**:**2.14**) without the fluorene cage. When the fluorene cage was used, as expected, the reaction rate was inhibited producing the benzyl alkylidene product **2.11** in 32 % conversion and the ethyl alkylidene product **2.14** in 9 % conversion (Figure 2.12). The ratio between the benzyl and ethyl alkylidene products was 3.3:1.0 (**2.11**:**2.14**). The contrasting ratios of alkylidene products **2.11** and **2.14** with and without the fluorene cage suggest the possibility of molecular recognition events favoring the benzyl alkylidene product. However, these events appear to be minor factors, as benzylcyanoacetate demonstrates higher reactivity compared to ethylcyanoacetate, both with and without the fluorene cage.

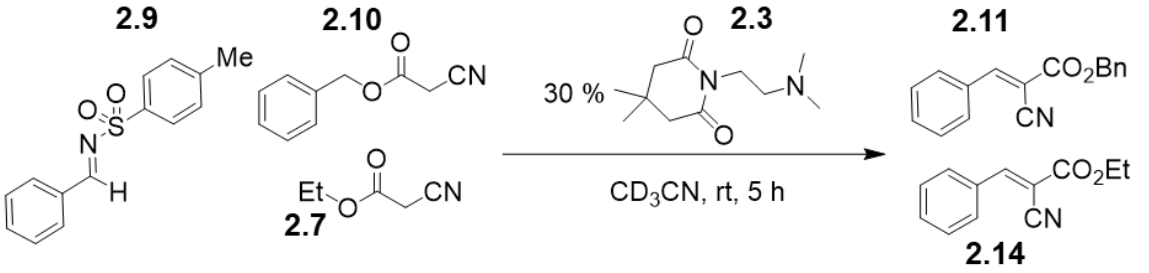

Cofactor	Cage	% conversion **2.11**	% conversion **2.14**
2.3	No cage	61	40
2.3	5 % **1.50**	30	9

Figure 2.12. Competitive nucleophile control study for the Knoevenagel condensation with **2.9**. [**1.50**/**2.1**/**2.2**] = 1.0 mM, [**2.9**] = 20 mM, [**2.7**/**2.10**] = 24 mM, [**2.3**] = 6.0 mM, CD_3CN, 298 K.

The lack of significant reactivity differences among cyanoacetates **2.10**, **2.12**, and **2.7** supports the notion that the fluorene cage's catalytic inhibition is not dependent on the reactants themselves, but rather on the cofactor. The cage's strong binding of conjugate acid species outcompetes the nucleophile and electrophile in both the conjugate addition and Knoevenagel condensation reactions. As a result, the reactivity of the reaction components is not significantly influenced by their simultaneous binding in the cage cavity. This is evident from the comparable reactivity observed in the Knoevenagel condensation of octylcyanoacetate **2.12** and ethylcyanoacetate **2.7**, despite their significant difference in size. Surprisingly, their reaction rates are identical (Figure 2.11). Further exploration of this phenomenon will be discussed extensively in Chapter 3.[7,19]

Within this system, the basicity of the cofactor is moderated, at least in the case of glutarimide catalyst **2.3**, which in turn modulates the reactivity. If the observed differences in reactivity between structurally different cyanoacetates cannot be attributed to the selective molecular recognition of the fluorene cage, it became necessary to explore

alternative strategies for discovering new reactivity. As the combination of 5 mol % **1.50** and 30 % **2.3** slowed the rate of the Knoevenagel condensation and almost completely shut down the conjugate addition, a competitive electrophile study may shed light on if this system could be used for chemoselective transformations. An equimolar solution of β-nitrostyrene **2.6** and ethylcyanoacetate **2.9** was prepared in CD_3CN in the presence of two molar equivalents of nucleophile ethylcyanoacetate **2.7** and 30 % glutarimide base catalyst **2.3** with and without fluorene cage **1.50**. Without any cage in the system both the Knoevenagel alkylidene product **2.14** and conjugate addition product **2.8** were produced in > 99 % and 67 % conversion, respectively (Figure 2.13). In the presence of the fluorene cage **1.50** a sole product was formed from the Knoevenagel condensation producing the alkylidene product **2.14**.

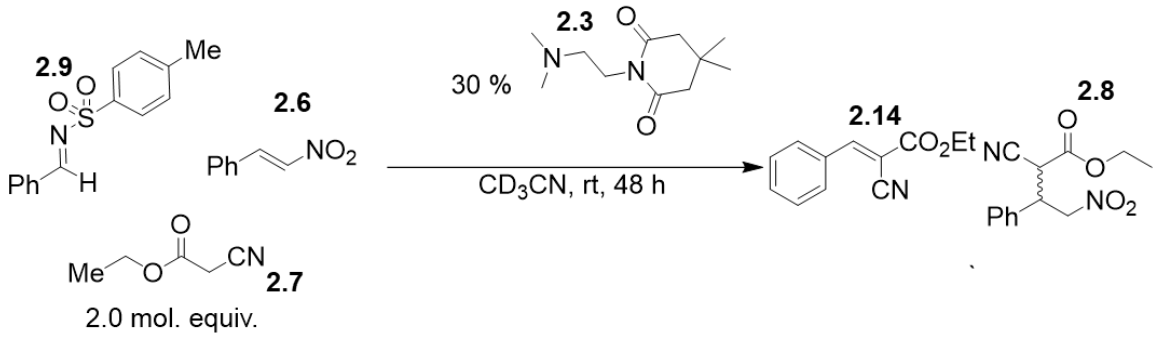

Cofactor	Cage	% conversion **2.14**	% conversion **2.8**
2.3	No cage	> 99	67
2.3	5 % **1.50**	> 99	0

Figure 2.13. a) Competitive electrophile control study. [**1.50**] = 1.0 mM, [**2.6**/**2.9**] = 20 mM, [**2.7**] = 24 mM, [**2.3**] = 6.0 mM, CD_3CN, 298 K.

The success of the competitive electrophile study prompted us to synthesize an electrophile that could accommodate a sulfonyl imine and a nitro styrene. Stille coupling serves a convenient and cost-effective method for the preparation of styrenes and due to the functional group tolerance of the reaction, the aldehyde does not require protection (Figure 2.14).[20] Following the purification of styrene **2.16**, a E-selective olefin nitration was performed using methods developed by the Maiti group to produce nitro styrene **2.17**.[21] From there the sulfonyl imine was prepared using standard procedures. Presently, studies are ongoing to fine-tune reaction conditions for the chemoselective transformation of **2.18**.

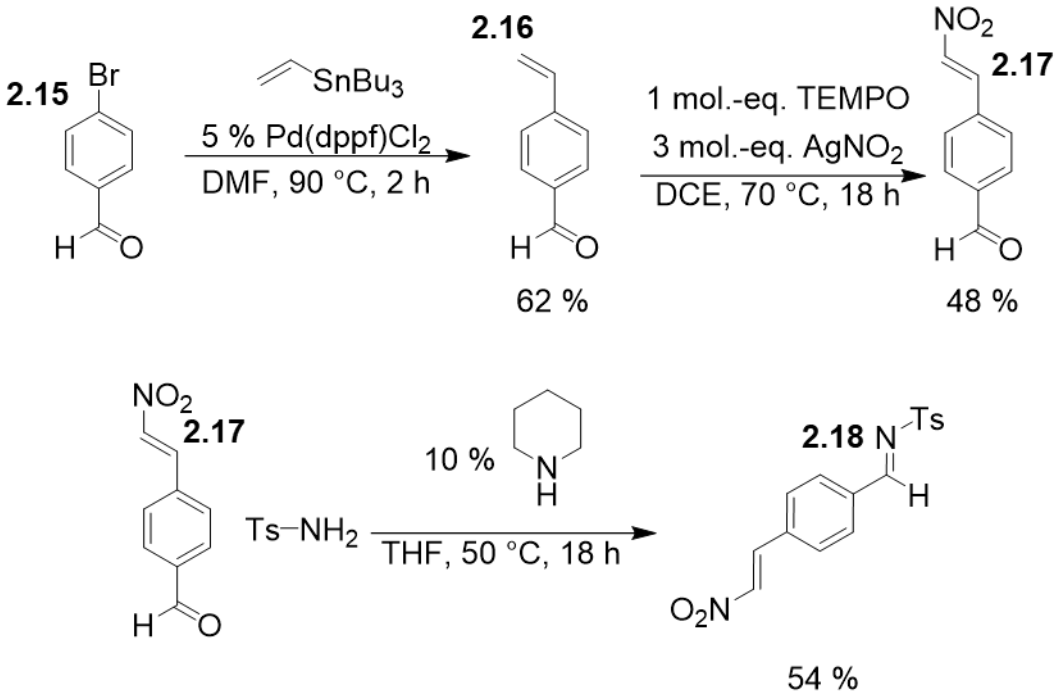

Figure 2.14. Reaction scheme of new electrophile for chemoselective studies.

2.6. Conclusion

In summary we have demonstrated that the fluorene cage **1.50** can catalytically inhibit conjugate additions as well as Knoevenagel condensations. The effect is more pronounced on the conjugate addition of **2.6** compared to Knoevenagel condensations of sulfonyl imine **2.9**. The mechanism of catalytic inhibition has been investigated thoroughly. Exogenous water in the reaction solution acts as a proton source for the protonation of various nitrogenous cofactors in the presence of **1.50**. This in turn protonates the bases, converting them to their conjugate acids which bind more favorably than their free base counterparts. In certain instances, this limits their ability to moderate base mediated reactions and in other circumstances the reactivity is completely shut off. UV-Vis binding studies demonstrated that the DABCO-H^+ binds more effectively than its free base counterpart, regardless of the fact that cage **1.50** possesses an overall 8+ charge. Finally, the moderated basicity of glutarimide catalyst **2.3** may see utility in mediating chemoselective transformations in the presence of fluorene cage **1.50**.

References

(1) Wang, Q.-Q.; Gonell, S.; Leenders, S. H. A. M.; Dürr, M.; Ivanović-Burmazović, I.; Reek, J. N. H. Self-Assembled Nanospheres with Multiple Endohedral Binding Sites Pre-Organize Catalysts and Substrates for Highly Efficient Reactions. *Nat. Chem*. **2016**, *8*, 225–230.

(2) Zhang, Q.; Catti, L.; Tiefenbacher, K. Catalysis inside the Hexameric Resorcinarene Capsule. *Acc. Chem. Res.* **2018**, *51*, 2107–2114.

(3) Catti, L.; Tiefenbacher, K. Brønsted Acid-Catalyzed Carbonyl-Olefin Metathesis inside a Self-Assembled Supramolecular Host. *Angew. Chem. Int. Ed.* **2018**, *57*, 14589–14592.

(4) Cullen, W.; Misuraca, M. C.; Hunter, C. A.; Williams, N. H.; Ward, M. D. Highly Efficient Catalysis of the Kemp Elimination in the Cavity of a Cubic Coordination Cage. *Nat. Chem*. **2016**, *8*, 231–236.

(5) Cullen, W.; Turega, S.; Hunter, C. A.; Ward, M. D. pH-Dependent Binding of Guests in the Cavity of a Polyhedral Coordination Cage: Reversible Uptake and Release of Drug Molecules. *Chem. Sci.* **2015**, *6*, 625–631.

(6) Ludden, M. D.; Taylor, C. G. P.; Tipping, M. B.; Train, J. S.; Williams, N. H.; Dorrat, J. C.; Tuck, K. L.; Ward, M. D. Interaction of Anions with the Surface of a Coordination Cage in Aqueous Solution Probed by Their Effect on a Cage-Catalysed Kemp Elimination. *Chem. Sci.* **2021**, *12*, 14781–14791.

(7) Ngai, C.; Bogie, P. M.; Holloway, L. R.; Dietz, P. C.; Mueller, L. J.; Hooley, R. J. Cofactor-Mediated Nucleophilic Substitution Catalyzed by a Self-Assembled Holoenzyme Mimic. *J. Org. Chem.* **2019**, *84* , 12000–12008.

(8) Maglic, J. B.; Lavendomme, R. MoloVol: An Easy-to-Use Program to Calculate Various Volumes and Surface Areas of Chemical Structures and Identify Cavities. *J. Appl. Crystallogr* **2021**, *55*, 1033-1044.

(9) Bryant, R. G. The NMR Time Scale. *J. Chem. Educ.* **1983**, *60*, 933.

(10) Fujita, M.; Oguro, D.; Miyazawa, M.; Oka, H.; Yamaguchi, K.; Ogura, K. Self-Assembly of Ten Molecules into Nanometre-Sized Organic Host Frameworks. *Nature* **1995**, *378*, 469–471.

(11) Biros, S. M.; Yeh, R. M.; Raymond, K. N. Design and Formation of a Large Tetrahedral Cluster Using 1,1'-Binaphthyl Ligands. *Angew. Chem. Int. Ed.* **2008**,

47, 6062–6064.

(12) Brynn Hibbert, D.; Thordarson, P. The Death of the Job Plot, Transparency, Open Science and Online Tools, Uncertainty Estimation Methods and Other Developments in Supramolecular Chemistry Data Analysis. *Chem. Commun.* **2016**, *52*, 12792–12805.

(13) Thordarson, P. Determining Association Constants from Titration Experiments in Supramolecular Chemistry. *Chem. Soc. Rev.* **2011**, *40*, 1305–1323.

(14) Holloway, L. R.; Bogie, P. M.; Lyon, Y.; Ngai, C.; Miller, T. F.; Julian, R. R.; Hooley, R. J. Tandem Reactivity of a Self-Assembled Cage Catalyst with Endohedral Acid Groups. *J. Am. Chem. Soc.* **2018**, *140*, 8078–8081.

(15) Ozeryanskii, V. A.; Pozharskii, A. F.; Antonov, A. S.; Filarowski, A. Out-Basicity of 1,8-Bis(Dimethylamino)Naphthalene: The Experimental and Theoretical Challenge. *Org. Biomol. Chem.* **2014**, *12*, 2360–2369.

(16) Taylor, C. G. P.; Argent, S. P.; Ludden, M. D.; Piper, J. R.; Mozaceanu, C.; Barnett, S. A.; Ward, M. D. One Guest or Two? A Crystallographic and Solution Study of Guest Binding in a Cubic Coordination Cage. *Chem. Eur. J.* **2020**, *26*, 3054–3064.

(17) Cullen, W.; Metherell, A. J.; Wragg, A. B.; Taylor, C. G. P.; Williams, N. H.; Ward, M. D. Catalysis in a Cationic Coordination Cage Using a Cavity-Bound Guest and Surface-Bound Anions: Inhibition, Activation, and Autocatalysis. *J. Am. Chem. Soc.* **2018**, *140*, 2821–2828.

(18) Vander Griend, D. A.; Bediako, D. K.; DeVries, M. J.; DeJong, N. A.; Heeringa, L. P. Detailed Spectroscopic, Thermodynamic, and Kinetic Characterization of Nickel(II) Complexes with 2,2‘-Bipyridine and 1,10-Phenanthroline Attained via Equilibrium-Restricted Factor Analysis. *Inorg. Chem.* **2008**, *47*, 656–662.

(19) da Camara, B.; Dietz, P. C.; Chalek, K. R.; Mueller, L. J.; Hooley, R. J. Selective, Cofactor-Mediated Catalytic Oxidation of Alkanethiols in a Self-Assembled Cage Host. *Chem. Commun.* **2020**, *56*, 14263–14266.

(20) McKean, D. R.; Parrinello, G.; Renaldo, A. F.; Stille, J. K. Synthesis of Functionalized Styrenes via Palladium-Catalyzed Coupling of Aryl Bromides with Vinyl Tin Reagents. *J. Org. Chem.* **1987**, *52*, 422–424.

(21) Maity, S.; Manna, S.; Rana, S.; Naveen, T.; Mallick, A.; Maiti, D. Efficient and Stereoselective Nitration of Mono- and Disubstituted Olefins with $AgNO_2$ and TEMPO. *J. Am. Chem. Soc.* **2013**, *135*, 3355–3358.

Chapter 3 - Size Selective Oxidation of Alkanethiols by a Self-Assembled Host

3.1. Introduction

Self-assembled cages have proven to be versatile catalysts, facilitating a wide range of different reactions, e.g. cycloadditions, acid/base catalysis, and transition metal mediated processes.[1–5] By encapsulating substrates within these host molecules, intriguing reaction behaviors can be achieved, such as size selectivity. Size selectivity in self-assembled cages is typically achieved by tightly binding guest molecules within a small cavity. However, this strong binding can hinder catalytic turnover. To enhance turnover rates, one approach is to increase the cavity size of the cage. However, larger cavities are less capable of discrimination between substrates, and self-assembled cages with "large" cavities (> 500 $Å^3$) are rarely capable of achieving size-selective catalysis. The development of a size-selective system is feasible when a large self-assembled cage exhibits a preference for binding guest molecules of different sizes and stoichiometries.[6,7]

3.2. Size-Selective Catalysis Using a Large Self-Assembled Cage

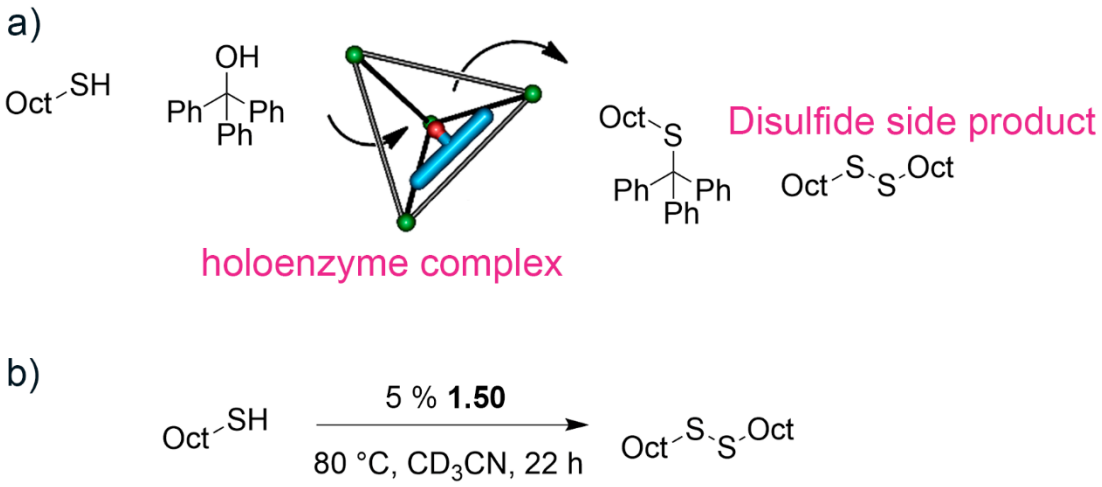

Figure 3.1. a) Holoenzyme mimic complex catalyzing the thioetherification of triphenylmethanol; b) **1.50** catalytic oxidation of octane thiol to disulfide.

Dr. Paul Bogie discovered that thiols are converted to their corresponding disulfides as a byproduct of the thioetherification of triphenyl methanol using fluorene cage **1.50** as catalyst, (Figure 3.1a). The cause of the oxidation of thiols to disulfides was not immediately obvious, as the only redox-active reagents in the solution are the putatively inert and electronically saturated vertices of **1.50**. We therefore began a study to understand this phenomenon. An 18 mM propanethiol and 1 mM **1.50** in CD_3CN was heated at 80 °C and monitored over time using ^1H NMR analysis. The results were surprising: the oxidative process occurred smoothly, the disulfide was the sole product and the cage remained mostly intact, even though there was *no obvious oxidant in the solution*. We hypothesized that **1.50** is delivering the active redox reagent, which is quite rare in supramolecular catalysis. Usually, hosts simply increase the effective concentration of species and promote reactivity, rarely do unfunctionalized cages directly participate in reactions.[8,9] But cage

1.50 is clearly an exception to this trend. The molecular recognition properties of **1.50** are unusual, and differently sized alkanethiols have been previously shown to prefer different binding modes, e.g., 1:1 versus 1:2.[7] To develop a size selective catalytic system employing **1.50**, we began conducting a mechanistic analysis on the oxidation mechanism of thiols to disulfides.

3.3. Mechanistic Analysis of Catalytic Oxidation of Alkanethiols by Self-Assembled Host

Control studies were employed surveying the effectiveness of $Fe(NTf_2)_2$ for the reaction process, as well as structurally similar Fe-iminopyridine self-assemblies with varying cavity sizes (Figure 3.2). Structurally similar cages such as xylene-based Fe_4L_6 cage **2.1** or suberone Fe_2L_3 helicate **2.2** were ineffective for the oxidation of octyl thiol to its corresponding disulfide, and so was the iron salt that is used to make cages **1.50**, **2.1**, and **2.2**, even after excessive heating and using a higher stoichiometry of Fe^{2+} (Figure 3.2). If $Fe(NTf_2)_2$ is ineffective for the dimerization process and so are the structurally similar cages **2.1** and **2.2**, likely coencapsulation of two molecules of thiol within cage **1.50** must be required for the oxidation to occur. As the cavities of **2.1** and **2.2** are too small to bind guests in a 1:2 stoichiometry, this is likely the cause of the inability to mediate the oxidation of octanethiol to its corresponding disulfide.

How then is **1.50** supplying a redox reagent to the reaction media to promote this oxidation? Cage **1.50** is not being consumed through the oxidative process, thus it is performing this reaction catalytically, so the actual nature of the catalytically active species is less obvious. The first important clue to the mechanism is that removal of oxygen from

the system slowed the oxidation process, suggesting that O_2 from air is the stoichiometric oxidant in the process.[10] As the Fe^{2+} vertices of **1.50** are electronically saturated and there is no visible ligand dissociation occurring by ^1H NMR spectroscopy, the reactivity cannot be mediated by an uncoordinated vertex of **1.50** from a ligand arm temporarily detaching.[11] What is most likely is small amounts of Fe(II) cations bleed from **1.50**, and act as the active catalyst while the bulk of the cage remains intact (Figure 3.3c), this is consistent with the observation that minimal peak broadening is observed in the ^1H NMR spectrum. If free Fe(II) in solution was oxidized to paramagnetic Fe(III), significant broadening in the ^1H NMR spectrum would be visible.

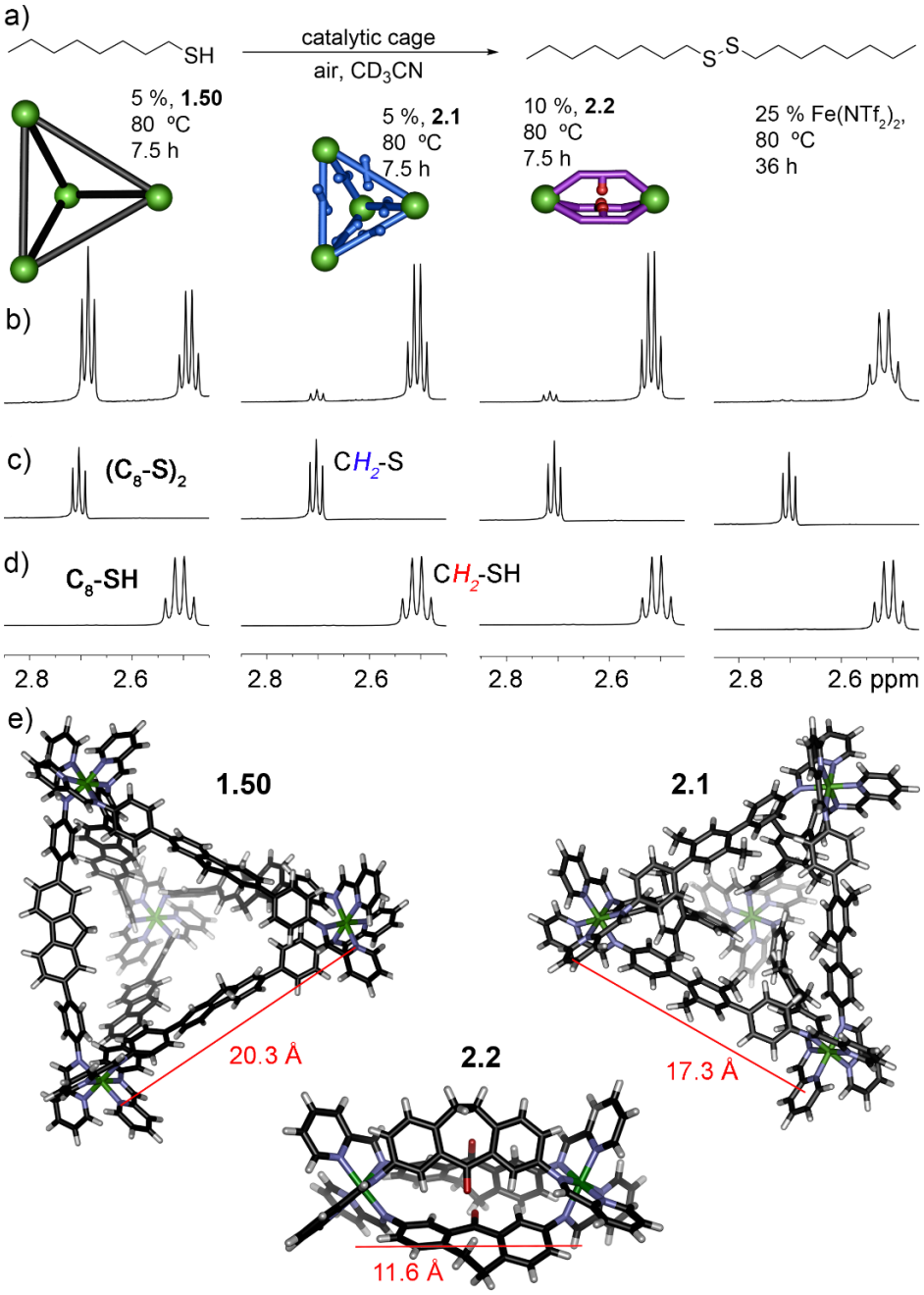

Figure 3.2. a) Reaction scheme of oxidative dimerization of octanethiol, ^{1}H NMR analysis of the reaction catalyzed by various Fe^{2+}-containing supramolecular species; b) expansion of the CH_2-S region of the ^{1}H NMR spectra reaction mixture for the indicated time; c) (**C_8-S**)$_2$; d) **C_8-SH**. CD_3CN, 400 MHz, spectra acquired at 298 K; e) energy minimized Spartan models of supramolecular species (AM 1 forcefield) **1.50**, **2.1**, and **2.2**. [**1.50**/**2.1**/**2.2**] = 1 mM, [**C_8-SH**] = 20 mM, [**Fe(NTf$_2$)$_2$**] = 24 mM, [**2.3**] = 6 mM, CD_3CN, 298 K.

To further probe for the catalytically active species doping studies were undertaken where a sample of 5 mol % **1.50** was doped with 0, 10, 25, and 50 mol % $Fe(NTf_2)_2$ (Figure 3.3) which gave 61 %, 35 %, 33 %, and 20 % conversion to disulfide, respectively. Surprisingly, addition of more Fe^{2+} in the presence of **1.50** lead to inhibition of disulfide formation. This is indicative of Fe^{2+} acting as a competitive guest which displaces octanethiol from the cavity of **1.50**. Fe^{3+} has been shown to stoichiometrically oxidize thiols to disulfides under more forcing conditions[12] but Fe^{2+} is unable to catalyze or stoichiometrically promote the dimerization of thiols under these mild conditions, but the reactivity Fe^{2+} is significantly enhanced in **1.50**s cavity.

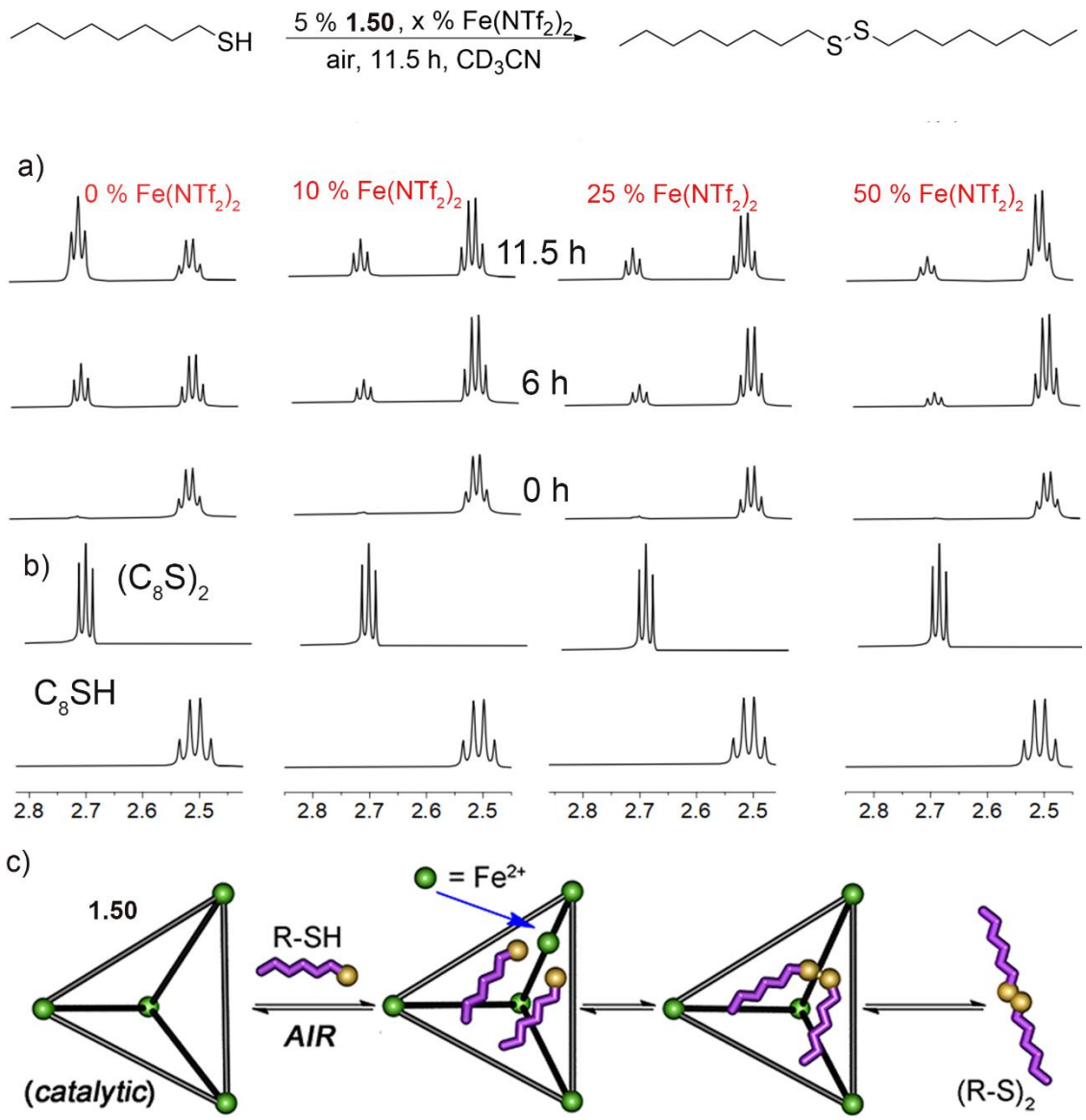

Figure 3.3. ^{1}H NMR spectra of the oxidation of **C_8-SH** with varying concentrations of $Fe(NTf_2)_2$ showing: a) relative rate of product formation using varying concentrations of $Fe(NTf_2)_2$ (2.85-2.45 ppm); b) (**C_8-S**)$_2$ and **C_8-SH**; c) cartoon of plausible oxidation mechanism. [**C_8-SH**] = 18.2 mM, [**1.27**] = 0.9 mM, [$Fe(NTf_2)_2$] = 0, 1.8, 4.6, 9.1 mM. Reactions were performed at 80 °C in 400 µL CD_3CN and monitored over time (600 MHz, 298 K, CD_3CN).

3.4. Binding Affinities and Modes of Thiols in Self-Assembled Cages

Table 3.1. Binding affinities and modes for thiols and disulfides in **1.50** and **2.1**.[a]

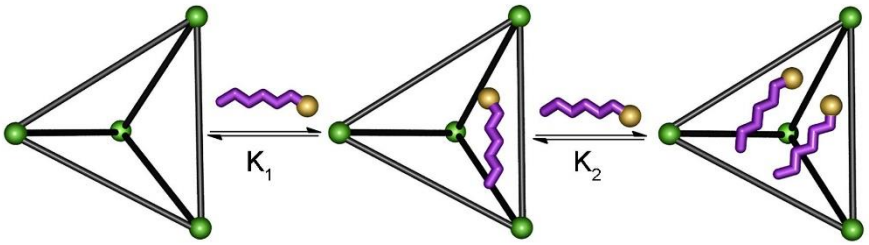

2:1 Substrate (**1.50**)	K_1 x 10^3 M^{-1}	K_2 x 10^3 M^{-1}	α ($4K_2/K_1$)
C_5-SH	2150 ± 650	1.2 ± 3.0	837 x 10^{-4}
C_6-SH	540 ± 130	2.4 ± 1.5	0.018
C_8-SH	174 ± 43	0.78 ± 0.53	0.018
1:1 Substrate (**1.50**)	K_a x 10^3 M^{-1}	1:1 Substrate (**1.50**)	K_a x 10^3 M^{-1}
C_{10}-SH	19.7 ± 6.4	$(C_6\text{-S})_2$	71.0 ± 14
C_{11}-SH	40.0 ± 19	$(C_8\text{-S})_2$	76.1 ± 3.8
C_{12}-SH	2.7 ± 0.6	$(C_{10}\text{-S})_2$	27.9 ± 9.4
$(C_3\text{-S})_2$	16.6 ± 2.4	$(C_{11}\text{-S})_2$	5.5 ± 0.5
$(C_5\text{-S})_2$	38.8 ± 7.1	$(C_{12}\text{-S})_2$	8.4 ± 0.9
1:1 Substrate (**2.1**)	K_a x 10^3 M^{-1}		
C_6-SH	420 ± 130		

[a]Titrations were performed in CH_3CN, [**1.50/2.1**] = 3 μM, absorbance changes measured at 300 and 370 nm for **1.50** and 275/335 nm for **2.1**.

To comprehensively understand the molecular recognition properties of **1.50** for the coencapsulation of thiols, UV-Vis titrations were performed using differently sized alkanethiols and disulfides. Each guest was titrated into a 3 μM solution of **1.50** (or **2.1**) in CH_3CN, and the changes in absorbance at both 330 and 370 nm (or 275/335 nm for **2.1**)

were recorded and analyzed. In each case, the binding isotherms were fit to both 1:1 and 1:2 binding models and the residuals were calculated.[13] The significance of the 1:2 model was judged based on the inverse ratio of the squared residuals compared to the 1:1 model, and quantified *via* p-value, please see chapter 6 for more in-depth details: Mathematica fitting was performed by Dr. Kevin Chalek (University of California – Riverside, department of chemistry). We decided that a conservative p-value cut off of 0.001 would provide the most honest analysis of binding modes of these host:guest complexes, where a smaller p value indicates the model is truly better. We defaulted to assuming that the complexes prefer the 1:1 stoichiometry but required an elevated level of proof that, in certain instances, the 1:2 complexes are preferred. It is important to note just because a model fits a binding isotherm "better" does not mean that other binding stoichiometry is forbidden, only that it is statistically less likely in solution.

The molecular recognition capabilities of **1.50** and **2.1** varied significantly, in both binding modes (1:2 or 1:1) and affinities, for alkyl thiols and disulfides of different chain lengths. Midsized thiols $C_{5\text{-}8}$ were found to fit the 1:2 model better than their larger $C_{10\text{-}12}$ analogues while all disulfides fit the 1:1 model. Disulfides $(C_6\text{-}S)_2$ and $(C_8\text{-}S)_2$ bound stronger than their smaller and larger counterparts. It should be noted that smaller alkanethiols, such as propanethiol, fit the 1:1 model better, which is not to say that the 1:2 is impossible, or that other higher order complexes such as 1:5 are inaccessible, but the Nelder-Mead cannot unambiguously support the presence of these higher order complexes. As such, the exact nature of the binding mode of 1-propanethiol in **1.50** is unclear: in that case, the isotherm fits best to a 1:1 model, but other stoichiometries are certainly possible.[10]

Considering that fluorene cage **150** has a volume of 572 $Å^3$ and propanethiol has a volume of 84 $Å^3$, a maximum of 6 molecules of 1-propanethiol could "fit" into the cavity of the fluorene cage. Interestingly, C_{12}-SH and $(C_{12}\text{-}S)_2$ both bound within the cavity of **1.50**, which implies that coencapsulation of 2 molecules of C_{12}-SH is not completely forbidden. Similarly, the long alkyl chains of C_{12}-SH can easily dangle outside the portal of **1.50** if they are coencapsulated. There is certainly enough space, and it is just a matter of favorability. Importantly, 1-hexanethiol is bound in **2.1** and fits the 1:1 model best, which supports the hypothesis that coencapsulation of two molecules of thiol is optimal for the oxidation process to occur as it is not possible in the smaller cavity of **2.1**, which is ineffective for the oxidative dimerization of alkanethiols. The difference in cavity size between **1.50** and **2.1** is clearly visible when viewing the minimized structures (SPARTAN, AM 1 forcefield) (Figure 3.4), one molecule of C_8-SH takes up the entire volume of **2.1**, while **1.50** can fit 2 molecules of C_8-SH. As self-assemblies **2.1** and **2.2** cannot coencapsulate multiple thiols and are equally as ineffective as $Fe(NTf_2)_2$ for the dimerization of thiols, we reason that the mechanism in Figure 3.3c is the most reasonable description of the catalytic oxidation mechanism of thiols by **1.50**.

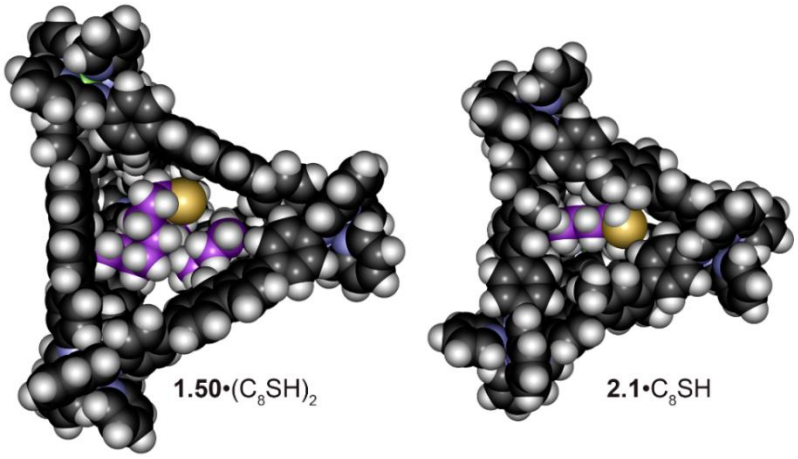

Figure 3.4. 1.50•(C_8-SH)$_2$ and **2.1•C_8-SH** (Spartan molecular model minimized structures, AM 1 forcefield).

3.5. Size-Selective Oxidation of Chemically Identical Thiols

As the binding modes and affinities of differently sized alkanethiols varied significantly in the formation of host:guest complexes when using **1.50**, we sought next to analyze the ability of the host to discriminate chemically identical alkanethiols based solely on size. Considering that large alkanethiols (such as C_{12}-SH) fit the 1:1 model the best, reasonably C_{12}-SH should not be oxidized by **1.50** or at the very least at a much slower rate. Thiols $C_{5\text{-}8}$-SH and $C_{10\text{-}12}$-SH were all oxidized to their corresponding dimers to completion at 80 °C after 22 h. To achieve selectivity in the oxidative system we oxidized $C_{5\text{-}8}$-SH and $C_{10\text{-}12}$-SH at 50 °C. Under these milder conditions, thiols $C_{5\text{-}8}$-SH and C_{10}-SH were oxidized at similar rates but when $C_{11\text{-}12}$-SH was used, the rate began to decrease, particularly for dodecyl thiol (Table 3.2).

Table 3.2. Reactivity of differently sized alkanethiols using **1.50**.[a]

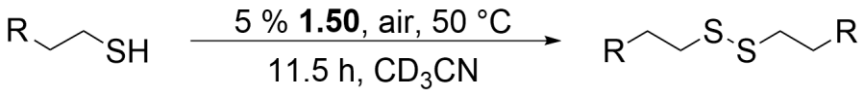

Reactant	Conversion, %	Reactant	Conversion, %
C_5-SH	49	C_{10}-SH	63
C_6-SH	47	C_{11}-SH	43
C_7-SH	54	C_{12}-SH	15

[a]Reactions performed at 50 °C, 11.5 h, CD_3CN and analyzed by ^1H NMR, concentrations determined using dioxane as an internal standard. [$\mathbf{C_x}$**-SH**] = 18.2 mM

The selectivity of the homodimerization of alkanethiols at 50 °C inspired us to examine if there would be any significant differences in the dimerization of equimolar heteromixtures of chemically identical alkyl thiols that differed only in their chain length. Various combinations of two differently sized alkyl thiols were evaluated and continually produced non-selective thermodynamic mixtures of disulfides, in a 1:2:1 ratio at 80 °C. We anticipated this might be the case, thiol-disulfide exchange has been rigorously studied for its importance in biological systems,[14] as the exchange can be facile under similar conditions at room temperature,[15,16] it is unsurprising that no selectivity was observed. Mixtures of alkanethiols and disulfides are known to equilibrate over time. As the initial oxidation selectivity of **1.50** cannot be studied under thermodynamic conditions, the temperature of the reaction was lowered and allowed to mix for 7 days to analyze the initial kinetics of the system (Figure 3.5). Under these new conditions the selectivity of **1.50** is easily determined *via* GC analysis of the product mixture.

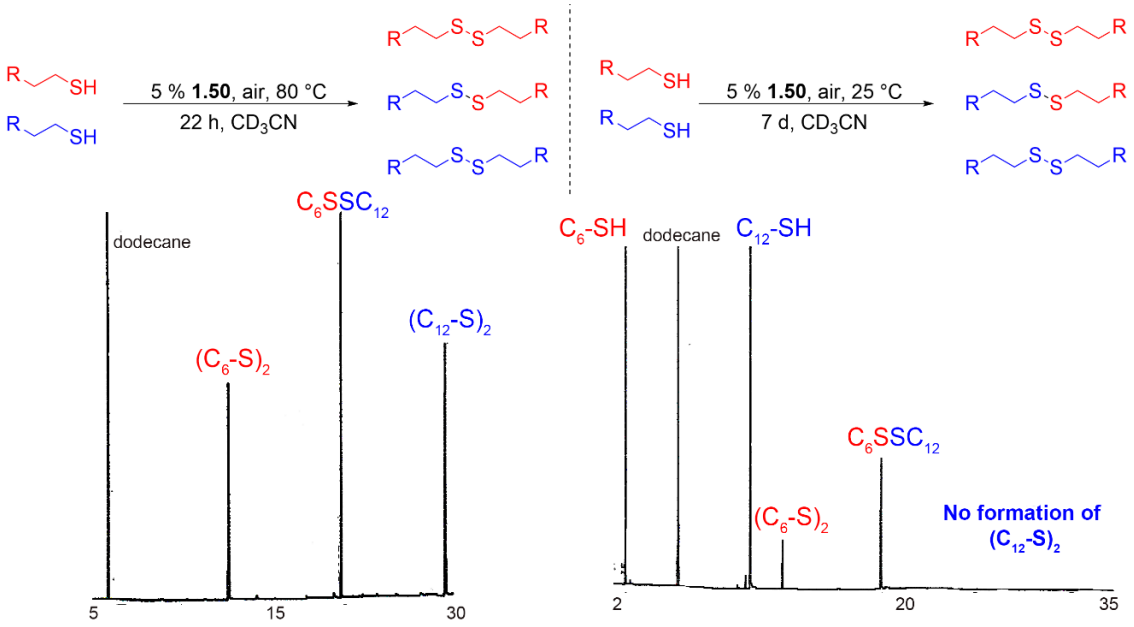

Figure 3.5. Gas chromatography chromatograms of product distribution of alkyl disulfides produced from equimolar mixtures of two differently sized alkanethiols.

The origins of the selectivity in this system are due to the selective molecular recognition of **1.50** favorably coenscapulating multiple molecules of thiol. Under these kinetic conditions the selectivity of the system is clear and mirrors the binding data (Table 3.1). We then explored the selectivity with various combinations of alkanethiols: C_3/C_8, C_3/C_{10}, C_6/C_7, C_6/C_{10} and C_6/C_{12}, (Figure 3.6). As might be expected when two similarly sized alkanethiols were used (such as C_6/C_7) a statistical 1:2:1 mixture of disulfides was produced: as there are minimal differences in the size of both thiols, their various binding modes are all equally favorable. In the case of C_3/C_{10}, the medium sized $C_3S\text{-}SC_{10}$ hetero-dimeric product and the larger $C_{10}S\text{-}SC_{10}$ homodimeric products were produced in excess over the smaller $C_3S\text{-}SC_3$, consistent with the observation that medium sized alkanethiols with a total chain length of C_{11}-C_{18} are favorably coencapsulated and thus their

corresponding disulfides are produced in higher yields. When the thiol is too large, e,g., C_{12}-SH, coencapsulation cannot occur, thus oxidation is far less favorable.

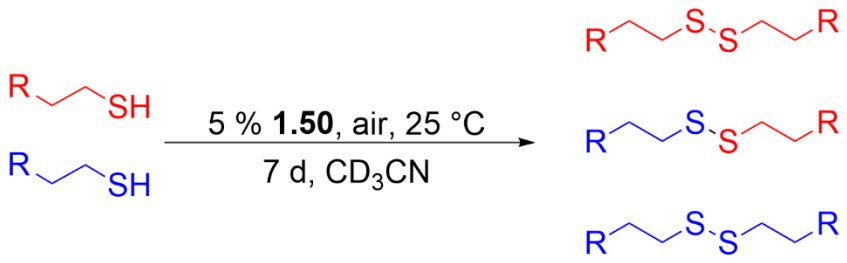

R_1	R_2	Conversion, %	R_1R_1	R_1R_2	R_2R_2
C_3	C_8	19	7	35	58
C_3	C_{10}	20	10	34	56
C_6	C_7	20	23	49	28
C_6	C_{10}	18	19	42	39
C_6	C_{12}	12	28	72	0

Figure 3.6. Reactions performed at 25 °C, 7 d, CD_3CN and analyzed by gas chromatography, concentrations determined using dodecane as internal standard. Equimolar amounts of each thiol used, overall [$\mathbf{C_x}$**-SH**] = 18.2 mM.

3.6. Conclusion

We have demonstrated that **1.50** is a redox active catalyst for the oxidation of alkanethiols to disulfides. It is unique, as it supplies its own metallic cofactor to be used for catalytic processes. Considering it possesses a large cavity, its capabilities as a size selective alkanethiol catalyst are impressive, which are driven by its selective molecular recognition of alkyl thiol substrates. Presently, we are looking towards new biomimetic reactivity, and the next chapter of this dissertation will discuss our efforts to achieve this goal *via* the synthesis of new cage scaffolds.

References

(1) Yoshizawa, M.; Takeyama, Y.; Kusukawa, T.; Fujita, M. Cavity-Directed, Highly Stereoselective [2+2] Photodimerization of Olefins within Self-Assembled Coordination Cages. *Angew. Chem. Int. Ed.* **2002**, *41*, 1347–1349.

(2) Ludden, M. D.; Taylor, C. G. P.; Tipping, M. B.; Train, J. S.; Williams, N. H.; Dorrat, J. C.; Tuck, K. L.; Ward, M. D. Interaction of Anions with the Surface of a Coordination Cage in Aqueous Solution Probed by Their Effect on a Cage-Catalysed Kemp Elimination. *Chem. Sci.* **2021**, *12*, 14781–14791.

(3) Cullen, W.; Misuraca, M. C.; Hunter, C. A.; Williams, N. H.; Ward, M. D. Highly Efficient Catalysis of the Kemp Elimination in the Cavity of a Cubic Coordination Cage. *Nat. Chem.* **2016**, *8*, 231–236.

(4) Gramage-Doria, R.; Hessels, J.; Leenders, S. H. A. M.; Tröppner, O.; Dürr, M.; Ivanović-Burmazović, I.; Reek, J. N. H. Gold(I) Catalysis at Extreme Concentrations inside Self-Assembled Nanospheres. *Angew. Chem. Int. Ed.* **2014**, *53*, 13380–13384.

(5) Wang, Z. J.; Brown, C. J.; Bergman, R. G.; Raymond, K. N.; Toste, F. D. Hydroalkoxylation Catalyzed by a Gold(I) Complex Encapsulated in a Supramolecular Host. *J. Am. Chem. Soc.* **2011**, *133*, 7358–7360.

(6) Ngai, C.; Bogie, P. M.; Holloway, L. R.; Dietz, P. C.; Mueller, L. J.; Hooley, R. J. Cofactor-Mediated Nucleophilic Substitution Catalyzed by a Self-Assembled Holoenzyme Mimic. *J. Org. Chem.* **2019**, *84*, 12000–12008.

(7) Bogie, P. M.; Holloway, L. R.; Ngai, C.; Miller, T. F.; Grewal, D. K.; Hooley, R. J. A Self-Assembled Cage with Endohedral Acid Groups Both Catalyzes Substitution Reactions and Controls Their Molecularity. *Chem. Eur. J.* **2019**, *25*, 10232–10238.

(8) Lu, Z.; Ronson, T. K.; Heard, A. W.; Feldmann, S.; Vanthuyne, N.; Martinez, A.; Nitschke, J. R. Enantioselective Fullerene Functionalization through Stereochemical Information Transfer from a Self-Assembled Cage. *Nat. Chem.* **2022**, *15*, 405–412.

(9) Hashikawa, Y.; Fujikawa, N.; Murata, Y. π-Extended Fullerenes with a Reactant Inside. *J. Am. Chem. Soc.* **2022**, *144*, 23292–23296.

(10) Bogie, P. M. Designing Functional Cages: From Luminescent Sensors to Artificial Enzymes. Doctor of Philosophy , University of California Riverside, 2019.

(11) Davis, A. V.; Raymond, K. N. The Big Squeeze: Guest Exchange in an M4L6 Supramolecular Host. *J. Am. Chem. Soc.* **2005**, *127*, 7912–7919.

(12) Wallace, T. J. Reactions of Thiols with Metals. II. Low-Temperature Oxidation by Soluble Metal Salts[1]. *J. Org. Chem.* **1966**, *31*, 3071–3074.

(13) Thordarson, P. Determining Association Constants from Titration Experiments in Supramolecular Chemistry. *Chem. Soc. Rev.* **2011**, *40*, 1305–1323.

(14) Nagy, P. Kinetics and Mechanisms of Thiol-Disulfide Exchange Covering Direct Substitution and Thiol Oxidation-Mediated Pathways. *Antioxid. Redox Signal.* **2013**, *18*, 1623–1641.

(15) Fernandes, P. A.; Ramos, M. J. Theoretical Insights into the Mechanism for Thiol/Disulfide Exchange. *Chem. Eur. J.* **2004**, *10*, 257–266.

(16) Wilson, J. M.; Bayer, R. J.; Hupe, D. J. Structure-Reactivity Correlations for the Thiol-Disulfide Interchange Reaction. *J. Am. Chem. Soc.* **1977**, *99*, 7922–7926.

Chapter 4 - Altering Anion Exchange Selectivity and Kinetics Using Self-Assembled Cages with Pendant Functional Groups

4.1. Introduction

The recognition of substrates in proteins relies on hydrogen bonding and other electrostatic interactions, wherein subtle structural changes dictate substrate affinity and significantly impact exchange kinetics.[1,2] Similarly, self-assembled cages exhibit the ability to bind guest molecules. The molecular recognition of substrates within cages possesses a kinetic and thermodynamic element, otherwise described as in/out exchange rate and affinity, respectively. The kinetics of guest ingress/egress within self-assembled cages are regulated by the size of the portals into the host cavity. Increasing the portal size generally results in faster exchange rates, as guests do not have to "squeeze" past small panel gaps into the cavity, which is what the binding kinetics of **1.50** demonstrated.[3,4] Alternatively, switchable entrance portals or ligand dissociation techniques can also be employed for controlled exchange.[5–9] We propose an alternative strategy for modulating guest exchange kinetics and selectivity involving "gating" the entrance portal of self-assembled cages, akin to enzymes that possess "lidded" active sites.[2] By incorporating this gating mechanism, we aim to investigate the effects on guest exchange kinetics and selectivity. Most ligands employed in sub-component self-assembly are typically unfunctionalized and symmetrical to ensure the self-assembly process is not hindered by competing coordinating groups. The use of functionalized ligand scaffolds to create self-assembled cages with pendant functional groups is relatively rare. Consequently, the

impact of these pendant functional groups on guest exchange kinetics and selectivity has not been extensively studied.[10–13]

4.2. The Synthesis of C_3-Symmetric Tris-Amine Ligands for the Self-Assembly of M_4L_4 Cages

Towards new strategies for incorporating functional groups into ligand frameworks we shifted our focus to the synthesis of C_3-symmetric tris-amine ligands, which are well known to produce tetrahedral cages *via* sub-component self-assembly.[14–16] One advantage of using these types of ligands is that they usually form *T*-symmetric cages, which significantly simplifies the ^{1}H NMR spectra and eases experimental analysis.[14,17] One draw-back to using functionalized C_3-symmetric ligands is that the resultant self-assembled cage could have the functional groups oriented *internally* or *externally*. If the panels cannot rotate and the self-assembly process positions the functional groups internally, then the cavity is filled. If the panels can rotate, then the cavity can potentially be blocked or unblocked *via* rotation. The biggest issue being if the cavity is blocked or filled then it possesses no obvious capacity for molecular recognition. If the functional groups are oriented externally, then potentially they can act as a gate at the cage entrance portals and distort guest exchange kinetics and selectivity.

Dibromo-fluorene can be easily functionalized *via* substitution reactions thus we thought the trimerized fluorenyl scaffold truxene, **4.1**, would be an ideal target for the synthesis of C_3-symmetric ligands (Figure 4.1). Truxene can be synthesized on gram scale from indanone which provided us with a promising starting point (Figure 4.1).[18] In our initial attempts, we performed alkylation on truxene, aiming to obtain the fully alkylated

product, **4.2**. However, the reaction yielded a mixture of various addition products, and unfortunately, the desired fully alkylated product was not detected in appreciable amounts. These findings prompted us to explore alternative molecular architectures for accessing C_3-symmetric ligands, such as, 1,3,5-trisubstituted triazine or benzene rings, such as **4.3** (Figure 4.2). These alternative molecular architectures are easily synthesized and possess a variety of handles for functionalization.

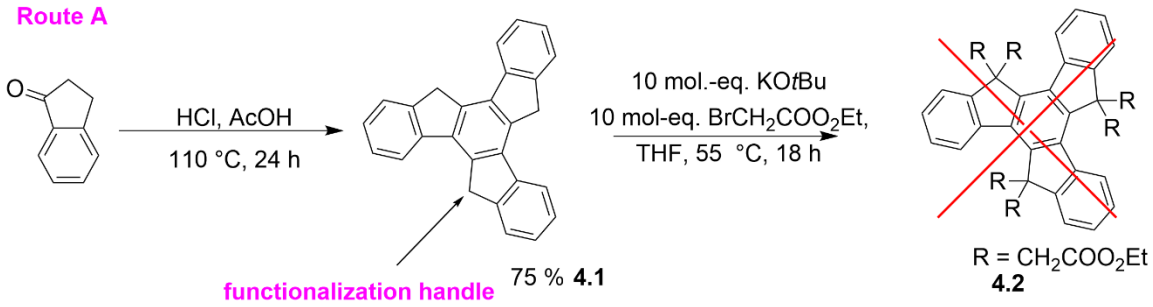

Figure 4.1. Route A for accessing C_3 symmetric tris-amine ligand precursors *via* the truxene scaffold.

Our proof-of-concept reaction involved the Friedel-Crafts arylation between **4.3** and **4.4** that produced **4.7** with a good yield of 82 %.[19] The strategic placement of the alcohol *ortho* to the triazine motif, in theory, could allow for the incorporation of various functional groups through substitution reactions, assuming the tris-amine ligand was accessible under these conditions. When the Friedel-Crafts arylation was attempted with **4.5**, only starting material was recovered, due to the electron-deficient nature of the aromatic ring, it proved ineffective as a nucleophile.

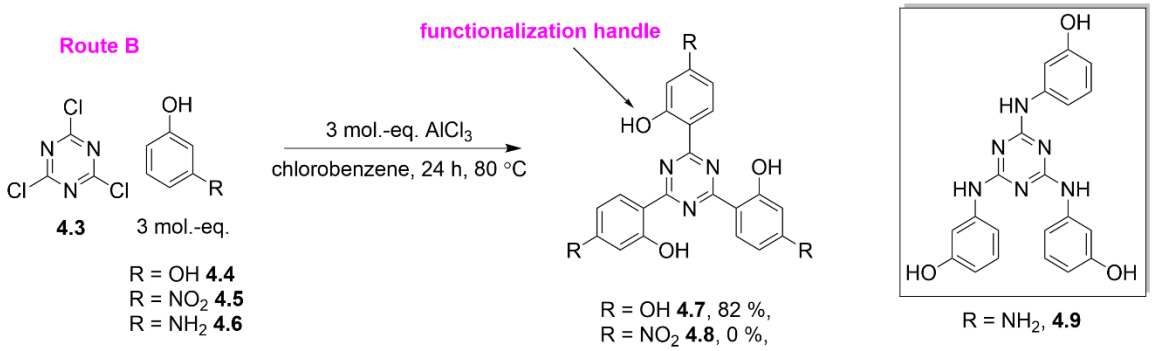

Figure 4.2. Route B for accessing C_3-symmetric tris-amine ligand precursors *via* the Friedel-Crafts arylation of cyanuric chloride (**4.3**).

Nucleophile, **4.6**, has a more electron rich ring than **4.5**, and so we performed the reaction with the free amine where crude ^{1}H NMR analysis revealed the major product as **4.9**, as the addition occurred from the nucleophilic amine of **4.6**. To mitigate this competing reaction pathway, we performed the same reaction using derivatives of **4.6**, where the amine was masked as a trifluoroacetamide, phthalimide, or tert-butyloxycarbonyl (Boc) protecting groups. In all cases there was no formation of product. Rather than contending with the competing reaction pathway, we used it as inspiration to reevaluate the most optimal route for accessing highly versatile C_3-symmetric ligands.

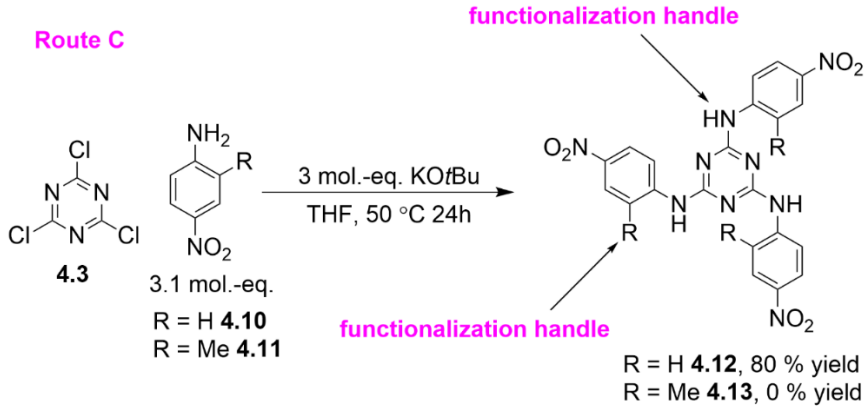

Figure 4.3. Route C for accessing C_3-symmetric tris-amine ligand precursors *via* the nucleophilic aromatic substitution of cyanuric chloride (**4.3**).

By employing the new synthetic route depicted in Figure 4.3, we achieved a 80 % yield in the synthesis of the unfunctionalized ligand precursor, **4.12**.[20] The synthetic and rotational flexibility afforded by this scaffold presents highly advantageous characteristics for self-assembled cages. The inclusion of the C-N-C bond in the scaffold theoretically could promote swifter rotation of the aryl ring panels after sub-component self-assembly, compared to the biphenyl scaffold **4.7**. Consequently, any functional groups integrated into the self-assembled cage could undergo external rotation, thus effectively "freeing" the cavity. The dual handles for functionalization are also very desirable. These dual locations provide opportunities for incorporating functional groups, or alternatively, accommodating two different functional groups within the final self-assembled cage structure. This versatility could expand the potential applications for altering guest exchange kinetics and selectivity using "gated' entrance portals of self-assembled cages. Unfortunately, attempts to derivatize **4.12** *via* substitution at the NH did not yield valuable ligand targets. When ortho-substituted anilines, such as **4.11**, were employed, there was no evidence for the formation of **4.13**, only starting material was retrieved from the reaction mixture. This outcome suggests that the steric bulk of the methyl group hindered the addition of **4.11**. To address this issue, we hypothesized that the use of ortho-substituted phenols might circumvent these issues, as oxygen is smaller than nitrogen.

With these new conditions, we were able to prepare C_3-symmetric tris-amine ligands possessing pendant functional groups. Ligands **4.17**, **4.19**, and **4.20** were obtained following route D (Figure 4.4). Notably, ligand **4.17** had been previously reported by multiple research groups, and our yields were consistent with the literature.[17] By utilizing

the core as a nucleophile in conjunction with electrophilic fluorinated aryl rings, we successfully prepared ligand **4.22** *via* route E. (Figure 4.4). With ligands in hand, we set out to develop conditions to convert these new ligands into cages.

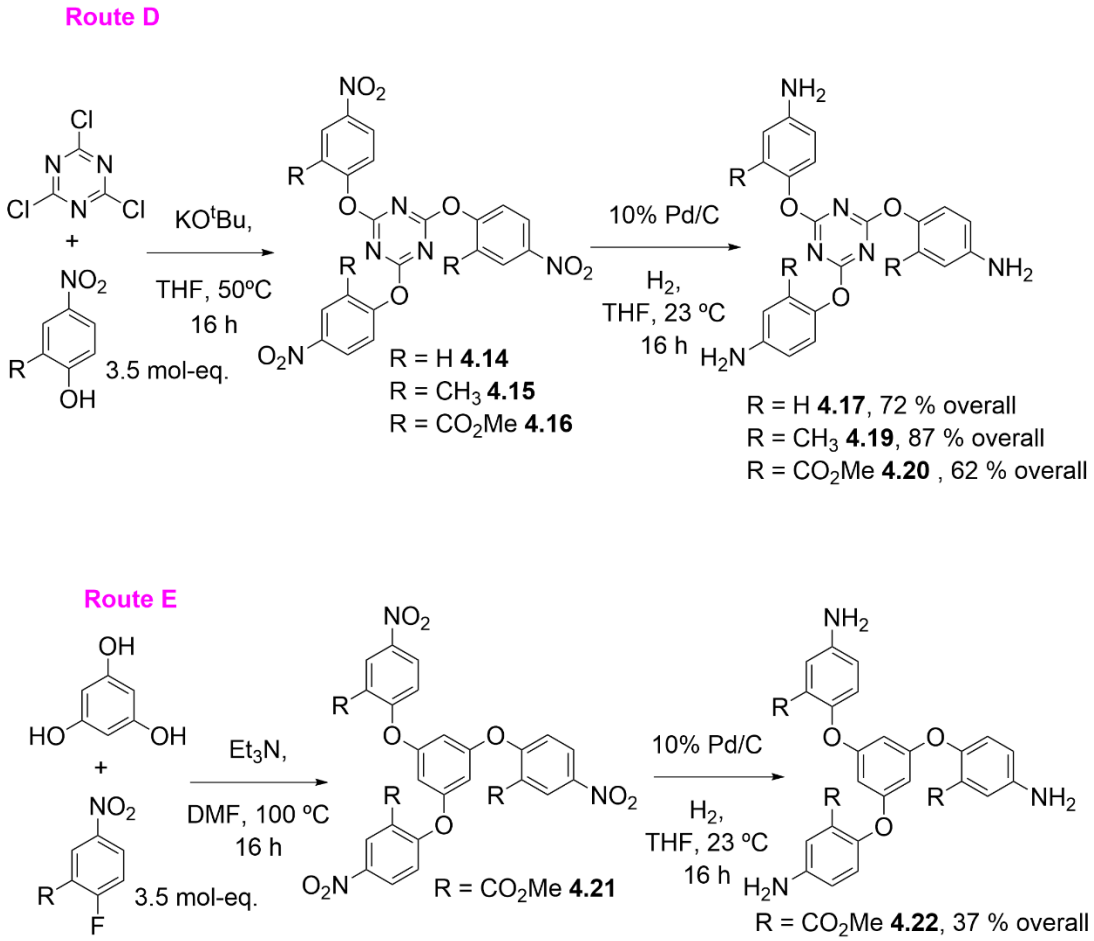

Figure 4.4. Route D and E to C_3-symmetric tris-amine ligand containing pendant functional groups, poised for the synthesis of self-assembled cages.

Related, albeit unfunctionalized ligands are present in the literature and have been used to produce M_4L_4 self-assembled cages that have been shown to bind anions.[14,15,17] A series of Fe^{2+} and Zn^{2+} salts were screened, and we discovered that $Zn(OTf)_2$ consistently yielded high-quality cage samples with good to excellent yields (85-97%) for all ligands (Figure

4.5a). As we hoped, all the cage samples have *T*-symmetry, as each ^{1}H NMR signal corresponds to its own set of chemically equivalent protons on the cage structure. The stoichiometry and structure of the cages was confirmed *via* electrospray ionization mass spectrometry.

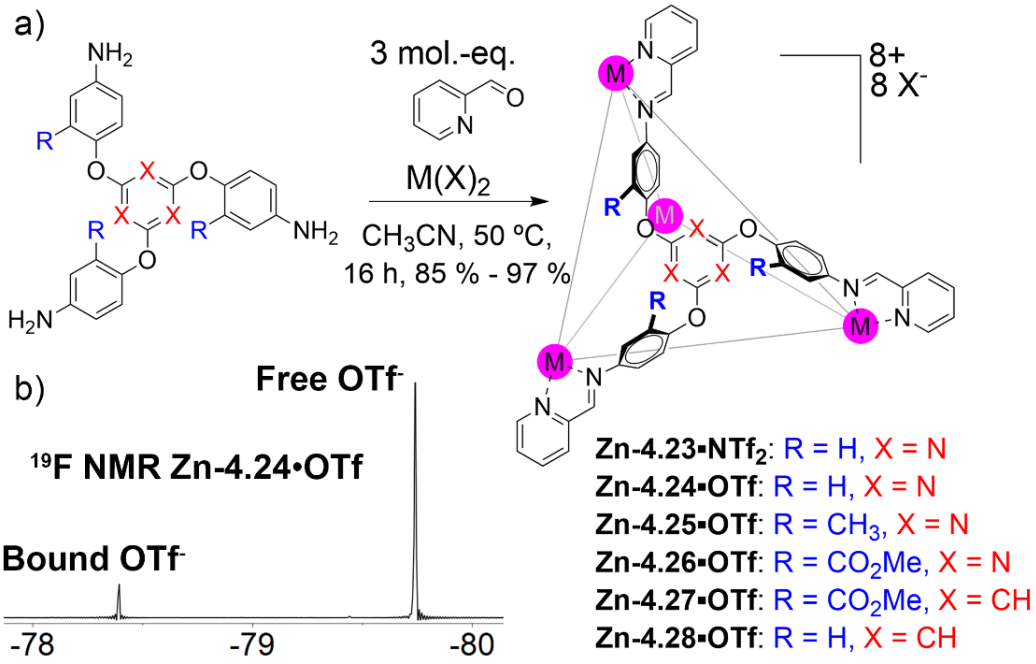

Figure 4.5. a) Self-assembled cage complexes; b) ^{19}F NMR of **Zn-4.24** demonstrating bound and free OTf^{-}.

In one instance using ligand **4.17**, pyridine carboxaldehyde, and $Zn(NTf_2)_2$ we were able to produce cage **Zn-4.23**, that possessed an empty cavity. Comparing the ^{19}F NMR of **Zn-4.23** and **Zn-4.24•OTf** a discrepancy was observed. The ^{19}F NMR of **Zn-4.23** contained a singular peak, compared to **Zn-4.24•OTf**, that contained two peaks (Figure 4.5b), this is consistent with cages **Zn-4.24-4.27•OTf**. The two peaks in the ^{19}F NMR are indicative that the cages synthesized from $Zn(OTf)_2$ each have one OTf^{-} anion on the interior, they are templated, and have seven OTf^{-} anions on the outside.

An interesting feature of the **Zn-4.23** cage, which has its cavity primarily occupied by solvent molecules in solution, is the rapid rotation of the aryl panels across the C-O-C axis. Compared to cage **Zn-4.24•OTf**, the templated OTf^- anion slows this rotation and can be easily visualized by the broadness of the aryl peaks in the ^1H NMR (Figure 4.6). Interestingly, there is no evidence that the aromatic panels of cages **Zn-4.24-4.27•OTf** are capable of rotation. Variable temperature (VT) ^1H NMR of **Zn-4.24•OTf** revealed that the pendant methyl groups do not rotate, as no slow equilibrium exchanging methyl peaks appeared in the VT ^1H NMR upon cooling to -30 °C. We were not able to obtain publication quality crystals structures of cages **Zn-4.24-4.27•OTf**, but we were able to obtain an X-ray structure of the structurally analogous Fe^{2+} cage, **Fe-4.27•SbF_6**, this confirmed the tetrahedral structure of the cages and demonstrated the pendant methyl esters are all externally oriented. With these new cages we can further explore the influence of "gating" the cage portals on the kinetics of anion exchange and selectivity.

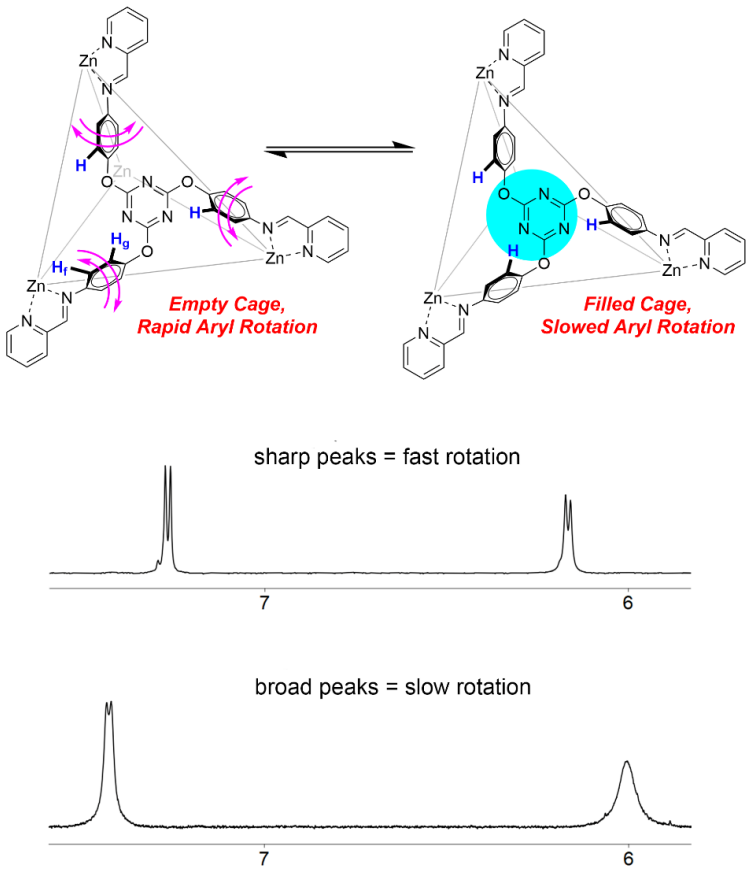

Figure 4.6. Comparing the rotational speed of "empty" cage **Zn-4.23** and filled cage **Zn-4.24**.

4.3. Anion Binding Selectivity and Kinetics of M_4L_4 Self-Assembled Cages with Pendent Functional groups

To investigate the influence of pendant functional groups on the binding properties of cages **Zn-4.24-4.27•OTf**, a preliminary binding study was conducted (Figure 4.7). Solutions of 1 mM concentrations of the respective cages in CD_3CN were prepared, and equimolar amounts of various pnictogen anions were added. The solutions were then heated and allowed to reach equilibrium before calculating the binding affinity relative to OTf^-. Cages **Zn-4.24-4.27•OTf** are templated with OTf^- anion, and the synthesis of empty variants of these cages is not possible, thus the binding affinities are determined relative to

OTf^-. Anion exchange with these cages exhibit slow exchange rates relative to the NMR time scale, as observed in Figure 4.7b, allowing for peak integration to derive the unknown values in the K_{rel} equation (Figure 4.7c). Despite the structural similarity in terms of an overall 8+ charge and identical cavity sizes of cages **Zn-4.24-4.27•OTf**, significant variations in anion selectivity and kinetics were observed. Specifically, when comparing the triazine-faced cages **Zn-4.23-4.26•OTf**, it became evident that cage **Zn-4.23** required a three-day heating period at 50 °C to reach equilibrium, while cages **Zn-4.24-4.26•OTf** necessitated a surprising two weeks under identical conditions. It is noteworthy that at the two-week mark, some cage decomposition was observed, indicating that both the time required for equilibrium and anion affinity represent lower limits. Consequently, it is highly likely that the actual time needed to reach equilibrium extends well beyond the two-week timeframe. Given that the only discernible difference among cages **Zn-4.23-4.26•OTf** lies in their pendant functional groups, these groups directly influence the kinetics of anion exchange.

a)

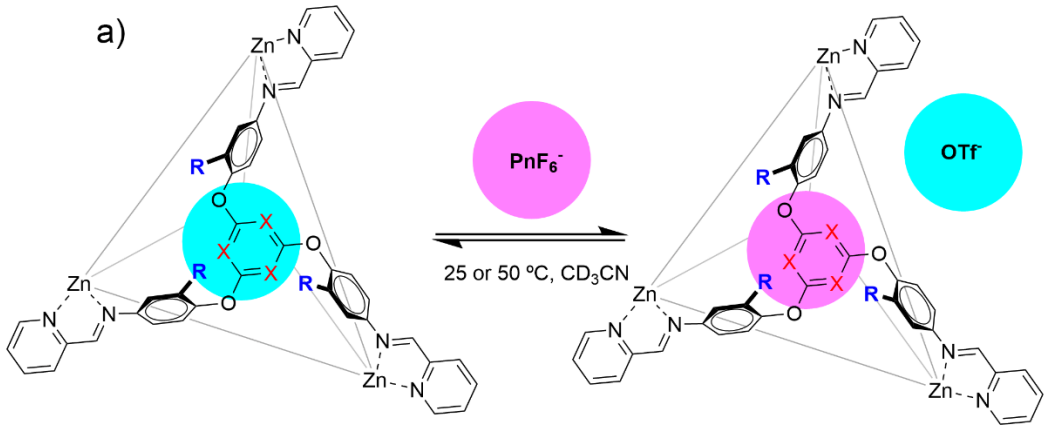

Zn-4.24•OTf: R = H, X = N
Zn-4.25•OTf: R = CH_3, X = N
Zn-4.26•OTf: R = CO_2Me, X = N
Zn-4.27•OTf: R = CO_2Me, X = CH
Zn-4.28•OTf: R = H, X = CH

b)

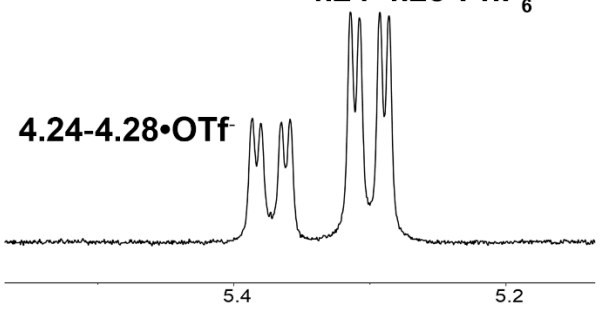

c)

$$k_{rel} = \frac{[HG2]([G1]_0 - [HG1])}{[HG1]([G2]_0 - [HG2])}$$

d)

Guest anion	K_{rel}(**4.24**)	K_{rel}(**4.25**)	K_{rel}(**4.26**)	K_{rel}(**4.27**)	K_{rel}(**4.28**)[4]
PF_6^-	19	20	2.4	0.1	n.d.
AsF_6^-	19	58	38	0.4	1.0
SbF_6^-	25	25	15	44	5.8
Time to equilibrium	72 h at 50 °C	336 h at 50 °C	336 h at 50 °C	seconds, at 25 °C	seconds, at 25 °C

Figure 4.7. a) Reaction scheme of anion exchange; b) ^{1}H NMR example of anion exchange that is slow relative to the NMR timescale; c) K_{rel} equation; d) K_{rel} affinities for various pnictogens and their time to reach equilibrium.

The results of the preliminary binding study revealed that the pendant functional groups installed onto cages **Zn-4.24-4.26•OTf** have a significant impact on their anion selectivity.

For example, **Zn-4.24•OTf** showed no selectivity for PF_6^-, AsF_6^-, and SbF_6^-. However, after the introduction of 12 pendant methyl groups, **Zn-4.25•OTf** exhibited a 2-fold increase in affinity for AsF_6^-, over PF_6^-, and SbF_6^-, Similarly, **Zn-4.26•OTf** demonstrated a remarkable 19-fold increase in affinity for AsF_6^- over PF_6^- and a 3-fold preference for AsF_6^- over SbF_6^-. **Zn-4.27•OTf** exchanged anions rapidly at room temperature in seconds, like its unfunctionalized empty predecessor **Zn-4.28**, which has been previously studied by another research group.[15] **Zn-4.27•OTf** exhibited staggeringly high selectivity for SbF_6^-, showing a 440-fold preference over PF_6^- and a 110-fold preference over AsF_6^-. To further investigate the effect of the pendant groups on anion binding selectivity and kinetics, we studied the anion exchange process using pseudo-first order rate plots.

While investigating the anion exchange process using pseudo-first order rate plots for cages **Zn-4.24-4.26•OTf**, 1 mM solutions of the cages were prepared in CD_3CN, and the concentration of each competitive anion was adjusted to 25 mM. The anion exchange process was monitored over time using ^1H NMR spectroscopy, revealing significant differences in anion exchange rates between cages **Zn-4.24–4.26•OTf**. For cage **Zn-4.24•OTf**, the panel gaps rotate slowly, behaving like a "revolving door," and the exchange process is governed by the size of the incoming anion. PF_6^-, being the smallest anion, exchanges at a rate of 0.1 mM/h, reaching completion in 9-12 hours. AsF_6^- and SbF_6^-, being larger anions, exchange at rates of 0.08 and 0.05 mM/h, respectively. Despite the similar relative binding affinities of PF_6^-, AsF_6^-, and SbF_6^-. for cage **Zn-4.24•OTf**, the exchange process does not seem to be driven by affinity but rather by the ability for the anions to "squeeze" through the gaps in the cage's panels.

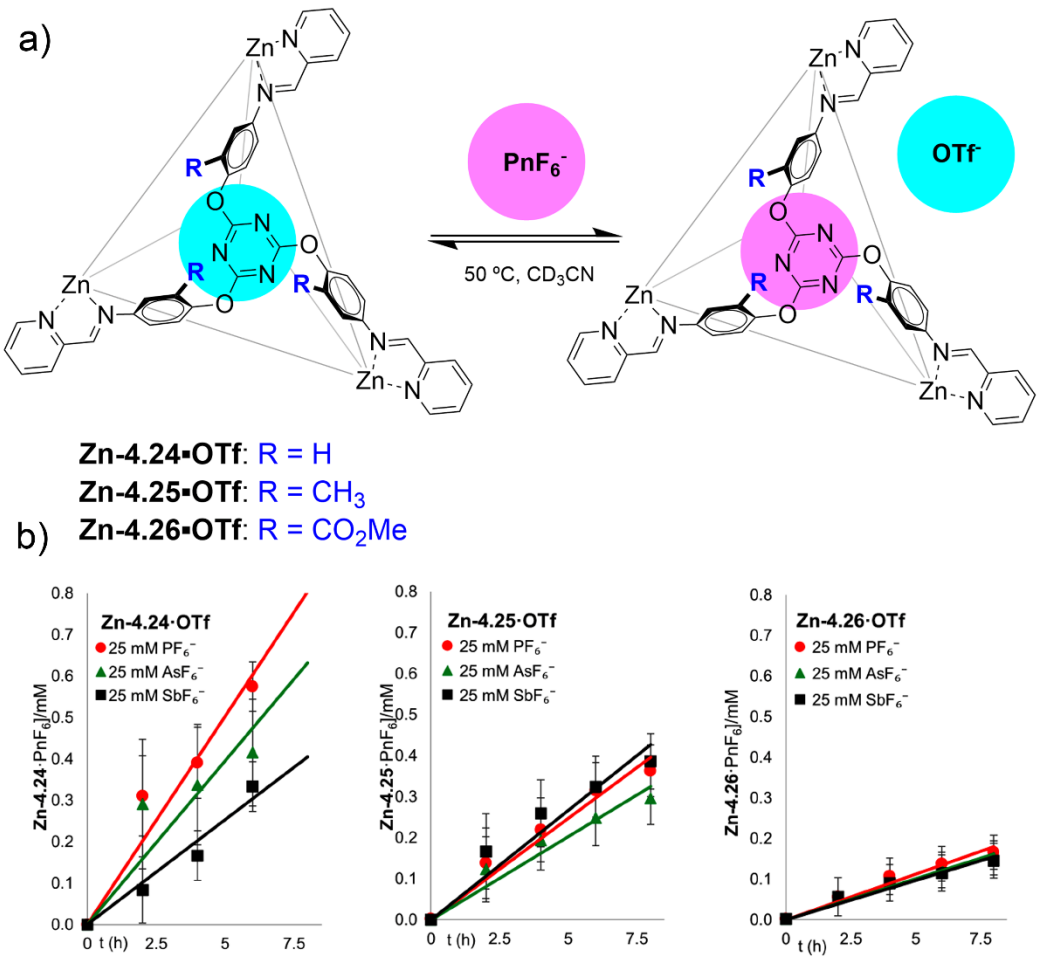

Figure 4.8. Reaction scheme depicting the anion exchange process; b) pseudo-first order rate plots for the exchange process, [**Zn-4.24-4.26•OTf**] = 1.0 mM, [PnF_6^-] = 25 mM, CD_3CN, 323 K.

Cage **Zn-4.25•OTf** exhibits about a 2-fold slower exchange rate for the pnictogen anions compared to **Zn-4.24•OTf** , and there is less dependence on the size of the incoming anion. Even with a significant excess of competitive anion, **Zn-4.25•OTf** does not fully exchange even after 24 hours. This is attributed to the steric congestion caused by the pendant methyl groups, which act as a "door stop" and restrict the free rotation of the aromatic walls, significantly impeding the ingress and egress of anions. The effect of the pendant methyl esters on cage **Zn-4.26•OTf** is even more pronounced. These groups prevent the aromatic

panels from rotating freely and introduce an additional degree of rotation across the C-C bond of the methyl ester and aromatic ring, which can potentially "block" the cage portal. Broadly, the exchange rate of **Zn-4.26•OTf** is 5-fold slower than **Zn-4.24•OTf** and 2-fold slower than **Zn-4.25•OTf** for the pnictogen anions. Interestingly despite **Zn-4.26•OTf** having a 19-fold preference for AsF_6^- over PF_6^-, the exchange rates are almost identical. Once again, anion affinity does not significantly impact the exchange process, instead, the governing effects are more nuanced. Perplexed by the lack of correlation between anion affinity and kinetics, further investigation was initiated to probe the mechanism of the exchange process and fully understand the effects of the pendant functional groups on the exchange of non-coordinating anions of different sizes.

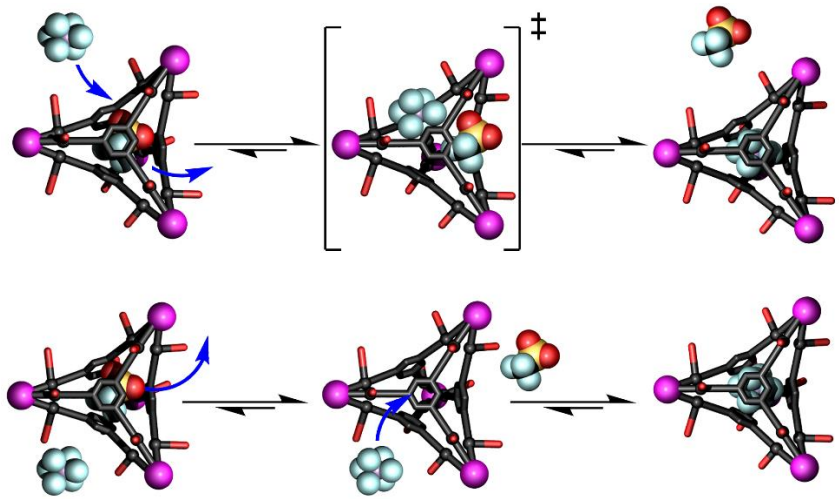

Figure 4.9. Cartoon of two competing mechanistic pathways for anion exchange, associative which is more S_N2 like and dissociative which is more S_N1-like.

The anion exchange process for cages **Zn-4.24-4.26•OTf** occurs slowly enough that the mechanism can be elucidated, which can go through either an associative or dissociative mechanism. Where the associative mechanism is akin to a S_N2 reaction mechanism and the dissociative is more like a S_N1 mechanism. It was not immediately

clear whether the existence or nature of the leaving group was relevant when considering the mechanism of the anion exchange process. So, we ran a simple anion capture experiment to see if there was a substantial difference in the rate of anion capture using PF_6^- with "empty" cage **Zn-4.23** and OTf^- templated cage **Zn-4.24•OTf**. As **Zn-4.23** is empty it has no "leaving group", which in the case of **Zn-4.24•OTf** is an anion of OTf^- templated during the subcomponent self-assembly process. The capturing of PF_6^- by **Zn-4.23•OTf** occurred rapidly in under three minutes at ambient temperature, while only 20 % of anion exchange occurred when using **Zn-4.24•OTf** heated at 50 °C for 24 hours (Figure 4.10). The ease with which the OTf^- can leave the cage structure is crucial in determining the rate of anion exchange. In the case of **Zn-4.24•OTf**, it is easier to leave compared to the sterically congested portals of **Zn-4.25–4.26•OTf**, thus the anion exchange is faster for **Zn-4.24•OTf**.

Clearly there are multiple elements to the anion exchange process, not only does the size of the incoming anion and the type of pendant functional group significantly impact the exchange kinetics, but potentially so does the nature of the leaving group. The incoming anion has to "squeeze" through the panel gaps but the templated anion OTf^- must also "squeeze" itself out, either during the approach of the incoming anion or before. To clarify the relationship between binding affinity and leaving group and their impact on anion exchange kinetics, anion exchange studies were conducted using cages containing a different leaving group.

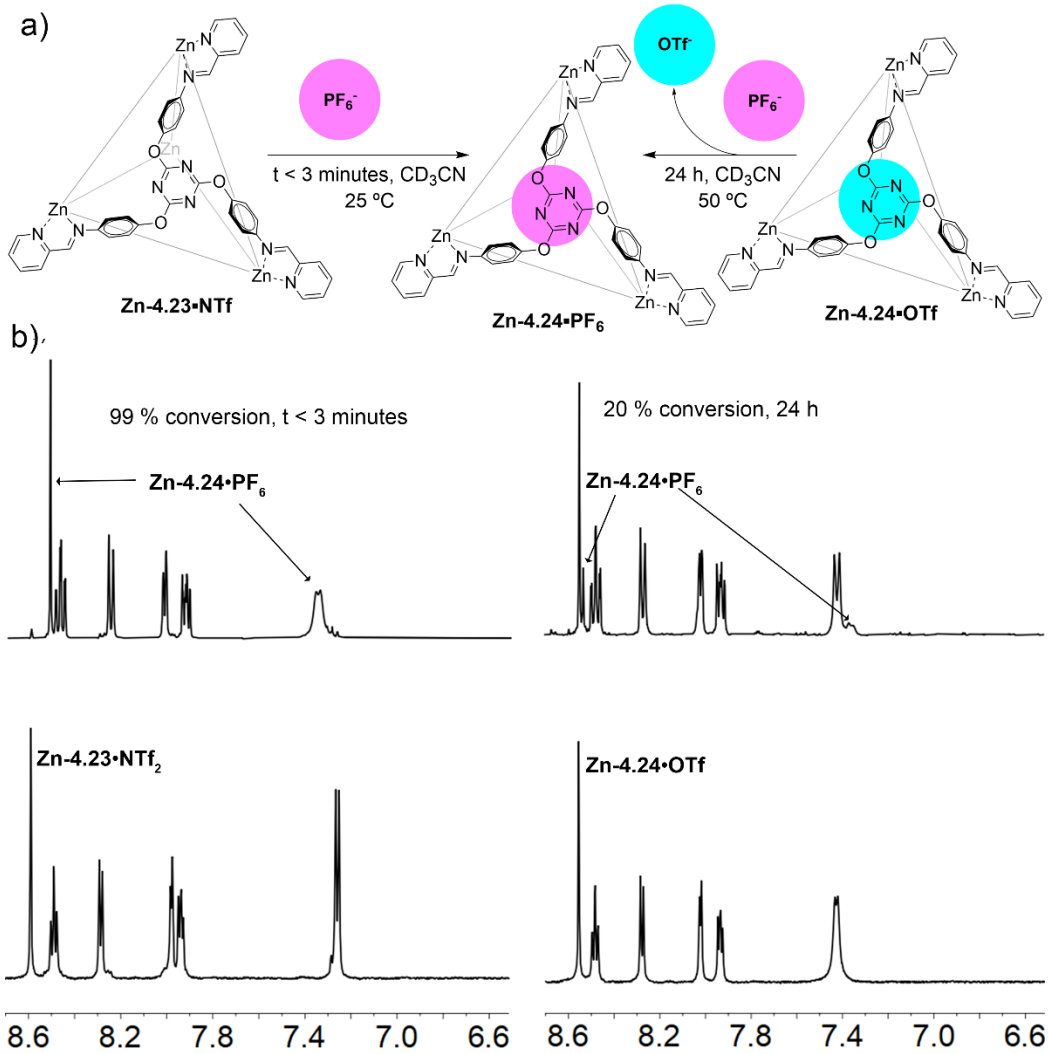

Figure 4.10. Testing the effect of the "leaving group" for anion exchange with unfunctionalized cages. a) Chemdraw illustration of "empty" cage **Zn-4.24** and templated cage **Zn-4.25•OTf** up taking PF_6^-; b) ^1H NMR spectra showing the initial cage spectra (bottom) and anion exchange measured as % conversion at the indicated time. [**Zn-4.24** and **4.25•OTf**] = 1.0 mM, [PF_6^-] = 1.0 mM, CD_3CN, 323 or 273 K.

The binding affinities of cages **Zn-4.24-4.26•OTf** towards OTf^- were consistently lower than their affinities towards the various screened pnictogen anions. When conducting the anion exchange experiments using **Zn-4.24•OTf** and different pnictogens, it was observed that despite having similar binding affinities, the rate of exchange was primarily influenced by the size of the anion rather than its binding affinity (Figure 4.8). However,

in the case of **Zn-4.25•OTf**, the relationship of size and affinity on the exchange rate was less pronounced. Interestingly, neither size nor affinity appeared to significantly affect the exchange using **Zn-4.26•OTf**. This suggests that the leaving group may be a crucial variable in the anion exchange process, while size and affinity play a lesser role when considering the exchange with **Zn-4.25-4.26•OTf**.

Zn-4.25-4.26•OTf were converted to their corresponding SbF_6^- templated cages *via* heating **Zn-4.25-4.26•OTf** with over 175 molar equivalents of $NaSbF_6$ at 50 °C overnight which produced templated variants **Zn-4.25-4.26•SbF_6**. The following day they were isolated and their ^1H NMR spectra revealed successful displacement of OTf^- and incorporation of SbF_6^-. Akin to other exchange rate studies **Zn-4.25–4.26•SbF_6** were prepared at 1 mM concentration, the concentration of competitive anion was brought to 25 mM and the solutions were heated at 50 °C and monitored over time (Figure 4.11). In both cases the exchange rate was significantly slower when the cages had SbF_6^- as a leaving group.

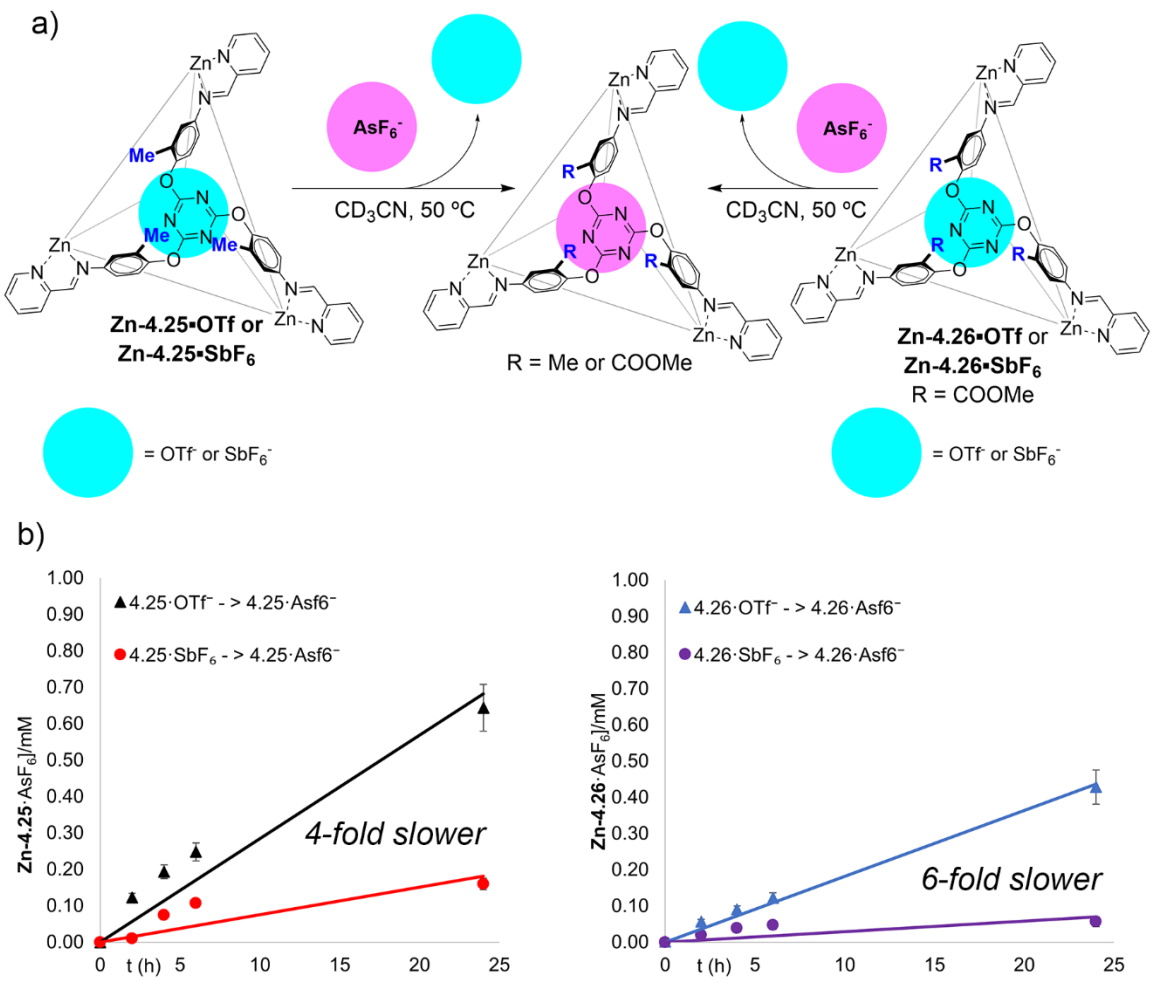

Figure 4.11. a) Scheme depicting the effect of leaving group OTf^- versus SbF_6^- for exchange with AsF_6^-; b) pseudo-first order rate plots for the exchange process of **Zn-4.25–4.26•OTf** to **Zn-4.25–4.26•SbF$_6$**. [**Zn-4.25–4.26•OTf/SbF$_6$**] = 1.0 mM, [AsF_6^-] = 25.0 mM, CD_3CN, 323 K.

For both cages **Zn-4.25-4.26•OTf** SbF_6^- binds tighter than OTf^- thus the observed rates of exchange are slower when displacing OTf^- compared to the more tightly bound SbF_6^- (Figure 4.11). Cage **Zn-4.25•OTf** has a 2.3-fold higher affinity for AsF_6^- over SbF_6^- and similarly cage **Zn-4.26•OTf** has a 2.5-fold higher affinity for AsF_6^- over SbF_6^-, meaning both cage's preference for AsF_6^- over SbF_6^- are almost identical. If the exchange rate was purely governed by the binding affinity of the incoming anion it would be expected that

the difference in the rate of anion exchange for cages **Zn-4.25–4.26•SbF_6** would be very close. Instead, the exchange rates are different, 4-fold slower for **Zn-4.25•SbF_6** and 6-fold slower for **Zn-4.26•SbF_6** when exchanging with AsF_6^-. This indicates that the size of the leaving group is also an important factor when considering the exchange rate, particularly when the leaving group anion must "squeeze" through the sterically congested portal of **Zn-4.26•OTf.**

Table 5.1. a) Rate as a function of increasing concentration of competing anion and order calculated *via* an algebraic approach. [**Zn-4.25-4.26•OTf**] = 1.0 mM, CD_3CN, 293 K.

Zn-4.25•OTf

8 mM	Rate (mM/h)	25 mM	Rate (mM/h)	75 mM	Rate (mM/h)	Order
PF_6^-	0.016	PF_6^-	0.024	PF_6^-	0.028	0.2
AsF_6^-	0.023	AsF_6^-	0.034	AsF_6^-	0.044	0.3
SbF_6^-	0.018	SbF_6^-	0.062	SbF_6^-	0.090	0.7

Zn-4.26•OTf

8 mM	Rate (mM/h)	25 mM	Rate (mM/h)	75 mM	Rate (mM/h)	Order
PF_6^-	0.007	PF_6^-	0.015	PF_6^-	0.020	0.5
AsF_6^-	0.013	AsF_6^-	0.018	AsF_6^-	0.020	0.2
SbF_6^-	0.007	SbF_6^-	0.012	SbF_6^-	0.024	0.6

To gauge the amount of associative and dissociative mechanism for various pnictogen anions and cages **Zn-4.25-4.26•OTf** pseudo-first order rate plots were produced using three different concentrations of incoming anion 8 mM, 25 mM, and 75 mM. The rates of the reactions were produced from the slope of the line and following the order was calculated which ranged from 0.2-0.7 (Table 5.1). Clearly both mechanisms are at play as the system is complex and many factors influence the anion exchange kinetics. For cages **Zn-4.25-4.26•OTf** we expected that PF_6^- would see the most significant associative

mechanism as it was the smallest anion and could easily squeeze through the cage's panel gaps. Instead, the largest anion, SbF_6^-, showed the greatest dependence on incoming anion concentration for cages **Zn-4.25-4.26•OTf**. I hypothesize this is likely due to a lower population of "unproductive" equilibria, where the SbF_6^- anion in cages **Zn-4.25-4.26•SbF_6** are displaced by another molecule of SbF_6^- thereby limiting the rate of formation of *new species of* **Zn-4.25-4.26•SbF_6** in solution. This unproductive equilibrium is less prevalent with the larger templated anion SbF_6^- as due to its size, it is more challenging to expel.

Although the variations in order are small, some trends can be cautiously and broadly summarized. The more hindered **Zn-4.26•OTf** displays a slightly increased order dependence on the nucleophile compared to **Zn-4.24•OTf**, suggesting that OTf^- egress is slowed, leading to a higher proportion of an S_N2-like associative mechanism. Seeing as the desolvation energies and charge of cage structures are universal across these kinetic experiments clearly the pendant functional groups profoundly impact the selectivity, kinetics, and mechanisms at play during anion exchange.

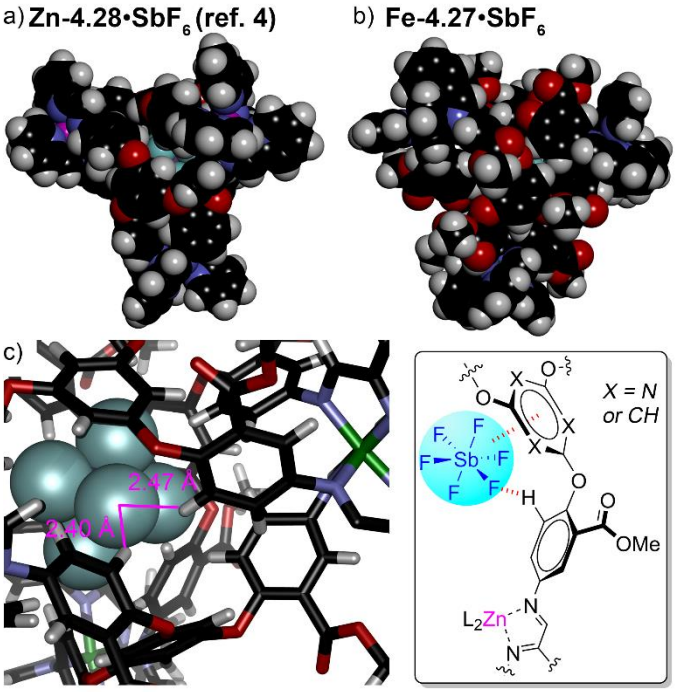

Figure 4.12. Structural analysis a) molecular structures determined by SCXRD a) **Zn-4.28•SbF_6** (ref. 4) and b) **Fe-4.28•SbF_6**, c) **Fe-4.28•SbF_6**, showing estimated CH-F distances between internal protons and the bound anion.

The exchange behavior of **Zn-4.27-4.28•OTf** differs significantly from their triazine counterparts. The presence of more electron-rich phenyl walls in cage **Zn-4.27-4.28•OTf** greatly enhances the rate of anion binding exchange compared to cages **Zn-4.24-4.26•OTf**. Upon adding PF_6^-, AsF_6^-, and SbF_6^- ions to **Zn-4.25•OTf**, complete equilibration occurs within seconds, for cages **Zn-4.24-4.26•OTf** equilibration takes days or weeks. The affinity data for phloroglucinol cage **Zn-4.25-4.26•OTf** also exhibits interesting characteristics. While **Zn-4.28•OTf** shows relatively similar affinities for similarly sized anions, with identical affinities for OTf^- and AsF_6^- and only a 6-fold higher affinity for SbF_6^-, cage **Zn-4.27•OTf** displays significant selectivity for the larger SbF_6^-, $K_{rel} = 44$. In contrast, AsF_6^- and PF_6^- bind more weakly than OTf^-. The crystal structure of **Zn-4.27•SbF_6** and the corresponding NMR data provide insights into the recognition process. The bound

guest is in close proximity to both the central ring in the ligand (triazine or benzene) and the C-H groups of the pendant phenyl arms, that create anion-pi and C-H anion interactions in the host:guest complex. The cavity sizes of cages **Zn-4.24-4.28•OTf** are extremely similar, ~145 $Å^3$, and the cages are slightly flexible, allowing them to adapt to the size and shape of the guest. Interactions with the central ring faces and the edge C-H bonds of the pendant benzenes play a role in determining the anion affinity. While the rotation of these bonds occurs in **Zn-4.24/4.28•OTf**, they are fixed in **Zn-4.25-4.27•OTf**. The fixed orientation and permanent introversion of the C-H groups on the arene ring in cages **Zn-4.25-4.27•OTf** may influence the effective cavity size or facilitate favorable C-H-anion interactions between the host and guest. The optimal size and shape match between the cavities and AsF_6^- explain its higher affinity in most cases. However, the significantly higher affinity for SbF_6^- in cage **Zn-4.27•OTf** compared to the other pnictogen anions and their affinities for cages **Zn-4.24-4.26•OTf**, can be attributed to the presence of a phenyl core instead of a triazine. The selectivity for the larger SbF_6^- is likely due to more favorable anion-pi interactions between the more electron-rich arene and the softer, more diffuse SbF_6^- ion. The enhanced CH-anion interactions in **Zn-4.27•OTf**, resulting from the presence of the external electron-withdrawing ester group, further contribute to its strong selectivity.

The favorable anion-pi interactions with the triazine ring significantly slow down the exchange rate. Among the highly similar cages **Zn-4.24-4.26•OTf**, which differ only in the nature of the external group, the exchange mechanism becomes more complex. Two mechanisms, associative and dissociative, are present, and their relative proportions

depend on the specific cage and incoming anion. The freely rotating groups in **Zn-4.24•OTf** facilitate a faster exchange rate for guests. When the aryl groups are "locked" by the presence of pendant methyl or methyl ester groups, the exchange rate decreases significantly. Increasing the size of the external group adds an additional hindrance layer to the cage exterior, limiting the access of incoming anions to the cage walls. The hindrance affects both the exit rate of the bound anion and the entry rate of the incoming anion, thereby influencing the reaction rate and the order of the process. This also explains the rate dependence of cages **Zn-4.24-4.26•OTf** on the type of incoming anion. For the unfunctionalized cage **Zn-4.24•OTf**, the rate depends on the size of the incoming anion, as smaller anions can more easily fit through the portals. However, this effect is not observed for the "locked" cage **Zn-4.26•OTf** as increasing the size of the anion no longer reduces the entry rate. Overall, small structural changes in the exterior of self-assembled cage complexes can have unexpected and significant effects on the affinity and exchange rate of bound guests, even when the interior cavity shapes and sizes are almost identical.

4.4. Conclusion

Within this chapter we successfully installed pendant functional groups on C_3-symmetric tris-amine ligands that undergo self-assembly to produce tetrahedral cages, that in most cases, are templated with a single anion of OTf^-. These types of cages and the effect of the pendant group on substrate exchange kinetics, selectivity, and mechanism are rare within the literature. As the pendant functional groups significantly impact guest exchange processes, we have demonstrated that this overlooked area of research inquiry is deserving of further research efforts. As the Hooley lab is predominately focused on biomimetic

catalysis future work is directed towards the extension of these functionalized C_3-symmetric tris-amine ligands for their applications to produce larger tetrahedral cages and positively affect biomimetic catalytic events.

References

(1) Sullivan, S. M.; Holyoak, T. Structures of Rat Cytosolic PEPCK: Insight into the Mechanism of Phosphorylation and Decarboxylation of Oxaloacetic Acid. *Biochemistry* **2007**, *46*, 10078–10088.

(2) Sullivan, S. M.; Holyoak, T. Enzymes with Lid-Gated Active Sites Must Operate by an Induced Fit Mechanism Instead of Conformational Selection. *Proc. Natl. Acad. Sci. U. S. A.* **2008**, *105*, 13829–13834.

(3) Ngai, C.; Bogie, P. M.; Holloway, L. R.; Dietz, P. C.; Mueller, L. J.; Hooley, R. J. Cofactor-Mediated Nucleophilic Substitution Catalyzed by a Self-Assembled Holoenzyme Mimic. *J. Org. Chem.* **2019**, *84*, 12000–12008.

(4) da Camara, B.; Dietz, P. C.; Chalek, K. R.; Mueller, L. J.; Hooley, R. J. Selective, Cofactor-Mediated Catalytic Oxidation of Alkanethiols in a Self-Assembled Cage Host. *Chem. Commun.* **2020**, *56*, 14263–14266.

(5) Tidmarsh, I. S.; Faust, T. B.; Adams, H.; Harding, L. P.; Russo, L.; Clegg, W.; Ward, M. D. Octanuclear Cubic Coordination Cages. *J. Am. Chem. Soc.* **2008**, *130*, 15167–15175.

(6) Cullen, W.; Metherell, A. J.; Wragg, A. B.; Taylor, C. G. P.; Williams, N. H.; Ward, M. D. Catalysis in a Cationic Coordination Cage Using a Cavity-Bound Guest and Surface-Bound Anions: Inhibition, Activation, and Autocatalysis. *J. Am. Chem. Soc.* **2018**, *140*, 2821–2828.

(7) Akine, S.; Miyashita, M.; Nabeshima, T. A Metallo-Molecular Cage That Can Close the Apertures with Coordination Bonds. *J. Am. Chem. Soc.* **2017**, *139*, 4631–4634.

(8) Wang, H.; Liu, F.; Helgeson, R. C.; Houk, K. N. Reversible Photochemically Gated Transformation of a Hemicarcerand to a Carcerand. *Angew. Chem. Int. Ed.* **2013**, *52*, 655–659.

(9) Liu, X.; Inagaki, S.; Gong, J. Heterogeneous Molecular Systems for Photocatalytic CO_2 Reduction with Water Oxidation. *Angew. Chem. Int. Ed.* **2016**, *55*, 14924–14950.

(10) Holloway, L. R.; Bogie, P. M.; Lyon, Y.; Ngai, C.; Miller, T. F.; Julian, R. R.; Hooley, R. J. Tandem Reactivity of a Self-Assembled Cage Catalyst with Endohedral Acid Groups. *J. Am. Chem. Soc.* **2018**, *140*, 8078–8081.

(11) Ngai, C.; Wu, H.-T.; da Camara, B.; Williams, C. G.; Mueller, L. J.; Julian, R. R.; Hooley, R. J. Moderated Basicity of Endohedral Amine Groups in an Octa-Cationic Self-Assembled Cage. *Angew. Chem. Int. Ed Engl.* **2022**, *61*, e202117011.

(12) Ngai, C.; da Camara, B.; Woods, C. Z.; Hooley, R. J. Size- and Shape-Selective Catalysis with a Functionalized Self-Assembled Cage Host. *J. Org. Chem.* **2021**, *86*, 12862–12871.

(13) Ngai, C.; Sanchez-Marsetti, C. M.; Harman, W. H.; Hooley, R. J. Supramolecular Catalysis of the Oxa-Pictet-Spengler Reaction with an Endohedrally Functionalized Self-Assembled Cage Complex. *Angew. Chem. Int. Ed Engl.* **2020**, *59*, 23505–23509.

(14) Ferguson, A.; Squire, M. A.; Siretanu, D.; Mitcov, D.; Mathonière, C.; Clérac, R.; Kruger, P. E. A Face-Capped $[Fe_4L_4]^{8+}$ Spin Crossover Tetrahedral Cage. *Chem. Commun.* **2013**, *49*, 1597–1599.

(15) Xu, L.; Zhang, D.; Ronson, T. K.; Nitschke, J. R. Improved Acid Resistance of a Metal-Organic Cage Enables Cargo Release and Exchange between Hosts. *Angew. Chem. Int. Ed.* **2020**, *59*, 7435–7438.

(16) Zhang, D.; Ronson, T. K.; Mosquera, J.; Martinez, A.; Guy, L.; Nitschke, J. R. Anion Binding in Water Drives Structural Adaptation in an Azaphosphatrane-Functionalized $FeII_4L_4$ Tetrahedron. *J. Am. Chem. Soc.* **2017**, *139*, 6574–6577.

(17) Ferguson, A.; Staniland, R. W.; Fitchett, C. M.; Squire, M. A.; Williamson, B. E.; Kruger, P. E. Variation of Guest Selectivity within $[Fe_4L_4]^{8+}$ Tetrahedral Cages through Subtle Modification of the Face-Capping Ligand. *Dalton Trans.* **2014**, *43*, 14550–14553.

(18) Alvi, S.; Ali, R. Design, Synthesis and Photophysical Properties of Novel Star-Shaped Truxene-Based Heterocycles Utilizing Ring-Closing Metathesis, Clauson-Kaas, Van Leusen and Ullmann-Type Reactions as Key Tools. *Beilstein J. Org. Chem.* **2021**, *17*, 1374–1384.

(19) Conn, G.; Eisler, S. Synthesis and Intramolecular Hydrogen Bonding Networks of 2,4,6-Tri(o-Hydroxyaryl)-1,3,5-Triazines. *Org. Lett.* **2011**, *13*, 5080–5083.

(20) Mao, J.; Wu, T.; Tang, Z.; Xia, L.; He, L.; Zeng, B.; Xu, Y.; Yuan, C.; Dai, L. Molecular Exchange of Dynamic Imine Bond for the Etching of Polymer Particles. *Macromol. Rapid Commun.* **2022**, *43*, e2200562.

Chapter 5 - Synthesis of Extended C_3-Symmetric Functionalized Tris-Amine Ligands and Their Capacity to Form Self-Assembled Cages

5.1. Introduction

In Chapter 4, the influence of pendant functional groups on anion exchange kinetics, selectivity, and mechanism in small M_4L_4 cage complexes was investigated. Since these cages were templated with an anion and had relatively small cavities (~145 $Å^3$), their ability to bind organic molecules and facilitate catalytic events was limited. As such, a method to form larger M_4L_4 scaffolds with pendant functional groups is required to use cages of this type to promote catalysis. This can be achieved by extending the C_3-symmetric tris-amine ligand subcomponent. Cages from this ligand type will have larger cavities but still maintain rather restricted entrance portals. By restricting the size of the entrance portal, we hypothesize that highly size and substrate selective processes can be achieved. While there are numerous extended C_3-symmetric tris-amine ligands documented in the literature, none of them contain functional groups on the periphery of the ligand.[1–9]

5.2. Synthesis of C_3-Symmetric Functionalized Tris-Amine Ligands and Their Sub-Component Self-Assembly Outcomes

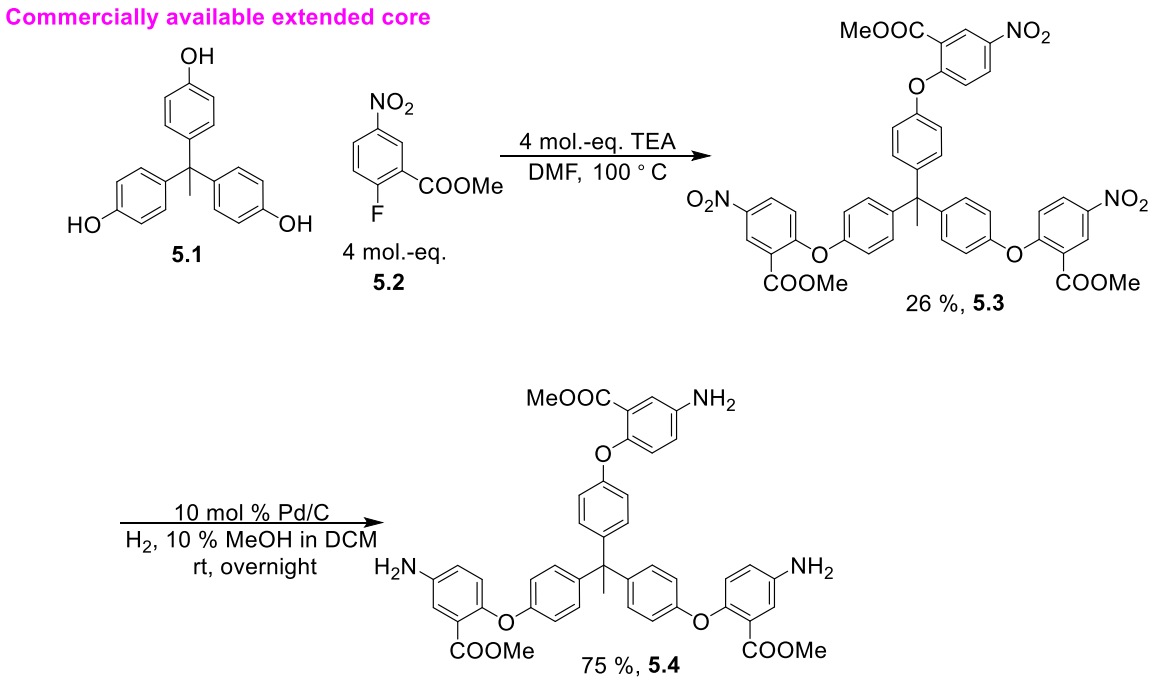

Figure 5.1. Synthetic route to C_3-symmetric ligand containing peripherally installed methyl ester group.

To efficiently produce extended C_3-symmetric tris-amine ligands and study their sub-component self-assembly properties, access to a commercially available aryl triol is key. 4,4',4''-(Ethane-1,1,1-triyl)triphenol (**5.1**) is a commercially available triphenol compound that can easily be extended by nucleophilic aromatic substitution and subsequently reduced to ligand **5.4** (Figure 5.1). The rapid access to the extended core was good. The presence of multiple degrees of freedom and conformations in ligand **5.4** raised concerns about its potential to effectively self-assemble into a well-defined species. Under our standard conditions we used ligand **5.4** with sub-components pyridine carboxaldehyde and $Fe(NTf_2)_2$ (Figure 5.2).

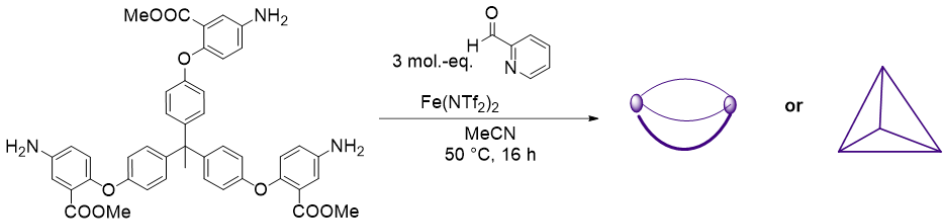

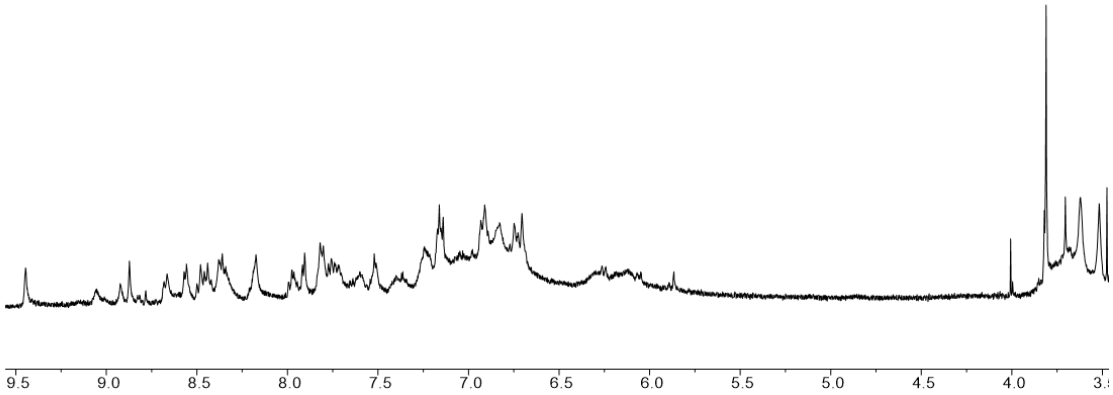

Figure 5.2. ^{1}H NMR spectra of self-assembly outcomes using ligand **5.4**.

The utilization of ligand **5.4** in conjunction with sub-components pyridine carboxaldehyde and $Fe(NTf_2)_2$ resulted in the formation of a complex but somewhat interpretable ^{1}H NMR spectrum (Figure 5.2). However, the presence of significant broadening in the methyl ester region (δ 3.5-4.0 ppm) posed challenges in fully elucidating if this was a mixture of diastereomers, different compounds, or both. Considering the self-assembly process, the two most plausible outcomes are a M_2L_3 helicate and a M_4L_4 tetrahedron. The tetrahedron, exhibiting *T* symmetry, would manifest as a singular peak for the methyl ester, 3 peaks for the S_4 diastereomer, and 4 peaks for the C_3 diastereomer. On the other hand, a helicate could exist in two stereochemical possibilities: if both metal

centers are homochiral, each chemically distinct proton would have its own peak, alternatively, if the metal centers are heterochiral, each proton would be split into 2 peaks. Additionally, in the formation of a helicate from ligand **5.4**, two esters would be chemically identical while the lone ester on the aryl ring would be in its own distinct environment due to the uncoordinated amine. In short, if the mixture from the self-assembly of ligand **5.4** produced three tetrahedral diastereomers and 2 helical diastereomers there would be a minimum of 10 peaks in the methyl ester region.

Deciphering the structure from this spectrum proves challenging as the broadening in the methyl ester region could be attributed to potentially free NH_2 groups, indicating helicate formation. Moreover, the methyl at the trityl position does not fall within the aliphatic region of the NMR, most likely it is clustered with the methyl ester peaks. This leads to unequal integrations (with significant error due to broadening) of the methyl ester peak region. Thes integrations could potentially include protons of both the methyl esters and the methyl at the trityl position. If the trityl methyl groups are significantly shifted down field potentially this is indicative of formation of a tetrahedron, which is juxtaposed to the observation that broadening at δ 3.5-4.0 ppm is from free NH_2. The significant broadening in the 3.5-4.0 ppm range renders the usefulness of the handles on the ligand futile. Furthermore, the aromatic region exhibits complex and overlapped splitting, typically indicative of a mixture of many products and stereoisomers. To determine the number of distinct species and their stoichiometry in the product mixture, efforts are currently underway to optimize mass spectrometry conditions.

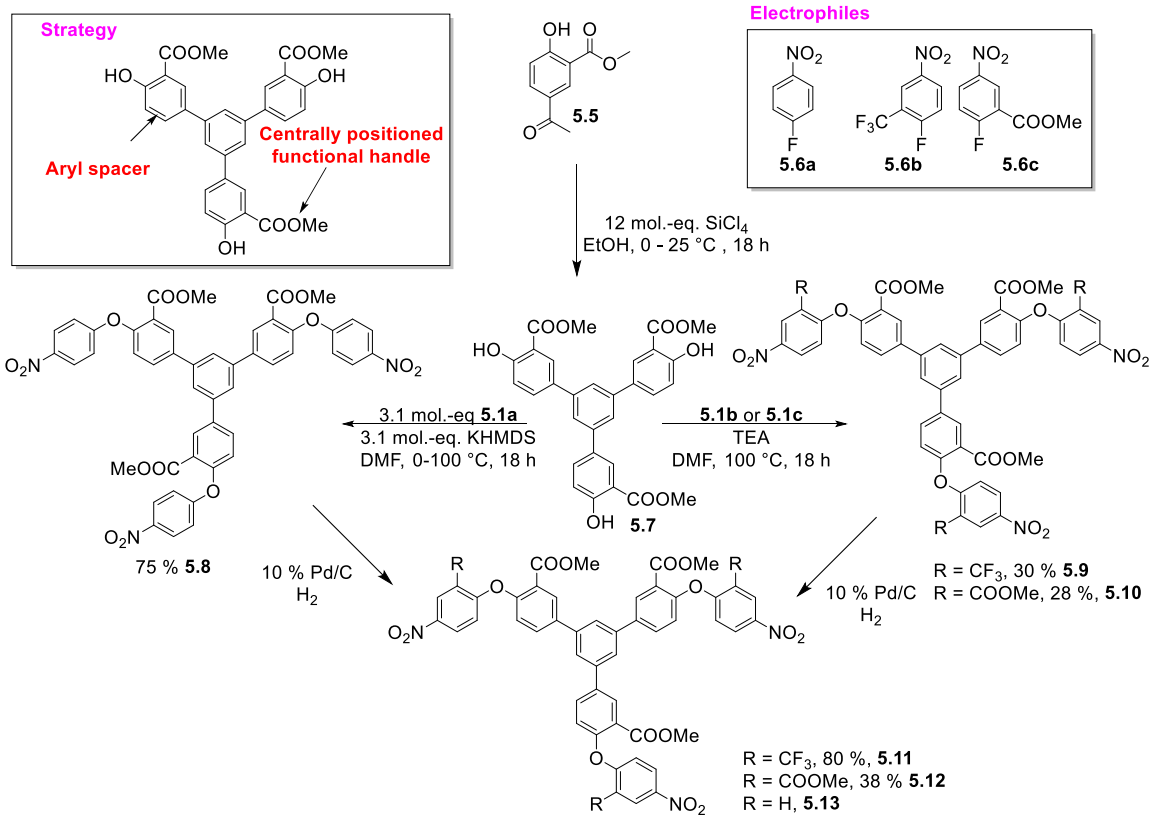

Figure 5.3. Synthetic route to new *C*$_3$-symmetric tris-amine containing peripherally installed methyl ester group.

To minimize the generation of multiple discrete species during subcomponent self-assembly, it is necessary to enhance the rigidity of the ligand scaffold. Many structures in the literature are related to **5.7** but it is one the most ideal candidates for producing extended *C*$_3$-symmetric tris-amine ligands. The reasons for this are twofold: the aryl spacer and biphenyl groups of the core make the structure highly rigid, which will pay dividends for sub-component self-assembly. Secondly, the methyl ester, after extension, will be positioned in the center of the ring, thus if it is an acid or a base it will be aptly positioned into the interior of the cavity to mediate biomimetic catalytic events. Luckily **5.7** is produced easily from cheap commercially available starting materials, is purified by washing, and can be prepared on a multigram scale.[10] It can easily be extended by

nucleophilic aromatic substitution and the ligand then by reduction (Figure 5.3). Three ligand scaffolds were prepared: **5.11**, **5.12**, **5.13** from extended core **5.7**. Scaffolds **5.12** is notable for possessing two methyl esters at two locations that could potentially allow for the assimilation of doubly basic, acidic, or alternatively two different functional groups in future work. Subcomponent self-assembly with **5.11** and **5.12** yielded extremely broad and illegible spectra, however ligand **5.13** was a different story as it produced a discrete Fe_4L_4 tetrahedron.

Self-assembly using ligand **5.13** and components pyridine carboxaldehyde and $Fe(NTf_2)_2$ produced a Fe_4L_4 tetrahedral species consisting solely of the S_4 isomer (Figure 5.4). DOSY analysis revealed that the complex multiplicity and overlapping peaks were due to a singular molecular entity. As the methyl ester peaks in the 3.5-4.0 ppm region of the ^{1}H NMR have an equal integration and are split into three different signals, this is consistent with a S_4-symmetric tetrahedral cage. Two similar ligand scaffolds have been reported in the literature that also selectively self-assembles into a S_4-symmetric tetrahedral cage.[11,12] We are currently optimizing mass spectrometry conditions to confirm the stoichiometry of the species with absolute certainty. Previous work from the Sessler group has demonstrated the methyl esters of trimerized salicylic derivative **5.7**s can be easily exchanged for acyl hydrazides, meaning functionalizing the ligand scaffold for its use as a biomimetic catalyst is possible.[13]

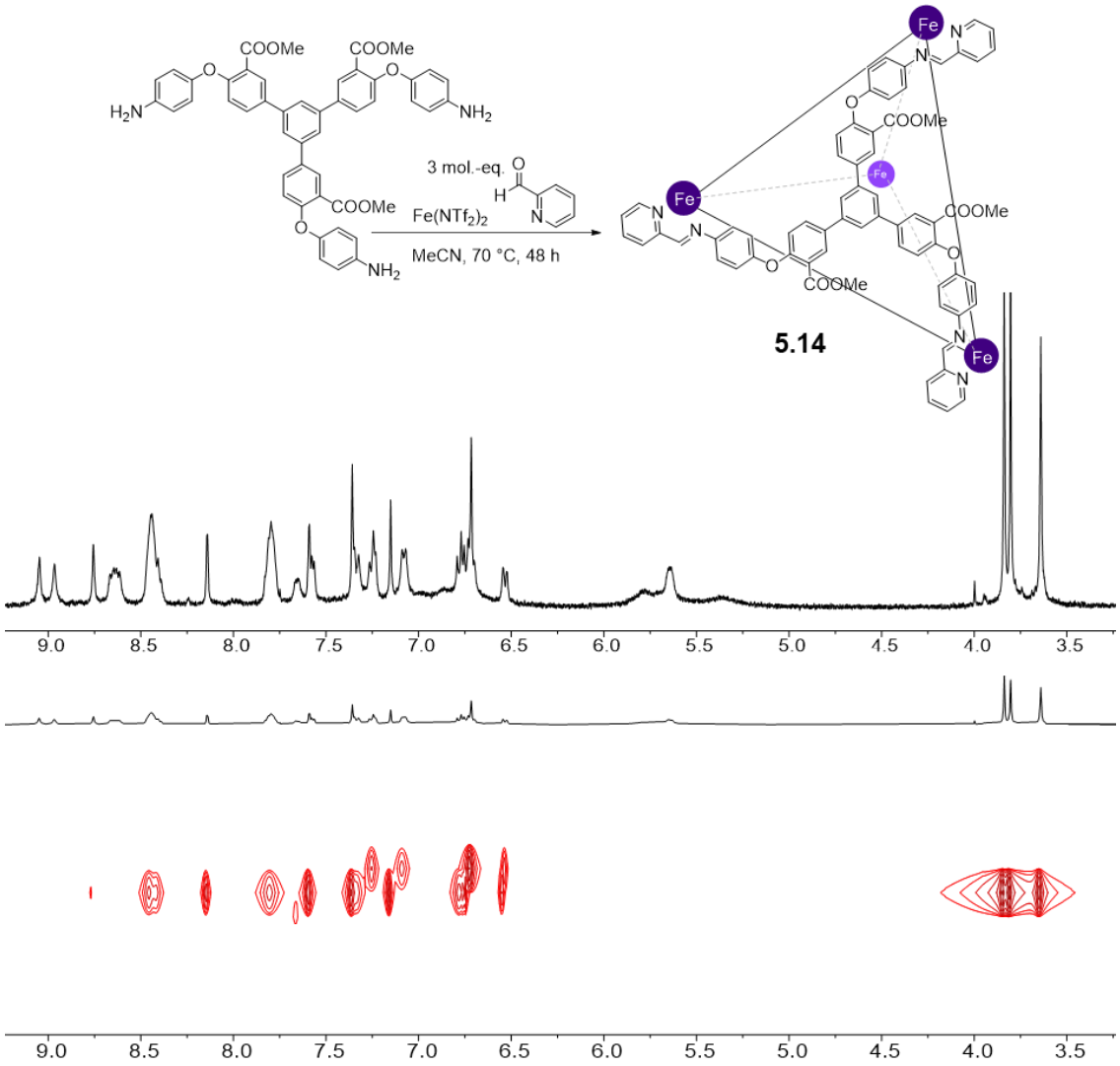

Figure 5.4. ^{1}H NMR spectrum of self-assembly outcome using ligand **5.13** producing a M_4L_4 tetrahedral cage **5.14** possessing S_4 symmetric and DOSY spectrum of cage.

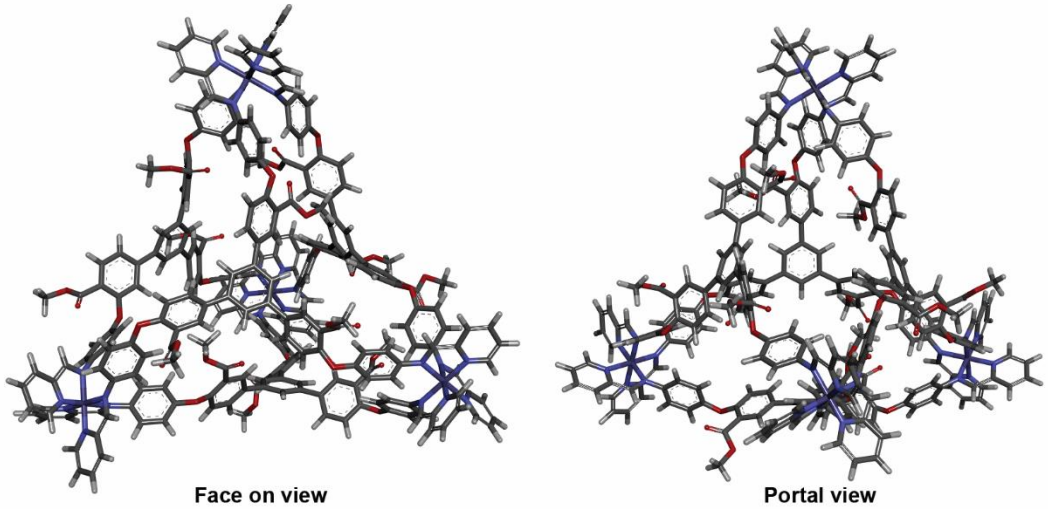

Figure 5.5. Energy minimized Spartan models of cage **5.14** from the face view and portal view (Hartree-Fock).

The cavity of cage **5.14** is about 472 $Å^3$ and energy minimized molecular models produced using Spartan demonstrate that 5 of the 12 pendant methyl esters are oriented towards the interior cavity (Figure 5.5). The difference between the orientation of the methyl esters causes desymmetrization of the ligand faces and agrees well with the S_4-symmetry of the self-assembled cage architecture. In addition to this 2D NOESY analysis of the cage clearly shows *no exchange peaks* between the methyl esters (Figure 5.6). Thus, rotation across the C-C biphenyl and C-O-C aryl ether axis, in light of their being more than enough space, may not be occurring in solution (Figure 5.6). This is indicative that in solution it not impossible for the methyl esters to be internally oriented. Thus, when they are converted to a functional group more adept at mediating organic transformations, we expect the cavity will act as a synthetic enzyme active site.

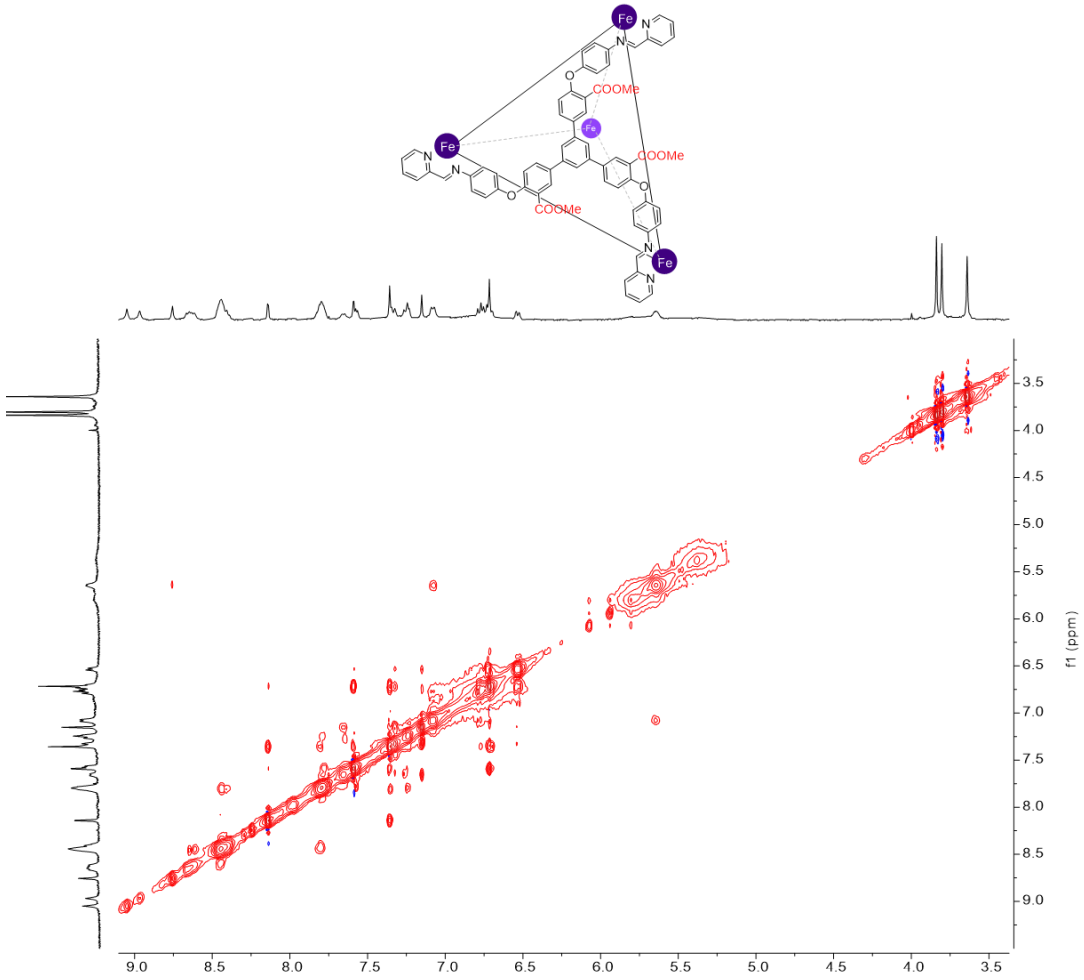

Figure 5.6. gNOESY NMR spectrum of cage **5.14** (CD_3CN, 400 MHz, 298 K, mixing time = 300 ms) demonstrating a lack of COOMe exchange peaks, thus there is no evidence for C-C and C-O-C rotation.

An initial ^1H NMR titration was performed with guests of varying sizes and charges to begin studying the molecular recognition capacity for cage **5.14** (Figure 5.6). Complete elucidation of the interaction between the various guests and cage **5.14** will require more thorough and rigorous testing. The addition of the guest generally produces a species with increased symmetry. Perplexingly, none of the new peaks can be related back to the cage subcomponents. What is potentially happening is conversion of the S_4 cage diastereomer to its *T*-symmetric conformation, which has been previously reported in the literature.[12]

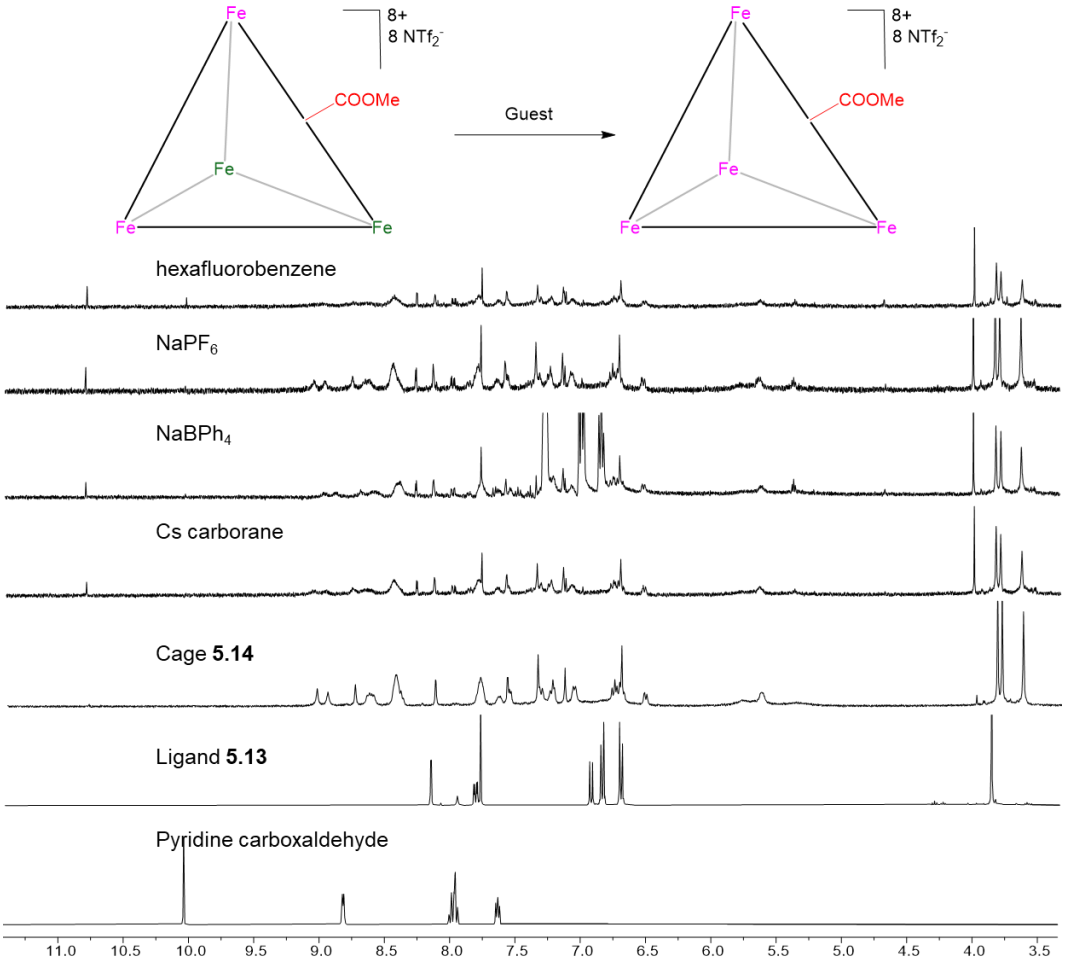

Figure 5.7. ^{1}HNMR titration spectra of various guests ([guest] = 1 mM]) to a 1 mM solution of cage **5.14**, compared to the cage without guest, the ligand, and pyridine carboxaldehyde, demonstrating an increase in symmetry for each titration likely due to conversion of the *S*$_4$ diastereomer of cage **5.14** to the *T*-symmetric diastereomer cage.

5.3. Conclusion

In conclusion a synthetic route for accessing a *C*$_3$-symmetric ligand was developed and successfully employed in subcomponent self-assembly to produce a *S*$_4$-symmetric tetrahedral M_4L_4 cage. The cavity of the cage is almost as spacious as the large fluorene cage discussed in chapters 2 and 3. The ability of cage **5.14** to be "tolerant" to various neutral and charged substrates will be vital for determining whether it can be used as a biomimetic catalyst. It seems reasonable that the rotation across the C-C biphenyl and C-

O-C aryl ether axis are rapid, thus the methyl ester can be endohedrally oriented in solution. The internal orientation of the methyl esters highlights the potential utility of this cage as a biomimetic catalyst.

References

(1) Yang, D.; Greenfield, J. L.; Ronson, T. K.; von Krbek, L. K. S.; Yu, L.; Nitschke, J. R. LaIII and ZnII Cooperatively Template a Metal-Organic Capsule. *J. Am. Chem. Soc.* **2020**, *142*, 19856–19861.

(2) Xu, L.; Zhang, D.; Ronson, T. K.; Nitschke, J. R. Improved Acid Resistance of a Metal-Organic Cage Enables Cargo Release and Exchange between Hosts. *Angew. Chem. Int. Ed.* **2020**, *59*, 7435–7438.

(3) Yang, Y.; Ronson, T. K.; Lu, Z.; Zheng, J.; Vanthuyne, N.; Martinez, A.; Nitschke, J. R. A Curved Host and Second Guest Cooperatively Inhibit the Dynamic Motion of Corannulene. *Nat. Commun.* **2021**, *12*, 4079.

(4) Nguyen, B.-N. T.; Thoburn, J. D.; Grommet, A. B.; Howe, D. J.; Ronson, T. K.; Ryan, H. P.; Bolliger, J. L.; Nitschke, J. R. Coordination Cages Selectively Transport Molecular Cargoes Across Liquid Membranes. *J. Am. Chem. Soc.* **2021**, *143*, 12175–12180.

(5) Ronson, T. K.; Carpenter, J. P.; Nitschke, J. R. Dynamic Optimization of Guest Binding in a Library of Diastereomeric Heteroleptic Coordination Cages. *Chem* **2022**, *8*, 557–568.

(6) Zhang, D.; Gan, Q.; Plajer, A. J.; Lavendomme, R.; Ronson, T. K.; Lu, Z.; Jensen, J. D.; Laursen, B. W.; Nitschke, J. R. Templation and Concentration Drive Conversion Between a $FeII_{12}L_{12}$ Pseudoicosahedron, a $FeII_4L_4$ Tetrahedron, and a $FeII_2L_3$ Helicate. *J. Am. Chem. Soc.* **2022**, *144*, 1106–1112.

(7) Ghosh, A.; Slappendel, L.; Nguyen, B.-N. T.; von Krbek, L. K. S.; Ronson, T. K.; Castilla, A. M.; Nitschke, J. R. Light-Powered Reversible Guest Release and Uptake from ZnL Capsules. *J. Am. Chem. Soc.* **2023**, *145*, 3828-3832.

(8) Martín Díaz, A. E.; Lewis, J. E. M. Structural Flexibility in Metal-Organic Cages. *Front. Chem.* **2021**, *9*, 706462.

(9) Ma, L.; Haynes, C. J. E.; Grommet, A. B.; Walczak, A.; Parkins, C. C.; Doherty, C. M.; Longley, L.; Tron, A.; Stefankiewicz, A. R.; Bennett, T. D.; Nitschke, J. R. Coordination Cages as Permanently Porous Ionic Liquids. *Nat. Chem.* **2020**, *12*, 270–275.

(10) Ballester, P.; Capó, M.; Costa, A.; Deyà, P. M.; Gomila, R.; Decken, A.; Deslongchamps, G. Dual Binding Mode of Methylmethanetriacetic Acid to Tripodal Amidopyridine Receptors. *J. Org. Chem.* **2002**, *67*, 8832–8841.

(11) Xue, W.; Wu, K.; Ouyang, N.; Brotin, T.; Nitschke, J. R. Allosterically Regulated Guest Binding Determines Framework Symmetry for an FeII 4 L4 Cage. *Angew. Chem. Int. Ed.* **2023**, e202301319.

(12) Hong, C. M.; Kaphan, D. M.; Bergman, R. G.; Raymond, K. N.; Toste, F. D. Conformational Selection as the Mechanism of Guest Binding in a Flexible Supramolecular Host. *J. Am. Chem. Soc.* **2017**, *139*, 8013–8021.

(13) Li, H.; Zhang, H.; Lammer, A. D.; Wang, M.; Li, X.; Lynch, V. M.; Sessler, J. L. Quantitative Self-Assembly of a Purely Organic Three-Dimensional Catenane in Water. *Nat. Chem.* **2015**, *7*, 1003–1008.

Chapter 6 - Experimental

6.1. General Information

Analytical Data: ^{1}H NMR and ^{13}C NMR spectra were recorded on Bruker Avance NEO 400 MHz and 600 MHz NMR spectrometer. The spectrometers were automatically tuned and matched to the correct operating frequencies. Proton (^{1}H), carbon (^{13}C), and fluorine (^{19}F) chemical shifts are reported in parts per million (δ) with respect to tetramethylsilane (TMS, $\delta = 0$) and referenced internally with respect to the protio solvent impurity or hexafluorobenzene for fluorine spectra (HFB, $\delta = -164.9$). Multiplicities are abbreviated: singlet, s; doublet, d; triplet, t; quartet, q; doublet of doublet, dd; multiplet, m. Deuterated NMR solvents were obtained from Cambridge Isotope Laboratories, Inc., Andover, MA, and used without purification, except for rigorously anhydrous studies, whereby the deuterated NMR solvent (CD_3CN) was distilled over calcium hydride. The distilled CD_3CN was transferred under nitrogen into a nitrogen-filled glovebox with standard techniques. Spectra were digitally processed (phase and baseline corrections, integration, peak analysis) using MestreNova. Infrared spectra were recorded on a Bruker IFS HR-FTIR spectrometer, and wavenumbers are reported in cm^{-1}. UV/Vis spectroscopy was performed on a Cary 60 Photospectrometer using the Varian Scans program to collect data. In chapter 4, the mass spectrometric sample of cages was prepared in 100 % CH_3CN and infused into a Thermo Orbitrap Velos Pro mass spectrometer (Thermo Fisher Scientific, San Jose, CA, USA) with a homebuilt nanoESI source. The spray voltage, capillary temperature, and the S-lens RF level were set to 0.9 kV, 150 °C, and 45% respectively. Full

mass spectra were acquired with a resolution of $r = 30\,000$. Thermo Xcalibur was used to analyze MS data and prepare the predicted isotope patterns. For all other molecules, high resolution accurate mass spectral data were obtained from the Analytical Chemistry Instrumentation Facility at the University of California, Riverside, on an Agilent 6545 QTOF LC/MS instrument.

Chromatography: Flash column chromatography was performed with Silicycle SiliaFlash P60 gel (60 Å porosity, 230-400 mesh) with indicated solvents. Silica gel was "wet-packed" using the column eluent, in the case of a gradient eluent, the lowest polarity solvent mixture was used for the slurry. Air pressure was then applied to the column for packing and separation of compounds. Thin layer chromatography was conducted using Sorbtech UV254 polyester backed silica plates (200 μm) with fluorescent indicator. Plates that were developed were visualized under UV light.

Reagents: Commercial reagents were purchased from Sigma Aldrich, Chem-Impex Int'l. Inc, Combi-Blocks, Alfa Aesar, Spectrum, Airgas, Acros, or Chemscene and used without further purification.

Solvents: Solvents were used as received from commercial sources and when required were dried and purified using standard techniques.[1] Dimethylformamide (DMF) sure seal bottles were purchased from Sigma Aldrich (CAS: 68-12-2). Tetrahydrofuran (THF), dichloromethane (CH_2Cl_2), toluene, and acetonitrile were dried through a commercial solvent purification system (Pure Process Technologies, Inc.).

6.2. SIVVU Binding Method for Chapter 2

Please see for information regarding the mathematical modeling method for SIVVU: Vander Griend, D.A.; DeVries, M. J.; Greeley, M.; Kim, Y.; Wang, N.; Buist, D; Ulry, C. SIVVU, http://sivvu.org, 2021.

General procedure for binding titrations for SIVVU. 3 mL of MeCN was added to a cuvette and an initial background scan was taken. Following 30 µL of a 0.3 mM solution of fluorene cage (**1.50**) was added to a cuvette and thoroughly mixed (3 µM fluorene cage in cuvette), a spectrum was then acquired. Then 1 µL of **titrant** solution (0.9 mM) was syringed into the cuvette (3 µM cage, 0.3 µM titrant), the cuvette solution was thoroughly mixed, and a spectrum was acquired. This was repeated 29 times. For "wet" titrations 5 µL of H_2O was added to solution before cage **1.50**, bringing the concentration of water to 0.09 M.

6.3. Nelder-Mead Method for Binding Calculations of UV/Vis Titrations for Chapter 3

General procedure for binding affinity calculations using the Nelder-Mead method.[2,3] A 1.5 µM solution of cage **1.50** or **2.1** was prepared in spectroscopic grade CH_3CN *via* dilutions from a 0.3 mM stock solution and added to a UV-Vis cuvette. To this solution was then added 0.1-5 µL aliquots from a 9 mM solution of the corresponding guest molecule, whereby the volume of added guest was equal to the molar equivalents of guest added. These additions were continued until there was no observable change in the absorption spectrum. Binding affinities were calculated *via* linear regression analysis using the Nelder-Mead method from the change in absorbance at two points (330 nm and 370

nm for **1.50**, 278/335 nm for **2.1**), the data was fit to either a 1:1 or 1:2 binding model and the variance used to determine best fit using a non-linear least-squares (maximum likelihood) approach written within the Mathematica programming environment.

Binding constants for 1:1 and 1:2 host-guest complex models were determined by UV/Vis titration experiments and binding constants extracted following the general approach outlined by Thordarson,[2,3] modified as described below. In brief, UV/Vis absorptions at 300 and 370 nm (for **1.50**, 278/335 nm for **2.1**), were monitored as a function of added guest and simultaneously fit using a non-linear least-squares (maximum likelihood) approach written within the Mathematica programming environment. For the 1:1 equilibrium model, the binding constant (K_a) and molar absorptivities (at both wavelengths) for the pure host (H) and host-guest (HG) complex were determined. For the 1:2 equilibrium model, both the first (K_1) and second (K_2) binding constants were determined, along with molar absorptivities for the host, host-guest (HG), and host-dual-guest (HG_2) complexes. The precise equilibria and corresponding equations are detailed below. Error bars for each of the fit parameters were determined by a numerical calculation of the covariance matrix and are reported above as ± standard error. The error analysis assumes normally distributed, random error that is independent of data point; in such a case, the sum of the squared-residuals follows the chi-squared distribution for N-k degrees of freedom, where N is the number of measured data points and k the number of fit parameters (5 and 8 for the 1:1 and 1:2 models, respectively). The significance of the 1:2 model was judged based on the inverse ratio of the squared residuals compared to the 1:1 model. Again, if the errors are normally distributed, this ratio follows the F-distribution for

N-5 (numerator) and N-8 (denominator) degrees of freedom. To be considered statistically "better," the 1:2 model must improve the residuals beyond what normal statistical fluctuations would be expected to sample with the observed noise and finite number of measured points. This is quantified *via* the p-value, which gives the probability that the observed improvement in residuals for the 1:2 complex model can be explained as statistical "luck." A small value indicates that the model truly is better – that is, that more of the underlying data trends are reproduced so that the residuals are smaller. To be considered significant in this context, we take p-values below 0.001.

Equilibrium Models:

The 1:1 host-guest binding

$$H + G \quad \underset{\longleftarrow}{\overset{K_a}{\longrightarrow}} \quad HG$$

has an association constant

$$K_a = \frac{[HG]}{[H][G]}$$

from which the concentration of the host, guest, and complex can be related back to initial (or total added) concentrations, H_0 and G_0, of each

$$[H] = \frac{1}{2}\left(H_0 - G_0 - \frac{1}{K_a} \right) + \frac{1}{2}\sqrt{\left(G_0 - H_0 - \frac{1}{K_a} \right)^2 + 4\frac{G_0}{K_a}}$$

$$[G] = \frac{1}{2}\left(G_0 - H_0 - \frac{1}{K_a} \right) + \frac{1}{2}\sqrt{\left(G_0 - H_0 - \frac{1}{K_a} \right)^2 + 4\frac{G_0}{K_a}}$$

$$[HG] = \frac{1}{2}\left(G_0 + H_0 + \frac{1}{K_a} \right) - \frac{1}{2}\sqrt{\left(G_0 - H_0 - \frac{1}{K_a} \right)^2 + 4\frac{G_0}{K_a}}$$

The absorbance at a given wavelength λ can then be written as

$$\begin{aligned} A^{\lambda} &= \varepsilon_H^{\lambda}[H] + \varepsilon_{HG}^{\lambda}[HG] \\ &= \varepsilon_H^{\lambda}\left\{ \frac{1}{2}\left(H_0 - G_0 - \frac{1}{K_a} \right) + \frac{1}{2}\sqrt{\left(G_0 - H_0 - \frac{1}{K_a} \right)^2 + 4\frac{G_0}{K_a}} \right\} + \\ &\varepsilon_{HG}^{\lambda}\left\{ \frac{1}{2}\left(G_0 + H_0 + \frac{1}{K_a} \right) - \frac{1}{2}\sqrt{\left(G_0 - H_0 - \frac{1}{K_a} \right)^2 + 4\frac{G_0}{K_a}} \right\} \end{aligned}$$

where it assumed that the guest on its own does not absorb. This is the expression that is used to simultaneously fit the experimental absorption data at 300 and 370 nm, A^{300} and A^{370}, as a function of added guest, G_o, to determine K_a and ε_H^{300}, ε_{HG}^{300}, ε_H^{370}, and ε_{HG}^{370}.

The 1:2 host-guest binding is assumed to be a non-cooperative, sequential two-step process

$$H + G \overset{K_1}{\rightleftharpoons} HG$$
$$HG + G \overset{K_2}{\rightleftharpoons} HG_2$$

which is characterized by two binding constants

$$K_1 = \frac{[HG]}{[H][G]}$$
$$K_2 = \frac{[HG_2]}{[HG][G]}$$

We analyze this for the case in which the approximation $[G] \approx G_0$ is valid, which corresponds to the limit in which $K_1[H] << 1$ or when G_0 is in large excess. This condition can be relaxed, but appears valid in our situation. With these caveats,

$$[H] = \frac{H_0}{1 + K_1 G_0 + K_1 K_2 G_0^2}$$

$$[G] \approx G_0$$

$$[HG] = \frac{K_1 H_0 G_0}{1 + K_1 G_0 + K_1 K_2 G_0^2}$$

$$[HG_2] = \frac{K_1 K_2 H_0 G_0^2}{1 + K_1 G_0 + K_1 K_2 G_0^2}$$

and the absorbance can be written

$$A^{\lambda} = \varepsilon_H^{\lambda}[H] + \varepsilon_{HG}^{\lambda}[HG] + \varepsilon_{HG_2}^{\lambda}[HG_2]$$
$$= \varepsilon_H^{\lambda} \frac{H_0}{1 + K_1 G_0 + K_1 K_2 G_0^2} + \varepsilon_{HG}^{\lambda} \frac{K_1 H_0 G_0}{1 + K_1 G_0 + K_1 K_2 G_0^2} + \varepsilon_{HG_2}^{\lambda} \frac{K_1 K_2 H_0 G_0^2}{1 + K_1 G_0 + K_1 K_2 G_0^2}.$$

This expression is used to simultaneously fit the experimental absorption data at 300 and 370 nm, A^{300} and A^{370}, as a function of added guest, G_o, to determine K_1, K_2, ε_H^{300}, ε_{HG}^{300}, $\varepsilon_{HG_2}^{300}$, ε_H^{370}, ε_{HG}^{370}, and $\varepsilon_{HG_2}^{370}$.

6.3. Experimental for Chapter 2

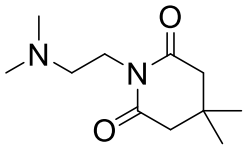

1-(2-(dimethylamino)ethyl)-4,4-dimethylpiperidine-2,6-dione: 2.3

Toluene (5 mL) was syringed into an oven dried two neck 10 mL round bottom flask equipped with a magnetic stir bar under nitrogen atmosphere. Following 3,3-dimethylglutaric anhydride (142 mg, 1 mmol, 1 eq.) was added followed by drop wise addition of N,N-dimethylethylenediamine (109 µL, 1 mmol, 1 eq.). The solution was brought to reflux and stirred overnight. The next day the flask was removed from heat and allowed to cool to room temperature before removing the solvent under reduced pressure. A glue-like residue with red highlights was left in the flask, hexanes (4 mL) was added, the flask was sonicated, and the hexanes was then run through a 3 cm tall silica plug, in a pasture pipette plugged with cotton, into a scintillation vial. Hexanes was removed under reduced pressure yielding a colorless sticky viscous oil used without further purification (209 mg, 98 %). ^{1}H NMR 400 MHz, ($CDCl_3$) δ 3.82 (t, *J* = 8 Hz, 2H), 2.49 (s, 4H), 2.35 (t, *J* = 8 Hz, 2H), 2.20 (s, 6H), 1.06 (s, 6H). $^{13}C\{^{1}H\}$ NMR (151 MHz, $CDCl_3$) δ 172.02, 56.60, 46.38, 45.41, 36.92, 29.14, 27.62. HRMS (ESI-TOF) *m/z* calc^{d} for $C_{11}H_{20}N_2O_2$ ($[M+H]^+$): 213.1597; found 213.1602. IR (neat) ν_{max} (cm^{-1}) 3123, 3013, 2979, 1515, 1443, 1383, 1073, 954, 660.

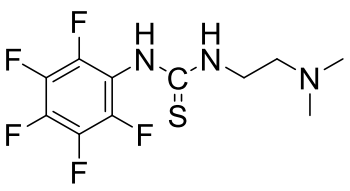

1-(2-(dimethylamino)ethyl)-3-(perfluorophenyl)thiourea: 2.5

N,N-dimethylethylenediamine (109 µL, 1 mmol, 1 eq.) and 1,2,3,4,5-pentafluoro-6-isothiocyanatobenzene (141 µL, 1 mmol, 1 eq.) were added to a 5 mL flame dried round bottom flask equipped with a magnetic stir bar and toluene (5 mL). After addition to the single neck flask, it was quickly put under an atmosphere of N_2 and brought to reflux in a sand bath and stirred overnight. The following day the reaction apparatus was taken out of the sand bath and allowed to cool to room temperature. Upon cooling clear crystals grew from the solution that were removed by filtration, the product was used without further purification. (80 mg, 25 %). ^{1}H NMR (400 MHz, $CDCl_3$) δ 7.16 (s, 1H), 3.47 (s, 2H), 2.71 (s, 2H), 2.40 (s, 6H).^{13}C{^{1}H} NMR (151 MHz, $CDCl_3$) δ 185.51, 144.56, 142.02, 139.08, 136.56, 116.34, 61.30, 44.95, 43.53. HRMS (ESI-TOF) *m/z* calc[d] for $C_{11}H_{12}F_5N_3S$ ($[M+H]^+$): 313.0745; found 313.0760. IR (neat) ν_{max} (cm^{-1}) 3210, 2985, 1625, 1501, 1243, 1035, 984, 711, 647, 475.

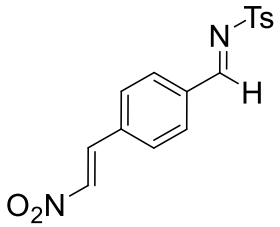

4-methyl-N-((E)-4-((E)-2-nitrovinyl)benzylidene)benzenesulfonamide: 2.18

(E)-4-(2-nitrovinyl)benzaldehyde[4,5] (400 mg, 2.3 mmol, 1 eq.) was placed in a 10 mL flame dried round bottom flask containing a magnetic stir bar and 300 mg of flame activated 4 Å molecular sieves. Following, benzenesulfonamide was added (362 mg, 2.3 mmol, 1 eq.) and then THF (4 mL) and piperidine (22.7 µL). The reaction was brought to 50 °C in a

sand bath and allowed to stir overnight. The following day the heterogeneous brown solution was taken out of the sand bath and passed through a celite plug atop a coarse frit filter and then allowed to cool to room temperature. THF was removed under reduced pressure and the crude material was refluxed in 250 mL of ethyl acetate. After refluxing for 45 seconds the solution was allowed to stop boiling and rapidly filtered and a brown solid was collected and used without further purification. (400 mg, 54 %). ^{1}H NMR (400 MHz, $CDCl_3$) δ 9.07 (s, 1H), 8.06 – 8.00 (m, 3H), 7.92 (d, *J* = 8.0 Hz, 2H), 7.73 – 7.61 (m, 3H), 7.39 (d, *J* = 8.0 Hz, 3H), 2.48 (s, 3H). ^{13}C{^{1}H} NMR (101 MHz, $CDCl_3$) δ 168.37, 145.07, 139.26, 137.08, 135.89, 135.15, 134.63, 131.88, 129.96, 129.54, 128.29, 21.71. HRMS (ESI-TOF) *m/z* calc[d] for $C_{16}H_{14}N_2O_4S$ ($[M+H]^+$): 331.0708; found 331.0750. IR (neat) ν_{max} (cm^{-1}) 3123, 3013, 2979, 1515, 1443, 1383, 1073, 954, 602, 545.

General procedure for NMR conjugate addition Reactions. If cage was being used Cage **1.50** (5.0 mol %, 0.31 μmol, 2 mg) was placed in a NMR tube filled with 360 μL of CD_3CN followed by the sequential addition of dioxane (0.5 mol.-eq., 0.0044 μmol , 10 μL of a 0.044 M solution in CD_3CN) β-nitrostyrene (1 mol.-eq., 7.26 μmol, 10 μL of a 0.073 M solution in CD_3CN), ethyl cyanoacetate (1.2 mol.-eq., 8.71 μmol, 10 μL of a 0.088 M solution in CD_3CN), and **2.3/2.5** or **2.4** (0.3 mol.-eq., 2.17 μmol, 5 or 10 μL of a 0.022 M solution in CD_3CN). The volume of the tube was then brought to 400 μL, capped, shaken, and an initial ^{1}H NMR was taken to verify the stoichiometry. The reaction progress was monitored over time. The percent conversion values were obtained *via* integration of the product and substrate peaks against the internal standard or comparing the change in integration values between the starting materials and product.

General procedure for NMR conjugate addition reactions employing anhydrous CD_3CN. If cage was being used Cage **1.50** (5.0 mol %, 0.31 μmol, 2 mg) was placed in a NMR tube filled with 370 μL of CD_3CN followed by the sequential addition β-nitrostyrene (1 mol.-eq., 7.26 μmol, 10 μL of a 0.073 M solution in CD_3CN), ethyl cyanoacetate (1.2 mol.-eq., 8.71 μmol, 10 μL of a 0.088 M solution in CD_3CN), and **2.3/2.5** (0.3 mol.-eq., 2.17 μmol, 10 μL of a 0.022 M solution in CD_3CN. *These stock solutions were prepared in the glovebox using rigorously anhydrous CD_3CN*. The volume of the tube was then brought to 400 μL, capped, shaken, and an initial ^1H NMR was taken to verify the stoichiometry. The reaction progress was monitored over time. The percent conversion values were obtained *via* the change in integration values between the starting materials and product.

General procedure for Knoevenagel condensation reaction. If cage was being used Cage **1.50** (5.0 mol %, 0.31 μmol, 2 mg) was placed in a NMR tube followed by 360 μL of CD_3CN and then the sequential addition of dioxane (0.5 mol.-eq., 0.0044 μmol , 10 μL of a 0.044 M solution in CD_3CN), (E)-N-benzylidene-4-methylbenzenesulfonamide (**2.9**) (1 mol.-eq., 7.26 μmol, 10 μL of a 0.073 M solution in CD_3CN), ethylcyanoacetate (1.2 mol.-eq., 8.71 μmol, 10 μL of a 0.088 M solution in CD_3CN), and **2.3** (0.3 mol.-eq., 2.17 μmol, 10 μL of a 0.022 M solution in CD_3CN). The tube was capped, shaken, and an initial ^1H NMR was taken to verify the stoichiometry. The reaction progress was monitored over time. The percent conversion values were obtained *via* integration of the product and substrate peaks against the internal standard or by comparing the change in integration values between the starting materials and product.

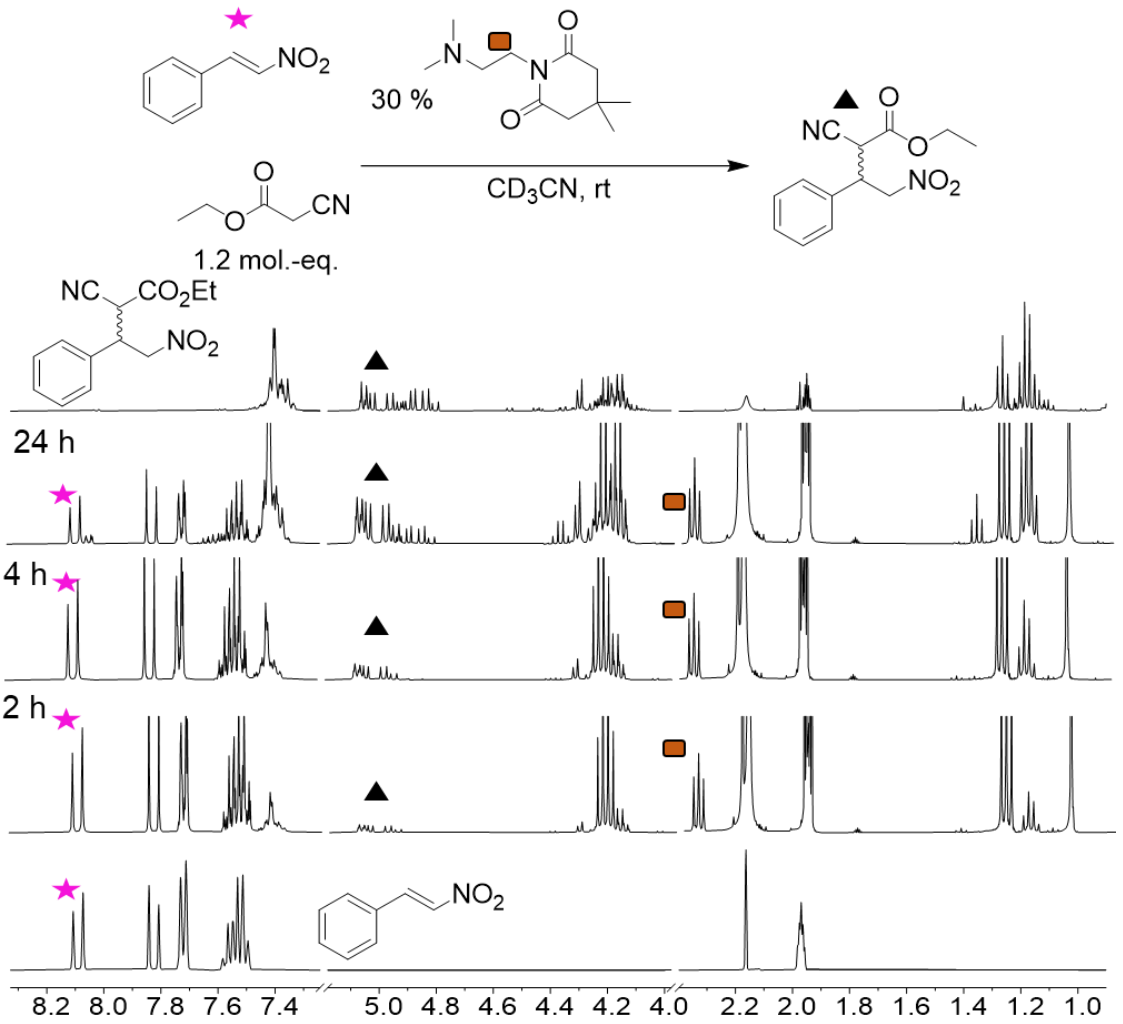

Figure 6.1. ^{1}H NMR spectra of the conjugate addition and subsequent product formation between **2.6** and **2.7** mediated by **2.3** in 400 µL CD_3CN. [**2.5**] = 20 mM, [**2.6**] = 24 mM, [**2.3**] = 6.0 mM, and [dioxane] = 10 mM. Reaction was performed at 25 °C and monitored over time. (400 MHz, 298 K, CD_3CN).

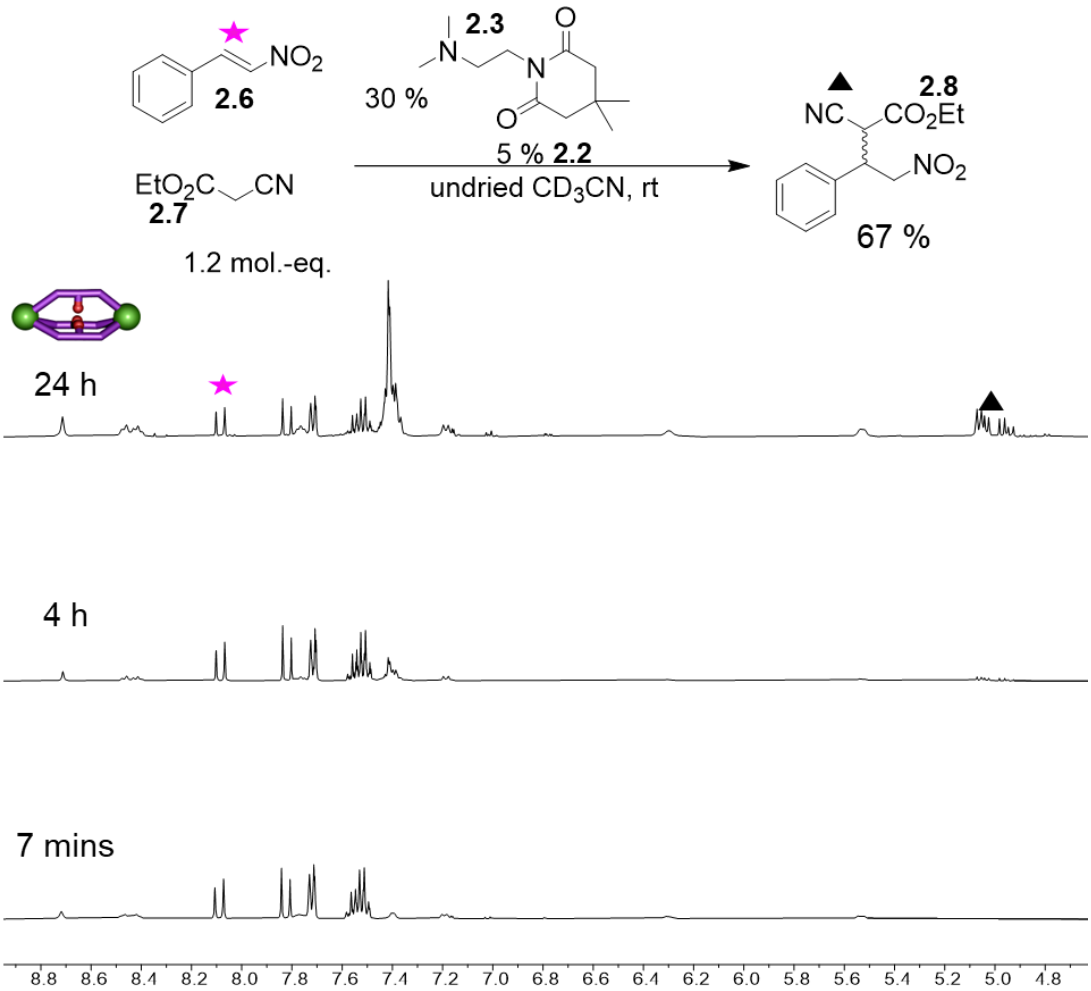

Figure 6.2. ^{1}H NMR spectra of the conjugate addition between **2.6** and **2.7** mediated by **2.3** in 400 µL CD_3CN. [**2.5**] = 20 mM, [**2.6**] = 24 mM, [**2.3**] = 6.0 mM, [**2.2**] = 1.0 mM, and [dioxane] = 10 mM. Reaction was performed at 25 °C and monitored over time. (400 MHz, 298 K, CD_3CN).

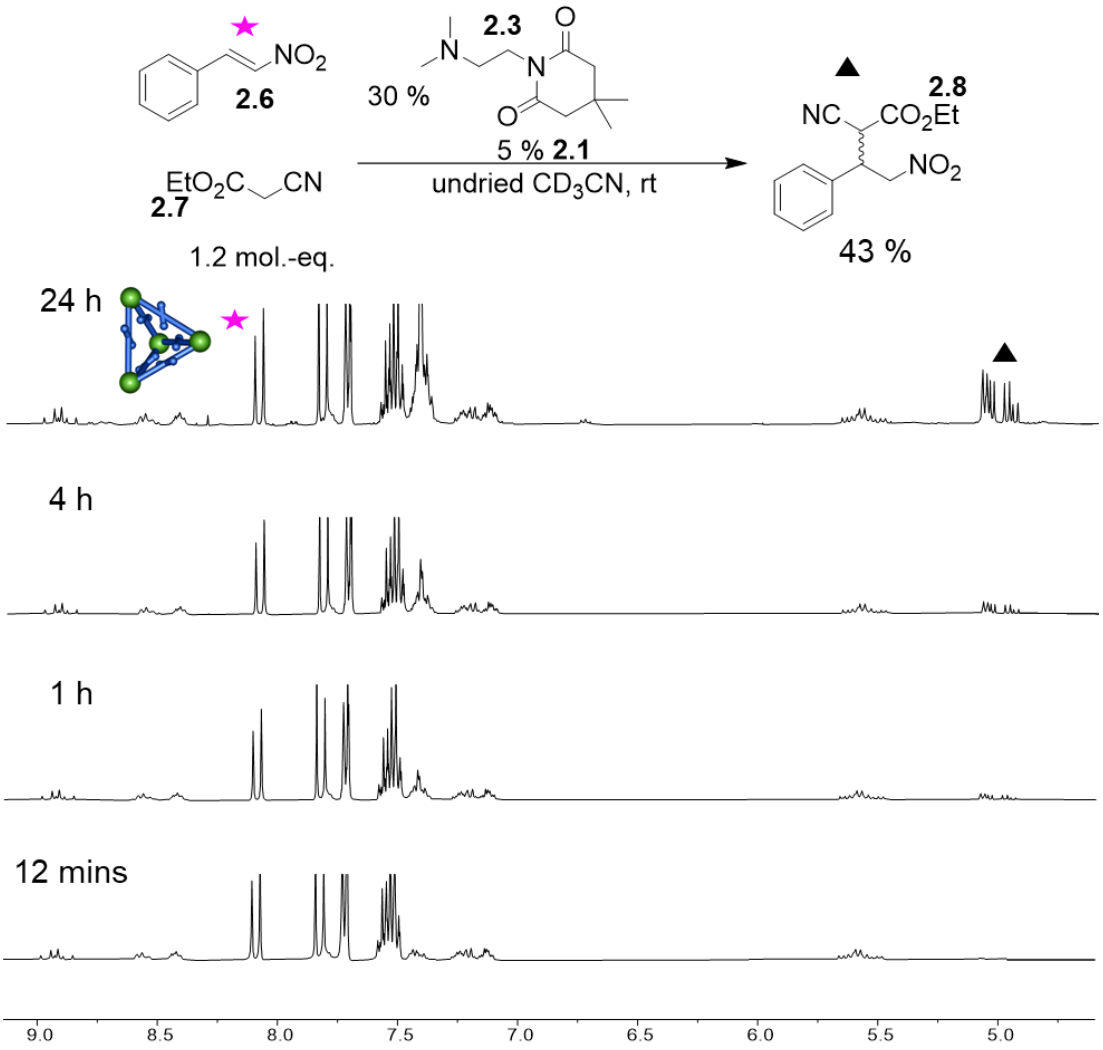

Figure 6.3. ^{1}H NMR spectra of the conjugate addition between **2.6** and **2.7** mediated by **2.3** in 400 µL CD_3CN. [**2.5**] = 20 mM, [**2.6**] = 24 mM, [**2.3**] = 6.0 mM, [**2.1**] = 1.0 mM, and [dioxane] = 10 mM. Reaction was performed at 25 °C and monitored over time. (400 MHz, 298 K, CD_3CN).

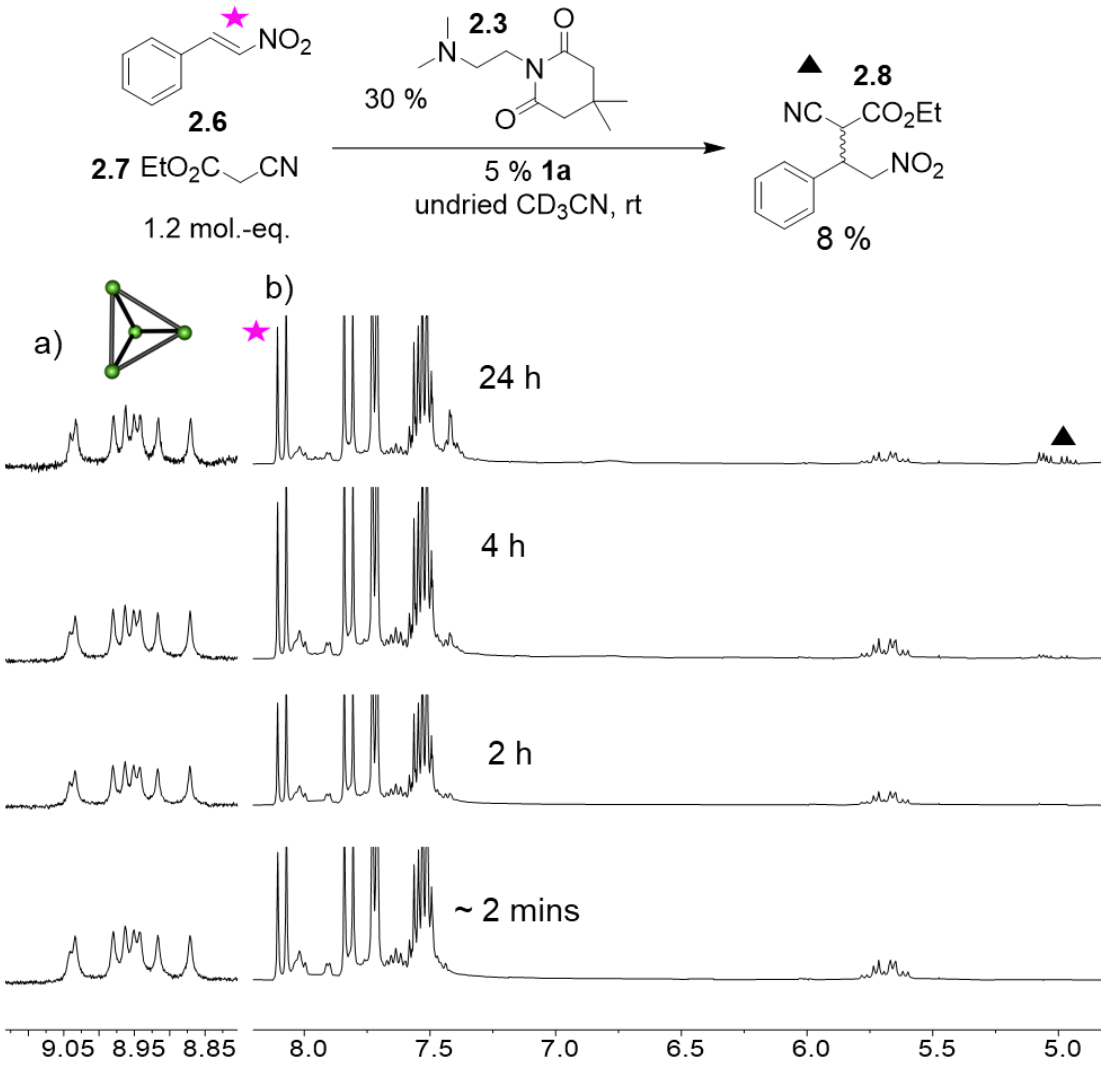

Figure 6.4. ^{1}H NMR spectra of the conjugate addition between β-nitrostyrene and ethylcyanoacetate catalyzed by glutarimide **2.3** in 400 µL CD_3CN. a) Cage imine peaks demonstrating stability; b) reaction monitored over time. [**2.6**] = 20 mM, [**2.7**] = 24 mM, [**2.3**] = 6.0 mM, [**1.50**] = 1.0 mM and [dioxane] = 10 mM. Reaction was performed at 25 °C and monitored over time. (400 MHz, 298 K, CD_3CN).

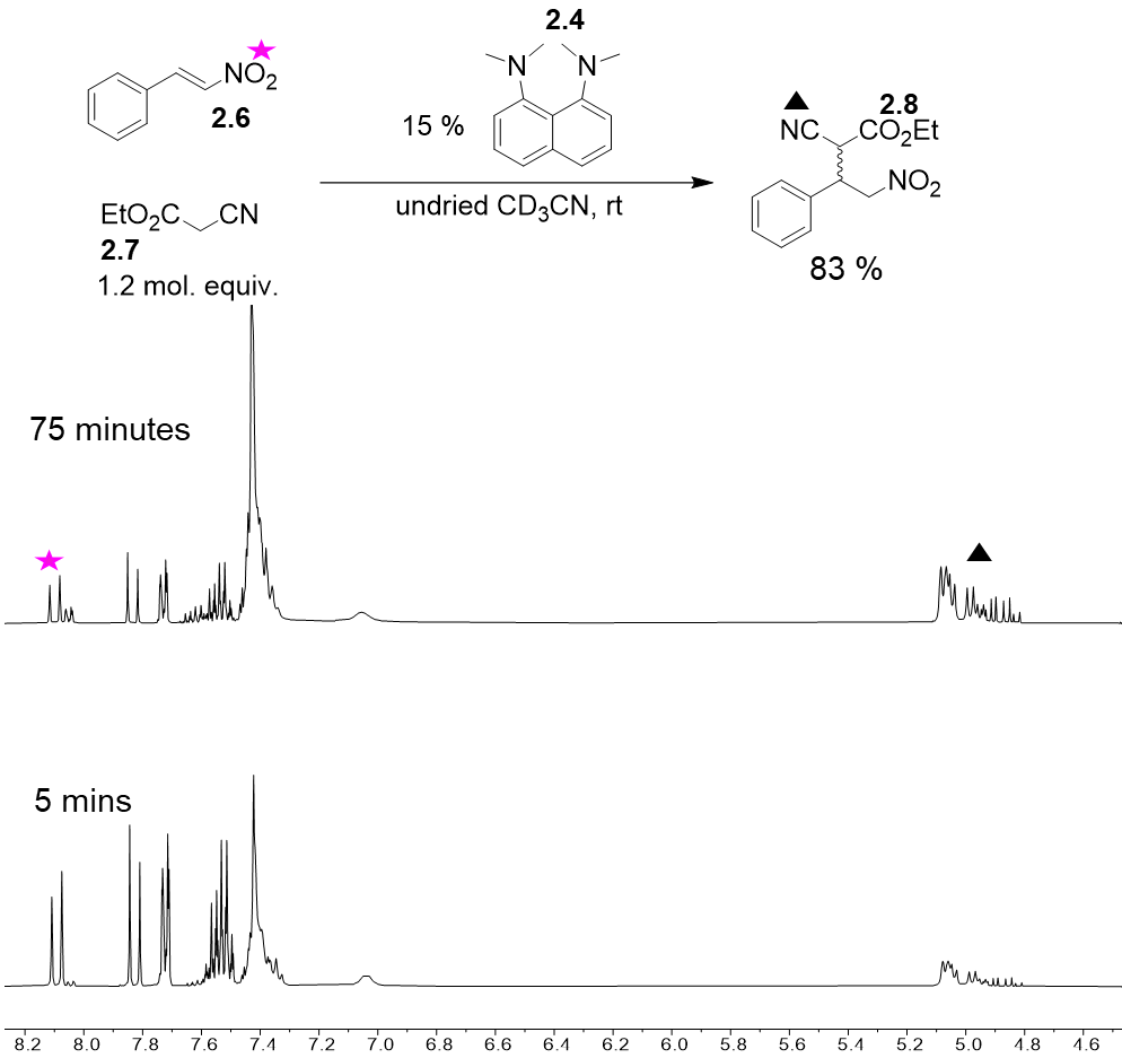

Figure 6.5. ^{1}H NMR spectra of the conjugate addition between **2.6** and **2.7** mediated by **2.3** in 400 µL CD_3CN. [**2.5**] = 20 mM, [**2.6**] = 24 mM, [**2.3**] = 6.0 mM, and [dioxane] = 10 mM. Reaction was performed at 25 °C and monitored over time. (400 MHz, 298 K, CD_3CN).

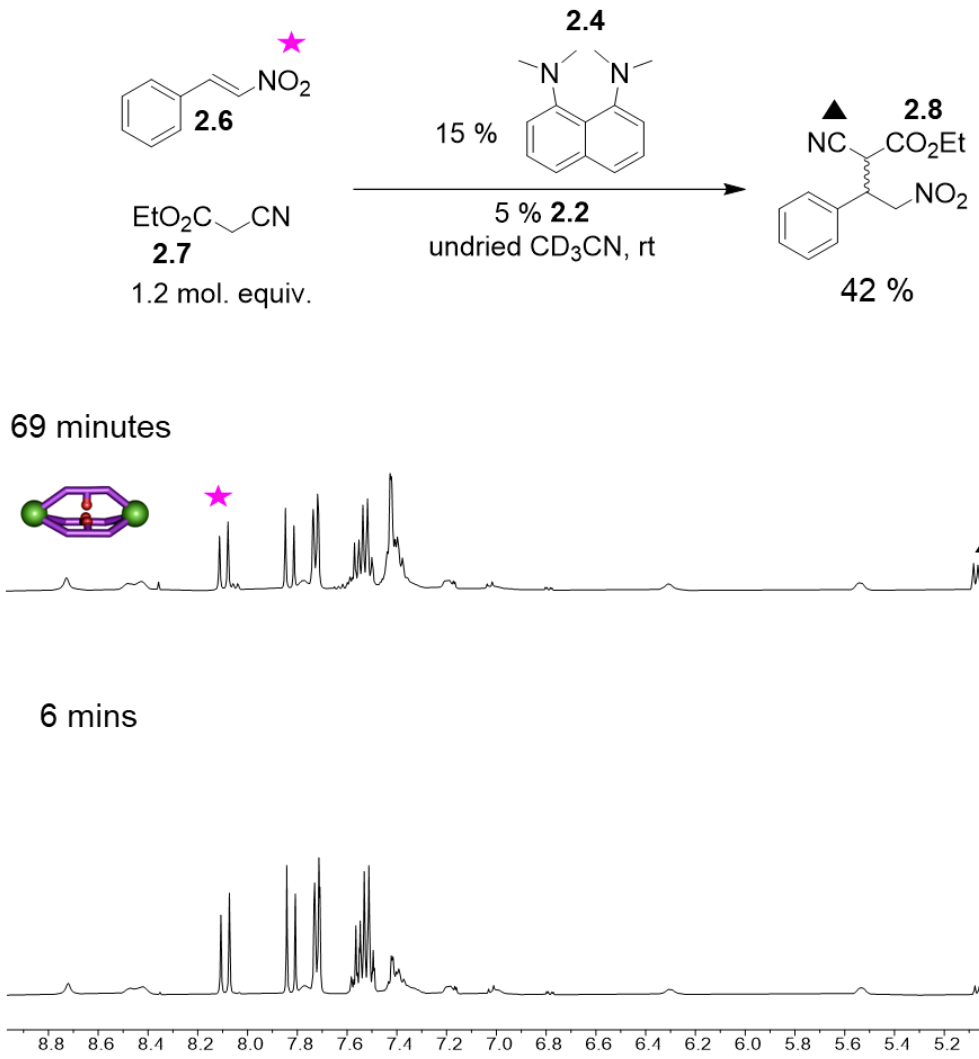

Figure 6.6. ^{1}H NMR spectra of the conjugate addition between **2.6** and **2.7** mediated by **2.3** in 400 µL CD_3CN. [**2.5**] = 20 mM, [**2.6**] = 24 mM, [**2.4**] = 3.0 mM, [**2.2**] = 1.0 mM and [dioxane] = 10 mM. Reaction was performed at 25 °C and monitored over time. (400 MHz, 298 K, CD_3CN).

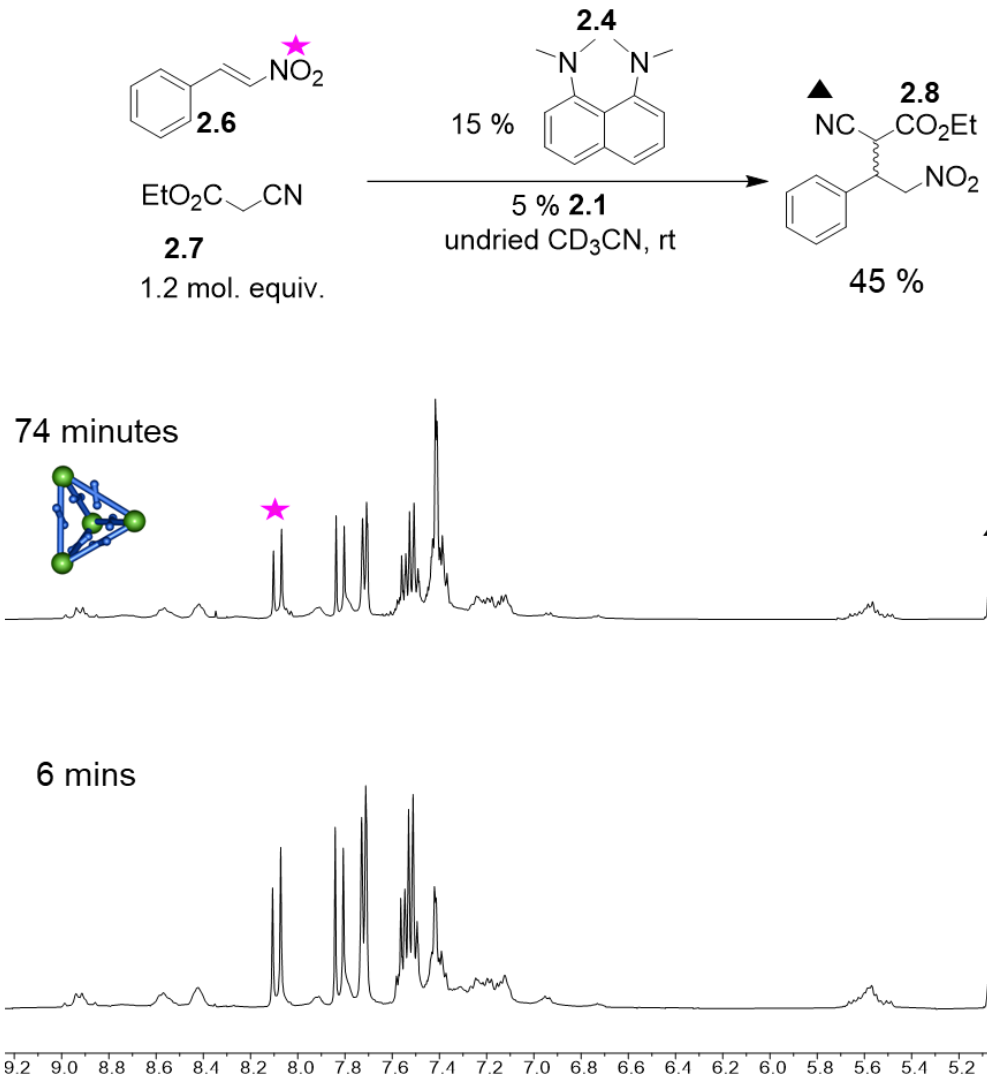

Figure 6.7. ^{1}H NMR spectra of the conjugate addition between **2.6** and **2.7** mediated by **2.3** in 400 µL CD_3CN. [**2.5**] = 20 mM, [**2.6**] = 24 mM, [**2.4**] = 3.0 mM, [**2.2**] = 1.0 mM and [dioxane] = 10 mM. Reaction was performed at 25 °C and monitored over time. (400 MHz, 298 K, CD_3CN).

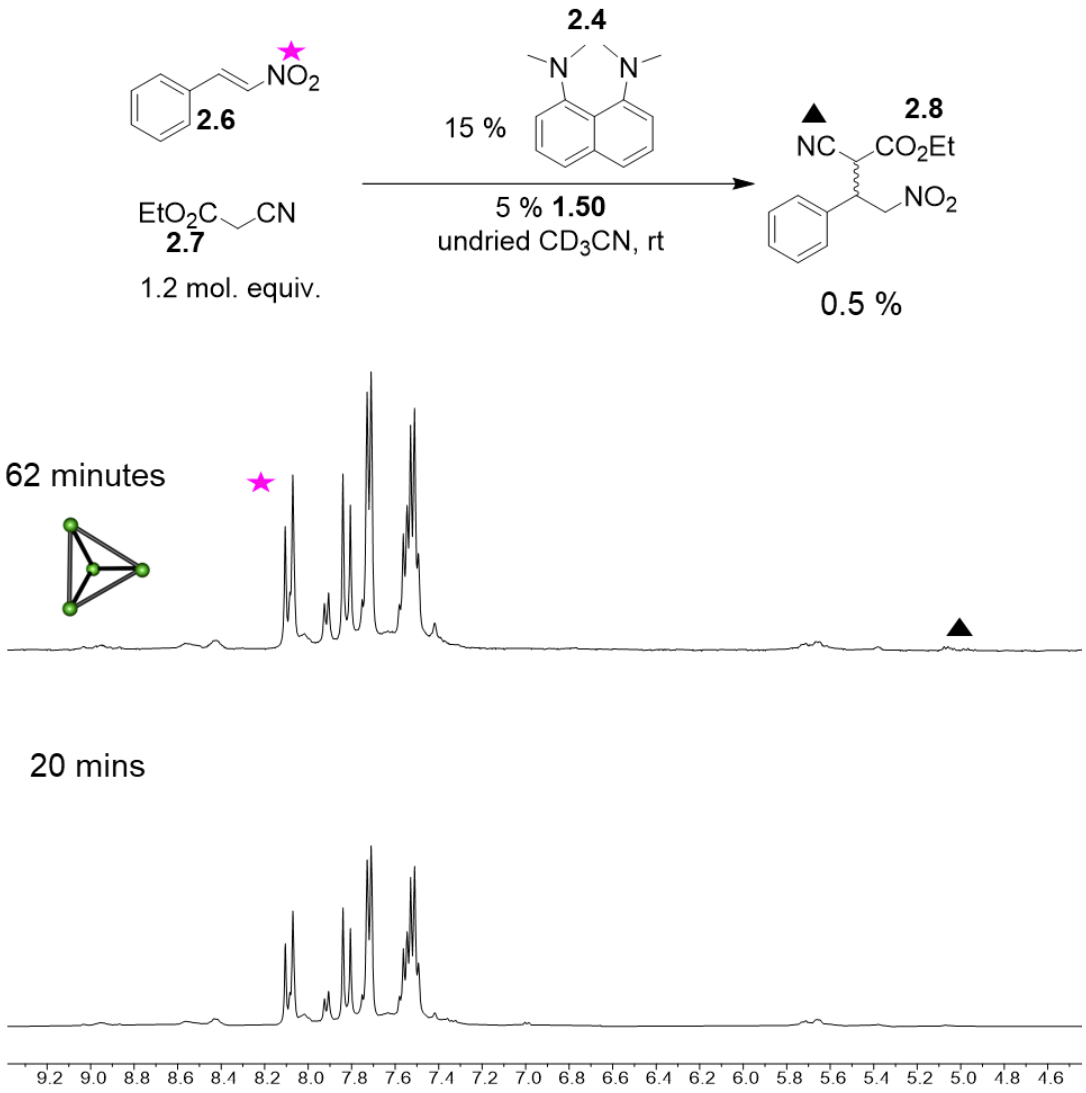

Figure 6.8. ^{1}H NMR spectra of the conjugate addition between **2.6** and **2.7** mediated by **2.3** in 400 µL CD_3CN. [**2.5**] = 20 mM, [**2.6**] = 24 mM, [**2.4**] = 3.0 mM, [**1.50**] = 1.0 mM and [dioxane] = 10 mM. Reaction was performed at 25 °C and monitored over time. (400 MHz, 298 K, CD_3CN).

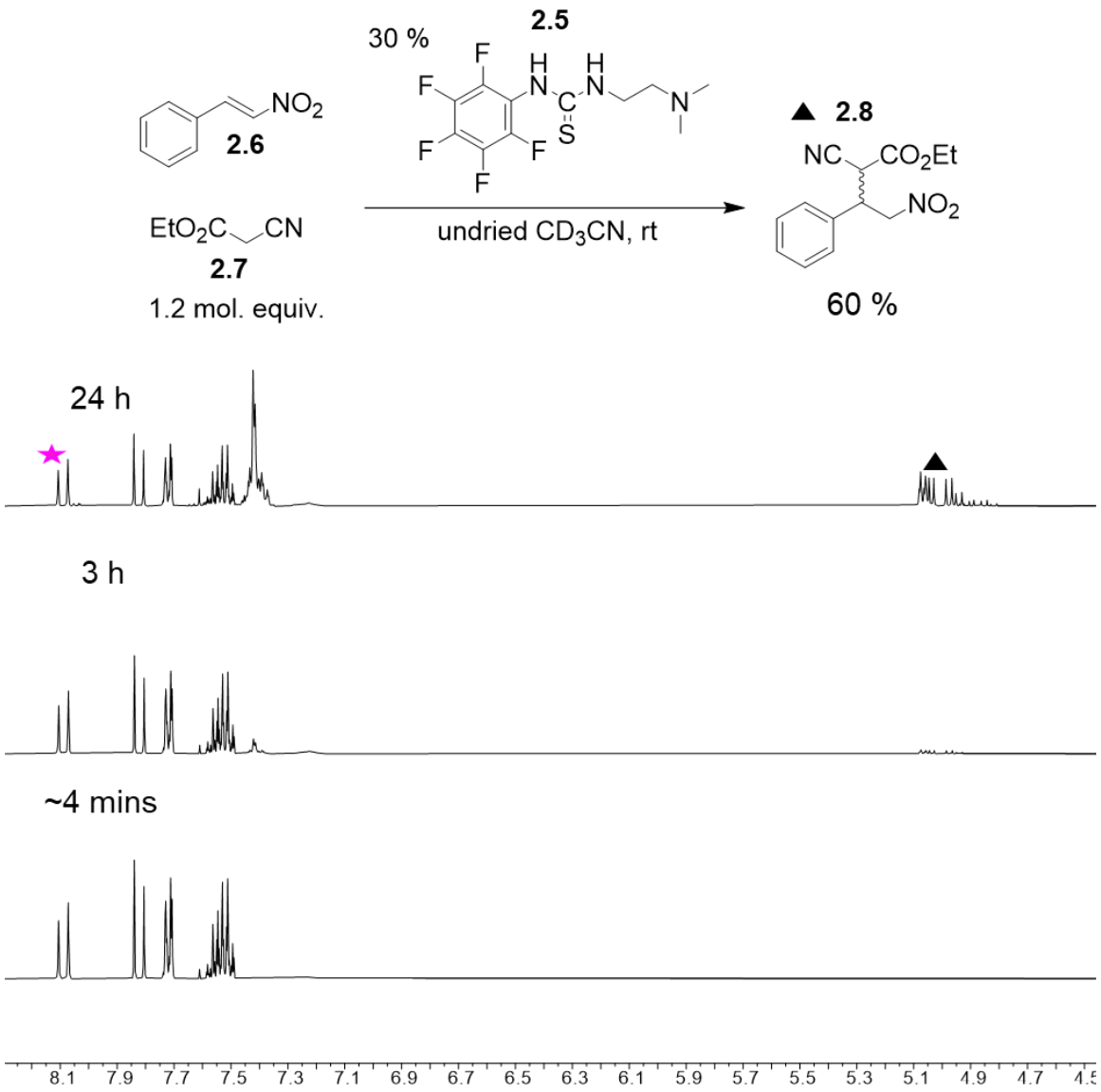

Figure 6.9. ^{1}H NMR spectra of the conjugate addition between **2.6** and **2.7** mediated by **2.3** in 400 µL CD_3CN. [**2.5**] = 20 mM, [**2.6**] = 24 mM, [**2.5**] = 6.0 mM, and [dioxane] = 10 mM. Reaction was performed at 25 °C and monitored over time. (400 MHz, 298 K, CD_3CN).

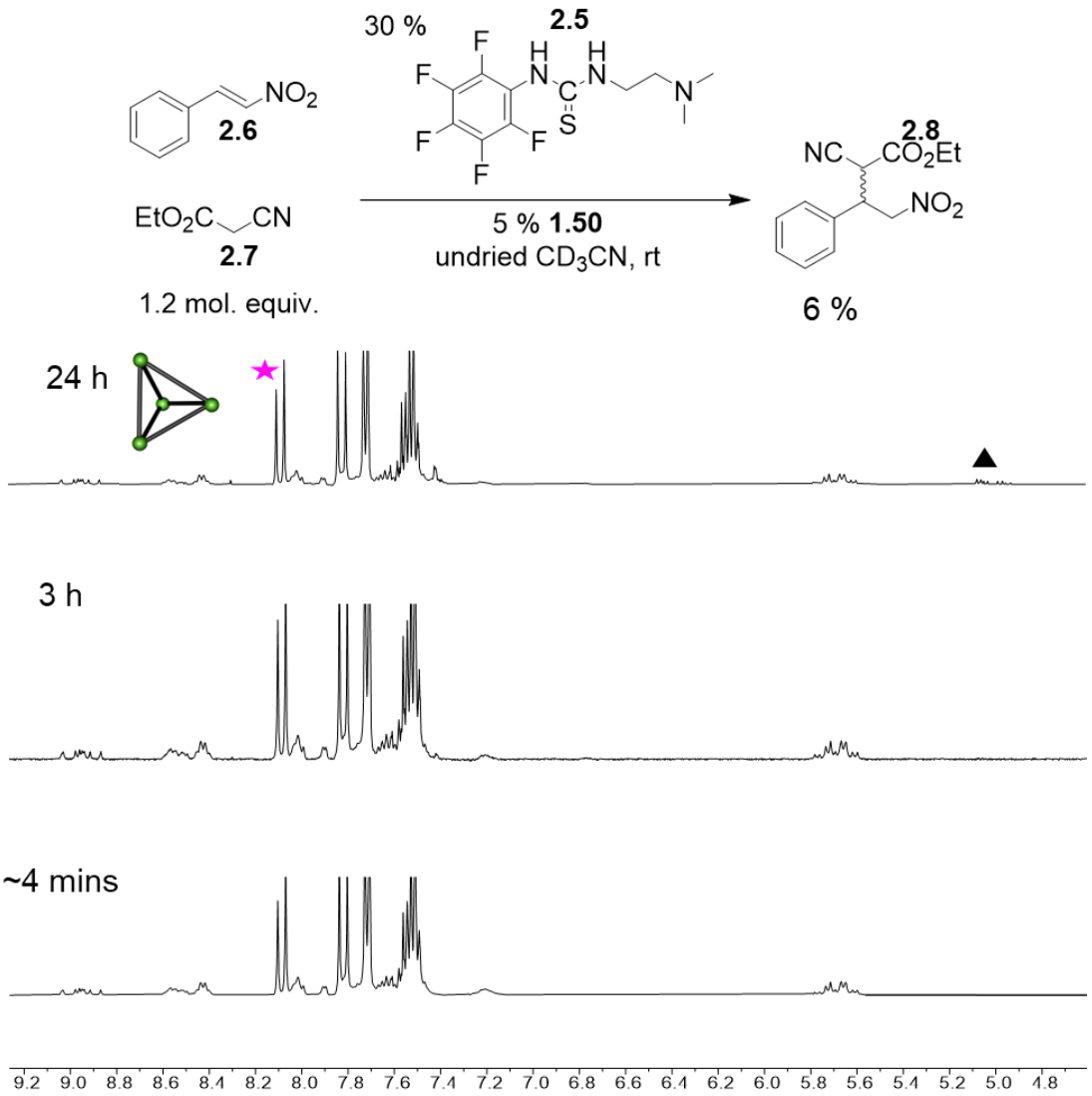

Figure 6.10. ^{1}H NMR spectra of the conjugate addition between **2.6** and **2.7** mediated by **2.3** in 400 µL CD_3CN. [**2.5**] = 20 mM, [**2.6**] = 24 mM, [**2.5**] = 6.0 mM, [**1.50**] = 1.0 mM, and [dioxane] = 10 mM. Reaction was performed at 25 °C and monitored over time. (400 MHz, 298 K, CD_3CN).

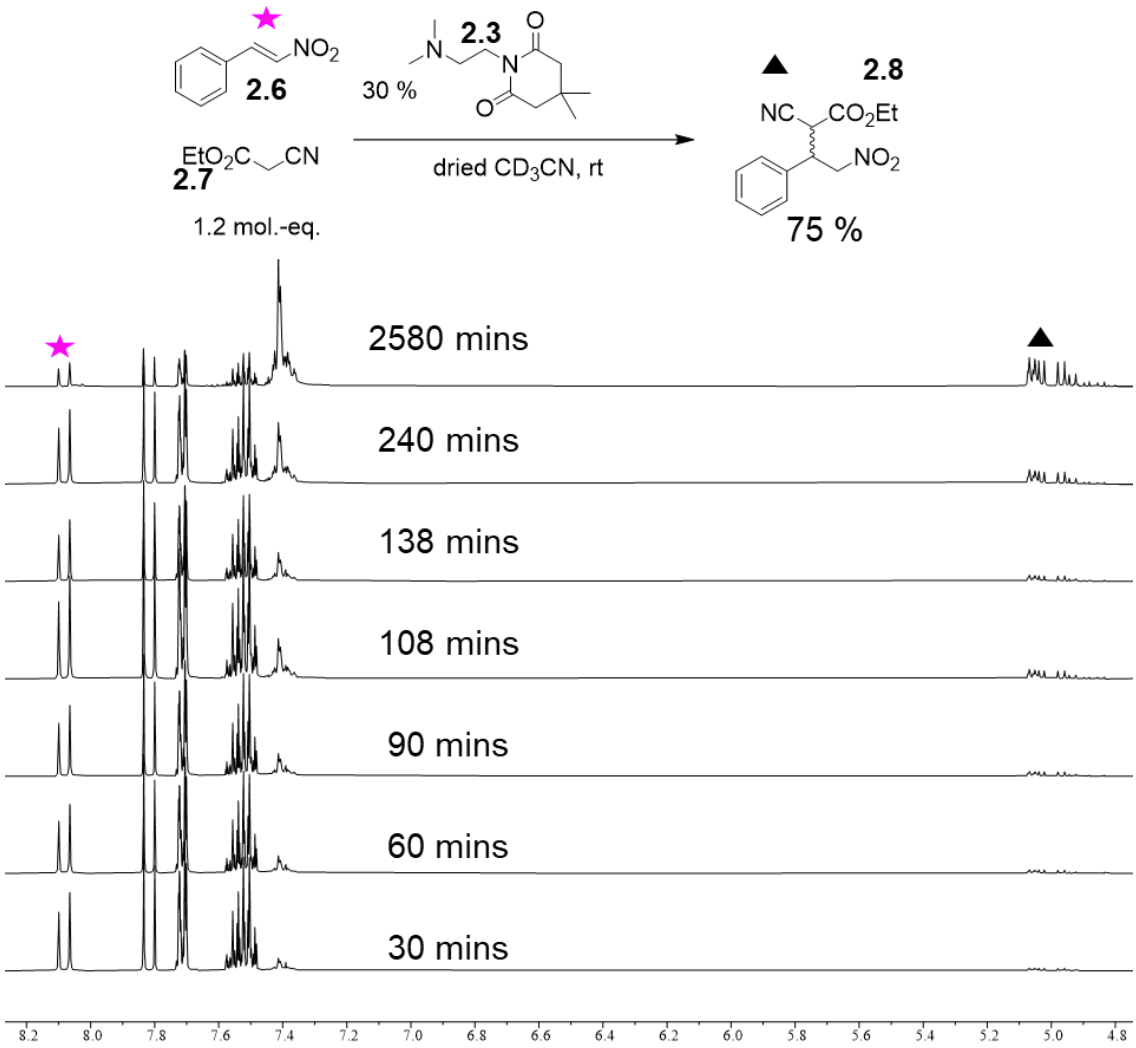

Figure 6.11. ^{1}H NMR spectra of the conjugate addition between **2.6** and **2.7** mediated by **2.3** in 400 µL CD_3CN. [**2.5**] = 20 mM, [**2.6**] = 24 mM, and [**2.3**] = 6.0 mM. Reaction was performed at 25 °C and monitored over time. (400 MHz, 298 K, anhydrous CD_3CN).

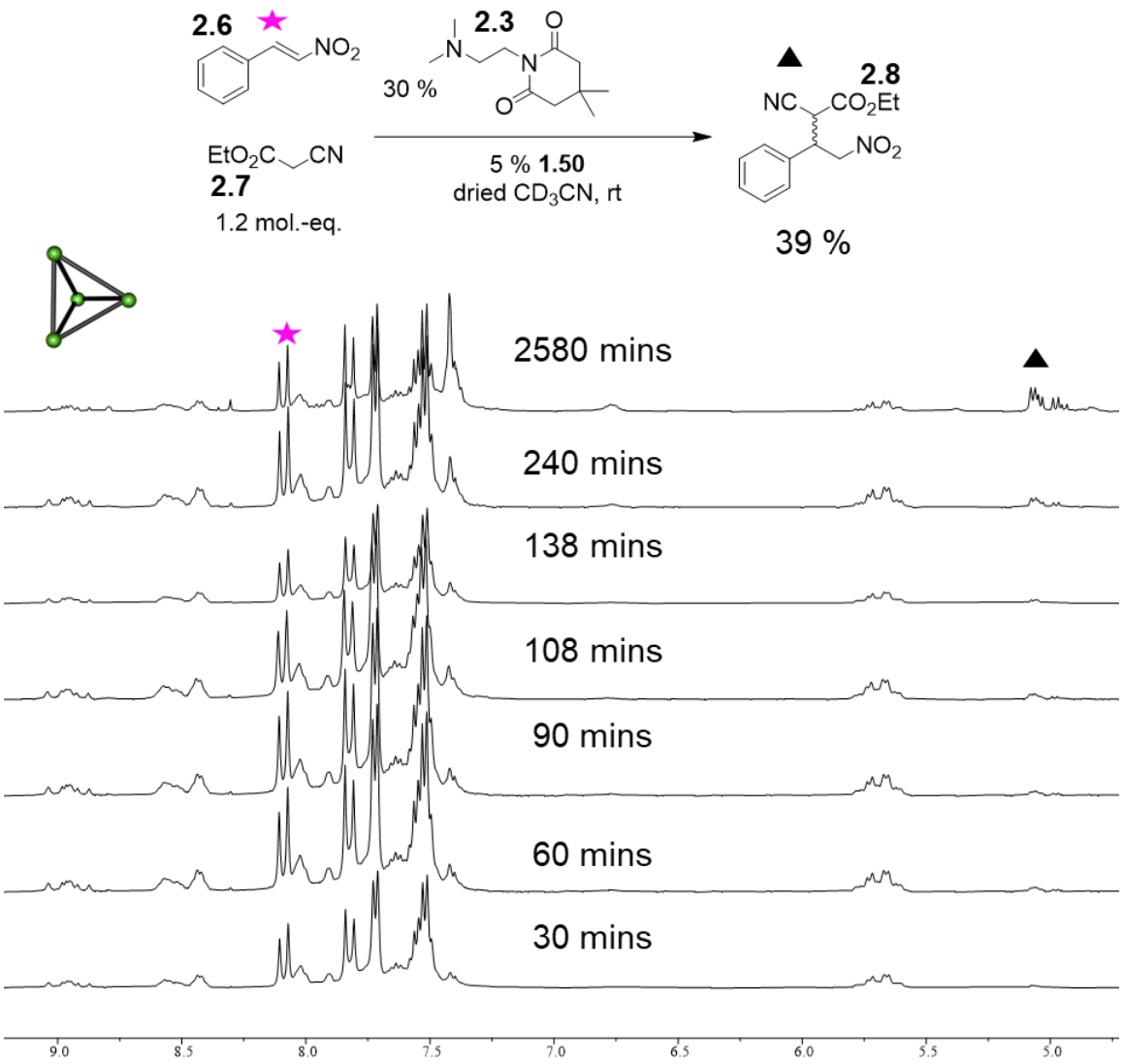

Figure 6.12. ^{1}H NMR spectra of the conjugate addition between **2.6** and **2.7** mediated by **2.3** in 400 µL CD_3CN. [**2.5**] = 20 mM, [**2.6**] = 24 mM, [**2.3**] = 6.0 mM, and [**1.50**] = 1.0 mM. Reaction was performed at 25 °C and monitored over time. (400 MHz, 298 K, anhydrous CD_3CN).

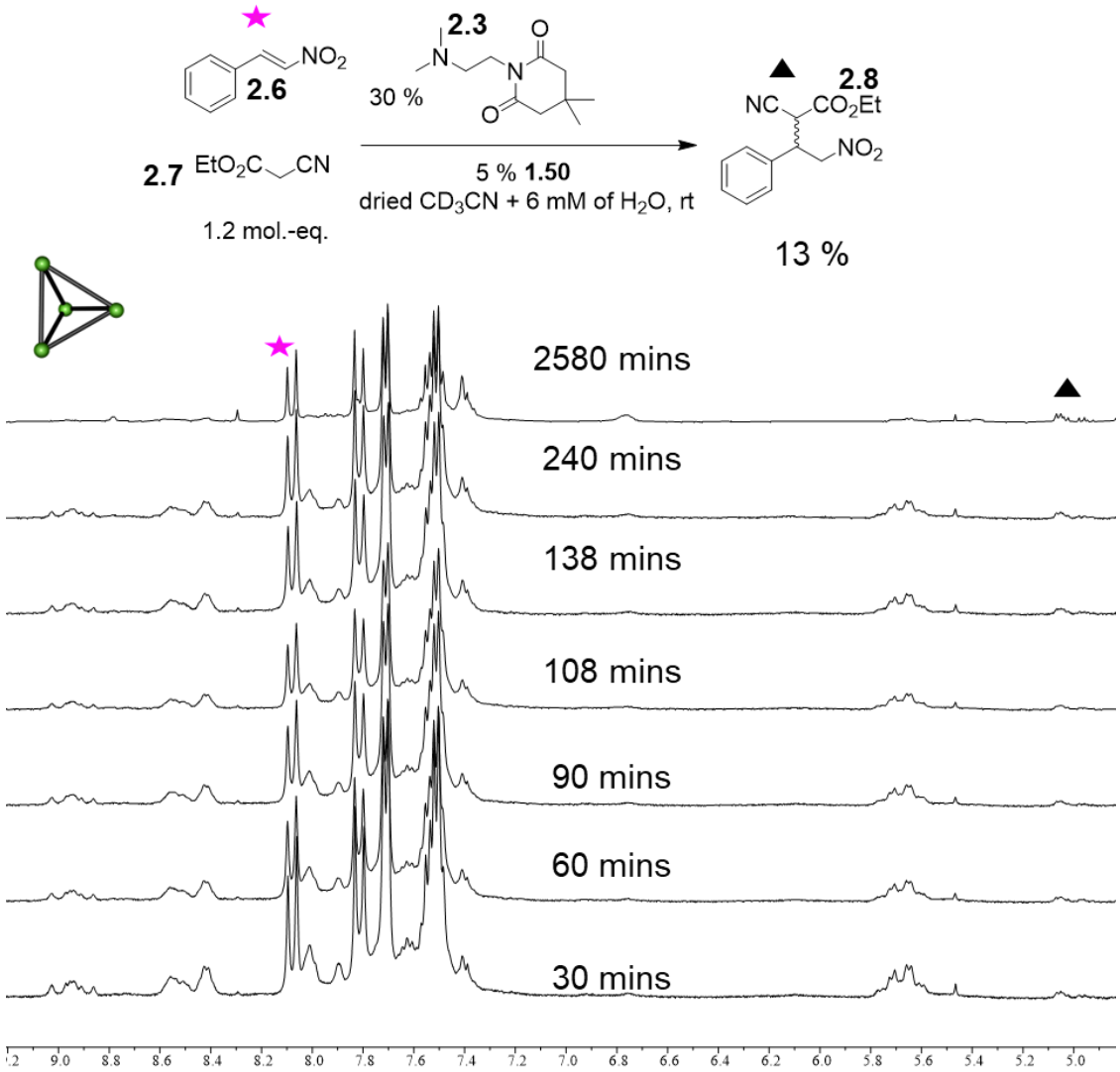

Figure 6.13. ^{1}H NMR spectra of the conjugate addition between **2.6** and **2.7** mediated by **2.3** in 400 µL CD_3CN. [**2.5**] = 20 mM, [**2.6**] = 24 mM, [**2.3**] = 6.0 mM, [H_2O] = 6.0 mM and [**1.50**] = 1.0 mM. Reaction was performed at 25 °C and monitored over time. (400 MHz, dried CD_3CN + 6.0 mM H_2O).

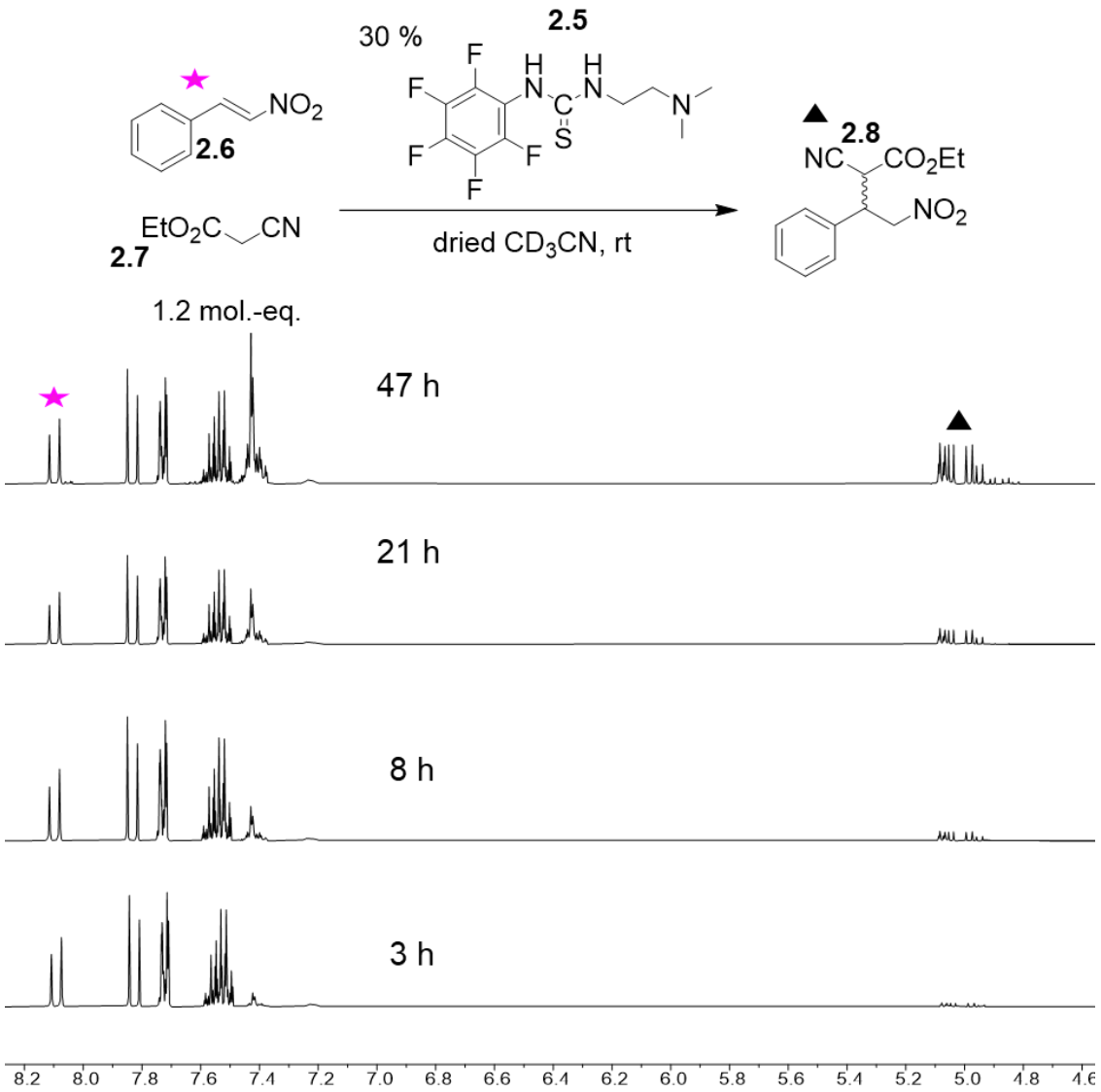

Figure 6.14. ^{1}H NMR spectra of the conjugate addition between **2.6** and **2.7** mediated by **2.3** in 400 µL CD_3CN. [**2.5**] = 20 mM, [**2.6**] = 24 mM, and [**2.5**] = 6.0 mM. Reaction was performed at 25 °C and monitored over time. (400 MHz, 298 K, dried CD_3CN).

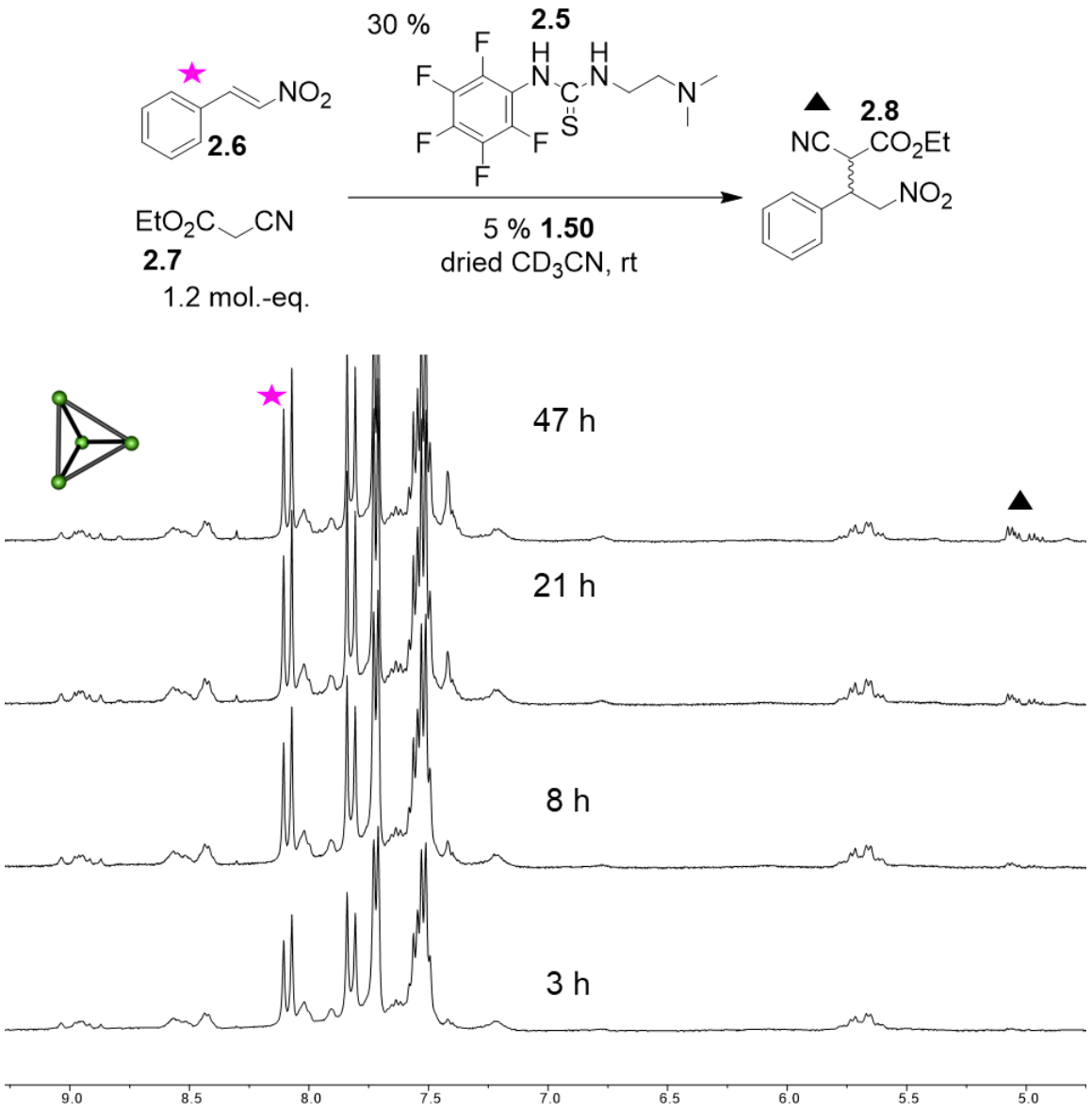

Figure 6.15. ^{1}H NMR spectra of the conjugate addition between **2.6** and **2.7** mediated by **2.3** in 400 µL CD_3CN. [**2.5**] = 20 mM, [**2.6**] = 24 mM, [**2.5**] = 6.0 mM, and [**1.50**] = 1.0 mM. Reaction was performed at 25 °C and monitored over time. (400 MHz, 298 K, dried CD_3CN).

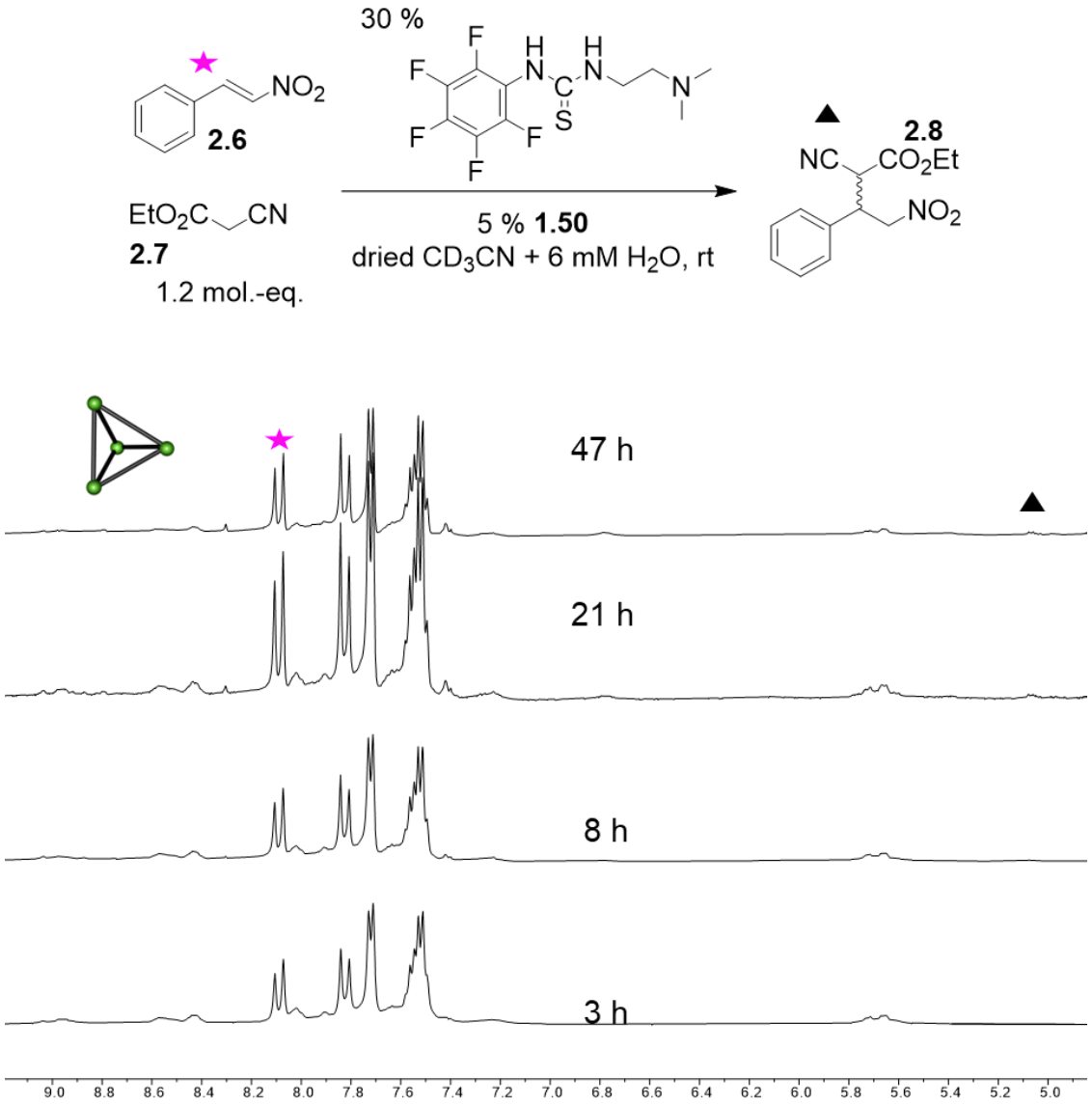

Figure 6.16. ^{1}H NMR spectra of the conjugate addition between **2.6** and **2.7** mediated by **2.3** in 400 µL CD_3CN. [**2.5**] = 20 mM, [**2.6**] = 24 mM, [**2.5**] = 6.0 mM, [H_2O] = 6.0 mM, and [**1.50**] = 1.0 mM. Reaction was performed at 25 °C and monitored over time. (400 MHz, 298 K, dried CD_3CN + 6.0 mM H_2O).

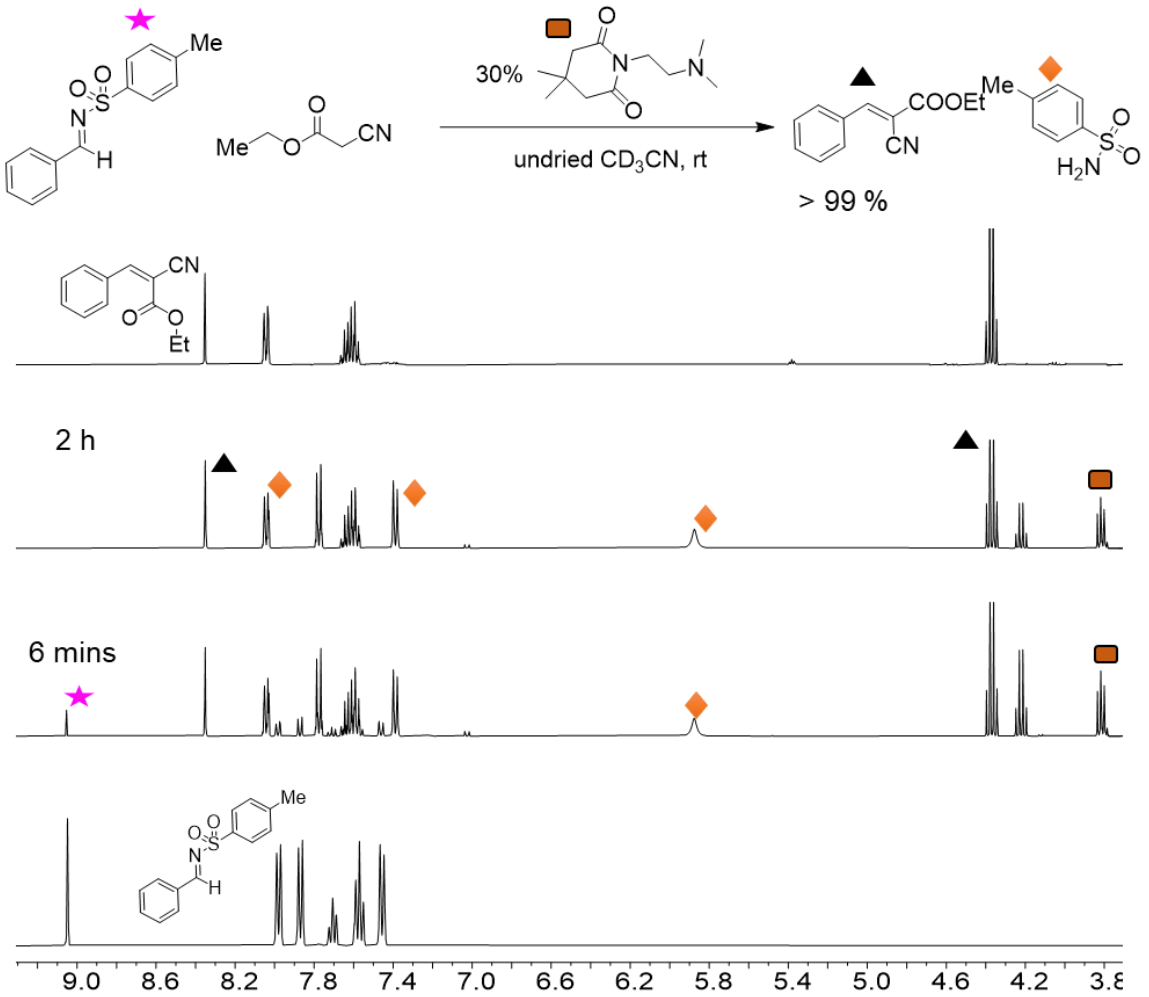

Figure 6.17. ^{1}H NMR spectra of the Knoevenagel condensation showing product formation between **2.9** and **2.10** mediated by **2.3** in 400 µL CD_3CN. [**2.9**] = 20 mM, [**2.10**] = 24 mM, [**2.3**] = 6.0 mM, and [dioxane] = 10 mM. Reaction was performed at 25 °C and monitored over time. (400 MHz, 298 K, CD_3CN).

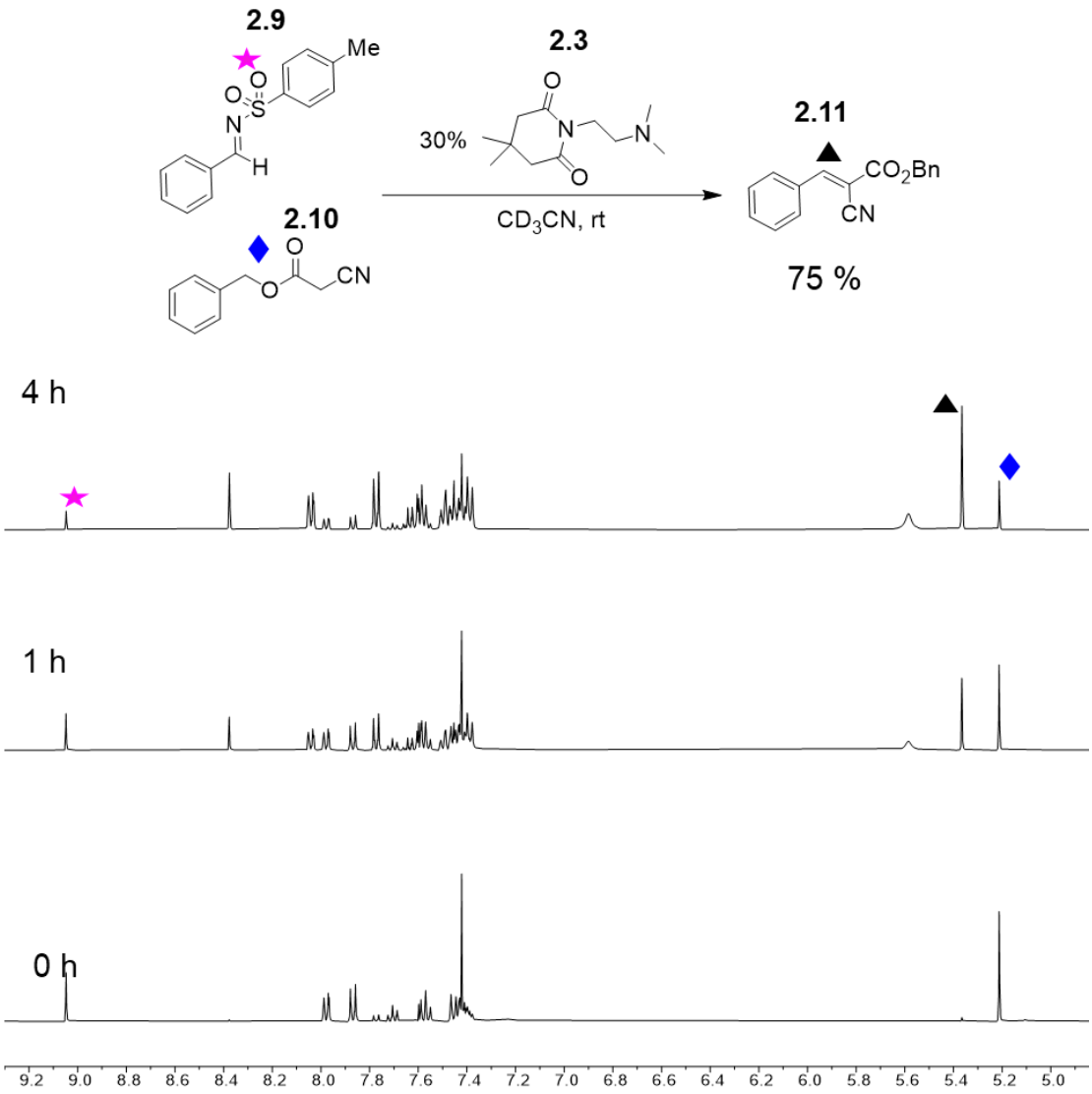

Figure 6.18. ^{1}H NMR spectra of the Knoevenagel condensation between **2.9** and **2.10** mediated by **2.3** in 400 µL CD_3CN. [**2.9**] = 20 mM, [**2.10**] = 24 mM, [**2.3**] = 6.0 mM, and [dioxane] = 10 mM. Reaction was performed at 25 °C and monitored over time. (400 MHz, 298 K, CD_3CN).

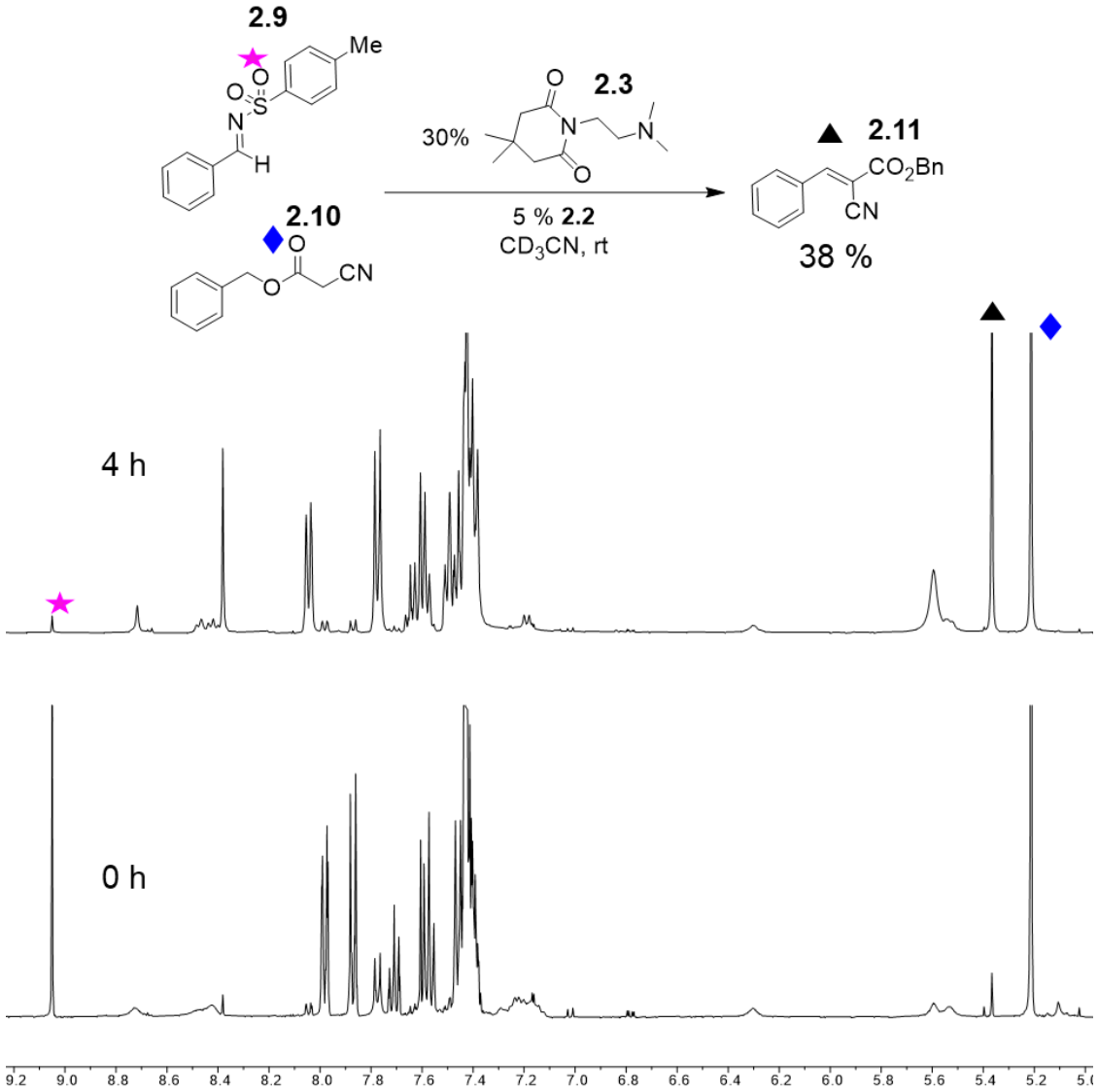

Figure 6.19. ^{1}H NMR spectra of the Knoevenagel condensation between **2.9** and **2.10** mediated by **2.3** in 400 µL CD_3CN. [**2.9**] = 20 mM, [**2.10**] = 24 mM, [**2.3**] = 6.0 mM, [**2.2**] = 1.0 mM and [dioxane] = 10 mM. Reaction was performed at 25 °C and monitored over time. (400 MHz, 298 K, CD_3CN).

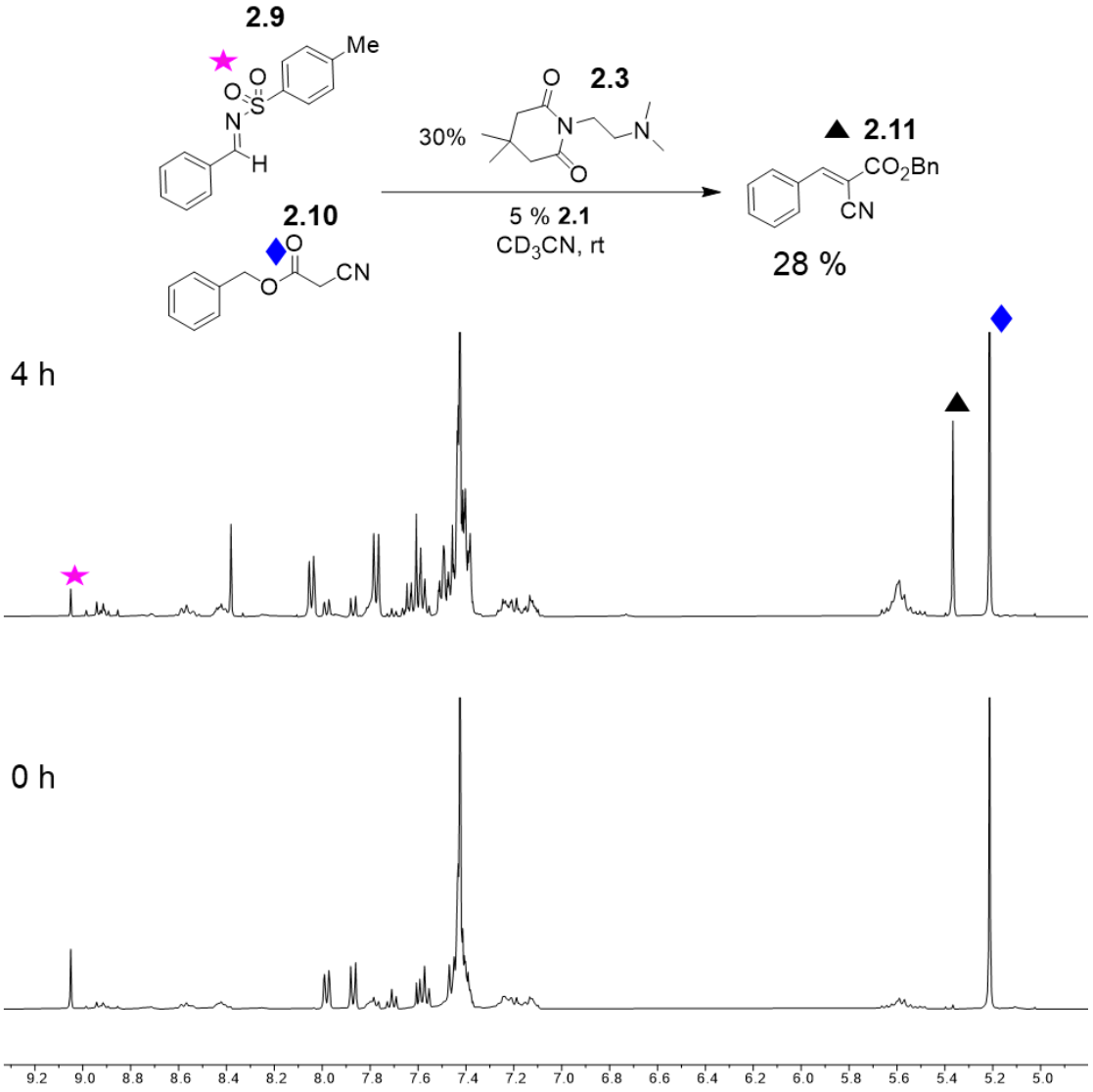

Figure 6.20. ^{1}H NMR spectra of the Knoevenagel condensation between **2.9** and **2.10** mediated by **2.3** in 400 µL CD_3CN. [**2.9**] = 20 mM, [**2.10**] = 24 mM, [**2.3**] = 6.0 mM, [**2.1**] = 1.0 mM and [dioxane] = 10 mM. Reaction was performed at 25 °C and monitored over time. (400 MHz, 298 K, CD_3CN).

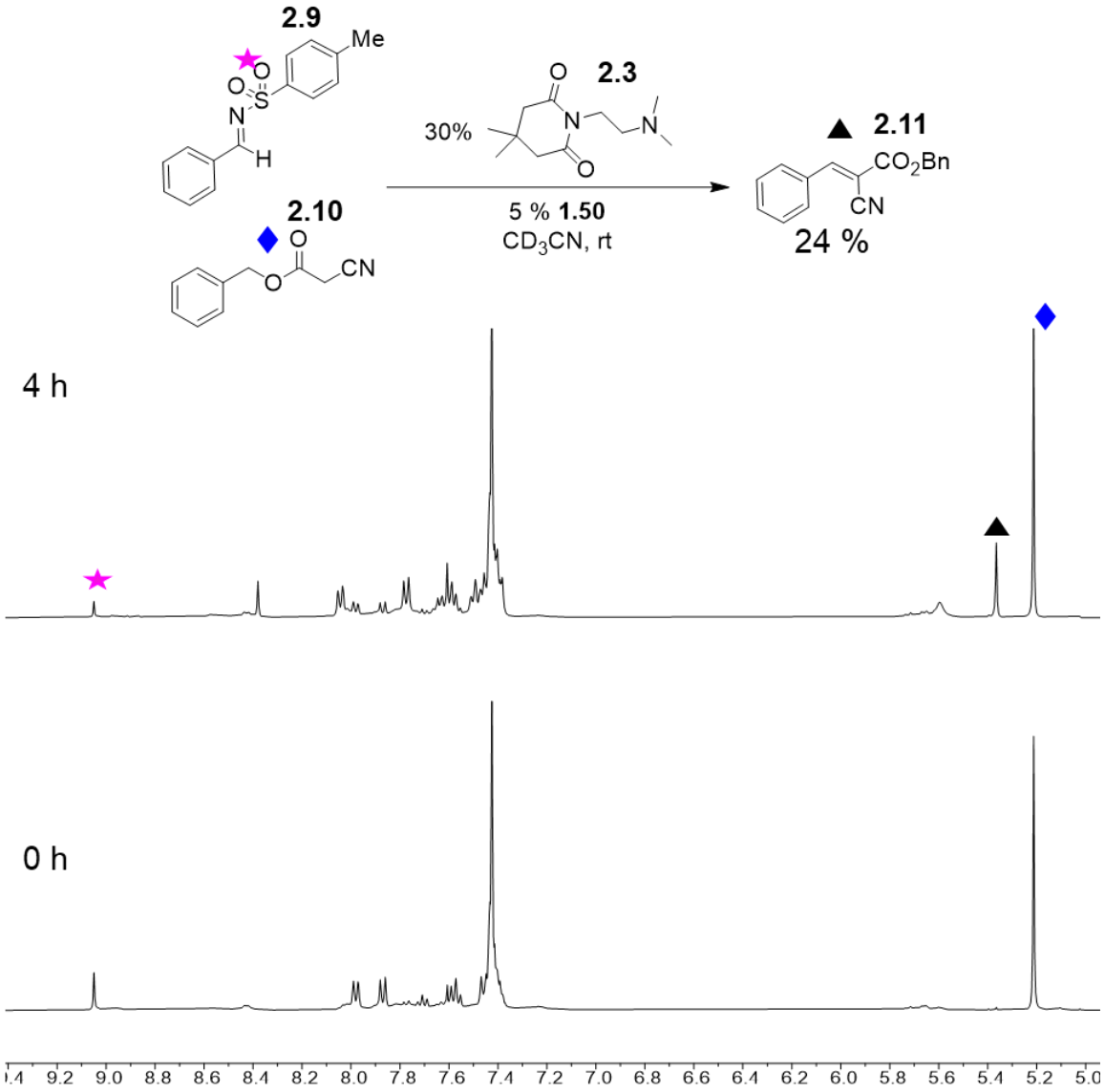

Figure 6.21. ^{1}H NMR spectra of the Knoevenagel condensation between **2.9** and **2.10** mediated by **2.3** in 400 µL CD_3CN. [**2.9**] = 20 mM, [**2.10**] = 24 mM, [**2.3**] = 6.0 mM, [**1.50**] = 1.0 mM and [dioxane] = 10 mM. Reaction was performed at 25 °C and monitored over time. (400 MHz, 298 K, CD_3CN).

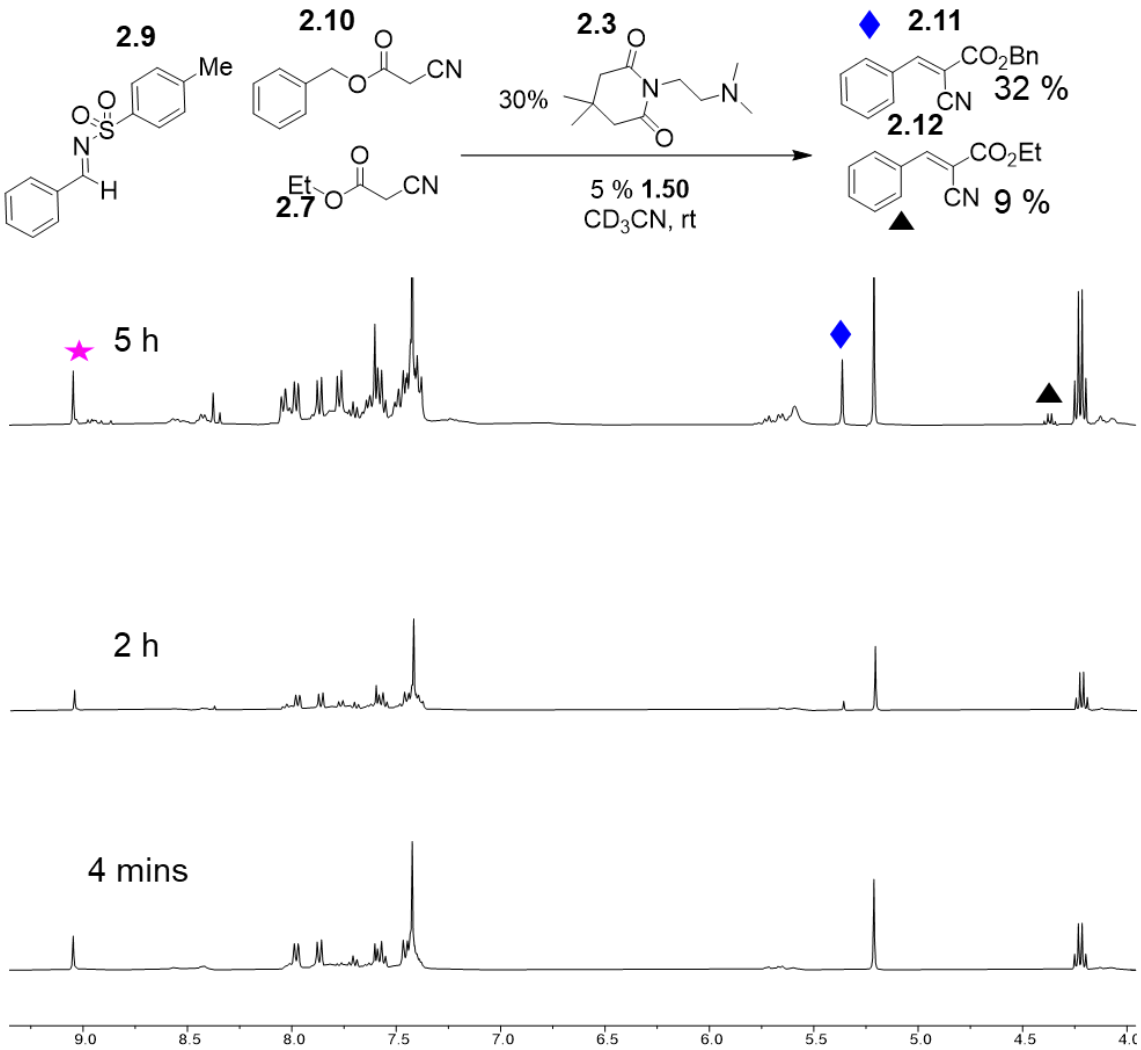

Figure 6.22. ^{1}H NMR spectra of competitive Knoevenagel condensation between **2.9**, **2.7** and **2.10** mediated by **2.3** in 400 µL CD_3CN. [**2.9**] = 20 mM, [**2.10**] = 24 mM, [**2.7**] = 24 mM, [**2.3**] = 6.0 mM, [**1.50**] = 1.0 mM and [dioxane] = 10 mM. Reaction was performed at 25 °C and monitored over time. (400 MHz, 298 K, CD_3CN).

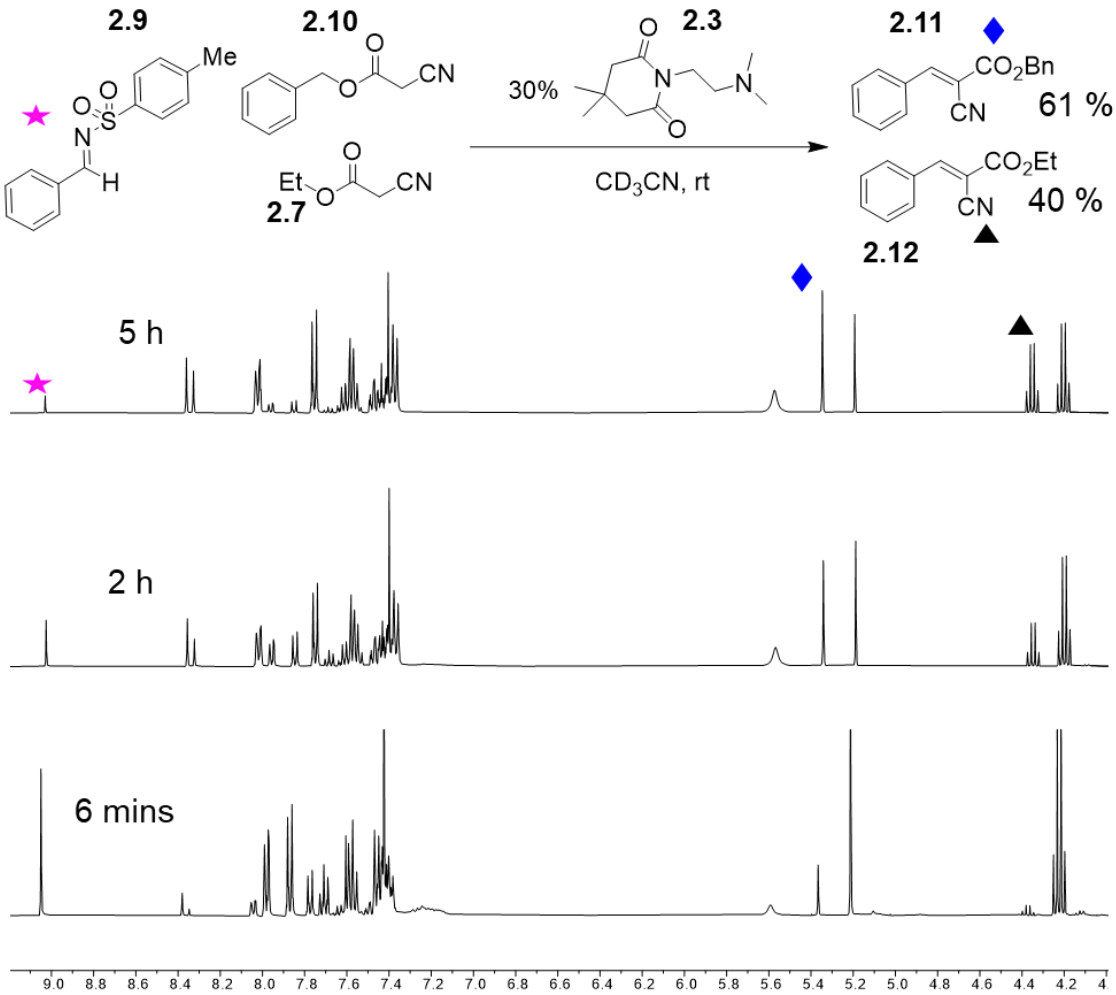

Figure 6.23. ^{1}H NMR spectra of competitive Knoevenagel condensation between **2.9**, **2.7** and **2.10** mediated by **2.3** in 400 µL CD_3CN. [**2.9**] = 20 mM, [**2.10**] = 24 mM, [**2.7**] = 24 mM, [**2.3**] = 6.0 mM, and [dioxane] = 10 mM. Reaction was performed at 25 °C and monitored over time. (400 MHz, 298 K, CD_3CN).

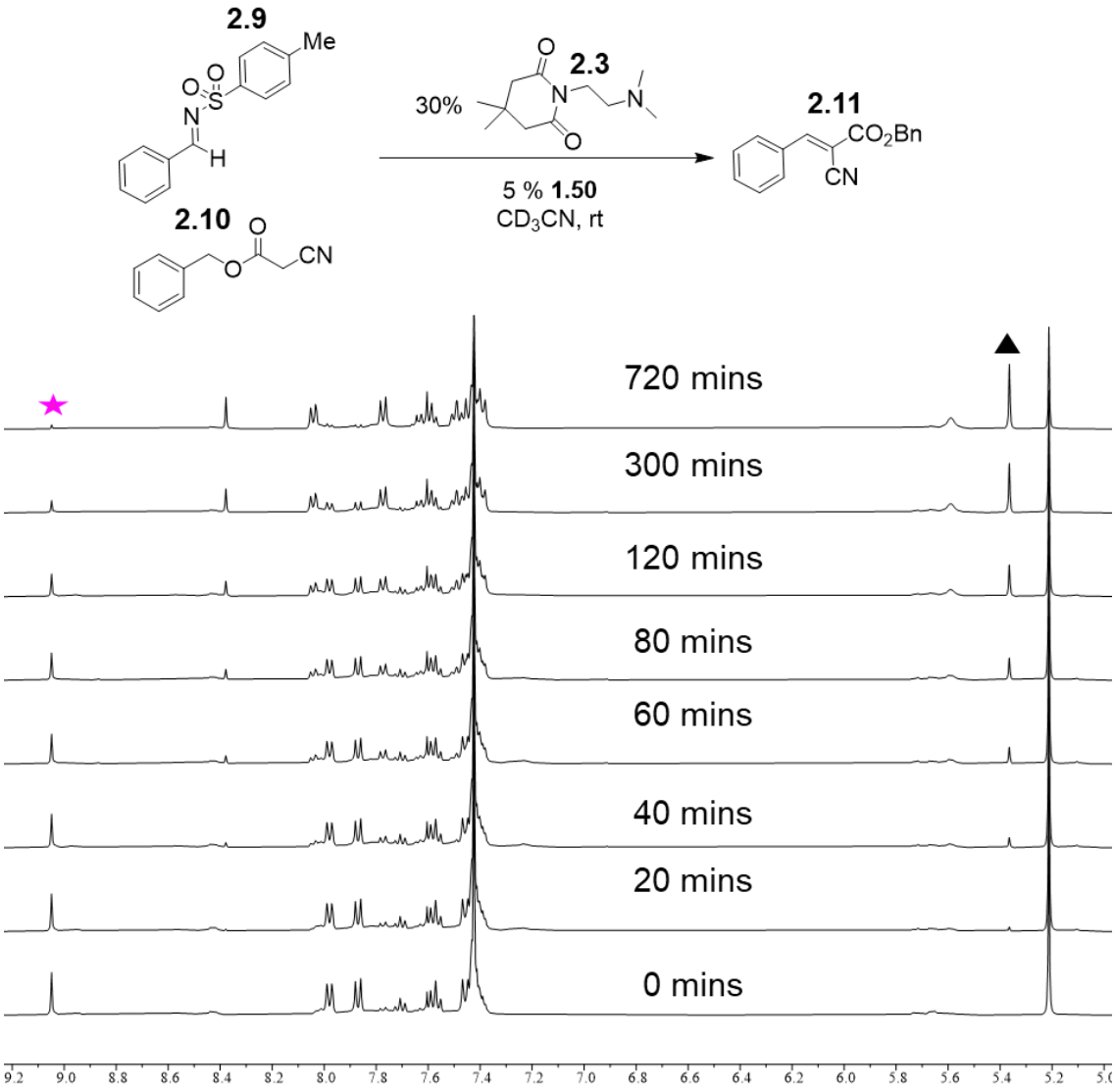

Figure 6.24. ^{1}H NMR spectra of competitive Knoevenagel condensation between **2.9** and **2.10** mediated by **2.3** in 400 µL CD_3CN. [**2.9**] = 20 mM, [**2.10**] = 24 mM, [**2.3**] = 6.0 mM, [**1.50**] = 1.0 mM and [dioxane] = 10 mM. Reaction was performed at 25 °C and monitored over time. (400 MHz, 298 K, CD_3CN).

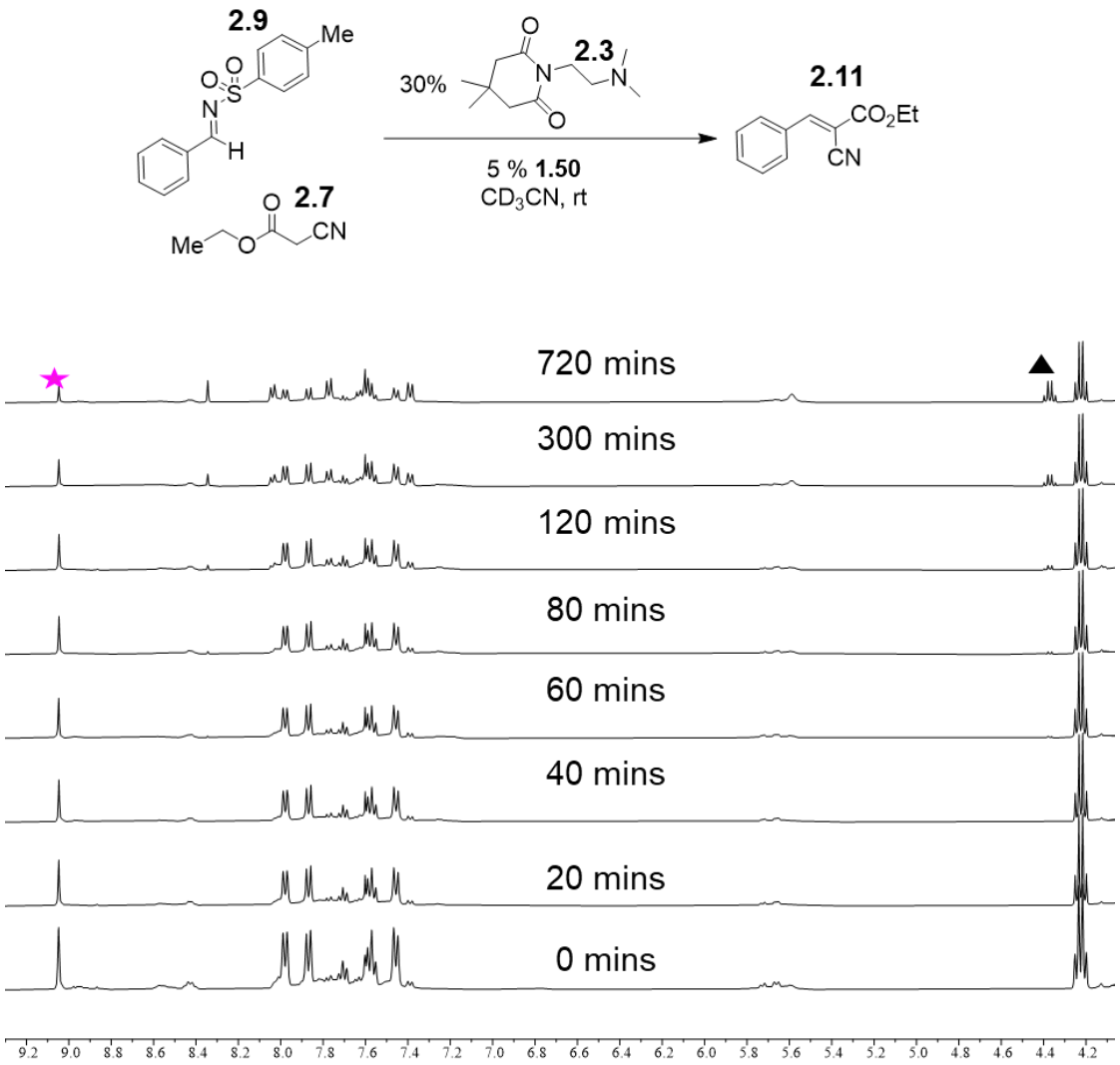

Figure 6.25. ^{1}H NMR spectra of competitive Knoevenagel condensation between **2.9** and **2.7** mediated by **2.3** in 400 µL CD_3CN. [**2.9**] = 20 mM, [**2.7**] = 24 mM, [**2.3**] = 6.0 mM, [**1.50**] = 1.0 mM and [dioxane] = 10 mM. Reaction was performed at 25 °C and monitored over time. (400 MHz, 298 K, CD_3CN).

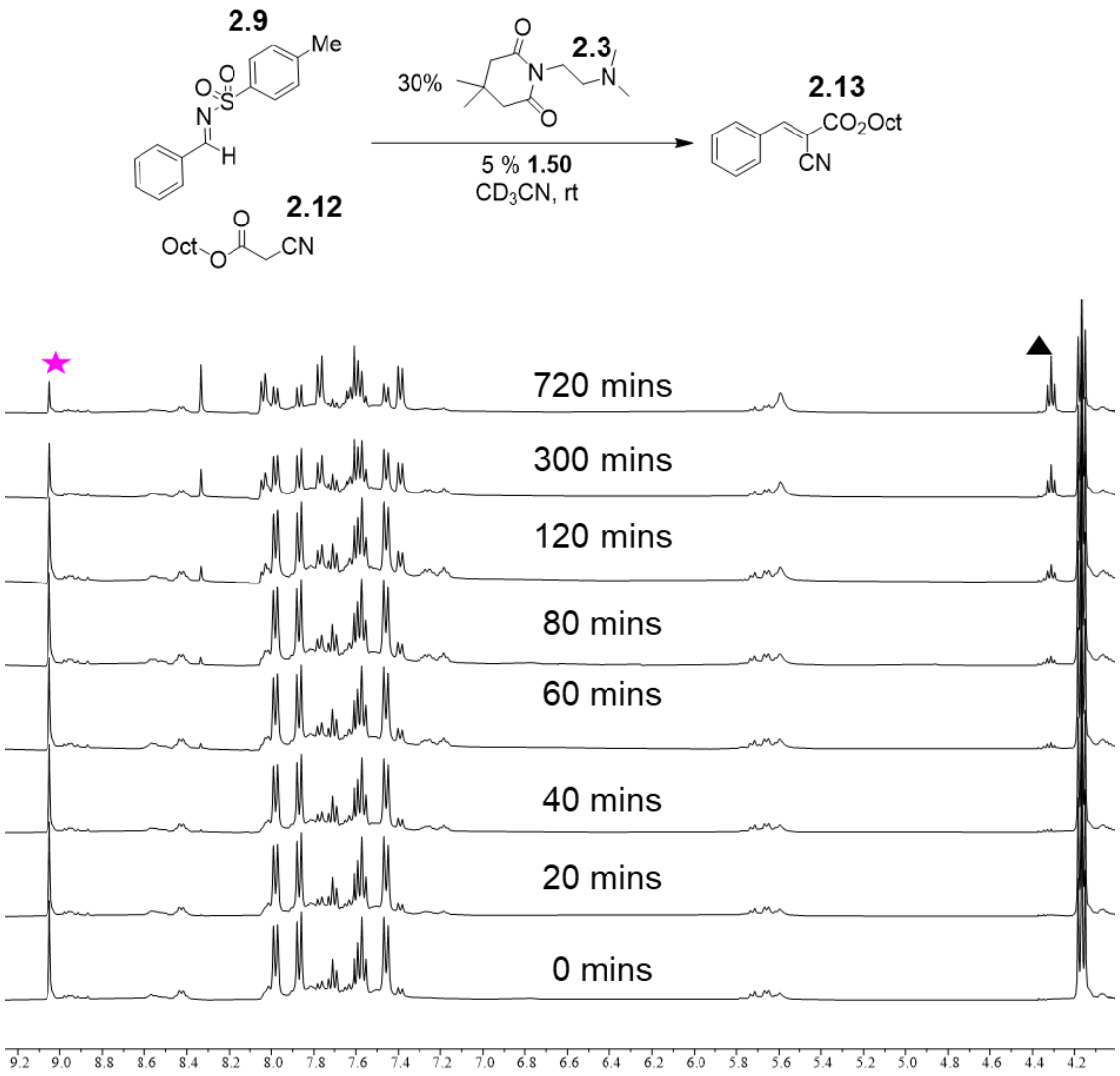

Figure 6.26. ^{1}H NMR spectra of competitive Knoevenagel condensation between **2.9** and **2.12** mediated by **2.3** in 400 µL CD_3CN. [**2.9**] = 20 mM, [**2.12**] = 24 mM, [**2.3**] = 6.0 mM, [**1.50**] = 1.0 mM and [dioxane] = 10 mM. Reaction was performed at 25 °C and monitored over time. (400 MHz, 298 K, CD_3CN).

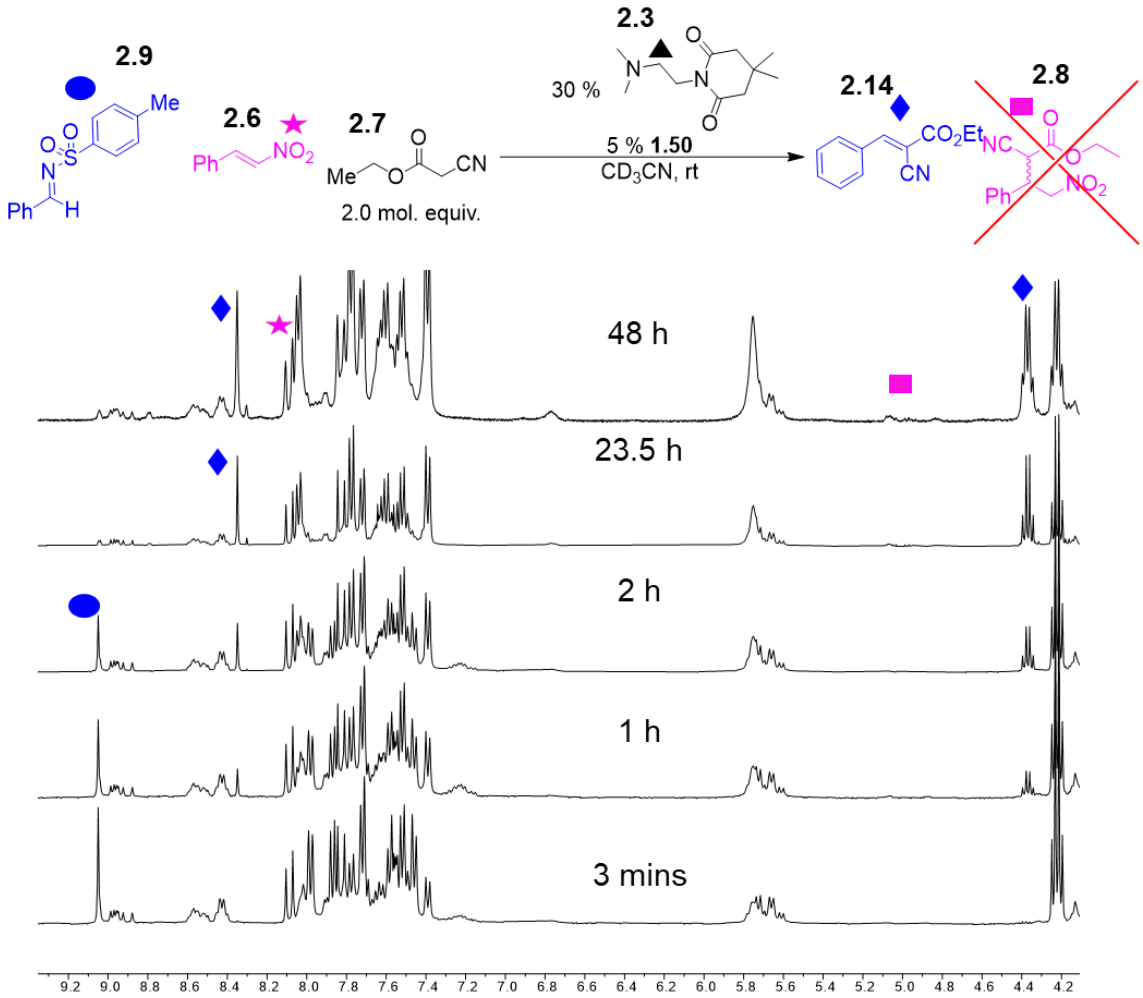

Figure 6.27. ^{1}H NMR spectra of competitive Knoevenagel condensation versus conjugate addition between **2.6**, **2.9**, and **2.7** mediated by **2.3** in 400 µL CD_3CN. [**2.9**] = 20 mM, [**2.6**] = 20 mM, [**2.7**] = 24 mM, [**2.3**] = 6.0 mM, [**1.50**] = 1.0 mM and [dioxane] = 10 mM. Reaction was performed at 25 °C and monitored over time. (400 MHz, 298 K, CD_3CN).

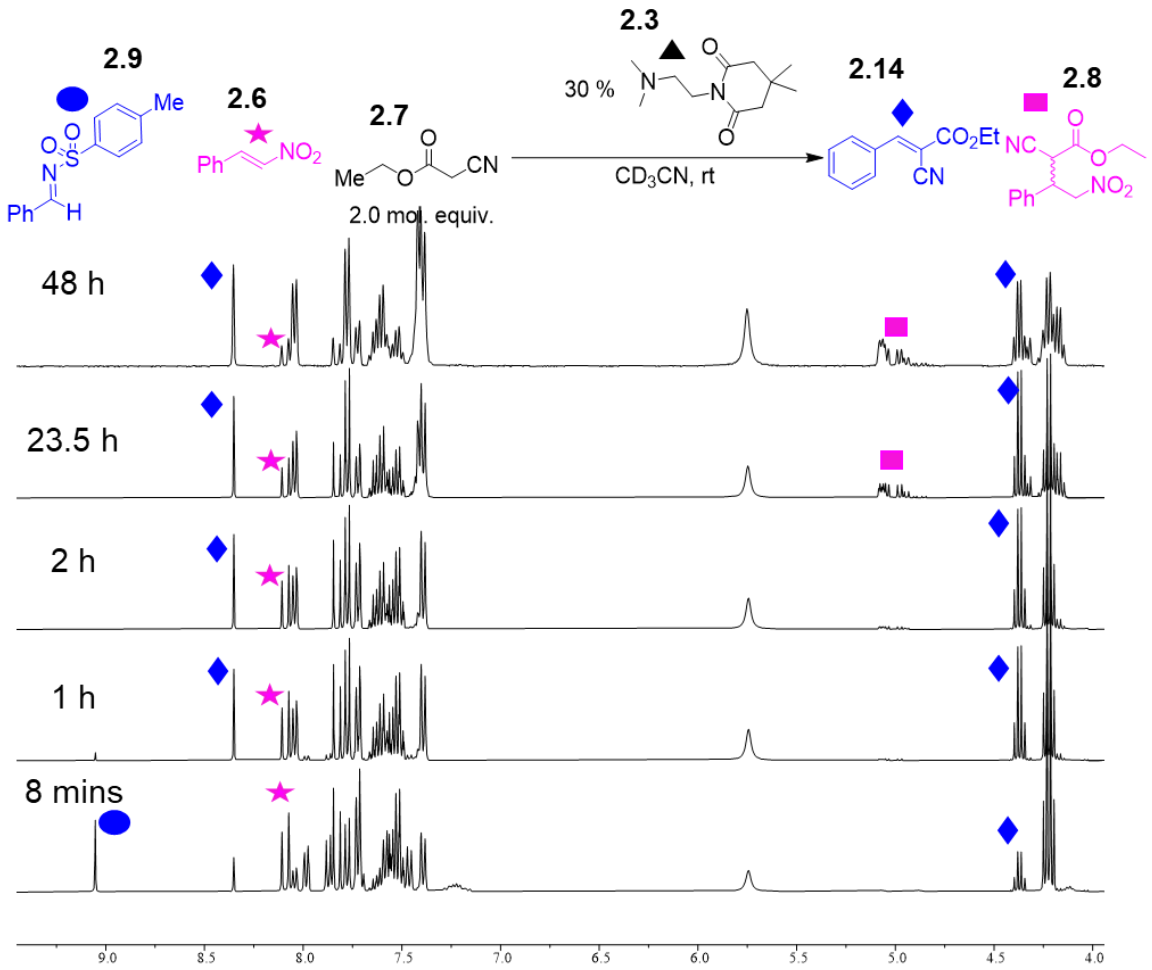

Figure 6.28. ^{1}H NMR spectra of competitive Knoevenagel condensation versus conjugate addition between **2.6**, **2.9**, and **2.7** mediated by **2.3** in 400 µL CD_3CN. [**2.9**] = 20 mM, [**2.6**] = 20 mM, [**2.7**] = 24 mM, [**2.3**] = 6.0 mM and [dioxane] = 10 mM. Reaction was performed at 25 °C and monitored over time. (400 MHz, 298 K, CD_3CN).

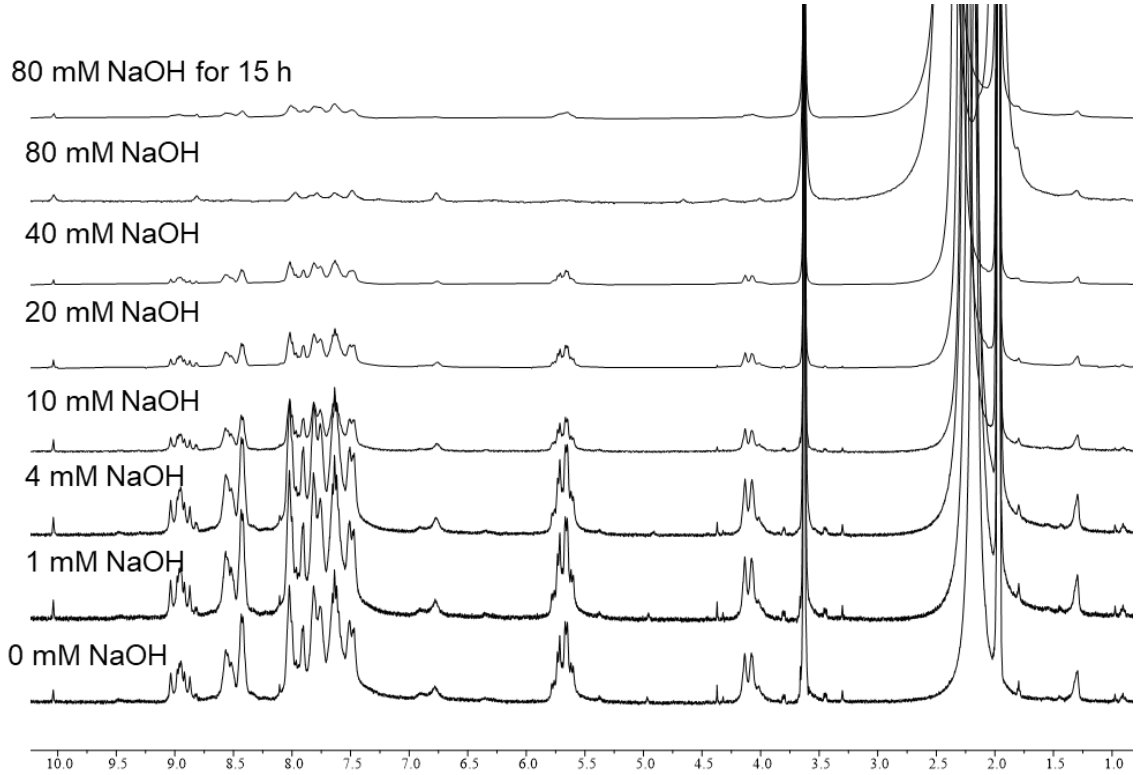

Figure 6.29. ^{1}H NMR titration of NaOH into a solution of **1.50**. [**1.50**] = 1.0 mM, performed at 25 °C and monitored over time. (400 MHz, 298 K, CD_3CN).

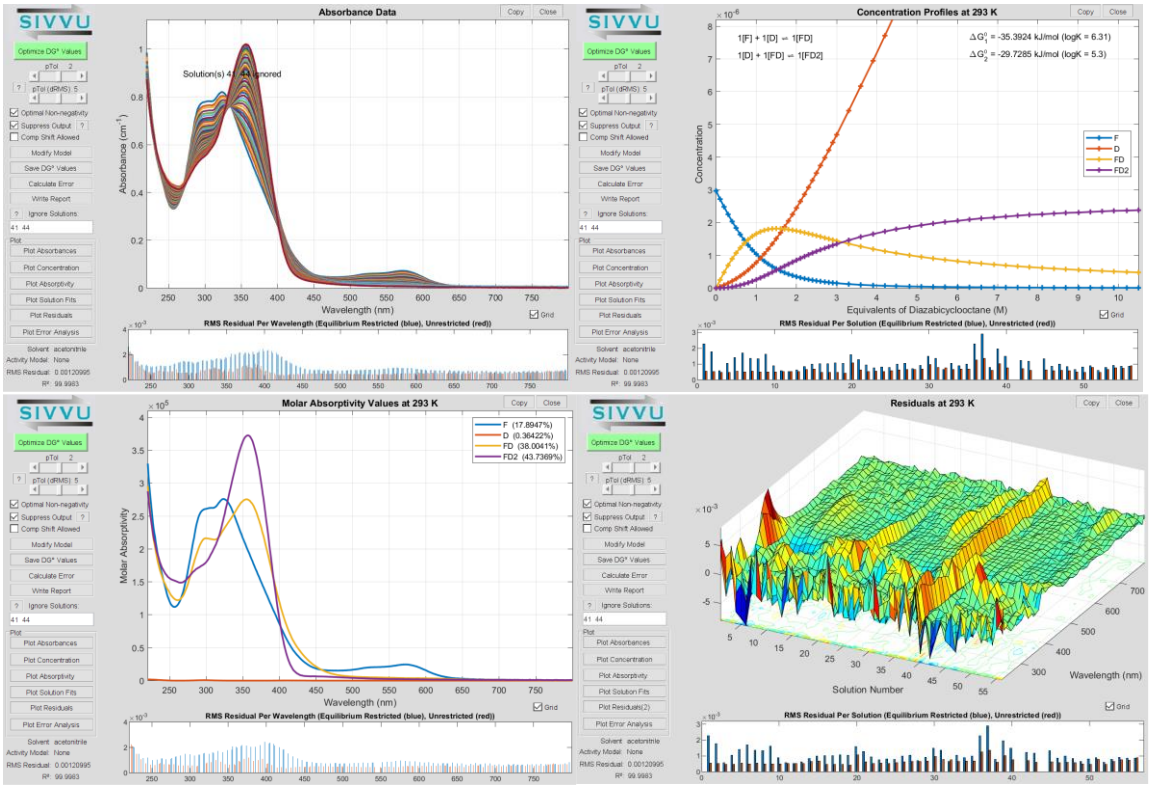

Figure 6.30. UV-Vis binding absorption spectrum for the addition of DABCO into fluorene cage (**1.50**, 3 μM). DABCO was added in 1 μL aliquots from a 0.9 mM stock solution in CH_3CN.

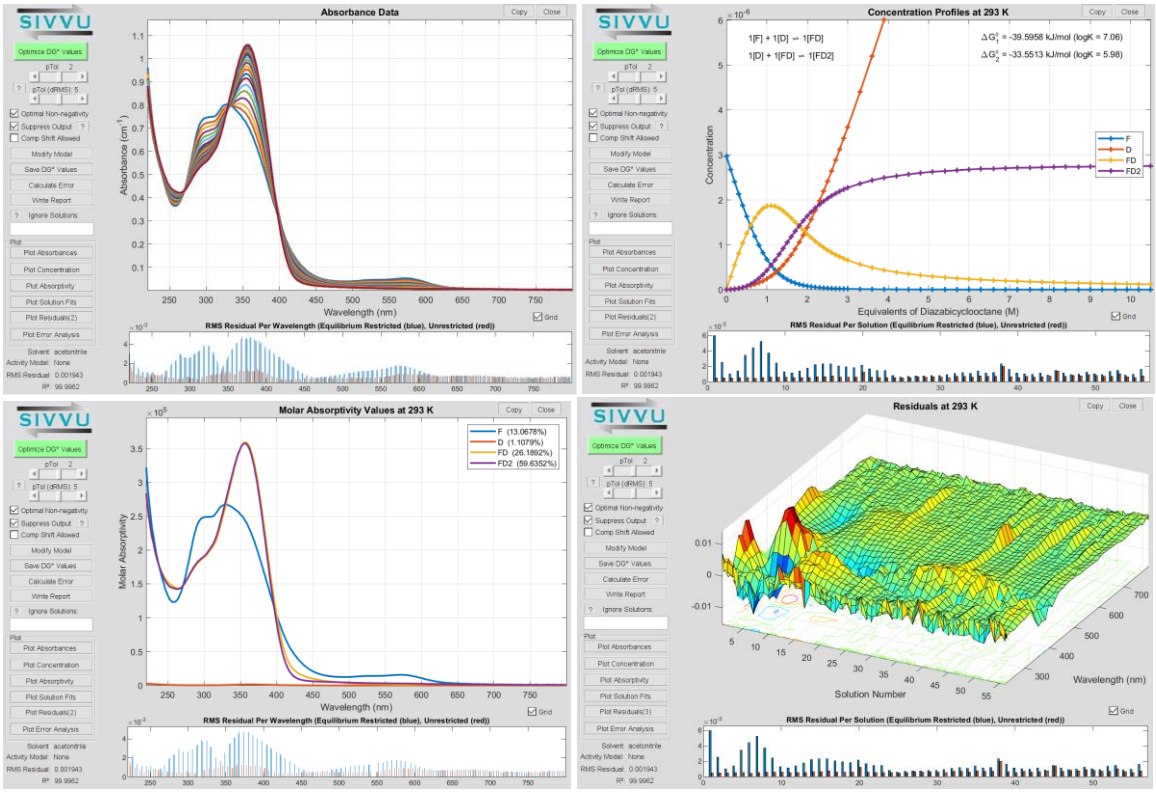

Figure 6.31. UV-Vis binding absorption spectrum for the addition of DABCO + H_2O into fluorene cage (**1.50**, 3 µM). DABCO was added in 1 µL aliquots from a 0.9 mM stock solution in CH_3CN. A 5 µL addition of water was added to the 3 mL cuvette brining the water concentration to about 0.09 M.

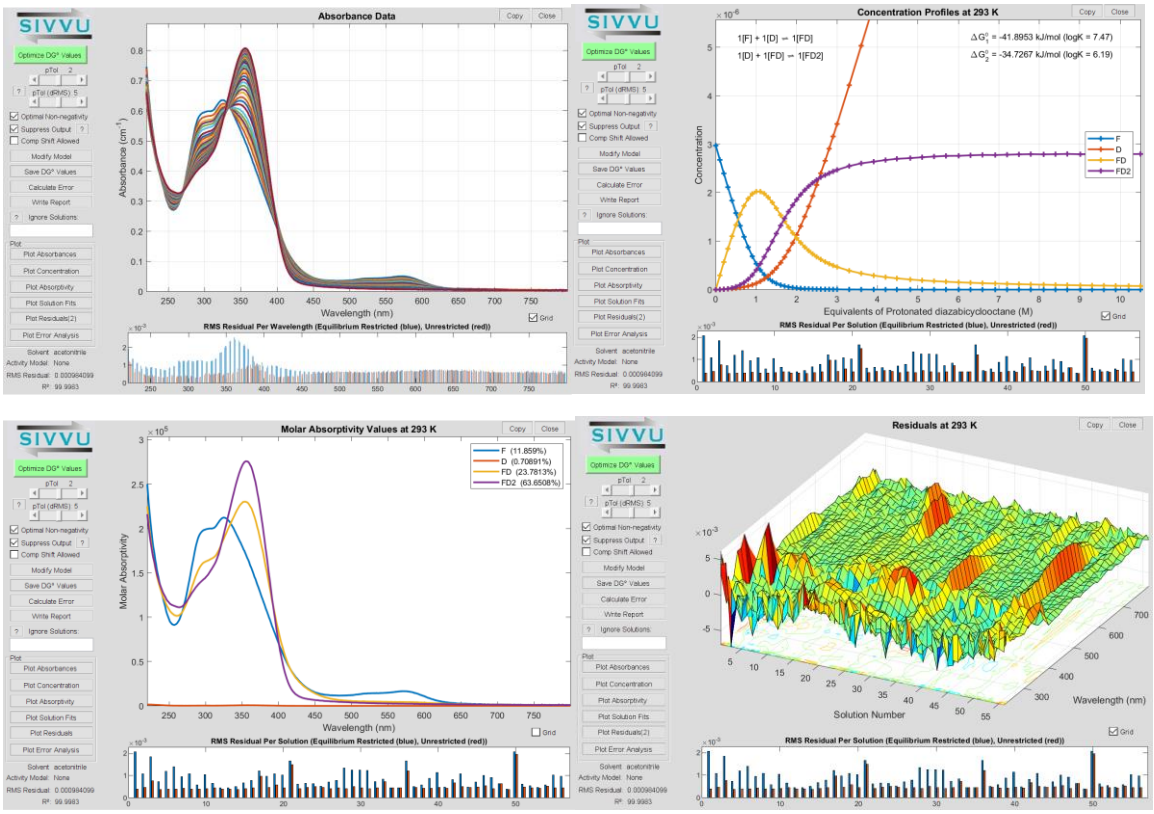

Figure 6.32. UV-Vis binding absorption spectrum for the addition of $DABCOH^{+}OTf^{-}$ into fluorene cage (**1.50**, 3 μM). DABCO was added in 1 μL aliquots from a 0.9 mM stock solution in CH_3CN.

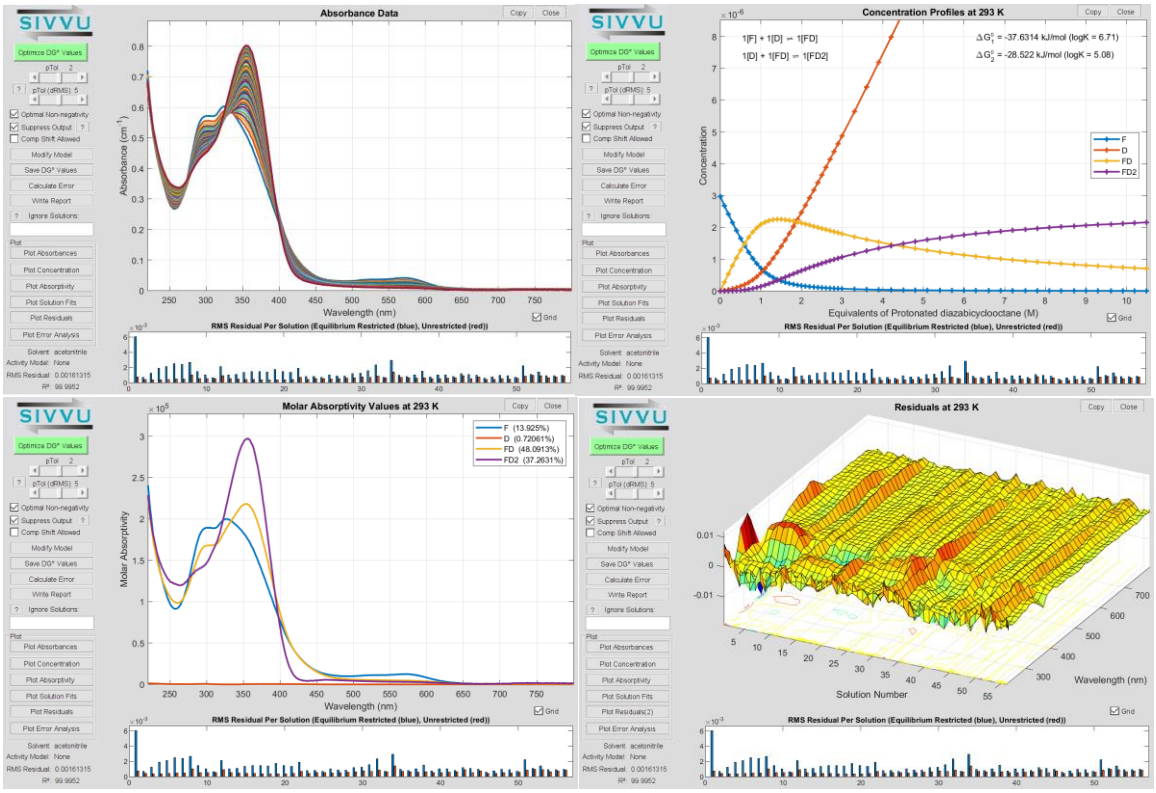

Figure 6.33. UV-Vis binding absorption spectrum for the addition of $DABCOH^{+}OTf^{-}$ + 5 µL into fluorene cage (**1.50**, 3 µM). DABCO was added in 1 µL aliquots from a 0.9 mM stock solution in CH_3CN. A 5 µL addition of water was added to the 3 mL cuvette brining the water concentration to about 0.09 M.

6.4. Experimental for Chapter 3

General procedure for oxidation reactions. Initially a 400 μL solution of thiol (1 mol.-eq., 7.3 μmol, 0.18 M solution in CD_3CN) and 1,4-dioxane as the internal standard (0.5 mol.-eq., 3.65 μmol, of 0.09 M solution in CD_3CN) was added to an NMR tube followed by 5 mol % cage **1.50** (0.31 μmol, 2 mg). The NMR tube was capped and quickly shaken to dissolve all solids. An initial ^1H NMR spectrum of the reaction mixture was obtained to verify the stoichiometry of the sample. The sample was then heated at 50 °C in a sand bath or left to sit in a test at room temperature while the reaction progress monitored over time. The percent conversion values were obtained *via* integration of the product and substrate peaks against the internal standard.

General procedure for control experiments. $Fe(NTf_2)_2$ doping studies**:** A volume of 300 μL of a solution containing thiol (1 mol.-eq., 7.3 μmol, 0.024 M solution in CD_3CN) and 1,4-dioxane as the internal standard (0.5 mol.-eq., 3.65 μmol, of 0.012 M solution in CD_3CN) was added to an NMR tube. The concentration of iron in the reaction solution was adjusted *via* the addition of aliquots from a $Fe(NTf_2)_2$ stock solution (0.1-0.5 mol.-eq., 0.7-3.7 μmol, of 0.14 mM solution in CD_3CN). 5 mol % **1.50** (0.36 μmol, 2 mg) was then added before finally adding CD_3CN so that the final reaction volume was 400 μL. The NMR tube was then capped and shaken to ensure proper solvation of **1.50**. An initial ^1H NMR spectrum of the reaction mixture was obtained to verify the stoichiometry of the sample. The sample was then heated at 50 °C in a sand bath and the reaction progress monitored over time. Supramolecular cage and assembly studies: Initially a 400 μL solution of thiol (1 mol.-eq., 7.3 μmol, 0.18 M solution in CD_3CN) and 1,4-dioxane as the internal standard

(0.5 mol.-eq., 3.65 μmol, of 0.09 M solution in CD_3CN) was added to an NMR tube followed by the addition of 5 mol % cage **1.50** (0.36 μmol, 2 mg), **2.1** (0.36 μmol, 1.8 mg), or **2.2** (0.72 μmol, 1.8 mg). The NMR tube was then capped and shaken to ensure proper solvation of supramolecular cages or assembly. An initial ^1H NMR spectrum of the reaction mixture was obtained to verify the stoichiometry of the sample. The sample was then heated at 80 °C in a sand bath and the reaction progress monitored over time.

General procedure for size selective studies and gas chromatography analysis. Initially 2 400 μL solutions of thiol A and B (1 mol.-eq., 7.3 μmol, 0.018 M solution in CD_3CN) and 1,4-dioxane as the internal standard (0.5 mol.-eq., 3.65 μmol, of 0.009 M solution in CD_3CN) were added to **separate** NMR tubes. An initial ^1H NMR spectrum of the reaction mixture was obtained to verify the stoichiometry of the sample. Following the NMR samples were combined into a new NMR tube followed by the addition of 5 mol % cage **1.50** (0.72 μmol, 4 mg). The NMR tube was capped and quickly shaken to dissolve all solids. Another ^1H NMR spectrum of the reaction mixture was obtained to ensure all reaction components were present. The sample was then left to sit in a test tube at room temperature while the reaction progress was monitored over time. Once ~20 % conversion had been achieved after 7 days the contents were flushed through a silica plug with 2 mL of ether, in addition to 450 μL solution of dodecane (0.6 mol.-eq., 4.05 μmol, 9 mM solution in diethyl ether) as an internal standard for GC analysis. The GC was then programmed with an initial temperature of 70 °C with a ramp rate of 10 °C per minute to 120 °C followed by a ramp rate of 20 °C per minute to 280 °C. The run was held at 280 °C until all reaction components had appeared on the chromatogram. The percent conversion

values were obtained *via* integration of the product and substrate peaks against the internal standard on the GC chromatogram.

Disulfide synthesis: Disulfides were synthesized and purified using previously established methods.[6]

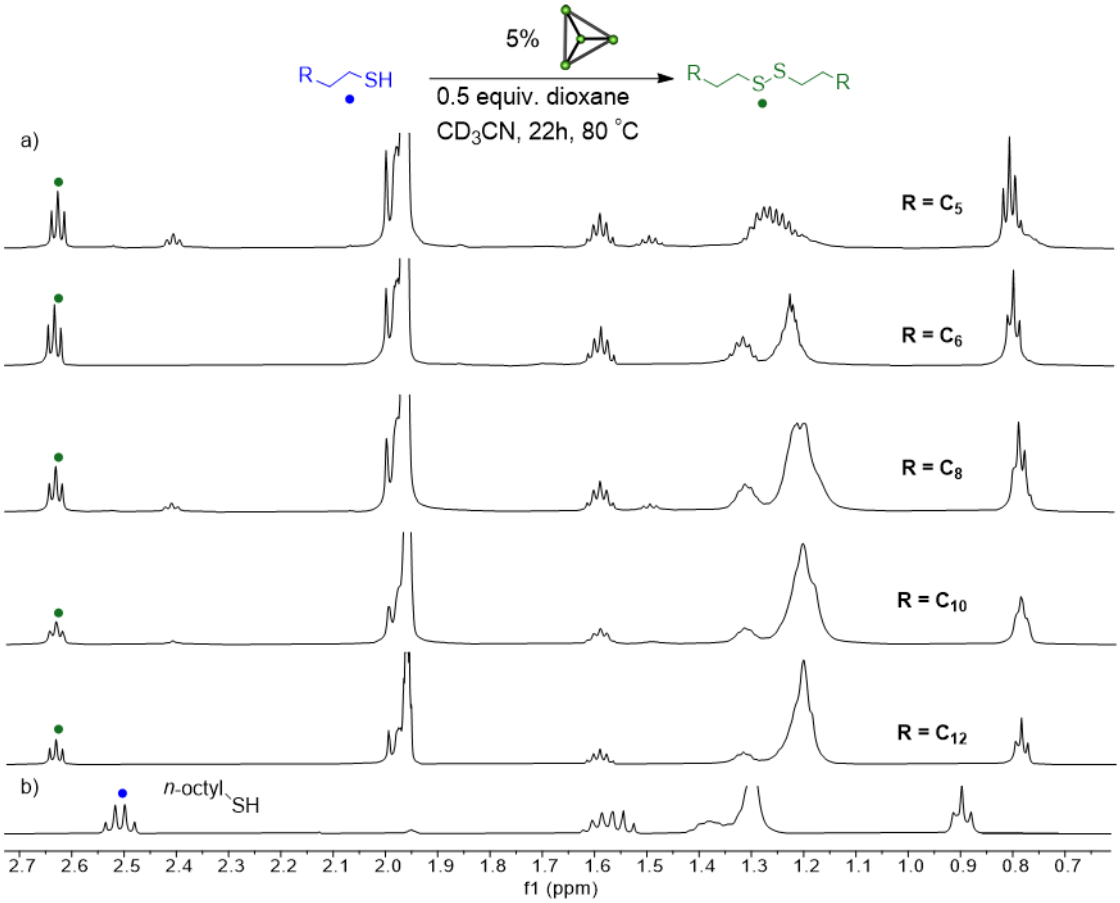

Figure 6.34. ^{1}H NMR spectra of the oxidative dimerization of various thiols with varying length in the presence of 5 mol % cage **1.50** showing: a) product formation (2.80-0.6 ppm); b) **C_8-SH** for comparison (2.80-0.6 ppm). [**C_x-SH**] = 18.2 mM, [**1.50**] = 0.9 mM, in CD_3CN. Reactions were performed at 80 °C in 400 µL CD_3CN and monitored over time (600 MHz, 298 K, CD_3CN).

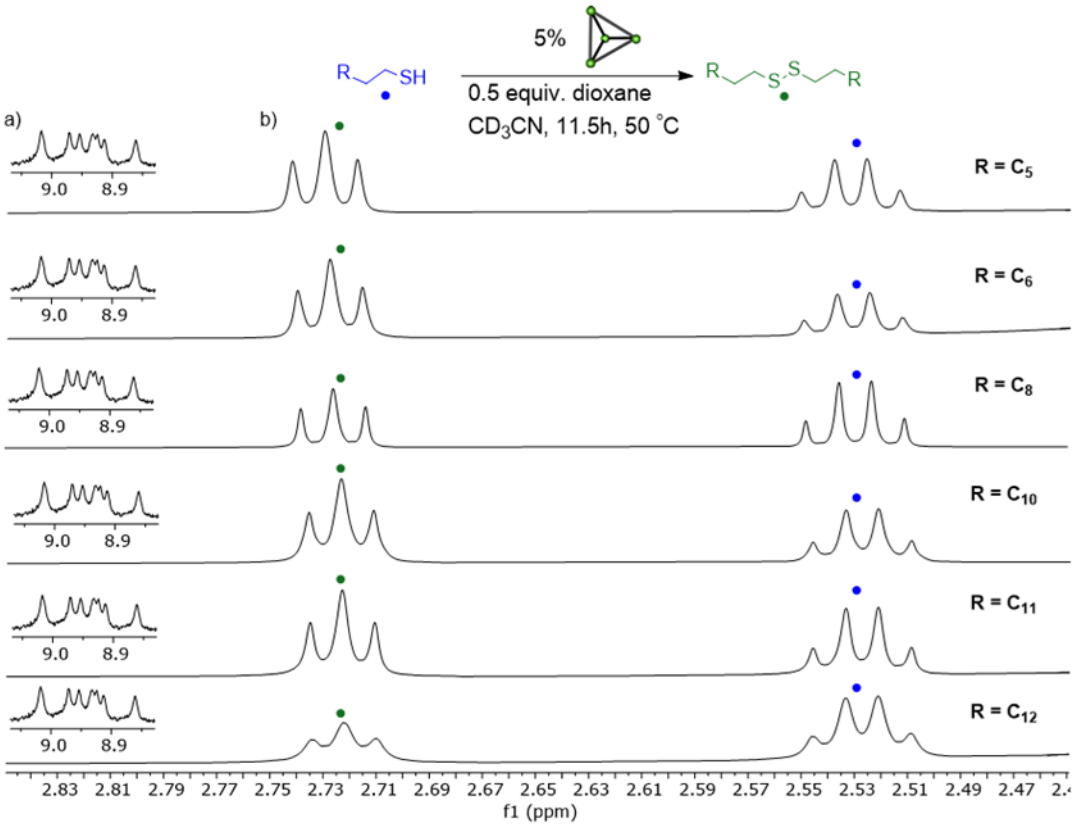

Figure 6.35. ^{1}H NMR spectra of the oxidative dimerization of various thiols with varying length in the presence of 5 mol % cage **1.50** showing: a) product formation (2.80-2.47 ppm); b) **C_8-SH** for comparison (2.80-0.6 ppm). [**C_x-SH**] = 18.2 mM, [**1.50**] = 0.9 mM, in CD_3CN. Reactions were performed at 50 °C in 400 µL CD_3CN and monitored over time (600 MHz, 298 K, CD_3CN).

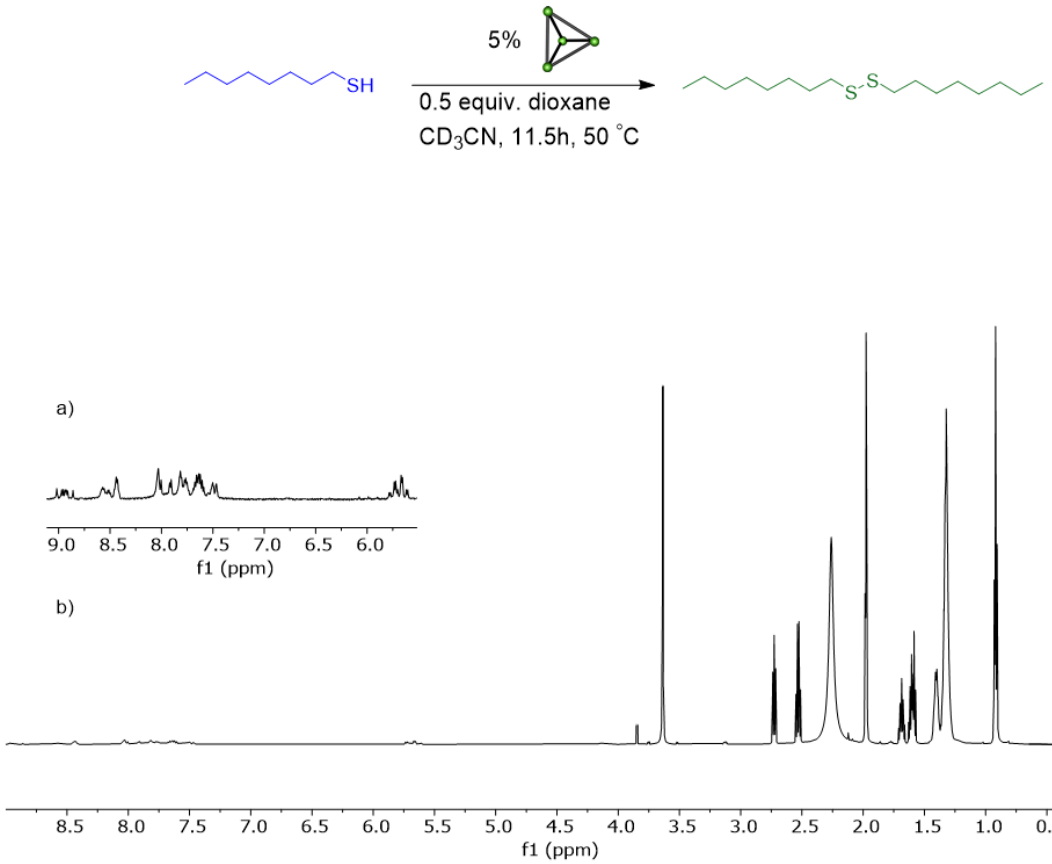

Figure 6.36. ^{1}H NMR spectrum of the oxidative dimerization of **C_8-SH** in the presence of 5 mol % cage **1.50** showing: a) presence and stability of cage (9.1-5.5 ppm); b) presence of reactant and product (9.0-0.0 ppm). [**C_8-SH**] = 18.2 mM, [**1.50**] = 0.9 mM, in CD_3CN. Reaction was performed at 50 °C in 400 µL CD_3CN and monitored over time (600 MHz, 298 K, CD_3CN).

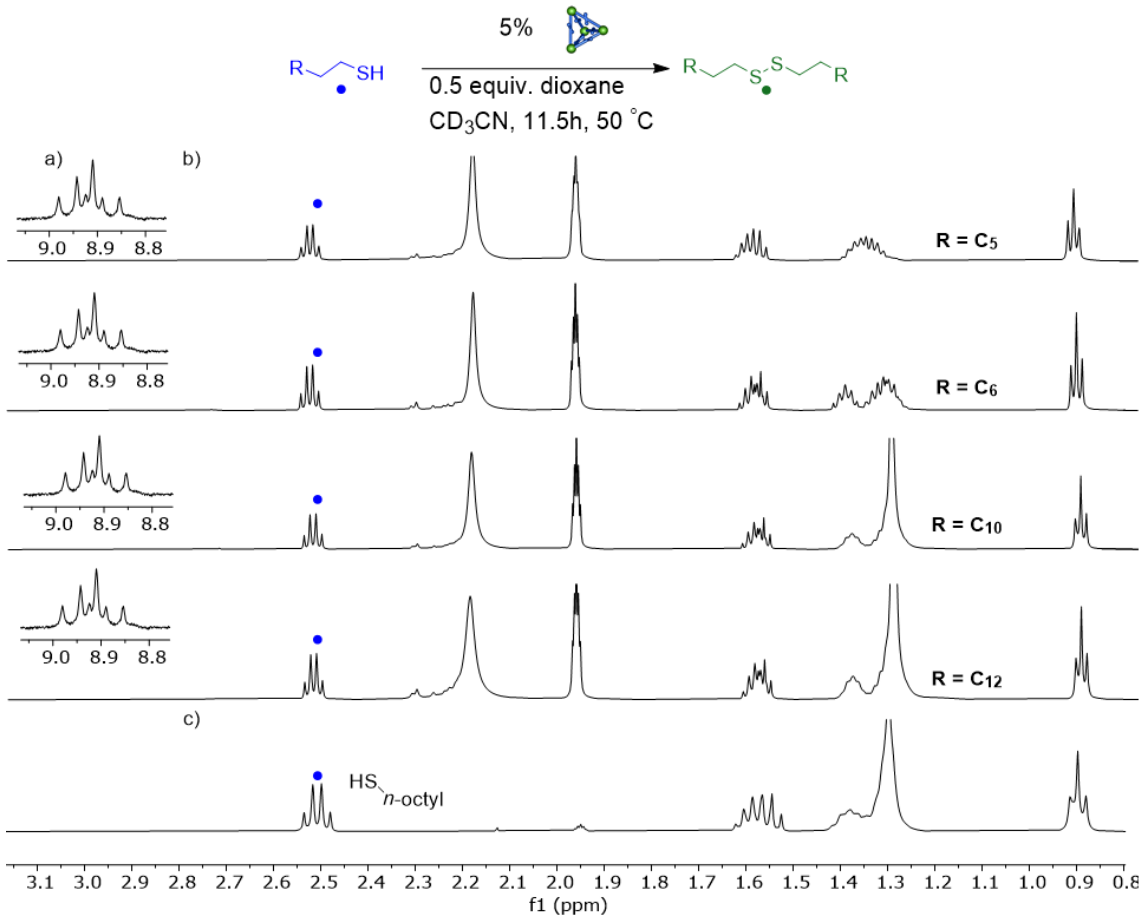

Figure 6.37. ^{1}H NMR spectra of the various thiols with varying length in the presence of 5 mol % cage **2.1** showing: a) presence and stability of cage (9.1-8.7 ppm); b) lack of product formation (2.80-0.6 ppm), c) **C_8-SH** for comparison. [**C_x-SH**] = 18.2 mM, [**2.1**] = 0.9 mM, in CD_3CN. Reactions were performed at 50 °C in 400 µL CD_3CN and monitored over time (600 MHz, 298 K, CD_3CN).

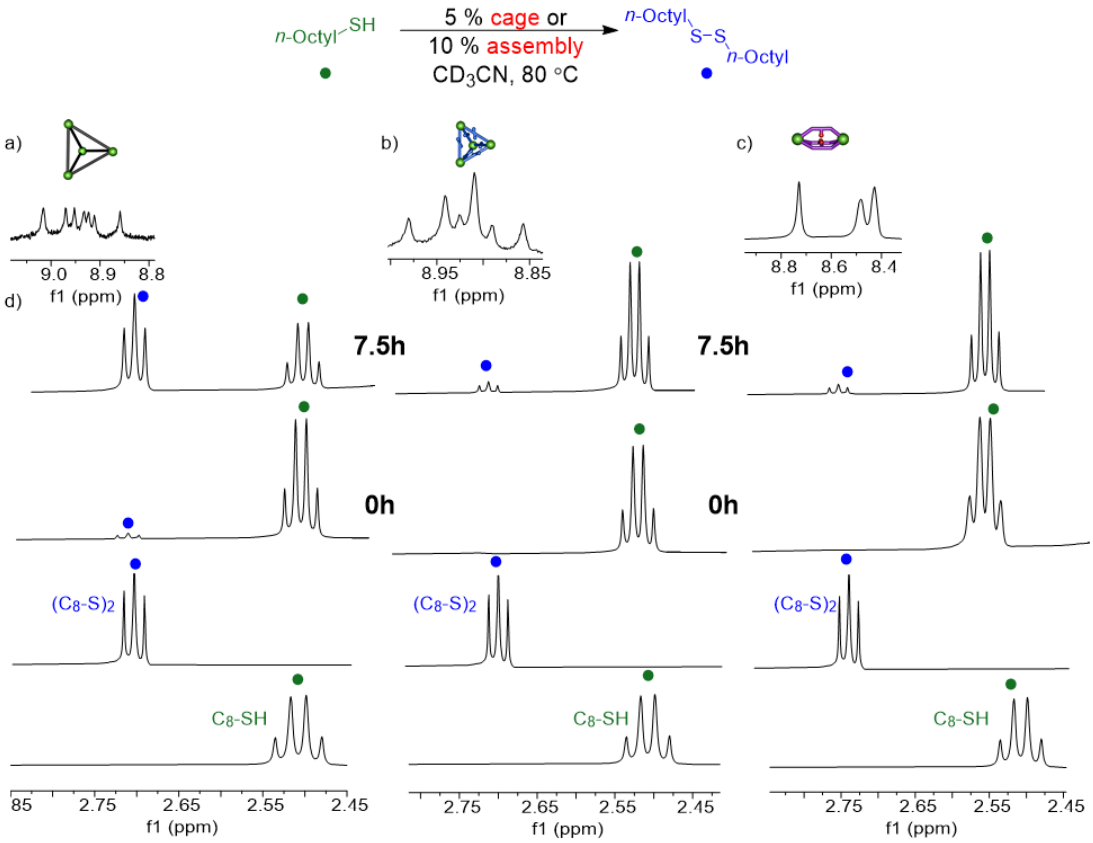

Figure 6.38. ^{1}H NMR spectra of the oxidative dimerization of **C_8-SH** in the presence of 5 mol % cage **1.50**, 5 mol % cage **2.1**, and 10 mol % assembly **2.2** showing: a); b); c) cage and assembly stability for the oxidation reaction (9.1-8.7 ppm); d) difference in relative rate of product formation for **1**, **2**, and **3** (2.85-2.45 ppm). [**C_8-SH**] = 18.2 mM, [**1.50**] = 0.9 mM, [**2.1**] = 0.9 mM, and [**2.2**] = 1.8 mM in CD_3CN. Reactions were performed at 80 °C in 400 µL CD_3CN and monitored over time (600 MHz, 298 K, CD_3CN).

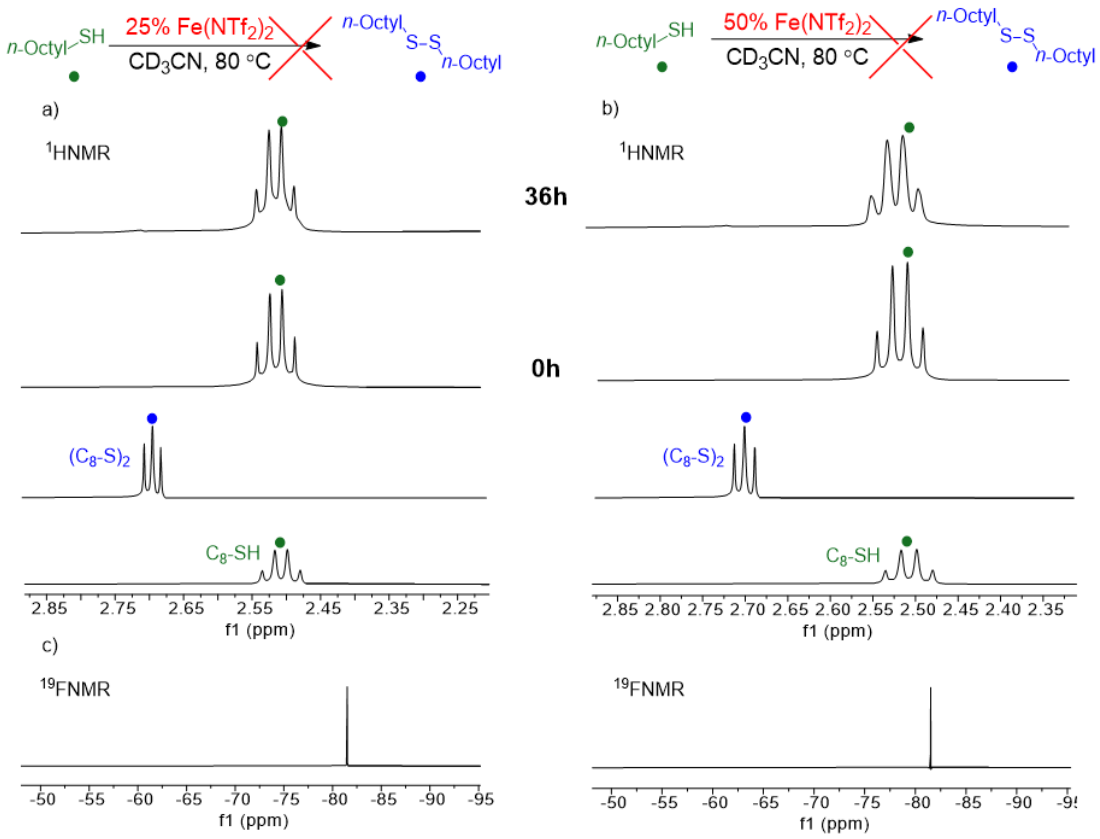

Figure 6.39. ^{1}H NMR spectra of **C_8-SH** in the presence of 25 and 50 mol % $Fe(NTf_2)_2$ showing: a); b) lack of product formation using 2 different concentrations of $Fe(NTf_2)_2$ (2.85-2.20 ppm); c) ^{19}F spectra confirmation that iron species are in solution (-55 – -95 ppm) in CD_3CN. [$Fe(NTf_2)_2$] = 4.6 mM and 9.1 mM, and [**C_8-SH**] = 18.2 mM. Reactions were performed at 80 °C in 400 µL CD_3CN and monitored over time (600 MHz, 298 K, CD_3CN).

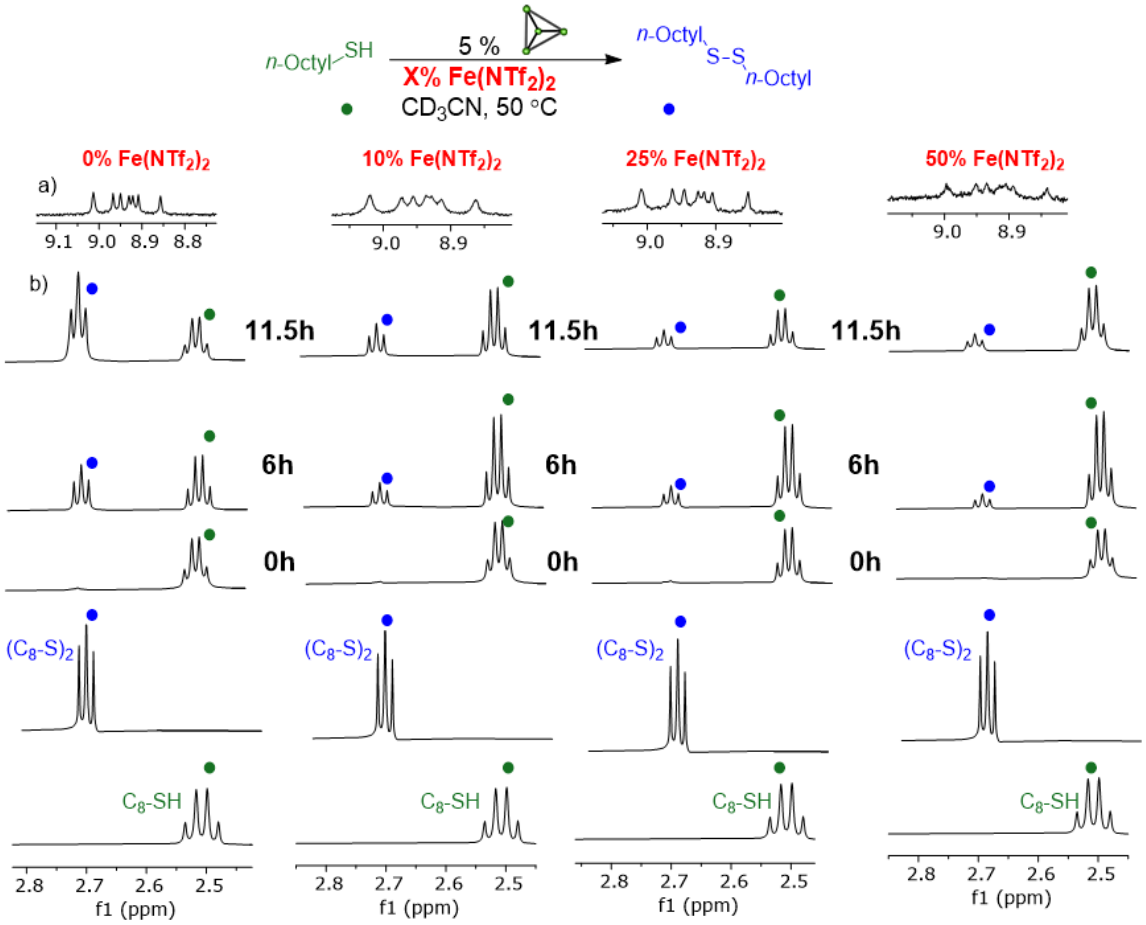

Figure 6.40. ^{1}H NMR spectra of the oxidation of **C_8-SH** with varying concentrations of $Fe(NTf_2)_2$ showing: a) cage stability at varying concentrations of $Fe(NTf_2)_2$; b) relative rate of product formation using varying concentrations of $Fe(NTf_2)_2$ (2.85-2.45 ppm). [**C_8-SH**] = 18.2 mM, [**1.50**] = 0.9 mM, [$Fe(NTf_2)_2$] = 0, 1.8, 4.6, 9.1 mM. Reactions were performed at 80 °C in 400 µL CD_3CN and monitored over time (600 MHz, 298 K, CD_3CN).

Gas Chromatography Data for Size Selective Alkanethiol Oxidation Studies

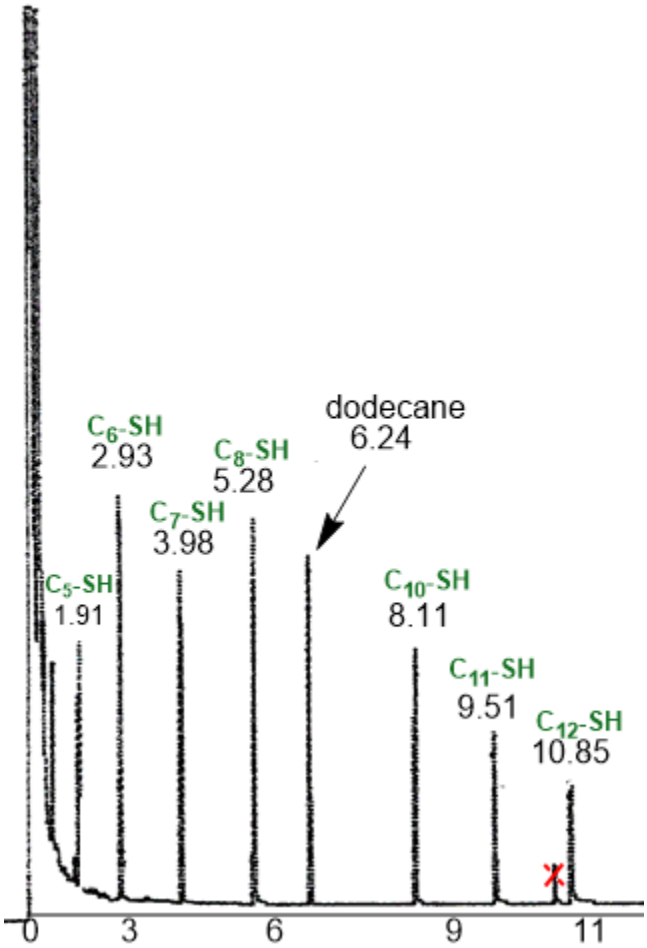

Figure 6.41. GC calibration displaying relative retention times of alkanethiols with varying lengths and dodecane.

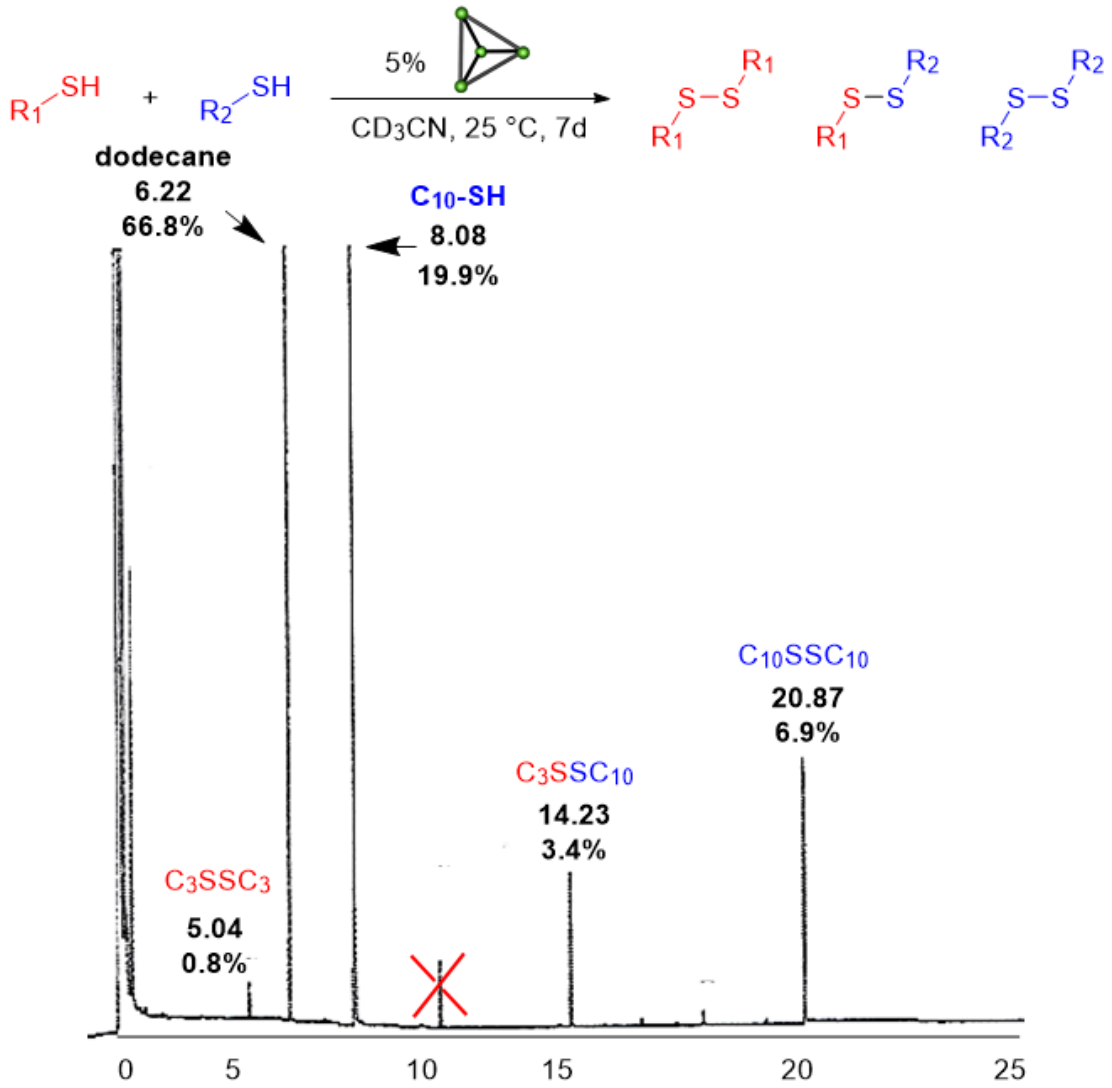

Figure 6.42. GC chromatogram trace of size selective alkanethiol oxidation of an equimolar mixture of **C_3-SH** and **C_{10}-SH** using dodecane as an internal standard. [**C_x-SH**] = 18.2 mM, [**1.50**] = 0.9 mM. Reaction was performed at 25 °C in 800 µL CD_3CN monitored over time (600 MHz, 298 K, CD_3CN). GC sample contained reaction solution flushed through a silica plug with diethyl ether, in addition to a 450 µL aliquot of 9 mM solution of dodecane in diethyl ether.

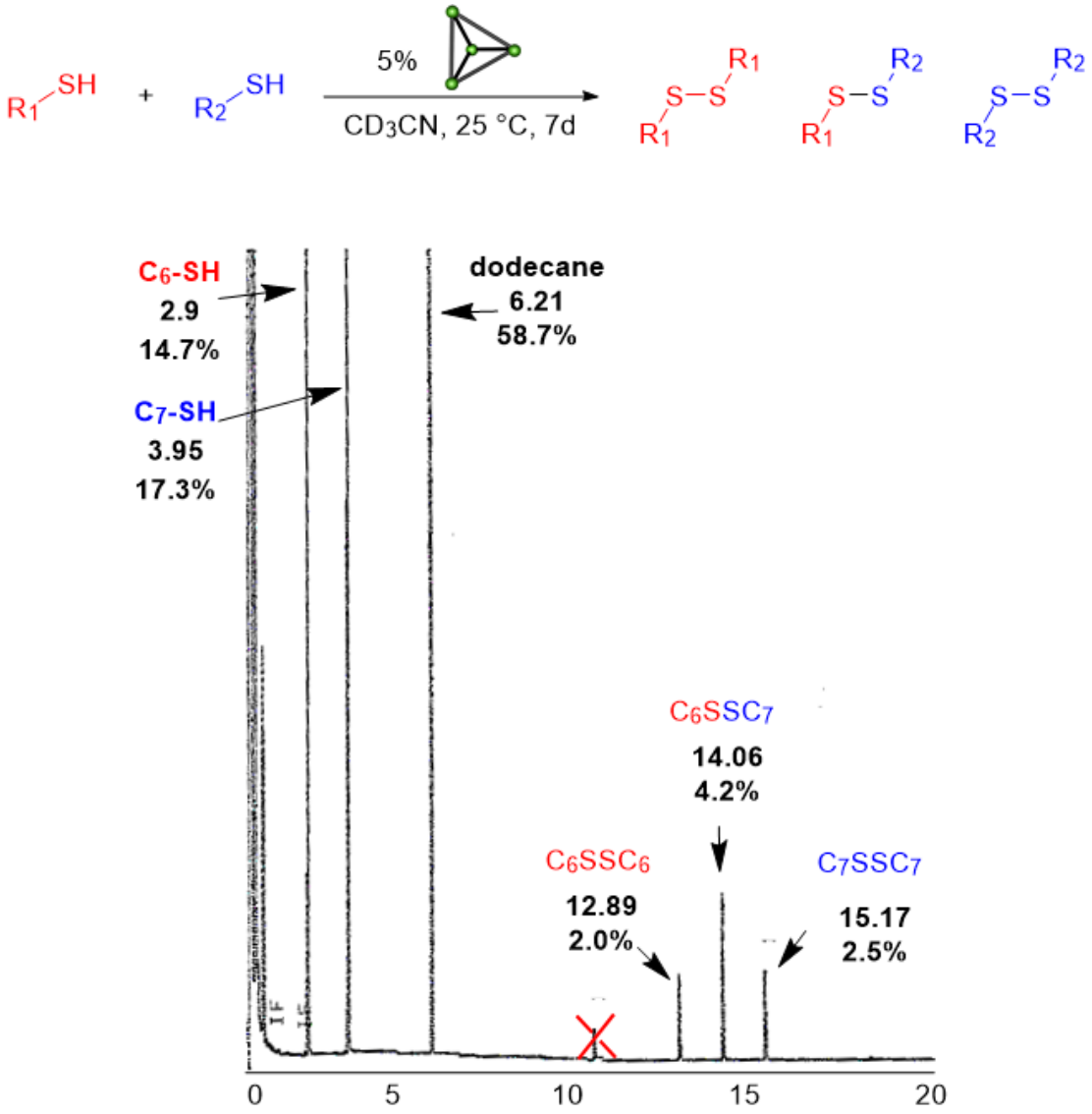

Figure 6.43. GC chromatogram trace of size selective alkanethiol oxidation of an equimolar mixture of **C_6-SH** and **C_7-SH** using dodecane as an internal standard. [**C_x-SH**] = 18.2 mM, [**1.50**] = 0.9 mM. Reaction was performed at 25 °C in 800 µL CD_3CN monitored over time (600 MHz, 298 K, CD_3CN). GC sample contained reaction solution flushed through a silica plug with diethyl ether, in addition to a 450 µL aliquot of 9 mM solution of dodecane in diethyl ether.

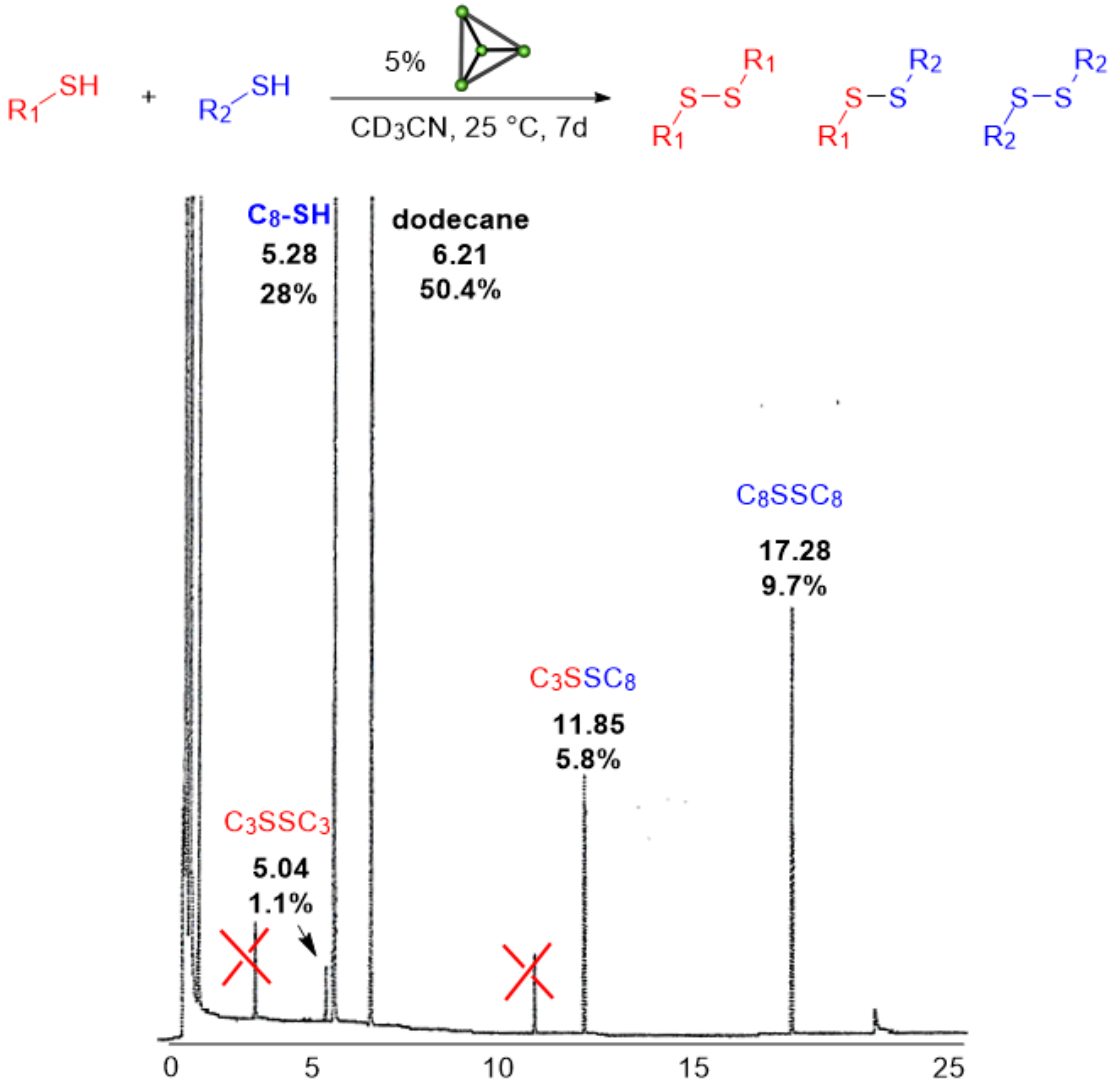

Figure 6.44. GC chromatogram trace of size selective alkanethiol oxidation of an equimolar mixture of **C_3-SH** and **C_8-SH** using dodecane as an internal standard. [**C_x-SH**] = 18.2 mM, [**1.50**] = 0.9 mM. Reaction was performed at 25 °C in 800 µL CD_3CN monitored over time (600 MHz, 298 K, CD_3CN). GC sample contained reaction solution flushed through a silica plug with diethyl ether in addition to a 450 µL aliquot of 9 mM solution of dodecane in diethyl ether.

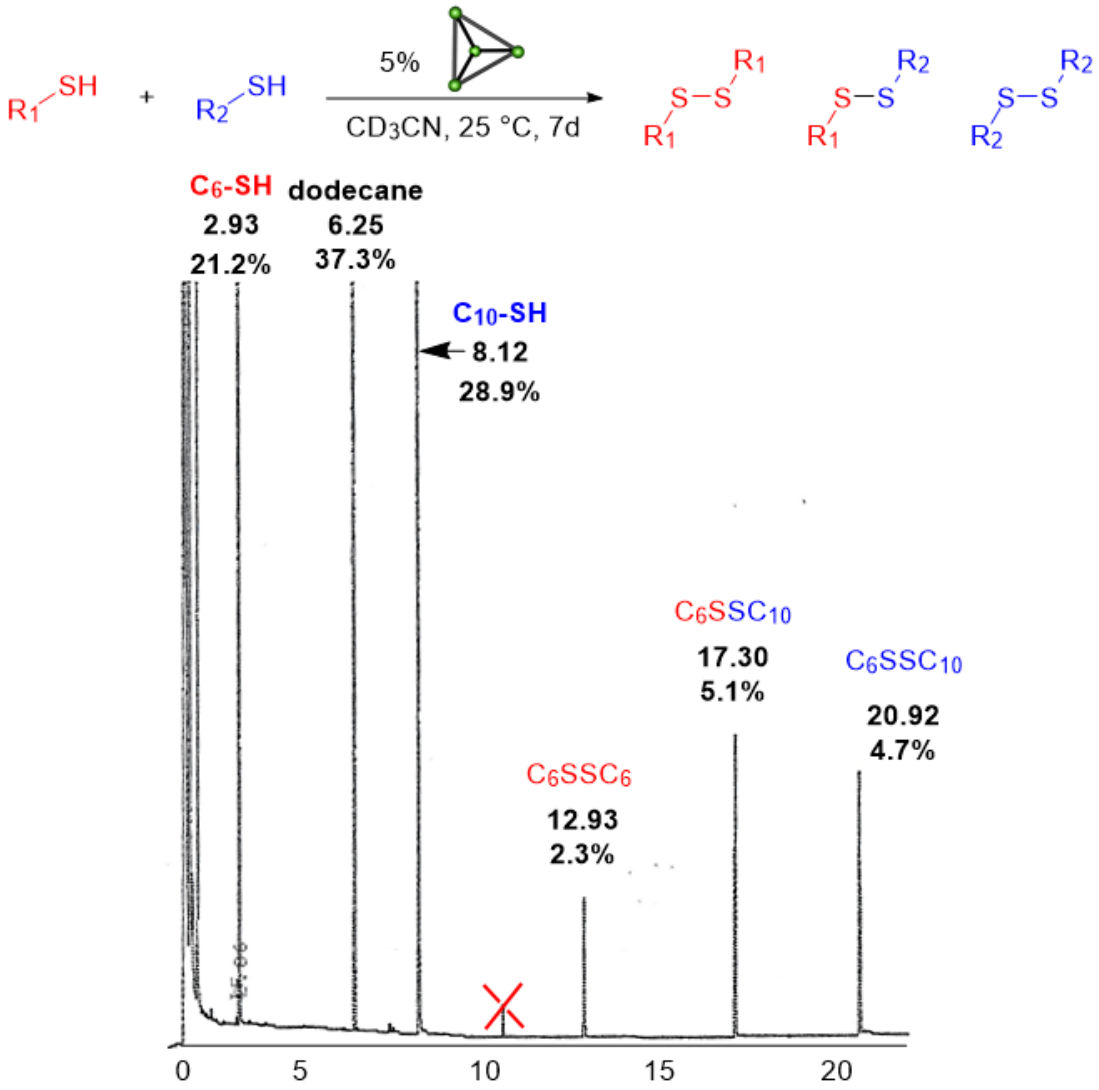

Figure 6.45. GC chromatogram trace of size selective alkanethiol oxidation of an equimolar mixture of **C_6-SH** and **C_{10}-SH** using dodecane as an internal standard. [**C_x-SH**] = 18.2 mM, [**1.50**] = 0.9 mM. Reaction was performed at 25 °C in 800 µL CD_3CN monitored over time (600 MHz, 298 K, CD_3CN). GC sample contained reaction solution flushed through a silica plug with diethyl ether in addition to a 450 µL aliquot of 9 mM solution of dodecane in diethyl ether.

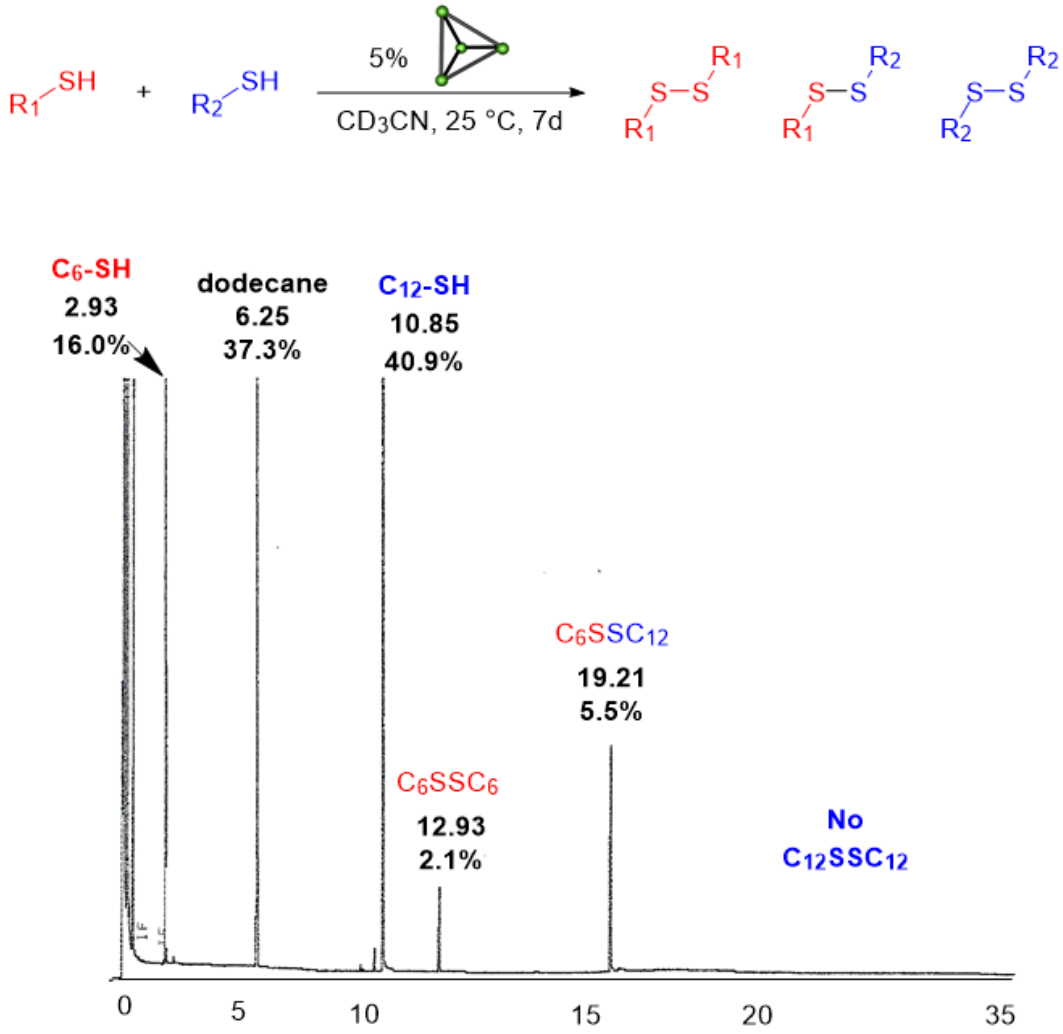

Figure 6.46. GC chromatogram trace of size selective alkanethiol oxidation of an equimolar mixture of **C_6-SH** and **C_{12}-SH** using dodecane as an internal standard. [**C_x-SH**] = 18.2 mM, [**1.50**] = 0.9 mM. Reaction was performed at 25 °C in 800 µL CD_3CN monitored over time (600 MHz, 298 K, CD_3CN). GC sample contained reaction solution flushed through a silica plug with diethyl ether in addition to a 450 µL aliquot of 9 mM solution of dodecane in diethyl ether.

UV-Vis Absorbance Titrations and Fitting Curves

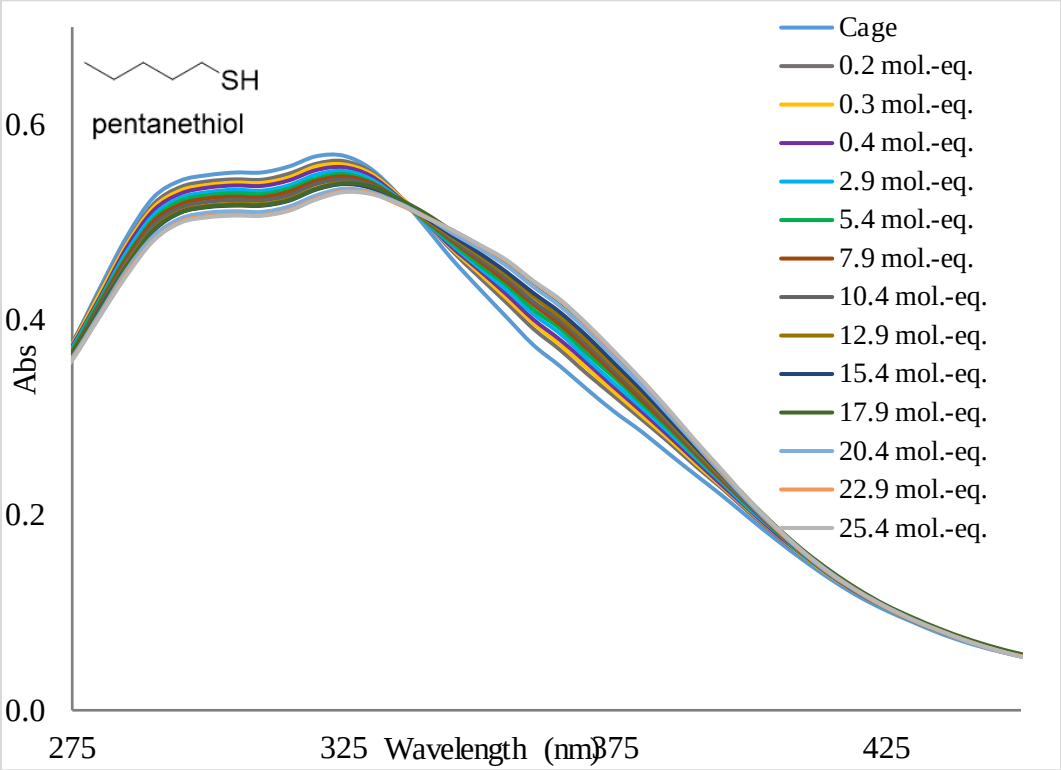

Figure 6.47. UV-Vis absorption spectrum of the titration of **C_5-SH** into a 3 µM solution of cage **1.50** in CH_3CN. **C_5-SH** was added in 0.2-3 µL aliquots from a 9 mM stock solution in CH_3CN.

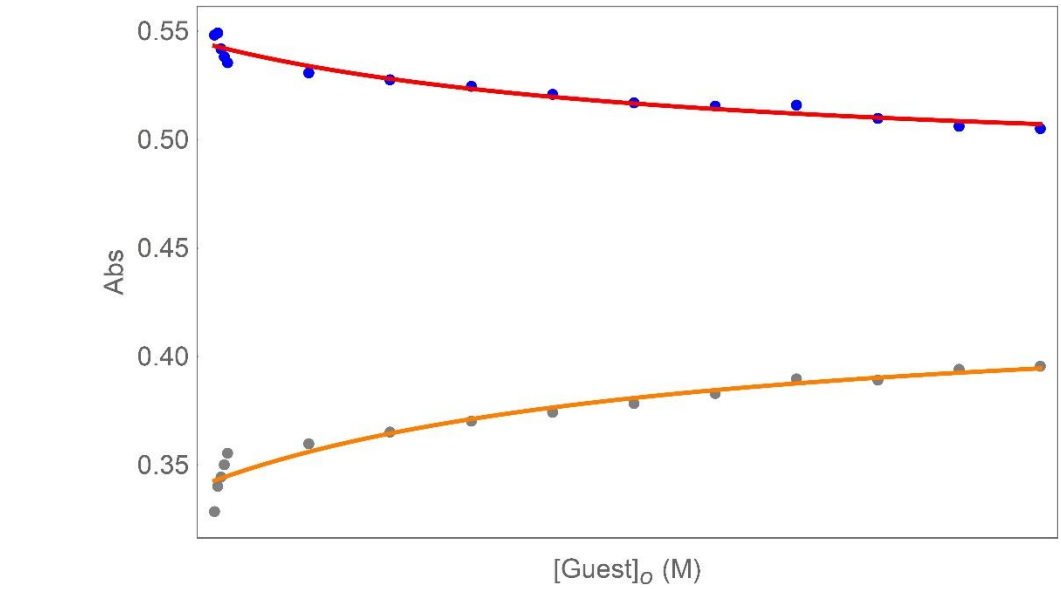

Residuals 330 nm

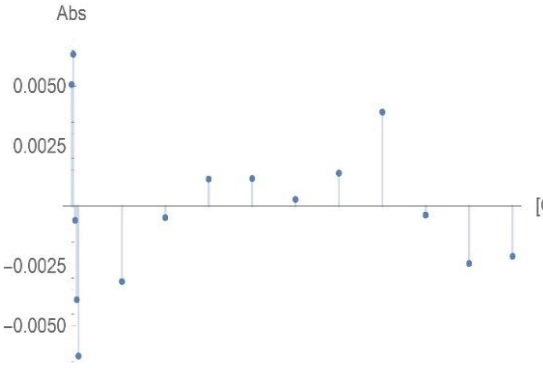

Residuals 370 nm

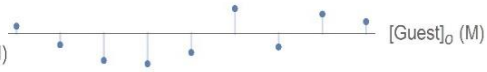

Figure 6.48. Fitting curves and plots of residual magnitude obtained when fitting the UV binding data for **C_5-SH** with cage **1.50** to the 1:1 binding model.

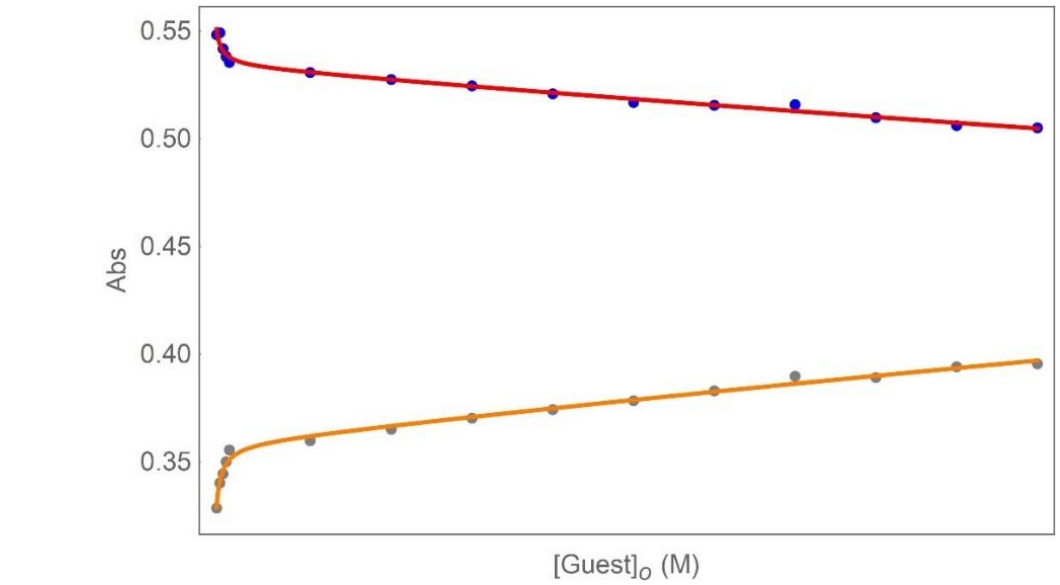

Residuals 330 nm

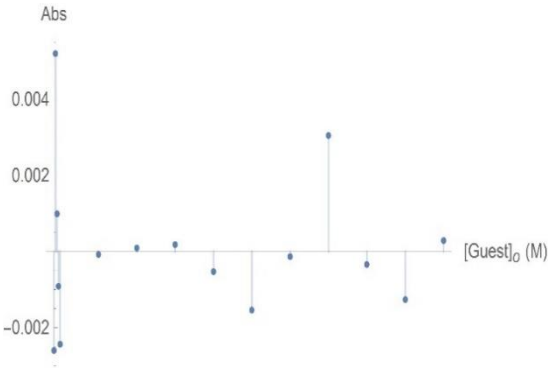

Residuals 370 nm

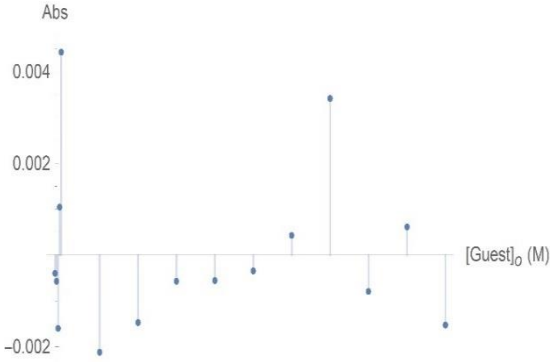

Figure 6.49. Fitting curves and plots of residual magnitude obtained when fitting the UV binding data for **C_5-SH** with cage **1.50** to the 1:2 binding model.

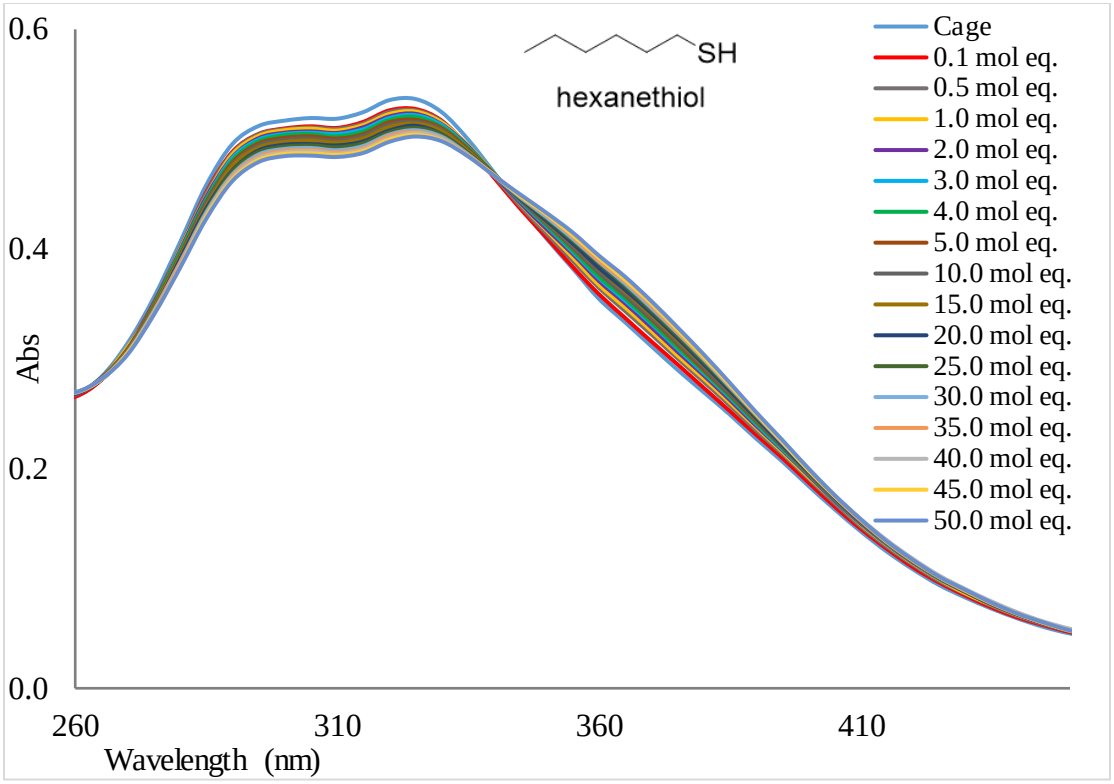

Figure 6.50. UV-Vis absorption spectrum of the titration of **C_6-SH** into a 3 µM solution of cage **1.50** in CH_3CN. **C_6-SH** was added in 0.1-5 µL aliquots from a 9 mM stock solution in CH_3CN.

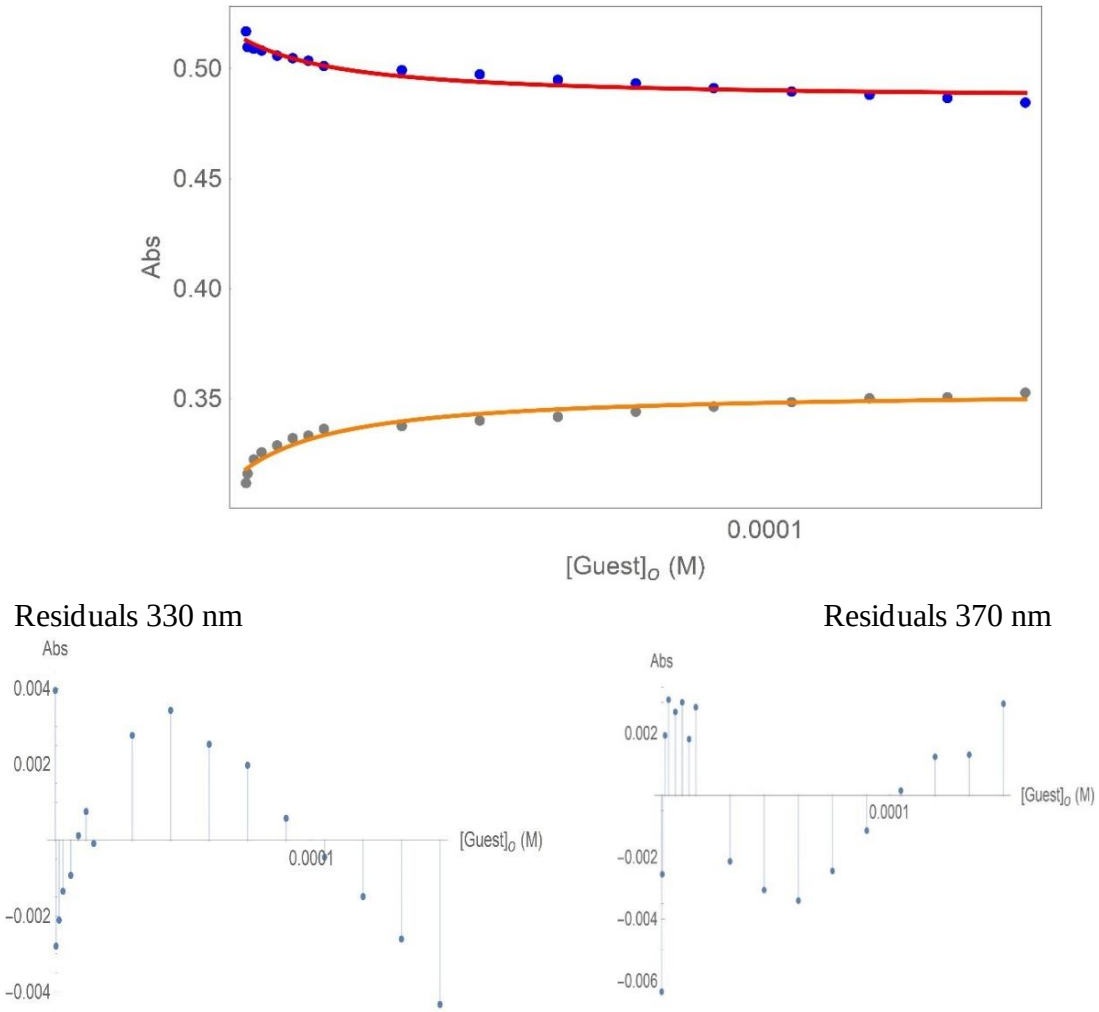

Figure 6.51. Fitting curves and plots of residual magnitude obtained when fitting the UV binding data for **C_6-SH** with cage **1.50** to the 1:1 binding model.

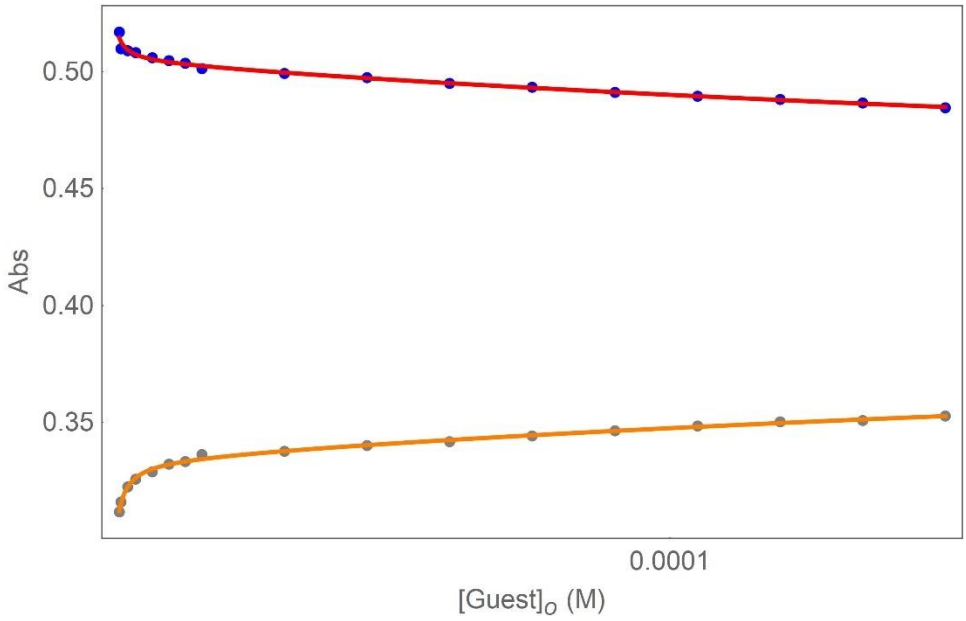

Residuals 330 nm

Residuals 370 nm

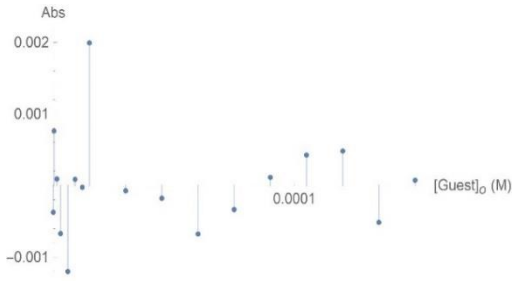

Figure 6.52. Fitting curves and plots of residual magnitude obtained when fitting the UV binding data for **C_6-SH** with cage **1.50** to the 1:2 binding model.

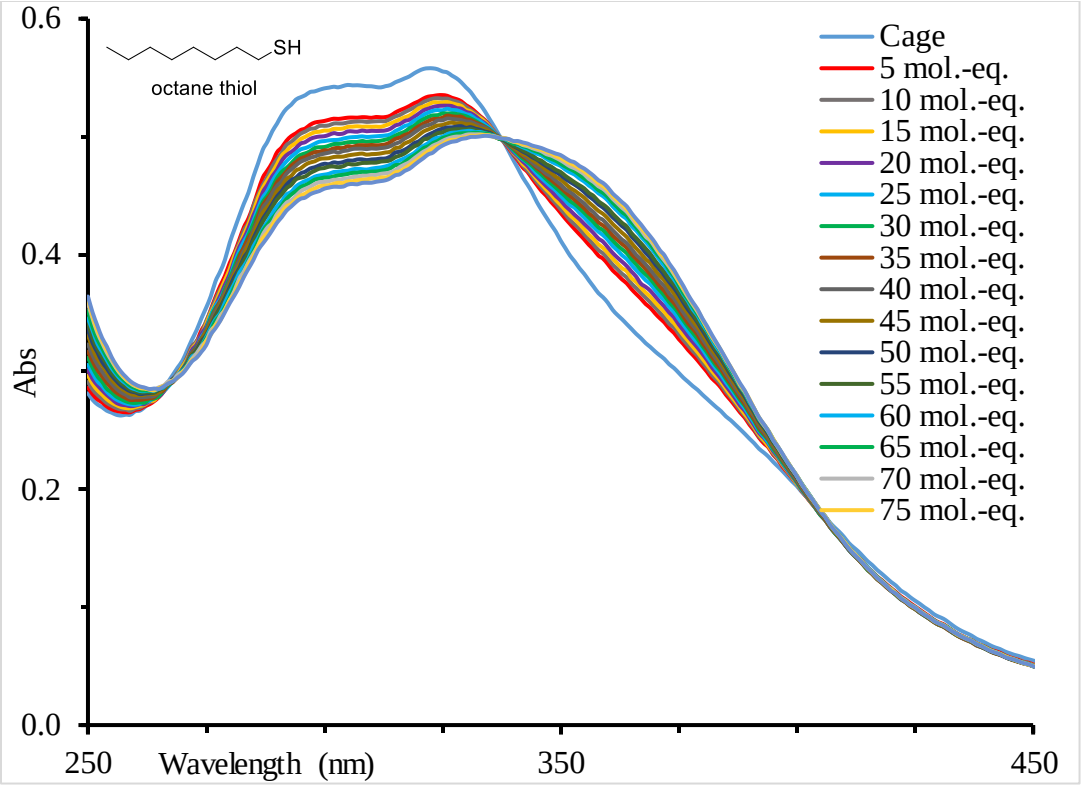

Figure 6.53. UV-Vis absorption spectrum of the titration of **C_8-SH** into a 3 µM solution of cage **1.50** in CH_3CN. **C_8-SH** was added in 5 µL aliquots from a 9 mM stock solution in CH_3CN.

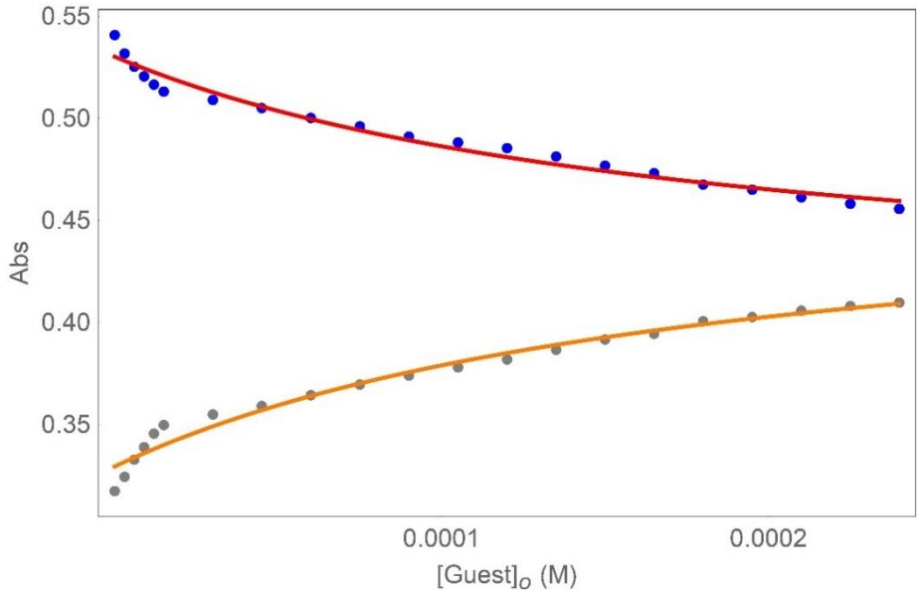

Residuals 330 nm

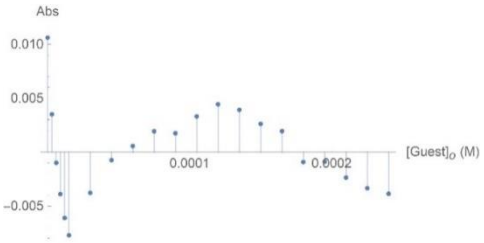

Residuals 370 nm

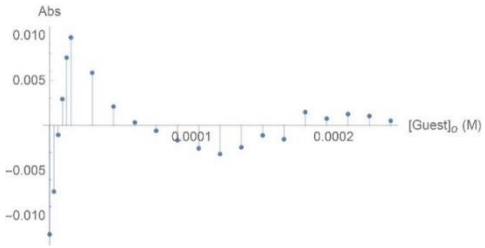

Figure 6.54. Fitting curves and plots of residual magnitude obtained when fitting the UV binding data for **C_8-SH** with cage **1.50** to the 1:1 binding model.

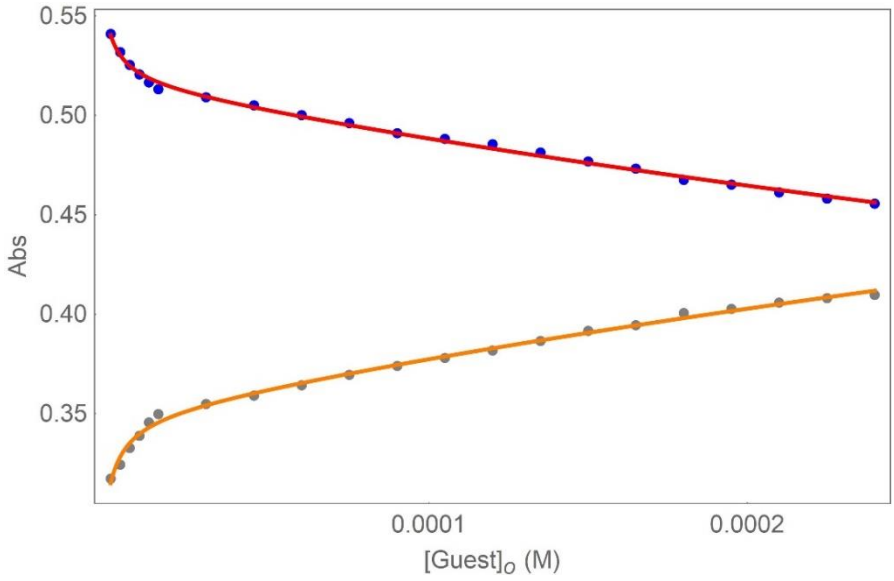

Residuals 330 nm

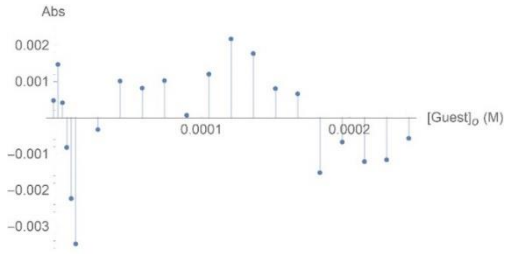

Residuals 370 nm

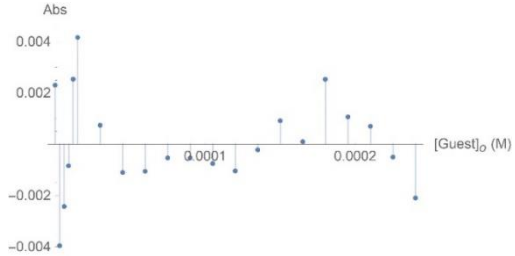

Figure 6.55. Fitting curves and plots of residual magnitude obtained when fitting the UV binding data for **C_8-SH** with cage **1.50** to the 1:2 binding model.

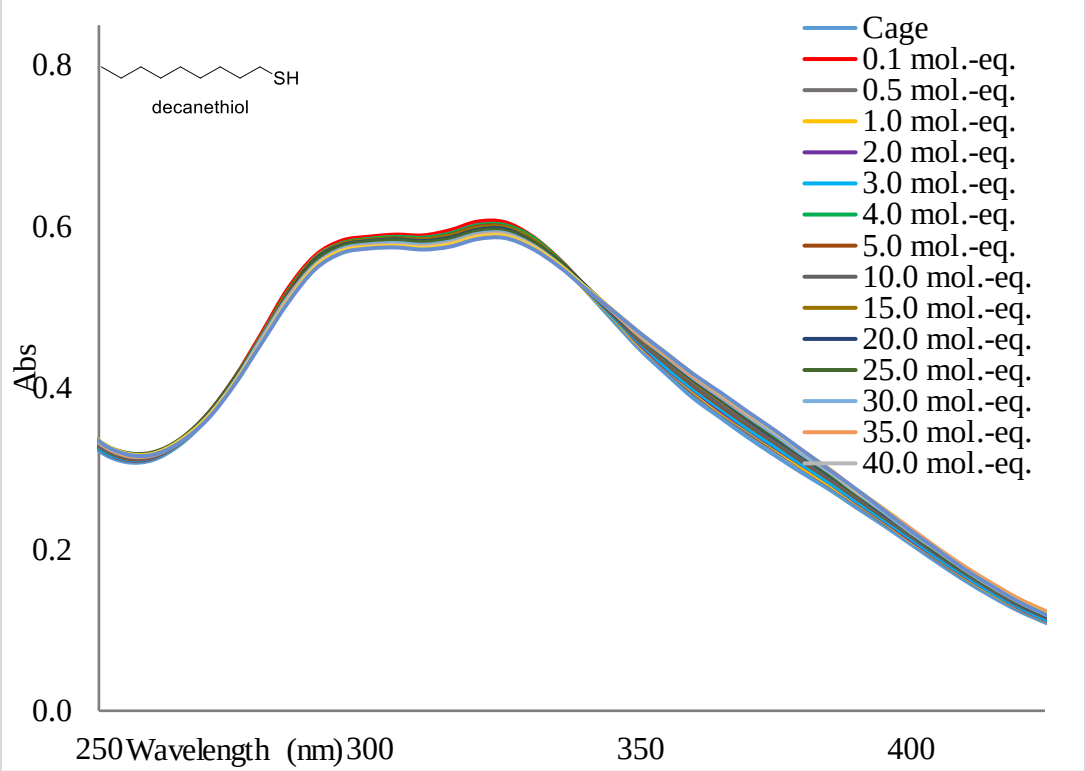

Figure 6.56 UV-Vis absorption spectrum of the titration of **C_{10}-SH** into a 3 µM solution of cage **1.50** in CH_3CN. **C_{10}-SH** was added in 0.1-5 µL aliquots from a 9 mM stock solution in CH_3CN.

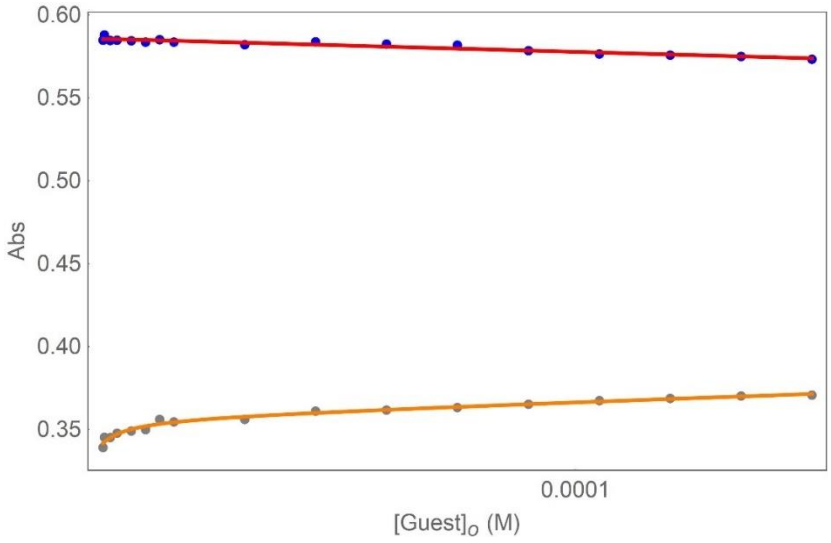

Residuals 330 nm Residuals 370 nm

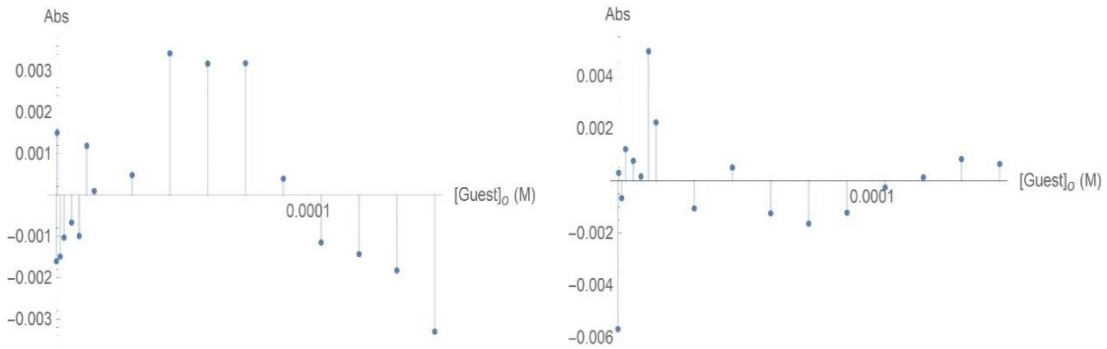

Figure 6.57. Fitting curves and plots of residual magnitude obtained when fitting the UV binding data for **C_{10}-SH** with cage **1.50** to the 1:1 binding model.

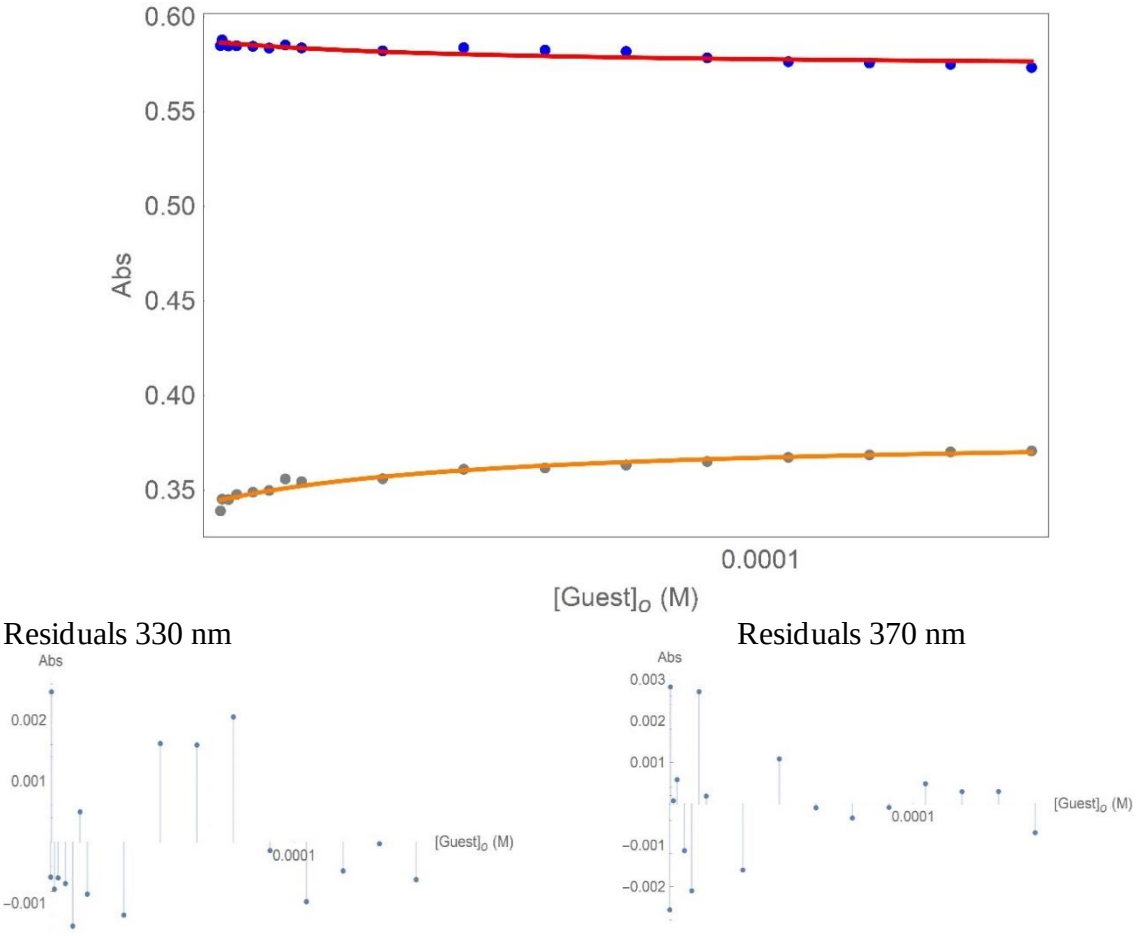

Figure 6.58. Fitting curves and plots of residual magnitude obtained when fitting the UV binding data for **C_{10}-SH** with cage **1.50** to the 1:2 binding model.

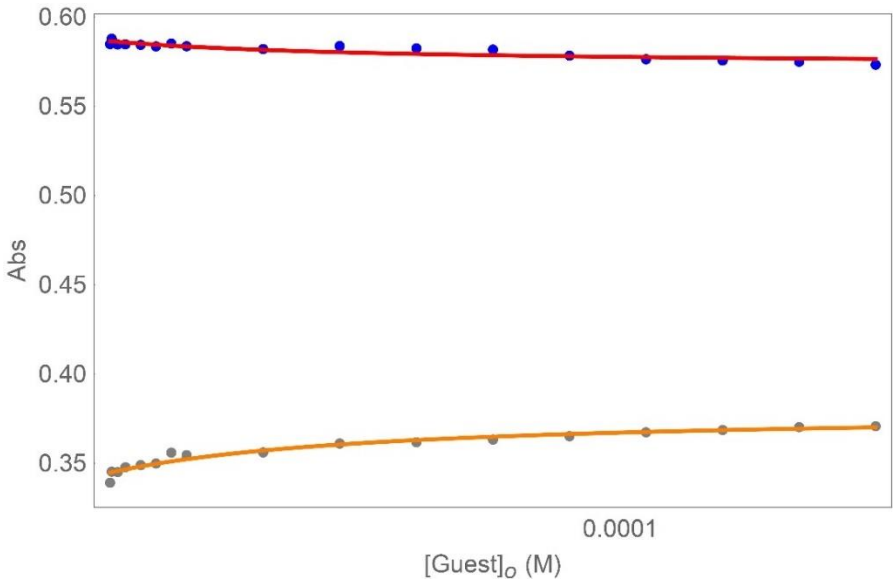

Residuals 330 nm

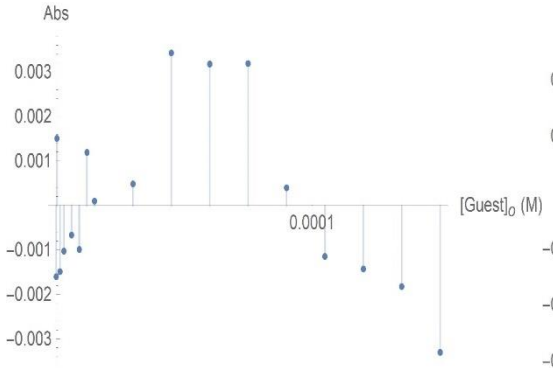

Residuals 370 nm

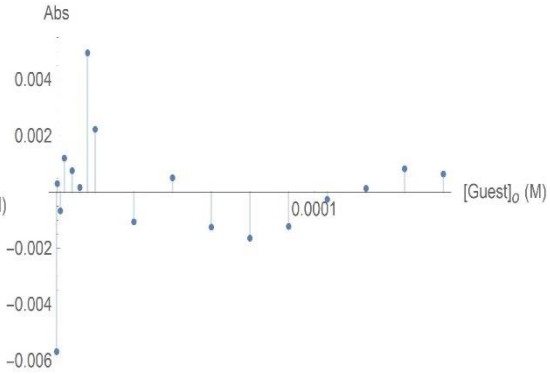

Figure 6.59. Fitting curves and plots of residual magnitude obtained when fitting the UV binding data for **C_{10}-SH** with cage **1.50** to the 1:1 binding model.

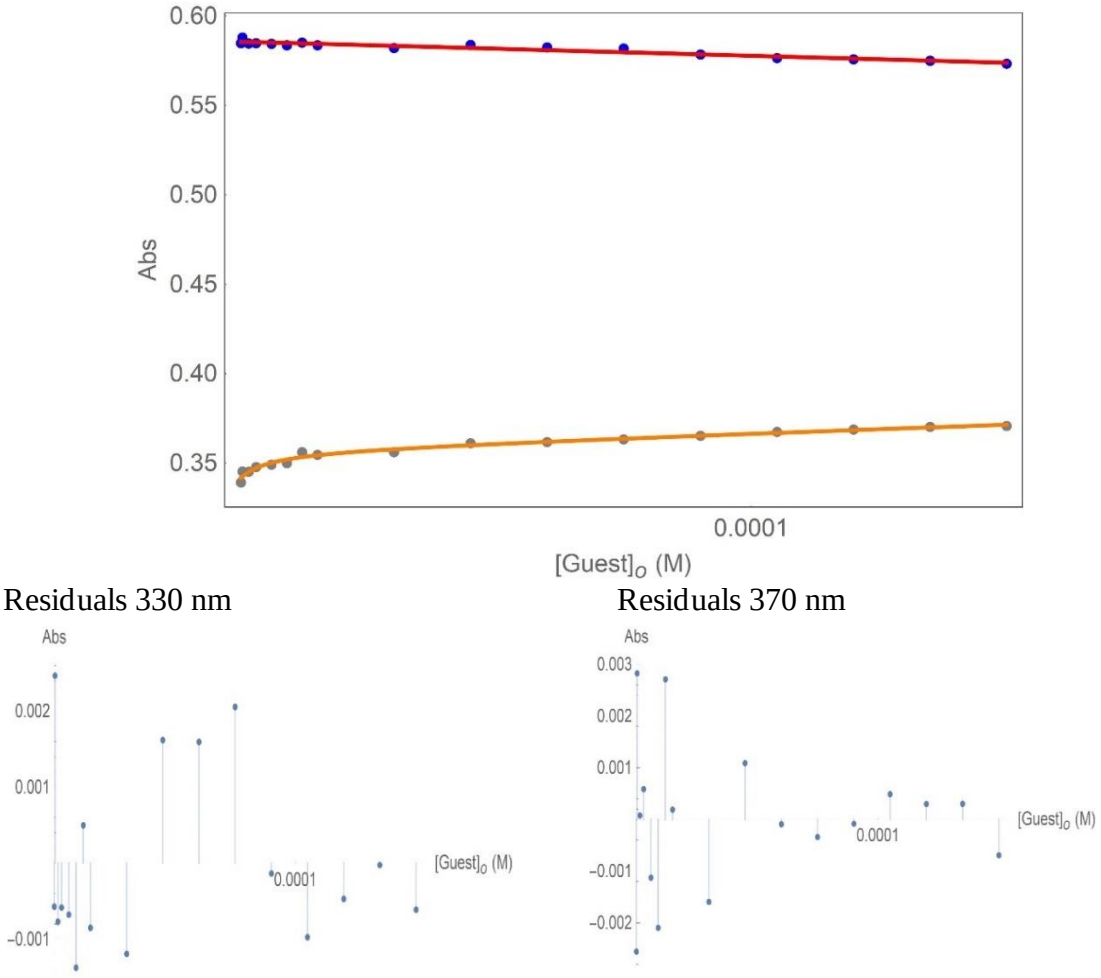

Figure 6.60. Fitting curves and plots of residual magnitude obtained when fitting the UV binding data for **C_{10}-SH** with cage **1.50** to the 1:2 binding model.

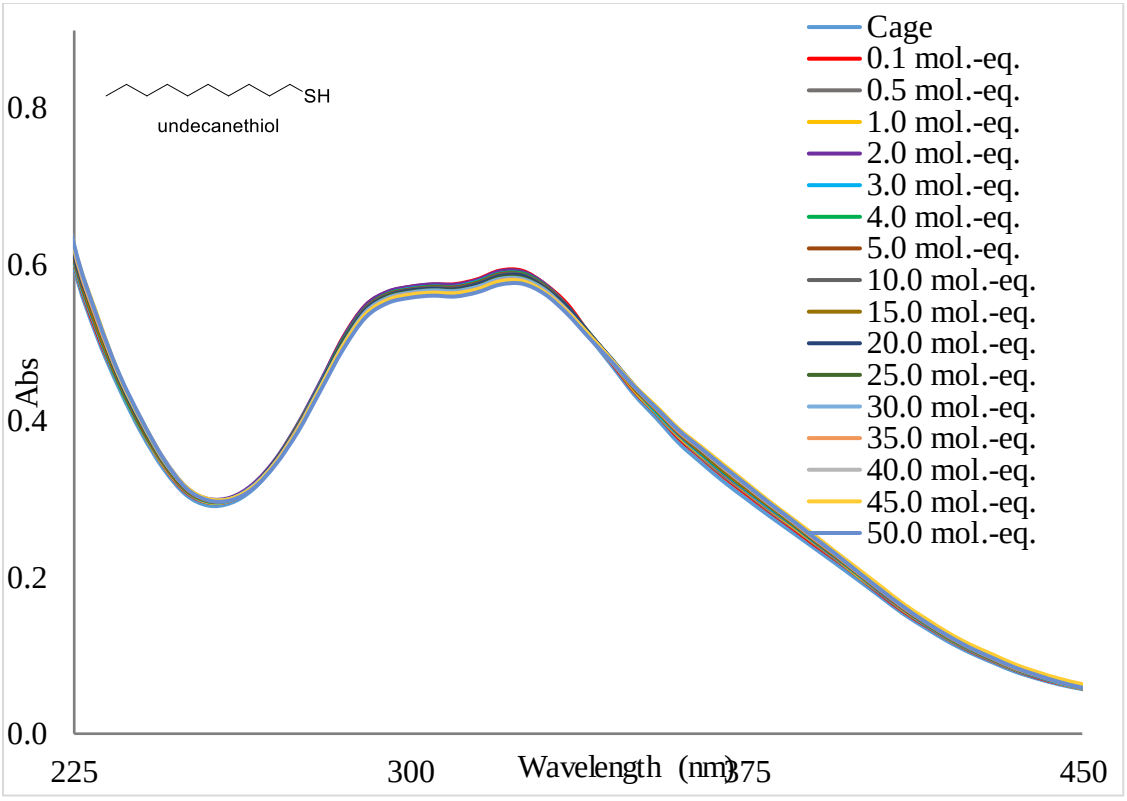

Figure 6.61. UV-Vis absorption spectrum of the titration **of C_{11}-SH** into a 3 µM solution of cage **1.50** in CH_3CN. **C_{11}-SH** was added in 0.1-5 µL aliquots from a 9 mM stock solution in CH_3CN.

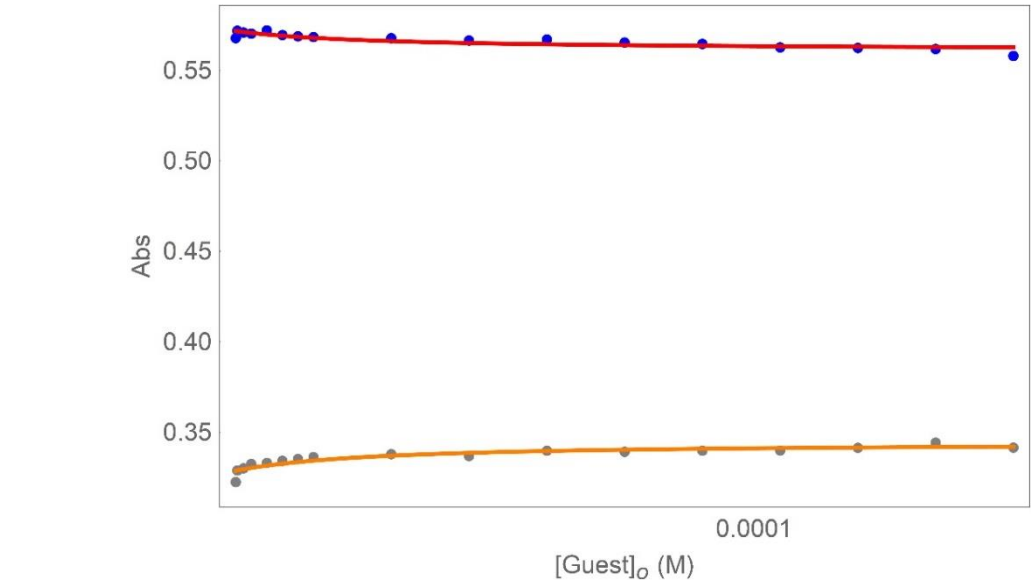

Residuals 330 nm

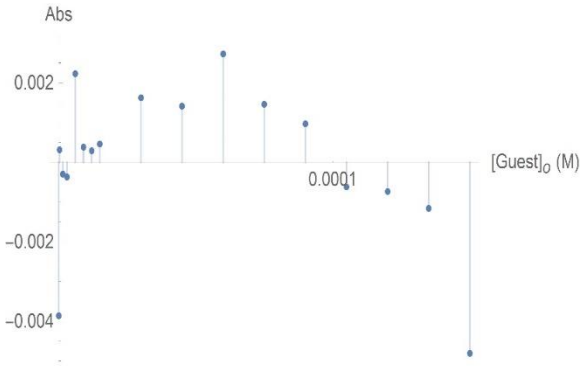

Residuals 370 nm

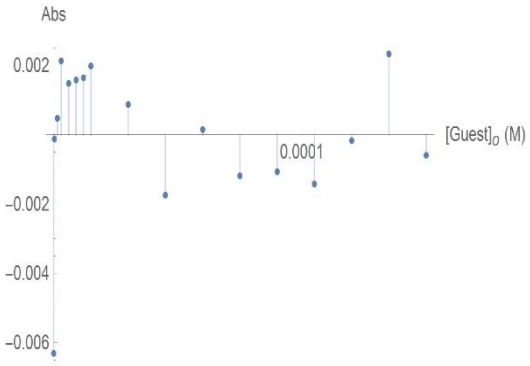

Figure 6.62. Fitting curves and plots of residual magnitude obtained when fitting the UV binding data for **C_{11}-SH** with cage **1.50** to the 1:1 binding model.

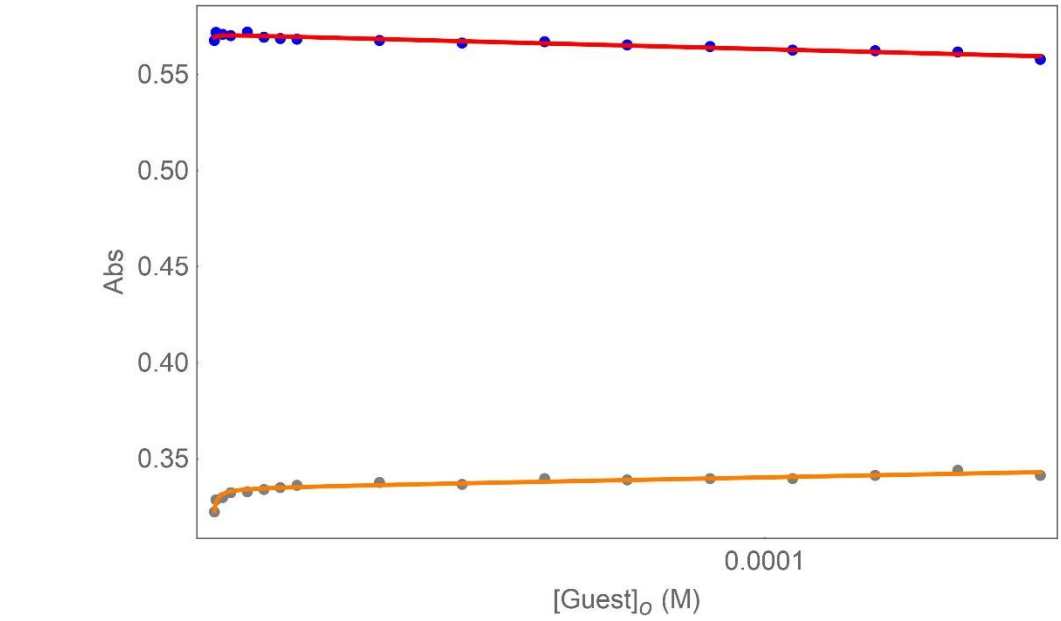

Residuals 330 nm

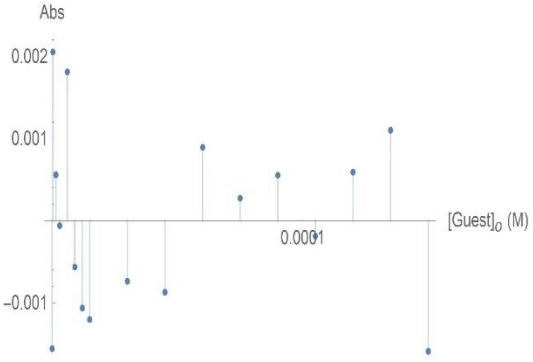

Residuals 370 nm

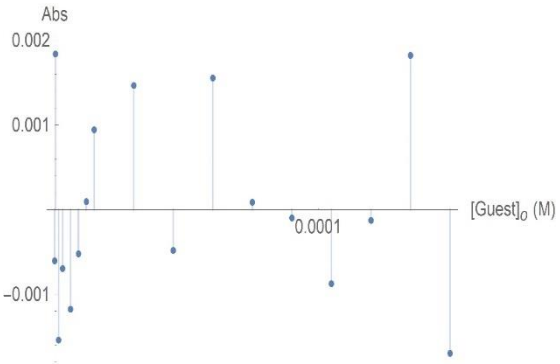

Figure 6.63. Fitting curves and plots of residual magnitude obtained when fitting the UV binding data for **C_{11}-SH** with cage **1.50** to the 1:2 binding model.

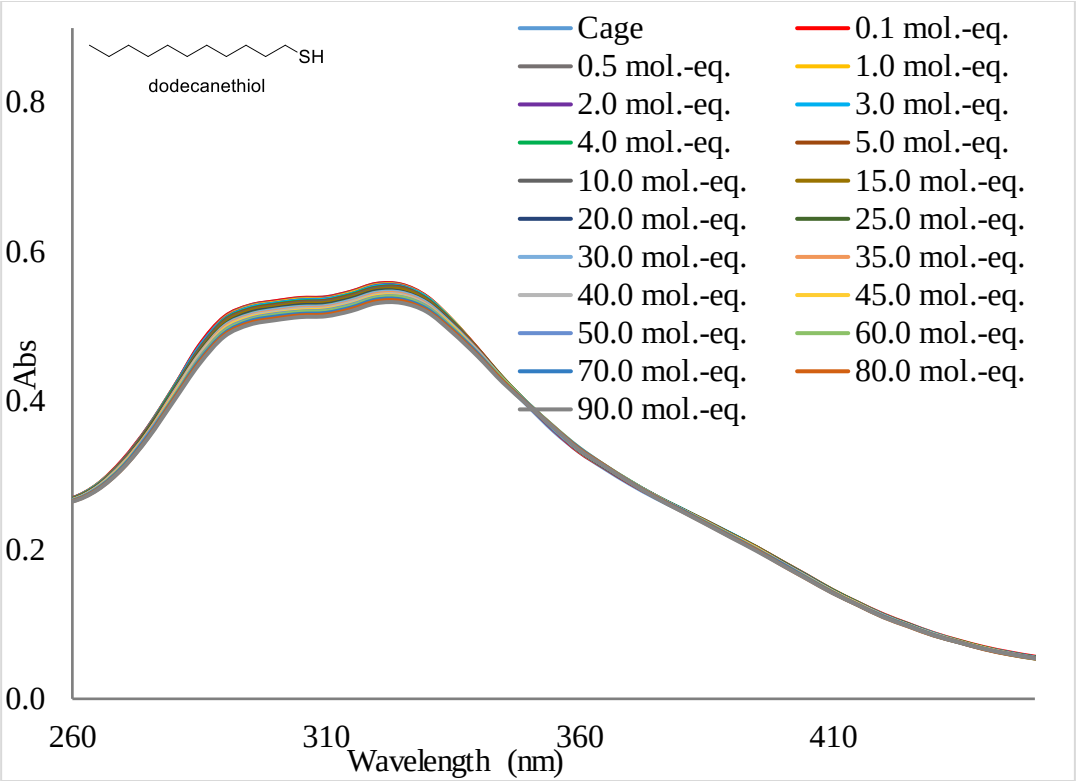

Figure 6.64. UV-Vis absorption spectrum of the titration of **C_{12}-SH** into a 3 µM solution of cage **1.50** in CH_3CN. **C_{12}-SH** was added in 0.1-5 µL aliquots from a 9 mM stock solution in CH_3CN.

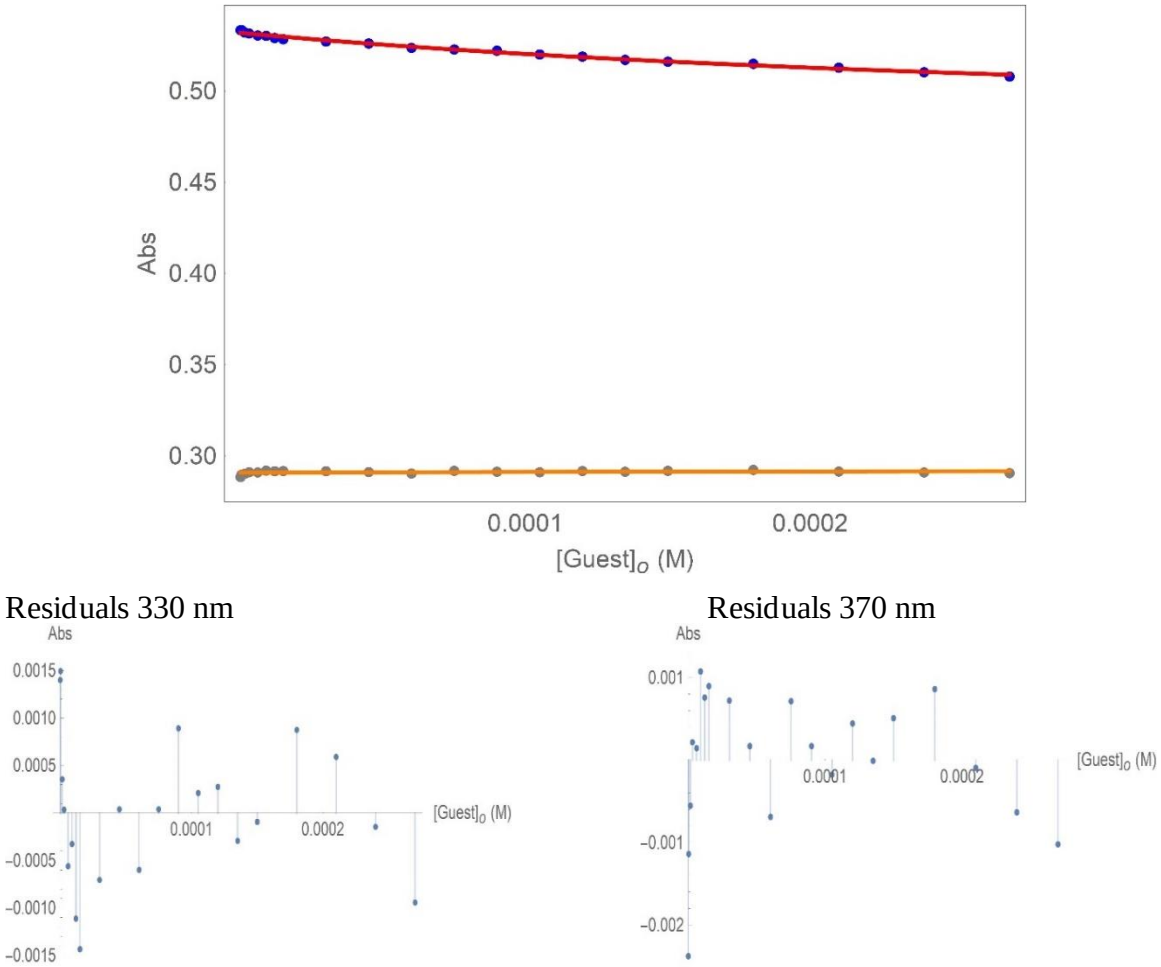

Figure 6.65. Fitting curves and plots of residual magnitude obtained when fitting the UV binding data for **C_{12}-SH** with cage **1.50** to the 1:1 binding model.

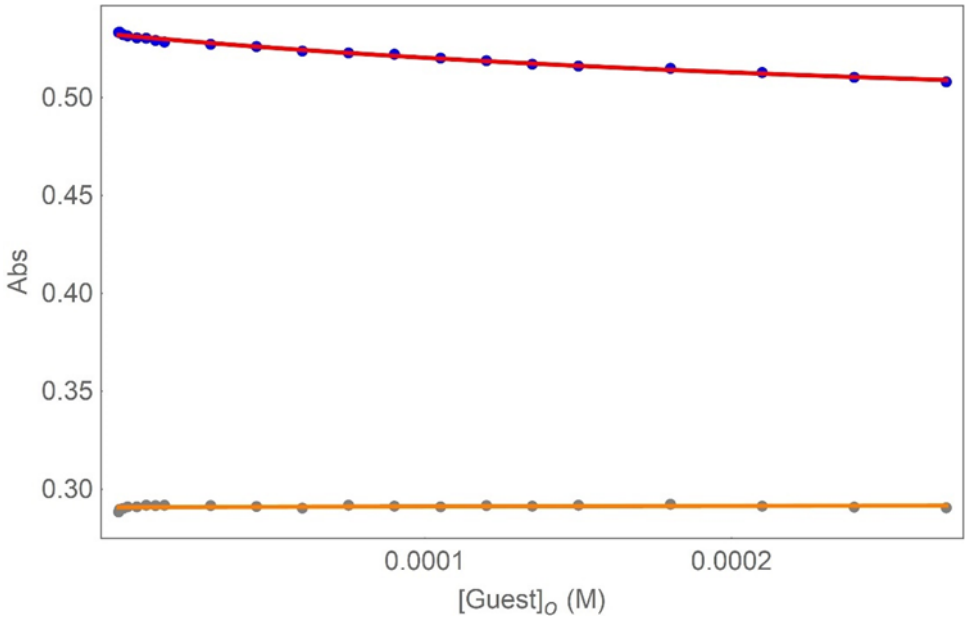

Residuals 330 nm

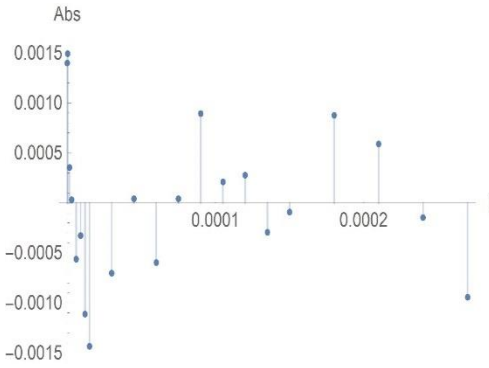

Residuals 370 nm

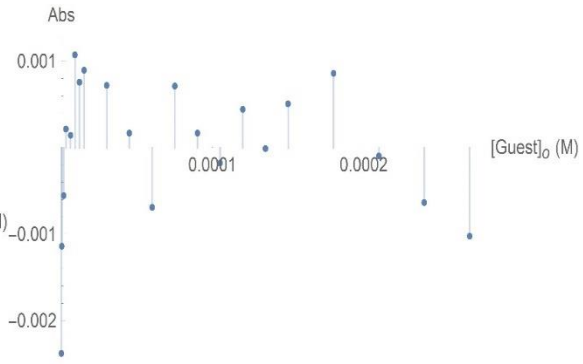

Figure 6.66. Fitting curves and plots of residual magnitude obtained when fitting the UV binding data for **C_{12}-SH** with cage **1.50** to the 1:2 binding model.

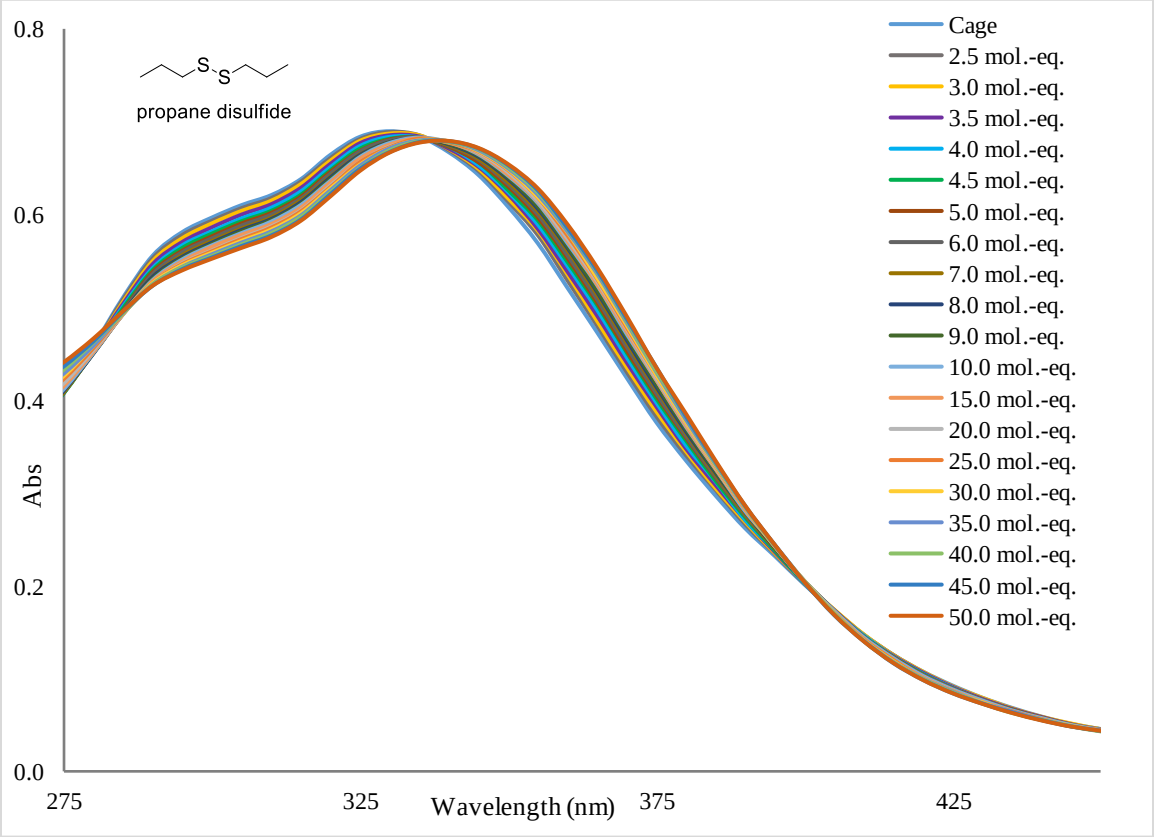

Figure 6.67. UV-Vis absorption spectrum of the titration of (**C_3-S**)$_2$ into a 3 µM solution of cage **1.50** in CH_3CN. (**C_3-S**)$_2$ was added in 2.5-5 µL aliquots from a 9 mM stock solution in CH_3CN.

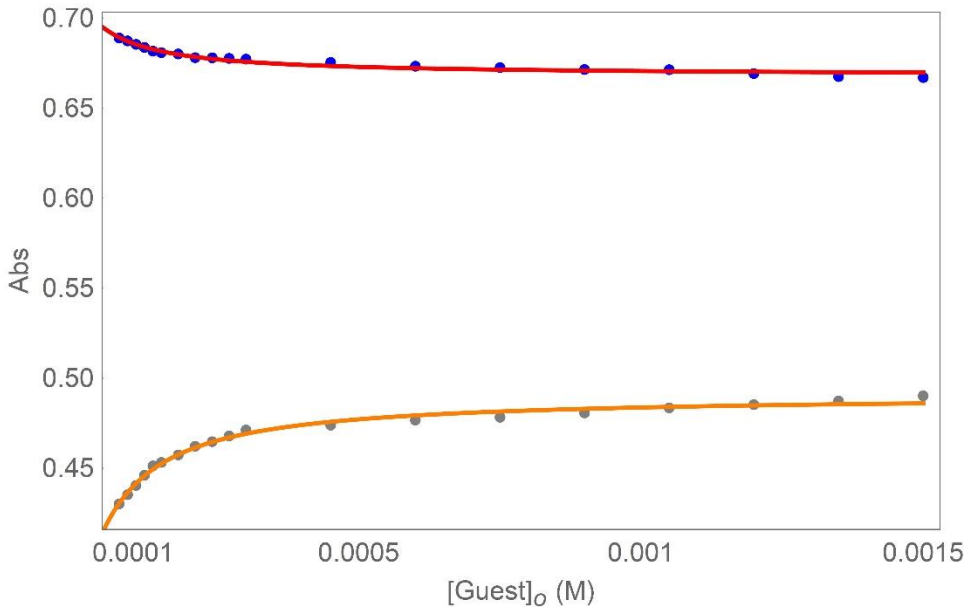

Residuals 330 nm

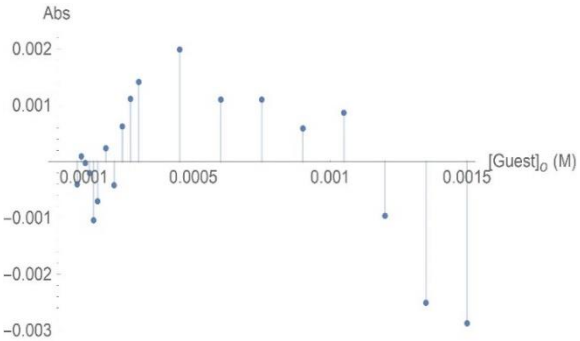

Residuals 370 nm

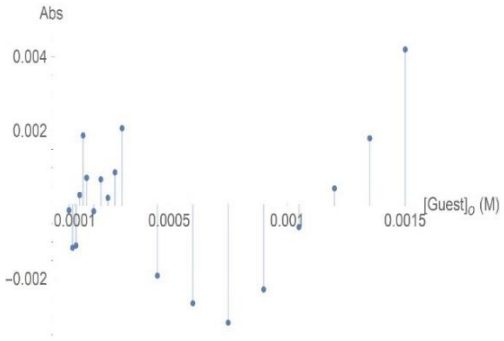

Figure 6.68. Fitting curves and plots of residual magnitude obtained when fitting the UV binding data for (**C$_3$-S**)$_2$ with cage **1.50** to the 1:1 binding model.

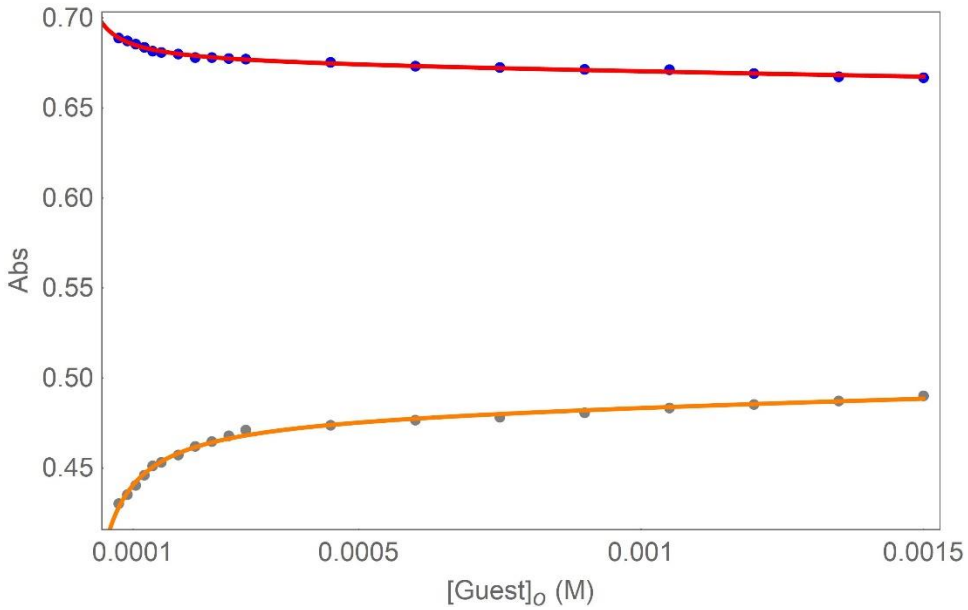

Residuals 330 nm

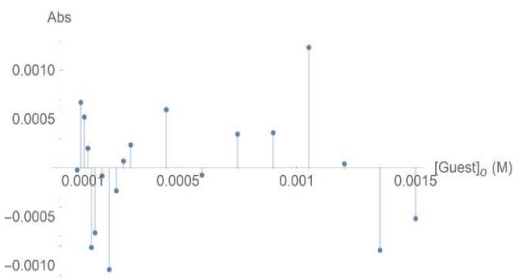

Residuals 370 nm

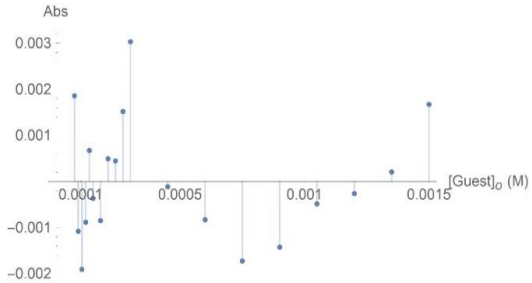

Figure 6.69. Fitting curves and plots of residual magnitude obtained when fitting the UV binding data for (**C$_3$-S**)$_2$ with cage **1.50** to the 1:2 binding model.

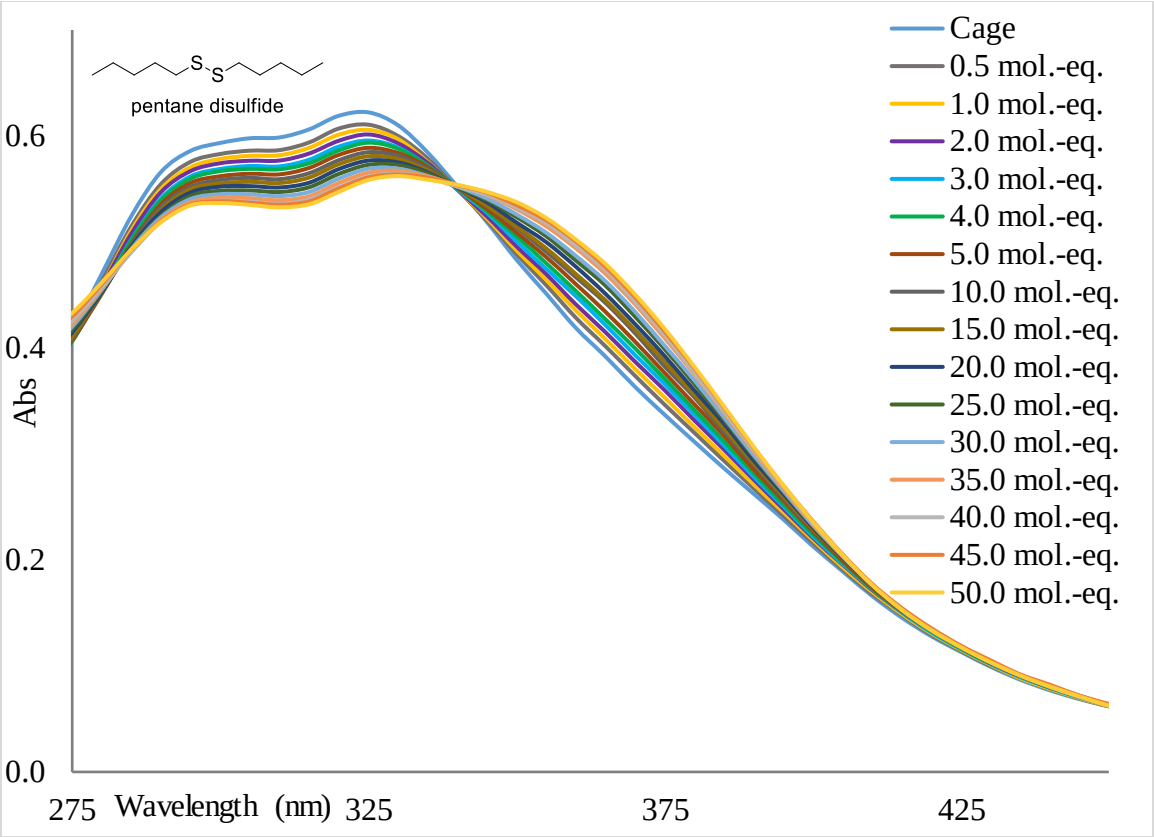

Figure 6.70. UV-Vis absorption spectrum of the titration of $(\mathbf{C_5\text{-}S})_2$ into a 3 µM solution of cage 1.50 in CH_3CN. $(\mathbf{C_5\text{-}S})_2$ was added in 0.5-5 µL aliquots from a 9 mM stock solution in CH_3CN.

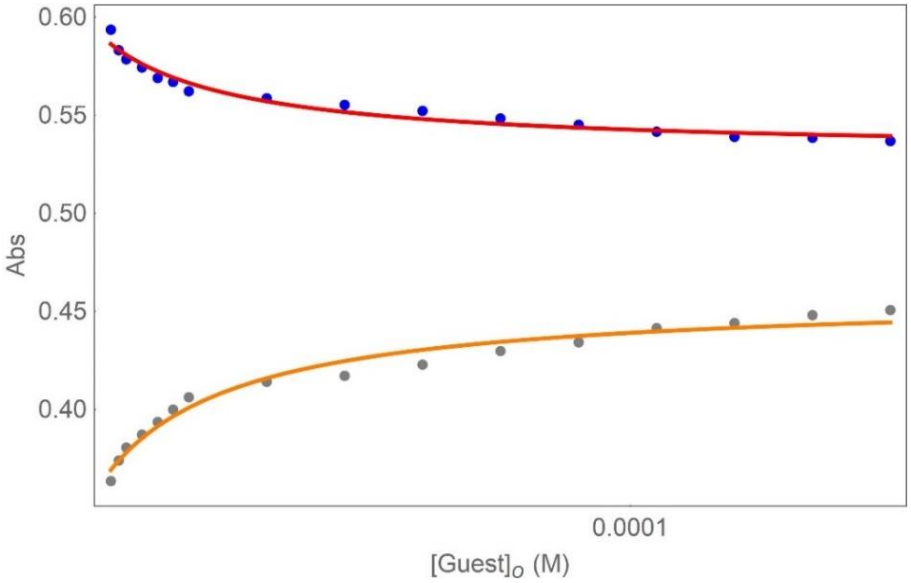

Residuals 330 nm

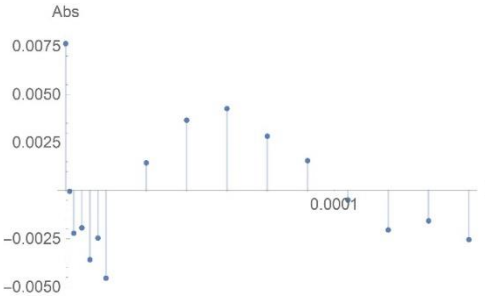

Residuals 370 nm

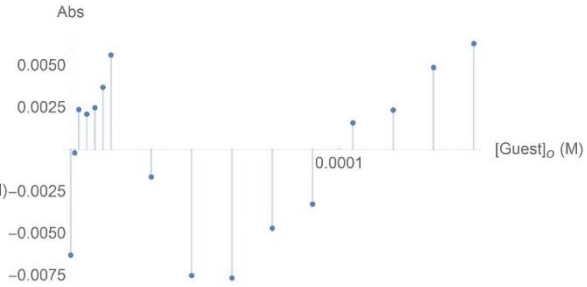

Figure 6.71. Fitting curves and plots of residual magnitude obtained when fitting the UV binding data for (**C$_5$-S**)$_2$ with cage **1.50** to the 1:1 binding model.

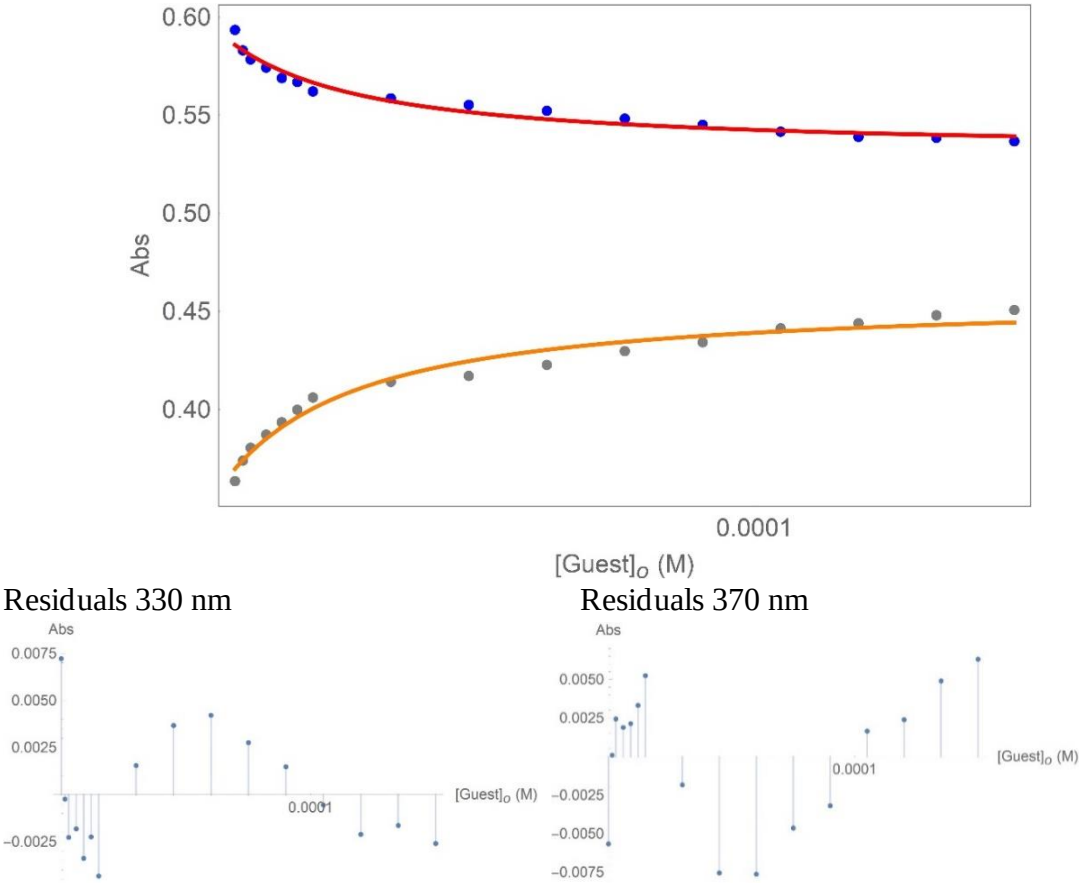

Figure 6.72. Fitting curves and plots of residual magnitude obtained when fitting the UV binding data for $(\mathbf{C_5\text{-}S})_2$ with cage **1.50** to the 1:2 binding model.

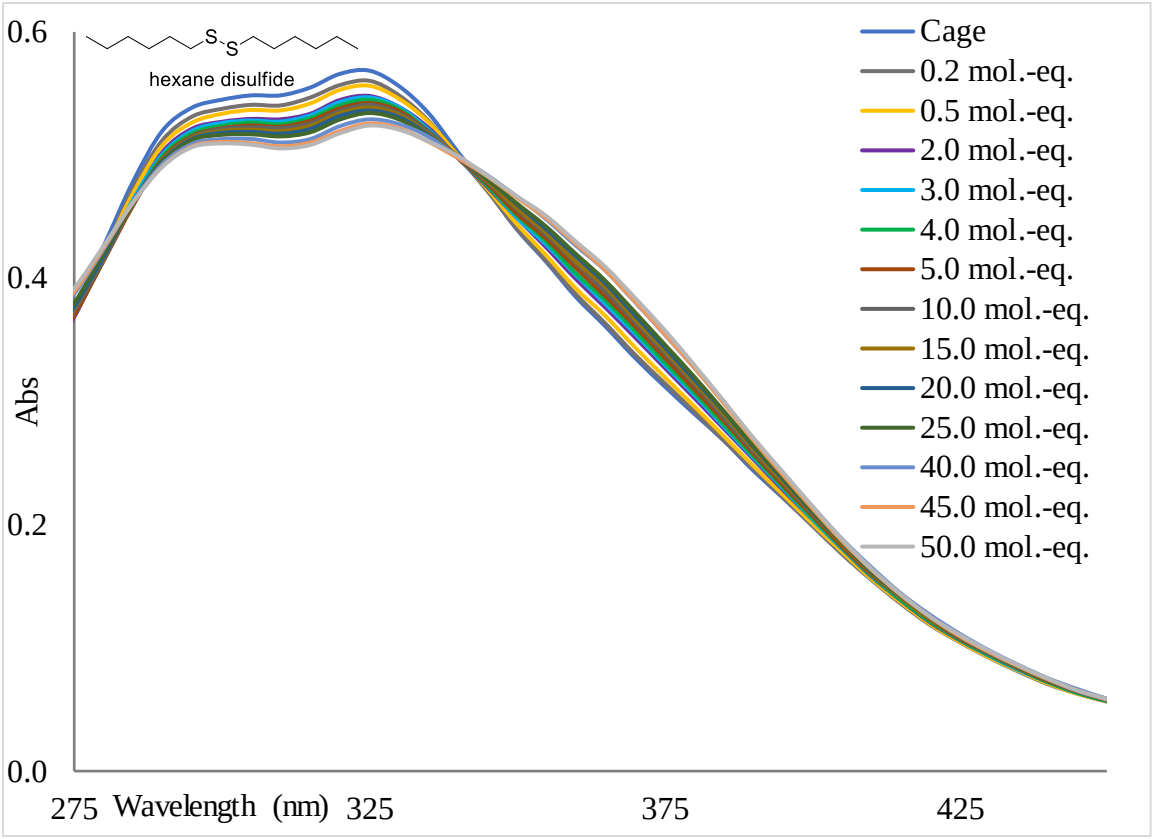

Figure 6.73. UV-Vis absorption spectrum of the titration of $(\mathbf{C_6\text{-}S})_2$ into a 3 μM solution of cage **1.50** in CH_3CN. $(\mathbf{C_6\text{-}S})_2$ was added in 0.5-5 μL aliquots from a 9 mM stock solution in CH_3CN.

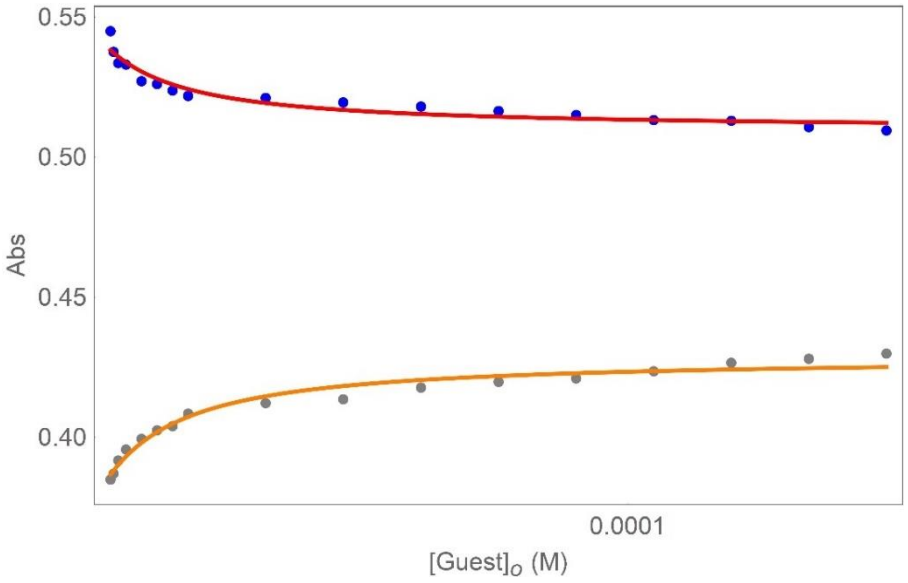

Residuals 330 nm

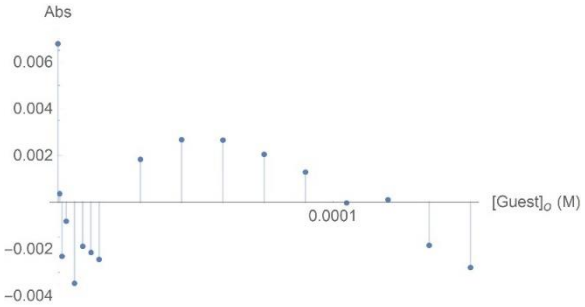

Residuals 370 nm

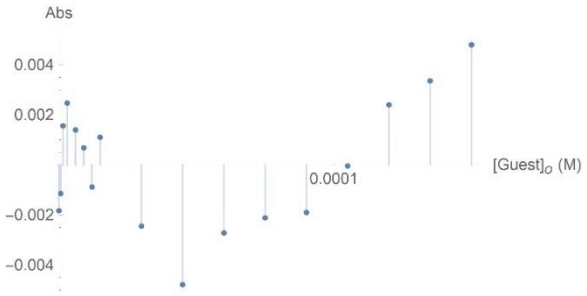

Figure 6.74. Fitting curves and plots of residual magnitude obtained when fitting the UV binding data for (**C_6-S**)$_2$ with cage **1.50** to the 1:1 binding model.

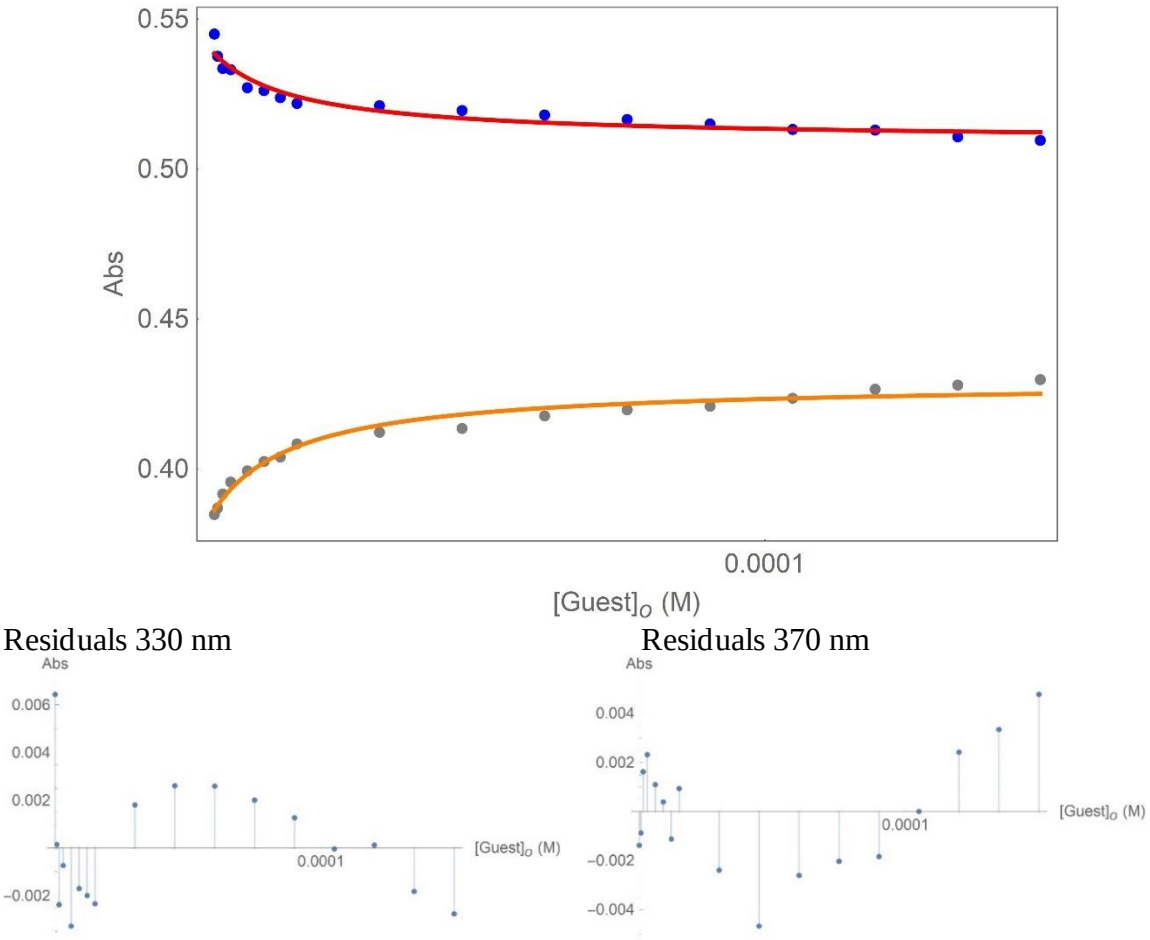

Figure 6.75. Fitting curves and plots of residual magnitude obtained when fitting the UV binding data for $(\mathbf{C_6\text{-}S})_2$ with cage **1.50** to the 1:2 binding model.

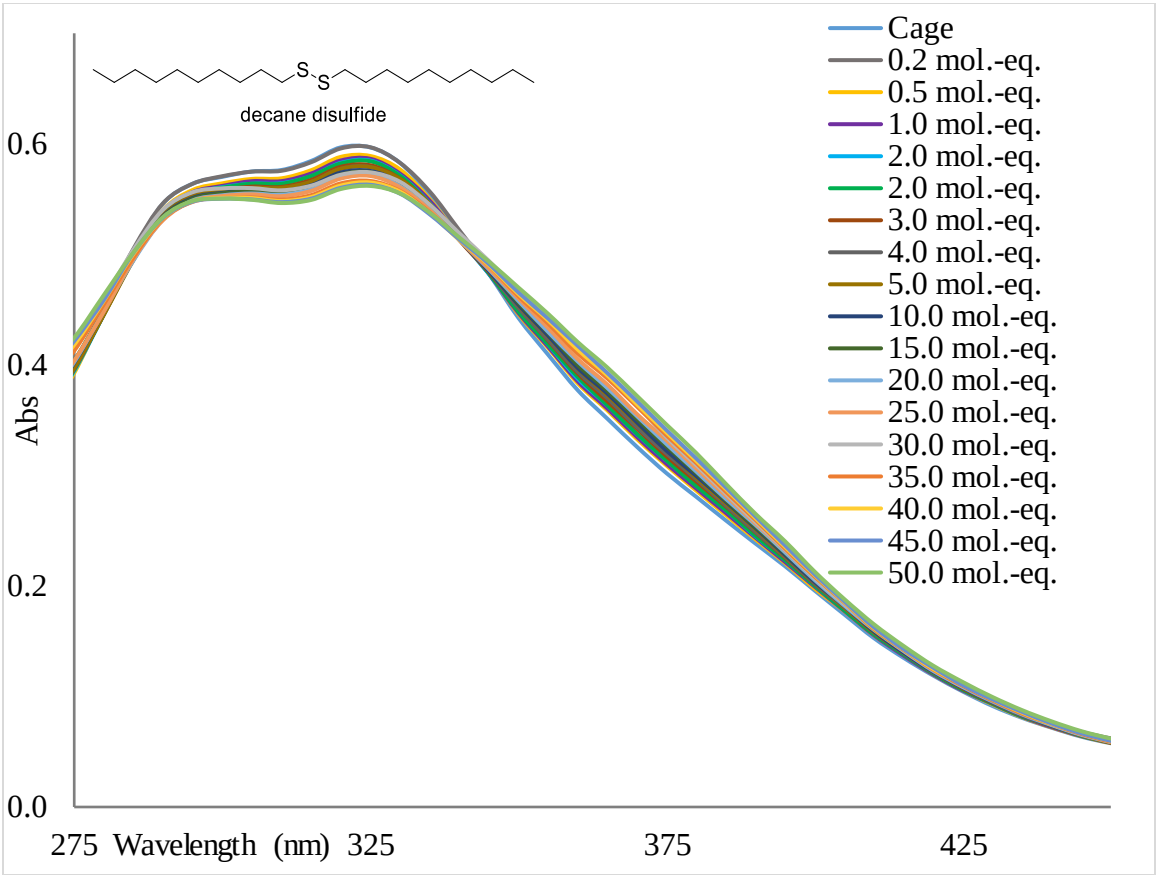

Figure 6.76. UV-Vis absorption spectrum of the titration of $(\mathbf{C_{10}\text{-}S})_2$ into a 3 µM solution of cage **1.50** in CH_3CN. $(\mathbf{C_{10}\text{-}S})_2$ was added in 0.2-5 µL aliquots from a 9 mM stock solution in CH_3CN.

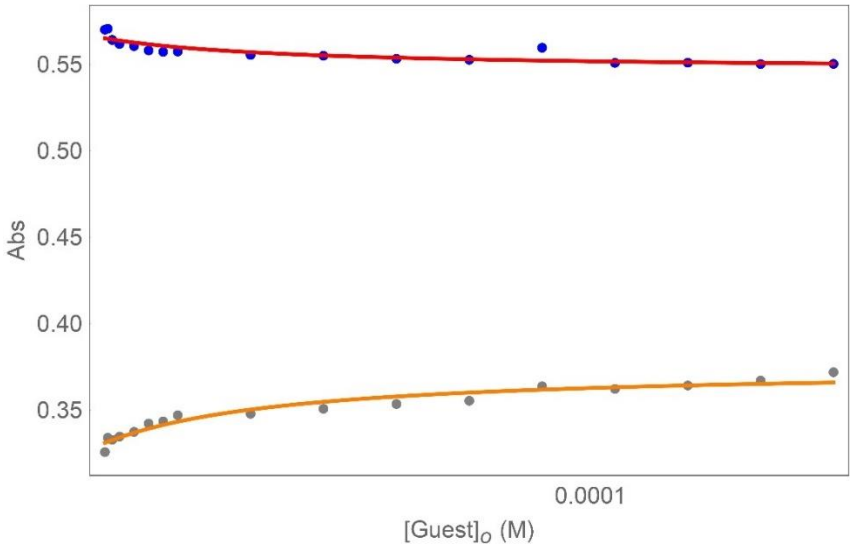

Residuals 300 nm

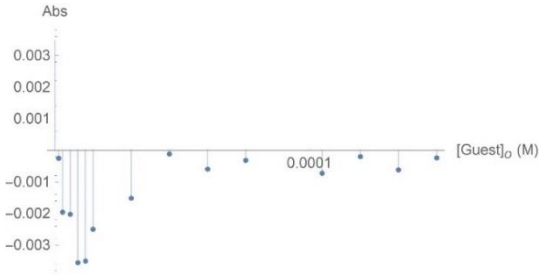

Residuals 370 nm

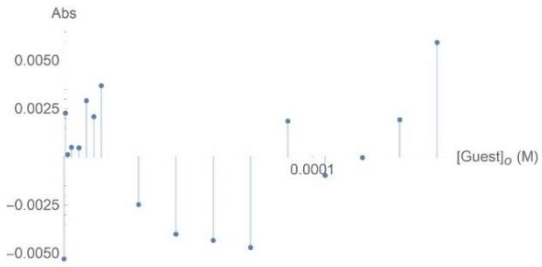

Figure 6.77. Fitting curves and plots of residual magnitude obtained when fitting the UV binding data for (**C_{10}-S**)$_2$ with cage **1.50** to the 1:1 binding model.

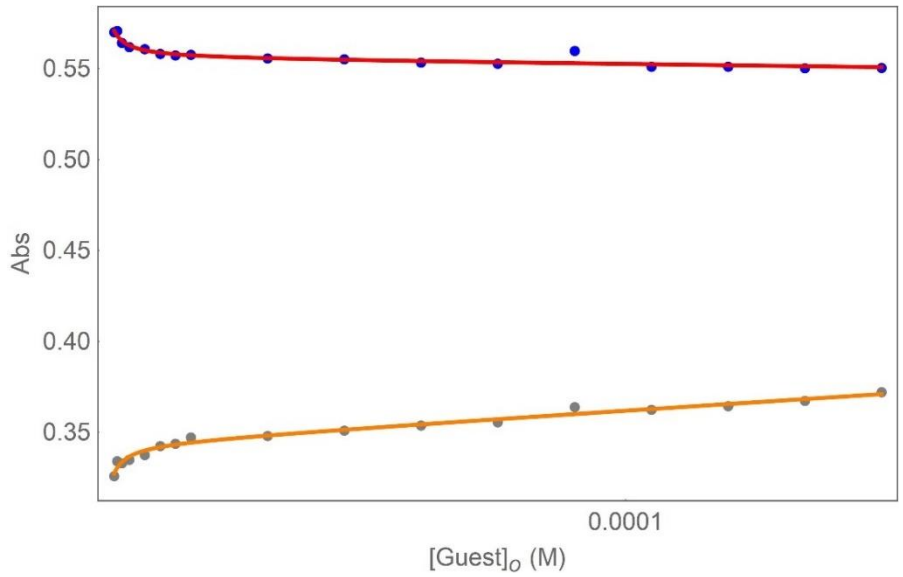

Residuals 300 nm

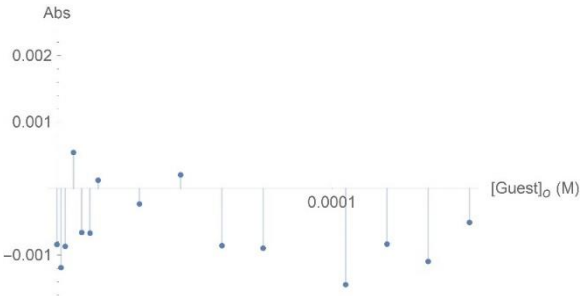

Residuals 370 nm

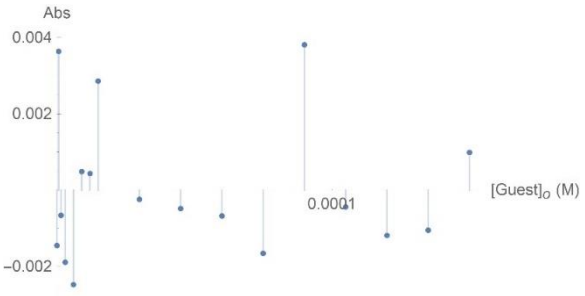

Figure 6.78. Fitting curves and plots of residual magnitude obtained when fitting the UV binding data for (**C_{10}-S**)$_2$ with cage **1.50** to the 1:2 binding model.

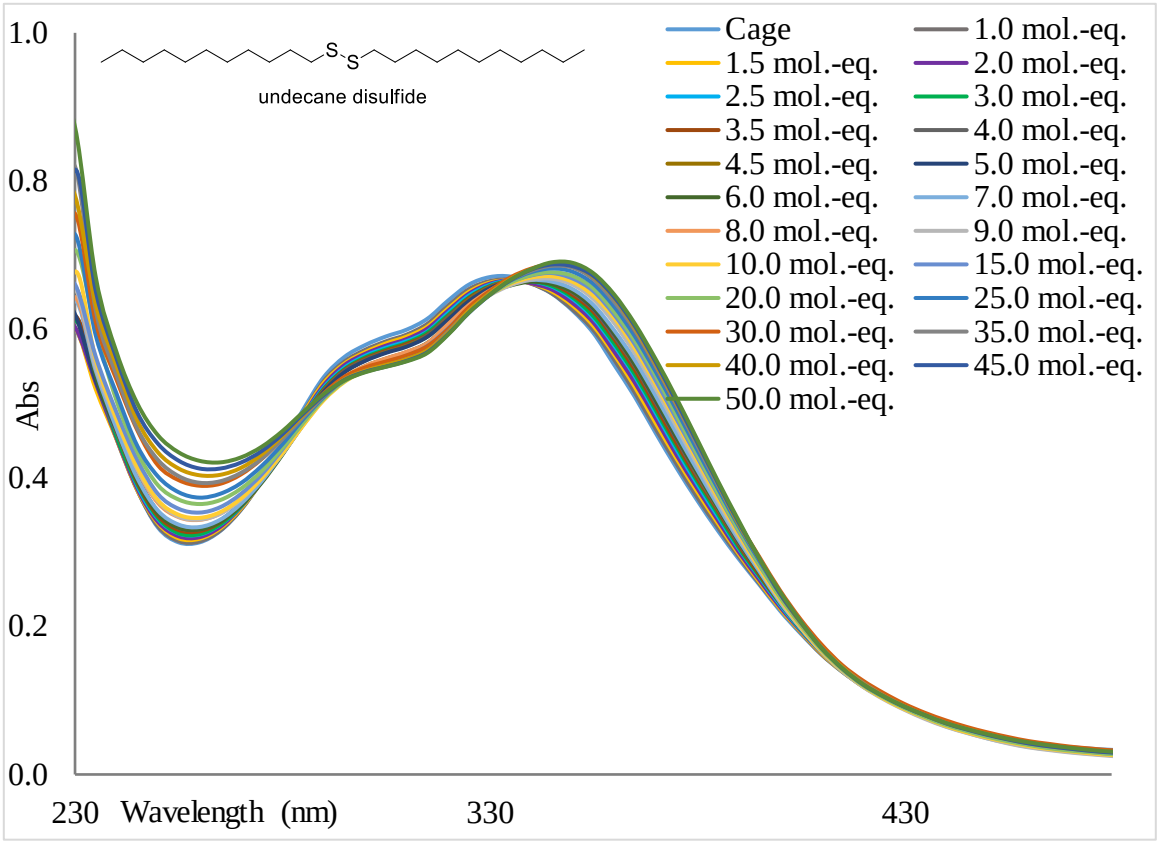

Figure 6.79. UV-Vis absorption spectrum of the titration of (**C_{11}-S**)$_2$ into a 3 µM solution of cage **1.50** in CH_3CN. (**C_{11}-S**)$_2$ was added in 1-5 µL aliquots from a 9 mM stock solution in CH_3CN.

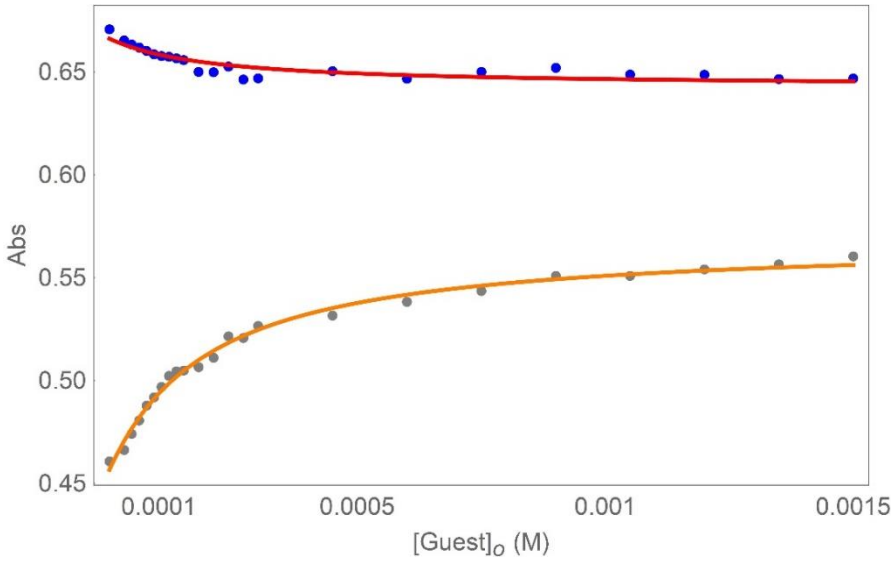

Residuals 330 nm

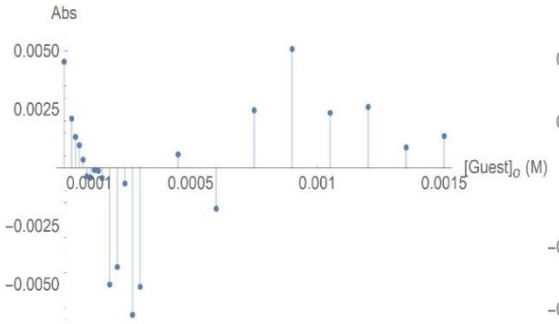

Residuals 370 nm

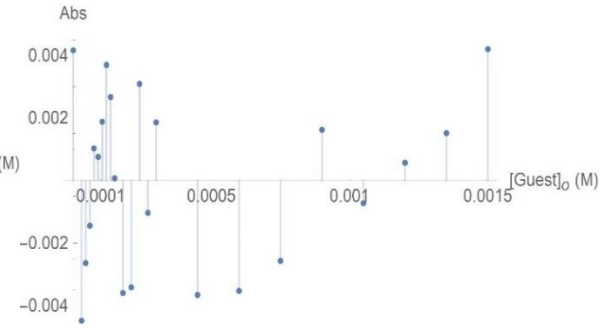

Figure 6.80. Fitting curves and plots of residual magnitude obtained when fitting the UV binding data for (**C$_{11}$-S**)$_2$ with cage **1.50** to the 1:1 binding model.

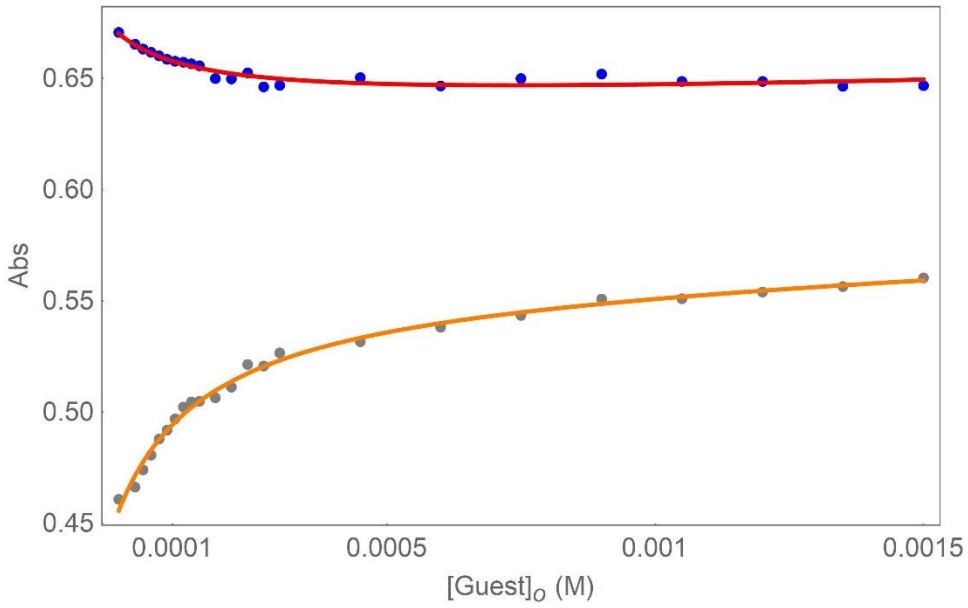

Residuals 330 nm

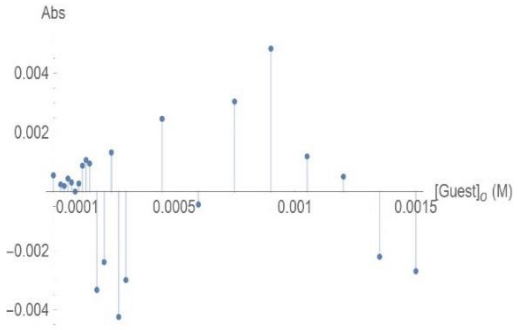

Residuals 370 nm

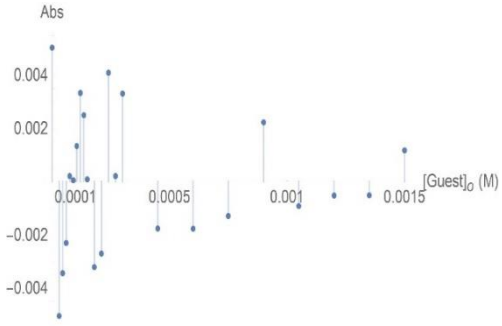

Figure 6.81. Fitting curves and plots of residual magnitude obtained when fitting the UV binding data for (**C_{11}-S**)$_2$ with cage **1.50** to the 1:2 binding model.

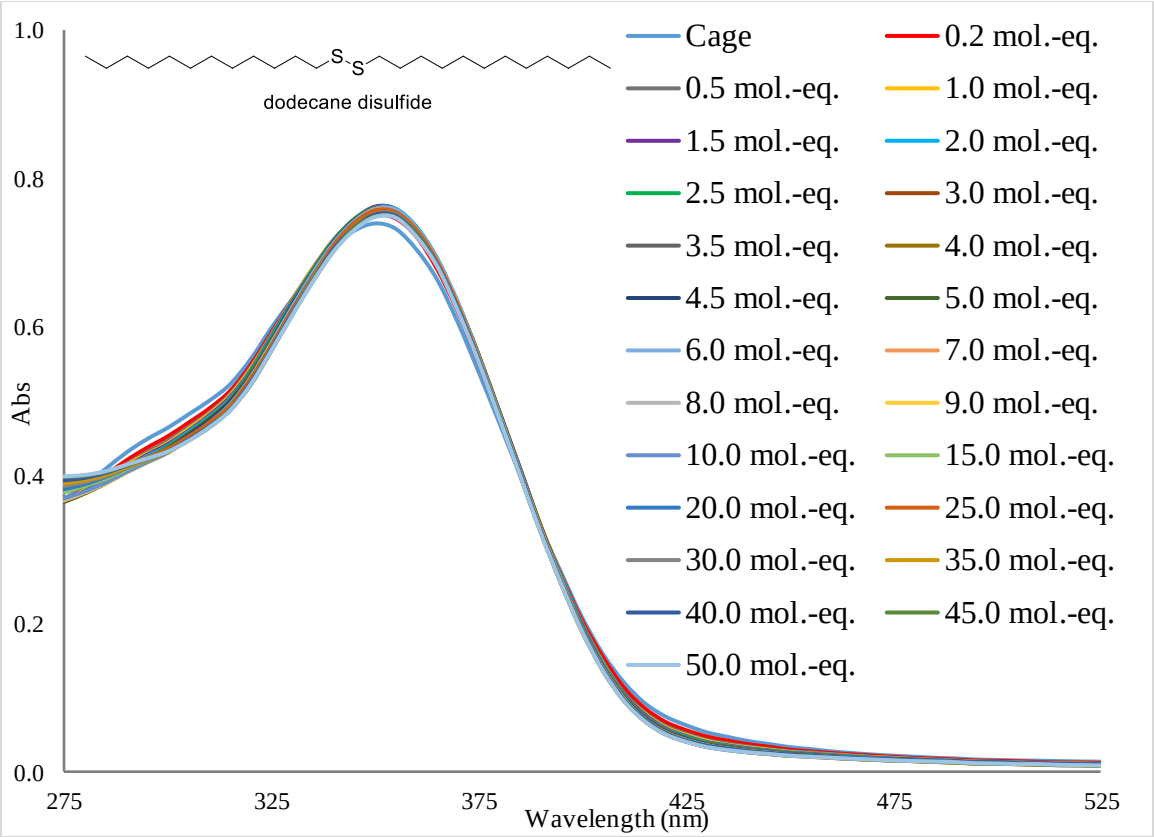

Figure 6.82. UV-Vis absorption spectrum of the titration of $(\mathbf{C_{12}\text{-}S})_2$ into a 3 μM solution of cage **1.50** in CH_3CN. $(\mathbf{C_{12}\text{-}S})_2$ was added in 1-5 μL aliquots from a 9 mM stock solution in CH_3CN.

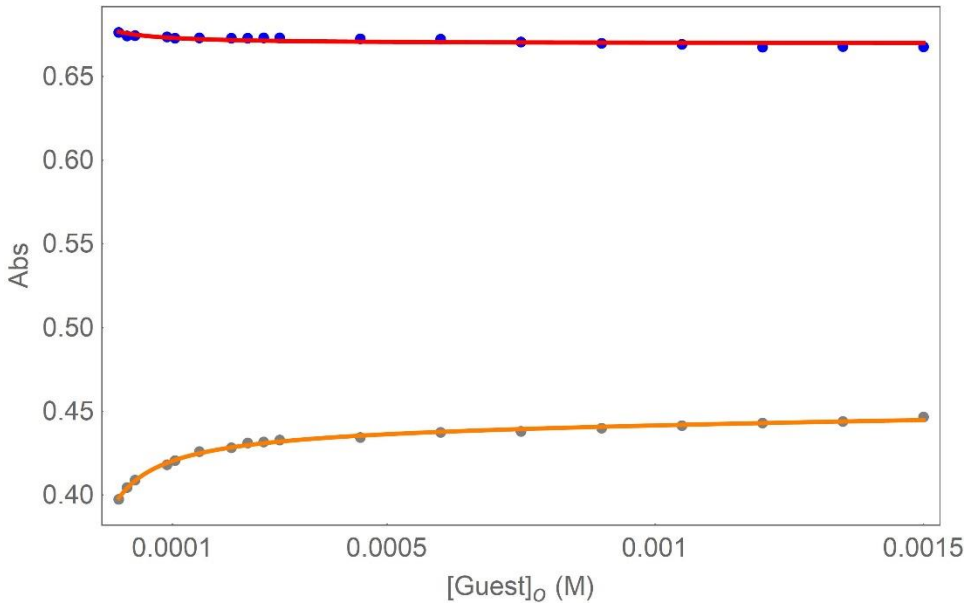

Residuals 330 nm

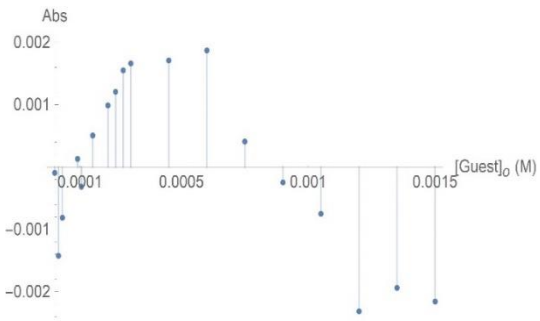

Residuals 370 nm

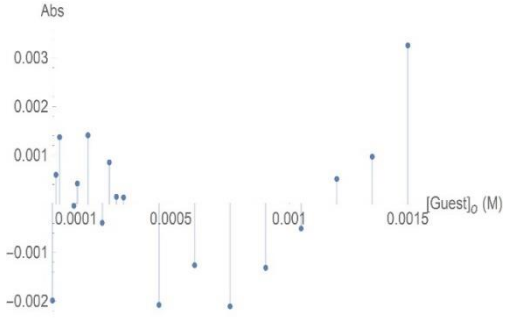

Figure 6.83. Fitting curves and plots of residual magnitude obtained when fitting the UV binding data for (**C_{12}-S**)$_2$ with cage **1.50** to the 1:1 binding model.

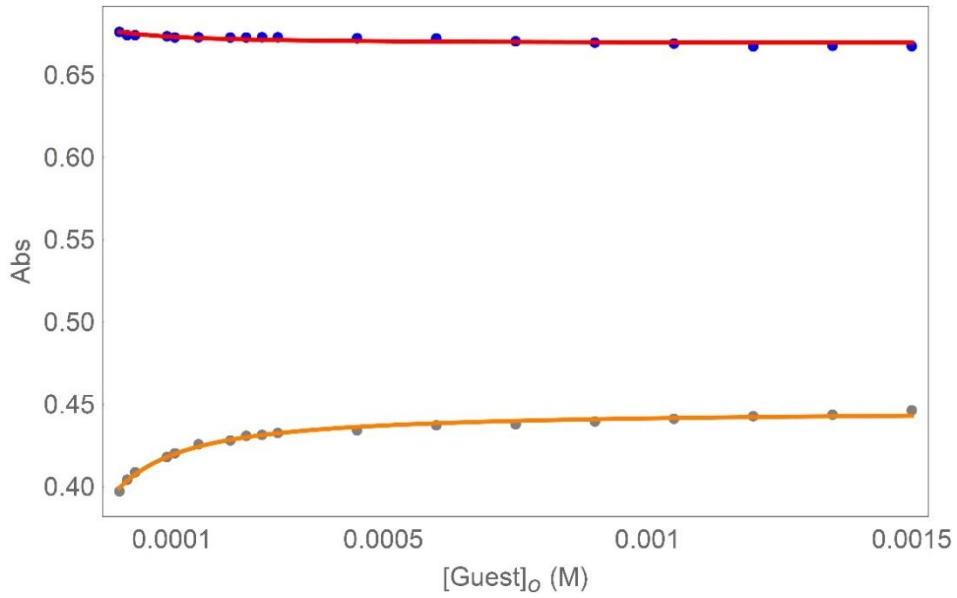

Residuals 330 nm

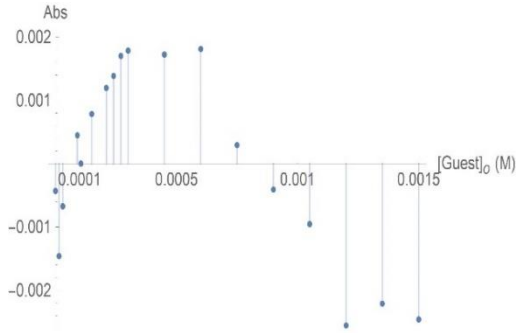

Residuals 370 nm

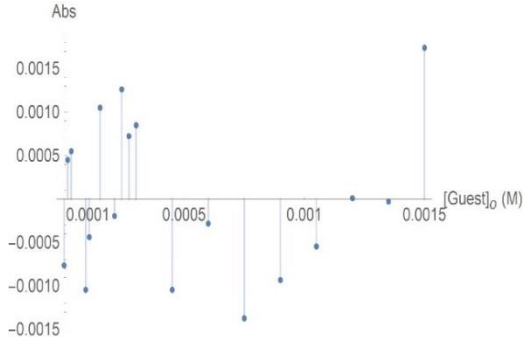

Figure 6.84. Fitting curves and plots of residual magnitude obtained when fitting the UV binding data for (**C_{12}-S**)$_2$ with cage **1.50** to the 1:2 binding model.

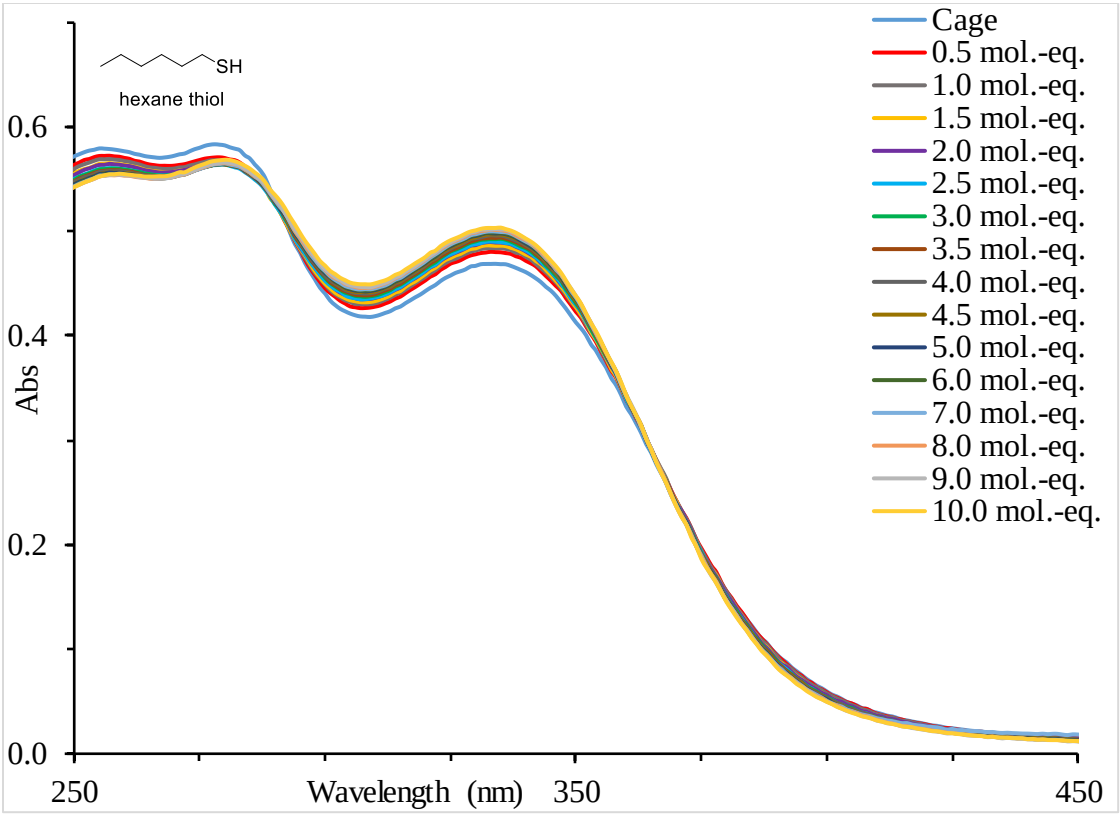

Figure 6.85. UV-Vis absorption spectrum of the titration of **C_6-SH** into a 3 µM solution of cage **2.1** in CH_3CN. **C_6-SH** was added in 0.5-1 µL aliquots from a 9 mM stock solution in CH_3CN.

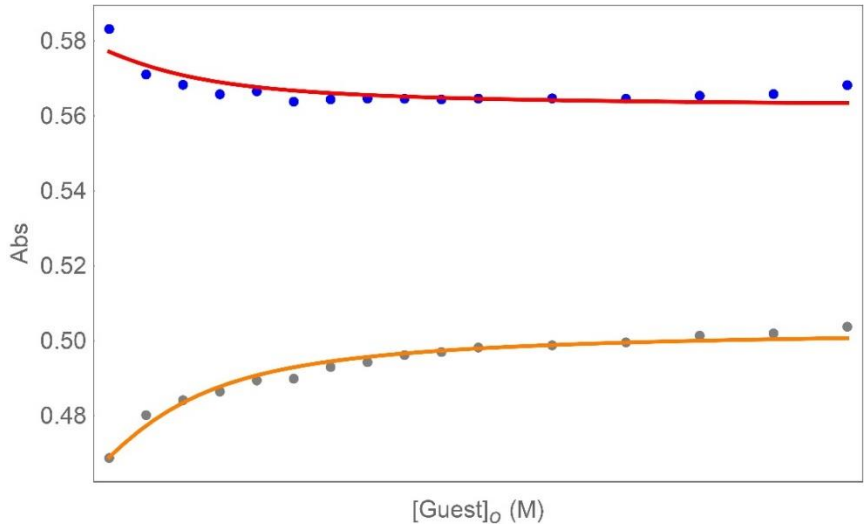

Residuals 278 nm

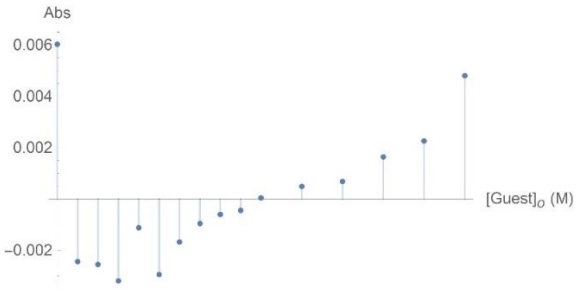

Residuals 335 nm

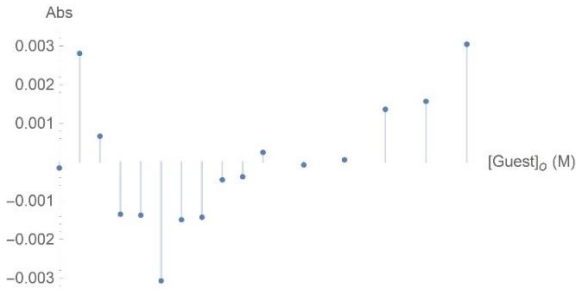

Figure 6.86. Fitting curves and plots of residual magnitude obtained when fitting the UV binding data for **C_6-SH** with cage **2.1** to the 1:1 binding model.

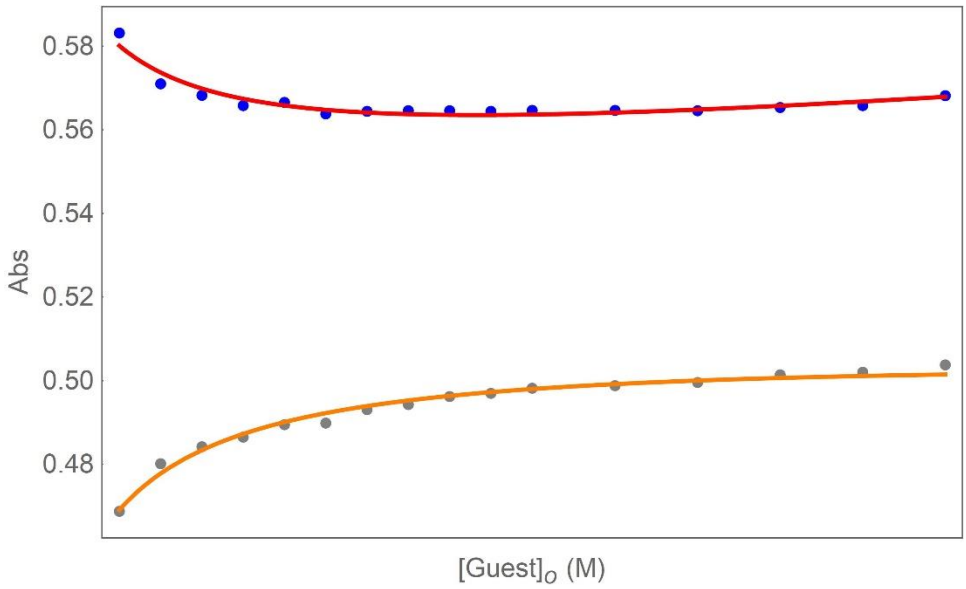

Residuals 278 nm

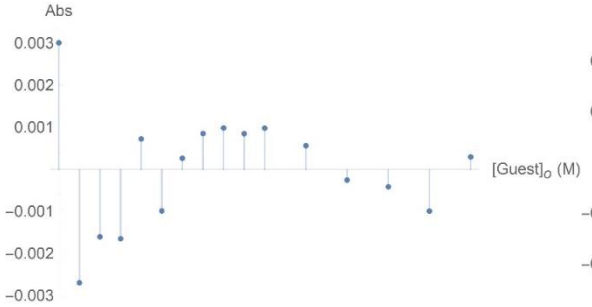

Residuals 335 nm

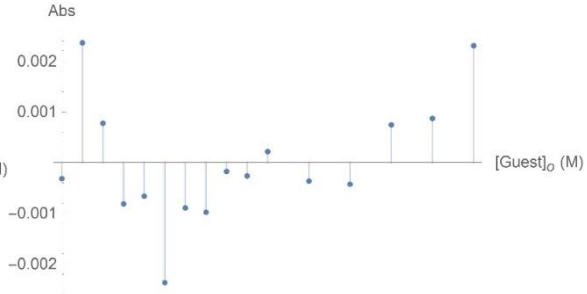

Figure 6.87. Fitting curves and plots of residual magnitude obtained when fitting the UV binding data for **C_6-SH** with cage **2** to the 1:2 binding model.

Table 6.1. Calculated Binding Affinities for Guests in Host **1.50** or **2.1**, showing only results from the model showing Best Fit (p-value < 0.001, **Sig = Yes**).

Substrate	1:1 model	1:2 Model			1:1 vs 1:2
	K_a (x 10^3 M^{-1})	K_1 (x 10^3 M^{-1})	K_2 (x 10^3 M^{-1})	4 K_2/K_1	p-value, Sig
Pentanethiol ***(1.50)***		2150 ± 650	1.2 ± 3.0	**8.7 x 10^{-4}**	**10^{-4}, Yes**
Hexanethiol ***(1.50)***		540 ± 130	2.4 ± 1.5	**0.018**	**10^{-6}, Yes**
Octanethiol ***(1.50)***		174 ± 43	0.78 ± 0.53	**0.018**	**10^{-7}, Yes**
Decanethiol ***(1.50)***	19.7 ± 6.4				0.02, No
Undecanethiol ***(1.50)***	40.± 19				0.004, No
Dodecanethiol ***(1.50)***	2.74± 0.60				0.40, No
Propyl Disulfide ***(1.50)***	16.6 ± 2.4				0.019, No
Pentyl Disulfide ***(1.50)***	38.8 ± 7.1				0.43, No
Hexyl Disulfide ***(1.50)***	71 ± 14				0.46, No
Octyl Disulfide ***(1.50)***	76.1 ± 3.8				0.006, No
Decyl Disulfide ***(1.50)***	27.9 ± 9.4				0.01, No
Undecyl Disulfide ***(1.50)***	5.53 ± 0.48				0.19, No
Dodecyl Disulfide ***(1.50)***	8.39 ± 0.85				0.36, No
Hexane Thiol ***(2.1)***	420 ± 130				0.01, No

6.5. Experimental Chapter 4

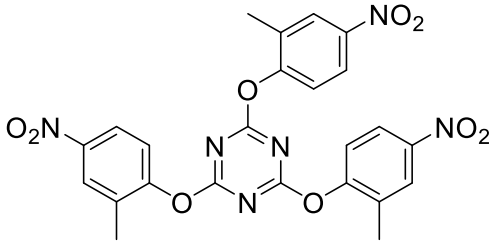

Synthesis of 4,4',4''-((1,3,5-Triazine-2,4,6-triyl)tris(oxy))tris(3-methylaniline): 4.15

2-methyl-4-nitrophenol (535 mg, 3.50 mmol) and potassium tert-butoxide (393 mg, 3.50 mmol) were placed in a 10 mL flame dried double necked round-bottomed flask equipped with a magnetic stir bar followed by the addition of dry THF (5.0 mL). The resulting heterogeneous orange solution was briefly stirred for 2 min under an atmosphere of N_2. Cyanuric chloride (184 mg, 1.00 mmol) was then added, the round-bottomed flask was equipped with a reflux condenser and brought to 50 °C in a sand bath and stirred overnight under N_2. The next day the flask was taken out of the sand bath and allowed to cool to room temperature before the solvent was removed in-vacuo which provided 2,4,6-tris(2-methyl-4-nitrophenoxy)-1,3,5-triazine **4.15** as a white powder. The white powder was then dissolved in CH_2Cl_2 and purified *via* column chromatography using CH_2Cl_2, which yielded a fine white powder (502 mg, 92 %), $R_f = 0.7$ (20 % EtOAc/hexanes). ^{1}H NMR (400 MHz, $CDCl_3$) δ 8.18 (d, $J = 2.6$ Hz, 3H), 8.12 (dd, $J = 8.9$, 2.8 Hz, 3H), 7.24 (d, $J = 8.9$ Hz, 3H), 2.31 (s, 9H). ^{13}C{^{1}H} NMR (151 MHz, $CDCl_3$) δ 173.11, 154.25, 1145.92, 131.98, 126.81, 122.78, 122.48, 16.46. HRMS (ESI-TOF) *m/z* calc[d] for $C_{24}H_{18}N_6NaO_9$ ($[M+Na]^+$): 557.1028; found 557.1020. IR (neat) ν_{max} (cm^{-1}) 3123, 3013, 2979, 1515, 1443, 1383, 1073, 954, 800, 454.

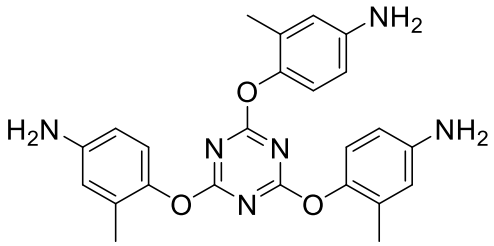

Synthesis of 4,4',4''-((1,3,5-Triazine-2,4,6-triyl)tris(oxy))tris(3-methylaniline): 4.19

Ligand precursor (**4.15**) (200 mg, 0.38 mmol) was added to a 25 mL pear shaped flask, followed by THF (20.0 mL), and then 10 % Pd/C (44.0 mg, 0.41 mmol). The flask was capped with a rubber septum and put under an atmosphere of H_2 and allowed to stir at room temperature overnight. The following day the solution was filtered over a small celite plug, the flask was washed with ~ 30 mL of CH_2Cl_2 and poured through a celite plug. The solvent of the filtrate was removed under reduced pressure yielding ligand **4.19** as a tan powder that was used without further purification (144 mg, 95 %). ^{1}H NMR (400 MHz, $CDCl_3$) δ 6.83 (d, *J* = 8.5 Hz, 3H), 6.52 (d, *J* = 3.1 Hz, 3H), 6.49 (dd, *J* = 8.5, 2.9 Hz, 3H), 2.07 (s, 9H). ^{13}C{^{1}H} NMR (151 MHz, $CDCl_3$) δ 168.80, 138.97, 137.58, 125.39, 116.74, 112.06, 108.03, 11.06. HRMS (ESI-TOF) *m/z* calc^d for $C_{24}H_{24}N_6O_3$ ($[M+H]^+$): 445.1983; found 445.1986. IR (neat) ν_{max} (cm^{-1}) 3435, 3364, 3258, 1625, 1588, 1507, 1352, 1209, 815, 535, 463.

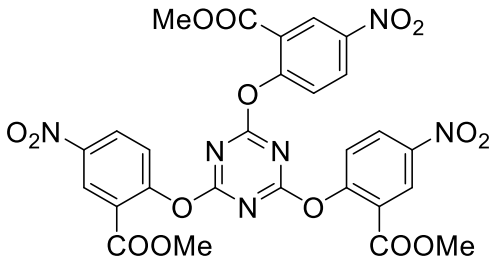

Synthesis of Trimethyl 6,6',6''-((1,3,5-triazine-2,4,6-triyl)tris(oxy))tris(3-nitrobenzoate): 4.16

Methyl 2-hydroxy-5-nitrobenzoate (1.87 g, 9.49 mmol) and potassium tert-butoxide (1.07 g, 9.49 mmol) were placed in a 50 mL flame dried double neck round-bottomed flask equipped with a magnetic stir bar followed by the addition of dry THF (30.0 mL), the resulting heterogeneous orange solution was briefly stirred for 2 minutes under an atmosphere of N_2. Cyanuric chloride (500 mg, 2.71 mmol) was then added, the round-bottomed flask was equipped with a reflux condenser and brought to 50 °C in a sand bath and stirred overnight under N_2. The next day the flask was taken out of the sand bath and allowed to cool to room temperature before the solvent was removed in-vacuo which provided a white powder. The white powder was then dissolved in CH_2Cl_2 and purified *via* column chromatography using a gradient eluent 20 % EtOAc/hexanes which yielded trimethyl 6,6',6''-((1,3,5-triazine-2,4,6-triyl)tris(oxy))tris(3-nitrobenzoate) **4.16** as a fine white powder (1.20 g, 71 %), R_f = 0.3 (20 % EtOAc/hexanes). ^{1}H NMR (400 MHz, $CDCl_3$) δ 8.90 (d, *J* = 2.8 Hz, 3H), 8.46 (dd, *J* = 8.9, 2.8 Hz, 3H), 7.40 (d, *J* = 8.9 Hz, 3H), 3.93 (s, 9H). ^{13}C{^{1}H} NMR (151 MHz, $CDCl_3$) δ 173.30, 162.58, 155.05, 145.70, 128.89, 127.57, 124.89, 124.40, 52.96. HRMS (ESI-TOF) *m/z* calc^d for $C_{27}H_{19}N_6O_{15}$ ($[M+H]^+$): 667.0903;

found 667.0906. IR (neat) ν_{max} (cm^{-1}) 3474, 3359, 3238, 3126, 3066, 2948, 1709, 1560, 1532, 1445, 1372, 1372, 1298, 1110, 1085, 962, 862, 845, 789, 772, 525.

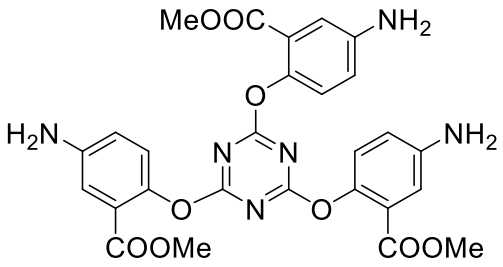

Synthesis of Trimethyl 6,6',6''-((1,3,5-triazine-2,4,6-triyl)tris(oxy))tris(3-aminobenzoate): 4.20

Ligand precursor **4.16** (200 mg, 0.32 mmol) was added to a 25 mL pear shaped flask, followed by THF (20.0 mL), and then 10 % Pd/C (42.0 mg, 0.35 mmol). The flask was capped with a rubber septum and put under an atmosphere of H_2 and allowed to stir at room temperature overnight. The following day the solution was filtered through a celite plug. The flask was washed with ~ 30 mL of CH_2Cl_2 and poured through a celite plug. The solvent of the filtrate was removed under reduced pressure yielding ligand **4.20** as a tan powder that was used without further purification (150 mg, 87 %). ^{1}H NMR (400 MHz, $CDCl_3$) δ 7.24 (d, *J* = 2.9 Hz, 3H), 6.92 (d, *J* = 8.6 Hz, 3H), 6.78 (dd, *J* = 8.6, 2.9 Hz, 3H), 3.75 (s, 9H).^{13}C{^{1}H} NMR (151 MHz, $CDCl_3$) δ 169.06, 159.67, 139.05, 138.04, 118.82, 118.11, 114.61, 112.12, 46.75. HRMS (ESI-TOF) *m/z* calc^d for $C_{27}H_{25}N_6O_9$ ($[M+H]^+$): 577.1677; found 577.1673. IR (KBr, powder) ν_{max} (cm^{-1}) 3567, 3474, 3339, 3215, 2982, 2889, 1715, 1571, 1375, 1237, 1203, 1099, 1054, 815, 713, 549, 539.

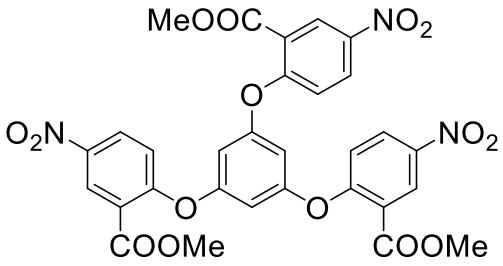

Synthesis of Trimethyl 6,6',6''-(benzene-1,3,5-triyltris(oxy))tris(3-nitrobenzoate): 4.21

Phloroglucinol (252 mg, 2.00 mmol) was added to a flame dried 25 mL pear shaped flask equipped with a magnetic stir bar, followed by DMF (4.00 mL), triethylamine (1.00 mL, 7.00 mmol), and methyl-2-fluoro-5-nitrobenzoate (1.40 g, 7.00 mmol). The reaction was brought to 100 °C in a sand bath and allowed to stir overnight. The following day the flask was removed from the sand bath and allowed to cool to room temperature. The reaction was diluted with 50 mL of CH_2Cl_2 and washed with 5 x 10 mL of H_2O followed by 3 x 15 mL of brine before being dried over sodium sulfate. The dried solution was then decanted, and the solvent was removed under reduced pressure. A ^1H NMR spectrum was taken of the crude material to confirm a majority of the DMF had been removed before the crude was purified *via* column chromatography with 0-20% EtOAc/hexanes yielding trimethyl 6,6',6''-(benzene-1,3,5-triyltris(oxy))tris(3-nitrobenzoate) **4.21** as an off-white powder (520 mg, 39 %), R_f = 0.3 (3 % EtOAc/hexanes). ^1H NMR (400 MHz, $CDCl_3$) δ 8.82 (d, J = 2.9 Hz, 3H), 8.37 (dd, J = 9.1, 2.8 Hz, 3H), 7.15 (d, J = 9.1 Hz, 3H), 6.59 (s, 3H), 3.95 (s, 9H). $^{13}C\{^1H\}$ NMR (151 MHz, $CDCl_3$) δ 163.43, 160.06, 158.20, 143.38, 128.76, 128.10, 123.16, 120.08, 106.54, 52.91. HRMS (ESI-TOF) *m/z* calc[d] for $C_{30}H_{22}N_3O_{15}$ ($[M+H]^+$):

664.1046; found 664.1025. IR (neat) ν_{max} (cm^{-1}) 3089, 2948, 1709, 1614, 1583, 144, 1352, 1268, 1133, 1007, 832, 756, 703.

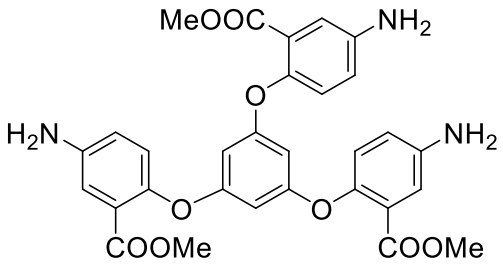

Synthesis of Trimethyl 6,6',6''-(benzene-1,3,5-triyltris(oxy))tris(3-aminobenzoate): 4.22

Ligand precursor (**4.21**) (200 mg, 0.30 mmol) was added to a 25 mL pear-shaped flask, followed by THF (20.0 mL), and then 10 % Pd/C (48.0 mg, 0.33 mmol). The flask was capped with a rubber septum and put under an atmosphere of H_2 and allowed to stir at room temperature overnight. The following day the solution was filtered over a small celite plug, the flask was washed with ~ 30 mL of dichloromethane and poured through a celite plug. The solvent of the filtrate was removed under reduced pressure yielding ligand **4.22** as a tan powder that was used without further purification (160 mg, 96 %). ^{1}H NMR (400 MHz, $CDCl_3$) δ 7.22 (d, *J* = 3.0 Hz, 3H), 6.90 (d, *J* = 8.6 Hz, 3H), 6.82 (dd, *J* = 8.6, 3.0 Hz, 4H), 6.08 (s, 3H), 3.78 (s, 9H), 3.71 (s, 6H). $^{13}C\{^1H\}$ NMR (151 MHz, $CDCl_3$) δ 165.98, 160.91, 146.70, 143.17, 124.03, 123.74, 120.25, 117.40, 99.16, 52.12. HRMS (ESI-TOF) *m/z* calc[d] for $C_{30}H_{27}N_3NaO_9$ ($[M+H]^+$): 596.1640; found 596.1637. IR (neat) ν_{max} (cm^{-1}) 3463, 3370, 3244, 2960, 1715, 1619, 1490, 1445, 1316, 1245, 1206, 1113, 1071, 1007, 841.

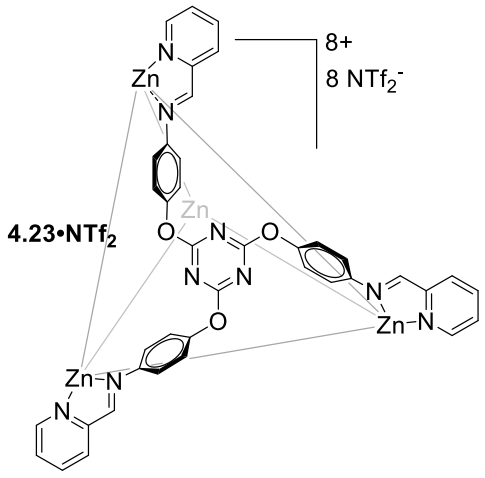

Synthesis of Cage 4.23•NTf_2: 4,4',4''-((1,3,5-triazine-2,4,6-triyl)tris(oxy))trianiline[7] (**4.14**) (25 mg, 0.06 mmol) was added to a 25 mL pear shaped flask equipped with a magnetic stir bar, followed by MeCN (10 mL), $Zn(NTf_2)_2$ (27.5 mg. 0.06 mmol), and 2-formylpyridine (17.1 µL, 0.18 mmol). The flask was equipped with a reflux condenser and brought to 50 °C in a sand bath and allowed to stir overnight. The flask was then taken out of the sand bath and allowed to cool to room temperature before the solvent was removed in vacuo which left a greasy residue on the walls of the flask. 20 mL of ether was then added which converted the greasy residue into a fine powder, the flask walls were scratched with a metallic spatula to ensure a maximum amount of material was collected. This solution was then filtered yielding an amber crystalline powder. (72 mg, 97 %). ^{1}H NMR (600 MHz, CD_3CN) δ 8.60 (s, 12H), 8.50 (t, J = 7.6 Hz, 12H), 8.29 (d, J = 7.6 Hz, 12H), 7.99 (d, J = 5.2 Hz, 12H), 7.97 – 7.92 (m, 12H), 7.27 (d, J = 9.0 Hz, 24H), 6.17 (d, J = 9.0 Hz, 24H).^{13}C{^{1}H} NMR (151 MHz, CD_3CN) δ 174.59, 166.65, 150.76, 150.23, 147.44, 146.52, 143.29, 131.90, 131.63, 123.84, 123.68. ^{19}F NMR (CD_3CN, 376 MHz, 298 K, referenced to C_6F_6): δ (ppm) -80.57. ESI-MS: m/z 460.0758 $[M+NTf_2]^{7+}$.

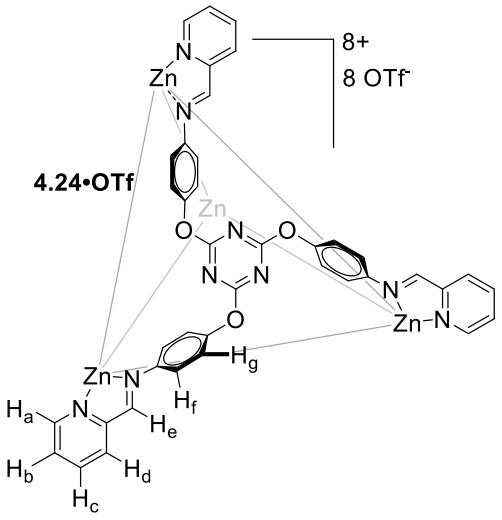

Synthesis of Cage 4.24•OTf: 4,4',4''-((1,3,5-triazine-2,4,6-triyl)tris(oxy))trianiline[7] (**4.1**) (25 mg, 0.06 mmol) was added to a 25 mL pear shaped flask equipped with a magnetic stir bar, followed by MeCN (10 mL), $Zn(OTf)_2$ (21.8 mg. 0.06 mmol), and 2-formylpyridine (17.1 μL, 0.18 mmol). The flask was equipped with a reflux condenser and brought to 50 °C in a sand bath and allowed to stir overnight. The flask was then taken out of the sand bath and allowed to cool to room temperature before the solvent was removed in vacuo which left a greasy residue on the walls of the flask. 20 mL of ether was then added which converted the greasy residue into a fine powder, the flask walls were scratched with a metallic spatula to ensure a maximum amount of material was collected. This solution was then filtered yielding an amber crystalline powder (60 mg, 96 %). ^{1}H NMR (400 MHz, CD_3CN) δ 8.55 (s, 12H), 8.48 (t, J = 7.7 Hz, 12H), 8.28 (d, J = 7.7 Hz, 12H), 8.02 (d, J = 6.5, 12H), 7.93 (t, J = 6.5 Hz, 12H), 7.43 (d, J = 8.5 Hz, 24H), 6.00 (br, 24H).^{13}C{^{1}H} NMR (151 MHz, CD_3CN) δ 174.52, 165.81, 151.53, 150.16, 146.69, 143.18, 131.57,

131.43, 124.84, 122.93. ^{19}F NMR (CD_3CN, 376 MHz, 298 K, referenced to C_6F_6): δ (ppm) -78.39, -79.74. ESI-MS: m/z 441.3665 $[M+OTf]^{7+}$.

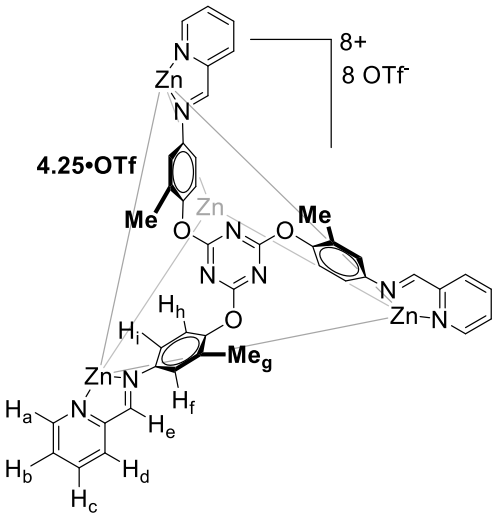

Synthesis of Cage 4.25•OTf: Ligand **4.19** (100 mg, 0.23 mmol) was added to a 100 mL round-bottomed flask equipped with a magnetic stir bar, followed by MeCN (40 mL), $Zn(OTf)_2$ (84 mg. 0.23 mmol), and 2-formylpyridine (66 µL, 0.69 mmol). The flask was equipped with a reflux condenser and brought to 50 °C in a sand bath and allowed to stir overnight. The flask was then taken out of the sand bath and allowed to cool to room temperature before the solvent was removed in vacuo which left a greasy residue on the walls of the flask. 50 mL of ether was then added which converted the greasy residue into a fine powder, the flask walls were scratched with a metallic spatula to ensure a maximum amount of material was collected. This solution was then filtered yielding an amber crystalline powder. (215 mg, 87 %). ^{1}H NMR (400 MHz, CD_3CN) δ 8.54 (s, 12H), 8.49 (td, *J* = 7.8, 1.6 Hz, 12H), 8.31 (d, *J* = 7.8 Hz, 12H), 8.08 (d, *J* = 5.2 Hz, 12H), 7.97 – 7.93 (m, 12H), 7.54 (d, *J* = 8.7 Hz, 12H), 6.10 (d, *J* = 2.7 Hz, 12H), 5.38 (dd, *J* = 8.7, 2.7 Hz,

12H), 2.13 (s, 36H). $^{13}C\{^{1}H\}$ NMR (151 MHz, CD_3CN) δ 173.56, 164.62, 149.92, 149.72, 146.38, 146.02, 142.86, 132.11, 130.88, 130.64, 125.50, 122.09, 120.48, 15.48. ^{19}F NMR (CD_3CN, 376 MHz, 298 K, referenced to C_6F_6): δ (ppm) -77.99, -79.73. ESI-MS: m/z 465.3914 $[M+OTf]^{7+}$.

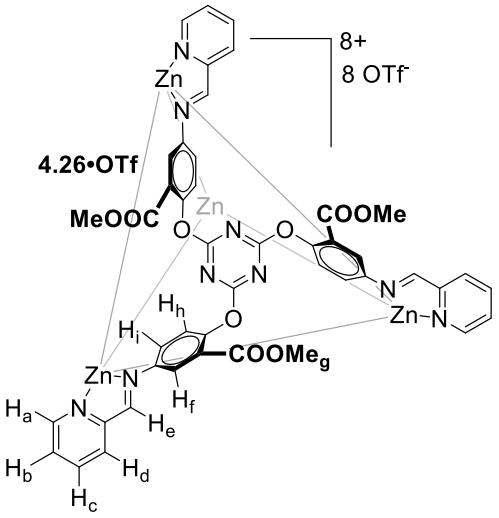

Synthesis of Cage 4.26•OTf: Ligand **4.20** (100 mg, 0.17 mmol) was added to a 100 mL round-bottomed flask equipped with a magnetic stir bar, followed by MeCN (40 mL), $Zn(OTf)_2$ (63 mg. 0.17 mmol), and 2-formylpyridine (49 μL, 0.51 mmol). The flask was equipped with a reflux condenser and brought to 50 °C in a sand bath and allowed to stir overnight. The flask was then taken out of the sand bath and allowed to cool to room temperature before the solvent was removed in vacuo which left a greasy residue on the walls of the flask. 50 mL of ether was then added which converted the greasy residue into a fine powder, the flask walls were scratched with a metallic spatula to ensure a maximum amount of material was collected. This solution was then filtered yielding a crystalline violet powder. (174 mg, 85 %). ^{1}H NMR (400 MHz, CD_3CN) δ 8.69 (s, 12H), 8.55 (td, *J* =

7.8, 1.6 Hz, 12H), 8.38 (d, J = 7.7, 1.1 Hz, 12H), 8.23 (d, 12H), 8.02 – 7.99 (m, 12H), 7.66 (d, J = 8.7 Hz, 13H), 6.88 (d, J = 2.8 Hz, 12H), 5.83 (dd, J = 8.7, 2.8 Hz, 12H), 3.80 (s, 36H). $^{13}C\{^{1}H\}$ NMR (151 MHz, $CDCl_3$) δ 172.81, 166.25, 163.39, 150.31, 149.69, 146.04, 145.85, 143.03, 131.37, 131.13, 126.97, 126.64, 124.75, 123.63, 52.46. ^{19}F NMR (CD_3CN, 376 MHz, 298 K, referenced to C_6F_6): δ (ppm) -79.00, -79.75. ESI-MS: m/z 540.8034 $[M+OTf]^{7+}$.

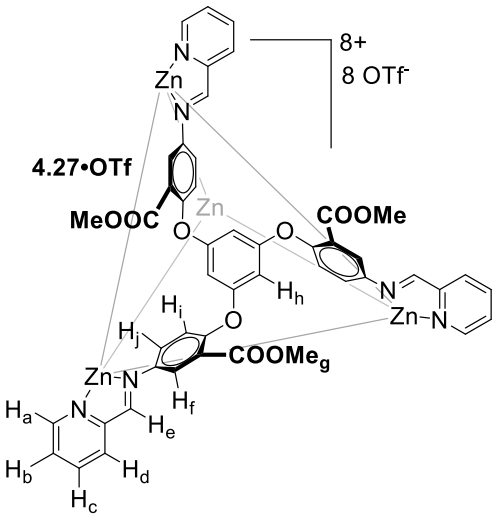

Synthesis of Cage 4.27•OTf: 4.22 (100 mg, 0.17 mmol) was added to a 100 mL round-bottomed flask equipped with a magnetic stir bar, followed by MeCN (40 mL), $Zn(OTf)_2$ (63 mg. 0.17 mmol), and 2-formylpyridine (49 µL, 0.51 mmol). The flask was equipped with a reflux condenser and brought to 50 °C in a sand bath and allowed to stir overnight. The flask was then taken out of the sand bath and allowed to cool to room temperature before the solvent was removed in vacuo which left a greasy residue on the walls of the flask. 50 mL of ether was then added which converted the greasy residue into a fine powder, the flask walls were scratched with a metallic spatula to ensure a maximum amount of

material was collected. This solution was then filtered yielding a crystalline amber powder. (176 mg, 86 %). ^{1}H NMR (400 MHz, CD_3CN) δ 8.62 (s, 12H), 8.55 (td, *J* = 7.8, 1.6 Hz, 12H), 8.30 – 8.26 (m, 24H), 8.03 – 7.99 (m, 12H), 7.60 (d, *J* = 8.6 Hz, 12H), 6.50 (d, *J* = 2.8 Hz, 12H), 6.06 (s, 12H), 5.99 (dd, *J* = 8.6, 2.8 Hz, 12H), 3.70 (s, 36H). ^{13}C NMR (151 MHz, CD_3CN) δ 166.76, 163.53, 161.04, 154.15, 150.63, 146.75, 144.87, 143.35, 131.84, 131.37, 127.13, 126.90, 126.13, 124.14, 98.91, 52.59.^{19}F NMR (CD_3CN, 376 MHz, 298 K, referenced to C_6F_6): δ (ppm) -79.20, -79.69. ESI-MS: m/z 539.0979 $[M+OTf]^{7+}$.

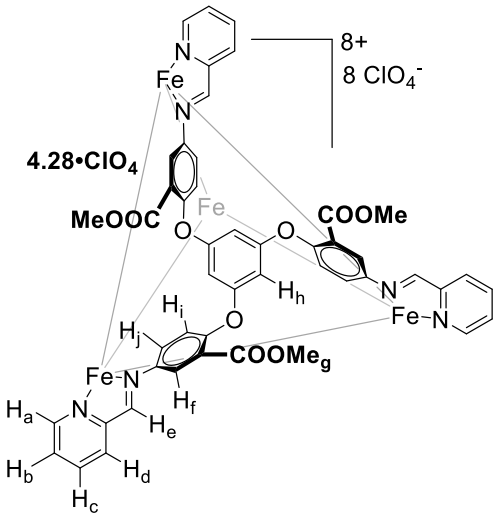

Synthesis of Cage Fe-4.28•ClO_4: 4.22 (25 mg, 0.043 mmol) was added to a 25 mL round-bottomed flask equipped with a magnetic stir bar, followed by MeCN (10 mL), $Fe(ClO_4)_2$ (11.7 mg, 0.043 mmol), and 2-formylpyridine (12.3 μL, 0.13 mmol). The flask was equipped with a reflux condenser and brought to 50 °C in a sand bath and allowed to stir overnight. The flask was then taken out of the sand bath and allowed to cool to room temperature before the solvent was removed in vacuo which left a greasy residue on the walls of the flask. 35 mL of ether was then added which converted the greasy residue into

a fine powder, the flask walls were scratched with a metallic spatula to ensure a maximum amount of material was collected. This solution was then filtered yielding a crystalline purple powder. (37 mg, 77 %) ^{1}H NMR (400 MHz, CD_3CN) δ 8.93 (s, 12H), 8.54 (d, *J* = 7.4 Hz, 12H), 8.48 (t, 12H), 7.83 (t, *J* = 5.9 Hz, 12H), 7.55 (d, *J* = 5.2 Hz, 12H), 7.39 (d, *J* = 8.6 Hz, 12H), 6.04 (d, *J* = 2.7 Hz, 12H), 6.00 (s, 12H), 5.50 (dd, *J* = 8.6, 2.8 Hz, 12H), 3.73 (s, 36H). ^{13}C NMR (101 MHz, CD_3CN) δ 175.46, 174.53, 158.45, 156.46, 152.00, 148.74, 140.23, 132.04, 130.43, 126.02, 124.85, 123.61, 122.38, 49.47. ESI-MS: m/z 465.3914 $[M+OTf]^{7+}$.

Synthesis of Cage 4.25•SbF_6: 4.25•OTf (150 mg, 0.04 mmol) and $NaSbF_6$ (1.8 g, 7.00 mmol) were placed in a single neck flask with MeCN (35 mL) equipped with a magnetic stir bar and reflux condenser. The flask was brought to 50 °C in a sand bath and allowed to stir overnight. The following day after being cooled to room temperature the solvent was removed in vacuo and provided a solid that was light pink. ~ 40 mL of ether was added to the flask, the solid was scratched off the walls and the following heterogeneous solution was filtered. The solid was then washed with ~ 600 ml of ether and 500 mL of H2O, providing a light pink powder (175 mg).

Cage 4.26•SbF_6: 4.26•OTf (150 mg, 0.03 mmol) and $NaSbF_6$ (1.7 g, 6.00 mmol) were placed in a single neck flask with MeCN (35 mL) equipped with a magnetic stir bar and reflux condenser. The flask was brought to 50 °C in a sand bath and allowed to stir for 48 h, following it was removed from heat and allowed to cool to room temperature. The solvent was removed in vacuo and provided a solid that was light pink. ~ 40 mL of ether

was added to the flask, the solid was scratched off the walls and the following heterogeneous solution was filtered. The solid was then washed with ~ 600 ml of ether and 500 mL of H_2O, providing a light pink powder (182 mg).

Cage Fe-4.28•SbF_6: Fe-4.28•ClO_4 (5 mg, 0.001 mmol) was placed in a 1.2 mL miniature test tube with MeCN (1 mL) and $NaSbF_6$ (3 mg, 0.011 mmol). The solution was placed in a scintillation vial with 2 mL of diisopropyl ether, sealed, and wrapped with parafilm. Crystals were allowed to grow over a period of 2 weeks and then analyzed by X-ray crystallography, deposited as CCDC 2213841.

General procedure for Determining Binding Affinities. 0.4 M solutions of $NaPnF_6$ anionic guests and 2 mM solutions of cage were prepared using CD_3CN. 200 µL of a stock solution of cage was added to an NMR tube. This solution was then diluted before the addition of the anion solution, with an appropriate volume of CD_3CN so that after the addition of the anion solution the desired concentrations of cage and anion would be obtained. For example, to obtain a 1 mM solution of cage with a 25 mM concentration of anion one would dilute a 200 µL solution of cage (2 mM) with 175 µL of CD_3CN followed by the addition of 25.0 µL of a solution of anion guest (0.4 M). As the speed of OTf^- displacement in cages ranged from moderate to slow, the solutions were heated to 50 ºC for a minimum of 3 days and a maximum of 2 weeks to ensure full equilibrium. After two weeks, heating was ceased as cage decomposition began to occur. Equilibrium was reached within seconds with **4.27•OTf**, unlike **4.24-4.26•OTf**. Solutions of **4.24-4.26•OTf** and anions were heated overnight to demonstrate that equilibrium was reached rapidly as

heating produced no notable changes in the ^{1}H NMR spectra. The cooled samples were analyzed by ^{1}H or ^{19}F NMR to determine K_{rel}, for calculations.

Calculating K_{rel}: As [HG2] and [HG1] can be determined by integrating the initial and resultant cage peaks and multiplying their ratio by $[HG1_0]$. $[G2]_0$ is the added anion, while $[G1]_0$ is OTf^-, K_{rel} can then be calculated.

$$k_{rel} = \frac{[HG2]([G1]_0 - [HG1])}{[HG1]([G2]_0 - [HG2])}$$

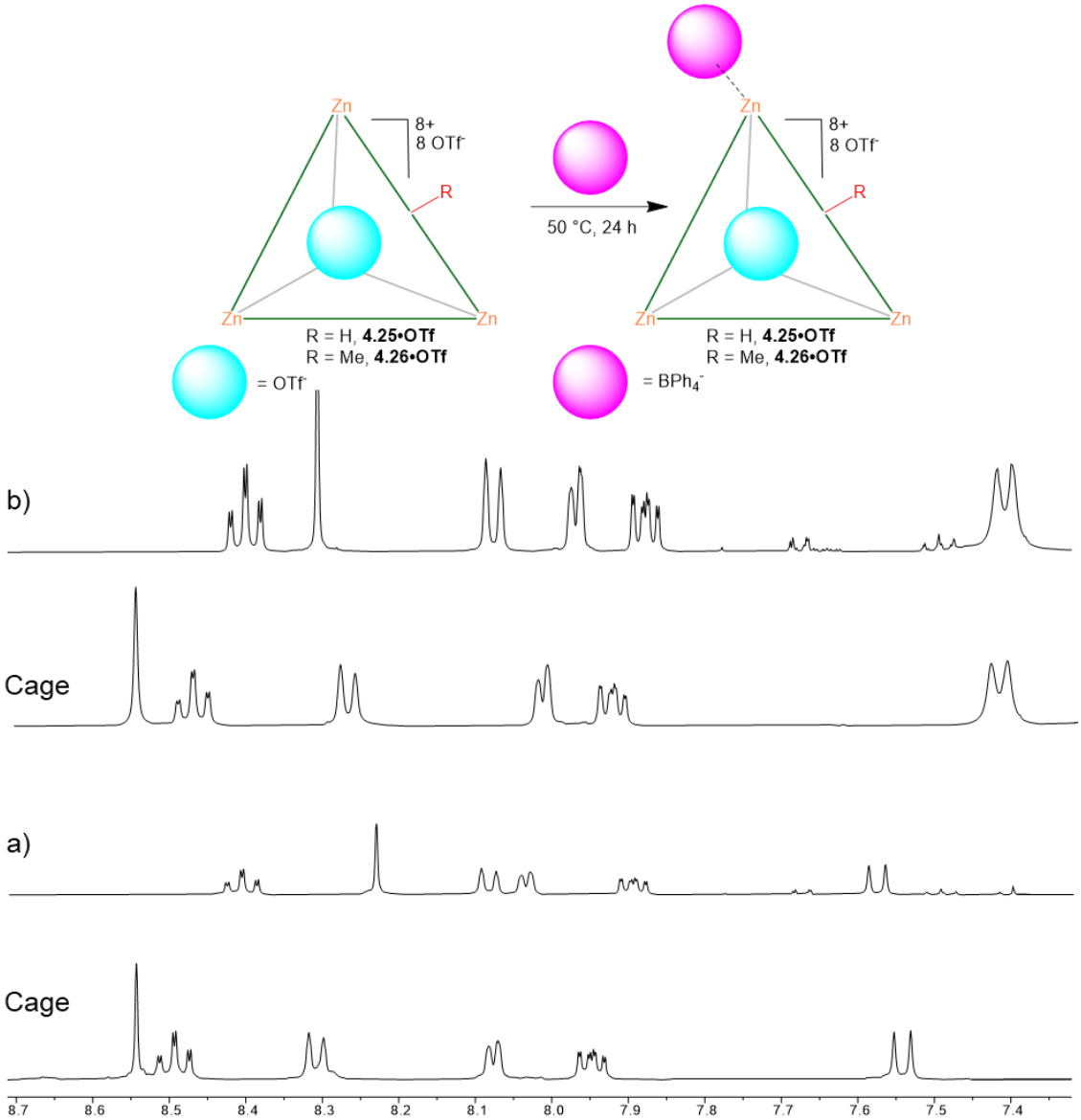

Figure 6.88. ^{1}H NMR (CD_3CN, 400 MHz, 298 K) spectra of a) **4.26•OTf** (1 mM) in the presence of BPh_4^- (10 mM) heated at 50 °C overnight; b) **4.25•OTf** (1 mM) in the presence of BPh_4^- (10 mM) heated at 50 °C overnight; demonstrating binding is on the pyridyl corners of the cage.

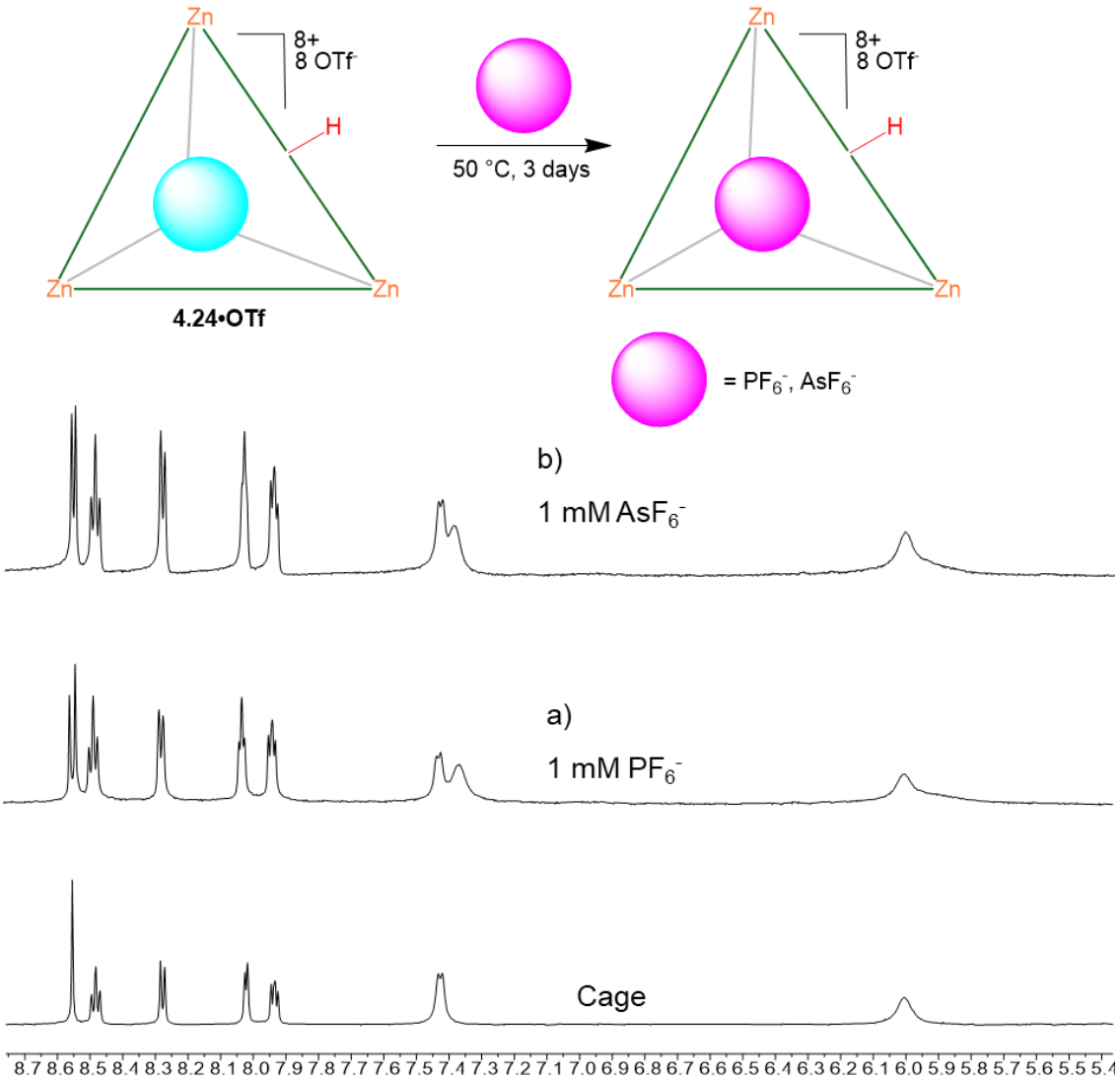

Figure 6.89. ^{1}H NMR (CD_3CN, 400 MHz, 298 K) spectra of a) **4.24•OTf** (1 mM) in the presence of PF_6^- (1 mM); b) **4.24•OTf** (1 mM) in the presence of AsF_6^- (1 mM) heated at 50 °C for 3 days.

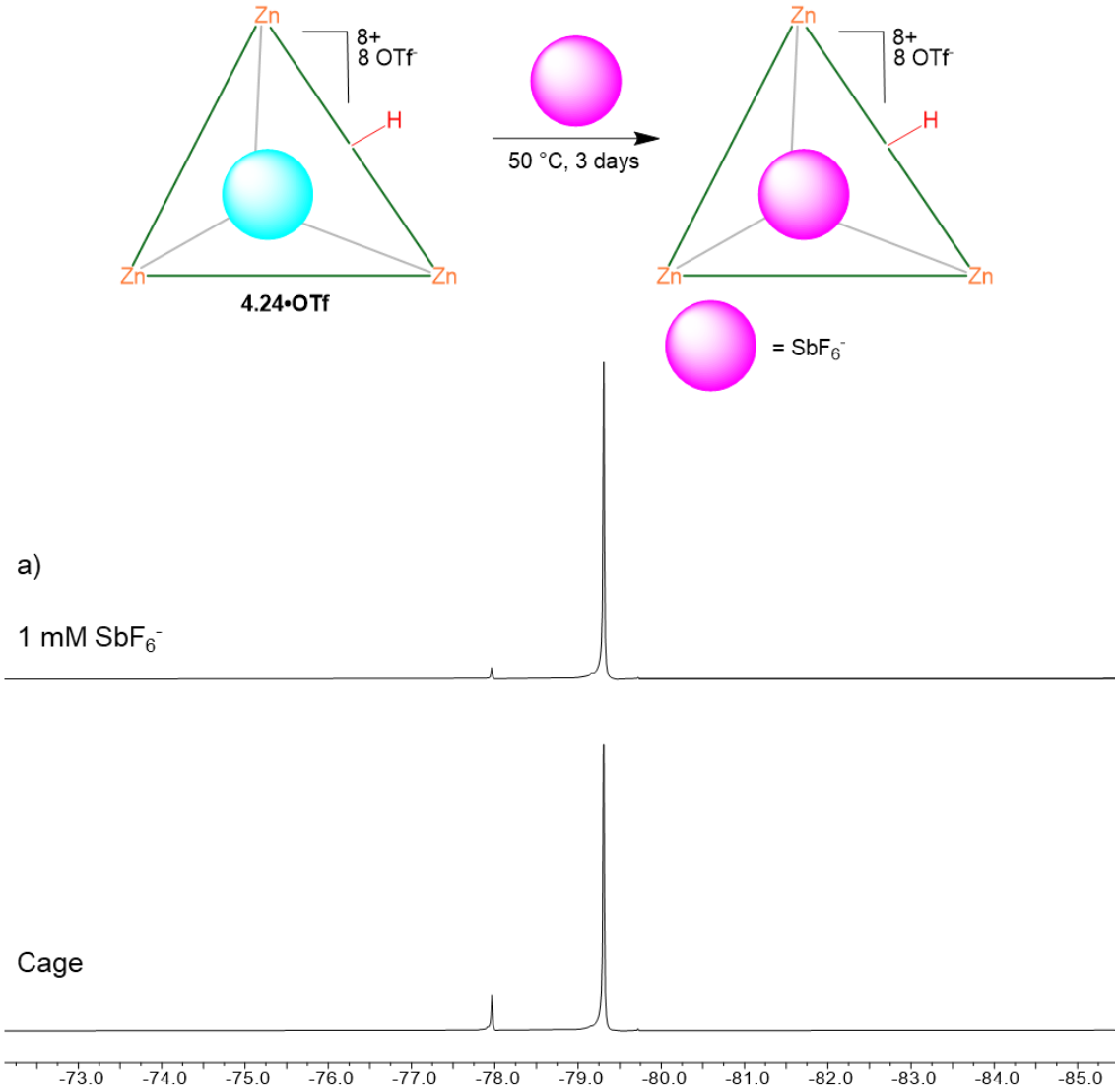

Figure 6.90. Expansion of ^{19}F NMR (CD_3CN, 151 MHz, 298 K) spectra of **4.24•OTf** (1 mM) in the presence of SbF_6^- (1 mM) heated at 50 °C for 3 days.

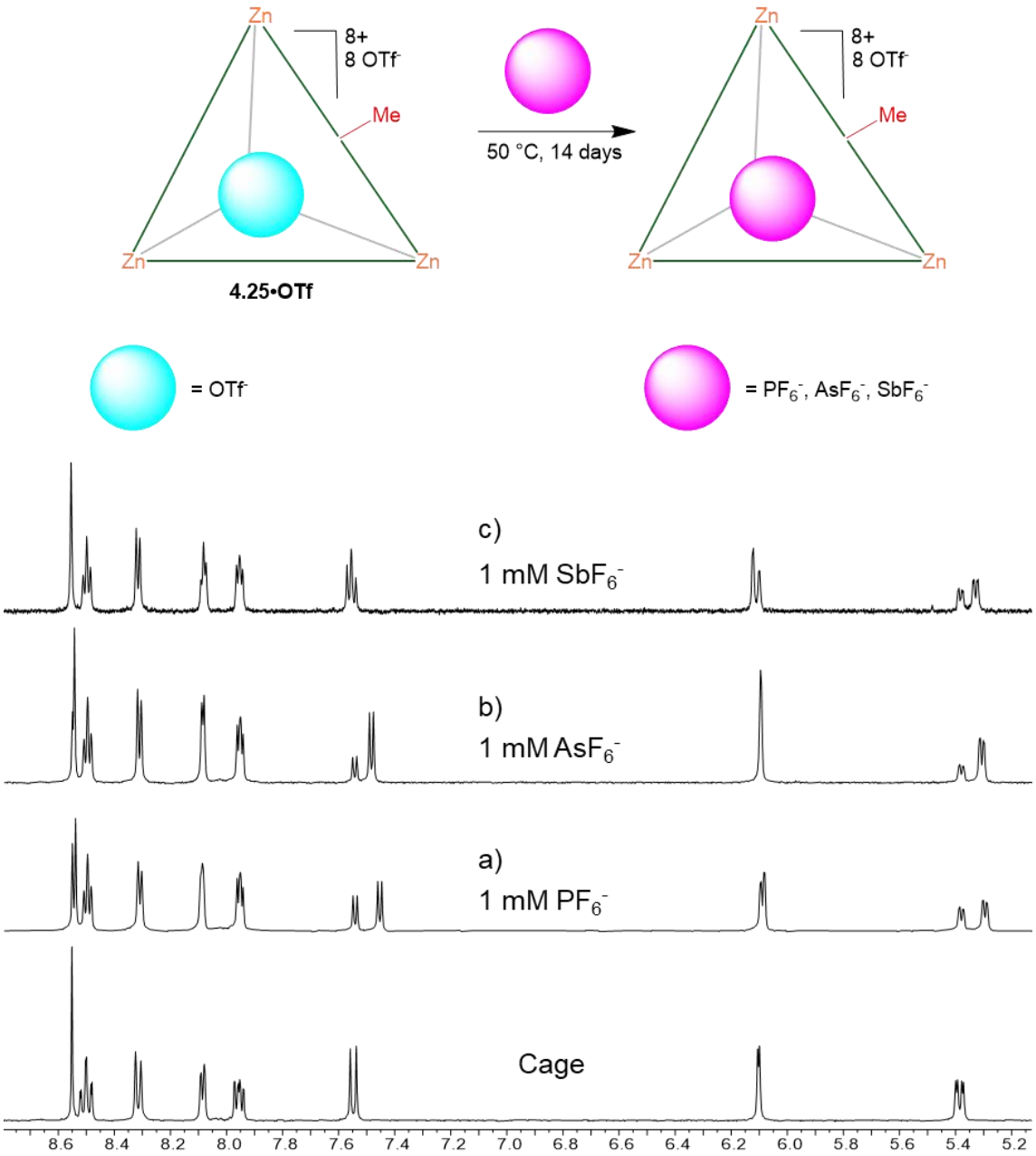

Figure 6.91. ^{1}H NMR (CD_3CN, 400 MHz, 298 K) spectra of a) **4.25•OTf** (1 mM) in the presence of PF_6^- (1 mM); b) **4.25•OTf** (1 mM) in the presence of AsF_6^- (1 mM); c) **4.25•OTf** (1 mM) in the presence of SbF_6^- (1 mM) heated at 50 °C for 14 days.

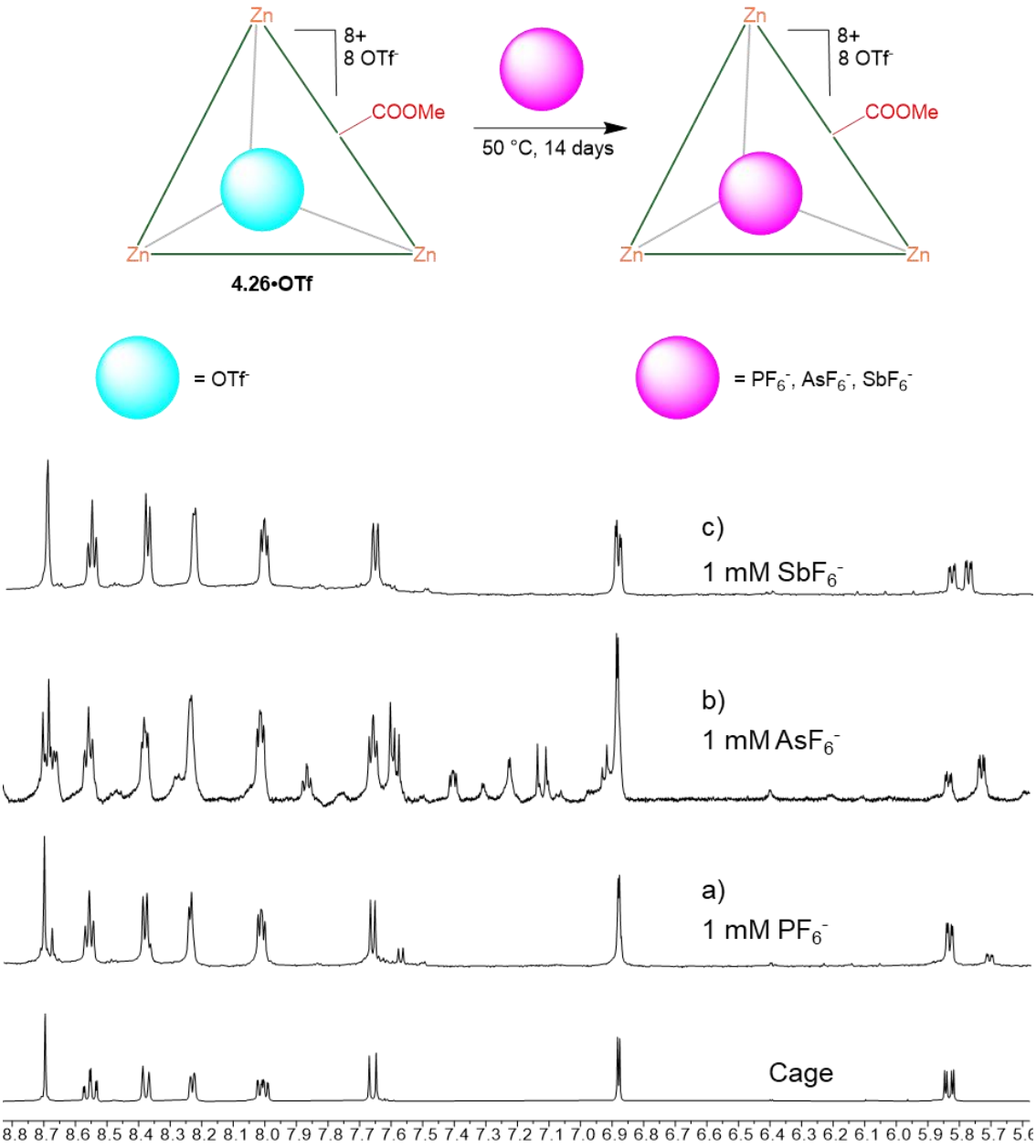

Figure 6.92. ^{1}H NMR (CD_3CN, 400 MHz, 298 K) spectra of a) **4.26•OTf** (1 mM) in the presence of PF_6^- (1 mM); b) **4.26•OTf** (1 mM) in the presence of AsF_6^- (1 mM); c) **4.26•OTf** (1 mM) in the presence of SbF_6^- (1 mM) heated at 50 °C for 14 days.

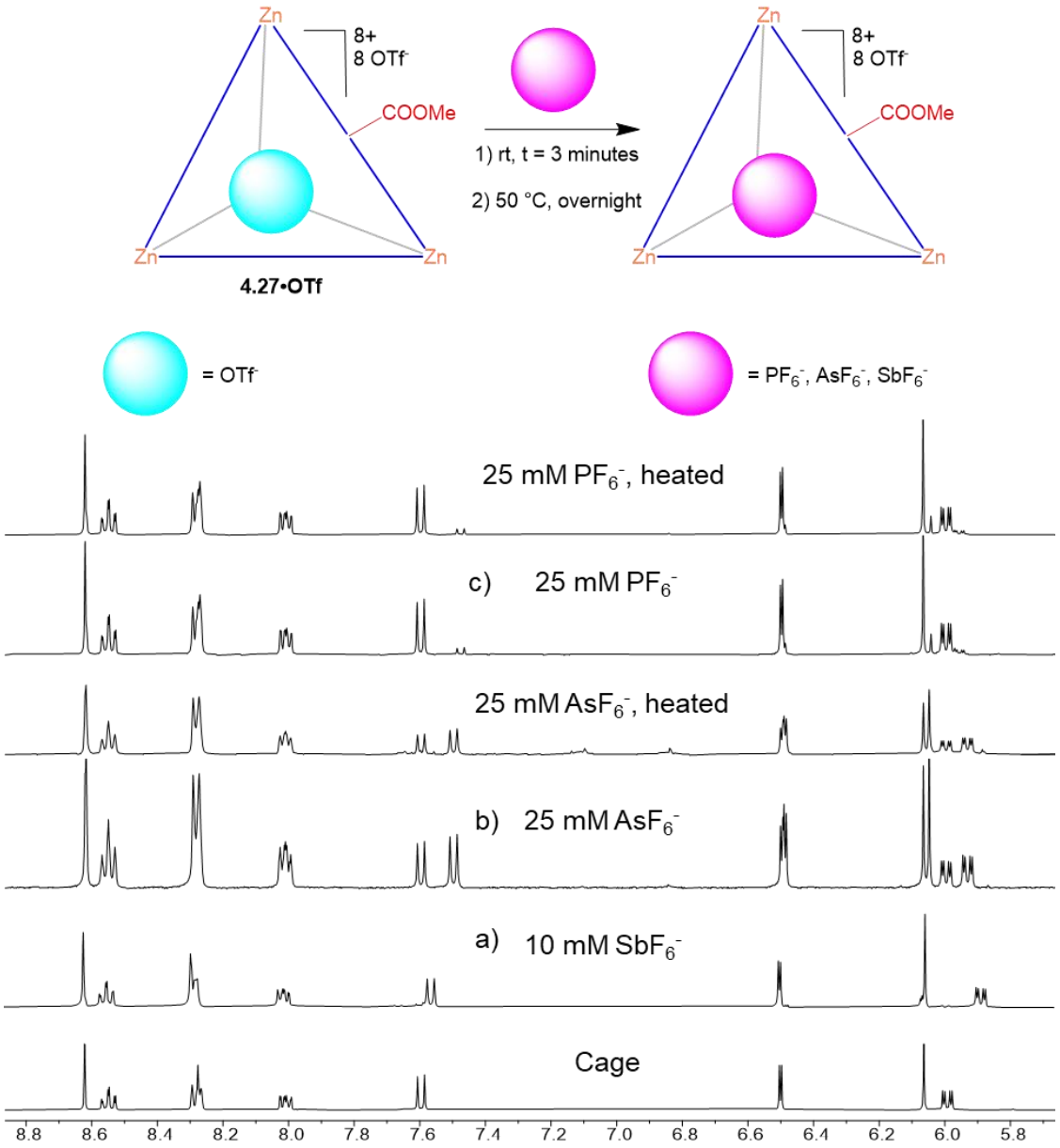

Figure 6.93. ^{1}H NMR (CD_3CN, 400 MHz, 298 K) spectra of a) **4.27•OTf** (1 mM) in the presence of SbF_6^- (10 mM), spectra was acquired after the addition of anion; b) **4.27•OTf** (1 mM) in the presence of AsF_6^- (25 mM), spectra was acquired after the addition of anion and then after heating overnight; c) **4.27•OTf** (1 mM) in the presence of PF_6^- (25 mM), spectra was acquired after the addition of anion and then after heating overnight.

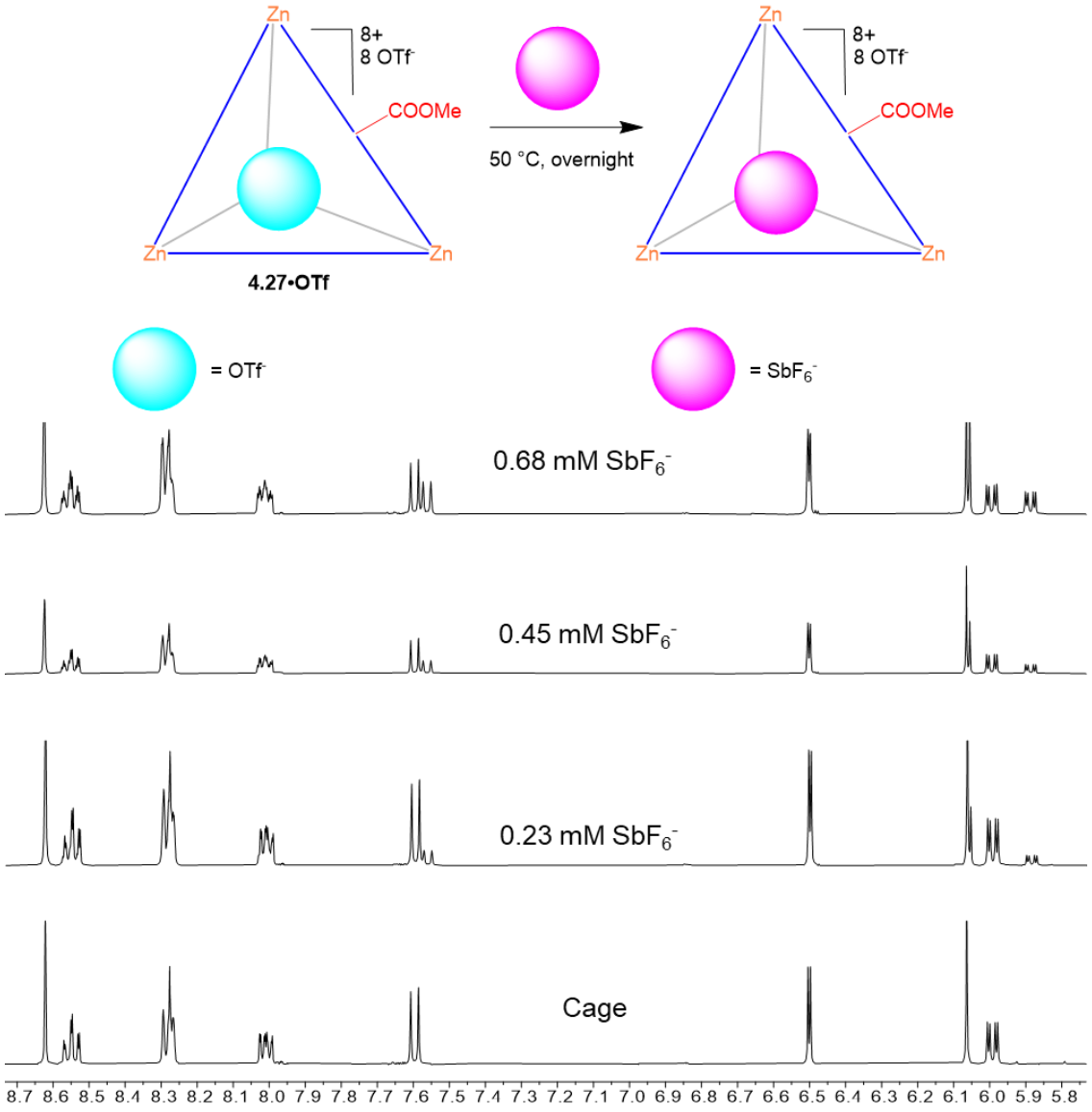

Figure 6.94. ^{1}H NMR (CD_3CN, 400 MHz, 298 K) spectra of the titration of SbF_6^- (0.23 – 0.68 mM) into a solution of **4.27•OTf** (1 mM) heated overnight to ensure equilibrium had been reached.

Exchange Rate Data for PnF_6^- Exchange with cages (4.9-4.11)•OTf

General procedure for determining exchange rates. Cage: guest solutions were formed in CD_3CN as described in section IV, placed into NMR tubes and the solutions heated at 50 ºC. After the specified timepoints, the solutions were removed from heat and ^1H and ^{19}F NMR spectra acquired at 23 ºC. Anion exchange proportions were determined by integration of the relevant NMR peaks.

Table 6.2. Rates of anion uptake for 1 mM solutions of cages **4.24-4.26•OTf** in the presence of 25 mM PnF_6^- anions.[a]

4.24•OTf		**4.25•OTf**		**4.26•OTf**	
Anion	Rate (mM/h)	Anion	Rate (mM/h)	Anion	Rate (mM/h)
PF_6^-	0.10	PF_6^-	0.05	PF_6^-	0.02
AsF_6^-	0.08	AsF_6^-	0.04	AsF_6^-	0.02
SbF_6^-	0.05	SbF_6^-	0.05	SbF_6^-	0.02

[a.] [**4.24-426**] = 1.0 mM; [PnF_6^-] = 25 mM, CD_3CN, 323 K.

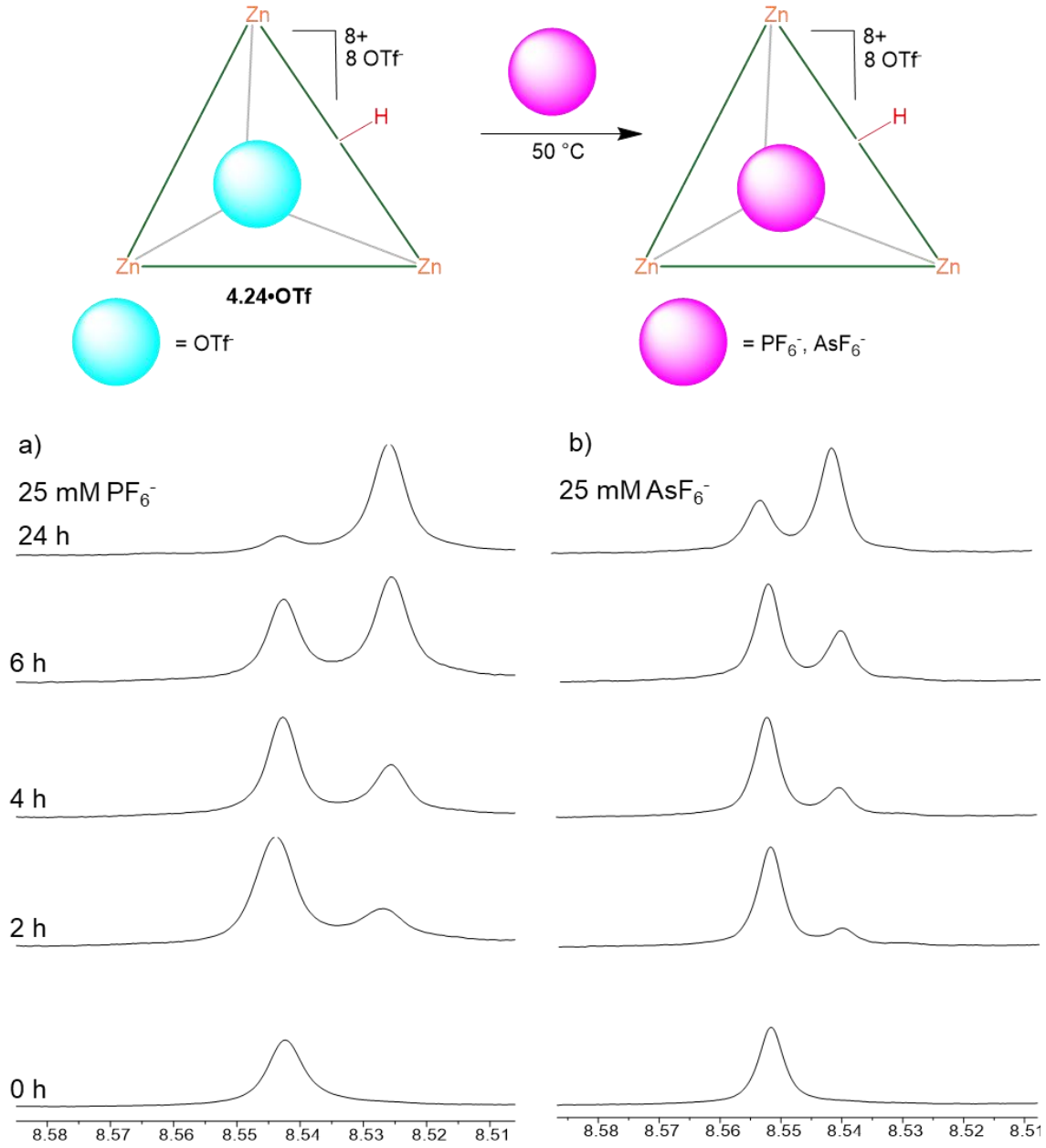

Figure 6.95. ^{1}H NMR (CD_3CN, 400 MHz, 298 K) spectra of **4.24•OTf** (1 mM) in the presence of a) jPF_6^- (25 mM); b) AsF_6^- (25 mM) heated at 50 °C and monitored over time.

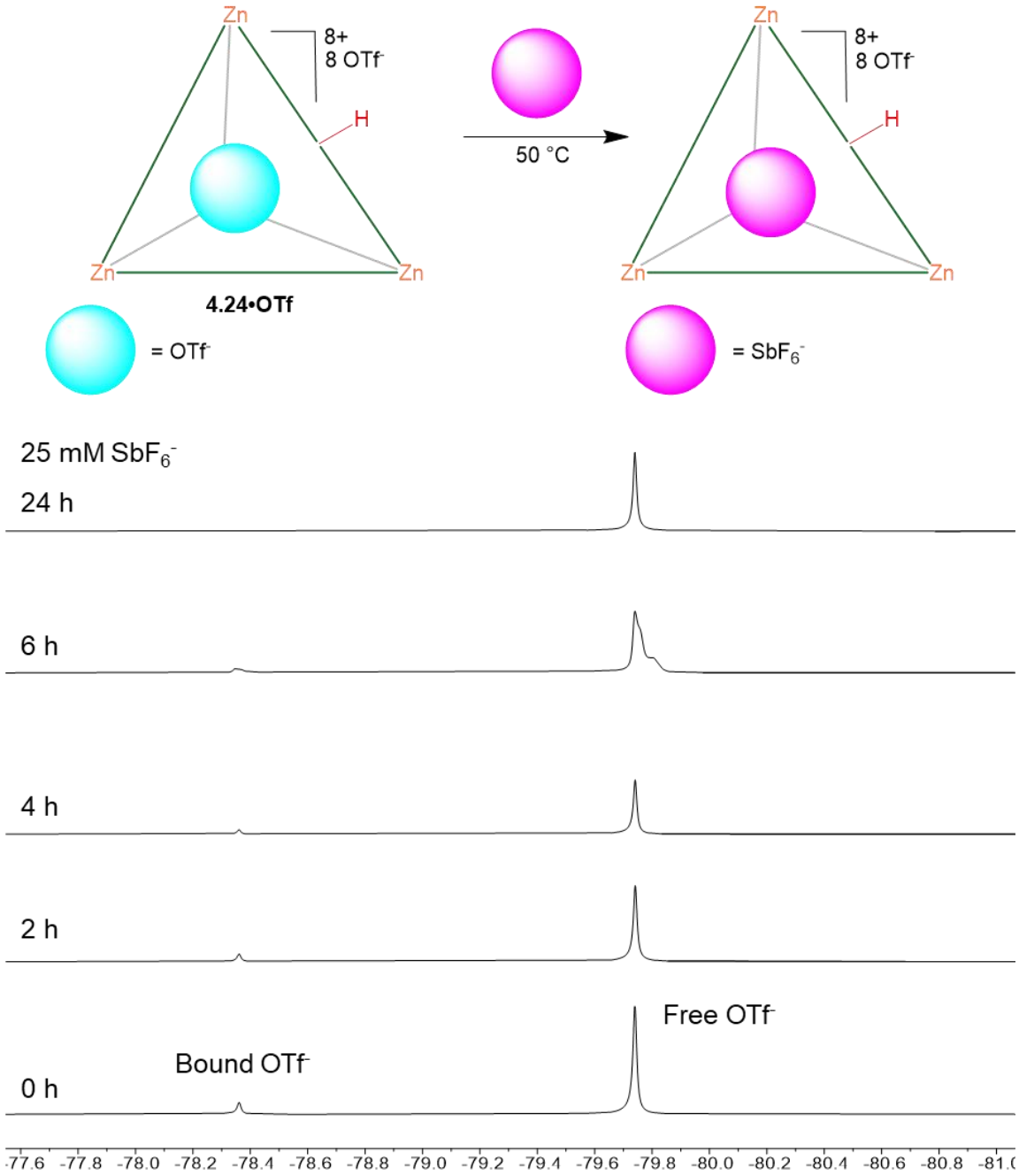

Figure 6.96. Expansion of the ^{19}F NMR (CD_3CN, 376 MHz, 298 K) spectra of **4.24•OTf** (1 mM) in the presence of SbF_6^- (25 mM) heated at 50 °C and monitored over time. ***Note:*** ^1H NMR analysis was ineffective at measuring the conversion of **4.24•OTf** to **4.24•SbF$_6$** due to the highly similar ^1H NMR spectrums of both cages.

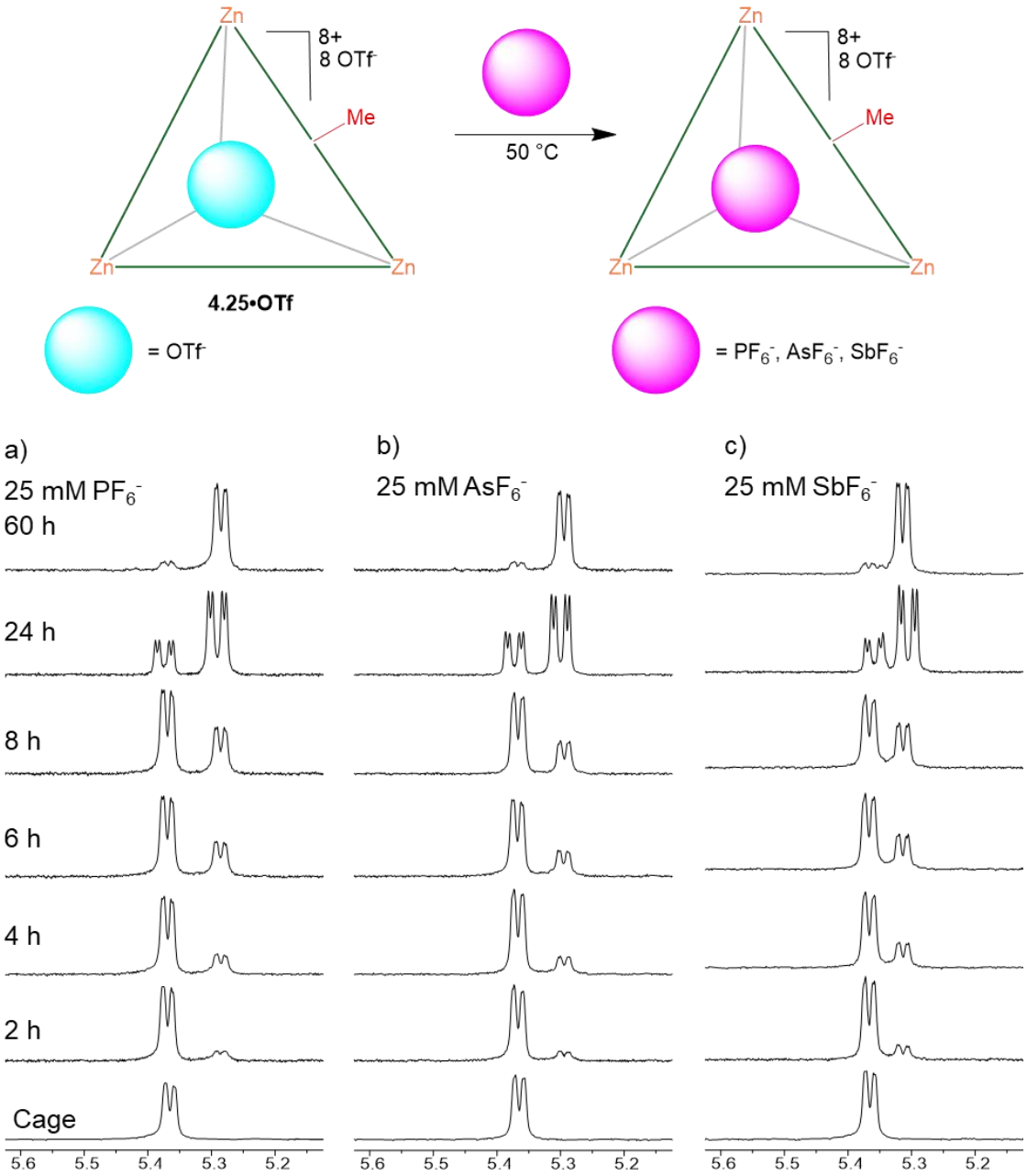

Figure 6.97. ^{1}H NMR (CD_3CN, 400 MHz, 298 K) spectra of **4.25•OTf** (1 mM) in the presence of a) PF_6^- (25 mM); b) AsF_6^- (25 mM); c) SbF_6^- (25 mM) heated at 50 °C and monitored over time.

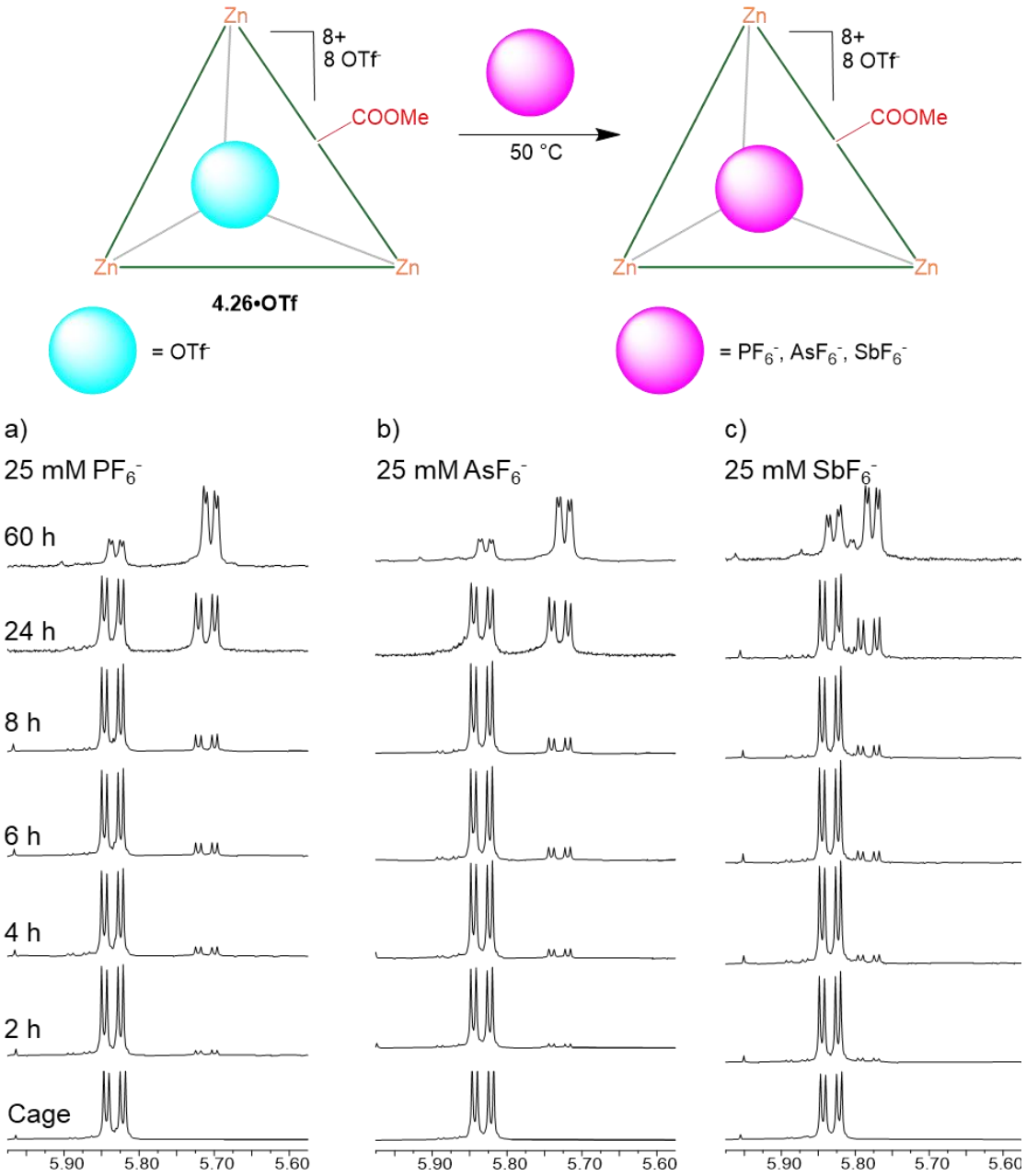

Figure 6.98. ^{1}H NMR (CD_3CN, 400 MHz, 298 K) spectra of **4.26•OTf** (1 mM) in the presence of a) PF_6^- (25 mM); b) AsF_6^- (25 mM); c) SbF_6^- (25 mM) heated at 50 °C and monitored over time.

Exchange Rate Data for AsF_6^- Exchange with (4.25-4.26)•OTf and (4.25-4.26)•SbF_6

Calculations: Concentration of the newly formed cage was calculated by integrating the initial and resultant cage peaks and multiplying their ratio by the initial concentration of cage.

Table 6.3. Rates of anion uptake for 1 mM solutions of cages **4.25-4.26•OTf** (1 mM) and **4.25-4.26•SbF_6** (1 mM) in the presence of AsF_6^- (25 mM).

Cage	Rate of **2/3**•AsF_6 formation (mM/h)
4.25•OTf	0.04
4.25•SbF_6	0.008
4.26•OTf	0.02
4.26•SbF_6	0.003

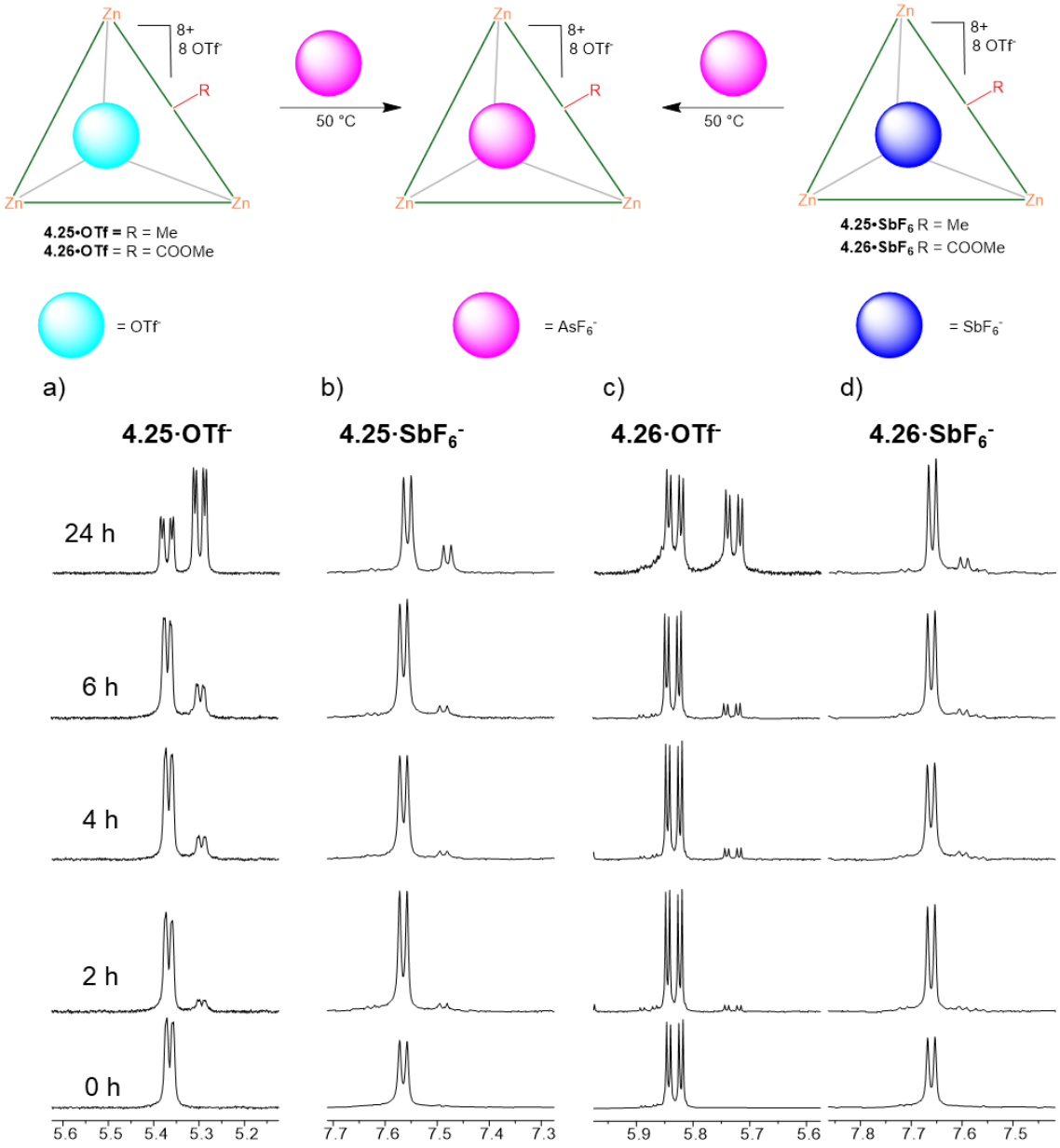

Figure 6.99. ^{1}H NMR (CD_3CN, 400 MHz, 298 K) spectra of a) **4.25•OTf** (1 mM) in the presence of AsF_6^- (25 mM); b) **4.25•SbF$_6$** (1 mM) in the presence of AsF_6^- (25 mM); c) **4.26•OTf** (1 mM) in the presence of AsF_6^- (25 mM), and d) **4.26•SbF$_6$** (1 mM) in the presence of AsF_6^- (25 mM), heated and monitored overtime.

Determination of Reaction Order with Respect to Incoming Anion

General procedure for mechanistic studies: 0.4 M solutions of $NaPnF_6$ anionic guests and 2 mM solutions of cage were prepared using CD_3CN. 200 µL of a stock solution of cage was added to an NMR tube. This solution was then diluted before the addition of the anion solution, with an appropriate volume of CD_3CN so that after the addition of the anion solution the desired concentrations of cage and anion would be obtained. For example, to obtain a 0.8 mM solution of cage with a 90 mM concentration of anion one would dilute a 200 µL solution of cage (2 mM) with 200 µL of CD_3CN followed by the addition of 90.0 µL of a solution of anion guest (0.4 M).

Calculations: Concentration of the newly formed cage was calculated by integrating the initial and resultant cage peaks and multiplying their ratio by the initial concentration of cage. Order was calculated *via* an algebraic approach comparing the ratio of the rate equations at two different concentrations.

$$\frac{\boldsymbol{Rate\,2}}{\boldsymbol{Rate\,1}} = \frac{\boldsymbol{k[HG1]^M[x_2]^N}}{\boldsymbol{k[HG1]^M[x_1]^N}} \rightarrow \frac{\boldsymbol{Rate\,2}}{\boldsymbol{Rate\,1}} = \frac{\boldsymbol{[x_2]^N}}{\boldsymbol{[x_1]^N}} \rightarrow \boldsymbol{Ln}\left(\frac{\boldsymbol{Rate\,2}}{\boldsymbol{Rate\,1}}\right) = \boldsymbol{nLn}\left(\frac{\boldsymbol{[x_2]}}{\boldsymbol{[x_1]}}\right) \rightarrow \boldsymbol{n} = \frac{\boldsymbol{Ln}\left(\frac{\boldsymbol{Rate\,2}}{\boldsymbol{Rate\,1}}\right)}{\boldsymbol{Ln}\left(\frac{\boldsymbol{[x_2]}}{\boldsymbol{[x_1]}}\right)}$$

Table 6.4. Rates of anion uptake for **4.25-4.26•OTf** (0.82 mM) with different concentrations of anionic guests.[a]

4.25•OTf

8 mM	Rate (mM/h)	25 mM	Rate (mM/h)	75 mM	Rate (mM/h)	Order
PF_6^-	0.016	PF_6^-	0.024	PF_6^-	0.028	0.2
AsF_6^-	0.023	AsF_6^-	0.034	AsF_6^-	0.044	0.3
SbF_6^-	0.018	SbF_6^-	0.062	SbF_6^-	0.090	0.7

4.26•OTf

8 mM	Rate (mM/h)	25 mM	Rate (mM/h)	75 mM	Rate (mM/h)	Order
PF_6^-	0.007	PF_6^-	0.015	PF_6^-	0.020	0.5
AsF_6^-	0.013	AsF_6^-	0.018	AsF_6^-	0.020	0.2
SbF_6^-	0.007	SbF_6^-	0.012	SbF_6^-	0.024	0.6

[a.] [**4.25-4.26•OTf**] = 0.8 mM; [PnF_6^-] = 8, 25, 75 mM, CD_3CN, 323 K.

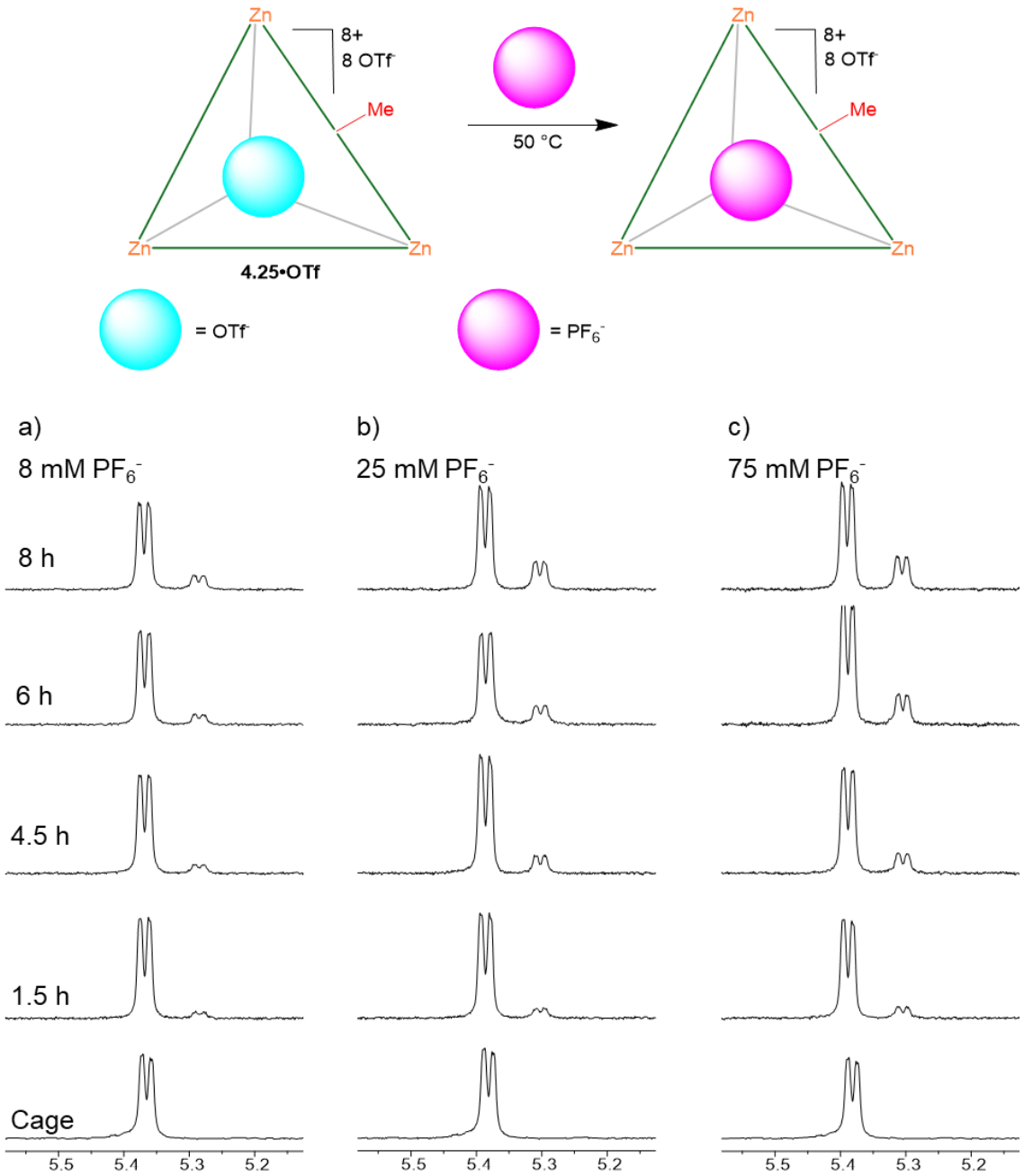

Figure 6.100. ^{1}H NMR (CD_3CN, 400 MHz, 298 K) spectra of **4.25•OTf** (0.82 mM) in the presence of a) PF_6^- (8 mM); b) PF_6^- (25 mM); c) PF_6^- (75 mM) heated at 50 °C and monitored over time.

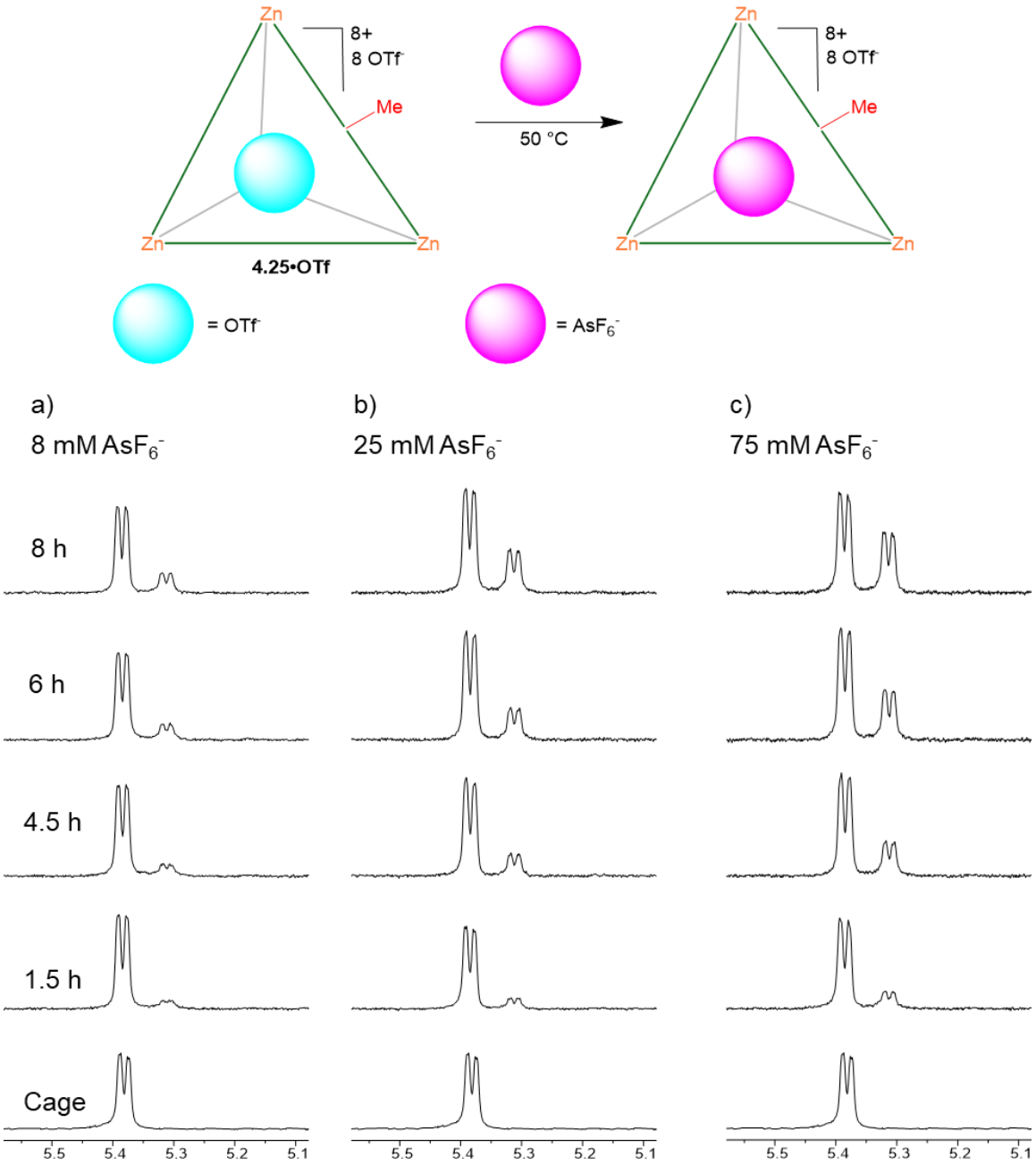

Figure 6.101. ^{1}H NMR (CD_3CN, 400 MHz, 298 K) spectra of **4.25•OTf** (0.82 mM) in the presence of a) AsF_6^- (8 mM); b) AsF_6^- (25 mM); c) AsF_6^- (75 mM) heated at 50 °C and monitored over time.

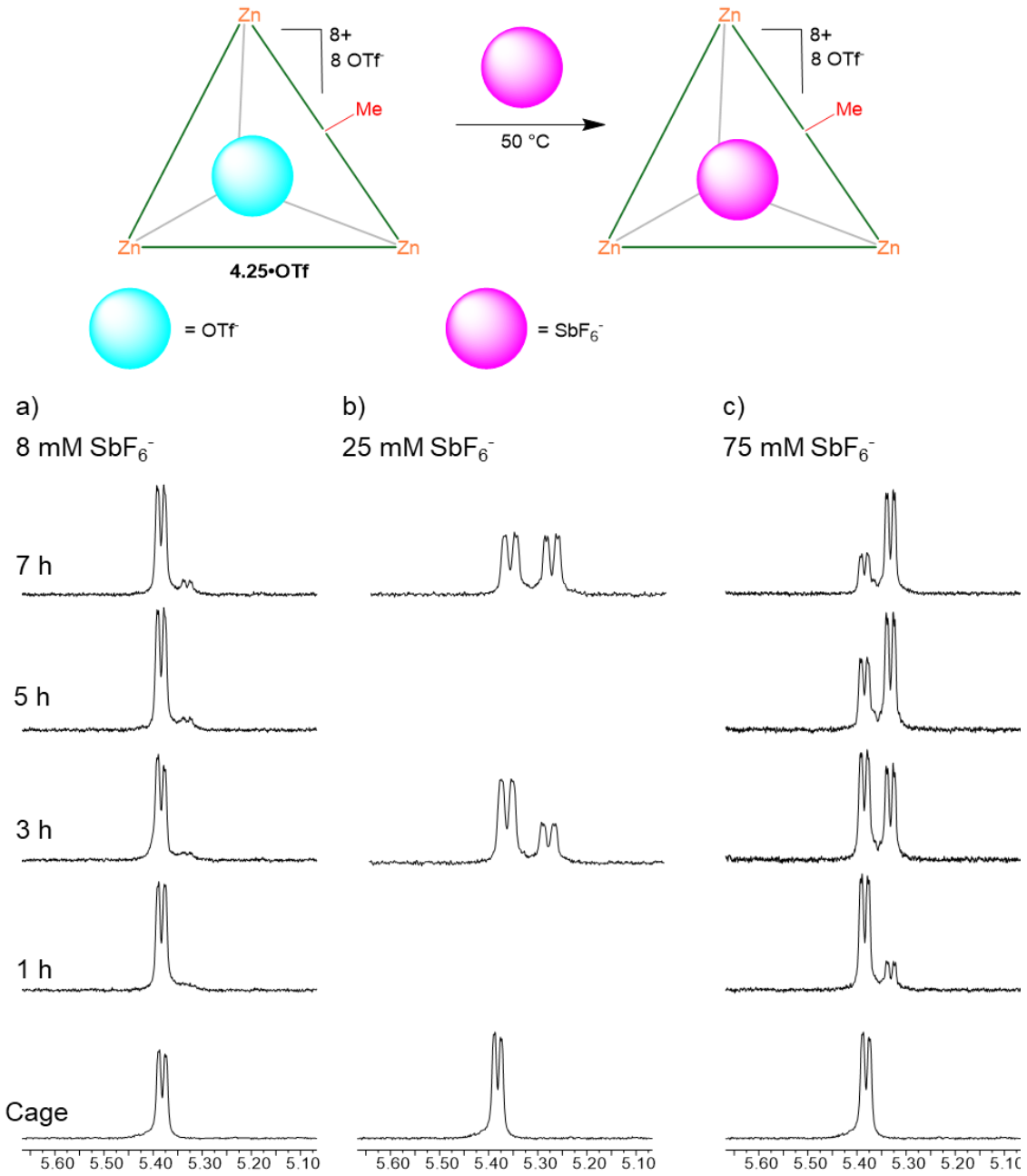

Figure 6.102. ^{1}H NMR (CD_3CN, 400 MHz, 298 K) spectra of **4.25•OTf** (0.82 mM) in the presence of a) SbF_6^- (8 mM); b) SbF_6^- (25 mM); c) SbF_6^- (75 mM) heated at 50 °C and monitored over time.

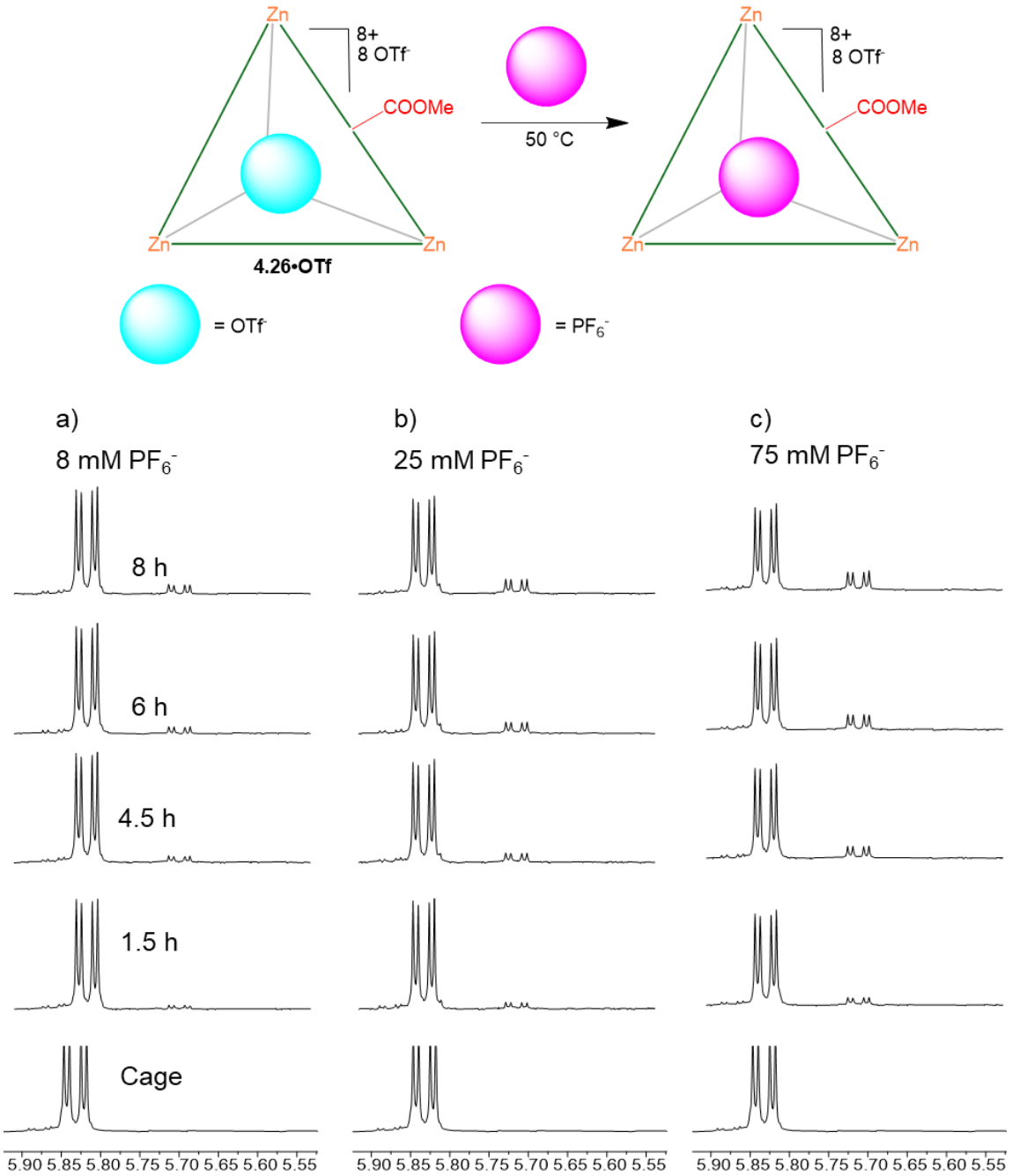

Figure 6.103. ^{1}H NMR (CD_3CN, 400 MHz, 298 K) spectra of **4.26•OTf** (0.82 mM) in the presence of a) PF_6^- (8 mM); b) PF_6^- (25 mM); c) PF_6^- (75 mM) heated at 50 °C and monitored over time.

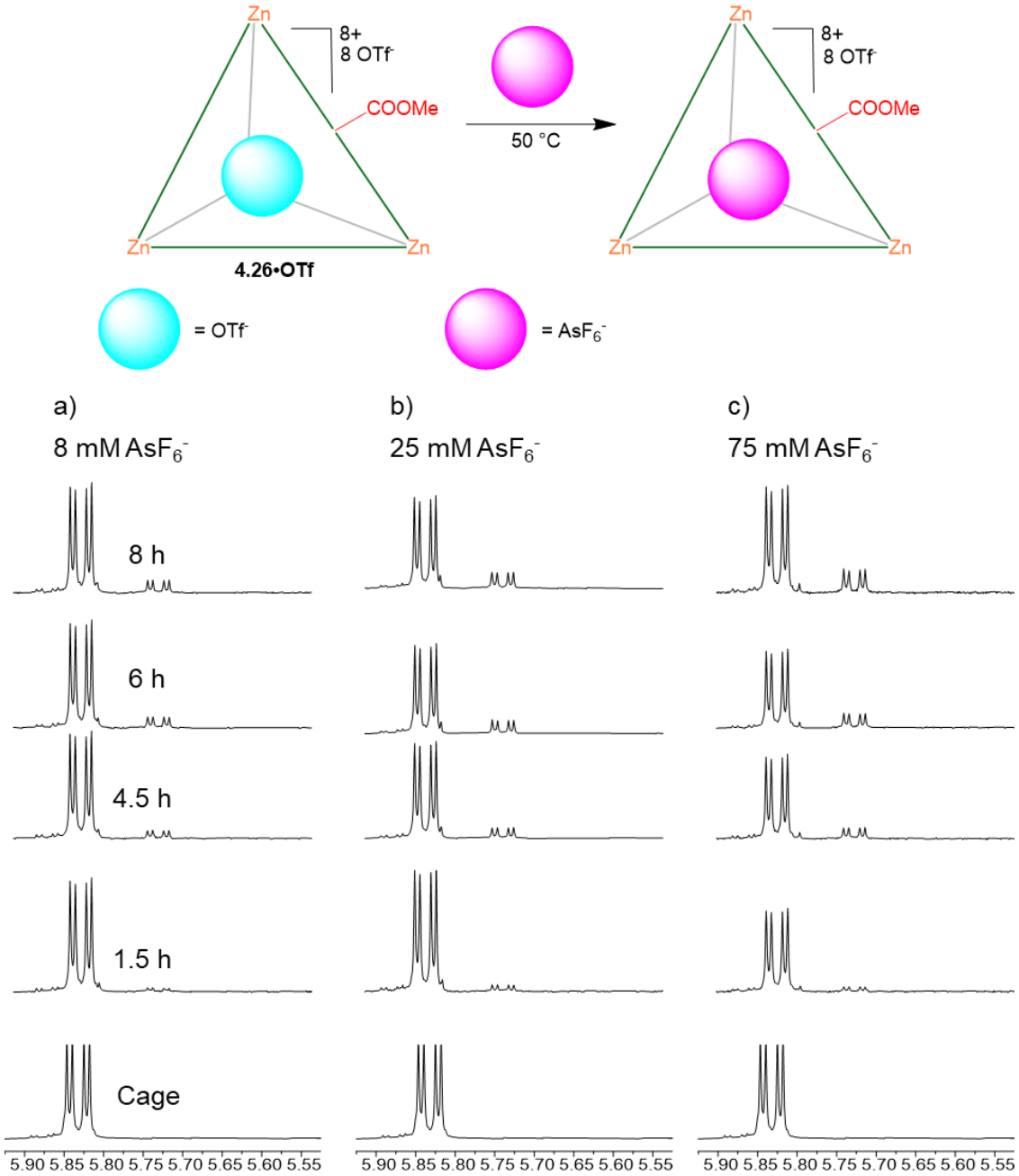

Figure 6.104. ^{1}H NMR (CD_3CN, 400 MHz, 298 K) spectra of **4.26•OTf** (0.82 mM) in the presence of a) AsF_6^- (8 mM); b) AsF_6^- (25 mM); c) AsF_6^- (75 mM) heated at 50 °C and monitored over time.

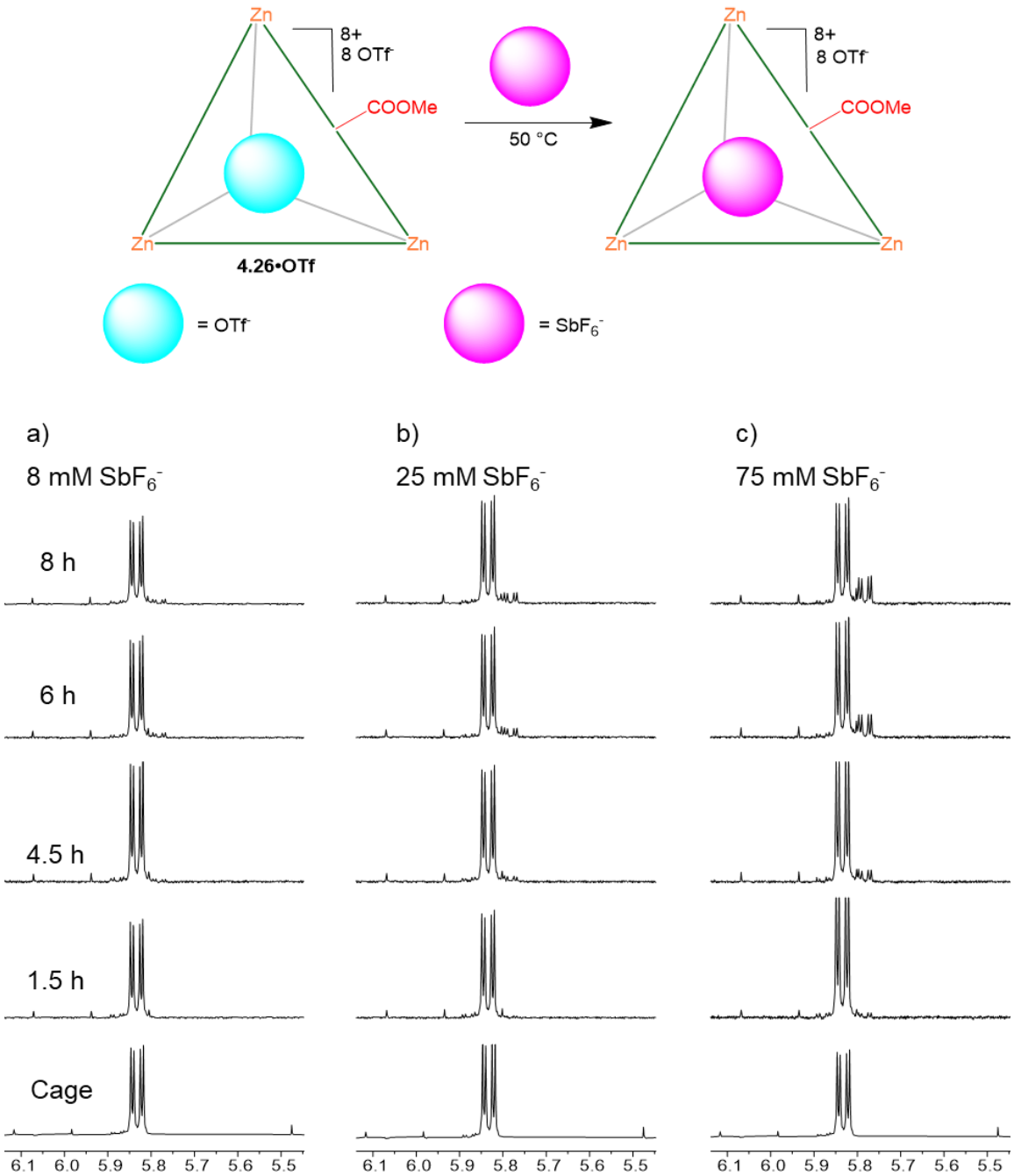

Figure 6.105. ^{1}H NMR (CD_3CN, 400 MHz, 298 K) spectra of **4.26•OTf** (0.82 mM) in the presence of a) SbF_6^- (8 mM); b) SbF_6^- (25 mM); c) SbF_6^- (75 mM) heated at 50 °C and monitored over time.

6.6. Crystallographic Analysis of Cage Fe-4.12•SbF_6

Data collection

Single crystals suitable for X-ray diffraction were grown by slow diffusion of diisopropyl ether into acetonitrile. A purple crystal (plate, approximate dimensions 0.25 × 0.19 × 0.1 mm^3) was placed onto the tip of a MiTeGen pin and mounted on a Bruker Venture D8 diffractometer equipped with a PhotonIII detector at 147.0 K. The data collection was carried out using Cu Ka radiation (l = 1.54178 Å, ImS micro-source) with a frame time of 15 seconds and a detector distance of 40 mm. A collection strategy was calculated and complete data to a resolution of 0.84 Å with a redundancy of 6.9 were collected. Crystals diffracted poorly, with intensity sharply dropping at high angles. For this reason, the data was integrated to 0.95 Å resolution using the Bruker SAINT software package with a narrow-frame algorithm. Data were corrected for absorption effects using the multi-scan method (SADABS). Please refer to Table 1 for additional crystal and refinement information. X-ray data has been deposited with the CCDC (CCDC 2213841).

Structure solution and refinement

The space group P-1 was determined based on intensity statistics and systematic absences. The structure was solved using the SHELX suite of programs[8,9] and refined using full-matrix least-squares on F^2 within the OLEX2 suite. An intrinsic phasing solution was calculated, which provided most non-hydrogen atoms from the E-map. Full-matrix least squares / difference Fourier cycles were performed, which located the remaining non-hydrogen atoms. All non-hydrogen atoms were refined with anisotropic displacement parameters, with the exception of some of the perchlorate and hexafluoroantimonate

anions. The hydrogen atoms were placed in ideal positions and refined as riding atoms with relative isotropic displacement parameters. The final full matrix least squares refinement converged to $R1 = 0.2093$ and $wR2 = 0.5297$ (F^2, all data). The goodness-of-fit was 1.474. On the basis of the final model, the calculated density was 1.540 g/cm^3 and F(000), 4950 e^{-1}. The compound is a molecular cage with 260 non-hydrogen atoms, a cavity with a host molecule, and several disordered counterion molecules. Attempts to grow better crystals were unsuccessful.

Table 6.5. Crystal data and structure refinement for Fe-4.28•SbF_6.

Empirical formula	C_{192} H_{142} $Cl_{3.92}$ $F_{24.51}$ Fe_4 N_{24} $O_{51.66}$ $Sb_{4.09}$	
Formula weight	4937.86	
Crystal color, shape, size	purple plate, 0.25 × 0.19 × 0.1 mm^3	
Temperature	147.0 K	
Wavelength	1.54178 Å	
Crystal system, space group	Triclinic, P-1	
Unit cell dimensions	a = 22.1047(16) Å	a = 91.048(6)°.
	b = 22.9465(18) Å	b = 105.276(5)°.
	c = 23.878(2) Å	□ = 113.021(5)°.
Volume	10652.1(15) Å^3	
Z	2	
Density (calculated)	1.540 g/cm^3	
Absorption coefficient	7.522 mm^3	
F(000)	4950	
Data collection		
Diffractometer	Bruker D8 Venture	
Theta range for data collection	2.272 to 54.605°.	
Index ranges	-23<=h<=23, -24<=k<=24, -25<=l<=24	
Reflections collected	78643	
Independent reflections	23288 [R_{int} = 0.2108]	
Observed Reflections	8951	

Completeness to θ = 54.605°	88.2 %
Solution and Refinement	
Absorption correction	Semi-empirical from equivalents
Max. and min. transmission	0.7507 and 0.3912
Solution	Intrinsic methods
Refinement method	Full-matrix least-squares on F^2
Weighting scheme	$w = [s^2Fo^2 + AP^2 + BP]^{-1}$, with $P = (Fo^2 + 2\,Fc^2)/3$, A = 0.200, B = 0.000
Data / restraints / parameters	23288 / 4141 / 2619
Goodness-of-fit on F^2	1.474
Final R indices [I>2s(I)]	$R1$ = 0.2093, $wR2$ = 0.4512
R indices (all data)	$R1$ = 0.3692, $wR2$ = 0.5297
Largest diff. peak and hole	1.852 and -1.226 e.Å^{-3}

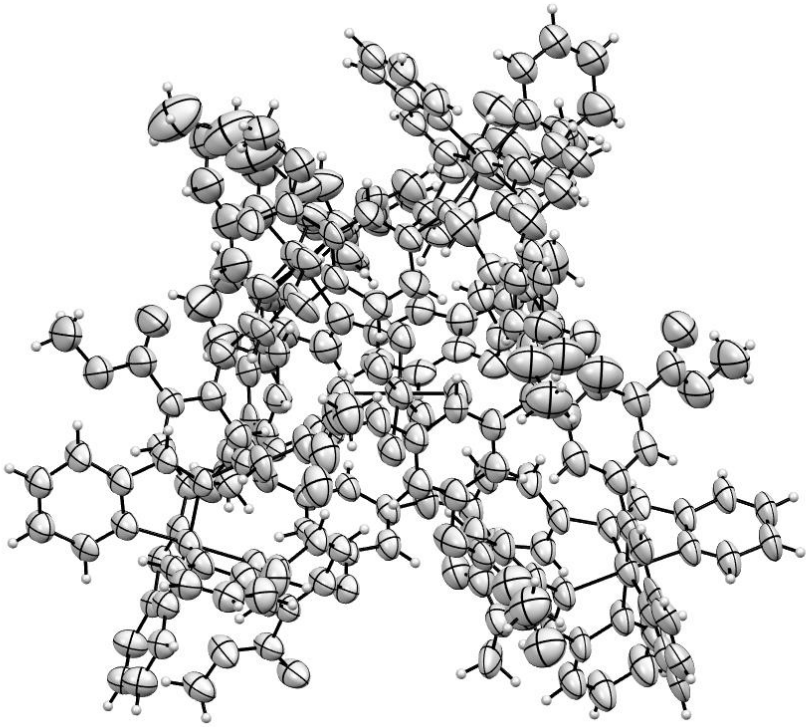

Figure 6.106. ORTEP structure of **Fe-4.28•SbF_6** (slow diffusion of diisopropyl ether into a solution of acetonitrile, diffracted at 147.0 K).

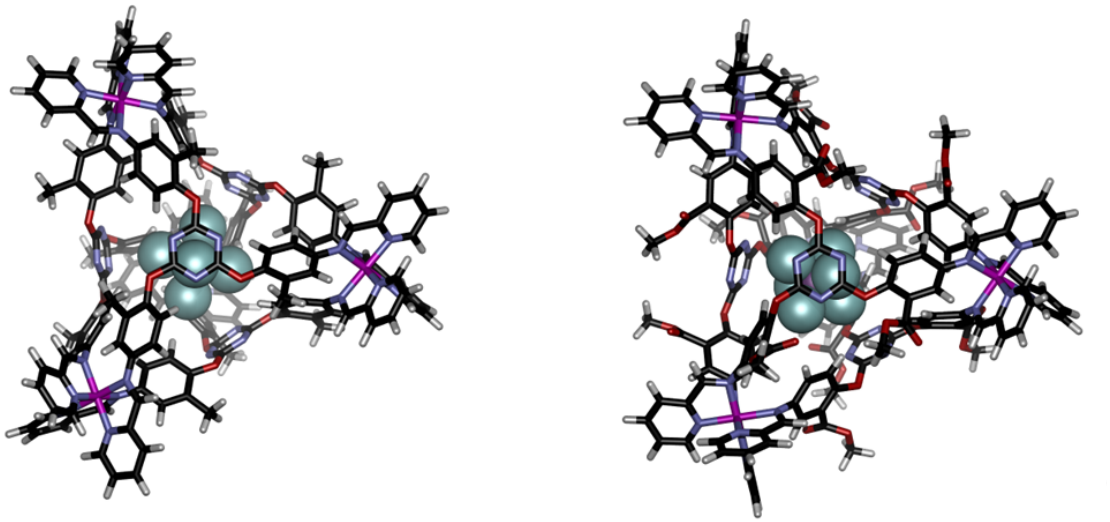

Figure 6.107. a) Spartan minimized representation of **4.25•SbF_6** and b) Minimized representation of **4.26•SbF_6** (SPARTAN 06, geometry optimization, 3-21G basis set).

6.7. Experimental Chapter 5

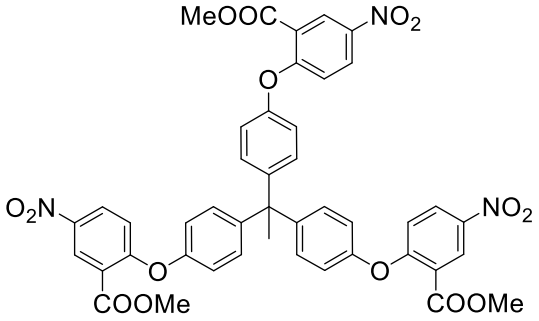

Synthesis of trimethyl 6,6',6''-((ethane-1,1,1-triyltris(benzene-4,1-diyl))tris(oxy))tris(3-nitrobenzoate): 5.3

4,4',4''-(ethane-1,1,1-triyl)triphenol (**5.1**) (306 mg, 1.00 mmol) was added to a flame dried 25 mL round bottom flask equipped with a magnetic stir bar, followed by DMF (3.00 mL), triethylamine (0.5 mL, 4.00 mmol, 4 mol.-eq.), and methyl-2-fluoro-5-nitrobenzoate (796 mg, 4.00 mmol, 4 mol.-eq.). The reaction was brought to 100 °C in a sand bath and allowed to stir overnight. The following day the flask was removed from the sand bath and allowed to cool to room temperature. The reaction was diluted with 50 mL of CH_2Cl_2 and washed with 5 x 10 mL of H_2O followed by 3 x 15 mL of brine before being dried over sodium sulfate. The dried solution was then decanted, and the solvent was removed under reduced pressure. A ^1H NMR spectrum was taken of the crude material to confirm a majority of the DMF had been removed, which revealed a complex mixture of various addition products. The crude was then purified *via* column chromatography using dichloromethane yielding **5.3** as an off-white powder (220 mg, 26 %), R_f = 0.4 (CH_2Cl_2). ^1H NMR (400 MHz, $CDCl_3$) δ 8.82 (d, *J* = 2.9 Hz, 3H), 8.29 (dd, *J* = 9.2, 2.9 Hz, 3H), 7.20 (d, *J* = 2.9 Hz, 7H), 7.06 (d,

J = 2.9, 7H), 7.01 (d, J = 9.1 Hz, 3H), 3.97 (s, 9H), 2.27 (s, 3H). $^{13}C\{^1H\}$ NMR (151 MHz, $CDCl_3$) δ 163.07, 160.95, 152.24, 144.59, 141.15, 129.43, 127.42, 127.00, 121.09, 118.75, 117.11, 59.38, 51.76, 50.61. HRMS (ESI-TOF) *m/z* calc[d] for $C_{44}H_{33}N_3O_{15}Na$ ([M+Na^+]): 866.1804; found 866.1777. IR (neat) ν_{max} (cm^{-1}) 3007, 2966, 1743, 1717, 1707, 1528, 1443, 1372, 1343, 1258, 1248, 1201, 1128, 1092, 801, 741.

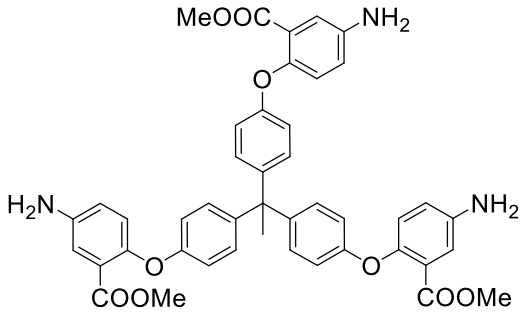

Synthesis of trimethyl 6,6',6''-((ethane-1,1,1-triyltris(benzene-4,1-diyl))tris(oxy))tris(3-aminobenzoate): 5.4

Ligand precursor (**5.3**) (100 mg, 0.12 mmol) was added to a 25 mL pear-shaped flask, followed by methanol (2.0 mL) and dichloromethane (18.0 mL), and then 10 % Pd/C (24.0 mg, 0.17 mmol). The flask was capped with a rubber septum and put under an atmosphere of H_2 and allowed to stir at room temperature overnight. The following day the solution was filtered over a small celite plug, the flask was washed with ~ 30 mL of methanol and poured through a celite plug. The solvent of the filtrate was removed under reduced pressure yielding ligand **5.4** as a tan powder that was used without further purification (67 mg, 75 %). ^1H NMR (400 MHz, $CDCl_3$) δ 7.23 (d, J = 3.0 Hz, 3H), 6.97 (d, J = 12 Hz,

6H), 6.92 (d, J = 8.0 Hz, 3H), 6.83 (dd, J = 8.6, 2.9 Hz, 3H), 6.77 (d, J = 12 Hz, 6H), 3.76 (s, 9H), 2.10 (s, 3H). $^{13}C\{^{1}H\}$ NMR (151 MHz, $CDCl_3$) δ 166.18, 157.16, 147.49, 142.86, 129.66, 124.22, 123.64, 120.27, 117.31, 115.78, 52.15, 50.84. HRMS (ESI-TOF) *m/z* calc[d] for $C_{44}H_{39}N_3NaO_9Na$ ([M+Na$^+$]): 776.2579; found 776.2576. IR (neat) ν_{max} (cm^{-1}) 3223, 3124, 2960, 1745, 1702, 1564, 1536, 1437, 1366, 1335, 1279, 1261, 1208, 1119, 1080, 807, 726.

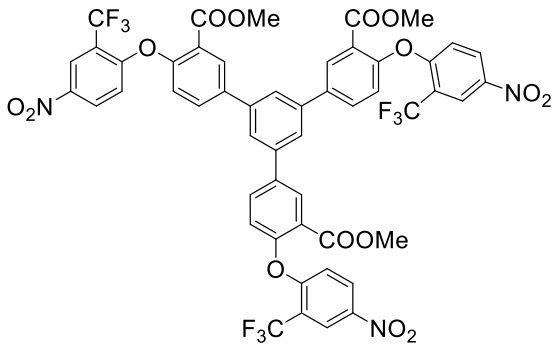

Synthesis of dimethyl 5'-(3-(methoxycarbonyl)-4-(4-nitro-2-(trifluoromethyl)phenoxy)phenyl)-4,4''-bis(4-nitro-2-(trifluoromethyl)phenoxy)-[1,1':3',1''-terphenyl]-3,3''-dicarboxylate: 5.8

Dimethyl 4,4''-dihydroxy-5'-(4-hydroxy-3-(methoxycarbonyl)phenyl)-[1,1':3',1''-terphenyl]-3,3''-dicarboxylate (**5.7**) (528 mg, 1.00 mmol) was added to a flame dried 25 mL round bottom flask equipped with a magnetic stir bar, followed by DMF (1.00 mL), triethylamine (0.43 mL, 3.10 mmol), and 1-fluoro-4-nitro-2-(trifluoromethyl)benzene (650 mg, 3.10 mmol). The reaction was brought to 100 °C in a sand bath and allowed to stir overnight. The following day the flask was removed from the sand bath and allowed to cool to room temperature. The reaction was diluted with 50 mL of CH_2Cl_2 and washed with

5 x 10 mL of H_2O followed by 3 x 15 mL of brine before being dried over sodium sulfate. The dried solution was then decanted, and the solvent was removed under reduced pressure. A ^1H NMR spectrum was taken of the crude material to confirm a majority of the DMF had been removed, which revealed a complex mixture of both starting materials and various addition products. The crude was then purified *via* column chromatography using dichloromethane yielding **5.8** as an off-white powder (300 mg, 30 %), Rf = 0.5 (DCM). ^1H NMR (400 MHz, $CDCl_3$) δ 8.66 (d, *J* = 2.7 Hz, 3H), 8.43 (d, *J* = 2.4 Hz, 3H), 8.34 (dd, *J* = 9.2, 2.8 Hz, 3H), 8.02 (dd, *J* = 8.4, 2.4 Hz, 3H), 7.91 (s, 3H), 7.37 (d, *J* = 8.4 Hz, 3H), 6.85 (d, *J* = 9.2 Hz, 3H), 3.81 (s, 9H).$^{13}C\{^1H\}$ NMR (151 MHz, $CDCl_3$) δ 164.78, 161.16, 152.13, 141.69, 140.82, 139.08, 133.23, 131.56, 128.84, 125.83, 124.78, 124.06, 123.98, 123.56, 120.07, 119.74, 115.53, 52.70. HRMS (ESI-TOF) *m/z* calc[d] for $C_{51}H_{31}F_9N_3O_{15}$ ($[M+H^+]$): 1096.1606; found 1096.1628. IR (neat) ν_{max} (cm^{-1}) 3098, 2952, 1724, 1627, 1589, 1542, 1479, 1337, 1271, 1133, 1115, 1046, 910, 857, 835, 758, 732, 708, 697, 673.

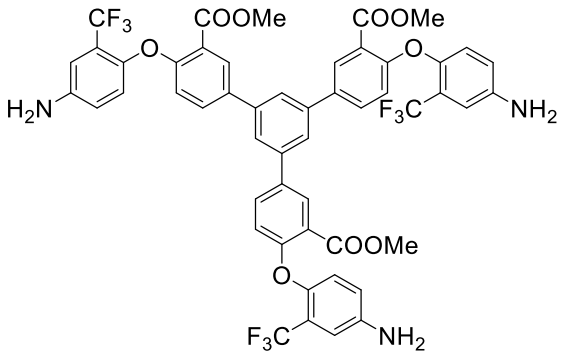

Synthesis of dimethyl 4,4''-bis(4-amino-2-(trifluoromethyl)phenoxy)-5'-(4-(4-amino-2-(trifluoromethyl)phenoxy)-3-(methoxycarbonyl)phenyl)-[1,1':3',1''-terphenyl]-3,3''-dicarboxylate: 5.11

Ligand precursor (**5.8**) (100 mg, 0.11 mmol) was added to a 25 mL pear-shaped flask, followed by methanol (20.0 mL), and then 10 % Pd/C (24.0 mg, 0.17 mmol). The flask was capped with a rubber septum and put under an atmosphere of H_2 and allowed to stir at room temperature overnight. The following day the solution was filtered over a small celite plug, the flask was washed with ~ 30 mL of methanol and poured through a celite plug. The solvent of the filtrate was removed under reduced pressure yielding ligand **5.11** as a tan powder that was used without further purification (70 mg, 80 %). ^{1}H NMR (400 MHz, $CDCl_3$) δ 8.21 (d, *J* = 2.4 Hz, 3H), 7.78 – 7.70 (m, 6H), 7.02 (d, *J* = 2.6 Hz, 3H), 6.97 (d, *J* = 8.6 Hz, 3H), 6.89 – 6.80 (m, 6H), 3.91 (s, 9H). ^{13}C{^{1}H} NMR (151 MHz, $CDCl_3$) δ 166.28, 156.56, 146.10, 142.51, 141.00, 135.61, 132.08, 130.49, 124.83, 124.51, 122.84, 122.69, 122.38, 121.80, 121.55, 119.30, 119.24, 113.24, 113.19, 52.35. HRMS (ESI-TOF) *m/z* calc[d] for $C_{51}H_{37}F_9N_3O_9$ ([M+H]$^+$):]$^+$): 1006.2381; found 1006.2837. IR (neat) ν_{max} (cm$^-$

[1]) 3473, 3365, 3215, 2958, 1722, 1633, 1489, 1445, 1340, 1265, 1234, 1212, 1127, 1078, 1046, 914, 880, 849, 821, 784, 675, 586, 545, 509, 497, 476.

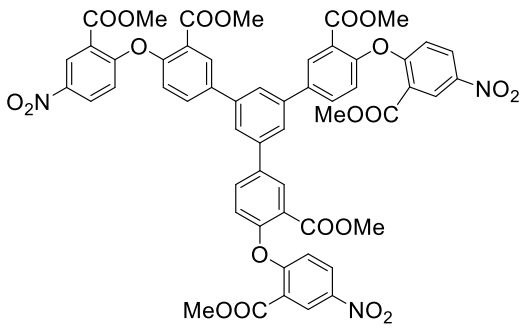

Synthesis of dimethyl 5'-(3-(methoxycarbonyl)-4-(2-(methoxycarbonyl)-4-nitrophenoxy)phenyl)-4,4''-bis(2-(methoxycarbonyl)-4-nitrophenoxy)-[1,1':3',1''-terphenyl]-3,3''-dicarboxylate: 5.9

Dimethyl 4,4''-dihydroxy-5'-(4-hydroxy-3-(methoxycarbonyl)phenyl)-[1,1':3',1''-terphenyl]-3,3''-dicarboxylate (**5.7**) (200 mg, 0.50 mmol) was added to a flame dried 25 mL round bottom flask equipped with a magnetic stir bar, followed by DMF (1.00 mL), triethylamine (0.43 mL, 3.1 mmol), and methyl 2-fluoro-5-nitrobenzoate (616 mg, 3.10 mmol). The reaction was brought to 100 °C in a sand bath and allowed to stir overnight. The following day the flask was removed from the sand bath and allowed to cool to room temperature. The reaction was diluted with 50 mL of CH_2Cl_2 and washed with 5 x 10 mL of H_2O followed by 3 x 15 mL of brine before being dried over sodium sulfate. The dried solution was then decanted, and the solvent was removed under reduced pressure. A ^1H NMR spectrum was taken of the crude material to confirm a majority of the DMF had been removed, which revealed a complex mixture of both starting materials and various addition

products. The crude was then purified *via* column chromatography using 0-5 % EtOAc/dichloromethane yielding **5.9** as an off-white powder (283 mg, 28 %), Rf = 0.2 (dichloromethane). ^{1}H NMR (400 MHz, $CDCl_3$) δ 8.87 (d, *J* = 2.8 Hz, 3H), 8.39 (d, *J* = 2.4 Hz, 4H), 8.28 (dd, *J* = 9.2, 2.9 Hz, 3H), 7.98 (dd, *J* = 8.4, 2.4 Hz, 3H), 7.88 (s, 3H), 7.32 (d, *J* = 8.4 Hz, 3H), 6.86 (d, *J* = 9.2 Hz, 3H), 4.01 (s, 9H), 3.81 (s, 9H).^{13}C{^{1}H} NMR (151 MHz, $CDCl_3$) δ 164.86, 164.03, 162.45, 142.07, 140.87, 138.41, 133.06, 131.37, 128.49, 128.07, 125.64, 124.28, 123.59, 121.44, 116.80, 52.83, 52.62. HRMS (ESI-TOF) *m/z* calc^{d} for $C_{54}H_{39}N_3O_{21}$ ([M+H$^+$]): 1066.2149; found 1066.2133. IR (neat) ν_{max} (cm^{-1}) 3120, 2962, 1720, 1613, 1585, 1522, 1479, 1445, 1344, 1263, 1133, 1068, 908, 856, 825, 808, 763.

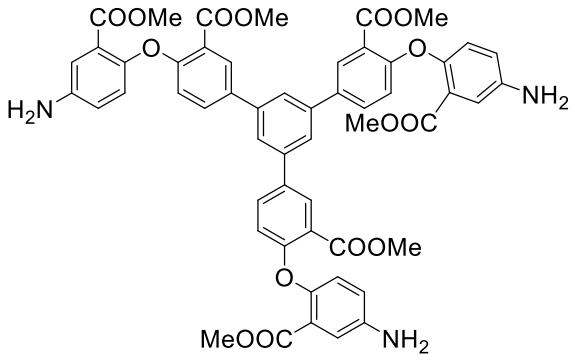

Synthesis of dimethyl 4,4''-bis(4-amino-2-(methoxycarbonyl)phenoxy)-5'-(4-(4-amino-2-(methoxycarbonyl)phenoxy)-3-(methoxycarbonyl)phenyl)-[1,1':3',1''-terphenyl]-3,3''-dicarboxylate: 5.12

Ligand precursor (**5.9**) (100 mg, 0.11 mmol) was added to a 25 mL pear-shaped flask, followed by methanol (20.0 mL), and then 10 % Pd/C (24.0 mg, 0.17 mmol). The flask was capped with a rubber septum and put under an atmosphere of H_2 and allowed to stir at room temperature overnight. The following day the solution was filtered over a small celite

plug, the flask was washed with ~ 30 mL of methanol and poured through a celite plug. The solvent of the filtrate was removed under reduced pressure yielding ligand **5.12** as a tan powder that was used without further purification (35 mg, 38 %). ^{1}H NMR (400 MHz, DMSO-*d*$_6$) δ 8.19 (d, *J* = 2.4 Hz, 3H), 7.98 (dd, *J* = 8.7, 2.5 Hz, 3H), 7.86 (s, 3H), 7.36 – 7.28 (m, 3H), 7.09 – 7.00 (m, 4H), 6.96 (d, *J* = 8.7 Hz, 4H), 6.82 (d, *J* = 9.1 Hz, 4H), 3.83 (s, 9H), 3.68 (s, 9H). ^{13}C{^{1}H} NMR (101 MHz, DMSO-*d*$_6$) δ 165.37, 164.57, 155.37, 150.37, 140.18, 137.28, 135.10, 132.62, 129.75, 122.83, 122.66, 121.45, 52.38, 52.29. HRMS (ESI-TOF) *m/z* calc^{d} for $C_{54}H_{47}N_3O_{15}$ ([M+H]$^{+}$): 976.2924; found 976.2912. IR (neat) ν_{max} (cm^{-1}) 3469, 3365, 2962, 2845, 1720, 1613, 1587, 1519, 1483 1322, 1272, 1103, 1068, 914, 855, 823, 811, 777, 693.

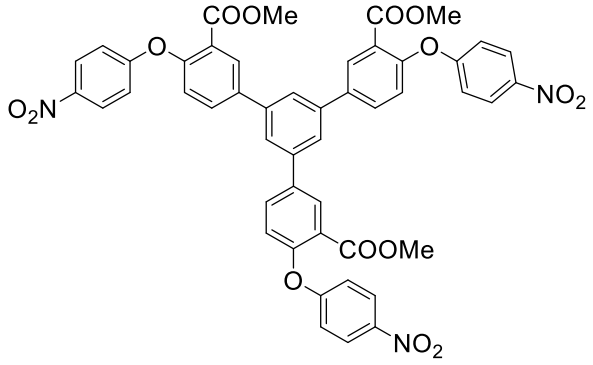

Synthesis of dimethyl 5'-(3-(methoxycarbonyl)-4-(4-nitrophenoxy)phenyl)-4,4''-bis(4-nitrophenoxy)-[1,1':3',1''-terphenyl]-3,3''-dicarboxylate: 5.10

Dimethyl 4,4''-dihydroxy-5'-(4-hydroxy-3-(methoxycarbonyl)phenyl)-[1,1':3',1''-terphenyl]-3,3''-dicarboxylate (**5.7**) (300 mg, 0.56 mmol) was added to a flame dried 25 mL two-neck round bottom flask equipped with a magnetic stir bar under an atmosphere

of N_2 through the reflux condenser equipped to the Schlenk manifold. Following the addition of DMF (1.00 mL) through a septum covering the second neck, the solution was allowed to stir and brought to 0 °C with an ice bath. KHMDS (1 M in toluene, 1.8 mL, 1.8 mmol) was added slowly *via* syringe *via* opening the second neck under a flux of N_2. The reaction was resealed and the solution was brought out of the ice bath and allowed to warm for 10 minutes. Following, 1-fluoro-4-nitrobenzene (253 mg, 1.8 mmol) was added slowly through the second neck under a flux of N_2 and then resealed. Once the reaction reached room temperature, the reaction was brought to 100 °C in a sand bath and allowed to stir overnight. The following day the flask was removed from the sand bath and allowed to cool to room temperature. The reaction was diluted with 50 mL of CH_2Cl_2 and washed with 5 x 10 mL of H_2O followed by 3 x 15 mL of brine before being dried over sodium sulfate. The dried solution was then decanted, and the solvent was removed under reduced pressure. A ^{1}H NMR spectrum was taken of the crude material to confirm a majority of the DMF had been removed, the crude ^{1}H NMR consisted mostly of product. The crude was then purified *via* column chromatography using dichloromethane yielding **5.7** as an off-white powder (376 mg, 75 %) Rf = 0.3 (dichloromethane). ^{1}H NMR (400 MHz, $CDCl_3$) δ 8.37 (d, *J* = 2.4 Hz, 3H), 8.27 (d, *J* = 8.0 Hz, 6H), 7.97 (dd, *J* = 8.4, 2.4 Hz, 3H), 7.88 (s, 3H), 7.32 (d, *J* = 8.4 Hz, 3H), 7.05 (d, *J* = 8.0 Hz, 6H), 3.83 (s, 9H).^{13}C{^{1}H} NMR (151 MHz, $CDCl_3$) δ 165.37, 164.57, 155.37, 150.37, 140.18, 137.28, 135.10, 132.62, 129.75, 128.23, 125.02, 124.41, 122.83, 122.66, 122.39, 121.45, 52.38, 52.29. HRMS (ESI-TOF) *m/z* calc[d] for $C_{48}H_{34}N_3O_{15}$ ($[M+H]^+$): 891.1912; found 891.1903. IR (neat) ν_{max} (cm^{-1})

3114, 3086, 2950, 2845, 1733, 1674, 1619, 1591, 1516, 1479, 1445, 1342, 1236, 1111, 1070, 874, 841, 750.

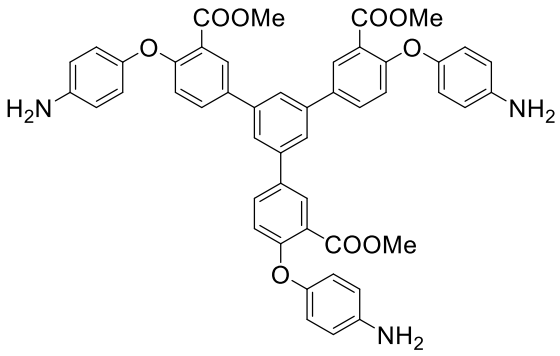

Synthesis of dimethyl 4,4''-bis(4-aminophenoxy)-5'-(4-(4-aminophenoxy)-3-(methoxycarbonyl)phenyl)-[1,1':3',1''-terphenyl]-3,3''-dicarboxylate: 5.13

Ligand precursor (**5.10**) (100 mg, 0.11 mmol) was added to a 25 mL pear-shaped flask, followed by tetrahydrofuran (20.0 mL), and then 10 % Pd/C (24.0 mg, 0.17 mmol). The flask was capped with a rubber septum and put under an atmosphere of H_2 and allowed to stir at room temperature overnight. The following day the solution was filtered over a small celite plug, the flask was washed with ~ 30 mL of methanol and poured through a celite plug. The solvent of the filtrate was removed under reduced pressure yielding ligand **5.10** as a tan powder that was used without further purification (87 mg, 99 %). ^{1}H NMR (400 MHz, DMSO-*d*$_6$) δ 8.17 (d, *J* = 2.4 Hz, 3H), 7.70 (d, *J* = 6.3 Hz, 6H), 6.98 (d, *J* = 8.6 Hz, 3H), 6.94 (d, *J* = 8.3 Hz, 6H), 6.73 (d, *J* = 8.5 Hz, 6H), 3.93 (s, 9H). ^{13}C{^{1}H} NMR (101 MHz, DMSO-*d*$_6$) δ 166.44, 157.67, 146.34, 145.67, 140.78, 134.04, 132.55, 129.78, 124.37, 122.39, 121.11, 118.31, 115.60, 52.66. HRMS (ESI-TOF) *m/z* calc[d] for

$C_{48}H_{40}N_3O_9$ ([M+H]$^+$): 801.2686; found 802.2773. IR (neat) ν_{max} (cm^{-1}) 3459, 3364, 3255, 3109, 3087, 2943, 2844, 1728, 1677, 1620, 1594, 1519, 1482, 1489, 1343, 1222, 1110, 877, 843, 744, 709

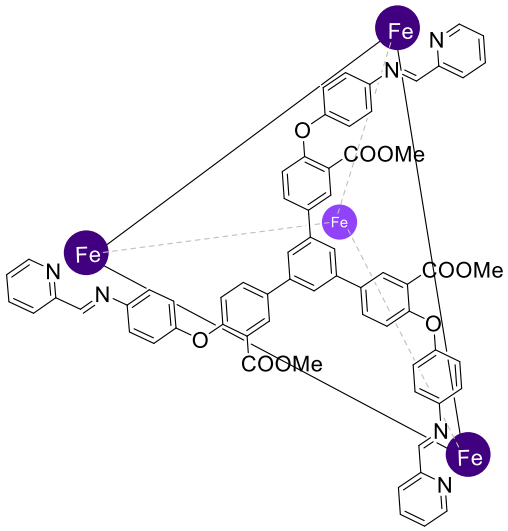

Synthesis of Cage 5.14: Dimethyl 4,4"-bis(4-aminophenoxy)-5'-(4-(4-aminophenoxy)-3-(methoxycarbonyl)phenyl)-[1,1':3',1"-terphenyl]-3,3"-dicarboxylate (**5.13**) (25 mg, 0.03 mmol) was added to a 25 mL pear shaped flask equipped with a magnetic stir bar, followed by MeCN (15 mL), $Fe(NTf_2)_2$ (19.2 mg. 0.03 mmol), and 2-formylpyridine (8.5 µL, 0.09 mmol). The flask was equipped with a reflux condenser and brought to 70 °C in a sand bath and allowed to stir overnight. The flask was then taken out of the sand bath and allowed to cool to room temperature before the solvent was removed in vacuo which left a rock like purple smear on the walls of the flask. 20 mL of ether was then added, the flask walls were scratched with a metallic spatula to ensure a maximum amount of material was collected. This solution was then filtered yielding a purple crystalline powder. (51 mg, 79 %).

6.8. Spectra for Chapter 2

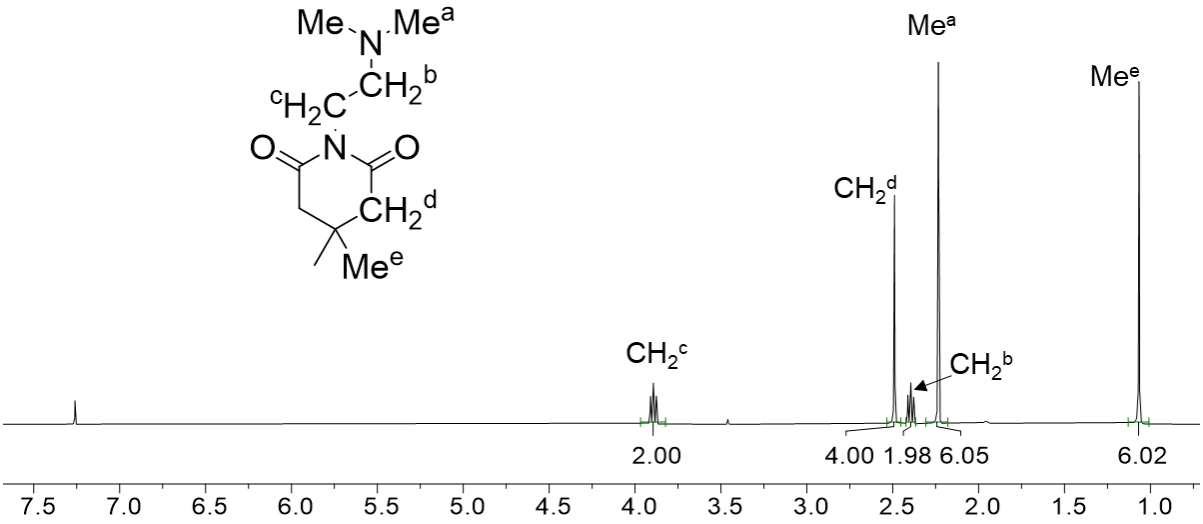

Figure 6.108. ^{1}H NMR spectrum of **2.4** ($CDCl_3$, 400 MHz, 298 K).

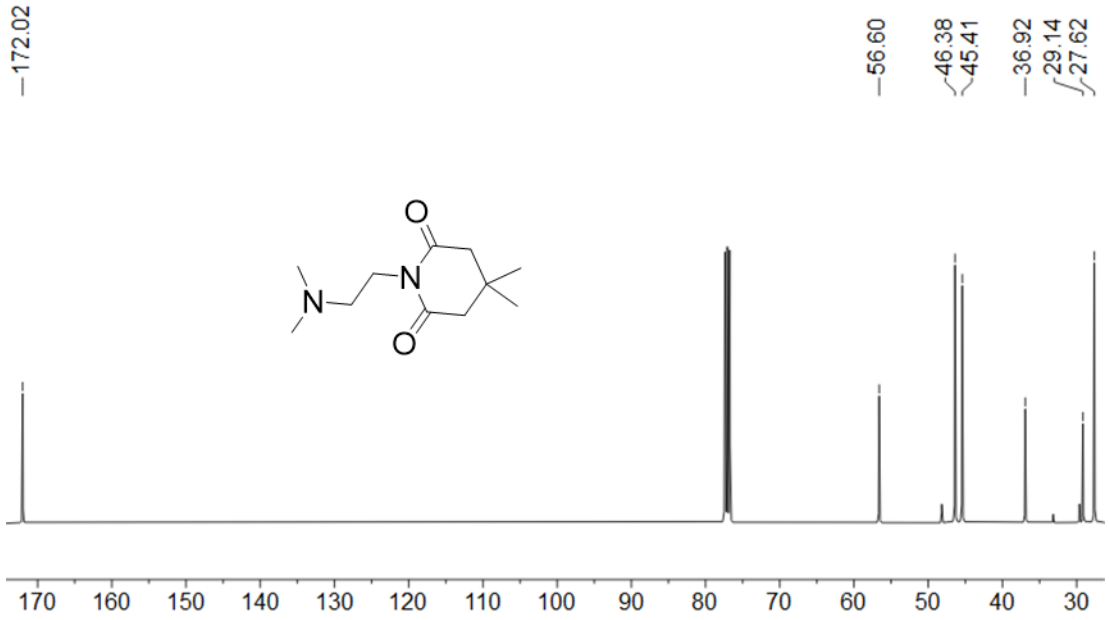

Figure 6.109. ^{13}C NMR spectrum of **2.4** ($CDCl_3$, 151 MHz, 298 K).

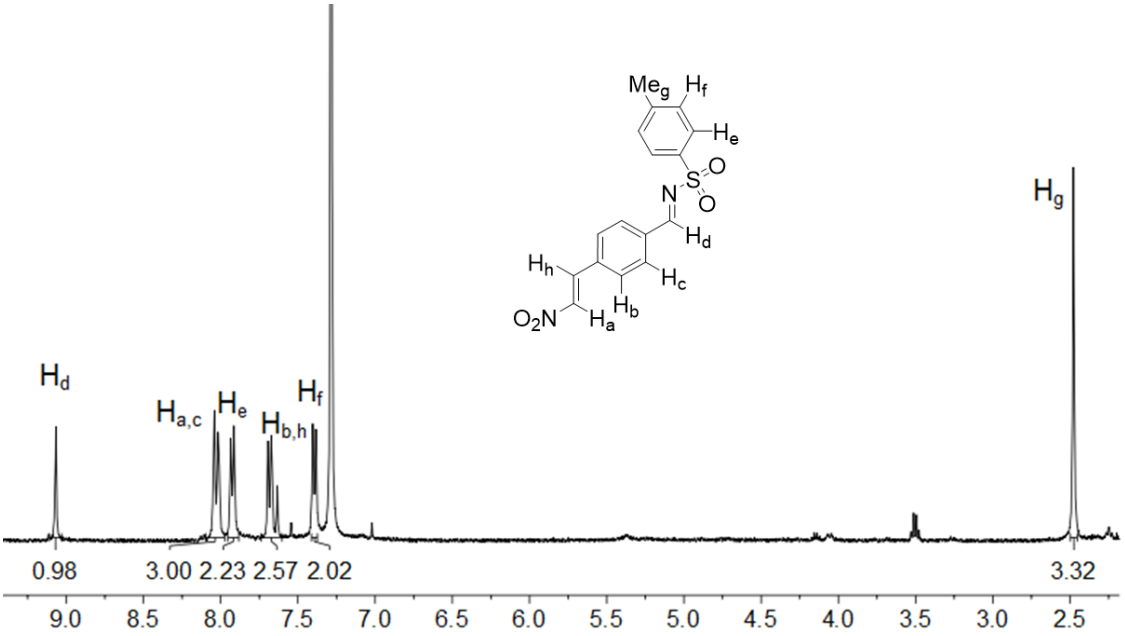

Figure 6.110. ^{1}H NMR spectrum of **2.18** ($CDCl_3$, 400 MHz, 298 K).

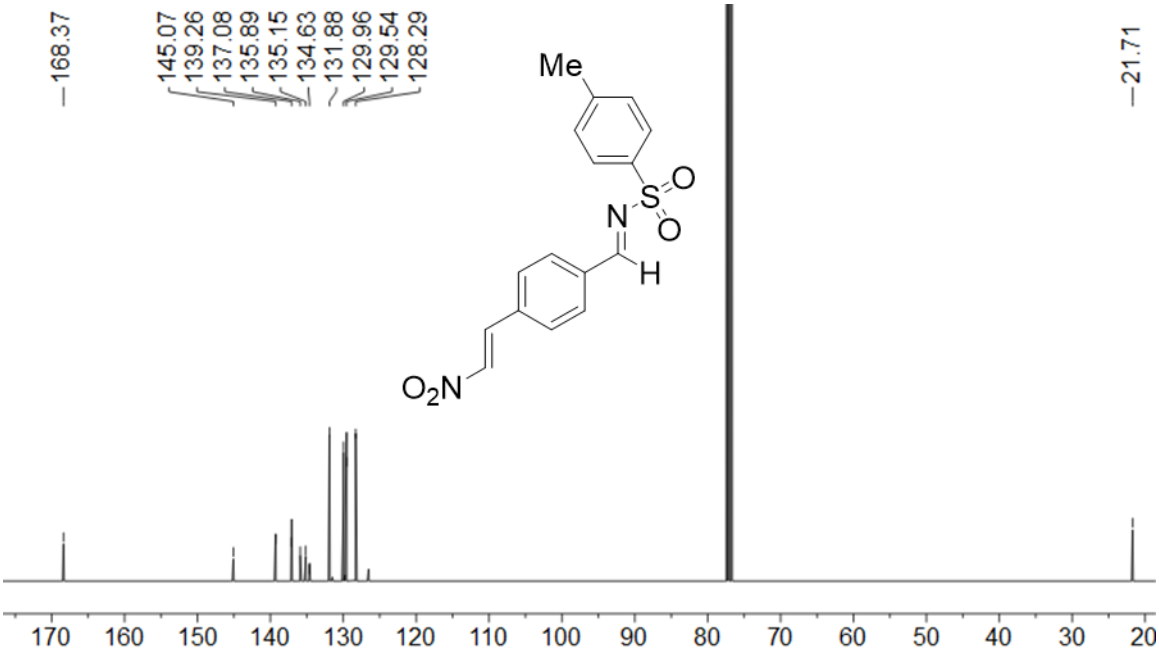

Figure 6.111. ^{13}C NMR spectrum of **2.18** ($CDCl_3$, 151 MHz, 298 K).

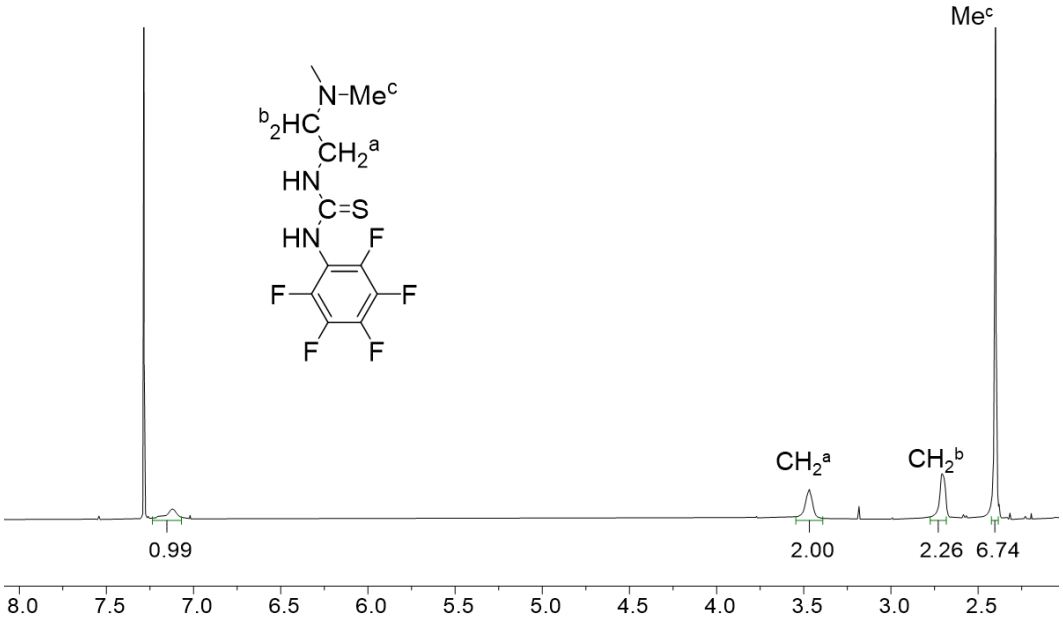

Figure 6.112. ^{1}H NMR spectrum of **2.5** ($CDCl_3$, 400 MHz, 298 K).

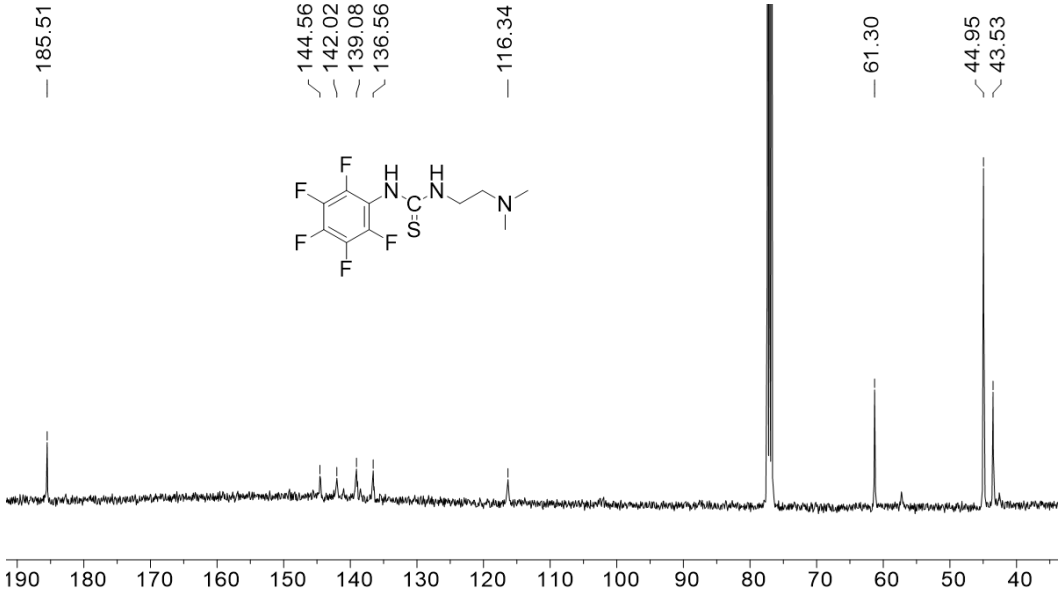

Figure 6.113. ^{13}C NMR spectrum of **2.5** ($CDCl_3$, 151 MHz, 298 K).

6.9. Spectra for Chapter 4

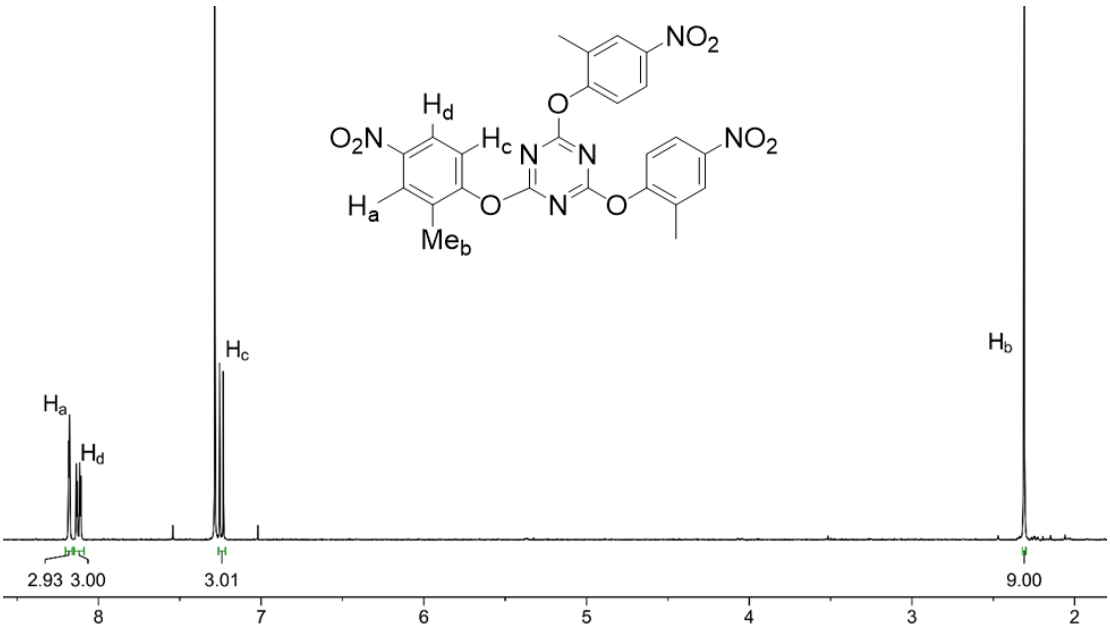

Figure 6.114. ^{1}H NMR spectrum of **4.15** ($CDCl_3$, 400 MHz, 298 K).

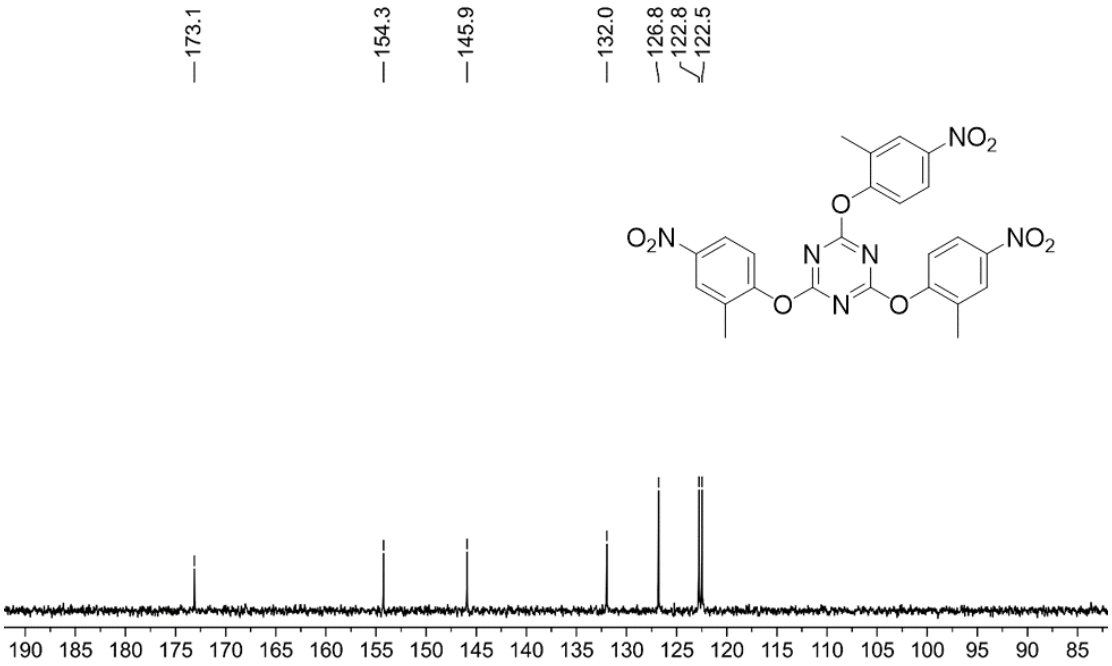

Figure 6.115. ^{13}C NMR spectrum of **4.15** ($CDCl_3$, 151 MHz, 298 K).

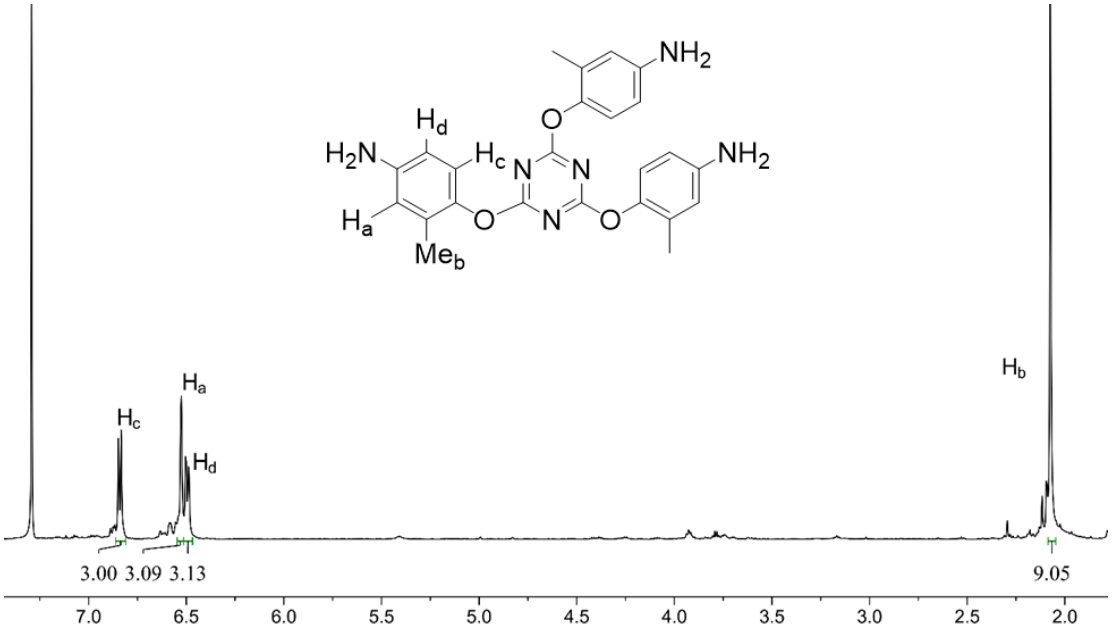

Figure 6.116. ^{1}H NMR spectrum of **4.19** ($CDCl_3$, 400 MHz, 298 K).

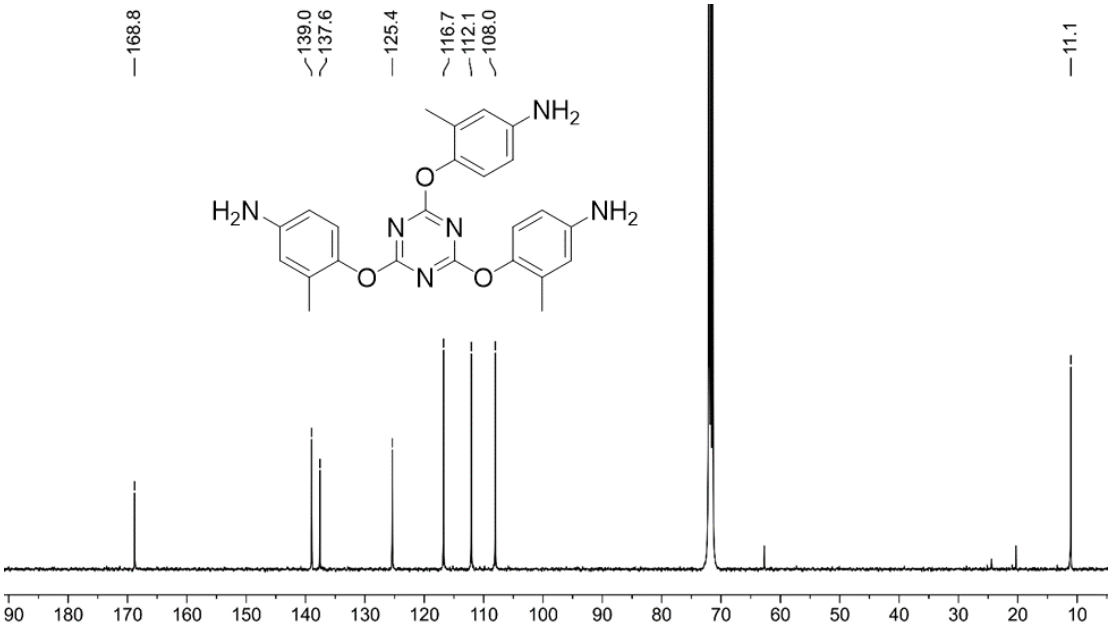

Figure 6.117. ^{13}C NMR spectrum of **4.19** ($CDCl_3$, 151 MHz, 298 K).

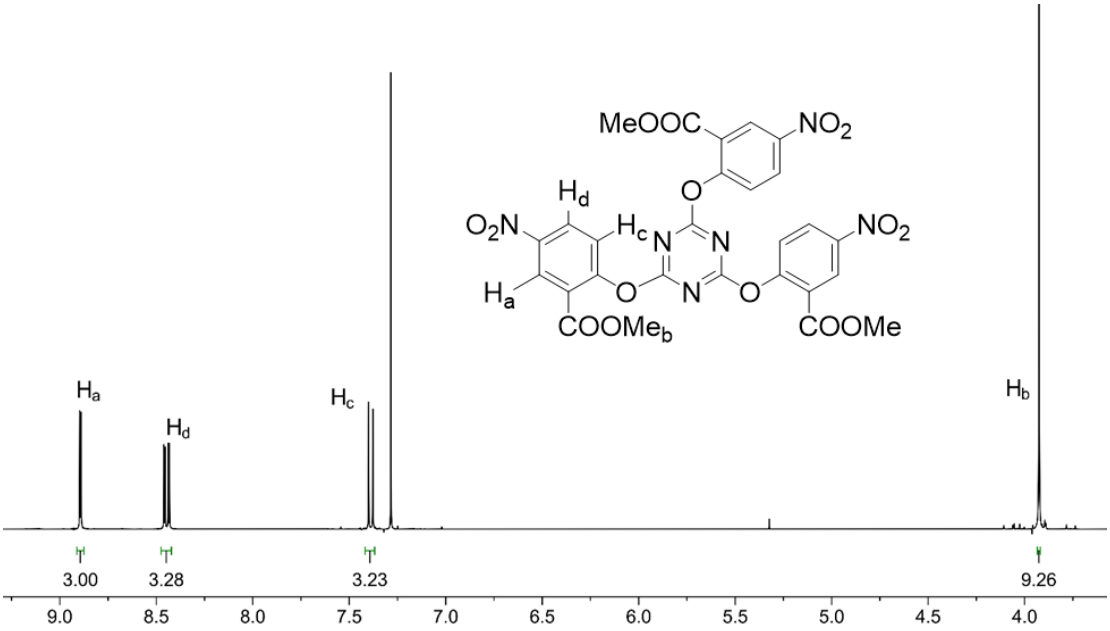

Figure 6.118. ^{1}H NMR spectrum of **4.16** ($CDCl_3$, 400 MHz, 298 K).

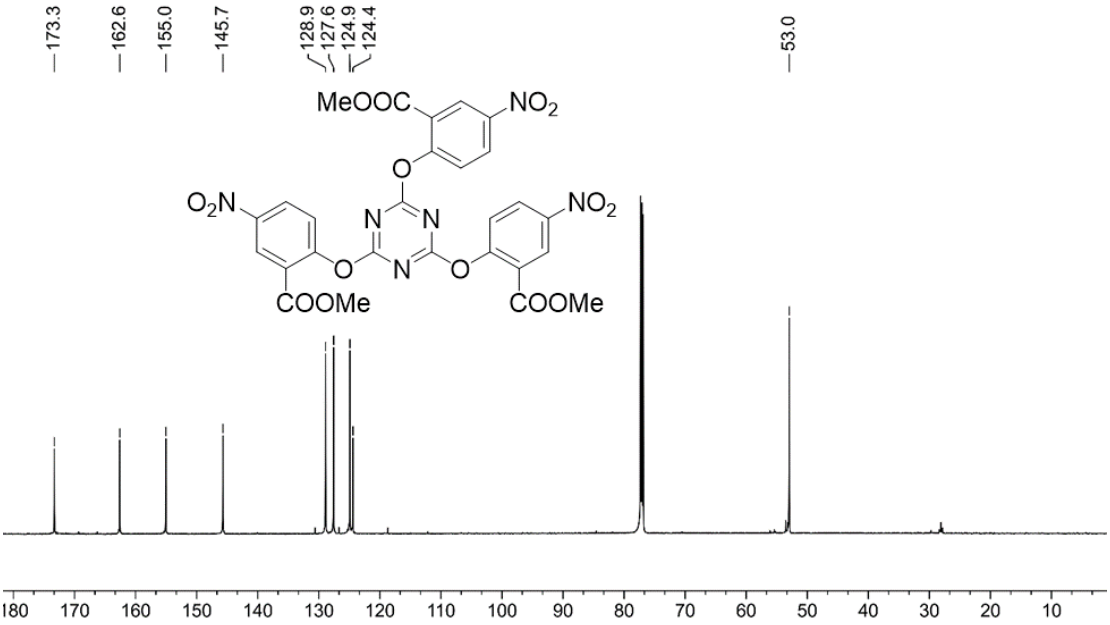

Figure 6.119. ^{13}C NMR spectrum of **4.16** ($CDCl_3$, 151 MHz, 298 K).

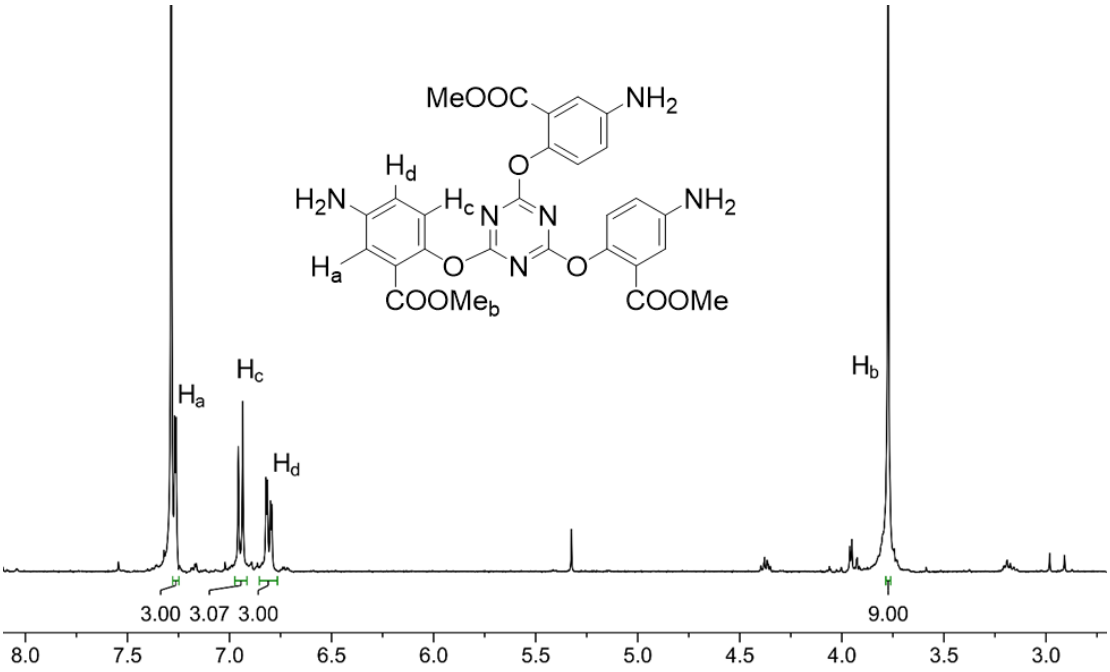

Figure 6.120. ^{1}H NMR spectrum of **4.20** ($CDCl_3$, 400 MHz, 298 K).

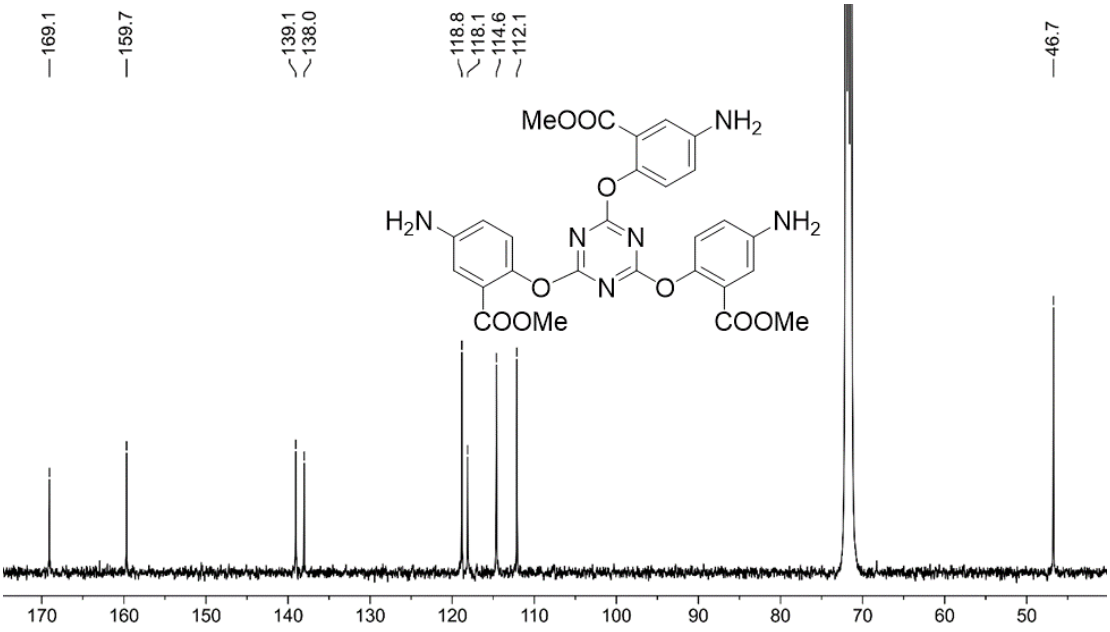

Figure 6.121. ^{13}C NMR spectrum of **4.20** ($CDCl_3$, 151 MHz, 298 K).

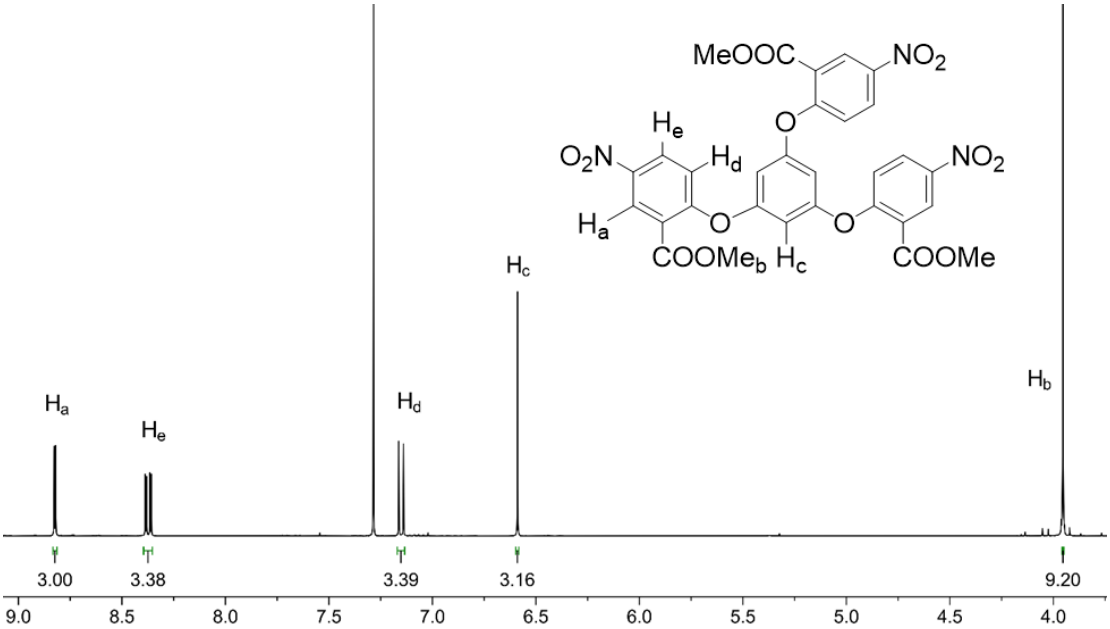

Figure 6.122. ^{1}H NMR spectrum of **4.21** ($CDCl_3$, 400 MHz, 298 K).

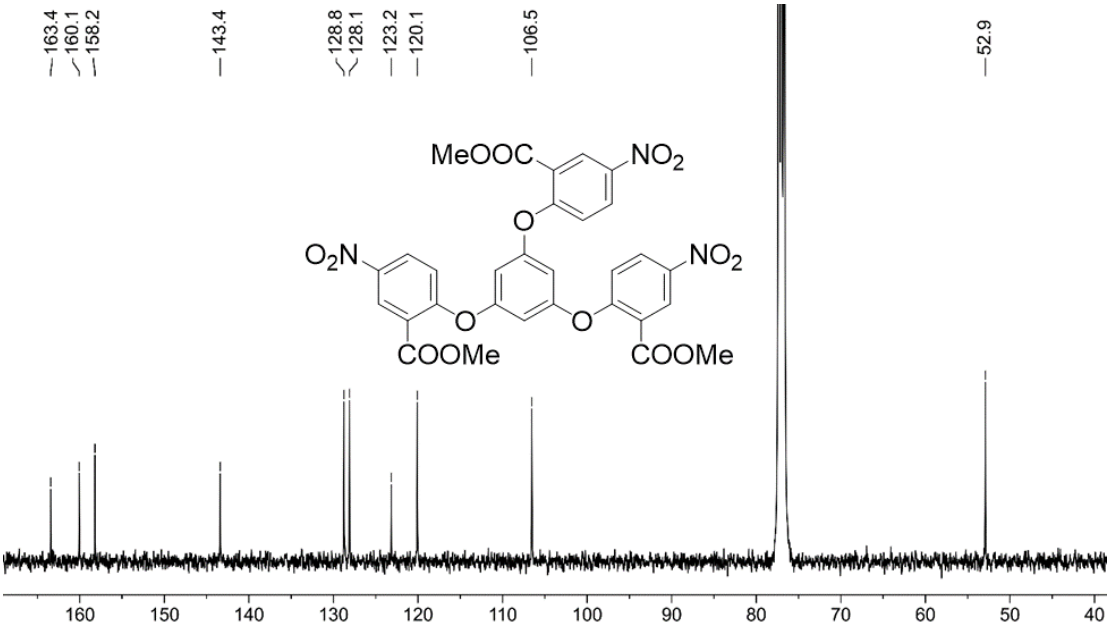

Figure 6.123. ^{13}C NMR spectrum of **4.21** ($CDCl_3$, 151 MHz, 298 K).

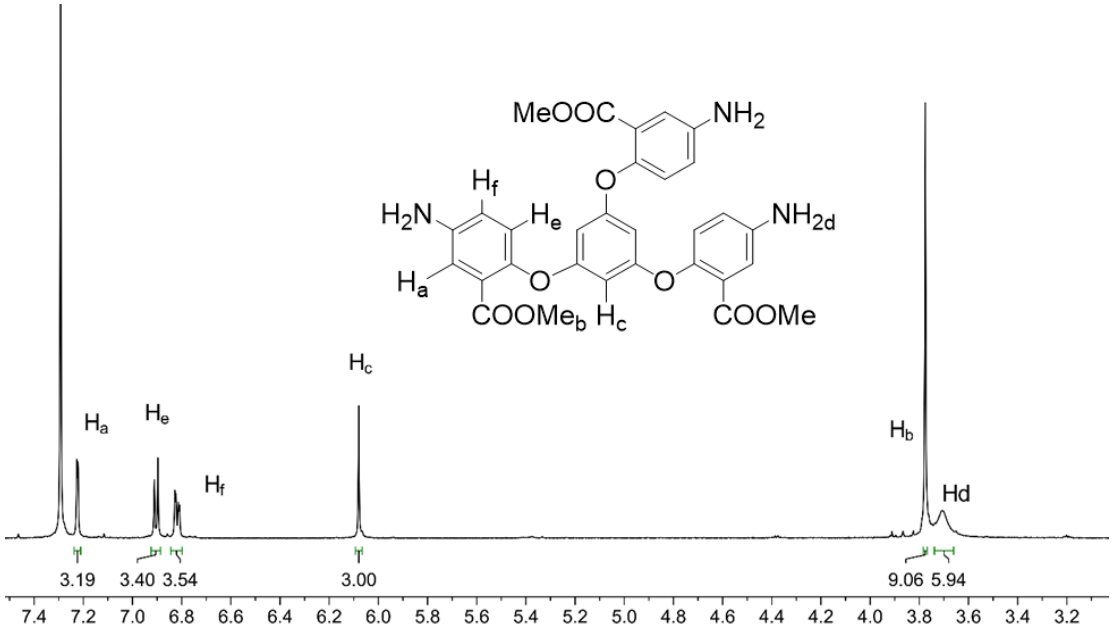

Figure 6.124. ^{1}H NMR spectrum of **4.22** ($CDCl_3$, 400 MHz, 298 K).

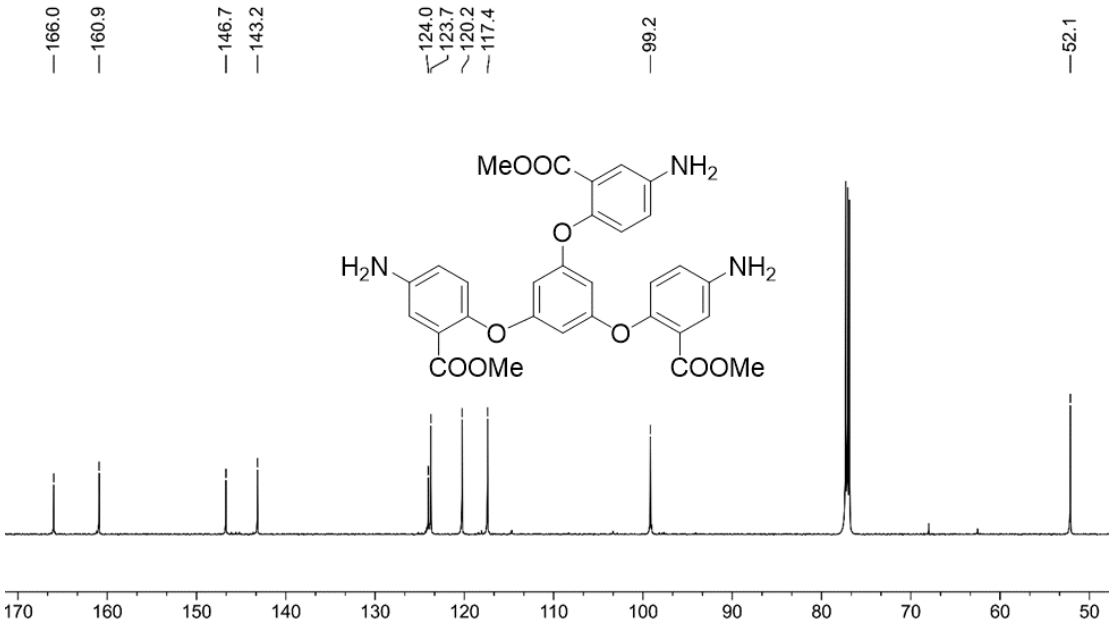

Figure 6.125. ^{13}C NMR spectrum of **4.22** ($CDCl_3$, 151 MHz, 298 K).

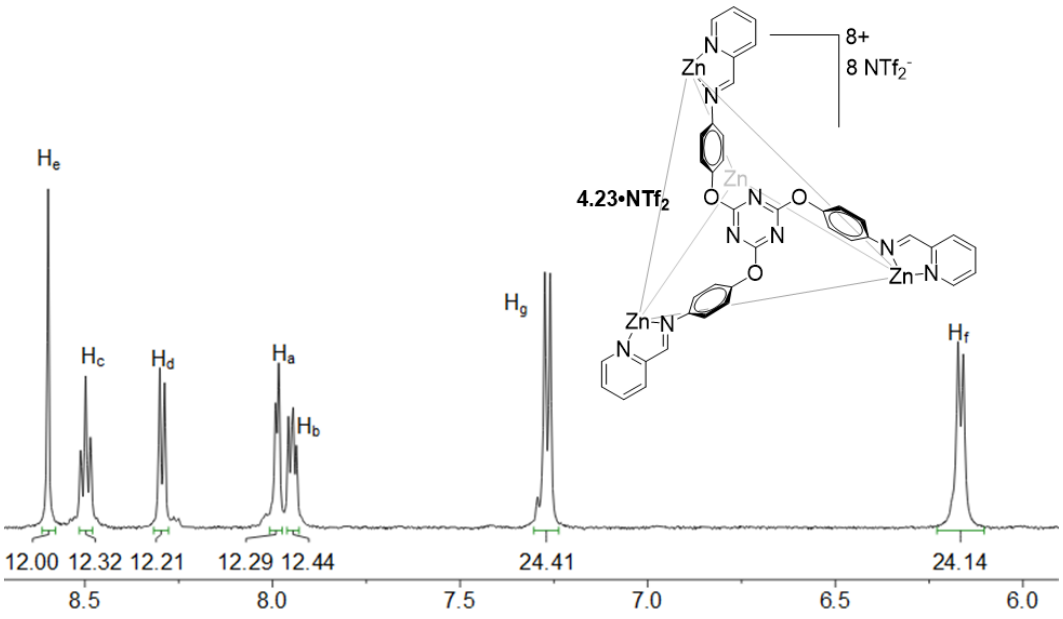

Figure 6.126. ^{1}H NMR spectrum of **4.23•NTf$_2$** (CD_3CN, 600 MHz, 298 K).

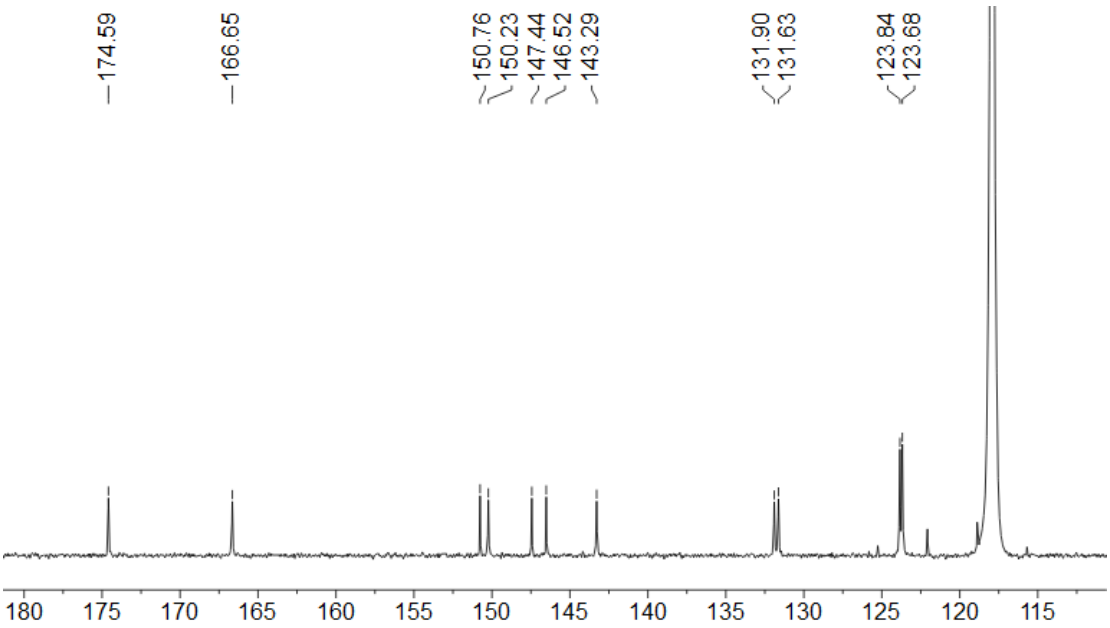

Figure 6.127. ^{13}C NMR spectrum of **4.23•NTf$_2$** (CD_3CN, 151 MHz, 298 K).

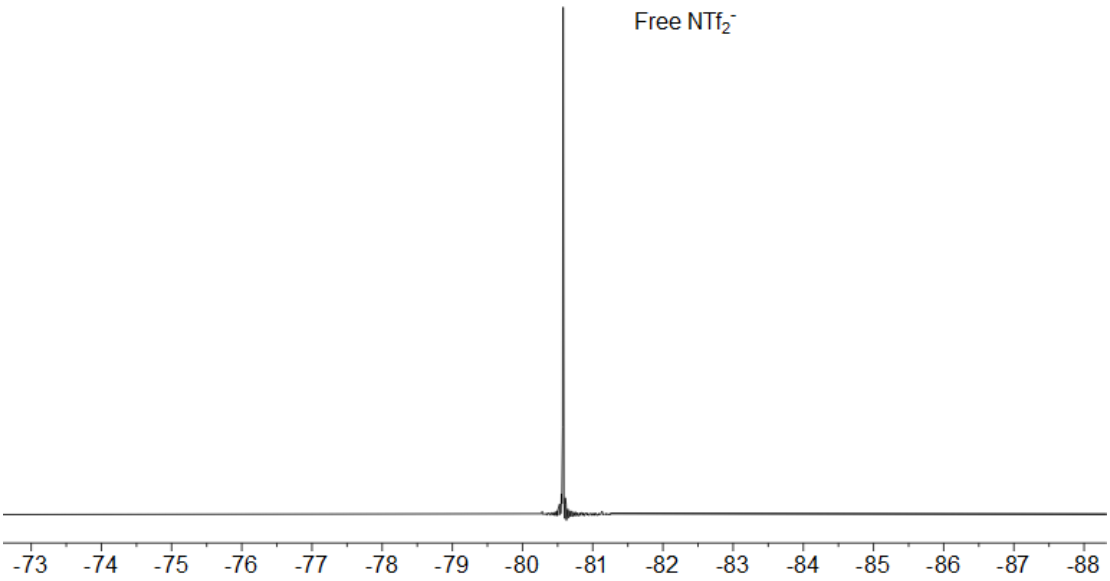

Figure 6.128. ^{19}F NMR spectrum of **4.23•NTf$_2$** (CD_3CN, 376 MHz, 298 K).

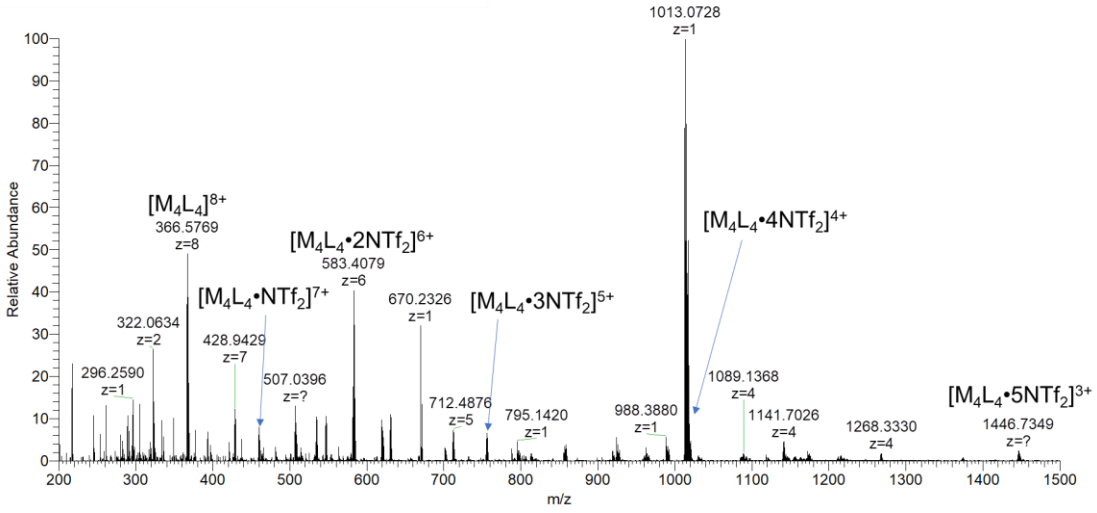

Figure 6.129. Full ESI-MS spectrum of **4.23•NTf$_2$**.

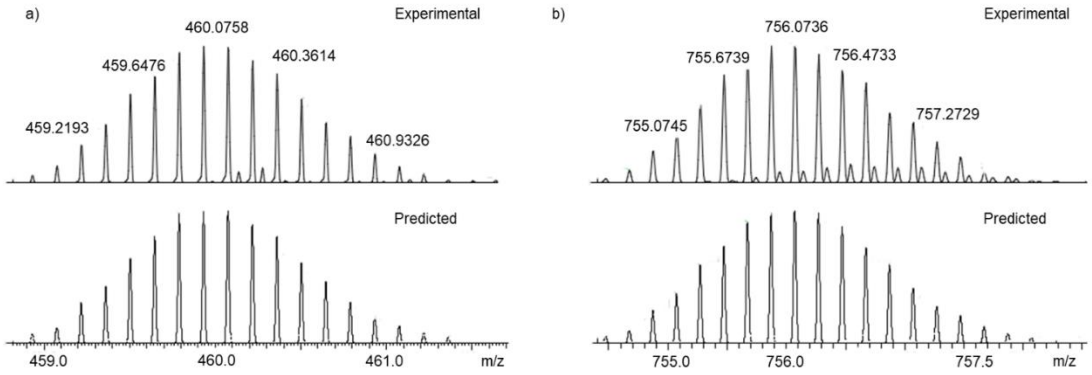

Figure 6.130. Expansion of the ESI-MS spectrum of **4.23•NTf_2**, showing obtained and simulated isotope regions a) [**4.23**•(NTf_2)]$^{7+}$ and b) [**4.23**•$(NTf_2)_3$]$^{5+}$ ion.

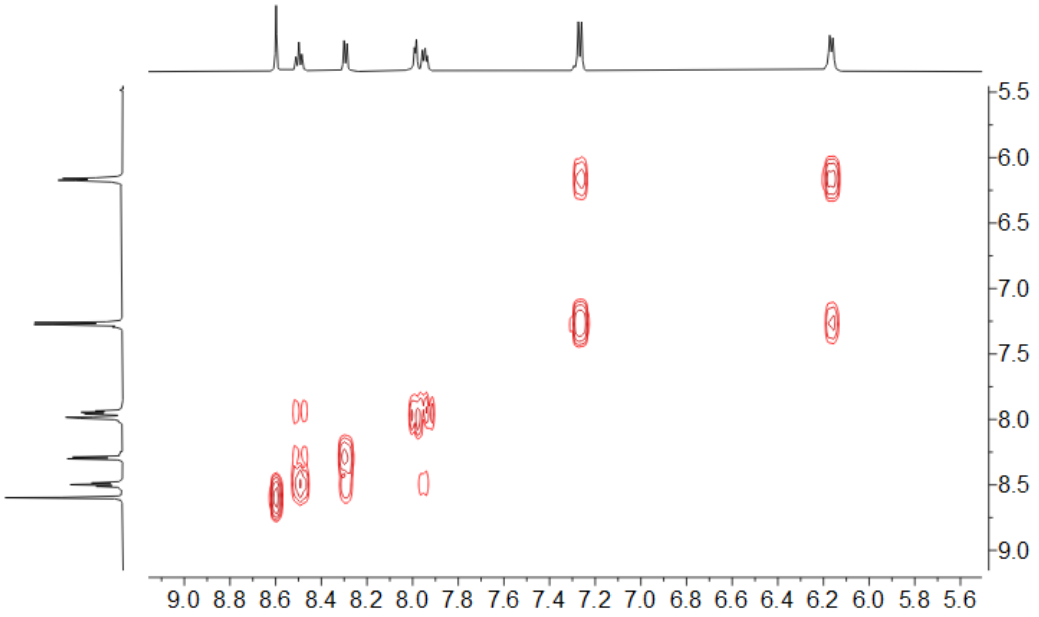

Figure 6.131. gCOSY NMR spectrum of **4.23•NTf_2** (CD_3CN, 400 MHz, 298 K).

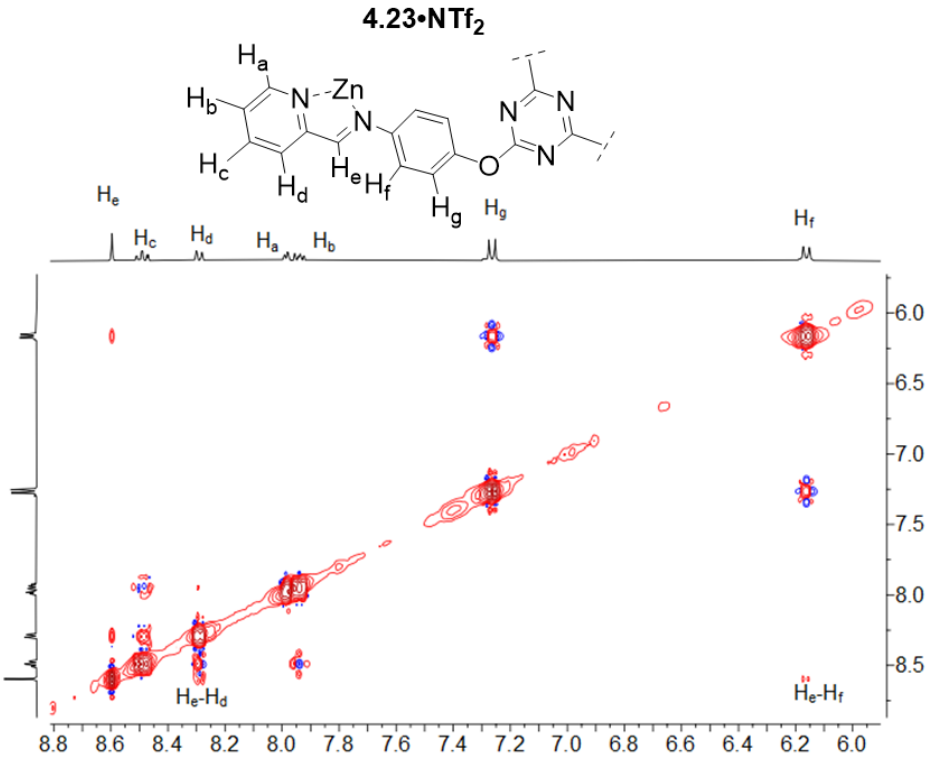

Figure 6.132. gNOESY NMR spectrum of **4.23•NTf$_2$** (CD_3CN, 400 MHz, 298 K, mixing time = 300 ms).

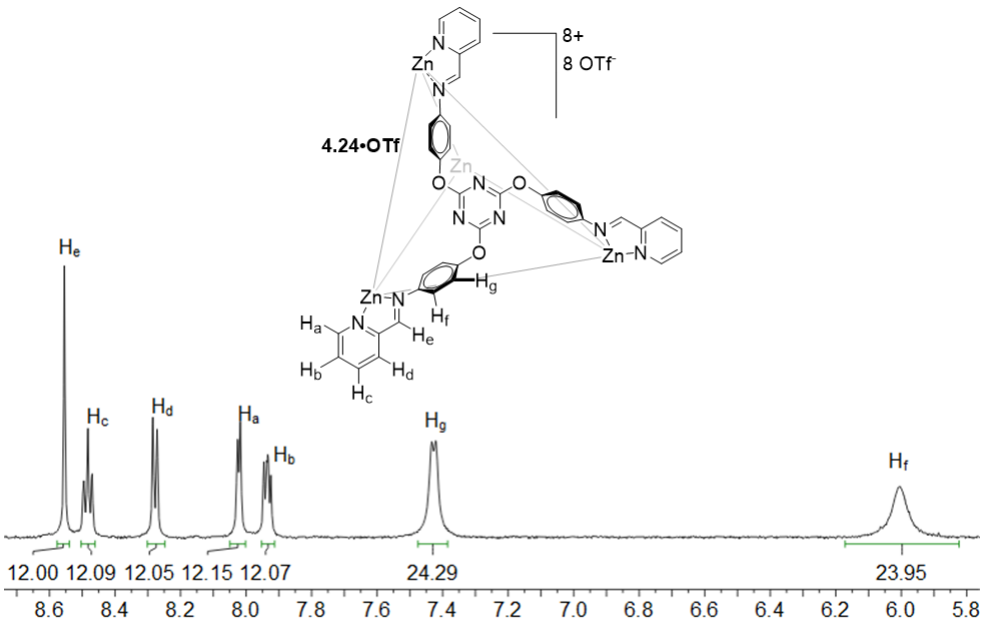

Figure 6.133. ^{1}H NMR spectrum of **4.24•OTf** (CD_3CN, 400 MHz, 298 K).

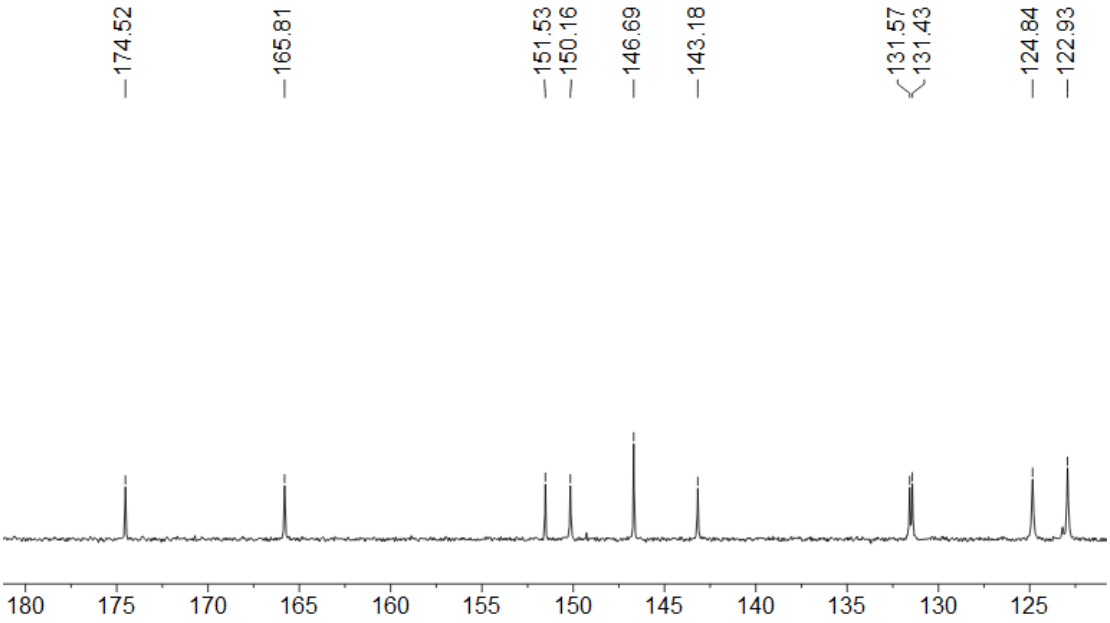

Figure 6.134. ^{13}C NMR spectrum of **4.24•OTf** (CD_3CN, 151 MHz, 298 K).

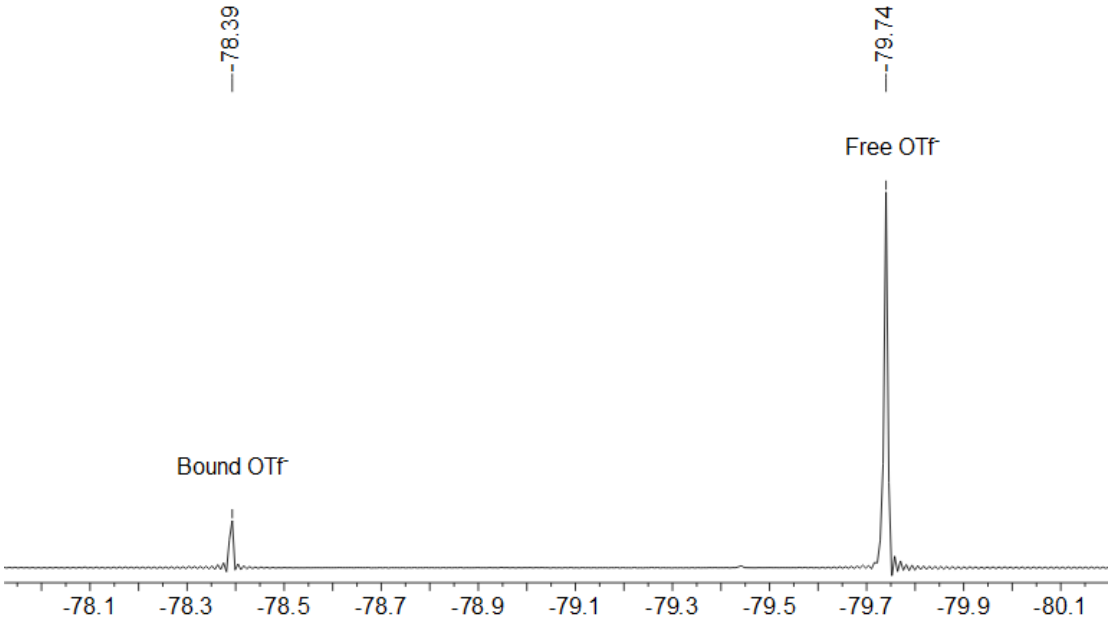

Figure 6.135. ^{19}F NMR spectrum of **4.24•OTf** (CD_3CN, 376 MHz, 298 K).

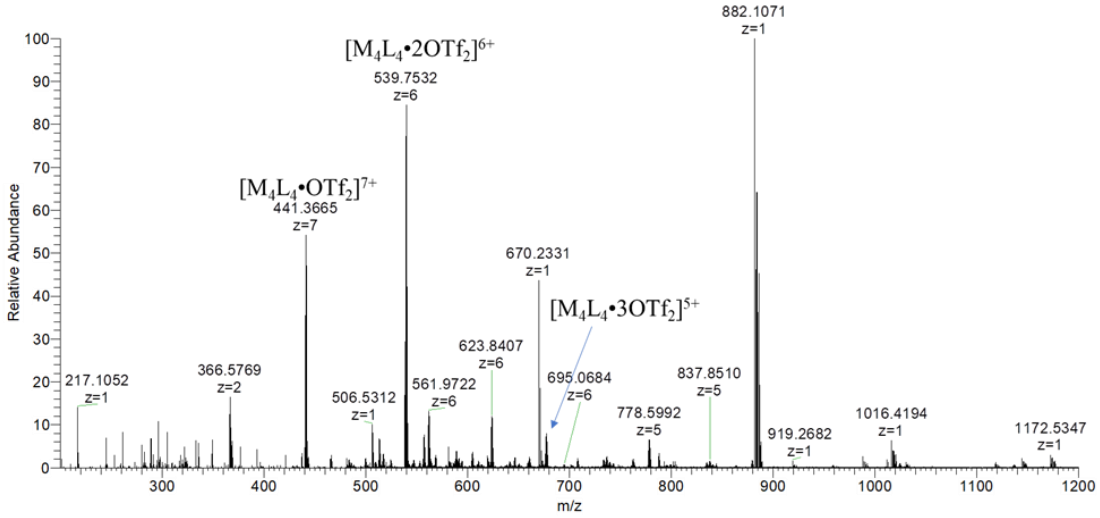

Figure 6.136. Full ESI-MS spectrum of **4.24•OTf**.

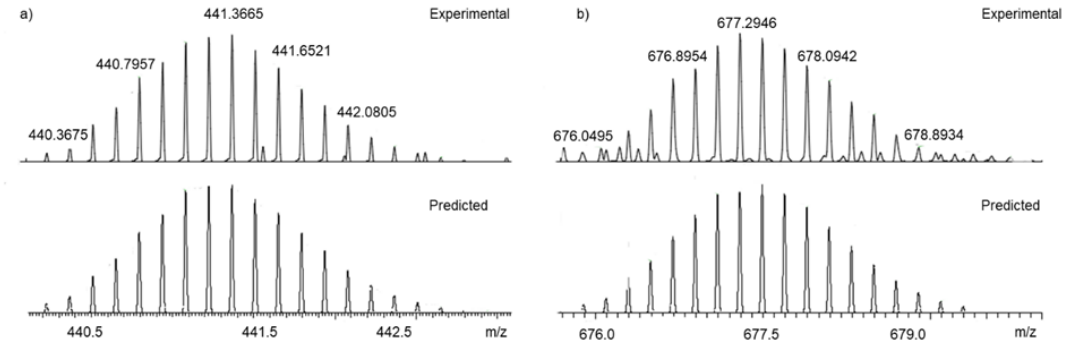

Figure 6.137. Expansion of the ESI-MS spectrum of **4.24•OTf**, showing obtained and simulated isotope regions for the [**4.24•OTf** •(OTf_2)]$^{7+}$ and [**4.24**•$(OTf_2)_3$]$^{5+}$ ion.

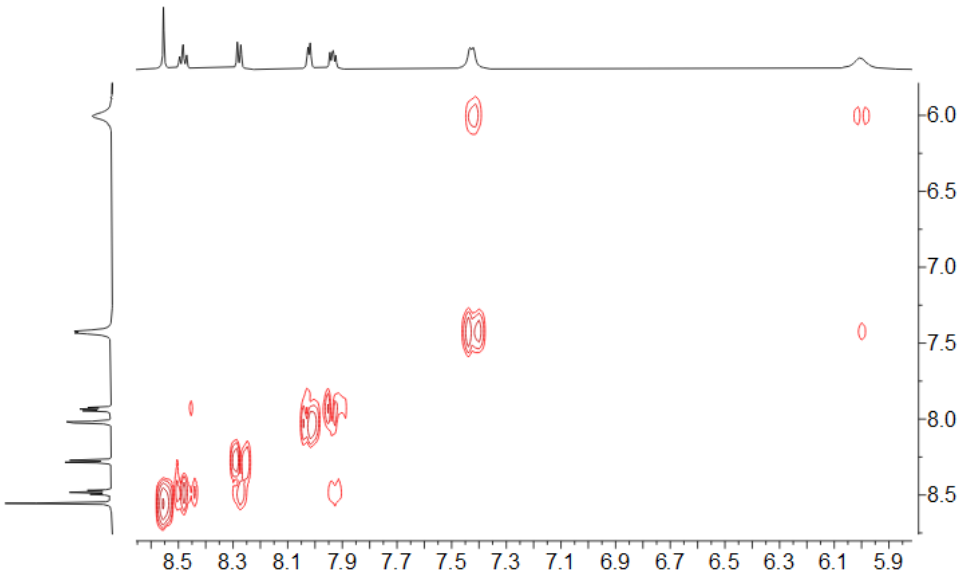

Figure 6.138. gCOSY NMR spectrum of **4.24•OTf** (CD_3CN, 400 MHz, 298 K).

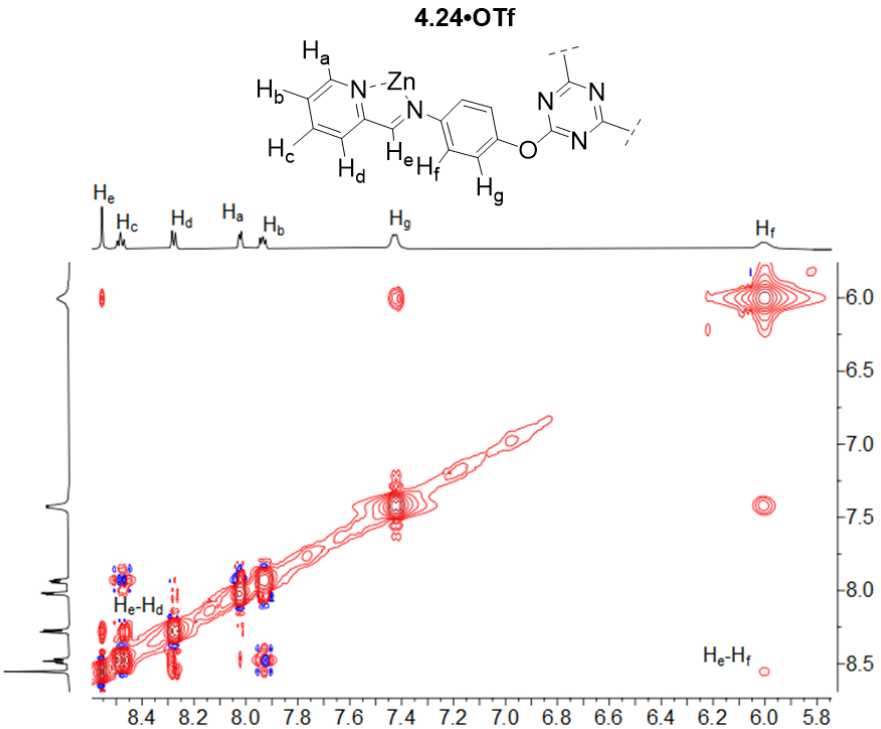

Figure 6.139. gNOESY NMR spectrum of **4.24•OTf** (CD_3CN, 400 MHz, 298 K, mixing time = 300 ms).

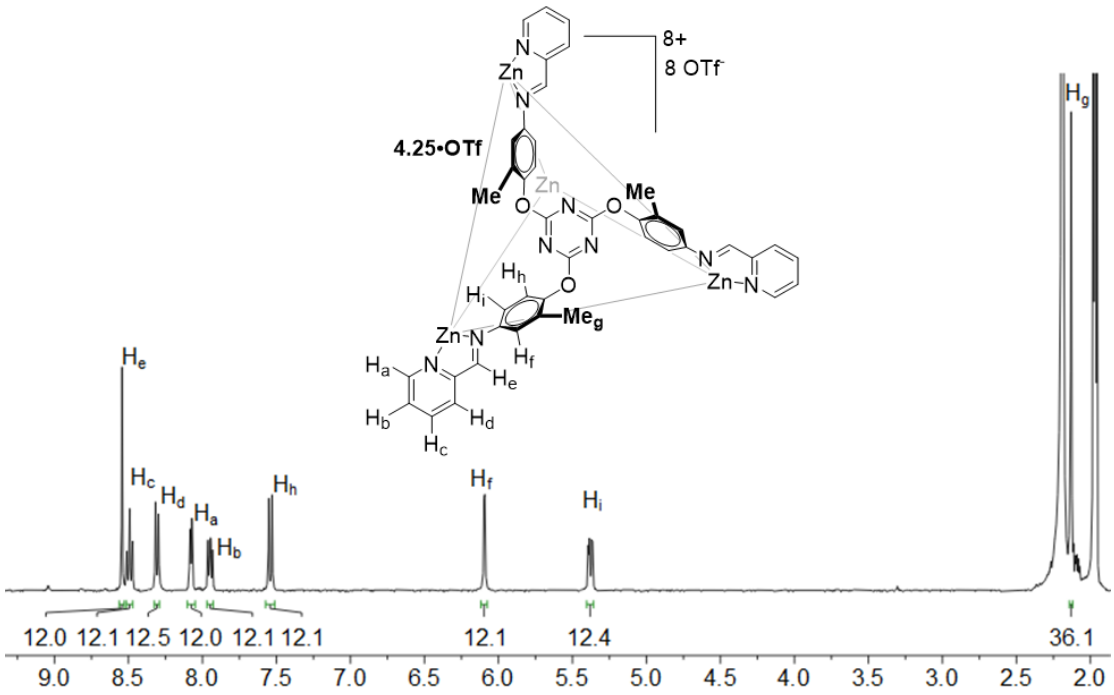

Figure 6.140. ^{1}H NMR spectrum of **4.25•OTf** (CD_3CN, 400 MHz, 298 K).

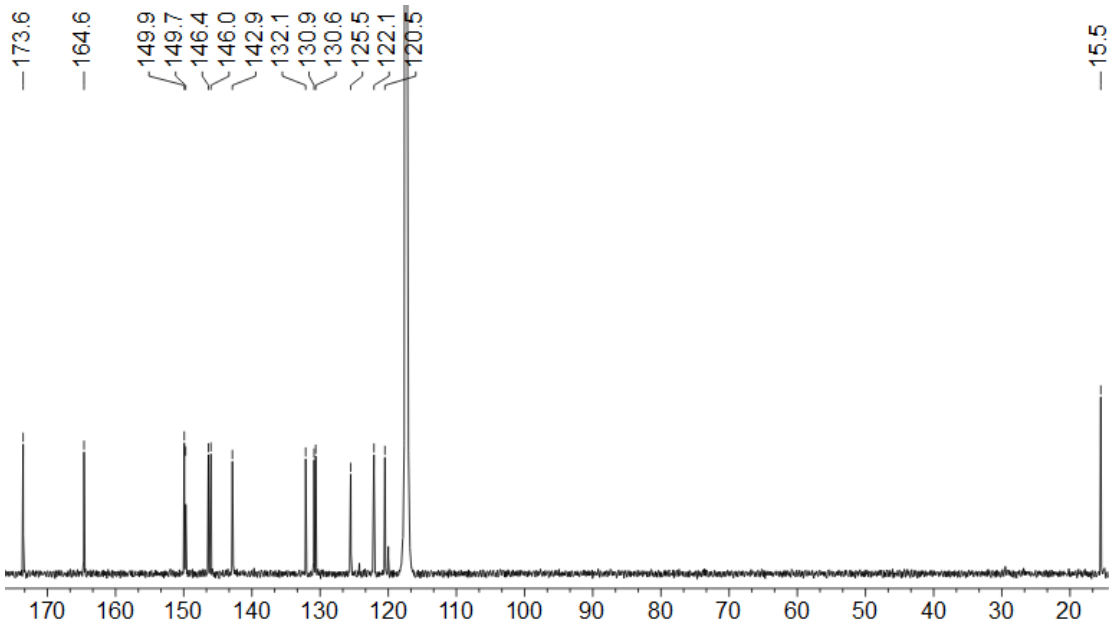

Figure 6.141. ^{13}C NMR spectrum of **4.25•OTf** (CD_3CN, 151 MHz, 298 K).

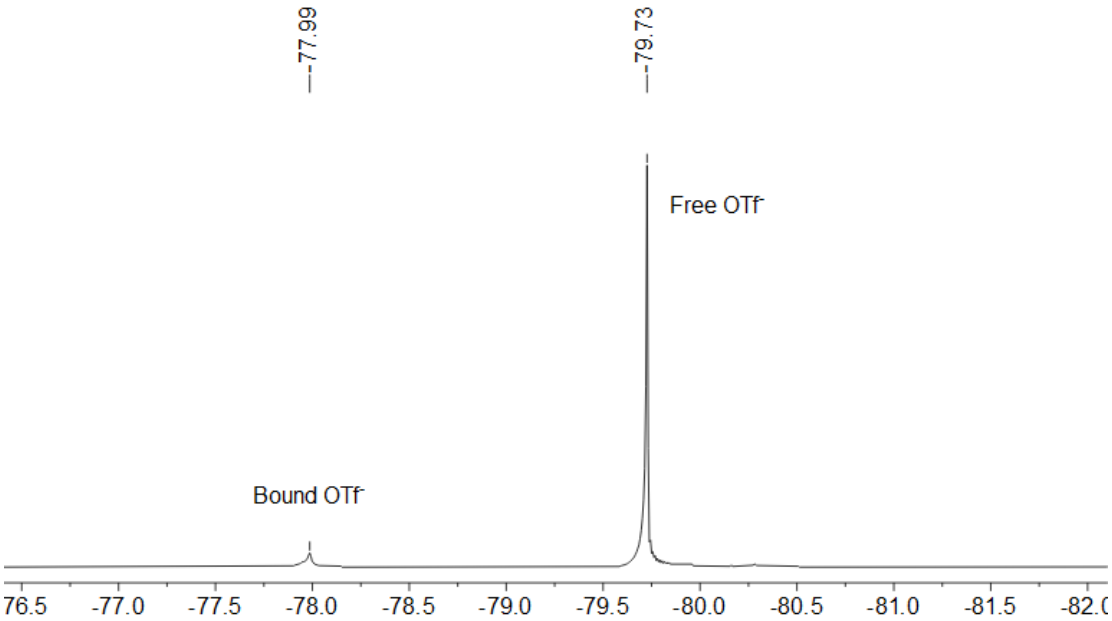

Figure 6.142. ^{19}F NMR spectrum of **4.25•OTf** (CD_3CN, 376 MHz, 298 K).

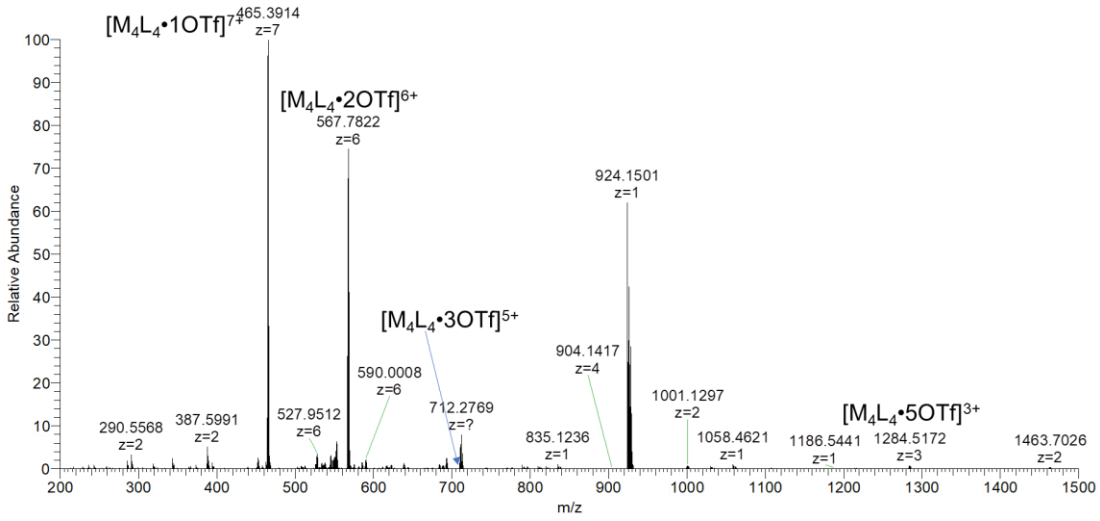

Figure 6.143. Full ESI-MS spectrum of **4.25•OTf**.

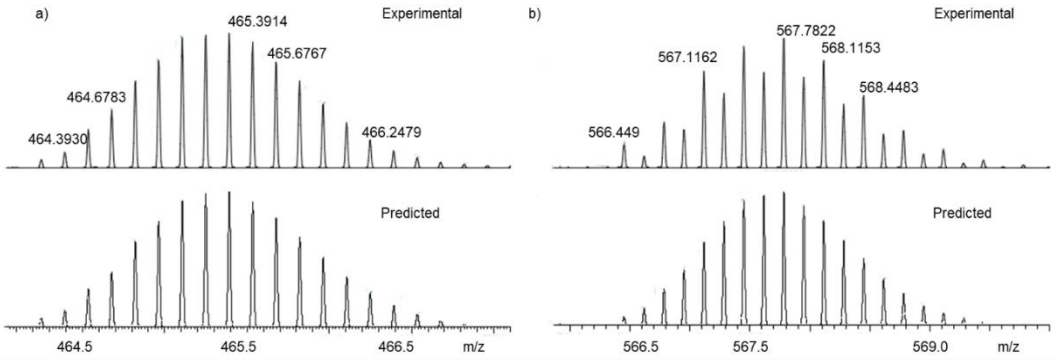

Figure 6.144. Expansion of the ESI-MS spectrum of **4.25•OTf**, showing obtained and simulated isotope regions a) $[\mathbf{4.25}\bullet(OTf)]^{7+}$ and b) $[\mathbf{4.25}\bullet(OTf)_2]^{6+}$ ion.

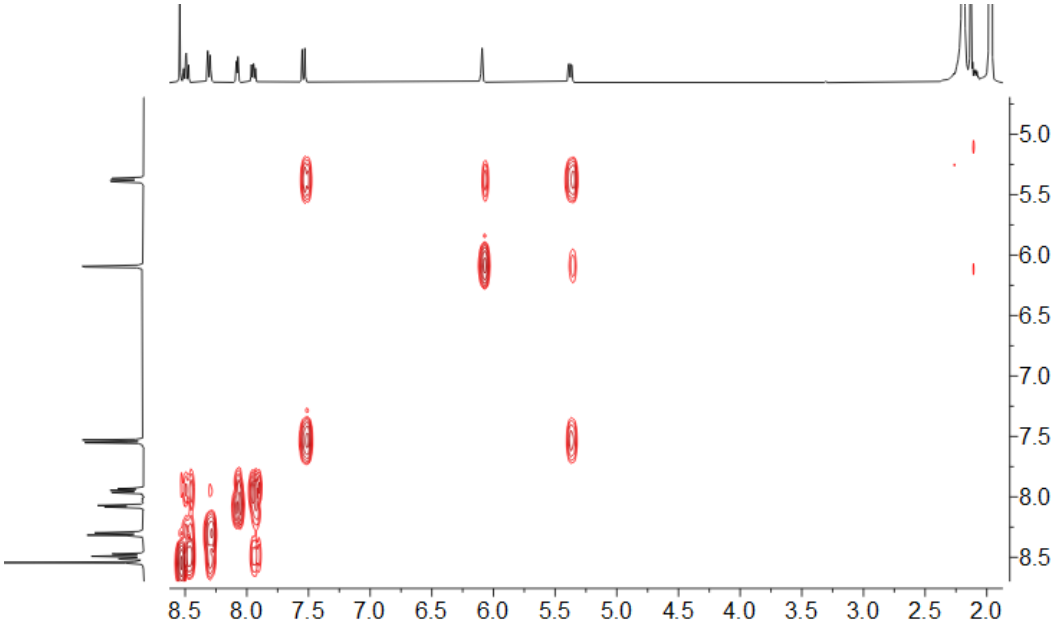

Figure 6.145. gCOSY NMR spectrum of **4.25•OTf** (CD_3CN, 400 MHz, 298 K).

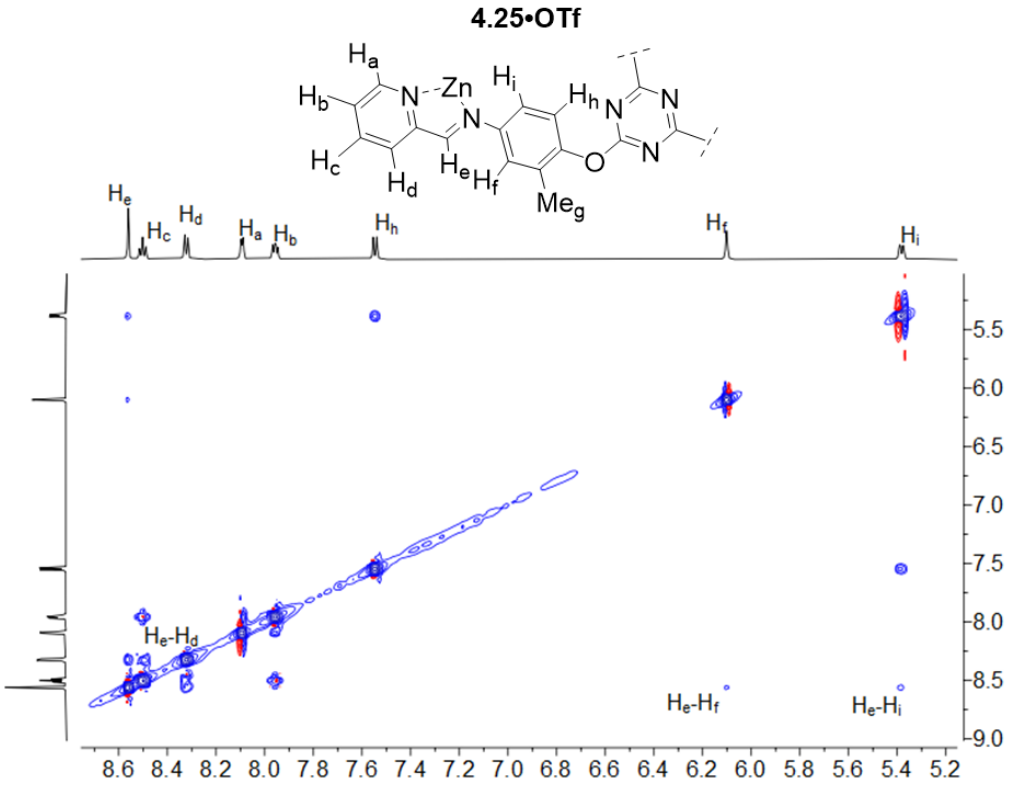

Figure 6.146. gNOESY NMR spectrum of **4.25•OTf** (CD_3CN, 400 MHz, 298 K, mixing time = 300 ms).

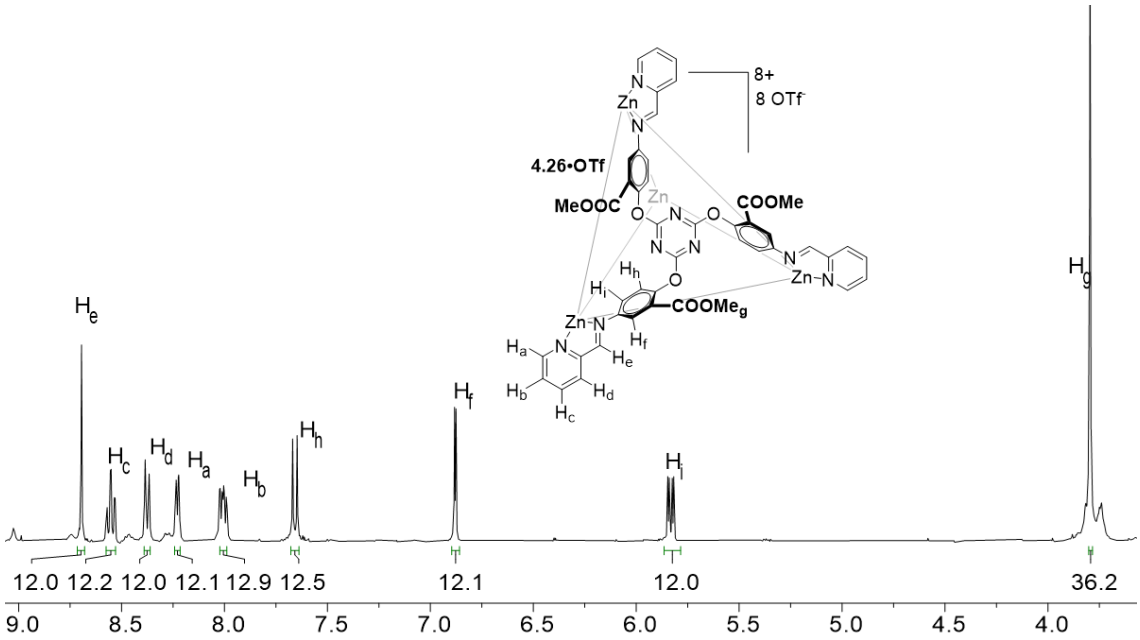

Figure 6.147. ^{1}H NMR spectrum of **4.26•OTf** (CD_3CN, 400 MHz, 298 K).

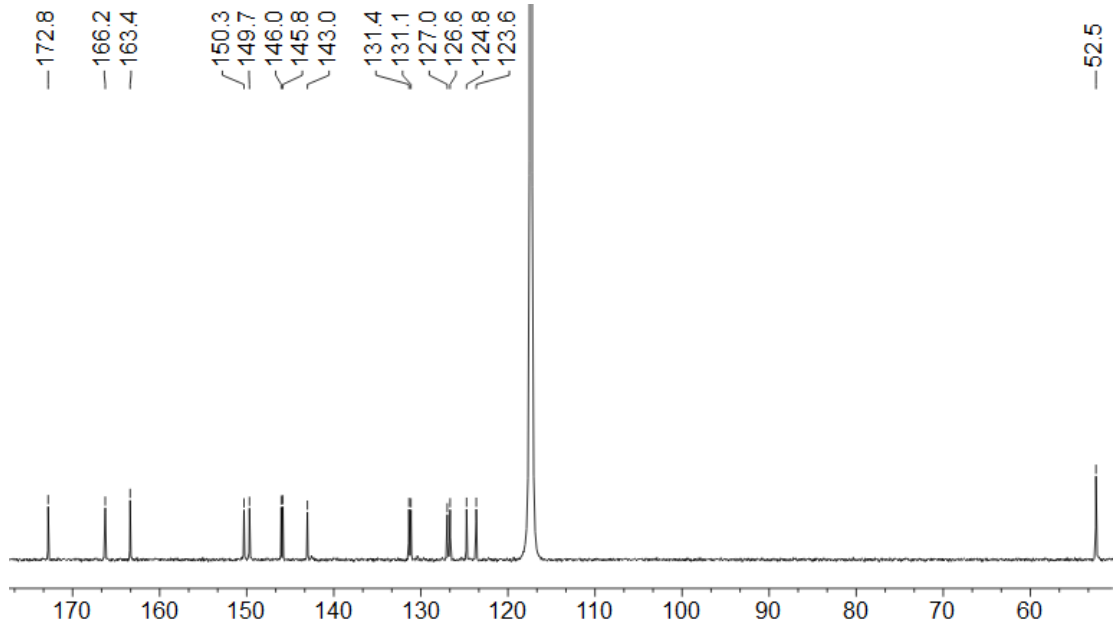

Figure 6.148. ^{13}C NMR spectrum of **4.26•OTf** (CD_3CN, 151 MHz, 298 K).

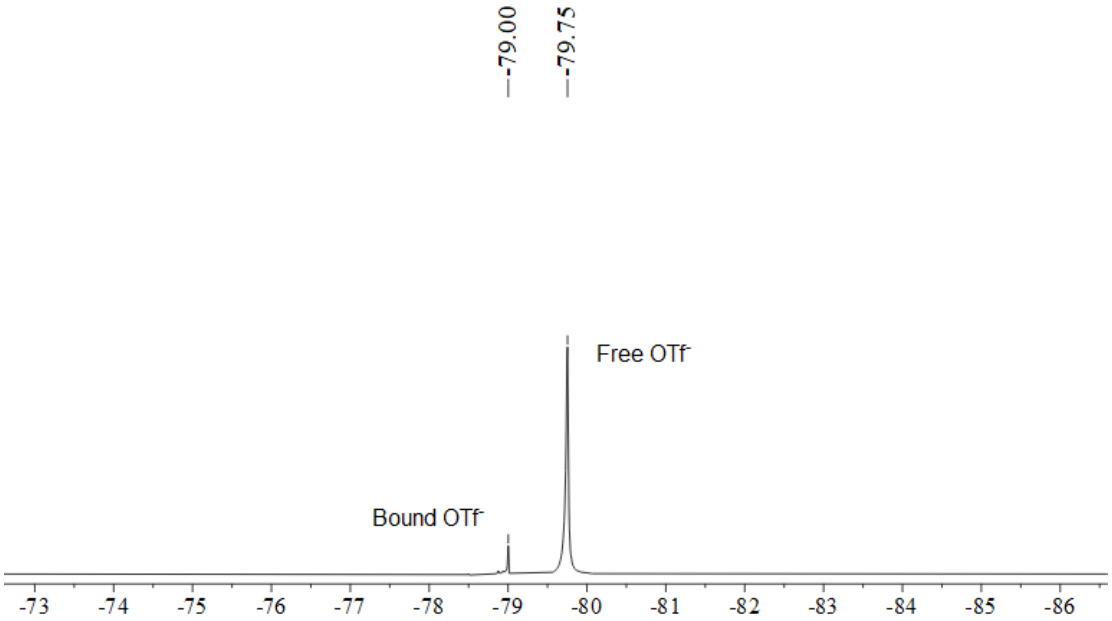

Figure 6.149. ^{19}F NMR spectrum of **4.26•OTf** (CD_3CN, 376 MHz, 298 K).

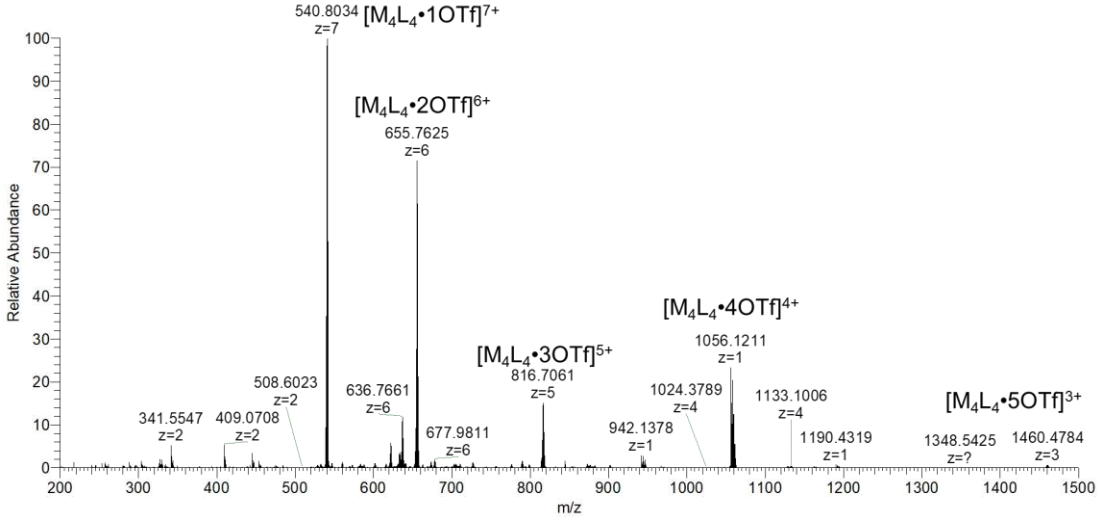

Figure 6.150. Full ESI-MS spectrum of **4.26•OTf**.

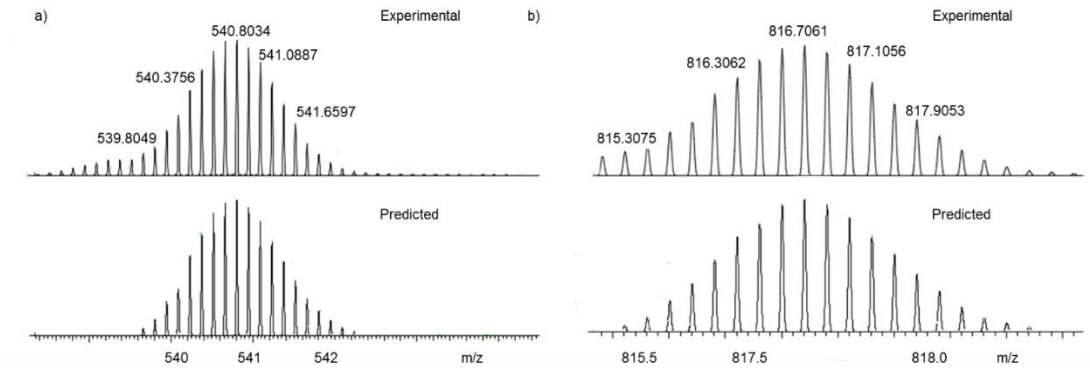

Figure 6.151. Expansion of the ESI-MS spectrum of **4.26•OTf**, showing obtained and simulated isotope regions for the $[\mathbf{4.26}\bullet(OTf_2)]^{7+}$ and $[\mathbf{4.26}\bullet(OTf_2)_3]^{5+}$ ion.

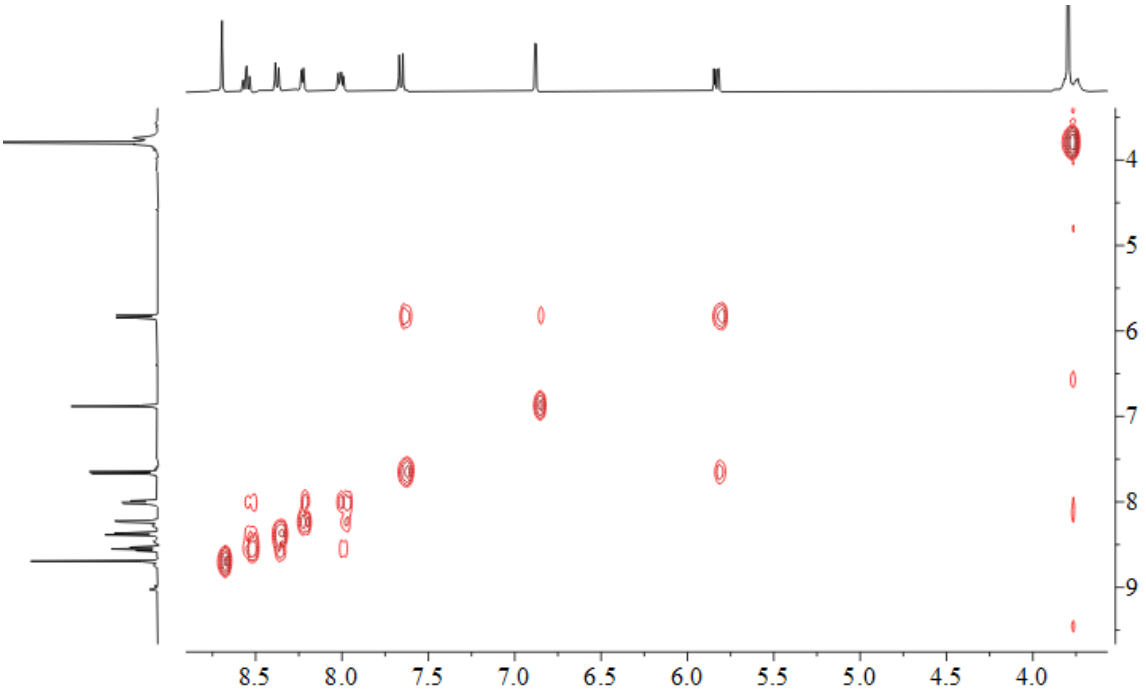

Figure 6.152. gCOSY NMR spectrum of **4.26•OTf** (CD_3CN, 400 MHz, 298 K).

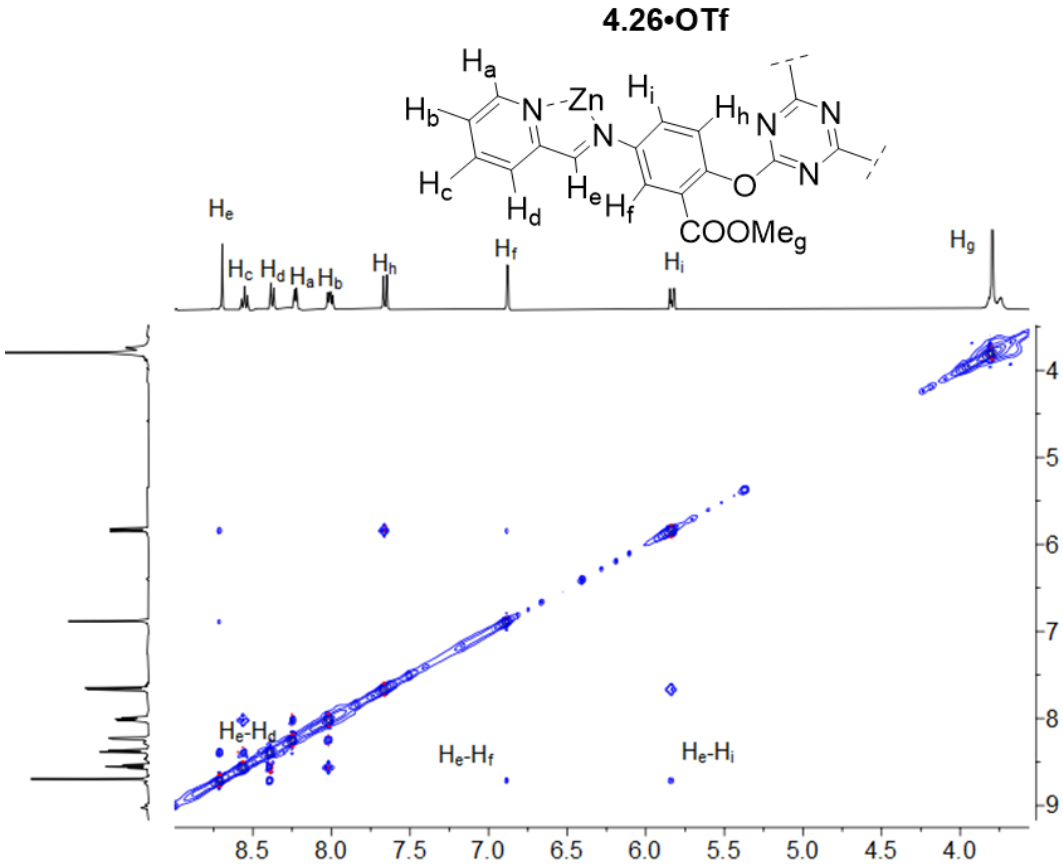

Figure 6.153. gNOESY NMR spectrum of **4.26•OTf** (CD_3CN, 400 MHz, 298 K, mixing time = 300 ms).

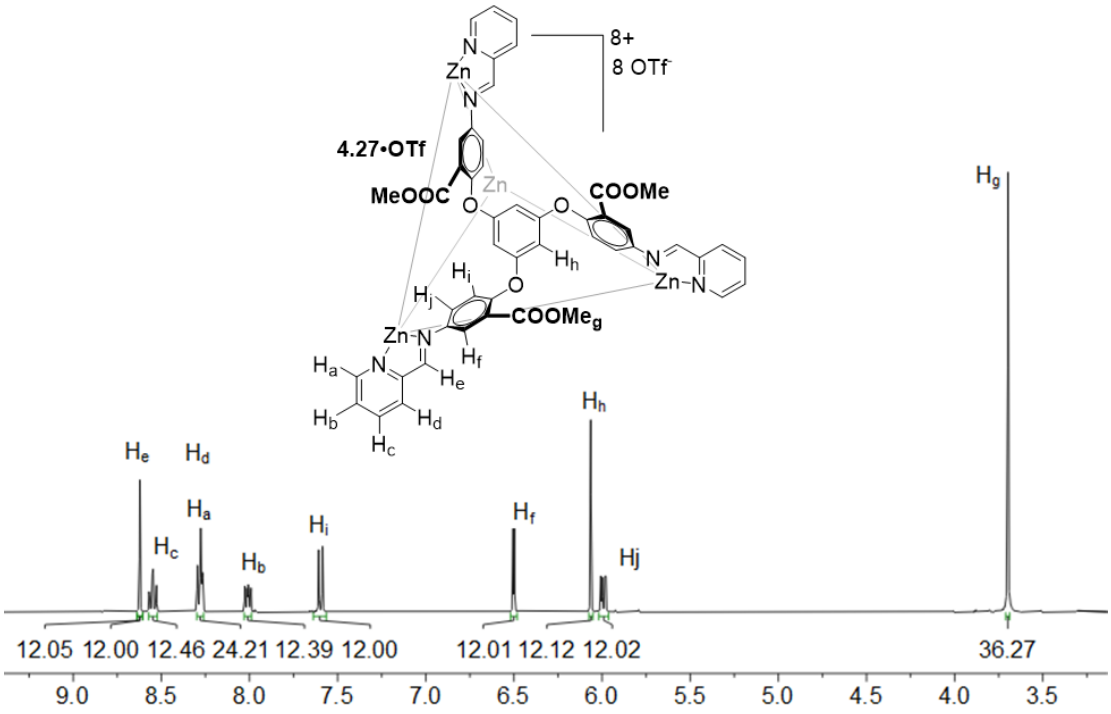

Figure 6.154. ^{1}H NMR spectrum of **4.27•OTf** (CD_3CN, 400 MHz, 298 K).

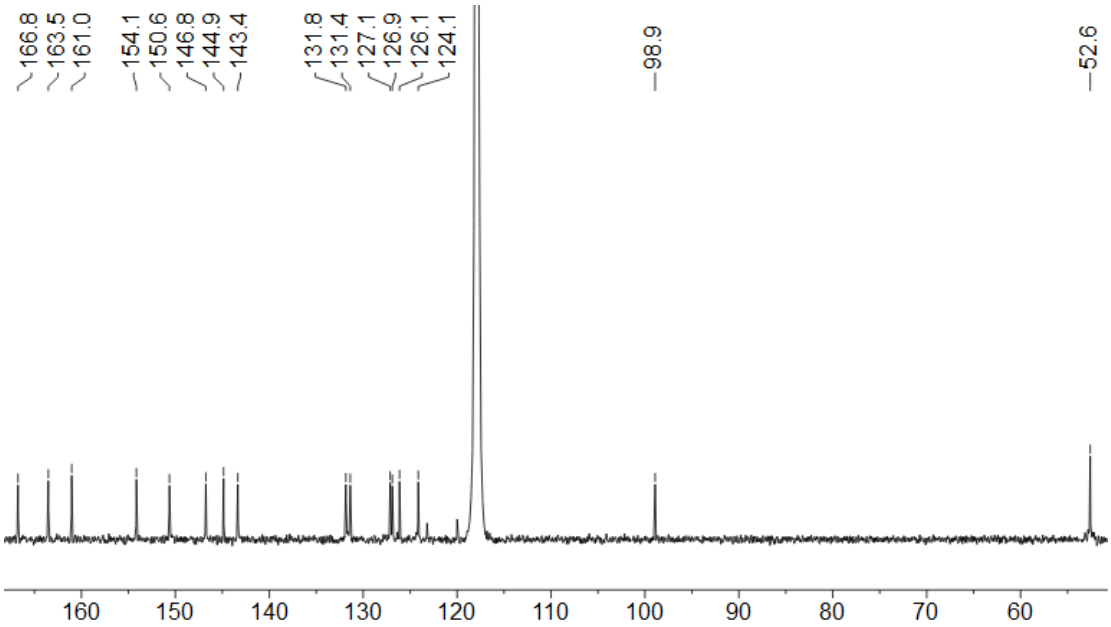

Figure 6.155. ^{13}C NMR spectrum of **4.27•OTf** (CD_3CN, 151 MHz, 298 K).

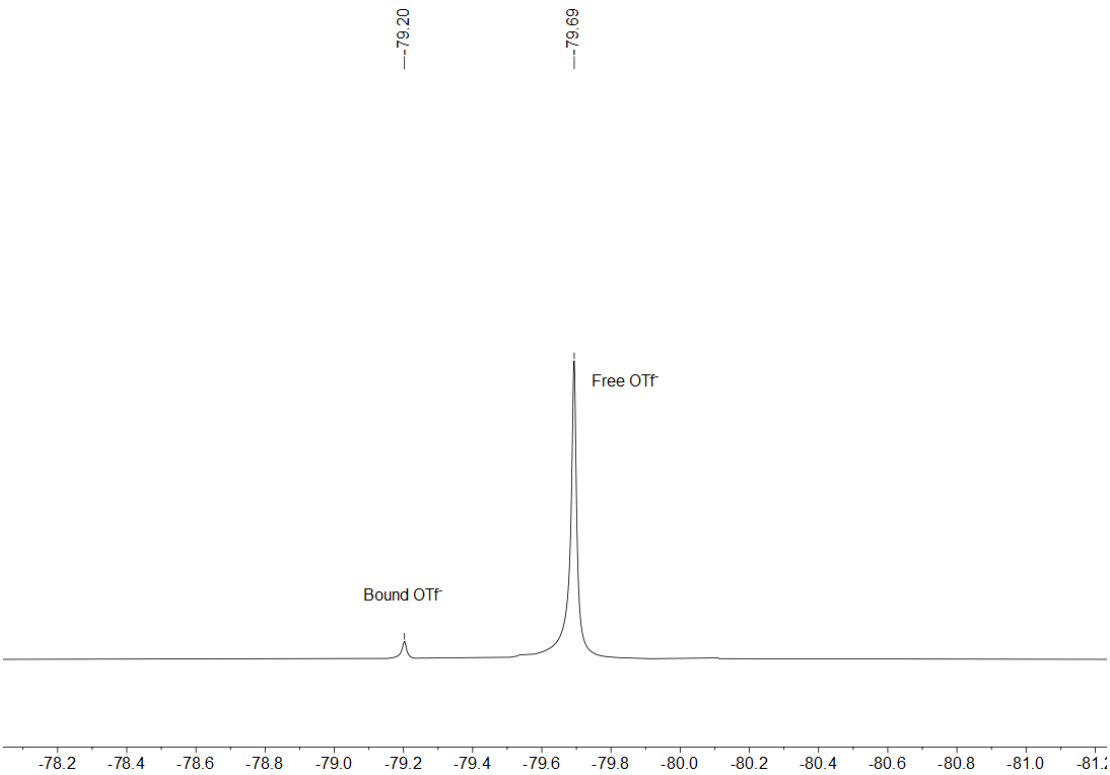

Figure 6.156. ^{19}F NMR spectrum of **4.27•OTf** (CD_3CN, 376 MHz, 298 K).

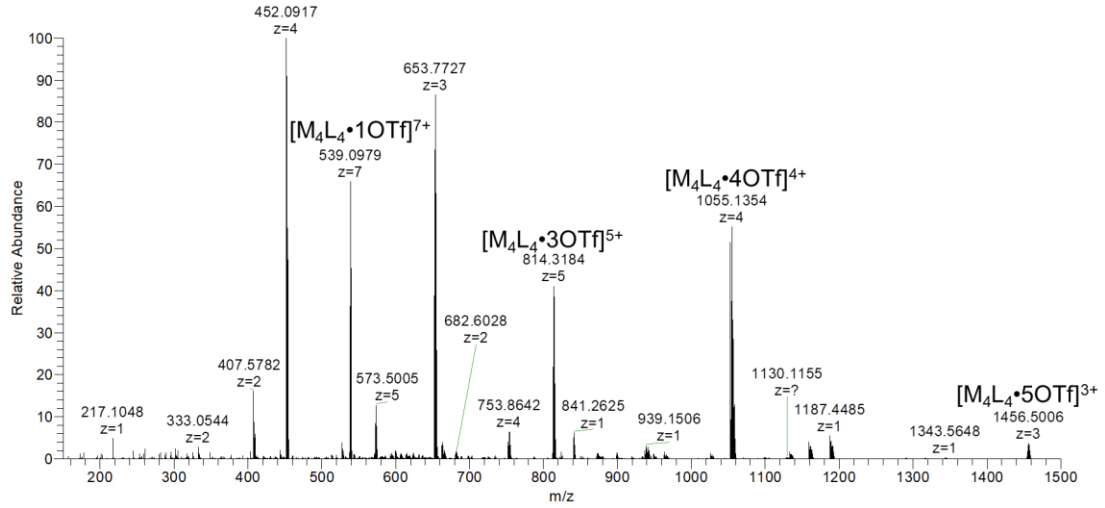

Figure 6.157. Full ESI-MS spectrum of **4.27•OTf**.

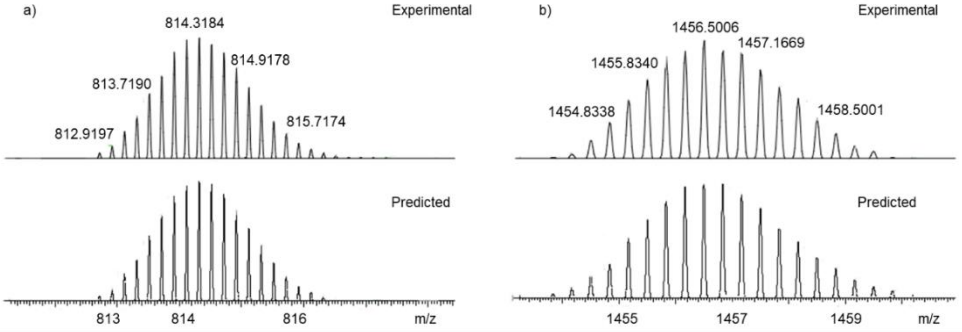

Figure 6.158. Expansion of the ESI-MS spectrum of **4. 27•OTf**, showing obtained and simulated isotope regions a) $[\mathbf{4.27}\bullet(OTf_2)_3]^{5+}$ and b) $[\mathbf{4.\ 27}\bullet(OTf_2)_5]^{3+}$ ion.

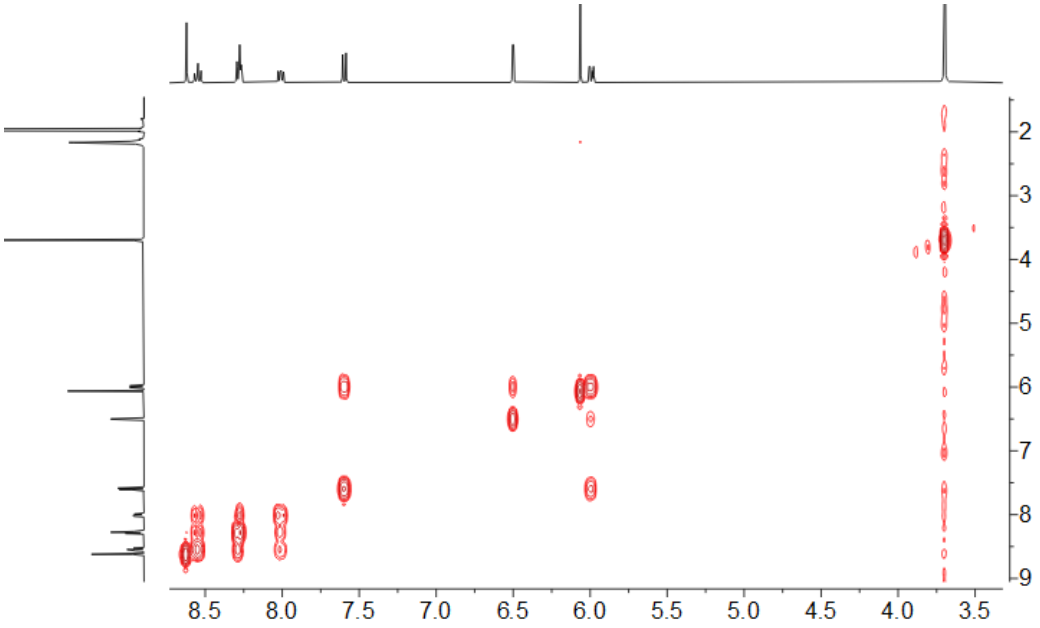

Figure 6.159. gCOSY NMR spectrum of **4.27•OTf** (CD_3CN, 400 MHz, 298 K).

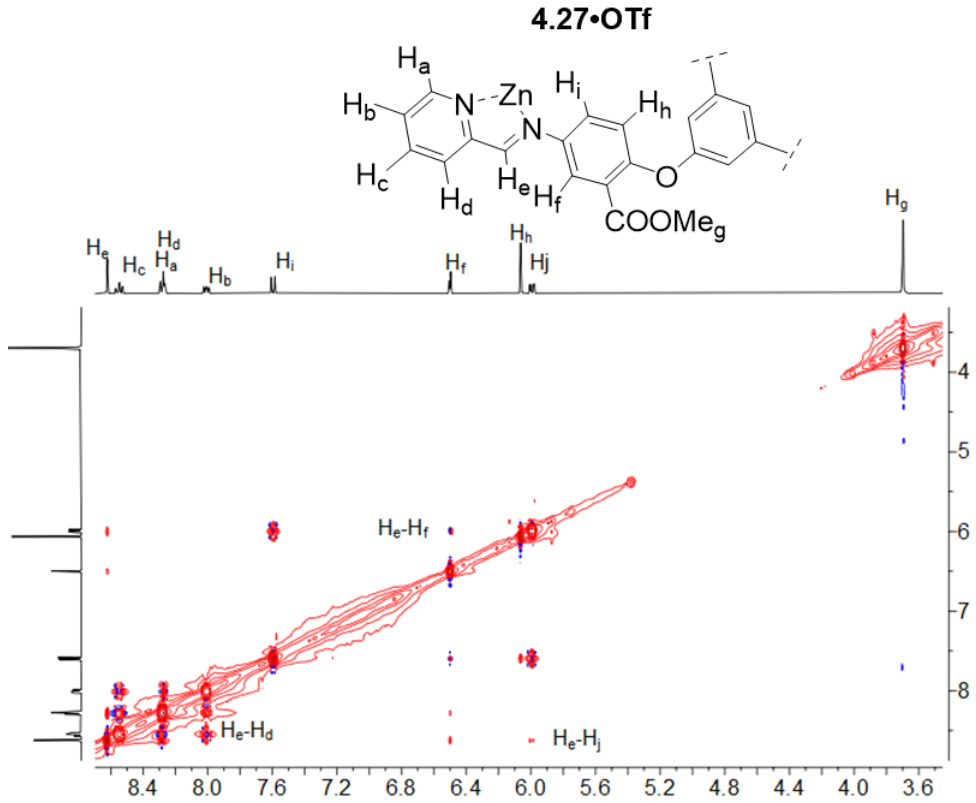

Figure 6.160. gNOESY NMR spectrum of **4.27•OTf** (CD_3CN, 400 MHz, 298 K, mixing time = 300 ms).

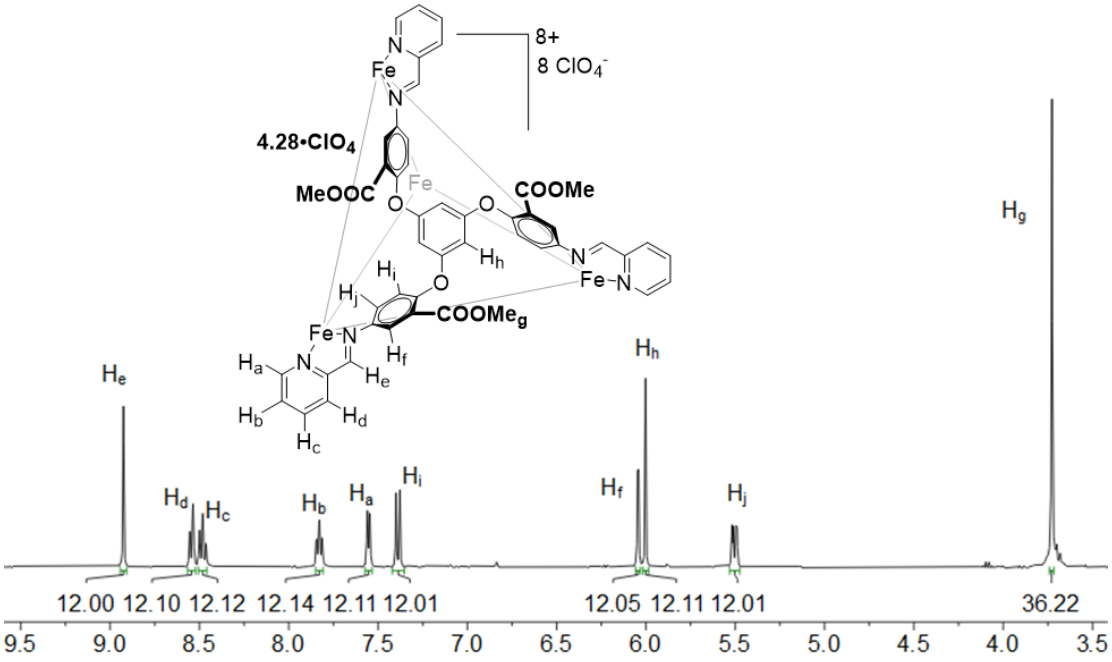

Figure 6.161. ^1H NMR spectrum of **Fe-4.28•ClO_4**. (CD_3CN, 400 MHz, 298 K).

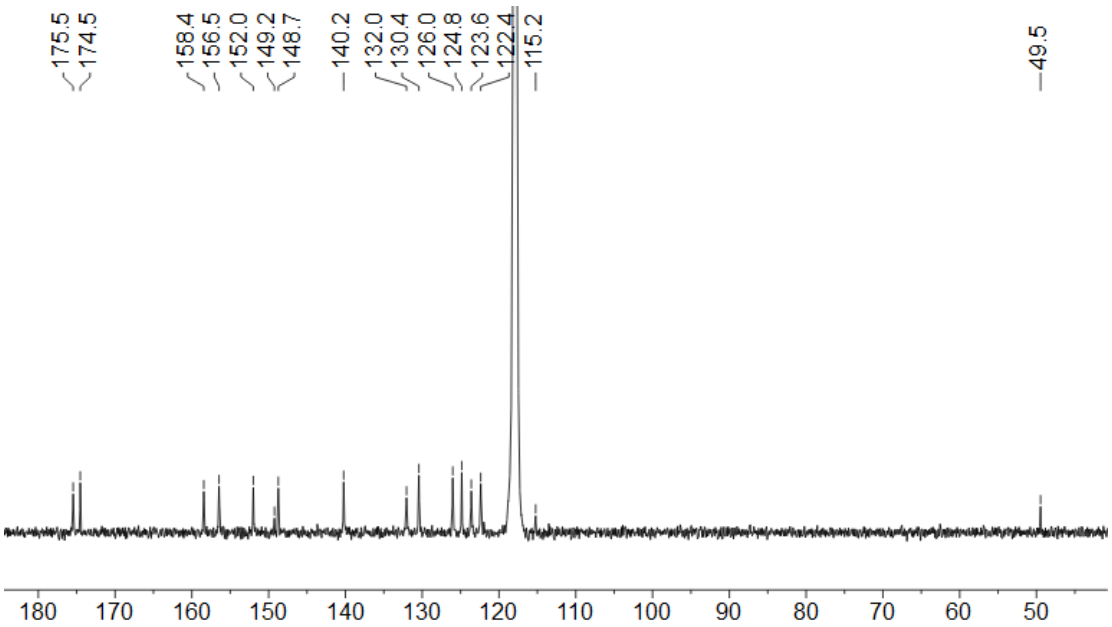

Figure 6.162. ^{13}C NMR spectrum of **Fe-4.28•ClO$_4$**. (CD_3CN, 151 MHz, 298 K).

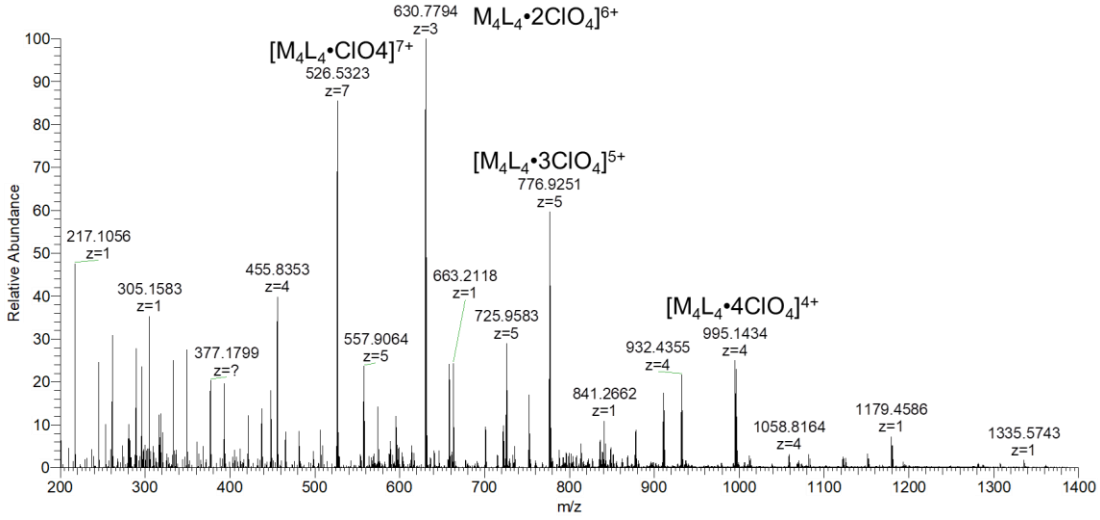

Figure 6.163. Full ESI-MS spectrum of **Fe-4.28•ClO$_4$**.

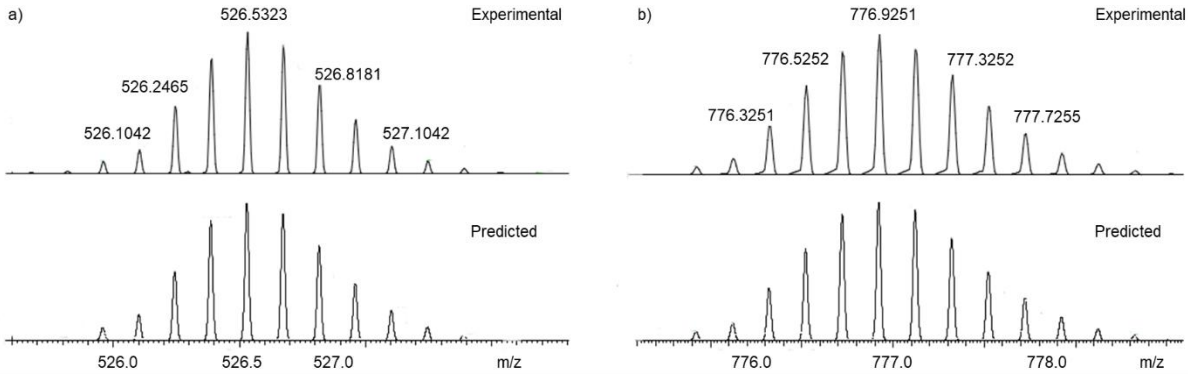

Figure 6.164. Expansion of the ESI-MS spectrum of **Fe-4.28•ClO_4** showing obtained and simulated isotope regions a) [**4.28**•$(ClO_4)_1$]$^{7+}$ and b) [**4.28**•$(ClO_4)_3$]$^{5+}$ ion.

6.10. Spectra for Chapter 5

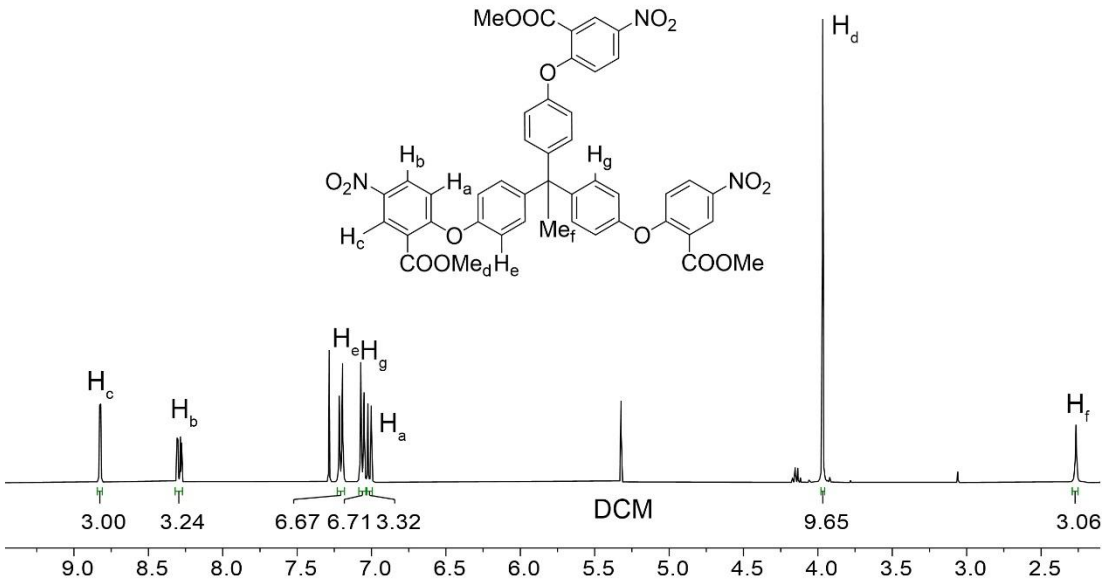

Figure 6.165. ^{1}H NMR spectrum of **5.3** ($CDCl_3$, 400 MHz, 298 K).

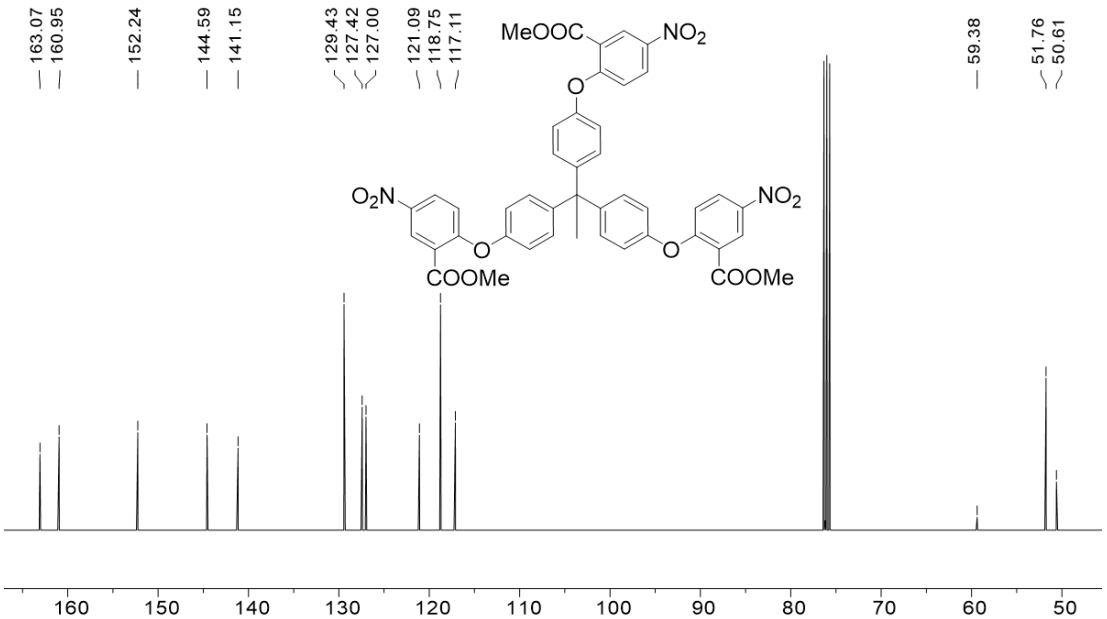

Figure 6.166. ^{13}C NMR spectrum of **5.3** ($CDCl_3$, 151 MHz, 298 K).

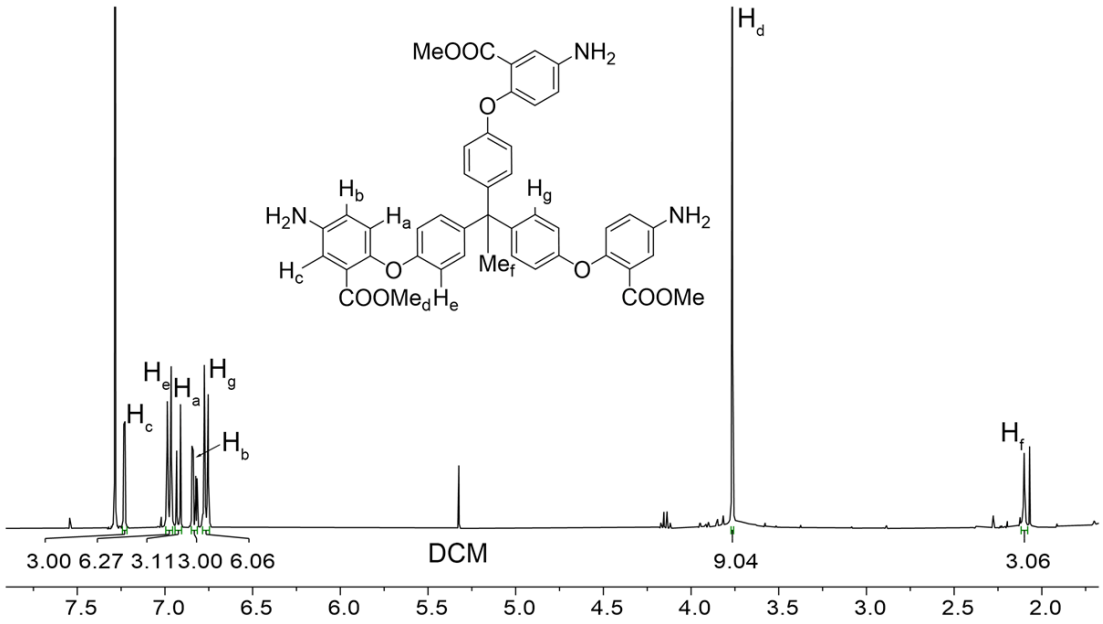

Figure 6.167. ^{1}H NMR spectrum of **5.4** ($CDCl_3$, 400 MHz, 298 K).

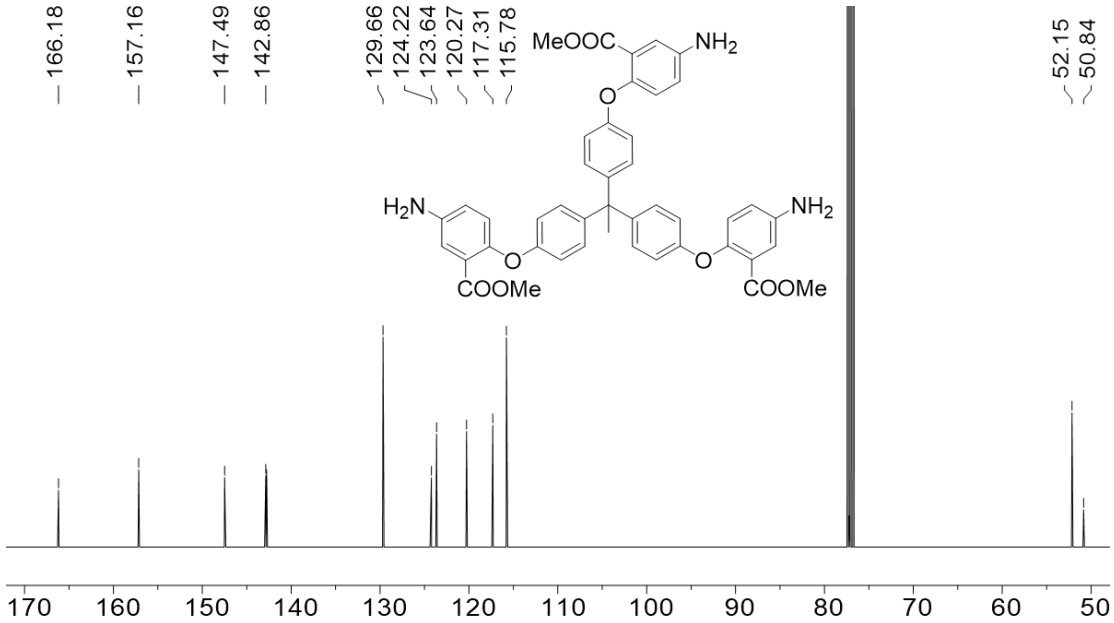

Figure 6.168. ^{13}C NMR spectrum of **5.4** ($CDCl_3$, 151 MHz, 298 K).

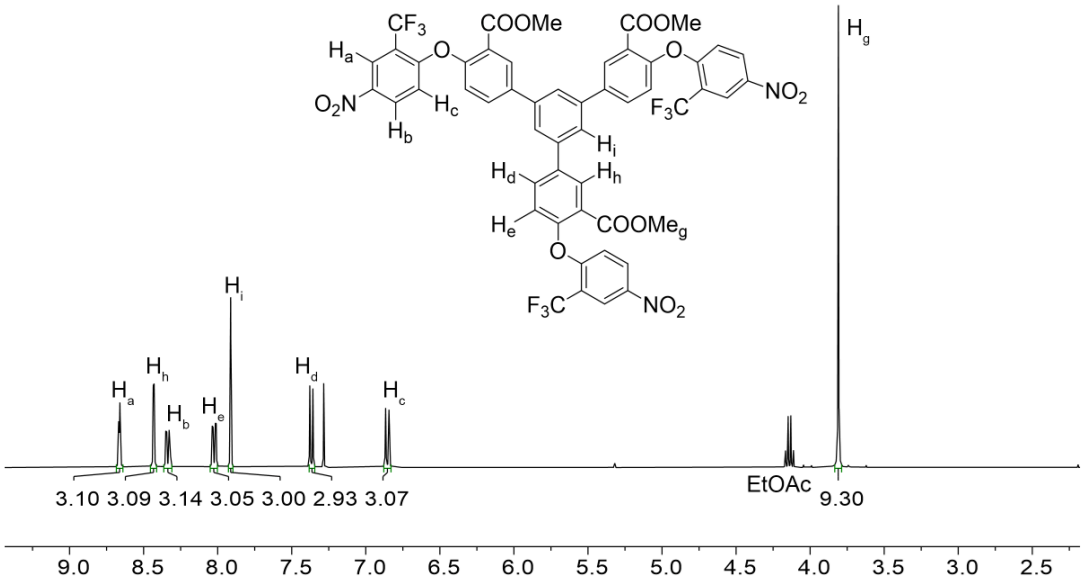

Figure 6.169. ^{1}H NMR spectrum of **5.9** ($CDCl_3$, 400 MHz, 298 K).

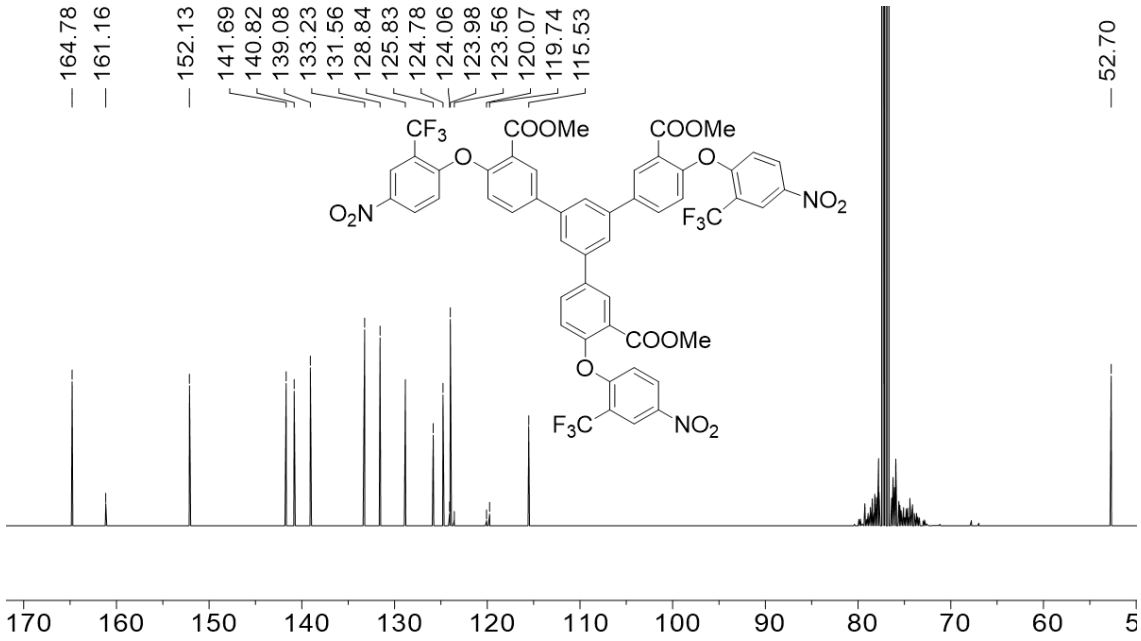

Figure 6.170. ^{13}C NMR spectrum of **5.9** ($CDCl_3$, 151 MHz, 298 K).

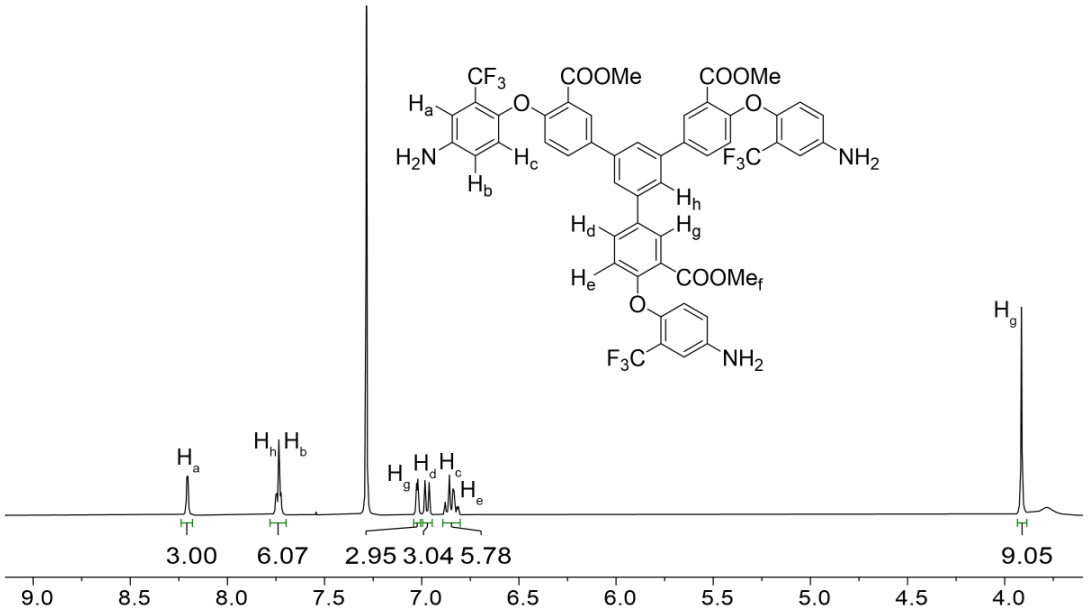

Figure 6.171. ^{1}H NMR spectrum of **5.11** ($CDCl_3$, 400 MHz, 298 K).

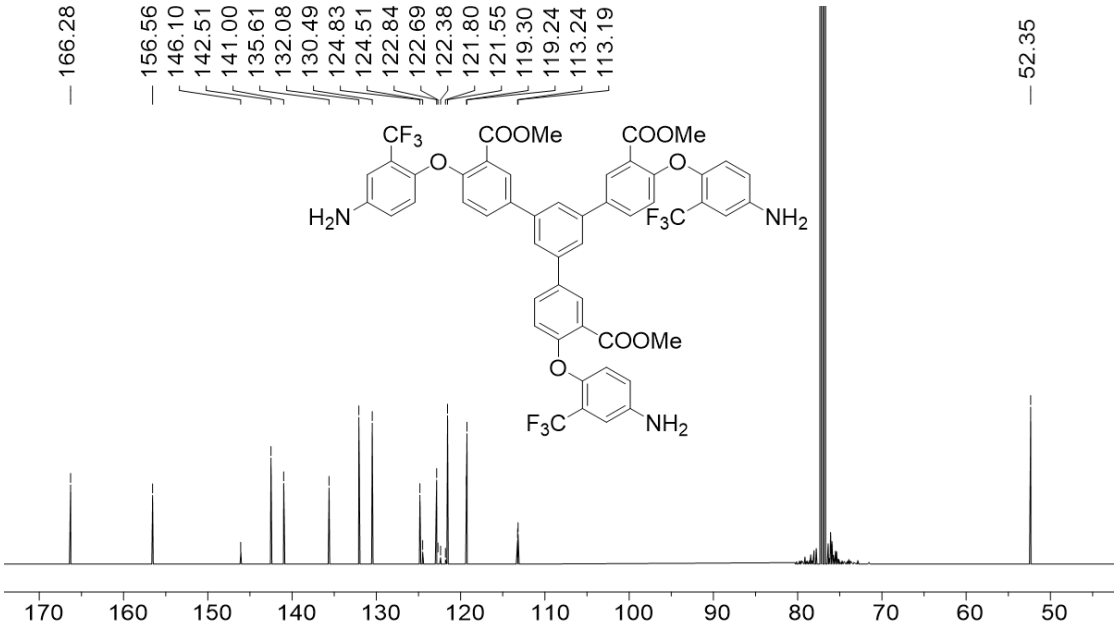

Figure 6.172. ^{13}C NMR spectrum of **5.11** ($CDCl_3$, 151 MHz, 298 K).

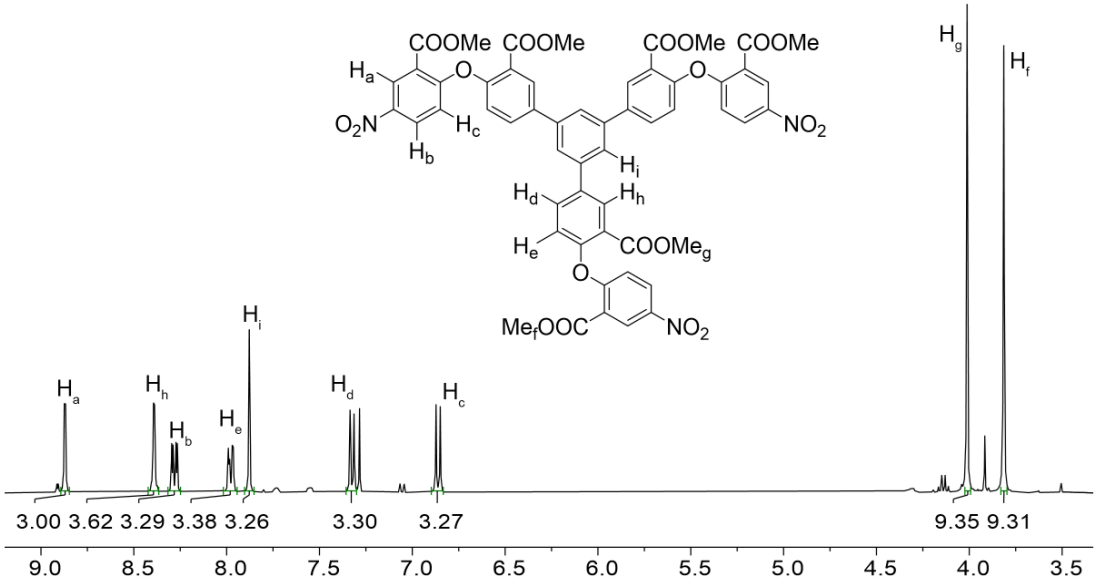

Figure 6.173. ^{1}H NMR spectrum of **5.10** ($CDCl_3$, 400 MHz, 298 K).

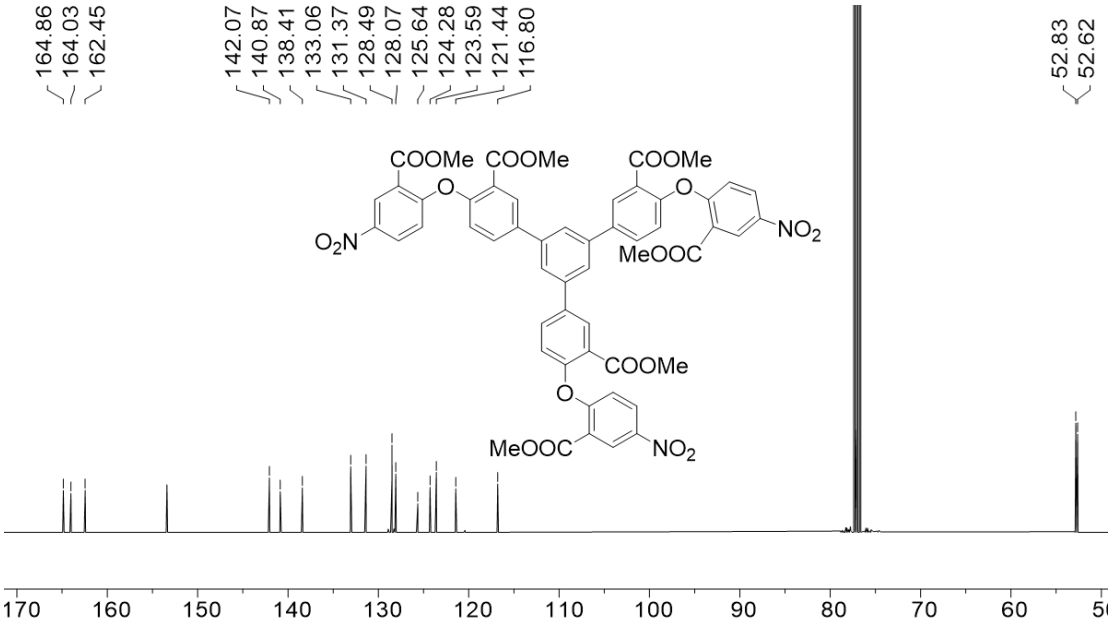

Figure 6.174. ^{13}C NMR spectrum of **5.10** ($CDCl_3$, 151 MHz, 298 K).

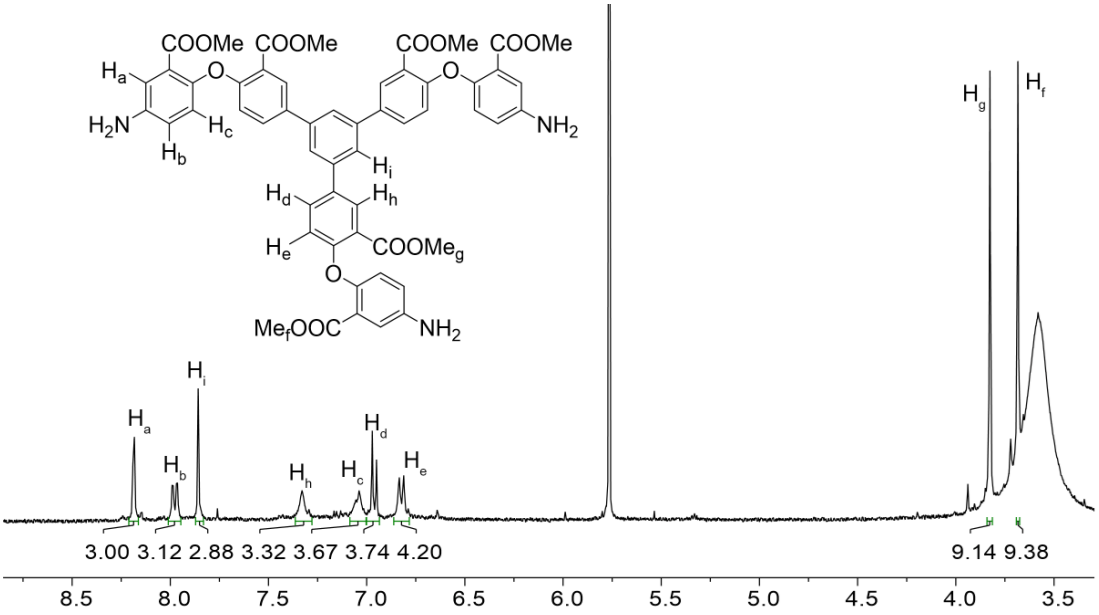

Figure 6.175. ^{1}H NMR spectrum of **5.12** (DMSO-*d*$_6$, 400 MHz, 298 K).

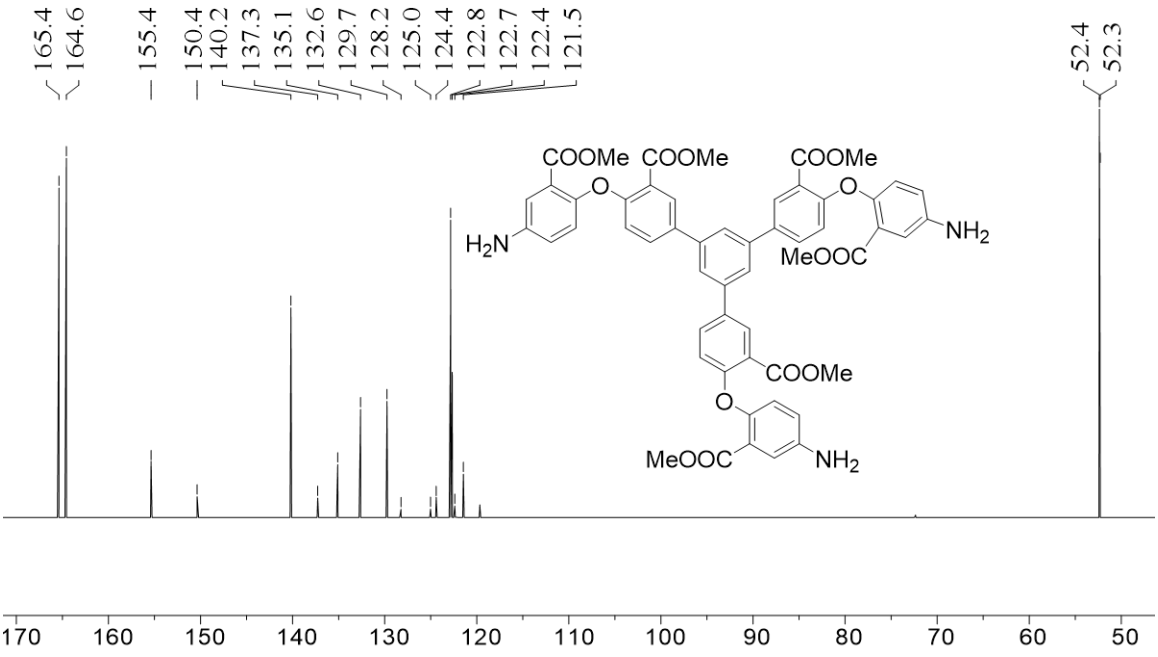

Figure 6.176. ^{13}C NMR spectrum of **5.12** (DMSO-*d*$_6$, 151 MHz, 298 K).

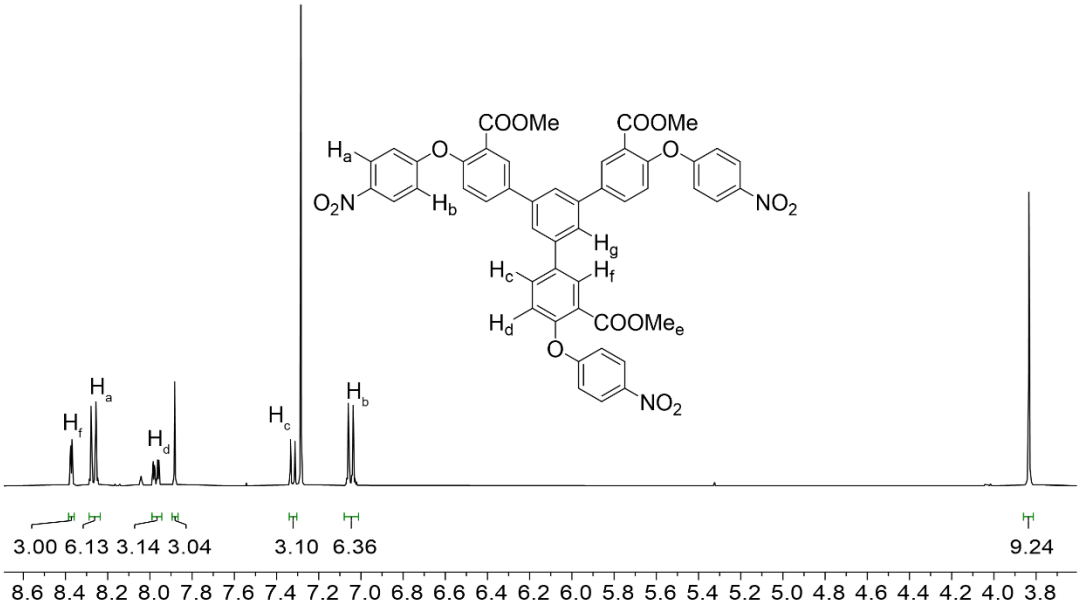

Figure 6.177. ^{1}H NMR spectrum of **5.8** ($CDCl_3$, 400 MHz, 298 K).

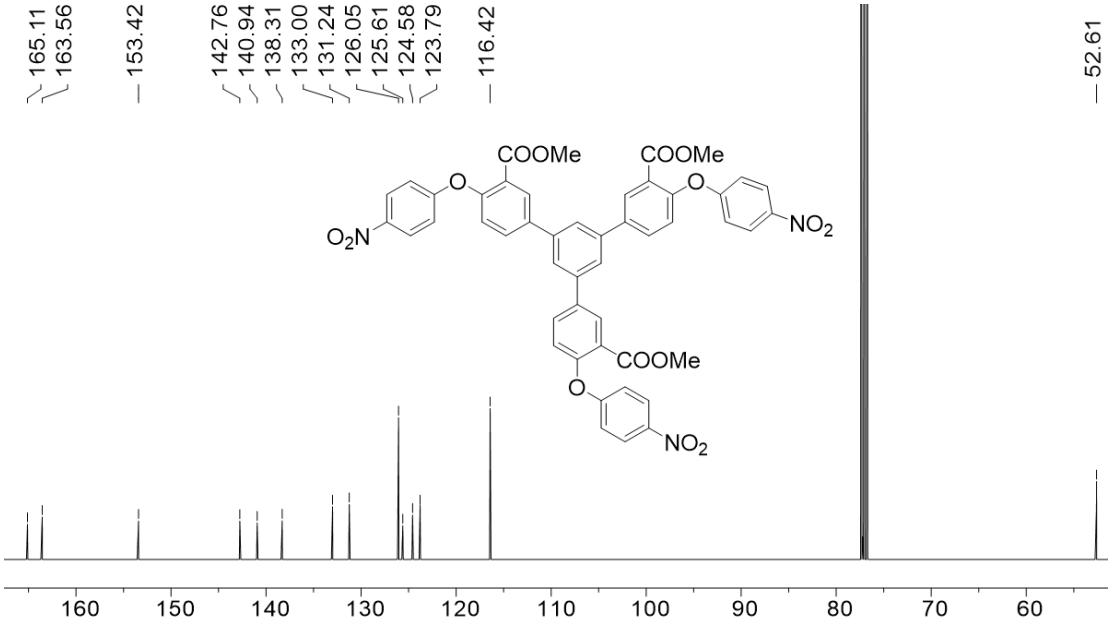

Figure 6.178. ^{13}C NMR spectrum of **5.8** ($CDCl_3$, 151 MHz, 298 K).

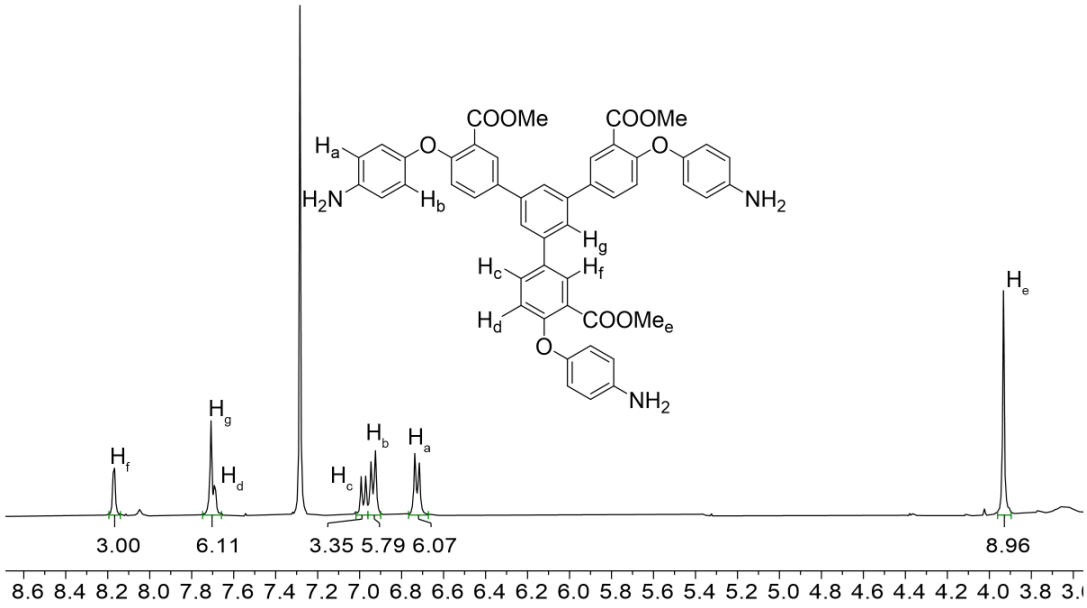

Figure 6.179. ^{1}H NMR spectrum of **5.13** ($CDCl_3$, 400 MHz, 298 K).

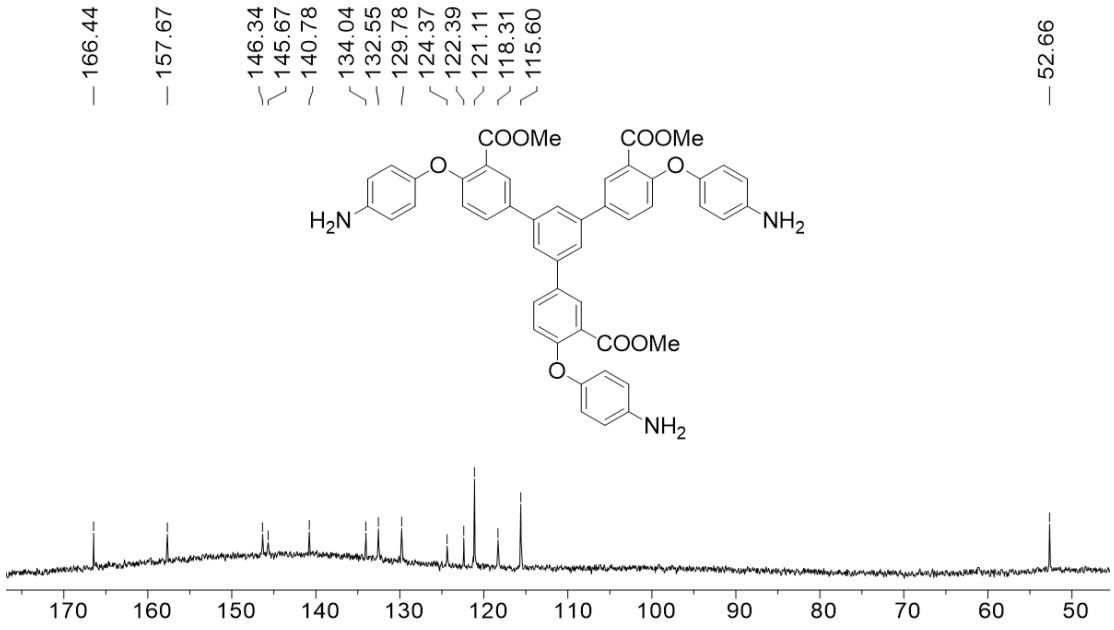

Figure 6.180. ^{13}C NMR spectrum of **5.13** (DMSO-*d*$_6$, 151 MHz, 298 K).

References

(1) Perrin, D. D. *Purification of Laboratory Chemicals*; Butterworth–Heinemann, 2009.

(2) Thordarson, P. Determining Association Constants from Titration Experiments in Supramolecular Chemistry. *Chem. Soc. Rev.* **2011**, *40*, 1305–1323.

(3) Hibbert, D. B.; Thordarson, P. The Death of the Job Plot, Transparency, Open Science and Online Tools, Uncertainty Estimation Methods and Other Developments in Supramolecular Chemistry Data Analysis. *Chem. Commun.* **2016**, *52*, 12792–12805.

(4) Maity, S.; Manna, S.; Rana, S.; Naveen, T.; Mallick, A.; Maiti, D. Efficient and Stereoselective Nitration of Mono- and Disubstituted Olefins with $AgNO_2$ and TEMPO. *J. Am. Chem. Soc.* **2013**, *135*, 3355–3358.

(5) McKean, D. R.; Parrinello, G.; Renaldo, A. F.; Stille, J. K. Synthesis of Functionalized Styrenes via Palladium-Catalyzed Coupling of Aryl Bromides with Vinyl Tin Reagents. *J. Org. Chem.* **1987**, *52*, 422–424.

(6) Khalili, D.; Iranpoor, N.; Firouzabadi, H. 4,4′-Azopyridine as an Easily Prepared and Recyclable Oxidant for Synthesis of Symmetrical Disulfides from Thiols or Alkyl Halides(Tosylates)/Thiourea. *J. Sulfur Chem.* **2015**, *36*, 544–555.

(7) Ferguson, A.; Squire, M. A.; Siretanu, D.; Mitcov, D.; Mathonière, C.; Clérac, R.; Kruger, P. E. A Face-Capped $[Fe_4L_4]^{8+}$ Spin Crossover Tetrahedral Cage. *Chem. Commun.* **2013**, *49*, 1597–1599.

(8) Sheldrick, G. M. A Short History of SHELX. *Acta Crystallogr. A* **2008**, *64*, 112–122.

(9) Sheldrick, G. M. SHELXT - Integrated Space-Group and Crystal-Structure Determination. *Acta Crystallogr A Found Adv* **2015**, *71*, 3–8.